

Syracuse University

SURFACE

Dissertations - ALL

SURFACE

June 2017

Cytotoxicity of Galvanically Coupled Magnesium and Titanium Particles for Therapeutic Effect

Jua Kim

Syracuse University

Follow this and additional works at: <https://surface.syr.edu/etd>



Part of the [Engineering Commons](#)

Recommended Citation

Kim, Jua, "Cytotoxicity of Galvanically Coupled Magnesium and Titanium Particles for Therapeutic Effect" (2017). *Dissertations - ALL*. 723.

<https://surface.syr.edu/etd/723>

This Dissertation is brought to you for free and open access by the SURFACE at SURFACE. It has been accepted for inclusion in Dissertations - ALL by an authorized administrator of SURFACE. For more information, please contact surface@syr.edu.

Abstract

This dissertation characterized how galvanic coupling of magnesium (Mg) with titanium (Ti) via sputtering enhanced the cytotoxicity of Mg particles due to increased corrosion rate. Mg and Mg-Ti particles were characterized using scanning electron microscopy (SEM), which showed that Mg and Mg-Ti particles have the average diameter of 50 μm , which makes them slightly larger than an average mammalian cell. Therefore, the cytotoxicity of the particles is not due to the ingestion of the particles by cells via phagocytosis, but solely due to electrochemical effects. Sputtering of Ti to partially cover Mg particles results in a very thin layer, in the range of nm. The surface area of Ti covering the Mg particles matters more than the thickness of the Ti layer, as the Ti layer serves as a catalyst for the reduction reactions, spatially separating the oxidation reaction of Mg and the reduction reaction of water/oxygen.

The first part of the dissertation focuses on the in vitro cell viability experiments to show that Mg and Mg-Ti particles kill cells in a dosage-dependent manner, where Mg-Ti particles kill cells more effectively than Mg alone. Cytotoxicity of Mg and Mg-Ti was measured on different types of cells, such as murine pre-osteoblast cells, human osteosarcoma cells, and bacterial *Escherichia coli* cells. For murine pre-osteoblast cells, Mg killed cells completely at 1500 $\mu\text{g/ml}$ (less than 1%), while Mg-Ti killed cells completely at 750 $\mu\text{g/ml}$, which is half of the concentration of Mg. Doubling and tripling the pre-osteoblast cell density did not increase the particle concentration that required to kill cells completely, but did decrease the rate of cell viability drop over particle concentration. Mg and Mg-Ti killed pre-osteoblast cells within 18-24 hours, and if many cells were viable, cells proliferated and recovered after 24 hours, while if more than 50% cells died, remaining cells stayed alive but did not proliferate. Cytotoxicity of Mg and Mg-Ti also depended on proximity, where only cells less than 2 mm away from the

cluster of particles were killed. For osteosarcoma cells, Mg could not kill cells completely even at 2500 $\mu\text{g/ml}$, while Mg-Ti killed cells completely at 1250 $\mu\text{g/ml}$ by 24 hours. By 72 hours, Mg killed cells completely at 2500 $\mu\text{g/ml}$, and Mg-Ti killed cells completely at 1000 $\mu\text{g/ml}$. Higher concentrations and longer periods of time were needed to kill osteosarcoma cells, compared to murine pre-osteoblast cells. Osteosarcoma cells also showed the same trend as pre-osteoblast cells, where at low particle concentrations, the cells were able to proliferate and recover, at medium particle concentrations, the remaining live cells did not proliferate, and at high particle concentrations, the cells died and did not recover. The remaining live cells and their daughter cells did not gain resistance to the particle treatment as they were killed again without having to increase the particle concentration. 24-hour grown *E. coli* biofilms and planktonic cells were also treated with high concentrations of particles, and compared to conventional antibiotics, such as ofloxacin, Mg and Mg-Ti were able to kill biofilm more significantly, although not completely (down to 2%). However, Mg and Mg-Ti showed great promise in killing and preventing biofilms.

The second part of the dissertation focuses on investigating whether pH is the main cause of Mg cytotoxicity as many studies have claimed, and if the pH is the major or sole cause of enhanced cytotoxicity of Mg-Ti. This study showed that the pH levels of Mg and Mg-Ti were the same at the same particle concentration, which does not explain the increased killing of Mg-Ti. Also, Mg and Mg-Ti did not just kill cells directly, but also affected the components, such as the proteins, in the cell culture medium.

Overall, this study provides better understanding of cytotoxicity of Mg and Mg-Ti, so that not only Mg and Mg-Ti can be used to target and kill cancer and bacterial infections for the

therapeutic effect, but to show that Mg and Mg-based alloys may not be as biocompatible, which is still the common conception of this biomaterial.

**Cytotoxicity of Galvanically Coupled Magnesium and Titanium Particles
for Therapeutic Effect**

By

Jua Kim

B.S., Syracuse University, Syracuse, NY, USA 2009

M.S., Syracuse University, Syracuse, NY, USA 2012

Dissertation

Submitted in partial fulfillment of the requirements for the degree of Doctor of Philosophy in

Bioengineering

Syracuse University

May 2017

©Copyright Jua Kim 2017

All Rights Reserved

Acknowledgement

I would first like to thank my advisor, Dr. Jeremy L. Gilbert, who is also my teacher and mentor. I met Dr. Gilbert as an undergraduate and worked on my senior thesis in his lab. I enjoyed doing research in his lab so much that I decided to stay and continue my education at Syracuse University, and of course, asked Dr. Gilbert if I can do my Ph.D. with him. I am so glad that he accepted me, giving me a chance to pursue this research project under his guidance. Dr. Gilbert is an endless source of knowledge in the area of biomaterials, and I am very lucky to have him as my advisor.

I would also like to thank my parents, YoungSun Kim (김영선) and JinBin Im (임진빈), for their continued encouragement, love, and financial support, while I was working on my dissertation. Without their support, I could not have come this far and earn my Ph.D. degree. I want to thank my husband, Huiyu Shi, who I met in Dr. Gilbert's lab. He was always there for me, in my darkest and best times, and he will always be number one in my heart. I also want to thank Huiyu's parents, my zhong guo papa, BenXian Shi (石本先), and my zhong guo mama, YueLan Xiang (向月兰), who accepted me as their daughter-in-law and gave their full support while I was finishing my dissertation.

I would like to thank Dr. Michelle Blum, Dr. Dacheng Ren, Dr. James Henderson, Dr. Julie Hasenwinkel, and Dr. Pranav Soman for taking their time and serving on my Ph.D. committee. I want to thank my colleagues, Dr. Viswanathan Swaminathan and Dr. Shiril Sivan. They taught me all the lab equipment and techniques I needed to know as a researcher, and they were always patient with me no matter how many times I asked for their help.

I really enjoyed my times at Syracuse University, and I will never forget the 11 years I stayed here doing my B.S., M.S., and Ph.D.!

Table of Contents

1	Overview.....	1
1.1	Motivation and Significance.....	1
1.2	General Objective.....	2
1.3	Specific Aims and Hypotheses.....	2
1.4	Structure of Dissertation.....	3
	References.....	5
2	Background.....	7
2.1	Historical Significance of Magnesium.....	7
2.2	Properties of Magnesium.....	12
2.3	Magnesium Ions.....	16
2.4	Current Assessment of Cytotoxicity of Magnesium and Its Alloys.....	18
2.5	Effect of Cathodic Potential on Cell Viability and Morphology.....	21
2.6	Reactive Oxygen Species (ROS).....	23
2.7	Galvanic Coupling of Mg-Ti.....	24
2.8	Mg-Ti Couple for Targeted Therapeutic Effect.....	27
2.9	Re-statement of Purpose.....	29
	References.....	30
3	Cytotoxic Effect of Galvanically Coupled Magnesium-Titanium Particles.....	38
3.1	Introduction.....	38
3.2	Materials and Methods.....	40
3.2.1	Characterization of Mg and Mg-Ti Microparticles using Scanning Electron Microscopy (SEM).....	40
3.2.2	Measuring Thickness of Ti layer using Atomic Force Microscopy (AFM).....	41
3.2.3	Analysis of MC3T3 Cell Viability over Mg and Mg-Ti Particle Concentrations.....	41
3.2.4	Determining Mg and Mg-Ti Particle Concentrations.....	42
3.2.5	Measuring pH for Mg and Mg-Ti Microparticles at Different Concentrations.....	43
3.2.6	Analysis of MC3T3 Cell Viability over pH Range Corresponding to the pH of Mg and Mg-Ti Particle Concentrations.....	43
3.2.7	Statistical Analysis.....	44
3.3	Results.....	44
3.3.1	SEM Images of Mg and Mg-Ti Microparticles.....	44
3.3.2	Measuring Ti Layer using AFM.....	46
3.3.3	Mg-Ti Cytotoxicity on MC3T3 Cells.....	48
3.3.4	pH Measurements of Mg and Mg-Ti Microparticles.....	52
3.3.5	MC3T3 Cell Viability at Different pH Range.....	53
3.4	Discussion.....	53
3.5	Conclusion.....	61
3.6	Acknowledgements.....	62
3.7	Supplementary Images.....	63
	References.....	67
4	The Effect of Cell Density, Proximity, and Time on the Cytotoxicity of Mg and Galvanically Coupled Mg-Ti Particles In Vitro.....	74

4.1	Introduction.....	74
4.2	Materials and Methods.....	77
	4.2.1 Preparation of Mg-Ti Microparticles.....	77
	4.2.2 Cell Density Effect.....	77
	4.2.3 Time Effect.....	78
	4.2.4 Proximity Effect.....	79
	4.2.5 Statistical Analysis.....	80
4.3	Results.....	80
	4.3.1 Cell Density Effect.....	80
	4.3.2 Time Effect.....	91
	4.3.3 Proximity Effect.....	100
4.4	Discussion.....	104
4.5	Conclusion.....	111
4.6	Acknowledgements.....	111
4.7	Supplementary Images.....	112
	References.....	130
5	In-Vitro Cytotoxicity of Galvanically Coupled Magnesium-Titanium Particles on Human Osteosarcoma SAOS2 Cells: A Potential Cancer Therapy.....	133
	5.1 Introduction.....	133
	5.2 Materials and Methods.....	136
	5.2.1 Preparation of Mg-Ti Microparticles.....	136
	5.2.2 SAOS2 Cell Viability vs. Mg and Mg-Ti Particle Concentrations.....	136
	5.2.3 Analysis of SAOS2's Acquired Resistance to Cytotoxicity of Mg and Mg-Ti Particles.....	137
	5.2.4 SEM Analysis of SAOS2 Morphology After Mg and Mg-Ti Particle Treatment.....	138
	5.2.5 Time-Lapse of SAOS2 Cells and Mg Particle Interactions.....	138
	5.2.6 Statistical Analysis.....	138
	5.3 Results.....	139
	5.4 Discussion.....	154
	5.5 Conclusion.....	162
	5.6 Acknowledgements.....	162
	References.....	163
6	In-Vitro Cytotoxicity of Galvanically Coupled Magnesium-Titanium Particles on <i>Escherichia Coli</i> Cells: Potential Bacterial Infection Therapy.....	166
	6.1 Introduction.....	166
	6.2 Materials and Methods.....	175
	6.2.1 Cathodic Potentials.....	175
	6.2.1.1 Metal Sample Preparation.....	175
	6.2.1.2 Bacterial Culture and Application of Cathodic Voltage.....	175
	6.2.1.3 Morphological Assessment using SEM and AFM.....	177
	6.2.1.4 Statistical Analysis.....	177
	6.2.2 Mg and Mg-Ti Particles.....	177
	6.2.2.1 E. Coli Biofilm Preparation for Mg and Mg-Ti Particle Treatment.....	177
	6.2.2.2 Sputtering of Mg with Ti.....	178

6.2.2.3	Distribution of Mg and Mg-Ti Particles.....	178
6.2.2.4	Flow Cytometry.....	178
6.2.2.5	Treatment of Planktonic Cells with Mg and Mg-Ti Particles....	179
6.2.2.6	Preparation of Cells for SEM Images.....	180
6.2.2.7	Inhibition Zone Test.....	180
6.2.2.8	Statistical Analysis.....	181
6.3	Results.....	181
6.3.1	Cell Viability of E. Coli Biofilm After Cathodic Voltage Treatment.....	181
6.3.2	Morphology Assessment of Cells using SEM.....	183
6.3.3	Length, Width, and Height Measurements using AFM.....	183
6.3.4	Cell Viability of E. Coli Biofilm After Mg and Mg-Ti Particle Treatment.....	189
6.3.5	Morphology Assessment of Biofilm Cells using SEM.....	200
6.3.6	Cell Viability of E. Coli Planktonic Cells After Mg and Mg-Ti Particle Treatment.....	203
6.3.7	Inhibition Zone Test.....	206
6.4	Discussion.....	208
6.5	Conclusion.....	214
6.6	Acknowledgements.....	214
	References.....	215
7	Effect of Mg and Mg-Ti Corrosion Preconditioning on Biological Medium and Cell Viability.....	220
7.1	Introduction.....	220
7.2	Materials and Methods.....	225
7.2.1	Hydrogen Gas Volume.....	225
7.2.2	Pre-Conditioning Media Part I.....	230
7.2.3	Pre-Conditioning Media Part II.....	230
7.2.4	pH Effect.....	231
7.3	Results.....	232
7.3.1	Hydrogen Gas Volume.....	232
7.3.2	Pre-Conditioning Media Part I.....	234
7.3.3	Pre-Conditioning Media Part II.....	238
7.3.4	pH Effect (Comparing Cell Viability of Mg and Mg-Ti Treated vs. NaOH Treated).....	244
7.4	Discussion.....	249
7.5	Conclusion.....	259
7.6	Acknowledgements.....	259
	References.....	260
8	Characterization of Mg-Ti Particle Corrosion in Different Solutions.....	264
8.1	Introduction.....	264
8.2	Materials and Methods.....	269
8.2.1	Mg Oxide Crystal Formation in Different Solutions.....	269
8.2.2	Gel Electrophoresis.....	269
8.2.2.1	Sample Preparation.....	269
8.2.2.2	SDS Page Preparation/Protocol.....	269
8.2.3	X-Ray Diffractometer (XRD) Analysis.....	273

8.2.4	Fourier Transform Infrared Radiation (FTIR) Analysis.....	273
8.3	Results.....	274
8.4	Discussion.....	288
8.5	Conclusion.....	298
8.6	Acknowledgements.....	298
	References.....	299
9	SEM Method Technique: Imaging Cells on Non-Conducting Substrate.....	305
9.1	Introduction.....	305
9.2	Materials and Methods.....	309
9.2.1	Experiment: Mg and Mg-Ti Particle Treatment.....	309
9.2.2	Cell Preparations for SEM Imaging.....	309
9.2.3	SEM Imaging.....	310
9.3	Results.....	310
9.4	Discussion.....	319
9.5	Conclusion.....	321
9.6	Acknowledgements.....	321
	References.....	322
10	Overall Conclusion.....	323
11	Future Work/Potential Applications.....	325
12	Biographical Data.....	327

List of Figures and Tables

Figure 2.1 Payr treating cavernous haemangioma by insertion of high-purity Mg arrows, where (A) X marks the insertion point in a child's chin. (B) A diagram of a Mg arrow. (C) A diagram showing Mg arrows embedded directly into the tumor. (D) A diagram showing platinum-iridium trocars used to insert Mg arrows into the haemangioma.¹.....8

Figure 2.2 6-year-old boy with persistent lymph- haemangioma in his cheek being treated with magnesium wires in 1975.².....9

Figure 2.3 (A) 7-months old baby with strawberry-type haemangioma. Mg wire is inserted by means of hyperthermic needles. (B) Same patient from (A) at the age of 3 years. The haemangioma has disappeared, with some scarring left at the site of ulceration which occurred at the age of 6 months. (C) 13-year old girl after implantation of Mg arrows in the lips. (D) The same patient from (C) after 2 years of Mg treatment.².....10

Figure 2.4 (A) 4-year old child with a haemangioma of the cheek before the Mg treatment. (B) The same patient as (A) at the age of 6 years, 2 years after the Mg treatment.².....11

Figure 2.5 (A) 3-months old child with proliferating haemangioma of the face, throat, and shoulder. (B) 3-months old child with the step incisions for the insertion of the magnesium arrows. (C) 9 months after the beginning of magnesium treatment at the age of 1 year. (D) 20 months after the start of magnesium therapy at the age of 2 years.¹⁻².....11

Figure 2.6 Pourbaix diagram of Mg in water at 25 Celsius. Lines (A) and (B) show stability of water, where water H₂O is more stable in a region between lines (A) and (B), oxygen O₂ is more stable in a region above line (A), and hydrogen H₂ is more stable in a region below line (B). (A) $O_2 + 4 H^+ + 4 e^- \rightarrow 2 H_2O$; $E_{red} = 1.233 V - 0.0591 pH$. (B) $2 H^+ + 2 e^- \rightarrow H_2$; $E_{red} = 0 V - 0.0591 pH$. (1) $Mg + 2 H_2O \rightarrow Mg(OH)_2 + H_2$. (2) Around pH of 8.5-11.5, a film of magnesium oxide or hydroxide may form to provide protection, and above 11.5, a stable film of magnesium hydroxide forms to protect magnesium from corrosion. (3) $Mg \rightarrow Mg^{2+} + 2 e^-$; $E_{red} = -2.34 V$ at all pH, intermediate monovalent ion Mg⁺ may be produced, but not stable.¹¹⁻¹³.....15

Figure 2.7 Galvanic series of metal. Ti is considered noble metal, and is almost always a cathodic member of the galvanic couple. Mg and Mg alloys are very active, and are always anodic members of the galvanic couple.⁵².....25

Figure 3.1 SEM images of (a-b) Mg particles, and (c-d) Mg particles sputtered with Ti for 5 minutes. There are no morphological differences between non-sputtered and sputtered samples. The Ti layer is too thin to be seen. The Mg particles are very irregularly-shaped, with rough surfaces, giving a larger surface area for corrosion. Average diameter of Mg particles is about 50 to 100 μm.....45

Figure 3.2 Ti was sputtered on glass for 5 minutes. AFM was used to take (a) deflection image and (b) height image at the border between sputtered and non-sputtered regions. The images show

different sized Ti domes on the sputtered regions, compared to the relatively flat non-sputtered regions.....47

Figure 3.3 Line profiles from images in Fig. 3.2. The heights of Ti domes measured are (a) 81.9 and (b) 9.6 nm, respectively. The size of the domes may vary, but the average thickness of Ti layer is still in nm range.....47

Figure 3.4 Live-dead images of MC3T3 cells with a cell density of 10,000 cells/cm² treated with Mg (a) Control, (b) 50, (c) 100, (d) 250, (e) 500, (f) 750, (g) 1000, (h) 1250, (i) 1500, and (j) 1750 µg/ml. Note the increase in dead cells with increasing concentration and near complete killing by 1500 µg/ml. Scale bar= 500 µm.....49

Figure 3.5 Live-dead images of MC3T3 cells with a cell density of 10,000 cells/cm² treated with Mg-Ti (a) Control, (b) 50, (c) 100, (d) 250, (e) 500, (f) 750, and (g) 1000 µg/ml. Note the more rapid increase in dead cells with increasing particle concentration with complete killing by 750 µg/ml. Scale bar= 500 µm.....50

Figure 3.6 SEM images of (a) control group, (b) 500 µg/ml Mg treated group, (c) 500 µg/ml Mg-Ti treated group. Note that only the Mg-Ti particles at 500 µg/ml concentration (c) are inducing significant changes in cell morphology and affecting viability (i.e., cells are balling up and dying). Also, note that these low kV images have secondary electron emission characteristics that highlight both cell structures and different protein agglomerates (dark and white spots) compared to the background culture dish.....51

Figure 3.7 Cell viability as a function of particle concentration when MC3T3 cells with cell density of 10,000 cells/cm² are treated with Mg or Mg-Ti particle groups for t= 24 hours.....51

Figure 3.8 The graph shows pH of Mg particles and Mg-Ti particles corroding in complete media for concentrations between 0 and 2500 µg/ml for t= 0 hour and t= 24 hours. The pH increase is particle concentration dependent (P < 0.05), but is not dependent on the presence of Ti coupling...52

Figure 3.9 Cell viability in NaOH adjusted media at pH of 7.5, 8, 8.5, and 9. This pH range roughly corresponds to the pH of Mg and Mg-Ti particle concentrations used to kill MC3T3 cells, from 50 to 1750 µg/ml.....53

Fig. 3.10 (a) Stainless steel (SS) disc after polished with 320, 400, and 600 grit sandpapers, (b) stainless steel disc with Mg powder placed inside the plastic ring (although there is leakage) and sputtered for ten minutes, showing yellowish discoloration of the SS disc, (c) SS disc with Mg powder sputtered for more than 20 minutes, showing blue discoloration of the SS disc, and (d) SS disc after Mg powder has been removed to show that there is no discoloration where the Mg powder has been since SS underneath Mg powder was not exposed.....63

Fig. 3.11 EDS on (a) mostly stainless steel (SS) disc (Mg is detected as well because there also must be some Mg particles), (b) mostly Mg powder (where Mg powder is densely packed), and (c) Ti6Al4V disc. Although Ti has been sputtered for very long time, and there was discoloration

of the disc, Ti could not be detected on both SS disc and Mg powder. EDS was measured on Ti6Al4V disc to show that EDS can detect Ti, just in larger amount.....64

Fig. 3.12 EDS on Mg powder shows magnesium (Mg) and oxygen (O).....65

Fig. 3.13 EDS on Mg-Ti powder still shows only magnesium (Mg) and oxygen (O).....66

Figure 4.1 Live/dead images of MC3T3 cells with cell densities of (i) 5,000, (ii) 10,000, (iii) 20,000, and (iv) 30,000 cells/cm². (a) Control, (b) 50 µg/ml Mg, (c) 50 µg/ml Mg-Ti, (d) 500 µg/ml Mg, and (e) 500 µg/ml Mg-Ti, n=3. The scale bar = 500 µm.....84

Figure 4.2 (a) Live/dead image of cells enveloping the particles. The cells are working together to engulf a large particle, which is impossible for an individual cell. This image was taken from a sample with cell density of 30,000 cells/cm² treated with 100 µg/ml of Mg-Ti. (b-d) SEM images of cells on top of the particles. Cells have somehow migrated on top of the cells, and while the cell body is on the particle, the cell filapodia are still attached to the surface. SEM images were taken from a sample with cell density of 30,000 cells/cm² treated with 500 µg/ml of Mg.....85

Figure 4.3 Cell viability graphs of Mg and Mg-Ti at different cell densities of (a) 5,000 cells/cm², (b) 10,000 cells/cm², (c) 20,000 cells/cm², and (d) 30,000 cells/cm², n=3. Cell viability is always significantly lower for those treated with Mg-Ti compared to Mg, p < 0.05.....87

Figure 4.4 Graphs showing how cell viability as a function of particle concentration drops at a different rate when cell density is varied for (a) Mg and (b) Mg-Ti, n=3. The graphs (a) and (b) were re-graphed as (c) Mg and (d) Mg-Ti by dividing the particle concentration by relative cell density ratio, where 5,000 cells/cm² was divided by 1, 10,000 cells/cm² by 2, 20,000 cells/cm² by 4, and 30,000 cells/cm² by 6, n=3.....89

Figure 4.5 The slopes of % average cell viability versus particle concentration, taken for different cell densities between 0 and 100 µg/ml for Mg group and Mg-Ti group, n=3. The more negative the slope, the faster the rate of cell killing. The lower the cell density, the slope also became more negative.....90

Figure 4.6 Graphs showing how cell viability changes over time at different particle concentrations for 10,000 cells/cm² cell density group (a) Mg and (b) Mg-Ti, n=3. At low particle concentrations, the cells can recover by t= 48 hours, but as the particle concentration is increased, cells cannot recover.....92

Figure 4.7 Mg and Mg-Ti groups graphed over time at concentrations of: (a) 0 µg/ml (control), (b) 250 µg/ml, (c) 500 µg/ml, (d) 750 µg/ml, and (e) 1500 µg/ml, n=3. Mg-Ti groups kill more cells over time than Mg groups.....96

Figure 4.8 The total number of live and dead cells over time for Mg and Mg-Ti groups at control, 50, 500, and 1000 µg/ml collected from 3 different samples.....97

Figure 4.9 The slopes of % average cell viability over particle concentrations for cell density of 10,000 cells/cm² were measured from t= 0 to 18 hours to measure (a) killing rates, and from t= 24 to 72 hours to measure (b) recover rates. Because these slopes were measured from the average % cell viability, there are no standard deviations.....98

Figure 4.10 Graphs showing pH values of complete media (AMEM + 10% FBS + 1% PSG) with different particle concentrations (from 0 to 1750 µg/ml) corroding from t= 0 to 72 hours, where (a) shows Mg and (b) shows Mg-Ti, n=3.....99

Figure 4.11 0.05 g of Mg (top row) and Mg-Ti (bottom row) are located at the center of the dish and live/dead images taken at (a) at site, (b) ~0.25-0.35 cm away, (c) 1 cm away, (d) 2 cm away, and (e) 3 cm away from the center of the bulk particles, where the diameter of the bulk particles is approximately 0.5 cm, n=3.....101

Figure 4.12 Images grouped to roughly show that the cells underneath the particles died completely, and the difference between the center and the edge of the particle bulk is very stark.102

Figure 4.13 Graph showing cell viability as a function of proximity, distance away from the center of the bulk particles, n=3. Cells are almost completely dead at the center, but significant number of cells survived even 1 cm away.....103

Figure 4.14 Graph showing pH as a function of proximity, distance away from the center of the bulk particles, n=3. There is no significant difference in pH at different locations.....103

Figure 5.1 Live/dead images of SAOS2 cells, where (a) Control (no particles), (b) Mg 500 µg/ml, (c) Mg-Ti 500 µg/ml, (d) Mg 1000 µg/ml, and (e) Mg-Ti 1000 µg/ml for (i-iii) groups, where the cells have been treated with particles for (i) t= 24 hours, (ii), t= 48 hours, and (iii) t= 72 hours, n=3. (iv) SAOS2 cells have been killed with Mg 1750 µg/ml for 24 hours, and the surviving cells were re-grown for almost seven weeks before treating them again with (a) Control (no particles), (b) Mg 500 µg/ml, and (c) Mg 1000 µg/ml for t= 24 hours, n=3.....141

Figure 5.2 Cells interact with Mg and Mg-Ti particles. At high cell density, like MC3T3 cells, SAOS2 cells envelop the particles and even at proximity, many cells are viable, such as (a) treated with Mg 750 µg/ml. At higher particle concentrations, the cells that have attached to the particles are eventually killed, such as (b) treated with Mg 1750 µg/ml. (c) shows cells with their membranes punctured, with red-stained nucleus either remaining inside the cell or bleeding out. This image has taken from a sample treated with Mg 500 µg/ml for t= 24 hours.....142

Figure 5.3 SEM images of (a-c) control, (d-f) Mg 100 µg/ml, (g-i) Mg 500 µg/ml, (j-l) Mg 1000 µg/ml, (m-o) Mg 1500 µg/ml, (p-r) Mg-Ti 100 µg/ml, (s-u) Mg-Ti 500 µg/ml, (v-x) Mg-Ti 1000 µg/ml, and (y-aa) Mg-Ti 1500 µg/ml. These SEM images were taken at low accelerating voltage of 4 kV, in order to highlight cellular features, such as filopodia and adsorbed proteins.....145

Figure 5.4 Graphs plotting % cell viability of SAOS2 cells as a function of Mg and Mg-Ti particle concentrations (0-2500 µg/ml) at (a) t= 24 hours, (b) t= 48 hours, and (c) t= 72 hours, n=3. Like

MC3T3 cells, SAOS2 cells are killed in a particle dosage-dependent manner, where Mg-Ti killed cells more significantly than Mg.....149

Figure 5.5 A graph of % cell viability of “recovered” SAOS2 cells killed again for t= 24 hours using the same Mg particle concentrations of 0-2500 µg/ml, which is compared to the cells killed only once with Mg shown in Fig. 5.4(a), n=3..... 149

Figure 5.6 Graphs showing % cell viability of SAOS2 cells over time, from t= 24 to 72 hours, for (a) Mg and (b) Mg-Ti, n=3. All the killings have occurred by 24 hours. There was no recovery of cells after 24 hours, even though for some particle concentrations, many cells remained viable.....150

Figure 5.7 A graph comparing SAOS2 and MC3T3 cell viability treated with Mg and Mg-Ti particle concentrations for t= 24 hours. Post hoc Tukey test shows that MC3T3 cell viability is significantly different from SAOS2 cell viability for high Mg particle concentrations of 1000 to 1750 µg/ml ($p < 0.05$), where SAOS2 cells have higher cell viability than that of MC3T3 cells at the same particle concentration. However, there is no significant difference in cell viability between MC3T3 and SAOS2 cells for all particle concentrations, except 500 µg/ml, for Mg-Ti groups ($p > 0.05$).....151

Figure 5.8 Total number of (a) live cells and (b) dead cells counted from ten images per sample, n=3, have been plotted for control, 50 µg/ml, 500 µg/ml, and 1000 µg/ml. For control groups and Mg 50 µg/ml, the number of live cells drastically increase, almost doubling and tripling from 1st day to 3rd day. Number of live cells treated with Mg-Ti 50 µg/ml increased very slightly, which is less than that of the control group and Mg 50 µg/ml. For 500 and 1000 µg/ml, the number of live cells remain relatively the same for both Mg and Mg-Ti groups, indicating that there is no proliferation of remaining live cells. The number of dead cells are highest for higher particle concentrations, where Mg-Ti groups showed higher number of dead cells, compared to that of Mg group of the same concentration. Control groups and 50 µg/ml showed relatively low number of dead cells, with a slight increase in number over time.....153

Figure 6.1 Fluorescent images of *E. Coli* HM 22 cells after live/dead stain. (a) Cells at OCP in NaCl solution, (b) cells at -1 V in NaCl solution, (c) cells at OCP in LB media, (d) cells at -1 V in LB media, and (e) cells at -1.2 V in LB media for t= 24 hours. All images were at 63x magnification. All the cells were dead after -1 V treatment in NaCl, while most of the cells in LB media remained alive, despite the voltage treatment.³⁰182

Figure 6.2 Cell viability fraction of bacterial biofilm measured from live/dead assay after OCP, -1 V, and -1.2 V voltage treatments in LB media or NaCl solution, n=3. Compared to voltage treatments of cells in LB media, the cells treated with -1 V in PBS show a significant decrease in cell viability.³⁰182

Figure 6.3 SEM images of *E. Coli* HM 22 cells after electrochemical treatment in secondary mode. (a) Cells at OCP in PBS, (b) cells at -1 V in PBS, (c) cells at OCP in LB media, and (d) cells at -1 V in LB media. Additional images are shown for (e) cells at OCP in PBS at higher magnification, and (f) cells at -1V in PBS at higher magnification. Cells at OCP in PBS and LB

media are rod-shaped, and the cells in LB media are starting to form clusters, which cannot be seen with cells in PBS. Most of the cells treated with -1 V voltage in PBS have cavitations in their surfaces and become shorter in the longitudinal direction, where there are more spherical than rod-shaped cells. For cells treated with -1 V in LB media, there are mixtures of cells with cavitation and shortened length and rod-shaped cells. Cells treated with -1 V voltage in LB media did not form clusters like the cells in OCP.³⁰184

Figure 6.4 AFM images of *E. coli* HM 22 after 2 hours at (a) OCP (5 μm scale bar) in LB media, (b) OCP (30 μm scale bar) in LB media, (c) -1V (5 μm scale bar) in NaCl solution, (d) -1V (30 μm scale bar) in NaCl solution, (e) -1V (5 μm scale bar) in LB media, and (f) -1V (30 μm scale bar) in LB media. Cells at OCP have intact and smooth membranes and are rod-shaped. Many cells at -1V in NaCl solution and LB media are lysed, with blebbed membranes. All voltages were versus Ag/AgCl.³⁰187

Figure 6.5 Cell length and width of bacteria on cpTi samples after two-hour voltage treatment in saline solution or LB media at -1 V, n=3. The OCP was measured in LB media for 2 hours, n=3. Post hoc Tukey test shows that voltage treatment of -1 V in saline solution reduced the length and the width of both intact and ruptured cells, compared to those of control cells at OCP ($p < 0.05$).³⁰188

Figure 6.6 Cell height of bacteria on cpTi samples after two-hour voltage treatment in saline solution or LB media for 24 hours -1 V, n=3. The OCP was measured in LB media for 2 hours, n=3. Post hoc Tukey test shows that the height of the ruptured cells due to voltage treatment decreased significantly to that of intact cells found in control and at -1 V ($p < 0.05$).³⁰188

Figure 6.7 Fluorescent images of *E. Coli* K12 biofilms treated with Mg particles. (a) Control, (b) 100 μg , (c) 200 μg , (d) 500 μg , (e) 1000 μg , (f) 1500 μg , (g) 2000 μg , (h) 2500 μg , (i) 3000 μg , and (j) 3500 μg , n=3. Fluorescent images cannot be taken at high particle concentrations because the particles interfere with imaging.....191

Figure 6.8 Flow cytometry data counting live and dead cells. Cells are stained with SYTO-9 and propidium (PI), where live cells fluoresce green and dead cells fluoresce red. Graph (a) shows correlated measurements of FSC and SSC, graph (b) shows FSC measurements of SYTO-9, graph (c) shows FSC measurements of PI, (d) shows correlated measurements of FSC of SYTO-9 and PI, graph (d) shows cell count of cells with SYTO-9, graph (e) shows cell count of cells with PI, and table (f) shows the actual cell numbers measured from the reading. Data is shown for (i) negative control without dyes, (ii) negative control with dyes, (iii) biofilm cells treated with Mg 7500 μg , (iv) biofilm cells treated with Mg 50000 μg , (v) positive control with 100 $\mu\text{g}/\text{ml}$ of ofloxacin, (vi) negative control planktonic cells, and (vii) planktonic cells treated with Mg 0.05g per 20 ml, n=3.....198

Figure 6.9 Cell viability of *E. Coli* K12 biofilms after Mg and Mg-Ti particle treatment for t= 6 hours in PBS, n=3. The biofilm was grown in a cell-treated cell culture dish ($A= 9.6 \text{ cm}^2$) for t= 24 hours in LB media before the particle treatment. The cells were treated with Mg from 0 to 50000 μg and Mg-Ti from 0 to 30000 μg in a total volume of 3 ml of PBS. The particles were randomly scattered in the dish. The % live cells decreased and the % dead cells increased as the

particle concentration increased. (a) shows complete data of % live and % dead from both Mg and Mg-Ti groups for all concentrations, and (b) shows % live between Mg and Mg-Ti groups for comparison.....199

Figure 6.10 Cell viability of *E. Coli* K12 biofilms after ofloxacin antibiotic treatment for t= 6 hours in PBS, n=3. Like the cells treated with Mg and Mg-Ti particles, biofilms were grown in a cell-treated cell culture dish (A= 9.6 cm²) for t= 24 hours in LB media before the antibiotic treatment. Even with high concentrations of antibiotics, more than 50% of cells in biofilm survived. There were no significant differences in % live and % dead between 50 µg/ml and 100 µg/ml, p > 0.05200

Figure 6.11 SEM images of biofilm cells after Mg and Mg-Ti treatment. Only negative control (a-b), Mg and Mg-Ti 100 µg (c-f), and Mg and Mg-Ti 2500 µg (g-j) are shown. SEM images of only low particle concentrations are shown because the higher particle concentration groups have too many particles in the sample, preventing proper SEM imaging. SEM images show the structure of the *E. Coli* K12 biofilm and its interaction with the particles. (a) shows biofilm grown for 24 hours on cell-treated polystyrene (PS) and (b) shows a close-up view. As expected, biofilm is consisted of many layers of cells. (c) shows biofilm treated with 100 µg of Mg, where in this particular site, the biofilm is very intact. (d) shows another area of the same sample treated with 100 µg of Mg as in (c), but in this location, there are hardly any cells to make up the biofilm. This discrepancy of local cell viability depends on the scattering of Mg particles. Some areas can have higher aggregation of the Mg particles, which will increase the local density of the particles, killing more cells than other areas. The variability of local cell viability also indicates that Mg particles only kill biofilm in close proximity around the particles, and so the cells do not get killed homogeneously across the sample. (e) and (f) show biofilm treated with 100 µg of Mg-Ti, where again like the 100 µg of Mg, the biofilm thickness is higher than that of control, although the thickness is not directly measured (just based on the observation). Therefore, at this particle concentration, Mg or Mg-Ti may be inducing cell proliferation and biofilm growth. At 2500 µg of both Mg (g-h) and Mg-Ti (i-j), many particles are visible, when compared to the bacterial cells (in nm range), the particles are much bigger (in µm range). Many cells have grown over the particles, integrating the particles into the biofilm, even though the particles have been added after 24-hour pre-formation of the biofilm.....202

Figure 6.12 Cell viability of *E. Coli* K12 planktonic cells after Mg and Mg-Ti treatment, n=3. For larger volume experiment, planktonic *E. Coli* K12 cells were grown in 25 ml of LB media for t= 18 hours, and then 1 ml of the planktonic cells were re-suspended in 19 ml of fresh LB media with 0.5 g of Mg particles in a flask for t= 24 hours. For smaller volume experiment, 0.1 g of Mg particles were corroded in 4 ml of cell solution for t= 24 hours. (a) % live and % dead cells and (b) viability fraction normalized by control, n=3.....204

Figure 6.13 Image of the solutions after treating 20 ml volume to 0.5 g of Mg for t= 24 hours. The solutions were transferred from a flask to the 6-well plate for visual purposes, 5 ml of solutions per well. As shown,the samples treated with 0.5 g of Mg are clear in optical density, while the control samples are very cloudy, indicating a significant difference in cell population.....205

Figure 6.14 SEM images of (a-b) control planktonic cells and (c-d) 0.5 g of Mg-treated planktonic cells. Compared to the control cells, the longitudinal lengths of Mg-treated cells have decreased, giving a round appearance than a rod-shaped.....205

Figure 6.15 Similar to the antibiotic resistance test, this is a particle proximity test to see how close the bacterial cells can grow near the particles. A ring with a diameter of 1.6 cm was placed in the center and then added 0.005 g or 0.02 g of Mg or Mg-Ti (in 100 μ l of LB media) in the ring to make a circular shape. There was no leakage of the particles. The inhibition ring zone is much smaller than a typical inhibition ring caused by an antibiotic. First, the particles were not able to corrode on the agar plate as they would in solution, which probably decreased the toxicity. Also, the particles are known to have small toxicity range of less than 2 mm from a previous study.....207

Figure 6.16 The thickness of the inhibition zone for Mg and Mg-Ti. The average distance the cells colonized away from the particles for Mg is 0.15 cm (1.5 mm) and for Mg-Ti is 0.2 cm (2 mm). Post hoc Tukey test shows that there is no difference between Mg and Mg-Ti inhibition zones.....207

Figure 7.1 Part I shows the schematic set-up of the experiment. 5 ml of pipette was used to measure the hydrogen gas volume. The tip (where it narrows) was cut and then a funnel was glued using silicone glue. The other end of the pipette tip was also glued to prevent hydrogen gas evaporation to the atmosphere. 0.05 g of Mg or Mg-Ti particles were added inside the funnel and as the particles corroded, hydrogen gas was produced, which floated up to the top of the pipette and displaced the same volume of liquid. Part II shows the step-by-step procedures. (a) First, the media was injected into the pipette using a syringe as shown. (b) The media was not filled all the way to the top so that when the pipette was inverted, the liquid was within the markers (to read the volume displacement, in ml). (c) 0.05 g of Mg or Mg-Ti was added into the cone. 0.05 g of particles was pre-mixed with small amounts of media (~1 ml) and then pipetted into the cone. Because there was an air gap between the liquid in the cone and the liquid in the pipette, the particles do not immediately fall into the pipette. (d) Additional media was added so that the cone is filled completely, but not overflowing. (e) The beaker was gently placed over the cone and then (f) the pressure was applied. (g) The entire system was then quickly inverted, without causing any spillage. (h) The pressure was still applied on the pipette as the liquid was displaced. (i-l) Once the liquid displacement was finished, 30 ml of media was added to the beaker. The hand still applied pressure on the pipette so that the pipette could not move while the media was being added. (m) Once done, the hand gently let go of the pipette. (n) This image shows the close-up of the bottom of the beaker, to ensure that the particles are all within the cone.....229

Figure 7.2 i) Pictures of (a) 0.01 g of Mg and (b) 0.01 g of Mg-Ti in complete media for $t=3$ days. For Mg, there are still hydrogen gas bubbles seen even at 3 days, while no hydrogen gas bubbles are visible for Mg-Ti. ii) Images are taken with optical microscope using time-lapse. Mg and Mg-Ti particles are corroded in complete media (AMEM + 10% FBS + 1% PSG) for (a) $t=1$ sec, (b) $t=3$ hours, (c) $t=6$ hours, and (d) $t=12$ hours, up to $t=3$ days, which is not shown. However, the time-lapse images also show that only Mg particles visibly produce hydrogen gas bubbles.....233

Figure 7.3 Hydrogen gas volume measured over time for 0.05 g of Mg and Mg-Ti corroding in complete media, n=3. There is significantly higher volume of hydrogen gas produced over time for the same amount of Mg-Ti than Mg, where Mg-Ti produces approximately twice the hydrogen gas volume than Mg, $p < 0.05$. Also, based on the hydrogen gas volume measured over time, Mg-Ti finished corroding more quickly, by $t = 18$ hours, compared to Mg, which kept producing hydrogen gas steadily over $t = 72$ hours.....234

Figure 7.4 Live/dead images of MC3T3 cells treated with the following media for $t = 24$ hours: (a) control (regular media) for $t = 1$ hour, (b) 0.05 g of Mg pre-corroded in complete media for $t = 1$ hour, (c) 0.05 g of Mg-Ti pre-corroded in complete media for $t = 1$ hour, (d) control (regular media) for $t = 5$ days, (e) 0.05 g of Mg pre-corroded in complete media for $t = 5$ days, and (f) 0.05 g of Mg-Ti pre-corroded in complete media for $t = 5$ days, n=3. Unlike the control groups, cells treated with “pre-conditioned” media, regardless of the conditioned time and particle type (Mg vs. Mg-Ti) that conditioned the media, were killed almost completely.....236

Figure 7.5 Cell viability measured for MC3T3 cells treated with pre-conditioned media for 24 hours. The pre-conditioned media has been made by corroding 0.05 g of Mg or Mg-Ti particles for $t = 1$ hour or 5 days in 15 ml of complete media, n=3. Post hoc Tukey test shows that there is a significant difference in cell viability between control and Mg/Mg-Ti groups, $p < 0.05$, but not between Mg and Mg-Ti groups, $p > 0.05$237

Figure 7.6 pH measured over time from $t = 0$ hour to 120 hours (5 days) for 0.05 g of Mg or Mg-Ti particles pre-corroded in 15 ml of complete media (AMEM + 10% FBS + 1% PSG), compared to control group, which is complete media without any particles, n=3. The pH shifted immediately after the particles have been added (within 1 minute) to pH of 9.3 and stayed between 9.5 and 9.9 over time. The pH of the control group at $t = 0$ hour was 7.6 and slightly increased to 8.1 by the end of $t = 5$ days. The pH measurements are significantly different among control, Mg and Mg-Ti groups, $p < 0.05$. Within a group, the pH measurements are significantly different between time points, except $t = 72$ hours and $t = 12$ hours.....237

Figure 7.7 (a) 0.5 g of Mg pre-corroded in 50 ml AMEM solution for $t = 5$ days at 4 Celsius, compared to regular AMEM. (b) 0.5 g of Mg-Ti pre-corroded in 50 ml FBS solution for $t = 5$ days at 4 Celsius, compared to regular FBS. The solution opacity looks clearly different. Both FBS and AMEM solutions with particles have more cloudy-appearance than its control counterparts, indicating that solution composition/chemistry due to particle corrosion have changed.....238

Figure 7.8 SEM images of (a) regular AMEM, (b) regular FBS, (c) modified AMEM treated with Mg, and (d) modified FBS treated with Mg. The solutions in the plastic dish were left in the desiccator and then sputtered with gold for SEM imaging. There were lots of particulates that were morphologically different for modified AMEM, compared to regular AMEM. The regular FBs and modified FBS did not show any morphological difference; there were just dried flakes of FBS.....239

Figure 7.9 pH measurements over time for the following solutions: Regular AMEM, Modified AMEM, Regular FBS, Modified in FBS from $t = 0$ to 120 hours, n=3. The pH of regular AMEM

and modified AMEM are significantly different from each other, $p < 0.05$, and likewise, the pH of regular FBS and modified FBS are significantly different from each other, $p < 0.05$240

Figure 7.10 pH measurements before and after pH changes of regular media using new products (control), (A) Regular AMEM + 10% Regular FBS (RR), (B) Regular AMEM + 10% Modified FBS (RM), (C) Modified AMEM + 10% Regular FBS (MR), and (D) Modified AMEM + 10% Modified FBS (MM), and (E) 50% (A) + 50% (D), $n=3$. The pH for groups A-D ranged from 8.5-12.1, and then the pH was re-adjusted closer to physiological pH using HCl. The pH after HCl for groups A-D ranged from 7.95-8.5. Although the pH could have been brought closer to the physiological pH of 7.4, adding more HCl would have started to affect the osmolality of the solution. Group E has a pH of 10.77, which is approximately the average pH of A and D, and this makes sense since E is a result of 50:50 ratio of A and D.....241

Figure 7.11 Live/dead images of MC3T3 cells treated with (A) Regular AMEM + 10% Regular FBS (RR), (B) Regular AMEM + 10% Modified FBS (RM), (C) Modified AMEM + 10% Regular FBS (MR), and (D) Modified AMEM + 10% Modified FBS (MM) for $t= 24$ hours, and (E) 50% (Regular AMEM + 10% Regular FBS) + 50% (Modified AMEM + 10% Modified FBS) (50%), $n=3$. Cells were treated with the following solutions either with or without pH adjustment using HCl solution. Group E is a result of mixing (A) and (D) by 1:1 ratio to change the pH without adding the HCl solution (and therefore, there is no cell viability reading “before pH change”).....243

Figure 7.12 Cell viability of MC3T3 cells treated with media with the following treatment conditions A-E that are explained in Fig. 7.10-7.11, $n=3$. Group A, which is control, shows high cell viability. Group B also shows high cell viability, although after the pH adjustment, cell viability is slightly lower than that of before pH adjustment. Groups C and D have very low cell viability, regardless of pH adjustments. Since group C also shows very low cell viability as group D, this indicates that modified AMEM has an effect on cell viability more significantly than modified FBS. Group E shows cell viability approximately between that of A and D.....244

Figure 7.13 pH of complete media (AMEM + 10% FBS + 1% PSG) adjusted with HCl or NaOH from 7 to 11. The pH was measured at $t= 0$ hour (immediately after adding HCl or NaOH), $t= 1$ hour, and $t= 24$ hours, $n=3$. The pH shifted over time and the range of pH from 7 to 11 flattened to the range from 7.5 to 8.2, due to the buffering of 5% CO_2 and buffers present in the media...246

Figure 7.14 Cell viability of MC3T3 cells treated with different pH of complete media, $n=3$. After $t= 1$ hour, the cells were still viable, even at the pH of 11. However, at $t= 24$ hours, the cell viability decreased as a function of pH, where the cell viability was lowest at the highest pH of 11.....246

Figure 7.15 Comparison of cell viability of MC3T3 cells treated with Mg and Mg-Ti particles to cell viability of MC3T3 cells treated with NaOH to compare the pH effect, $n=3$. As shown in (a), at $t= 1$ hour, the NaOH induced killing did not have any effect yet at this time point, even at the highest pH of 11. However, Mg and Mg-Ti particles had significant decrease in cell viability at

t= 1 hour, where the highest particle concentration had pH of 8.5, for both Mg and Mg-Ti. Post hoc Tukey tests showed that at t= 1 hour, Mg and Mg-Ti groups were significantly different from NaOH group and from each other ($p < 0.05$), except NaOH group compared to control groups (0 $\mu\text{g/ml}$ and no NaOH), $n=3$. (b) At t= 24 hours, cell viability of NaOH group decreased proportionally to the increase of pH. Post hoc Tukey test showed that at t= 24 hours, Mg and Mg-Ti groups were significantly different from NaOH group ($p < 0.05$), but not from each other, $n=3$247

Figure 7.16 Comparison of cell viability between pre-conditioned media before and after adjusting pH groups (from Fig. 7.12) and NaOH-treated groups, $n=3$. Cell viability of pre-conditioned media before pH adjustment (groups A-D) dropped proportionally to the increase of pH. Cell viability of NaOH group also dropped proportionally to the increase of pH. However, cell viability of pre-conditioned media after pH adjustment (groups A-E) showed no correlation to pH levels. This shows that while pH is a contributing factor, pH is not the major factor killing cells after the media is pre-conditioned.....249

Figure 7.17 pH titration curve with phosphate buffering.²⁷253

Figure 7.18 Formulations of AMEM by Corning, MediaTech Inc.³¹258

Figure 8.1 A table showing amino acids in proteins that can be oxidized and the oxidized products that are formed.^{13,19}266

Figure 8.2 The polypeptide organization of fibrinogen (top) and the domain organization of fibrinogen (bottom), where fibrinogen consists of two sets of $A\alpha$, $B\beta$, and γ polypeptide chains, which are connected by disulfide bonds.²²268

Figure 8.3 0.01 g of Mg particles in 5 ml of FBS solution from t= 1 hour to 24 hours, $n=3$. Cuboidal Mg oxides form within t= 1 hour and then disappear by t= 24 hours. All images were taken at 20x magnification.....275

Figure 8.4 0.01 g of Mg particles in 5 ml of AMEM solution from t= 1 hour to 24 hours, $n=3$. Mg particles become transparent over time, where Mg metal is oxidized to form Mg oxide. All images were taken at 20x magnification.....276

Figure 8.5 0.01 g of Mg particles in 5 ml of AMEM + 10% FBS solution from t= 1 hour to 24 hours, $n=3$. Mg particles become transparent over time, where Mg metal is oxidized to form Mg oxide. Mg oxide needles are formed in areas where particles are aggregated. Images (a)-(c) were taken at 20x (the scale bar 100 μm), (d) taken at 10x (the scale bar 50 μm), and (e) at 5x (the scale bar 20 μm).....277

Figure 8.6 0.01 g of Mg particles in 5 ml of LB media for t= 24 hours, $n=3$. Mg particles become transparent over time, and some may form rectangular oxides. All images were taken at 20x magnification.....277

Figure 8.7 0.01 g of Mg particles in 5 ml of AMEM + 10% FBS for $t= 24$ hours. Mg particles form these needle-shaped oxides, where each needle is hexagon-shaped.....278

Figure 8.8 Gel electrophoresis of control (just fibrinogen dissolved in PBS), Mg-treated fibrinogen, MgTi-treated fibrinogen, $n=3$. The first row consists of protein markers (shown in black bands with the molecular weights labeled on the left accordingly in kDa), but part of control group leaked. The molecular weights are within 70 and 55 kDa, because the molecular weights of $A\alpha$, $B\beta$, and γ chains are 63.5 kDa, 56 kDa, and 47 kDa, respectively. Fibrinogen molecule has a molecular weight of 340 kDa, which is too large to travel, and so may remain in the wells if fibrinogen is not reduced.....279

Figure 8.9 SEM images of (a)-(c) 0.1 g of Mg in 10 ml of PBS with fibrinogen (2 mg/ml) and (d)-(f) 0.1 g of Mg-Ti in 10 ml of PBS with fibrinogen (2 mg/ml). Although predominantly showing Mg oxide needles and Mg particles, these oxide needles seemed “glued” by fibrinogen.....281

Figure 8.10 XRD analysis of (a) Mg (before)- red line and Mg (after)- black line, and (b) Mg-Ti (before)- red line and Mg-Ti (after)- black line.....283

Figure 8.11 XRD analysis of (a) just fibrinogen (Fb) powder and (b) Mg with or without Fb and Mg-Ti with or without Fb. Mg and Mg-Ti without fibrinogen in graph (b) are Mg (after) and Mg-Ti (after) from Fig. 8.10.....283

Figure 8.12 XRD analysis comparing Mg-Ti with and without Fb.....284

Figure 8.13 Overall XRD graphs comparing all the groups.....285

Figure 8.14 FTIR spectrums for (a) CoCr background, (b) fibrinogen, (c) Mg before corrosion, (d) Mg-Ti before corrosion, (e) Mg corroded in PBS for $t= 4$ days, (f) Mg-Ti corroded in PBS for $t= 4$ days, (g) Mg corroded in fibrinogen solution for $t= 4$ days, and (h) Mg-Ti corroded in fibrinogen solution for $t= 4$ days.....287

Figure 8.15 XRD analysis of (a) as-cast pure Mg and Mg-1X alloy ($X= Al, Ag, In, Mn, Si, Sn, Y, Zn, Zr$) samples at room temperature²⁷, (b) pure MgO (thin line) and MgO loaded with 1 wt% Au by DIM (thick line), which shows 99% $Mg(OH)_2$ phase²⁸, and (c-i) Mg nano-powder before corrosion, (c-ii) Mg nano-powder during corrosion, (c-iii) Mg nano-powder after corrosion is complete²⁹. These XRD graphs show characteristic peaks of $32^\circ, 34^\circ, 36^\circ,$ and 48° , which all show up for all Mg and Mg-based alloys. These characteristic peaks only show up before corrosion and all disappear after corrosion. $Mg(OH)_2$ can be distinguished by a large peak right below 40° , while MgO can be distinguished by a large peak right above 40°290

Figure 8.16 This table shows $Mg(OH)_2$ oxide crystals with different morphologies formed under different experimental conditions, such as different Mg source, different solvent, temperature, reaction time.⁴².....292

Figure 8.17 (a) The growth of MgO using oxalic acid diahydrate, which uses two complexation sites to bind Mg^{2+} to grow MgO. (b) The growth of MgO using tartaric acid, which uses four

complexation sites to bind Mg^{2+} to grow MgO. Due to different number of complexation sites, MgO crystals grow linearly in (a), while branched in (b).⁴⁵293

Figure 8.18 The NH_2 groups from ethyldiamine can attack the metal ion, forming a covalent bond with the metal ion with the two lone pairs on the outer energy level, where ethyldiamine acts as a lewis base (electron donors).....294

Figure 8.19 Molecular structures of (a) ascorbic acid, (b) biotin, (c) D-calcium pantothenate, (d) choline chloride, (e) folic acid, (f) i-inositol, (g)nicotinamide, (h) pyridoxine*HCl, (i) riboflavin, (j) thiamine*HCl, and (k) vitamin B12.....296

Figure 9.1 Schematic diagram of SEM.....305

Figure 9.2 (a) Non-sputtered and imaged at 1 kV; (b) sputtered with gold for 30 seconds and imaged at 4 kV at the same location (two red circles show the same cells). The non-sputtered sample at 1 kV does not show spread out cells very clearly. Balled-up cells, which are greater in height, can be better distinguished. However, there are more details shown in the sputtered sample imaged at higher accelerating voltage. The spread-out cells are clearly visible, in contrast with the background.....311

Figure 9.3 Images taken using digital microscope and SEM, where (a) and (b) are taken at the same location, and (c) and (d) are taken at the same location. For SEM, the samples are non-sputtered, and the images are taken at 1 kV. Only the balled-up cells, blade marks, and large Mg particles can be distinguished at 1 kV. The red circles show how even for the balled-up cells, the SEM only shows the cell bodies, while the digital microscope also shows the retracting filopodia. The blade mark on the sample was made to be able to find the same location.....312

Figure 9.4 Cells with cell seeding density of 5,000 cells/cm² treated with 500 μ g/ml for t= 24 hours and imaged from 1-4 kV accelerating voltages. The cells can be seen at 1 kV, but difficult to tell how far the cells are spread out on the surface. As the accelerating voltage is increased, the cells start to become brighter, showing more details of the cells, such as the nucleus and microfilaments. The particulates covering the surfaces and cells also become brighter along with the cells as the accelerating voltage is increased, indicating that the particulates are made up of same type of materials (i.e. organic substances).....313

Figure 9.5 A Mg-Ti particle imaged at accelerating voltages of 1-4 kV. The particle becomes brighter as the accelerating voltage is increased. The particulates that became bright along with cells in Fig. 9.4 did not become bright with the Mg-Ti particle, which indicates that the particulates, organic in substance, is chemically different than a Mg-Ti particle, which is inorganic.....314

Figure 9.6 A cell imaged at accelerating voltages of 1-4 kV. The cell imaged at 1 kV cannot be easily distinguished, since the boundary of cell membrane cannot be seen. A part of a cell at the upper-left corner cannot be seen at this voltage at all. At 2 kV, the cell boundary is now more clearly visualized, with microfilaments as well. At 3 and 4 kV, the details of the cell nucleus can

be seen, where the cell has a nucleus split into two, in the process of cell division, which was hard to tell in 1-2 kV accelerating voltages.....315

Figure 9.7 Gold-coated cells imaged at accelerating voltages from 5-8 kV. The details of the nucleus and microfilaments are lost, although the cells can still be seen. The images look very grainy, as if there is not a lot of signal being detected (i.e. not enough secondary electrons).....317

Figure 9.8 Gold-coated cells imaged at 1-2 kV after being exposed to the accelerating voltage of 8 kV for few minutes. At this high accelerating voltage of 8 kV, the electrons penetrate deeper into the sample than lower accelerating voltages. Because the sample is not conductive, the electrons accumulate and get trapped underneath the sample surface, and then the electrons will start to repel each other. The samples are now permanently “charged” with electrons, and so when the samples are imaged even at optimal accelerating voltage of 4 kV, the cells look very puffy and swollen.....318

Figure 9.9 Cells imaged at 15 kV after sputtering the sample with gold for 30 seconds and then grounding the sample to the metal stage of SEM using metallic wires or conducting tape. The images look very detailed, even though the accelerating voltage was increased to 15 kV. This is because grounding the sample using metallic wires or conducting tape creates a pathway for electrons to flow out of the sample, instead becoming permanently trapped, as shown in Fig. 9.8.....319

1 Overview

1.1 *Motivation and Significance*

Cathodic polarization of metal implants is known to cause adverse effects on morphology and viability of cells directly on the implant surface [1-3]. Voltages from -1000 mV to +1000 mV were applied on the commercially pure titanium (cpTi) with cells cultured directly on the surface to observe changes in cell viability and morphology [1]. Cells cultured on the cpTi surfaces above -300 mV up to +1000 mV showed no significant effect of voltage on the cell viability and morphology, while cells cultured on the cpTi surfaces below -300 mV showed significant decrease in cell viability and cell area [1]. Further analysis showed that there is a subtle transition of cell morphology and viability that occurs between -300 mV and -400 mV (vs. Ag/AgCl) primarily, where cells go from viable to dead in as little as -100 mV change in potential [2]. Cathodic polarization of cobalt chromium molybdenum (CoCrMo) surface also showed the same effect on viability and morphology of cells cultured on the metal surface [3]. The direct killing of cells on the metal surface may be due to a combination of oxygen depletion, hydroxide ion generation (shifting pH), and reactive oxygen species (ROS) generation due to reduction of water and oxygen [1-3]. While the consequences were deleterious in vitro, cathodic potentials (DC electrical stimulation) in vivo stimulates bone healing in the vicinity of the electrode [4-6]. This showed that there was a disparity in cell response between cells directly cultured on the metal surface and cells in the surrounding tissue, which can be exploited further, to treat orthopedic device-related infections (ODRIs), for example.

ODRI is impossible to eradicate with antibiotics, due to the formation of biofilm on the implant surface. Cathodic polarization of the implant surface in an animal model in combination of antibiotics have shown significant reduction of biofilms, compared to just antibiotic or

cathodic polarization treatment alone [7-9]. However, the three electrode system (working/counter/reference electrodes) used to apply cathodic voltages on the implant is not clinically applicable, because additional incisions need to be made for counter and reference electrodes and these incisions need to stay open during electrical stimulation, which increases the risk for additional infections and patient discomfort/pain. Alternatively, coupling of Mg can drop the voltage of Ti significantly, which produces the same effect as the application of the cathodic voltage, without the complications of the three electrode system [10].

1.2 General Objective

The focus of this dissertation is to investigate whether Mg and Mg-Ti can adversely affect cells as occurs with cathodic voltage stimulation. This study used Mg microparticles that have large surface areas and sputtered with only small amount of Ti to maximize the corrosion of Mg. The cytotoxicity of Mg and Mg-Ti particles was assessed through in-vitro experiments that culture cells with different particle concentrations and time to determine cell morphology, viability, and proliferation. Different types of cells were used, such as mammalian, cancerous, and bacterial cells, to determine whether the cytotoxicity of Mg and Mg-Ti can extend to other types of cells. Mechanisms of cytotoxicity of Mg and Mg-Ti were analyzed by studying the effects of particle corrosion on cell culture medium and the protein fibrinogen, measuring pH and hydrogen gas volume, and observing Mg and Mg-Ti corrosion product growth in different solutions.

1.3 Specific Aims and Hypotheses

- (1) Galvanic-coupling of Mg and Ti enhances the cytotoxicity of Mg, killing cells and reducing cell proliferation at lower particle concentration and in shorter time, compared to Mg alone.

- (2) Cytotoxicity of Mg and Mg-Ti can kill all types of cells, but may vary in particle concentrations and duration of killing depending on the cell types.
- (3) Mg and Mg-Ti particles can only kill cells in very close proximity.
- (4) High concentrations of Mg ions and hydroxide ions, which ultimately increases osmolality and pH, respectively, are not the major causes of Mg cytotoxicity or the enhanced cytotoxicity of Mg-Ti.
- (5) Mg and Mg-Ti particles not only kill cells directly, but their corrosion products also modify components in the cell culture medium, such as proteins and free amino acids, rendering them cytotoxic as well.

The specific aims of this research efforts are:

- (1) Characterize Mg and Mg-Ti particles and the Ti layer produced via sputtering technique.
- (2) Understand how Mg and Mg-Ti particles affect the behavior and viability of cells near the particles and if these effects are dependent on particle concentrations, cell densities, time, proximity, and cell types.
- (3) Determine the effects of Mg and Mg-Ti particle corrosion on the constituents of the cell culture media, such as proteins and free amino acids, and whether the constituents of the cell cultured media exposed to particle corrosion can affect the behavior and viability of cells.
- (4) Study the mechanisms of Mg and Mg-Ti particle corrosion in order to understand the cytotoxic effect of the particles.

1.4 Structure of Dissertation

Chapter 1 introduces the motivation and significance, general objective, hypotheses and specific aims of this dissertation. Chapter 2 provides the background review of Mg as a

biomaterial and galvanic corrosion of bi-metallic couples. Chapter 3 summarizes the in vitro experiments used to show that Mg-Ti galvanic couple is more cytotoxic than Mg. Chapter 4 summarizes the effect of Mg and Mg-Ti on mammalian cell viability over particle concentration, cell density, proximity, and time. Chapter 5 summarizes the effect of Mg and Mg-Ti on osteosarcoma cell viability over particle concentration and time. Chapter 6 summarizes the effect of Mg and Mg-Ti on bacterial biofilm and planktonic cell viability over particle concentration. Chapter 7 summarizes the significance of pH on the cytotoxicity of Mg and Mg-Ti. Chapter 8 summarizes the effect of Mg and Mg-Ti corrosion on cell culture medium and proteins and also the effect of different solutions on the Mg and Mg-Ti corrosion, specifically Mg/Mg-Ti oxide formation. Chapter 9 explains the SEM methodology to effectively image cells on non-conducting surfaces. Chapter 10 includes future work, potential applications of Mg-Ti couple, and conclusions. It should be noted that chapter 3 to 7 are written as stand-alone papers to be submitted for publication, and so there may be some overlap and redundancy of the background and method sections among these chapters.

References

1. Ehrensberger MT, Sivan S, Gilbert JL. Titanium is Not “the Most Biocompatible Metal” under Cathodic Potential: The Relationship between Voltage and MC3T3 Preosteoblast Behavior on Electrically Polarized CpTi Surfaces, *J. Biomed. Mater. Res. A* 2010; 93A(4): 1500-9.
2. Sivan S, Kaul S, Gilbert JL. The Effect of Cathodic Electrochemical Potential of Ti-6Al-4V on Cell Viability: Voltage Threshold and Time Dependence, *J. Biomed. Materials Res. Part B Appl. Biomater.* 2013; 101(8): 1489-497.
3. Haeri M, Wollert T, Langford GM, Gilbert JL. Electrochemical Control of Cell Death by Reduction-Induced Intrinsic Apoptosis and Oxidation-Induced Necrosis on CoCrMo Alloy *In Vitro*, *Biomaterials* 2012; 33(27): 6295-304.
4. Mikus P. Method for Direct Bone Stimulation During Interventional Procedure to Assist in Bone Healing. Misonix, Incorporated (Farmingdale, NY, US), assignee. Patent 20160129284. 12 May 2016.
5. Ciombor DM, Aaron RK. The Role of Electrical Stimulation in Bone Repair, *Foot Ankle Clin.* 2005; 10(4): 579-93.
6. Sostaric BR, Zook BC. Electrically Stimulated Bone Healing- Morphologic Study in Rabbits, *Exp. Pathol.* 1987; 31(3): 129-46.
7. Ehrensberger MT, Tobias ME, Nodzo SR, Hansen LA, Luke-Marshall NR, Cole RF, Wild LM, Campagnari AA. Cathodic Voltage-Controlled Electrical Stimulation of Titanium Implants as Treatment for Methicillin-Resistant *Staphylococcus Aureus* Periprosthetic Infections, *Biomaterials* 2015; 41: 97-105.

8. Nodzo S, Tobias M, Hansen L, Luke-Marshall NR, Cole R, Wild L, Campagnari AA, Ehrensberger MT. Cathodic Electrical Stimulation Combined with Vancomycin Enhances Treatment of Methicillin-Resistant *Staphylococcus Aureus* Implant-Associated Infections, *Clin. Orthop. Relat. Res.* 2015; 473: 2856-64.
9. Nodzo SR, Tobias M, Ahn R, Hansen L, Luke-Marshall NR, Howard C, Wild L, Campagnari AA, Ehrensberger MT. Cathodic Voltage-Controlled Electrical Stimulation Plus Prolonged Vancomycin Reduce Bacterial Burden of a Titanium Implant-Associated Infection in a Rodent Model, *Clin. Orthop. Relat. Res.* 2016; 474(7): 1668-75.
10. Gilbert JL. Electrochemical Coupling of Metallic Biomaterial Implants for Biological Effect. Syracuse University (Syracuse, NY, US), assignee. Patent US9039764 B2. 26 May 2015.

2 Background

2.1 *Historical Significance of Magnesium*

Magnesium (Mg) was actually found to be of clinical importance as early as in the late 1800s, mainly due to the work of Payr, a physician who used pure Mg for various applications, such as bone fracture stabilizers, blood vessel connectors, and sutures [1]. In 1900, Payr investigated Mg as connectors (made as tubes or rings) for vessel anastomosis, and found that although the vessel ends thickened initially, the thickening disappeared over time and no thrombosis occurred [1]. The same year, Payr also used Mg in musculoskeletal applications, using Mg implants as intramedullary stabilizer in bone fractures and pseudarthrosis [1]. Following Payr's steps, Lambotte used Mg plate with steel screws to stabilize a fracture at the tibia of a human patient, and found the patient in extreme pain with local swelling and extensive subcutaneous gas cavities only one day after the operation [1]. Lambotte later learned that Mg dissolved very quickly due to electrochemical reaction between Mg plate and steel screws, producing large volume of gas. Lambotte and Verbrugge treated patients with humerus fractures with Mg nails and found that the fracture healed completely, without any pain in the operated area [1]. Lambotte concluded that Mg is a good biodegradable implant, as long as Mg is not combined with other metallic implants. Some researchers argued that Mg is not suitable for orthopedic applications, due to excessive gas cavities forming at the fracture site and quick disintegration of Mg implant even before any significant healing of the fracture [1]. However, despite some doubts on Mg implants, Lambotte and Verbrugge continued to use Mg and observed that the gas formation was only temporary and usually disappeared over time, in few weeks, without any adverse effects. Lambotte and Verbrugge noted that the corroding of Mg did not cause any permanent damage to the surrounding tissue or bone and no signs of infection or

inflammation were observed [1]. Like Lambotte and Verbrugge, Payr and other researchers also found no signs of post-operative infections during their animal experiments and clinical trials on humans, even though the operations were performed under non-sterile conditions [1].

Payr also discovered that Mg has tumor killing properties [1]. In 1900, Payr inserted Mg rods in children to treat haemangioma and lymphangioma tumors (Fig. 2.1).

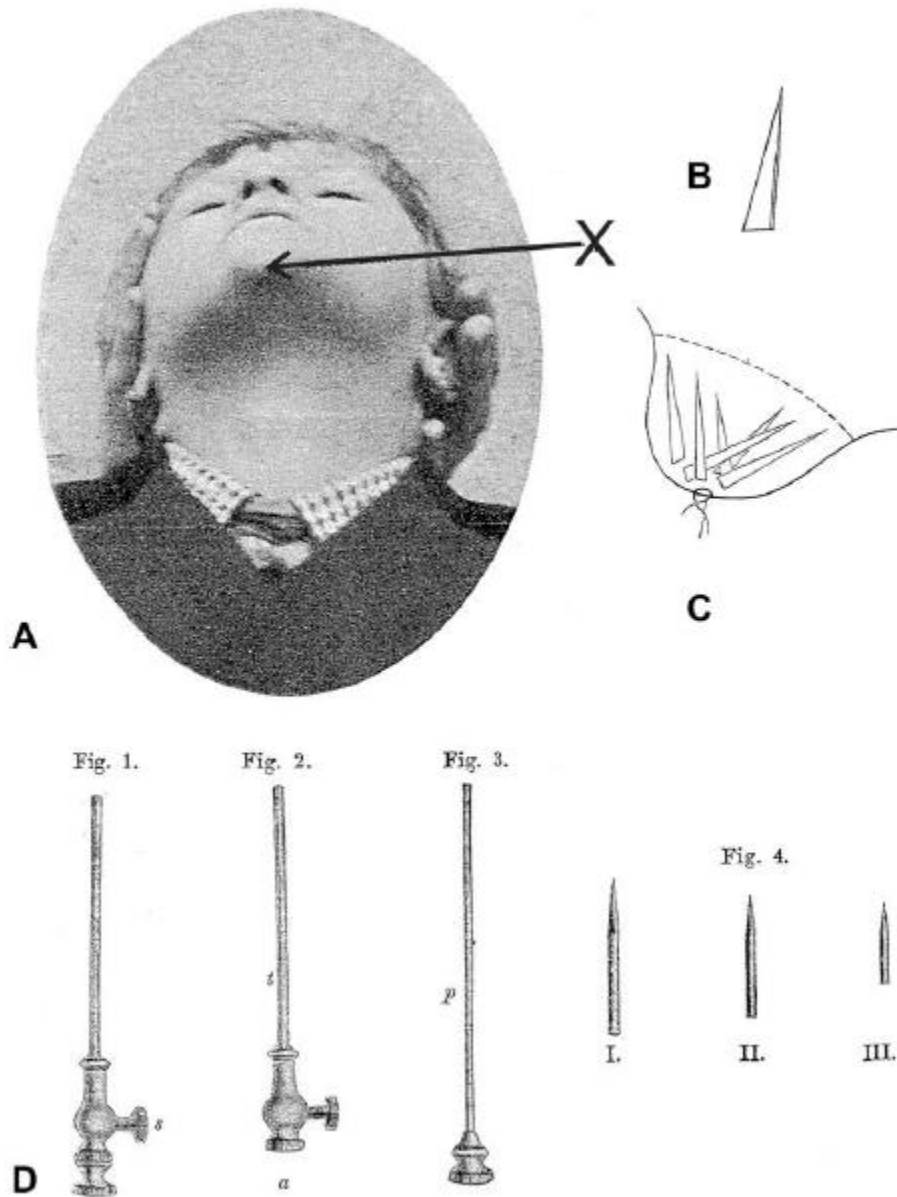


Figure 2.1 Payr treating cavernous haemangioma by insertion of high-purity Mg arrows, where (A) X marks the insertion point in a child's chin. (B) A diagram of a Mg arrow. (C) A diagram showing Mg arrows embedded directly into the tumor. (D) A diagram showing platinum-iridium trocars used to insert Mg arrows into the haemangioma.¹

In 1981, plastic surgeon Wilflingseder repeated Payr's Mg treatment of haemangioma in 27 patients [1-2]. Wilflingseder tried to treat different types of haemangioma and got 50% success rate, from which he confirmed Payr's previous results that the outcome of the treatment depended on the type of haemangioma, and the amount and the distribution of Mg arrows in the tumor, where Wilflingseder noted that tumors in the subcutaneous layer of skin were treated most effectively with Mg [2]. Fig. 2.2 shows a procedure of a boy being treated for haemangioma of the cheek with Mg wires [2].

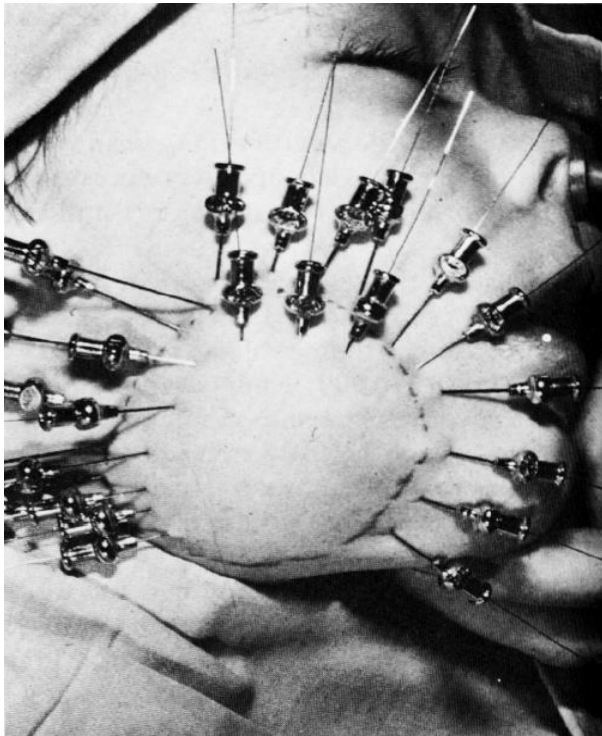


Figure 2.2 6-year-old boy with persistent lymph-haemangioma in his cheek being treated with magnesium wires in 1975.²

Wilflingseder showed many successful cases using Mg arrows for haemangioma treatments, where he reported that all patients showed complete or partial reduction in tumor, and only 2 cases with no effect. One successful case Wilflingseder reported was of a 7-months old child suffering from extensive capillary haemangioma of the strawberry type on the dorsum of her right hand (Fig. 1.3 a-b).

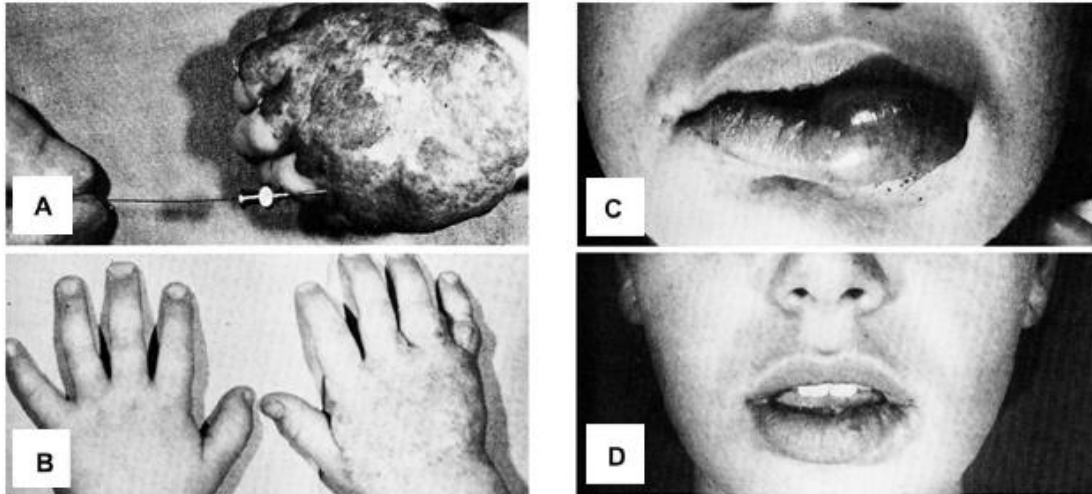


Figure 2.3 (A) 7-months old baby with strawberry-type haemangioma. Mg wire is inserted by means of hyperthermic needles. (B) Same patient from (A) at the age of 3 years. The haemangioma has disappeared, with some scarring left at the site of ulceration which occurred at the age of 6 months. (C) 13-year old girl after implantation of Mg arrows in the lips. (D) The same patient from (C) after 2 years of Mg treatment.²

Her hand had repeated hemorrhages and ulceration, and so Mg wires were used for treatment. The treatment consisted of 3 sessions, where different sized Mg wires were implanted within 4 months. Two years later, her hands looked healthy, besides some scarring and contour of the hands. Another successful case was of 13-year-old girl who had persistent haemangioma on her lower lip (Fig. 2.3 c-d). The first treatment consisted of 3 Mg arrows, followed by 5 Mg wire sessions, where different sized wires with increasing lengths were implanted. The tumor became very fibrous in 2 years, which was corrected by excision. Fig. 2.4 shows a boy with proliferating haemangioma of the right cheek, which was first treated at the age of 6 months by instilling hypertonic saline. However, at the age of 12 months, the tumor grew rapidly, and arterial ligations were performed, followed by more hypertonic saline injections, with no effect. And so at the age of 4 years, Mg wires were implanted three times at 3 month intervals, and the tumor, which turned fibrous, shrank. And lastly, one of his most successful cases is of a three months old child with cavernous haemangioma, where the child had tumor in his face, throat, and shoulder (Fig. 2.5).

After insertions of Mg rods at the tumor sites, the child's face became almost normal after 20 months of treatment.

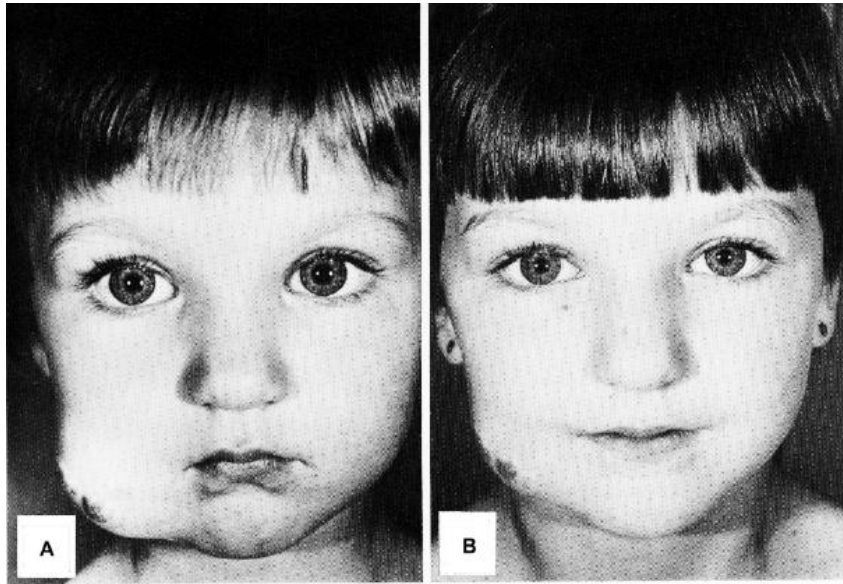


Figure 2.4 (A) 4-year old child with a haemangioma of the cheek before the Mg treatment. (B) The same patient as (A) at the age of 6 years, 2 years after the Mg treatment.²

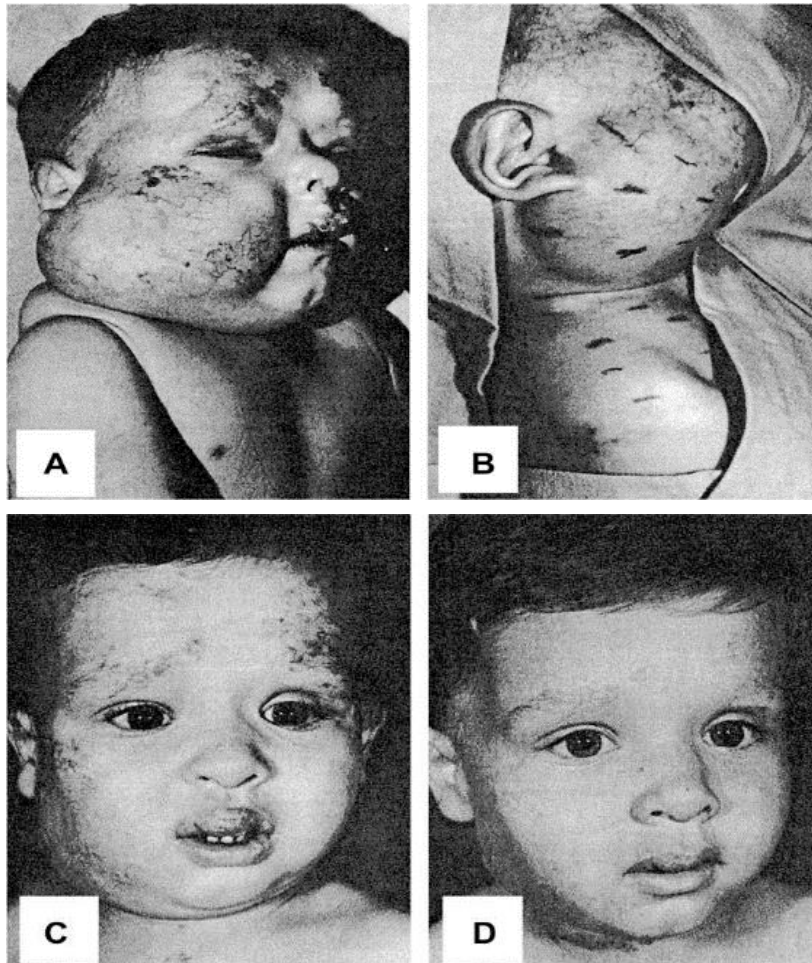


Figure 2.5 (A) 3-months old child with proliferating haemangioma of the face, throat, and shoulder. (B) 3-months old child with the step incisions for the insertion of the magnesium arrows. (C) 9 months after the beginning of magnesium treatment at the age of 1 year. (D) 20 months after the start of magnesium therapy at the age of 2 years.¹⁻²

Even in a case where lympho-haemangioma was found in the lumbar region, deep in the body, next to adjacent vital organs, in a location where surgery was not an option, Mg treatment reduced the tumor after 2 years. And moreover, while treating these patients, Wilflingseder found that the structure and function of nerves and muscle fibers (especially in the face) in close proximity to Mg rods were not disturbed, so Wilflingseder concluded that Mg is safe to treat haemangioma without harming the surrounding tissue.

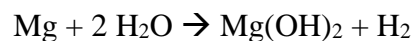
Due to Payr and other researchers' efforts in investigation of Mg for various applications, Mg as a potential biodegradable implant material has been discovered very early on, over a decade ago. And eighty years later, Wilflingseder was able to successfully re-use Payr's Mg approach for tumor treatment, although the exact mechanism of tumor involution due to Mg was not known at the time. Despite Mg's potential for antibacterial and tumor-killing properties, pure Mg is too brittle and corrosive, making Mg difficult to use as a biomaterial. For orthopedic implants, the surgeons began to prefer more corrosion-resistant materials, such as stainless steel (SS) and titanium (Ti), and Mg as an orthopedic biomaterial was abandoned for several decades. Since Wilflingseder, Mg was also not widely used for tumor treatment due to advancement of cancer chemotherapy, which can target and treat different cancers. And so Mg has not been considered as a biomaterial altogether, until recently, Mg is now again receiving attention as a biodegradable implant material, especially for orthopedic and cardiovascular applications.

2.2 Properties of Magnesium

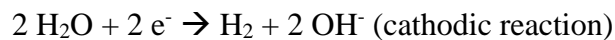
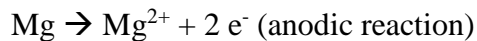
Mg has many favorable properties as a biodegradable implant material. First, Mg has a similar density ($1.74\text{-}2.0\text{ g/cm}^3$) as that of natural bone ($1.8\text{-}2.1\text{ g/cm}^3$) than other metals, such as titanium ($4.4\text{-}4.5\text{ g/cm}^3$), cobalt-chromium alloy ($8.3\text{-}9.2\text{ g/cm}^3$), and stainless steel ($7.8\text{-}8.1\text{ g/cm}^3$) [3]. Elastic modulus and compressive yield strength of Mg is also closer to that of natural

bone, reducing stress shielding, which is a common problem for other metallic implants [3]. Second, Mg ions are found as one of the most abundant ions in the body, and so toxicity due to high Mg ion accumulation is very unlikely [3]. Third, Mg ions released from Mg implants during degradation are known to stimulate bone regeneration, due to Mg ions increasing osteoblast activity [4-6]. Despite all these desirable qualities of Mg, Mg and its alloys have not been widely used as implant materials because of their fast degradation rates. A major drawback of using pure Mg is that it corrodes too quickly, especially in chloride containing solutions, such as body fluid, because Mg is susceptible to forming magnesium chloride (MgCl_2 ; $\text{Mg}(\text{OH})_2 + 2 \text{HCl} \rightarrow \text{MgCl}_2 + 2 \text{H}_2\text{O}$) [7-8]. Magnesium hydroxide ($\text{Mg}(\text{OH})_2$) converts into soluble magnesium chloride when chloride concentration exceeds 30 mmol/l in solution, where the body fluid contains chloride of about 150 mmol/l [9]. The corrosion rate of Mg is approximately 19-44 mg/cm²/day in simulated body fluid, which means that Mg implants will degrade over days and lose functionality without giving enough time for any wound healing, such as during bone fracture [10].

For pure Mg, the corrosion of Mg metal can be written as an oxidation reaction of Mg and reduction reaction of water. The overall corrosion reaction of Mg in aqueous solution is:



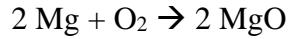
Where the overall equation can be broken down into anodic and cathodic reactions:



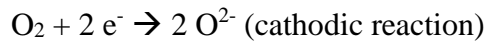
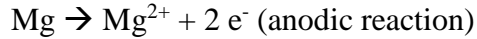
Anodic reaction involves Mg metal oxidizing to produce Mg ions and releasing two electrons.

Anodic reaction may produce an intermediate monovalent Mg ion, Mg^+ , which is not stable and has a short lifetime [11]. Cathodic reaction involves reduction of water into hydrogen gas and

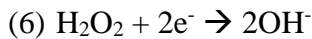
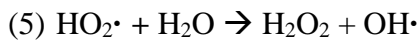
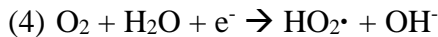
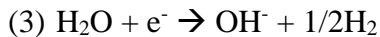
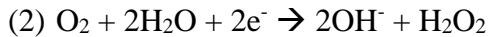
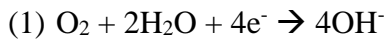
hydroxide, which will increase the pH of the solution. There are other possible reduction reactions, such as Mg reacting with oxygen, although in aqueous solution, Mg will more likely react with water than oxygen [11]. The overall equation for this reaction is:



And the anodic and cathodic reactions are:



Oxygen molecules will split to bind with each Mg ion. Magnesium oxide (MgO), however, is replaced by MgOH, which is more stable [11]. Other types of reduction reactions of water and oxygen are also possible, which are shown as follows:



Reduction of water and oxygen may produce hydrogen peroxide, hydroxyl radicals, and other types of reactive oxygen species (ROS). ROS produced due to reduction reactions of water/oxygen will be discussed further in a later section. The corrosion mechanisms of Mg alloys have not been systematically studied, but Mg still dominates the corrosion reactions [11].

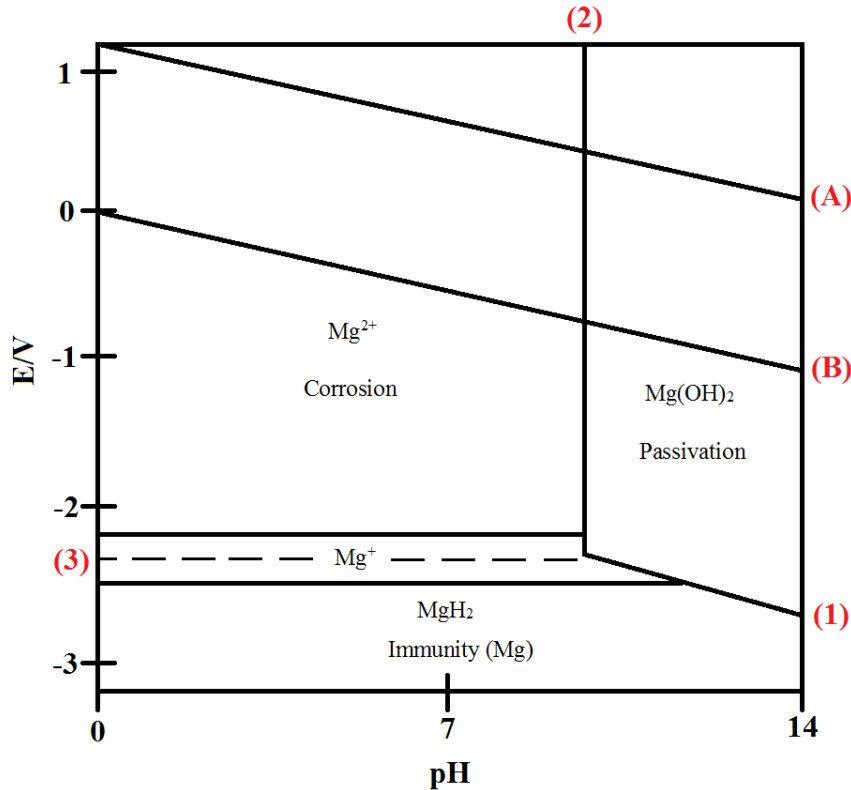


Figure 2.6 Pourbaix diagram of Mg in water at 25 Celsius. Lines (A) and (B) show stability of water, where water H_2O is more stable in a region between lines (A) and (B), oxygen O_2 is more stable in a region above line (A), and hydrogen H_2 is more stable in a region below line (B). (A) $O_2 + 4 H^+ + 4 e^- \rightarrow 2 H_2O$; $E_{red} = 1.233 V - 0.0591 pH$. (B) $2 H^+ + 2 e^- \rightarrow H_2$; $E_{red} = 0 V - 0.0591 pH$. (1) $Mg + 2 H_2O \rightarrow Mg(OH)_2 + H_2$. (2) Around pH of 8.5-11.5, a film of magnesium oxide or hydroxide may form to provide protection, and above 11.5, a stable film of magnesium hydroxide forms to protect magnesium from corrosion. (3) $Mg \rightarrow Mg^{2+} + 2 e^-$; $E_{red} = -2.34 V$ at all pH, intermediate monovalent ion Mg^+ may be produced, but not stable.¹¹⁻¹³

When Mg is in solution, the standard potential of Mg at 25 Celsius is -2.34 V (vs. standard hydrogen electrode, SHE), although the actual potential measured is around -1.7 V (vs. SHE), due to the thin oxide film of either hydroxide, $Mg(OH)_2$, or oxide, MgO [11]. The Pourbaix diagram shows that Mg metal spontaneously corrodes and forms Mg ions, Mg^{2+} , at the standard potential higher than -2.34 V and at pH lower than 8.5 (Fig. 2.6) [11-13]. This region is called the active state. As stated before, anodic reaction of Mg can produce an intermediate monovalent Mg ion, Mg^+ , but this species is not very stable, immediately converting to Mg^{2+} . As pH is increased to 8.5, $Mg(OH)_2$ or MgO may form at the metal surface to provide some protection from corrosion. As pH is increased to 11.5, a stable film of $Mg(OH)_2$ is formed to protect Mg metal from corrosion, so that Mg is in a passive state. And at potential below -2.34 V, Mg will not spontaneously corrode and can even form magnesium hydride, MgH_2 , which is very inert.

2.3 Magnesium Ions

Many studies usually focus on the oxidation reactions of the metal and the cytotoxicity of the released metal ions, especially transition metals, such as iron and chromium, in determining the biocompatibility of the metallic biomaterials [14-18]. Although certain metal ions are known to cause cytotoxic and allergic effects, such as nickel ions, Mg ions are known to be very biocompatible. As previously stated, Mg ions are found as the fourth most abundant ions in the body, where the daily intake of Mg for an average human adult is about 300-400 mg, with approximately 21-28 g of Mg ions stored in the body, of which almost half is found in muscle and soft tissue and the other half in bone [19]. Mg ions play an important role in various functions of the body, such as enzyme activities, signal transduction, energy metabolism, and nucleic acid and protein synthesis [19]. Early signs of Mg ion toxicity develop at plasma concentration of 3.5-5 mmol/l, which include vomiting, nausea, double vision, etc. [19]. More severe and permanent damage due to high Mg ion toxicity shows at high plasma concentration of 5-15 mmol/l, which include muscular paralysis, respiratory arrest, and cardiac arrest [19]. However, such level of cytotoxicity is extremely rare, because body usually can effectively excrete excess Mg via urine [19]. While Mg ion toxicity is very rare in vivo, in vitro Mg ion toxicity may occur, around 365-375 mg/l, for MC3T3-E1 murine pre-osteoblast cells (the toxicity level may be different for different cell types) [20-21].

As Mg and Mg alloys are being investigated as a potential biodegradable implant, especially in orthopedic applications to temporarily stabilize bone fractures, studies have found that Mg enhances bone growth around the implant. Witte et al. implanted four different types of Mg alloys, two aluminum and zinc containing Mg alloys (AZ31 and AZ91) and two rare earth containing Mg alloys (WE43 and LAE442), where the alloying elements did not exceed 10% wt,

to compare bone growth and implant degradation rates to that of biodegradable self-reinforced poly-96L/4D-lactide-polymer-based implant of the same size [22]. Witte et al. observed that although the polymer-based implant degraded more uniformly than the Mg-based implant, there were significant increases in the mineralization of bone around the Mg implants at 6 and 18 weeks postoperative compared to that of the polymer group [22]. Janning et al. implanted a cylindrical Mg(OH)₂ implant in the rabbit knee and compared osteoblast and osteoclast activity and bone growth around the implant compared to that of the control group, which had bone defects that were left empty [23]. Histology and staining showed that there was an increase in bone apposition rate around the Mg(OH)₂ implant and a decrease in the number of osteoclasts temporarily, usually between 2-4 weeks after the surgery. The results obtained from this study paralleled with in vitro studies showing increased osteoblast activity and decreased osteoclast activity in alkaline environments [23-24], and another study showed a reverse effect of increase in osteoclast activity and decrease in bone density in a rat model due to magnesium reduction diet [23, 25-28]. Yoshizawa et al. studied the role of Mg ions on osteogenic response in bone marrow stromal cells, and found that 10 mM of magnesium sulfate (MgSO₄) concentration affected extracellular matrix (ECM) proteins and transcription factors that cause ECM mineralization, which in turn induces osteogenesis [29-30]. These studies also suggest that Mg²⁺ released from Mg-based implants enhances bone regeneration by increasing the production of collagen type X and vascular endothelial growth factor (VEGF) of osteogenic cells in bone tissue. Feyerabend et al. supported Yoshizawa's results and found that up to 10 mM concentration of MgSO₄ increased chondrocyte proliferation rate compared to untreated control, while higher concentrations (15-30 mM) decreased chondrocyte proliferation [31]. High Mg concentrations of higher than 10 mM increased the production of components of the extracellular

matrix, such as glycosaminoglycans (GAGs), which is an important component of ECM that can attract and maintain water. Based on gene and protein expressions, chondrocytes treated with Mg ions during both proliferation and differentiation showed higher degree of differentiation than chondrocytes exposed to Mg ions during just differentiation stage alone. However, during chondrogenesis, the supplementation of Mg showed adverse effect, where the ECM matrix formation decreased significantly. This study shows that Mg ions can be beneficial in chondrocyte proliferation and differentiation, depending on the maturation of the cells.

2.4 Current Assessment of Cytotoxicity of Magnesium and Its Alloys

Mg metal is considered very biocompatible, mainly because as discussed earlier, Mg ions released are harmless in vivo, and in fact, can help heal and regenerate bone. However, Mg metal does show some cytotoxicity, especially in vitro. When assessing cytotoxicity of Mg and its alloys, one of the most common and traditional method is to pre-corrode the metal in the culture media and then use that media to culture cells to measure cell viability. Fischer et al. proposed an improved cytotoxicity testing of Mg materials by using extraction medium (Mg pre-corroded in medium supplemented with serum) to measure in-vitro cytotoxicity [32]. The extract medium was prepared according to EN ISO standards, where the relation of specimen weight of Mg to extraction medium is 0.2 g/ml, which is considered as 1x. Less concentrated extracts were also prepared by increasing the volume of the medium. The extract media with different series of dilutions (1x, 2.5x, 5x, 15x, 20x, and 25x) were then given to the cells to evaluate cytotoxicity by measuring cell viability. This study showed that cell viability was inversely correlated with higher osmolality and higher Mg concentration. For pure Mg, cell viability higher than 75% was reached at 5x dilution for the osteoblast cells and 15x dilution for

MG63 (human osteoblast-like) cells. This study concluded that higher osmolality and higher Mg concentration showed higher cytotoxic potential of the Mg-based material.

Gu et al. performed an in vitro viability test for different cell types, murine fibroblast cells L-929 and NIH3T3, murine pre-osteoblast cells MC3T3-E1, human umbilical vein endothelial cells ECV304, and rodent vascular smooth muscle cells VSMC, by culturing these cells in cell culture media that had pure Mg or Mg alloyed to another element (Mg-X) pre-corroded for 72 hours [33]. Based on this experiment, Gu et al. attributed the decrease of cell viability to the alloy metal ions, concluding that some elements, such as manganese, are highly cytotoxic for all cell types, while cytotoxicity of other elements, such as aluminum and tin, depended on the cell types and ion concentration. Gu et al. measured Mg ion concentrations and found that Mg ions released from the binary alloys varied between 130 and 210 $\mu\text{g/ml}$, which is much lower than IC_{50} (half maximal inhibitory concentration, measuring the effectiveness of a substance in inhibiting a specific biological or biochemical function) measured for osteoblast cells, and therefore this study concluded that Mg ions are not the cause of cytotoxicity [33-34]. pH was also measured but since these cells were viable for certain range of pH and the pH of the extracted solution was within this range, pH was also eliminated as a possible cytotoxic factor for this study. The study focused on the alloyed elements as the cause of cytotoxicity, but the result clearly showed that pure Mg yielded lower cell viability than most of Mg alloyed with another element, and this study failed to explain why pure Mg is more cytotoxic than Mg alloys. Gao et al. also pre-corroded cast 4N-Mg alloy in the cell culture media, which was then diluted with a saline solution, in order to determine cytotoxicity of this alloy on L929 fibroblast cells [35]. Gao et al. observed that cell viability decreased significantly for those given 1/2 and 1/3 dilutions (Mg^{2+} : 343-315 mg/l), while cell viability was almost the same as negative control for

those given 1/6 dilution (Mg^{2+} : 181 mg/l), and cell viability increased for those given 1/15 and 1/30 dilutions (Mg^{2+} : 97-112 mg/l) due to cell proliferation. pH was measured for some dilutions, but the pH did not vary significantly, and so this study concluded that although lower Mg ion concentrations supported osteoblast proliferation, higher Mg ion concentrations killed osteoblast cells.

Robinson et al. tested antibacterial properties of Mg by treating *Escherichia coli*, *Pseudomonas aeruginosa*, and *Staphylococcus aureus* with different concentrations of Mg metal [36]. Robinson et al. waited 90 minutes after the inoculation of bacteria before adding Mg metal, which forms a premature biofilm, which is less persistent and easier to kill than a fully-developed biofilm. Robinson et al. stated that cell viability was decreased significantly for the groups treated with Mg compared to the negative control and that both pH and Mg ion concentration increased correspondingly. Robinson et al. then tested cell viability by giving $MgCl_2$ solution to the cells to see if high concentrations of Mg ions caused cell deaths, but found that Mg ions did not affect cell viability. However, when hydroxide ions were added, cell viability decreased, and so Robinson et al. concluded that the corrosion of Mg kills bacteria in vitro due to pH shift.

As shown, many studies analyze cytotoxicity of Mg and its alloys by pre-corroding the metal in solution and measuring the Mg ion concentrations, hydrogen gas volume, osmolality, and pH. In vitro studies have contributed to our understanding of cytotoxicity of pure Mg mainly to high Mg ion concentrations and increase of pH. Hydrogen gas is not a factor in vitro since hydrogen gas will directly escape to the atmosphere [33]. Osmolality, which increases as Mg ion concentration increases, had no significant influence; a study shows that when osmolality increased from 300 to 500 mOsmol/kg, only 10% cell viability was reduced (isotonic solution

ranges from 270 to 300 mOsmol/kg) [37]. In vivo studies have attributed cytotoxicity of Mg to mainly hydrogen gas volume and pH shift. In vivo, if hydrogen gas is produced moderately, it does not seem to cause any clinically important effects because hydrogen gas can easily diffuse. However, if hydrogen gas is produced at large volume too quickly, it can cause separation of the tissue layers and necrosis of the tissue [38]. However, hydrogen gas accumulation within the tissue can be easily detected, and can be syringed out [4]. Increase of pH from physiological pH is known to adversely affect cells and tissue both in vivo and in vitro, where local in vivo pH exceeding 7.8 may lead to alkaline poisoning effect [39]. Overall, current assessments of cytotoxicity are focused primarily on the byproducts produced due to corrosion of Mg; however, these studies fail to investigate the corrosion reactions themselves or any role the reduction reactions may play.

2.5 Effect of Cathodic Potential on Cell Viability and Morphology

All metals, when they corrode, have an associated reduction reaction occurring at the same rate as the oxidation reaction to achieve an equilibrium. However, application of cathodic voltage on the metal drives the reduction reactions of water and oxygen due to excess electrons at the metal surface, while anodic voltages drives the oxidation reactions of the metal due to depletion of electrons at the metal surface. The effects of reduction reactions on cells and tissue have been largely ignored until recently, when studies have shown that cathodic voltage (i.e. reduction reactions dominating at the metal surface) can have adverse effects on the cells. According to Ehrensberger et al., potentials ranging from -300 mV to +1000 mV on commercially pure titanium (cpTi) showed no difference in cell viability, while cathodic polarization below -300 mV showed significant reduction in cell spreading and cell viability [40]. Haeri et al. also noticed a similar behavior with cobalt chromium molybdenum (CoCrMo)

alloy, where cells were less viable below -400 mV [41]. No significant difference in cell viability was shown from -100 mV to +300 mV compared to that of OCP (approximately -200 mV at 24 hours), but at +500 mV, cell viability again dropped for CoCrMo alloy. This difference in cell behavior between cpTi and CoCrMo in anodic potentials is due to the breakdown of chromium oxide film (above transpassive potential), while titanium oxide film does not break but continues to grow at anodic potentials. Interestingly, cells in cathodic and anodic voltages die under different mechanisms [41]. While cell area decreased for those cells that died under cathodic voltages, cell area increased for those under anodic voltages above +500 mV. Presence of caspase proteins, which are released during cell apoptosis process and found by staining the voltage-treated samples, showed that while the cells that were exposed to cathodic voltages had high concentrations of caspase proteins in the cells, the cells exposed to anodic voltages did not. In conclusion, cells exposed to cathodic voltages were prone to undergo cell apoptosis, while cells exposed to anodic voltages underwent cell necrosis [41]. This meant that oxidation reaction dominating at anodic voltage and reduction reaction dominating at cathodic voltage kill cells differently.

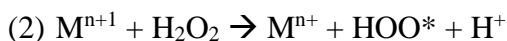
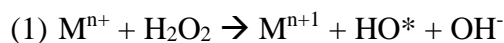
Sivan et al. showed similar results, but closer investigation of cathodic voltages showed that there was a significant drop of cell viability and cell area from -300 mV to -350 mV, which shows a very narrow range of voltage drop that changes cell viability, as if there is a “threshold potential” that triggers the cells to die [42]. Also, the cells died in time-dependent manner, where cells applied with higher cathodic voltages died faster [42]. The times were measured for 50% of cells to die at different voltages, and showed that $t_{0.50}$ (time it takes for 50% of cells to die) exponentially decreases as the potentials become more cathodic. This exponential curve fits the Butler-Volmer equation, which governs the rates of generation and accumulation of the

killing species [42]. Therefore, the hypothesis of this study is that the reduction reactions produces reactive oxygen species (ROS), which at high concentration, can induce cell death.

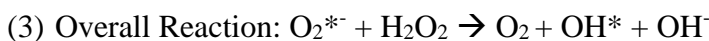
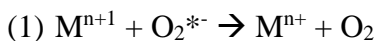
2.6 *Reactive Oxygen Species (ROS)*

Reactive oxygen species (ROS) is a term used to describe radicals with an unpaired electron, such as short-lived diffusible species like hydroxyl, alkoxy, or peroxy, and medium-lived species like superoxide and nitroxyl radical [43]. But ROS also include non-radicals such as hydrogen peroxide, organic hydroperoxides, and hypochlorous acid [43]. The effect of ROS on cellular behavior is known to be very dose-dependent. At low concentrations, ROS is known to induce cell signaling and proliferation, at intermediate concentrations, ROS is known to cause growth arrest, and at high concentrations, ROS is known to disrupt normal cell function, damage DNA, RNA, cellular proteins, and lipids, and promote cell death [44-49]. For example, Sugiyama et al. observed that hydrogen peroxide killed human mesangial cells in dosage-dependent manner and also fragmented DNA [50].

ROS are known to form in the presence of free metal ions via two types of reactions: Fenton and Haber-Weiss reactions. Fenton reaction involves oxidizing a metal ion to produce a hydroxyl radical and a hydroxide ion or reducing a metal ion to produce hydroperoxyl radical and a proton.



Haber-Weiss reaction generates hydroxyl radicals from hydrogen peroxide and superoxide.



Although transition metals, such as $\text{Fe}^{2+}/\text{Fe}^{3+}$ and $\text{Cr}^{3+}/\text{Cr}^{5+}/\text{Cr}^{6+}$, are known to participate in Fenton and Haber-Weiss reactions, Mg ions, $\text{Mg}^+/\text{Mg}^{2+}$, can also participate in this type of reactions.

2.7 Galvanic Coupling of Mg-Ti

Galvanic corrosion is a phenomenon where one metal preferentially corrodes over the other metal, especially at the junction of the two metals. The overall voltage established at bi-metal surface depends on the OCP's associated with each metal and the relative area of each present [51]. The higher the difference of OCP between the two metals, and the greater the cathodic area compared to the anodic area, the greater the galvanic effect. Mg is a very active metal, with a standard electrode potential of -1.6 V to -2.0 V, whereas Ti has a standard electrode potential of -0.3 V to 0.1 V [51]. Galvanic series of metals show that Mg-Ti couple will have a large galvanic effect due to this large difference in potential (Fig. 2.7) [52].

In this study, galvanic coupling of Mg and Ti is produced via sputtering, which allows only a very thin layer of Ti film to partially cover Mg in line of sight, so that there are areas of Mg exposed in solution. The cathodic area of Ti is small comparable to the anodic area of Mg via sputtering, which also produces a significant galvanic effect.

Galvanic Series in Seawater

Series	Metal
Cathodic End (Noble Metals)	Platinum
	Gold
	Silver
	Titanium
	Cr-Ni Stainless Steels, Passive
	Ni-Cu Alloys (Monels)
	Ni-Cr-Fe Alloys (Inconels), Passive
	Nickel, Passive
	Silver Solder
	Tin Bronzes
Anodic End (Active Metals)	Copper Nickels
	Silicon Bronzes
	Copper
	Red and Yellow Brasses
	Aluminum Bronzes
	Ni-Cr-Fe Alloys (Inconels), Active
	Nickel, Active
	High-Zn Yellow Brasses (>30% Zn)
	Manganese Bronzes
	Tin
	Lead
	Cr-Ni Stainless Steels, Active
	Cast Iron
	Wrought Iron
	Low-Carbon Steel
	2xxx and 7xxx Aluminum Alloys
	Cadmium
	Alclad Aluminum Alloys
	6xxx Aluminum Alloys
	Galvanized Steel
Zinc	
Magnesium Alloys	
Magnesium	

Figure 2.7 Galvanic series of metal. Ti is considered noble metal, and is almost always a cathodic member of the galvanic couple. Mg and Mg alloys are very active, and are always anodic members of the galvanic couple.⁵²

The partial covering of Ti layer on Mg surfaces enhances the rates of both oxidation reactions of Mg and reduction reaction of water/oxygen on the Ti surface. The surface of Ti essentially provides a catalyst for the reduction reactions, separating the oxidation and reduction spatially. Ti surfaces may also preferentially generate ROS during reduction on their surfaces, which is a known effect during photoelectrochemistry of titanium dioxide (TiO₂) [53-56]. Ti spontaneously passivate and form TiO₂, which produces ROS during reduction on the surface. Photocatalytic reaction of TiO₂ is started by excitation of light with wavelength less than 385 nm that create a photon energy that produces an electron hole pair on the surface of TiO₂ [55]. The hole in the valence band can react with water, oxygen, or hydroxide ions adsorbed on the surface to produce hydroxyl radicals or superoxide ions [55]. Other ROS, such as hydrogen peroxide and singlet oxygen, are also known to form from this photocatalytic process [55].

Although this study focuses specifically on Mg-Ti couple, galvanic coupling of other metals is possible and may have similar effects in terms of cell killing. For example, iron (Fe), zinc (Zn), and copper (Cu) are all essential metals that are found in the body that can easily replace Mg. Zn is considered a very active metal, like Mg, and so Zn will be a very good alternative to Mg (Fig. 2.7 shows that Zn is immediately above Mg and Mg alloys in galvanic series). Cu and Fe, on the other hand, is not as active as Zn and Mg, and so the galvanic effect will not be as large as that of Zn and Mg. There are studies reporting other galvanic-couples to control biological processes. A metal that is widely being investigated for antibacterial properties is silver (Ag). Cao et al. embedded Ag nanoparticles on Ti surface via silver plasma immersion ion implantation process so that these Ag nanoparticles can inhibit the growth of bacteria, with a potential application of utilizing this method on Ti-based implantable devices [57]. Although the exact mechanism is still being debated, one hypothesis is that the Ag ions

released is contributing to cell death, by disrupting cell membrane. However, in this case, Ti is slightly more cathodic than Ag (Fig. 2.7) shows Ag is one of few metals more anodic than titanium). Therefore, Ti-Ag galvanic couple will actually slow the oxidation reaction of Ag and instead, cause the Ti surrounding the Ag to oxidize. In applications of Ag particles in Ti-based implants, this galvanic couple is not ideal since Ag can assist in the corrosion of Ti implant. The antimicrobial effect of Ag is dependent upon size and shape of Ag particles, where Ag is most effective as nanoparticles, small enough to interact with the bacterial membrane and enter inside the cell, reacting with sulfur containing proteins and phosphorus-containing DNA, and ultimately disrupting the normal functions of the bacteria [58]. Ag also produces ROS that influence the bacterial cells. However, unlike Mg, large release of Ag ions can travel and accumulate at distant locations and adversely affect human body [58].

2.8 Mg-Ti Couple for Targeted Therapeutic Effect

Currently, the most common methods of treating tumor are surgery, radiation, and chemotherapy [59]. Surgery is most effective in removing solid tumors that are localized in one area (not leukemia or metastatic cancer that have spread). Surgery will physically remove the tumor, but also some healthy tissue surrounding the tissue to make sure the tumor is completely removed. However, sometimes removing the entire tumor may damage vital organs, depending on the location of the tumor, and so tumor may be only partially removed by surgery, and other treatments, such as radiation and chemotherapy, may follow. There are two types of radiation therapy, external and internal. External beam radiation involves an equipment that aims radiation to the specific part of the body with cancer. Internal radiation involves putting a source of radiation inside the body, either in solid (i.e. capsule) or liquid (i.e. through intravenous line) form. Mg-Ti galvanic couple possibly may be injected to the tumor site to give synergistic

effect. While radiation, for example, affects larger area, killing surrounding healthy tissue, Mg-Ti may be used to target tumor more effectively. And while radiation therapy needs to be given in multiple doses, Mg-Ti, once injected, will continue to produce ROS as long as Mg corrodes (Mg corrosion can be controlled by Mg size, surface area, and concentration). As mentioned before, photocatalytic reaction of TiO_2 can produce ROS when TiO_2 is excited using UV light or radiation. And so Mg-Ti galvanic couple may be used in combination with radiation therapy to effectively kill either remaining tumor or prevent re-growth.

Another major potential application of Mg-Ti is to treat orthopedic device-related infection (ODRI). Although the risk of orthopedic-device infection (ODRI) is less than 1-2%, the number of patients receiving total hip replacements is over 200,000 per year in the United States [60-61]. Another study stated that over a half million hip and knee replacements are performed each year in the US alone [62]. A different study showed that there was an increase of infection for both rheumatoid arthritis (RA) and osteoarthritis (OA) patients who received total hip replacement in the last decade, from 2002-2010, compared to the decade before, from 1995-2001, requiring revision of the implant [62]. A total of 390,671 received total hip replacements due to rheumatoid arthritis or osteoarthritis (377,287 from OA group and 13,384 from RA group) from 1995 to 2010, where 2,315 received revision due to infection (2,228 from OA group and 87 from RA group) [63]. And so although the incidence of ODRI is considered low, the number is still significantly high due to large numbers of patients receiving hip and joint replacements each year and infection is considered to be the second main cause of revision, especially during the first 2 years of surgery [62]. Antibiotics and chemotherapy with antimicrobial agents are used to treat ODRI, but these treatment options are not so effective if the infection has already significantly formed on the implant, and the only remaining option is the

removal of the implant, which causes more trauma on the patient and also increases the risk of implant replacement [62]. Peri-implant infections are considered more resistant than other post-operative infections, due to the presence of foreign biomaterial [62]. The critical dose of bacteria required to produce infection is significantly lower when a foreign material is present at the surgery site, partly due to lower immune defenses [62]. Also, the implant material can provide a surface where bacteria can adhere and colonize, by anchoring onto the host extracellular proteins adsorbed onto the biomaterial using receptorial proteins like adhesins and producing polysaccharide glycocalyx, essentially creating an adherent biofilm on implant surfaces that gives enhanced protection from host defense and antibiotic treatments [62]. Adding a small fraction of Mg onto the Ti surface drops the potential of the implant or fracture devices significantly, which is known to cause adverse effects on cells cultured on the surface, which may also affect biofilms [51].

2.9 Re-statement of Purpose

Based on previous literature, it is expected that Mg-Ti galvanic couple can be clinically used for targeted therapeutic effect, especially in treating cancer and bacterial infections. Mg-Ti alloy causes large voltage drop on the Ti surface, producing large doses of ROS that can kill cells/tissue at the Ti surface without adversely affecting cells/tissue at distant locations (since ROS is not stable, they cannot travel very far). At the same time, corrosion of Mg-Ti releases Mg ions essential to biological systems and help induce bone growth, which is a beneficial side effect. Therefore, this dissertation focuses to characterize Mg-Ti couple to determine whether this galvanic couple can effectively eradicate cancerous cells and biofilms as hypothesized, and also begin to address the mechanism of killing by Mg-Ti galvanic couple.

References

1. Witte F, Hort N, Vogt C, Cohen S, Kainer KU, Willumeit R, Feyerabend F. The History of Biodegradable Magnesium Implants: A Review. *Curr. Opin. Solid State Mater. Sci.* 2008; 6(5):1680-92.
2. Wilflingseder P, Martin R, Papp C. Magnesium Seeds in the Treatment of Lymph- and Haemangiomas. *Chir. Plast.* 1981; 6(2): 105-16.
3. Staiger MP, Pietak AM, Huadmai J, Dias G. Magnesium and Its Alloys as Orthopedic Biomaterials: A Review. *Biomaterials* 2006; 27(9): 1728-734.
4. Witte F, Kaese V, Haferkamp H, Switzer E, Meyer-Lindenberg A, Wirth CJ, Windhagen H. In Vivo Corrosion of Four Magnesium Alloys and the Associated Bone Response. *Biomaterials* 2005; 26(17): 3557-563.
5. Zhang E, Xu L, Yu G, Pan F, Yang K. In Vivo Evaluation of Biodegradable Magnesium Alloy Bone Implant in the First 6 Months Implantation. *J. Biomed. Mater. Res. A* 2009; 90A(3): 882-93.
6. Kraus T, Fischerauer SF, Hanzi AC, Uggowitzer PJ, Löffler JF, Weinberg AM. Magnesium Alloys for Temporary Implants Osteosynthesis: In Vivo Studies of Their Degradation and Interaction with Bone. *Acta Biomater.* 2012; 8(3): 1230-238.
7. Song G. The Anodic Dissolution of Magnesium in Chloride and Sulphate Solutions. *Corros. Sci.* 1997; 39(10-11): 1230-238.
8. Inoue H, Sugahara K, Yamamoto A, Tsubakino H. Corrosion Rate of Magnesium and Its Alloys in Buffered Chloride Solutions. *Corros. Sci.* 2002; 44(3): 603-10.

9. Witte F, Hort N, Vogt C, Cohen S, Kainer KU, Willumeit R, Feyerabend F. Degradable Biomaterials Based on Magnesium Corrosion. *Curr. Opin. Solid State Mater. Sci.* 2008; 12(5-6): 63-72.
10. Song G, Atrens A. Understanding Magnesium Corrosion- A Framework for Improved Alloy Performance. *Advanced Engineering Materials* 2003; 5(12): 837-58.
11. Song G, Atrens A. Corrosion Mechanisms of Magnesium Alloys. *Adv. Eng. Mater.* 1999; 1(1): 11-33.
12. Pourbaix M. Atlas of Electrochemical Equilibria in Aqueous Solutions. 2nd Edition. P. 141. 1975.
13. Revie RW, Uhlig HH. Corrosion and Corrosion Control: An Introduction to Corrosion Science and Engineering. 4th Edition. John Wiley & Sons, Inc. 2008.
14. Stohs S. Oxidative Mechanisms in the Toxicity of Metal Ions. *Free Radical Bio. Med.* 1995; 18(2): 321-36.
15. Sun Z, Wataha JC, Hanks CT. Effects of Metal Ions on Osteoblast-like Cell Metabolism and Differentiation. *J. Biomed. Mater. Res.* 1997; 34(1): 29-37.
16. Wataha JC, Hanks CT, Sun Z. Effect of Cell Line on *In Vitro* Metal Ion Cytotoxicity. *Dent. Mater.* 1994; 10(3): 156-61.
17. Li Y, Wong C, Xiong J, Hodgson P, Wen C. Cytotoxicity of Titanium and Titanium Alloying Elements. *J. Dent. Res.* 2010; 89(5): 493-97.
18. Issa Y, Brunton P, Waters C, Watts D. Cytotoxicity of Metal Ions to Human Oligodendroglial Cells Human Gingival Fibroblasts Assessed by Mitochondrial Dehydrogenase Activity. *Dent. Mater.* 2008; 24(2): 281-87.

19. Saris NEL, Mervaala E, Karppanen H, Khawaja JA, Lewenstam A. Magnesium: An Update on Physiological, Clinical and Analytical Aspects. *Clin. Chim. Acta* 2000; 294(1-2): 1-26.
20. Gao J-C, Qiao L-Y, Xin R-L. Effect of Mg²⁺ Concentration on Biocompatibility of Pure Magnesium, *Front. Mater. Sci. China* 2010; 4(2): 126-31.
21. Walker J, Shadanbaz S, Woodfield TBF, Staiger MP, Dias GJ. The *In Vitro* and *In Vivo* Evaluation of the Biocompatibility of Mg Alloys, *Biomed. Mater.* 2014; 9(1): 1-11.
22. Witte F, Kaese V, Haferkamp H, Switzer E, Meyer-Lindenberg A, Wirth C, Windhagen H. In Vivo Corrosion of Four Magnesium Alloys and the Associated Bone Response. *Biomaterials* 2005; 26(17): 3557-563.
23. Janning C, Wilbold E, Vogt C, Nellesen J, Meyer-Lindenberg A, Windhagen H, Thorey F, Witte F. Magnesium Hydroxide Temporarily Enhancing Osteoblast Activity and Decreasing the Osteoclast Number in Per-Implant Bone Remodelling. *Acta Biomater.* 2010; 6(5): 1861-868.
24. Bushinsky DA. Metabolic Alkalosis Decreases Bone Calcium Efflux by Suppressing Osteoclasts and Stimulating Osteoblasts. *Am. J. Physiol.* 1996; 271(1): F216–22.
25. Rude RK, Gruber HE, Norton HJ, Wei LY, Frausto A, Kilburn J. Reduction of Dietary Magnesium by Only 50% in the Rat Disrupts Bone and Mineral Metabolism. *Osteoporosis Int.* 2006; 17(7):1022–32.
26. Rude RK, Kirchen ME, Gruber HE, Meyer MH, Luck JS, Crawford DL. Magnesium Deficiency-Induced Osteoporosis in the Rat: Uncoupling of Bone Formation and Bone Resorption. *Magnes. Res.* 1999; 12(4): 257–67.

27. Rude RK, Gruber HE, Wei LY, Frausto A, Mills BG. Magnesium Deficiency: Effect on Bone and Mineral Metabolism in the Mouse. *Calcif. Tissue Int.* 2003; 72(1): 32–41.
28. Rude RK, Gruber HE, Norton HJ, Wei LY, Frausto A, Mills BG. Bone Loss Induced by Dietary Magnesium Reduction to 10% of the Nutrient Requirement in Rats is Associated with Increased Release of Substance P and Tumor Necrosis Factor-Alpha. *J. Nutr.* 2004; 134(1): 79–85.
29. Yoshizawa S, Brown A, Barchowsky A, Sfeir C. Role of Magnesium Ions on Osteogenic Response in Bone Marrow Stromal Cells. *Connect. Tissue Res.* 2014; 55(S1): 155-59.
30. Yoshizawa S, Brown A, Barchowsky A, Sfeir C. Magnesium Ion Stimulation of Bone Marrow Stromal Cells Enhances Osteogenic Activity, Simulating the Effect of Magnesium Alloy Degradation, *Acta Biomater.* 2014; 10: 2834-42.
31. Feyerabend F, Witte F, Kammal M, Willumeit R. Unphysiologically High Magnesium Concentrations Support Chondrocyte Proliferation and Redifferentiation. *Tissue Eng.* 2006; 12(12): 3545-556.
32. Fischer J, Pröfrock D, Hort N, Willumeit R, Feyerabend F. Improved Cytotoxicity Testing of Magnesium Materials. *Mater. Sci. Eng. B* 2011; 176(11): 830-4.
33. Gu X, Zheng Y, Cheng Y, Zhong S, Xi T. In Vitro Corrosion and Biocompatibility of Binary Magnesium Alloys. *Biomaterials* 2009; 30(4): 484-98.
34. Hallab NJ, Vermes C, Messina C, Roebuck KA, Glant TT, Jacobs JJ. Concentration- and Composition-dependent Effects of Metals Ions on Human MG-63 Osteoblasts. *J. Biomed. Mater. Res.* 2002; 60(3): 420-33.
35. Gao JC, Qiao LY, Xin RL. Effect of Mg²⁺ Concentration on Biocompatibility of Pure Magnesium. *Front. Mater. Sci. China* 2010; 4(2): 126-31.

36. Robinson DA, Griffith RW, Shechtman D, Evans RB, Conzemius MG. In Vitro Antibacterial Properties of Magnesium Metal against Escherichia Coli, Pseudomonas Aeruginosa and Staphylococcus Aureus. *Acta Biomater.* 2010; 6(5): 1869-877.
37. Wang J, Witte F, Xi T, Zheng Y, Yang K, Yang Y, Zhao D, Meng J, Li Y, Li W, Chan K, Qin L. Recommendation for Modifying Current Cytotoxicity Testing Standards for Biodegradable Magnesium-Based Materials, *Acta Biomater.* 2015; 21: 237-49.
38. Song G, Song S. A Possible Biodegradable Magnesium Implant Material, *Adv. Eng. Mater.* 2007; 9(4): 298-302.
39. Song G. Control of Biodegradation of Biocompatible Magnesium Alloys, *Corr. Sci.* 2007; 49: 1696-1701.
40. Ehrensberger MT, Sivan S, Gilbert JL. Titanium is Not the Most Biocompatible Metal under Cathodic Potential: The Relationship between Voltage and MC3T3 Preosteoblast Behavior on Electrically Polarized CpTi Surfaces. *J. Biomed. Mater. Res. A* 2010; 93A(4): 1500-509.
41. Haeri M, Wollert T, Langford GM, Gilbert JL. Electrochemical Control of Cell Death by Reduction-Induced Intrinsic Apoptosis and Oxidation-Induced Necrosis on CoCrMo Alloy In Vitro. *Biomaterials* 2012; 33(27): 6295-304.
42. Sivan S, Kaul S, Gilbert JL. The Effect of Cathodic Electrochemical Potential of Ti-6Al-4V on Cell Viability: Voltage Threshold and Time Dependence. *J. Biomed. Mater. Res. B Appl. Biomater.* 2013; 101(8): 1489-497.
43. Simon HU, Haj-Yehia A, Lev-Schaffer F. Role of Reactive Oxygen Species (ROS) in Apoptosis Induction. *Apoptosis* 2000; 5(5): 415-18.

44. Bergamini CM, Gambetti S, Dondi A, Cervellati C. Oxygen, Reactive Oxygen Species and Tissue Damage, *Curr. Pharm. Des.* 2004; 10: 1611-26.
45. Harris RM, Williams TD, Hodges NJ, Waring RH. Reactive Oxygen Species and Oxidative DNA Damage Mediate the Cytotoxicity of Tungsten-Nickel-Cobalt Alloys *In Vitro*, *Toxicol. Appl. Pharmacol.* 2011; 250: 19-28.
46. Ziech D, Franco R, Georgakilas AG, Georgakila S, Malamou-Mitsi V, Schoneveld O, Pappa A, Panayiotidis MI. The Role of Reactive Oxygen Species and Oxidative Stress in Environmental Carcinogenesis and Biomarker Development, *Chem. Biol. Interact.* 2010; 188: 334-9.
47. Cabisco E, Tamarit J, Ros J. Oxidative Stress in Bacteria and Protein Damage by Reactive Oxygen Species, *Internatl. Microbiol.* 2000; 3: 3-8.
48. Circu ML, Aw TY. Reactive Oxygen Species, Cellular Redox Systems, and Apoptosis, *Free Radic. Biol. Med.* 2010; 48: 749-62.
49. Martin KR, Barrett JC. Reactive Oxygen Species as Double-Edged Swords in Cellular Processes: Low-Dose Cell Signaling Versus High-Dose Toxicity, *Hum. Exp. Toxicol.* 2002; 21: 71-5.
50. Sugiyama H, Kashihara N, Makino H, Yamasaki Y, Ota Z. Reactive Oxygen Species Induce Apoptosis in Cultured Human Mesangial Cells. *J. Am. Soc. Nephrol.* 1996; 7(11): 2357-63.
51. Gilbert JL. Electrochemical Coupling of Metallic Biomaterial Implants for Biological Effect. Syracuse University (Syracuse, NY, US), assignee. Patent US9039764 B2. 26 May 2015.

52. Donachie, Matthew J. "Corrosion Resistance." *Titanium: A Technical Guide*. Metals Park, OH: ASM International, 1988. 126.
53. Blake DM, Maness PC, Huang Z, Wolfrum EJ, Huang J. Application of the Photocatalytic Chemistry of Titanium Dioxide to Disinfection and the Killing of Cancer Cells. *Separ. Purif. Methods* 1999; 28(1): 1-50.
54. Tsuang YH, Sun JS, Huang YC, Lu CH, Chang W, Wang CC. Studies of Photokilling of Bacteria Using Titanium Dioxide Nanoparticles. *Artif. Organs* 2008; 32(2): 167-74.
55. Maness PC, Smolinski S, Blake DM, Huang Z, Wolfrum EJ, Jacoby WA. Bactericidal Activity of Photocatalytic TiO₂ Reaction: Toward an Understanding of Its Killing Mechanism. *Appl. Environ. Microbiol.* 1999; 65(9): 4094-98.
56. Fujishima A, Rao TN, Tryk DA. Titanium Dioxide Photocatalysis. *J. Photochem. Photobiol. C* 2000; 1(1): 1-21.
57. Cao H, Liu X, Meng F, Chu PK. Biological Actions of Silver Nanoparticles Embedded in Titanium Controlled by Micro-Galvanic Effects. *Biomaterials* 2011; 32(3): 693-705.
58. Morones JR, Elechiguerra JL, Camacho A, Holt K, Kouri JB, Ramírez JT, Yacaman MJ. The Bactericidal Effect of Silver Nanoparticles. *Nanotechnology* 2005; 16(10): 2346-353.
59. "Cancer Treatment." National Cancer Institute. U.S. Department of Health and Human Services, National Institutes of Health, National Cancer Institute, 29 Apr. 2015. Web. 22 May 2015. <<http://www.cancer.gov/about-cancer/treatment/types/surgery>>.
60. Widmer AF. New Developments in Diagnosis and Treatment of Infection in Orthopedic Implants. *Clin. Infect. Dis.* 2001; 33(2): S94-106.
61. Fitzgerald RH Jr. Total Hip Arthroplasty Sepsis: Prevention and Diagnosis. *Orthop. Clin. North Am.* 1992; 23(2): 259-64.

62. Campoccia D, Montanaro L, Arciola CR. The Significance of Infection Related to Orthopedic Devices and Issues of Antibiotic Resistance. *Biomaterials* 2006; 27(11): 2331-339.
63. Schrama JC, Fenstad AM, Dale H, Havelin L, Hallan G, Overgaard S, Pedersen AB, Kärrholm J, Garellick G, Pulkkinen P, Eskelinen Antti, Mäkelä K, Engesæter LB, Fevang BT. Increased Risk of Revision for Infection in Rheumatoid Arthritis Patients with Total Hip Replacements. *Acta Orthop.* 2015; 86(3): 1-7.

3 Cytotoxic Effect of Galvanically Coupled Magnesium-Titanium

Particles

3.1 Introduction

Magnesium (Mg) and its alloys are currently being widely investigated as potential degradable biomaterials, especially in orthopedic and cardiovascular applications [1-4]. Pure Mg metal was used clinically as early as in the late 1800s, when Mg was used as ligatures to stop bleeding, connectors to treat vessel anastomosis, and fixtures to treat bone fractures [5]. Many physicians noticed that Mg was very biocompatible, allowing the bones and soft tissues to heal without any major adverse effects [5]. In fact, many investigators noticed that insertion of Mg in surgical sites prevented infections, even when the operation was performed under non-sterile conditions [5]. Mg even showed potential in treating tumors, mostly subcutaneous hemangioma, in children [5-7]. Further investigations of Mg recently showed that insertion of Mg rods at bone fracture sites increases the rate of bone mineralization during Mg corrosion [8-10]. This has been speculated to be due to the Mg ions playing an important role in increasing osteoblast activity, since Mg ion is an essential active-site component of many enzymes [8, 11-15]. However, despite its desirable qualities discovered early on, Mg as a biomaterial was discarded until recently because of its fast and unpredictable corrosion rate in vivo mainly depending on the size of the implant, chloride-containing environment, purity of the material (alloying elements), and the implant site (tissue type and degree of vascularization) [16-17]. Therefore, many studies began to focus on the alloying of Mg, coating the metal surface, or treating the metal to increase the ductility and slow the corrosion rate [18-20].

Toxicity of Mg ions has been studied and is considered very biocompatible with little adverse effects. Mg corrodes and releases Mg ions, which are already present in the body in

large amount (fourth most abundant ion in the body), with approximately 21-28 g of Mg ions stored in an average body, more than half is stored in bone and the rest in muscle and soft and tissue, and so the release of Mg ions rarely causes any toxicity [21-22]. The corrosion of Mg may rapidly release unwanted by-products in high concentrations, such as hydrogen gas, which may lead to dissociation and even necrosis of the tissues, and also hydroxide ions, which leads to the increase of local pH [23]. However, hydrogen gas usually disappears over time or can be quickly removed with syringe or incision [23-24]. The initial increase of pH can also have an adverse effect, but pH usually recovers rapidly, due to the body's natural buffer system [23, 25]. The in vitro cytotoxicity of Mg is mainly attributed to the increase of pH, very high concentrations of Mg ions, which will have more significant adverse effects in vitro since the closed system does not offer any means to buffer the pH or eliminate excess Mg ions or other metal elements alloyed to Mg [26-27].

In addition to the oxidation products (ions and hydroxide), there are reduction reactions that must be present to balance all of the oxidation taking place. Reduction reactions in vivo are thought to be dominated by reduction of oxygen and reduction of water, both of which ultimately generate hydroxide, and potentially hydrogen gas. However, these reduction reactions also have intermediate products that include hydrogen peroxide, hydroxyl radical, and other chemical species that may have significant biological effects [28]. Thus, high corrosion rates result in high rates of generation of these reduction intermediates and it may be these species that are affecting cell viability during corrosion [29-31].

When highly corrodible Mg alloys are galvanically coupled to a metal like titanium whose open circuit potential is a volt more positive than Mg, two effects result. First, the rate of corrosion of the Mg is galvanically increased, and second, the reduction reactions are focused

onto the Ti surface (i.e. spatially separated from the oxidation). It is hypothesized that galvanic couples of Mg and Ti will result in a significant enhancement in cell-killing ability.

This study proposes that galvanically coupled particles consisting of Mg and Ti in direct contact with one another could be used therapeutically to deliver a killing effect in proximity to the particles. This could be used, for example, to treat tumors or local infections. Thus, the goal of this study is to show that Mg galvanically coupled to Ti will be more effective in killing cells than Mg alone, by giving Mg or Mg-Ti microparticles to cells in dose-dependent manner. This study will also show that pH is unlikely to be the sole factor in killing cells in vitro.

3.2 *Materials and Methods*

3.2.1 *Characterization of Mg and Mg-Ti Microparticles using Scanning Electron Microscopy (SEM)*

Mg particles (Goodfellow, Product #: MG006021), generated by mechanical abrasion, with 99.8% Mg purity, were galvanically coupled with Ti (Alfa Aesar, Stock #: 13975 and Lot #: C19N26), with 99.99% Ti purity. These particles are formed from a mechanical process (e.g., cutting or milling). Mg particles are then sieved to the required particle range so that most of the particles have the maximum diameter of approximately 50 μm . Mg and Ti were galvanically coupled via direct current sputtering (Denton Systems) for 5 minutes, at 1.2 kV, 50 mA, and 100-200 mTorr. Sputtering allowed the Ti layer to cover only half of the Mg microparticles (the top that was exposed during sputtering) due to the line-of-sight nature of the sputter process, while leaving the bottom half of the Mg microparticles uncovered. SEM images of Mg and Mg-Ti microparticles were taken in secondary emission mode. Scanning electron microscopy (SEM, JEOL 5600, Dearborn, MA) with energy dispersive spectrometry (EDS, Princeton Gamma Tech, Princeton, NJ) were also used to characterize the particles.

In preliminary studies, Mg and Mg-Ti particles were sterilized by exposing the particles in UV light for t= 12-24 hours and these particles were compared to the non-sterilized Mg and Mg-Ti particles by giving them to the cells for t= 24 hours. However, there was no difference in cytotoxic effect between sterilized particles and non-sterilized particles (data not shown). Therefore, the sterilization steps were skipped for all the cell viability experiments reported in this chapter and the following chapters in order to increase the efficiency because the sterilization steps resulted in further loss of the particles.

3.2.2 Measuring Thickness of Ti layer using Atomic Force Microscopy (AFM)

Due to the extremely thin layer of Ti developed during sputtering, the thickness deposited was investigated by covering half of silicon dioxide (glass) slides while the other half was left exposed during sputtering with Ti. Prior to sputtering, the glass surface was washed in soap and water, rinsed in distilled water and then rinsed in pure ethanol. The sputtering conditions remained the same, as mentioned above. AFM (Digital Instruments Nanoscope IIIa) was then used to take height and deflection images at the border in contact mode using a standard silicon nitride tip. AFM software was used to measure the height and morphology of the sputtered layer.

3.2.3 Analysis of MC3T3 Cell Viability over Mg and Mg-Ti Particle Concentrations

Mouse fibroblast cells, MC3T3 (ATCC #: CRL-2593), were seeded in a 6-well plate (A= 9.6 cm²) with a cell density of 10,000 cells/cm², and were left for 12 hours in the incubator at 37°C and 5% CO₂ to allow cells to attach to the plate. The cells were cultured in a media made of minimum essential medium alpha medium MEM (Cellgro Corning 15-012-CV), 10% fetal bovine serum FBS (Invitrogen 16000044), and 1% penicillin-streptomycin-glutamine PSG (Invitrogen 10378-016). Mg and Mg-Ti microparticle concentrations ranging from 50 to 1750

$\mu\text{g/ml}$ were given to the cells for $t= 24$ hours, with 2 ml of the solution given per well. The particles were randomly scattered, and so the local density of particles in different regions in the sample varied. Live/dead assay (Invitrogen #: L3224) was performed at the end of each time period to measure cell viability using an optical microscope (Leica Instruments). Ten images were taken per sample at random for three separate samples and the number of live and dead cells was counted manually in each image using Image J software (Image J, NIH Bethesda MD), using the manual cell counter feature. Manual counting of live and dead cells was most effective and accurate due to the software's inability to differentiate between cells and particles. Viability was determined as the number of live cells divided by the total number of cells in each image.

$$\%CV = \frac{\# \text{ of live cells}}{\# \text{ of live cells} + \# \text{ of dead cells}} \times 100$$

This approach does not account for dead cells that have separated from the surface, however, it represents the upper limit in percent viable (since detached dead cells would have increased the denominator of the viability).

3.2.4 Determining Mg and Mg-Ti Particle Concentrations

Since Mg particles can only be measured down to a certain concentration using the weight scale, the particles had to be diluted in media solution and then divided into aliquots to achieve a smaller concentration. Mg particles were initially measured as 0.002 g, 0.008 g, and 0.01 g on non-treated petri dishes. These particles were then added to 4 ml of media in a 15 ml centrifuge tube. In order to minimize loss of the particles during this transfer from the dish to the tube, media was added to the dish 1 ml of media at a time to collect the particles as the media is withdrawn by the micropipette gun (using 1000 μl pipette tips), so that by 4 ml, the dish has been washed with media 4 times and most of the particles have been transferred. Only 1000 μl pipette tips were used since microparticles did not fit through any tips with smaller openings. In order to

achieve the final desired concentration of Mg particles, more concentrated particle solutions were diluted to achieve the appropriate value. For example, to achieve 50 $\mu\text{g/ml}$, 0.2 ml was taken from a 500 $\mu\text{g/ml}$ particle-solution, which was made by mixing 0.002 g of Mg particles in 4 ml of media. There are 100 μg of Mg particles in 0.2 ml of particle solution and 1.8 ml of additional media is then added to make the total volume of 2 ml, yielding the final concentration of 50 $\mu\text{g/ml}$ per sample. Since the particles sink quickly, in order to achieve maximum homogeneity in the particle-containing solutions, the micropipette gun was used to suck the particle-solution up and down few times to insure thorough mixing before withdrawing the final amount of 0.2 ml. In this way, the particle-solution concentrations of 50, 100, 250, 500, 750, 1000, 1250, 1500, and 1750 $\mu\text{g/ml}$ were created from both Mg and Mg-Ti particles.

For Mg-Ti particles, the same procedure was taken to calculate the final concentration of particles as Mg particles. However, because there was a significant loss of particles during sputtering due to the suction of vacuum, the weight of the empty dish was measured and the final weight of the dish and the particles sputtered were measured to calculate the weight of the Mg-Ti particles. The volume withdrawn from 4 ml of particle-solution had to be calculated each time to get the desired final Mg-Ti concentration. Once prepared, the solutions were used in cell culture immediately, within 15 minutes of mixing.

3.2.5 Measuring pH for Mg and Mg-Ti Microparticles at Different Concentrations

pH's were measured, using an electrochemical pH meter (Omega PHB-45), at particle concentrations ranging from 0 to 2500 $\mu\text{g/ml}$ for Mg and Mg-Ti groups at $t= 0$ hour, which was immediately after the particles were added in solution (within 5 minutes), and at $t= 24$ hours.

3.2.6 Analysis of MC3T3 Cell Viability over pH Range Corresponding to the pH of Mg and Mg-Ti Particle Concentrations

To investigate the role of pH alone on cell viability, sodium hydroxide (NaOH, Fisher Scientific Cat. No. SS266) was used to change the pH of the complete media (AMEM + 10% FBS + 1% PSG). The pH was measured using an electrochemical pH meter to get the pH desired. The pH was adjusted to 8, 8.5, and 9, and compared to control, which had a pH of 7.5. Cells were cultured in this media at different pH for $t = 24$ hours and live/dead assay was performed to measure cell viability, where ten images were taken randomly per sample for a total of three samples for each pH.

3.2.7 *Statistical Analysis*

Two-way analysis of variance (ANOVA) statistical methods were used to analyze the results, along with post-hoc Tukey tests, using SPSS Statistics Software, version 17.0. The two factors were particle type and concentration. Statistically significant differences were determined with $p < 0.05$.

3.3 *Results*

3.3.1 *SEM Images of Mg and Mg-Ti Microparticles*

SEM images of Mg and Mg-Ti microparticles show they are very irregular in shape and size (Fig. 3.1), resulting from the grinding method used to make them. The maximum diameter of these particles was upwards of 100 μm . These particles also have a rough surface, with many grooves, which means there are more surface areas exposed in solution for corrosion. Mg powder on stainless steel (SS) disc was sputtered for up to 2 hours to detect Ti, but EDS was unable to confirm the Ti layer on Mg microparticles and SS disc. However, there was discoloration of the SS disc, where the surface showed yellow-goldish color when the disc was sputtered, and the color changed to dark blue as the sample was sputtered longer, indicating Ti deposition onto the SS disc surface (data not shown here; but in [3.7 Supplementary Images](#)). To

ensure that the EDS can indeed detect Ti element, Ti-6Al-4V disc was used as a control, and EDS detected Ti on Ti-6Al-4V disc (3.7 Supplementary Images). All the results seem to indicate that there is deposition of Ti on the exposed surface of Mg particles and any metal surface in line of sight to the Ti source, but Ti just cannot be detected using EDS because the Ti layer is just too thin (~nm), which is reasonable since EDS can usually detect only few microns. The particles did not exhibit any gross evidence of corrosion or oxidation prior to mixing in the solutions, however, they will likely have a thin oxide film on their surface from exposure to air (not observable in SEM).

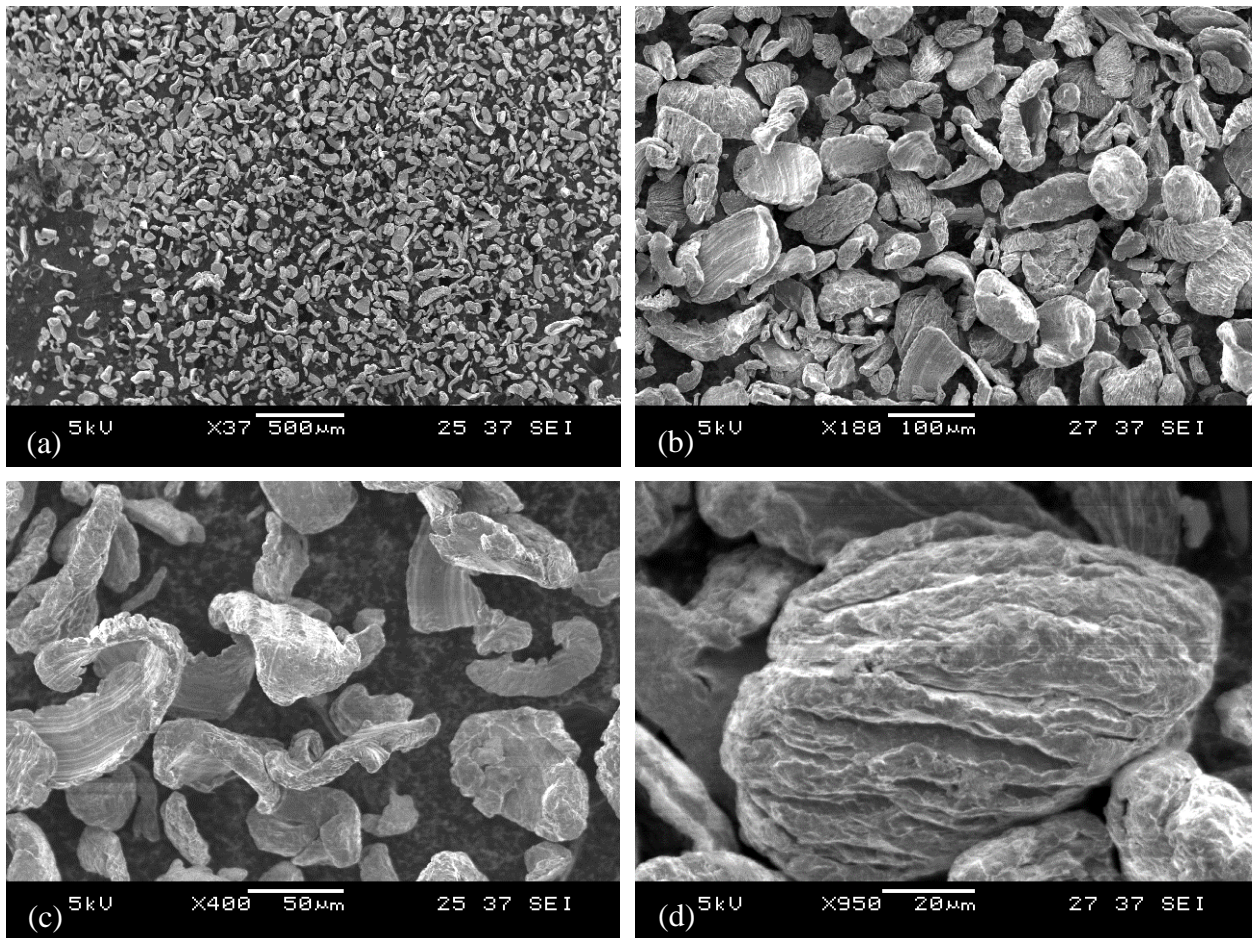


Figure 3.1 SEM images of (a-b) Mg particles, and (c-d) Mg particles sputtered with Ti for 5 minutes. There are no morphological differences between non-sputtered and sputtered samples. The Ti layer is too thin to be seen. The Mg particles are very irregularly-shaped, with rough surfaces, giving a larger surface area for corrosion. Average diameter of Mg particles is about 50 to 100 μm.

3.3.2 *Measuring Ti Layer using AFM*

Atomic force microscopy (AFM) was used to detect the Ti layer when sputtered for 5 minutes. When the border between the Ti sputtered and non-sputtered regions were imaged on a glass slide, it was clear that Ti was not homogeneously covering the sputtered area (Fig. 3.2). Shown in Figures 3.2a and 3.2b are the deflection and height images of the border between Ti-sputtered and non-sputtered areas on a glass slide. Ti formed many domes, which varied in height, as small as 9 nm or as tall as 81 nm (Fig. 3.3). The reason for the heterogeneous deposition is not known, however, this experiment demonstrated the presence of the titanium due to the sputtering process.

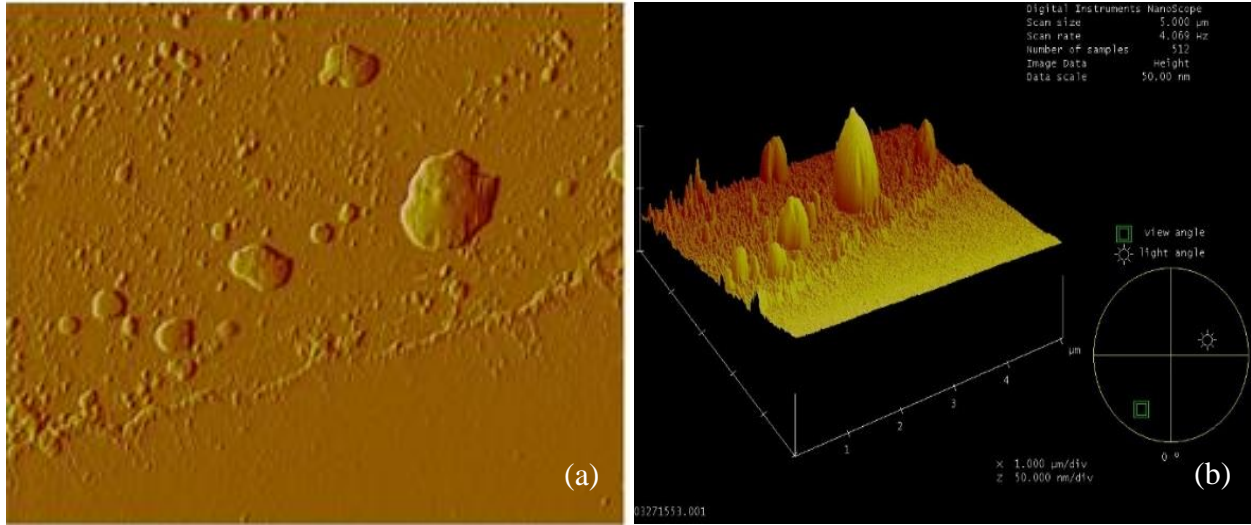


Figure 3.2 Ti was sputtered on glass for 5 minutes. AFM was used to take (a) deflection image and (b) height image at the border between sputtered and non-sputtered regions. The images show different sized Ti domes on the sputtered regions, compared to the relatively flat non-sputtered regions.

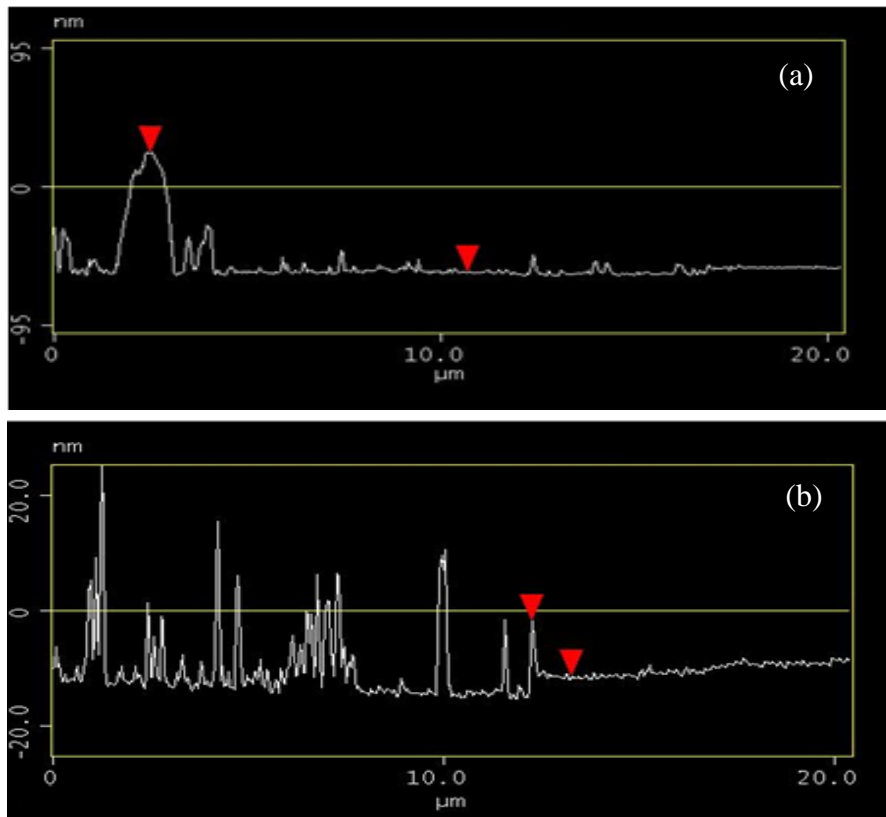
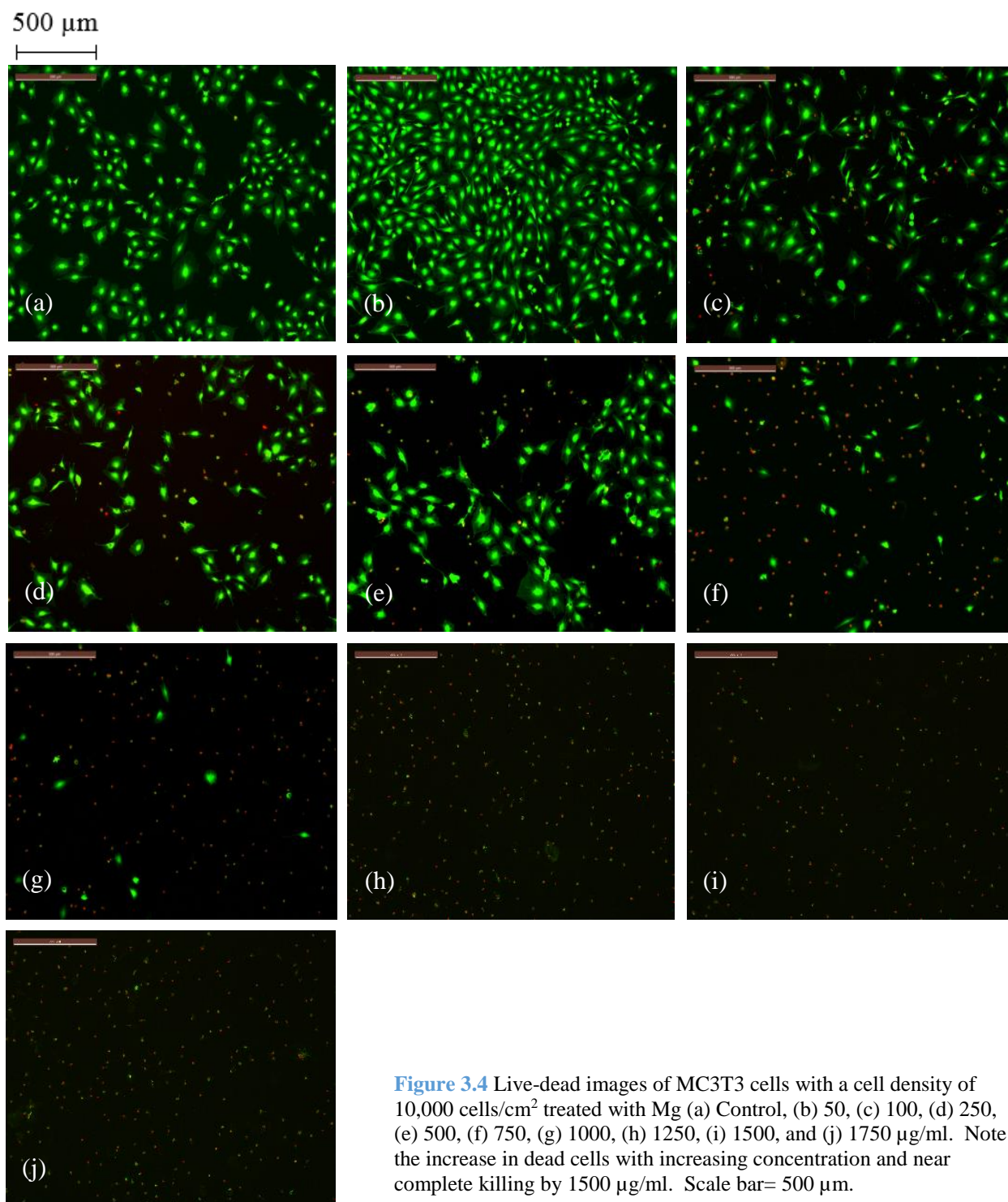


Figure 3.3 Line profiles from images in Fig. 3.2. The heights of Ti domes measured are (a) 81.9 and (b) 9.6 nm, respectively. The size of the domes may vary, but the average thickness of Ti layer is still in nm range.

3.3.3 Mg-Ti Cytotoxicity on MC3T3 Cells

Live/dead images of MC3T3 cells with cell seeding density of 10,000 cells/cm² treated with Mg concentrations ranging from 0-1750 µg/ml for 24 hours are shown (Fig. 3.4). Control group (non-treated) is nearly entirely viable, with most of the cells alive and spread out on the surface. As the particle concentration of Mg is increased, the cell viability begins to decrease, with more cells balled up and dead. The same trend is shown for MC3T3 cells treated with Mg-Ti particles (Fig. 3.5). SEM images (Fig. 3.6) of MC3T3 cells after 24 hours of exposure to 500 µg/ml of Mg particles (Fig. 3.6b) or 500 µg/ml of Mg-Ti particles (Fig. 3.6c) are compared to control samples (Fig. 3.6a) with no particles present. The cells in the control groups and cells treated with 500 µg/ml Mg only are well attached, well spread and viable. Cells treated with Mg-Ti at 500 µg/ml, however, are in the process of retracting their membranes or have completely balled up and died. It should be noted that the use of low kV secondary electron imaging of gold coated samples (which are not grounded to the SEM stage) provides significant contrast between cells, the substrate polymer, and various protein-based structures (dark and bright spots) seen on the cells and on the substrate. The percent cell viability versus particle concentrations of Mg and Mg-Ti groups (Fig 3.7) shows a decrease in viability with concentration for both particle types. The cells are completely dead for Mg-Ti group at 750 µg/ml and higher, while cells completely died for Mg group at 1500 µg/ml. Twice the particle concentration is needed to kill all cells for the Mg group than the Mg-Ti group. Tukey's post hoc test showed that there are significant differences in cell viability among all particle concentrations within each particle-type group ($p < 0.05$, Mg and Mg-Ti), except between 750 and 1000 µg/ml ($n=3$). Also, Tukey's post hoc test showed that there are significant differences in cell viability between the particle-type groups ($p < 0.05$, $n=3$). It should be noted that

particles were visually observed to remain present in the solution for over 12 h and were continuing to corrode for at least this time period.



500 μm

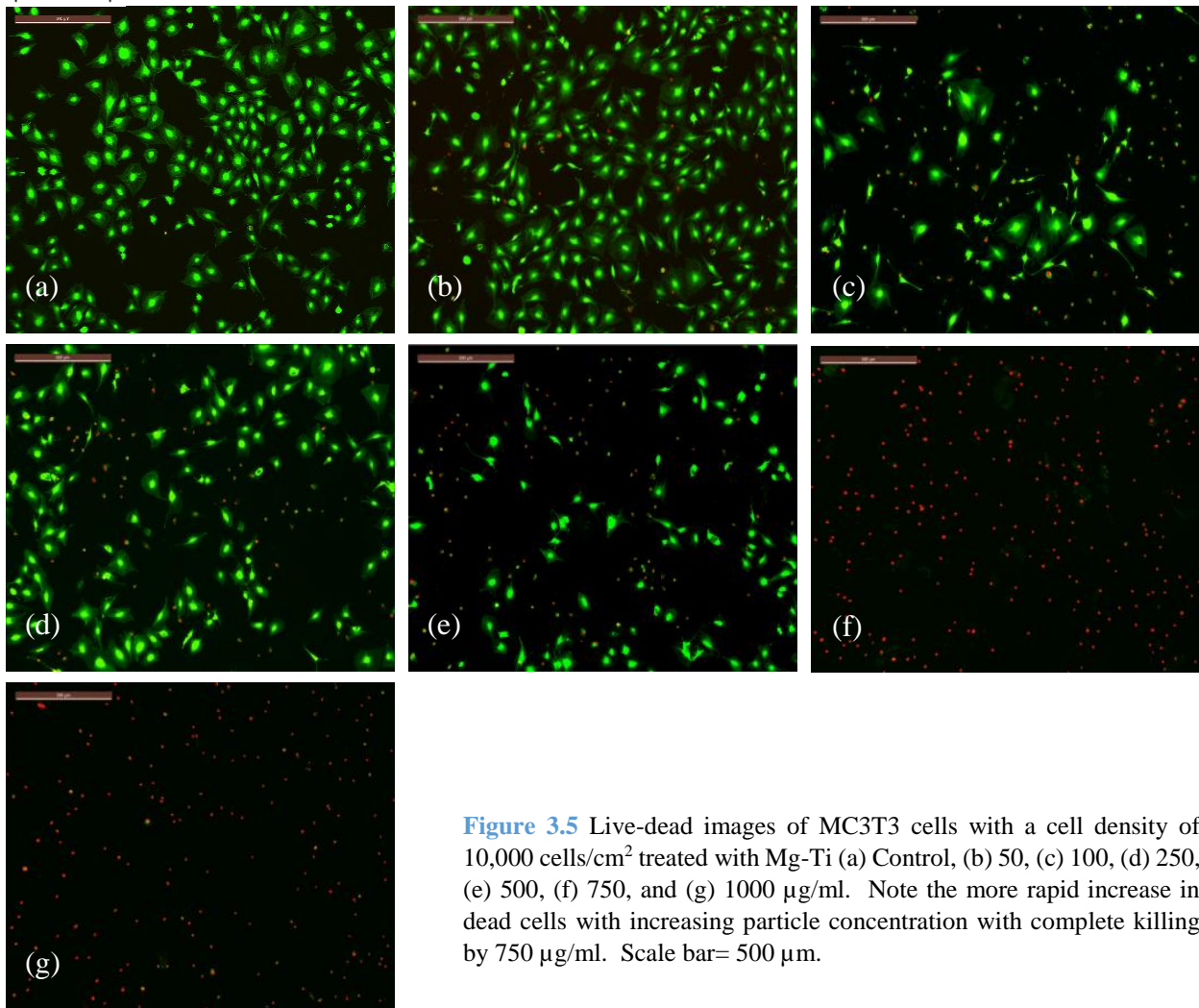


Figure 3.5 Live-dead images of MC3T3 cells with a cell density of 10,000 cells/cm² treated with Mg-Ti (a) Control, (b) 50, (c) 100, (d) 250, (e) 500, (f) 750, and (g) 1000 $\mu\text{g/ml}$. Note the more rapid increase in dead cells with increasing particle concentration with complete killing by 750 $\mu\text{g/ml}$. Scale bar= 500 μm .

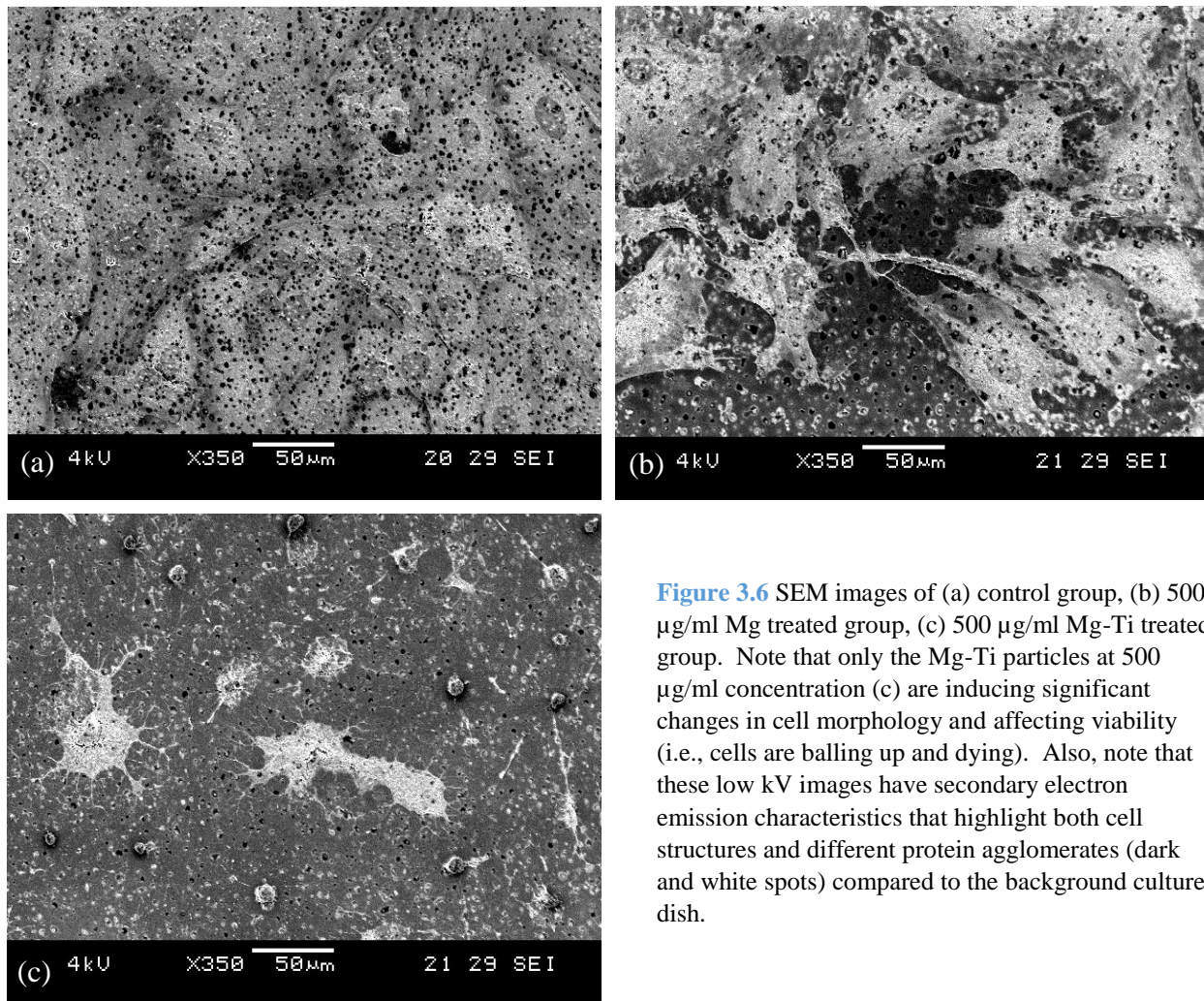


Figure 3.6 SEM images of (a) control group, (b) 500 µg/ml Mg treated group, (c) 500 µg/ml Mg-Ti treated group. Note that only the Mg-Ti particles at 500 µg/ml concentration (c) are inducing significant changes in cell morphology and affecting viability (i.e., cells are balling up and dying). Also, note that these low kV images have secondary electron emission characteristics that highlight both cell structures and different protein agglomerates (dark and white spots) compared to the background culture dish.

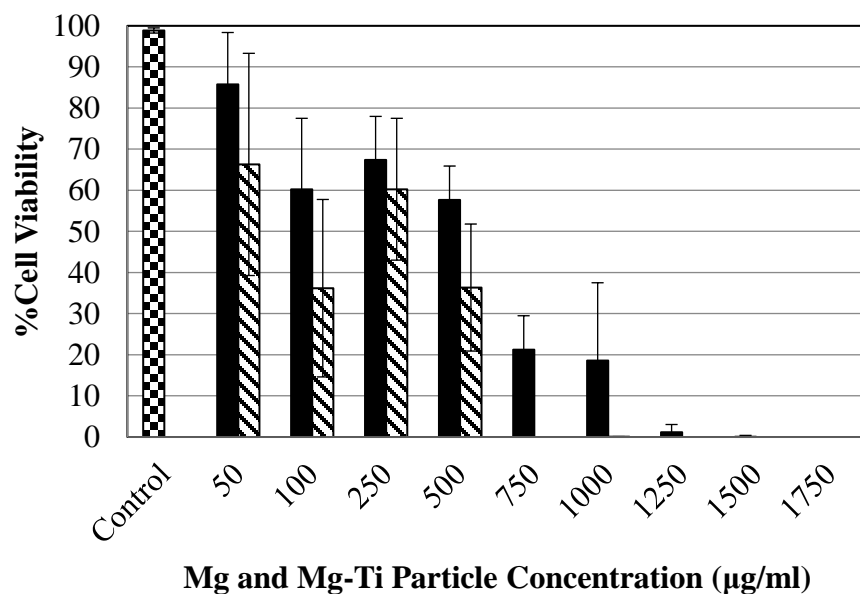


Figure 3.7 Cell viability as a function of particle concentration when MC3T3 cells with cell density of 10,000 cells/cm² are treated with Mg or Mg-Ti particle groups for t= 24 hours.

3.3.4 pH Measurements of Mg and Mg-Ti Microparticles

pH increased as particle concentration increased, with pH at 7.5 when no particles were added and around 9.0 at particle concentrations of 2500 $\mu\text{g/ml}$ at $t=0$ hour (i.e., as soon as the measurement could be taken after creating the solutions and taking the measurement), for both Mg and Mg-Ti groups (Fig. 3.8). This pH drops slightly to 8.6 for 2500 $\mu\text{g/ml}$ at $t=24$ hours. The pH at the particle concentrations required to kill all cells was 8.5 (for Mg at 1500 $\mu\text{g/ml}$) and 8.2 (for Mg-Ti at 750 $\mu\text{g/ml}$), respectively, which did not vary that much over time for $t=0$ to 24 hours. Post hoc Tukey tests were performed to show that there were no significant differences in pH between Mg and Mg-Ti groups for both times ($p < 0.05$, $n=3$).

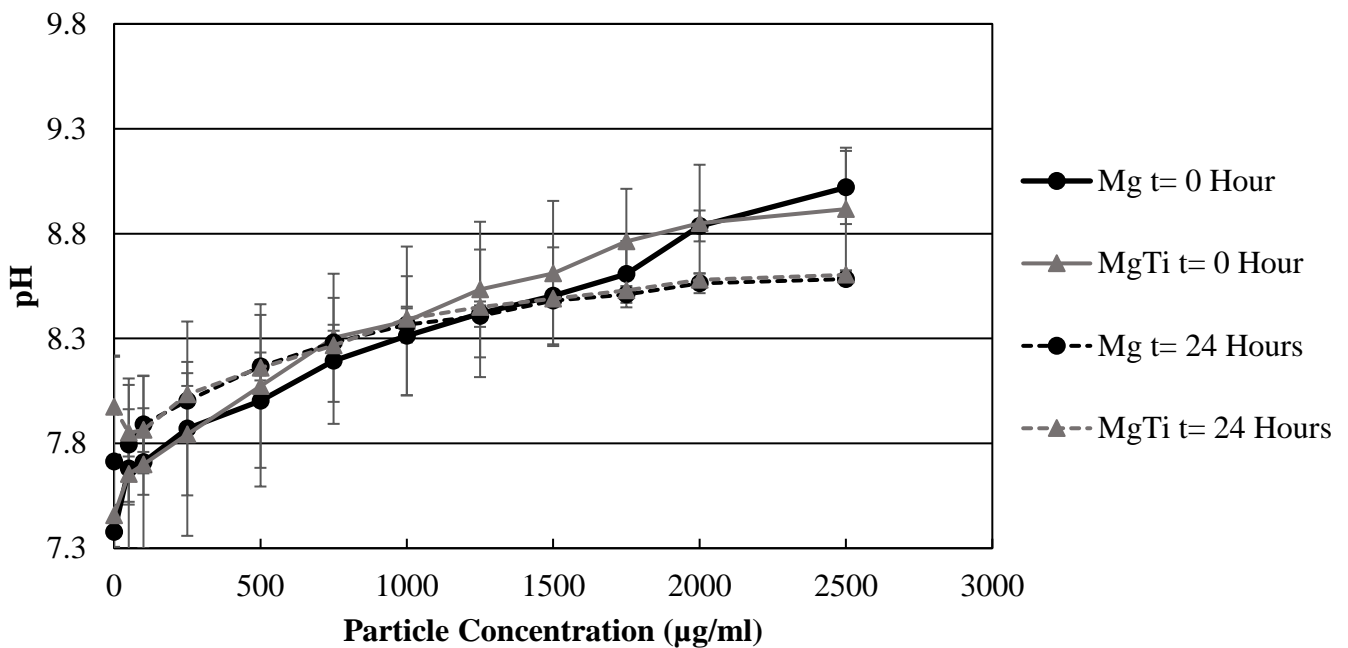


Figure 3.8 The graph shows pH of Mg particles and Mg-Ti particles corroding in complete media for concentrations between 0 and 2500 $\mu\text{g/ml}$ for $t=0$ hour and $t=24$ hours. The pH increase is particle concentration dependent ($P < 0.05$), but is not dependent on the presence of Ti coupling.

3.3.5 MC3T3 Cell Viability at Different pH Range

Cell viability at pH ranging from 7.5 to 9 adjusted by sodium hydroxide (without particles) was measured at $t = 24$ hours. Average cell viability is 99.31%, 93.71%, 85.77%, and 80.92% for pH of 7.5, 8, 8.5, and 9, respectively (Fig. 3.9). Tukey's post hoc tests show that pH of 7.5 group is significantly different from all groups except pH of 8 group. pH of 8 group is only significantly different from pH of 9 group, while pH of 8.5 is only significantly different from pH of 7.5 group. pH of 9 group is significantly different from all groups except pH of 8.5 group. It should be noted that there is significantly greater ($p < 0.05$) killing of cells at identical pH's, in the particle containing samples.

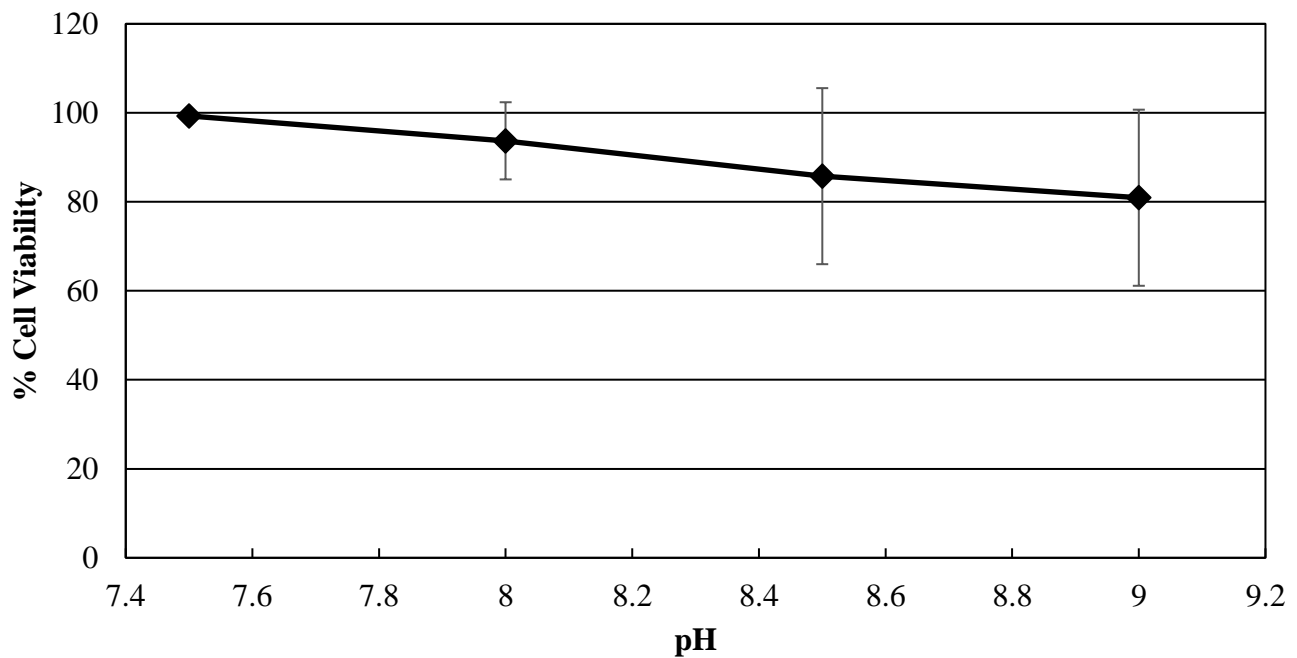


Figure 3.9 Cell viability in NaOH adjusted media at pH of 7.5, 8, 8.5, and 9. This pH range roughly corresponds to the pH of Mg and Mg-Ti particle concentrations used to kill MC3T3 cells, from 50 to 1750 $\mu\text{g/ml}$.

3.4 Discussion

This study has demonstrated that particles of Mg and galvanically coupled Mg-Ti can kill MC3T3 cells relatively rapidly (within 24 hours). Shetty et al. did a similar study using

mechanically alloyed Mg-Ti microparticles to investigate its in-vitro cytotoxicity and also found that Mg-Ti is more potent than Mg alone [32]. Mechanically alloyed Mg-Ti couple is obtained by powder processing technique called ball milling, which involves mixing or grinding metallic powder particles to form an alloy in a high energy ball mill. Unlike sputtering, which deposits a very small fraction of Ti, mechanical alloying allows a larger ratio of Ti on Mg, where Shetty et al. used 50:50 Mg and Ti ratio [32]. Due to larger ratio of Ti for mechanically alloyed Mg-Ti microparticles, Shetty et al. was able to detect both Mg and Ti using EDS, unlike the sputtering [32], which only deposited such small Ti layer that EDS could not detect the Ti element. When Shetty et al. treated MC3T3 cells with 1000 $\mu\text{g/ml}$ of Ti, Mg, and Mg-Ti particles for $t=24$ hours, the cell viability was 66.3%, 26.9%, and 0.2%, respectively [32]. This result is very similar to the result reported here, where the cell viability of 1000 $\mu\text{g/ml}$ of Mg and Mg-Ti particles was 18.62% and 0.02%. Experimental procedures were exactly the same between this study and the study done by Shetty et al., except for the galvanic coupling technique (sputtering vs. mechanically-alloyed) and the sterilization process. While the sterilization steps were all eliminated in this study, Shetty et al. sterilized the particles by soaking the particles in 100% ethanol and then transferred to a cell culture plate, where the particles were air dried in the cell culture hood. The samples were then further sterilized with UV light for 5-10 minutes. Therefore, different galvanic coupling methods and sterilization process of the particles did not have significant effect on the Mg and Mg-Ti microparticles, since the cytotoxic effect of these particles were the same.

The galvanically coupled Mg-Ti particles were statistically more potent than Mg particles alone at killing cells, requiring a lower concentration of particles to have the same level of killing. In fact, complete cell killing with Mg-Ti occurred at about half the concentration of Mg

alone (750 $\mu\text{g/ml}$ Mg-Ti vs. 1500 $\mu\text{g/ml}$ Mg, respectively). There were no significant differences in the pH measurements between Mg and Mg-Ti groups either immediately after the exposure or after 24 hours of immersion and yet, there was greater killing in particle-containing solutions at equivalent pH's, which implies that the pH is not the only cause of cell killing. That is, cells treated with media adjusted with sodium hydroxide (NaOH) only to the same pH level as those with highest particle concentration that killed all cells (pH of 8.5 for Mg group at 1500 $\mu\text{g/ml}$ and pH of 8.2 for Mg-Ti group at 750 $\mu\text{g/ml}$) had high viability. Although the pH levels were the same, the pH adjusted by NaOH did not have the same killing effect on cells as the Mg and Mg-Ti particles. So the question remains: why does Mg-Ti group kill more cells than Mg?

Local variations of cell viability based on random particle distribution throughout the dish showed that the particles have to be close to the cells to cause cell death. Cells in regions where there were few or almost no particles tended to be viable, even if there were particles some distance away, killing cells immediately next to them. Although the actual distance from the particle that affects cell killing is unknown, it is clear that proximity of particles affects cell viability. This observation also shows that pH is not the only factor that affects cell viability. pH is increased homogeneously throughout the entire solution, and yet, only the cells immediately next to the particles were found dead. Since the particles are roughly the same or slightly larger than an average mammalian cell, phagocytosis of particle by individual cells is not possible, and therefore unlikely to be a source of cell killing.

Many studies focus on the oxidation reactions of metal and cytotoxicity of the released metal ions, especially transition metals, such as iron and chromium [33-36]. Indeed, cytotoxicity of Mg studies have used the corrosion product solution extracts in cell culture [18, 26, 37] and these have generally found that Mg ions alone are not cytotoxic except at high concentrations.

However, reduction reactions have also been found to be important in affecting cell viability due to the production of reactive oxygen intermediate species. Dhar et al. reported that during oxygen reduction, about 10 % of the products are reactive oxygen intermediates that can have killing effects on bacteria [28].

Ehrensberger et al. showed that applying cathodic potential on Ti affects cell viability in a voltage- and time-dependent manner [29-30]. Haeri et al. also showed reduction-induced apoptosis of cells when cathodic potential is applied to CoCrMo alloy [31]. Both studies imply that excess electrons drive reduction reactions of water and/or oxygen in solution and produce ROS, such as super oxide anion, hydroxyl radicals, peroxy radicals, alkoxy, and hydrogen peroxide, which can be very harmful to cells by disrupting cell function, damaging DNA, and promoting cell apoptosis [38-39]. The partial covering of the Ti layer on Mg particle via sputtering will enhance the rates of both oxidation reactions of Mg and reduction reaction of water and/or oxygen on the Ti surface. The surface of Ti essentially provides a catalyst for the reduction reactions, separating the oxidation and reduction spatially. Ti surfaces may also preferentially generate ROS during reduction on their surfaces. This is a known effect during photoelectrochemistry of TiO₂ [40-44]. Therefore, this study hypothesizes that galvanic coupling of Mg and Ti is expected to have higher cytotoxic ability than Mg alone due to the increase in reduction reactions, thereby producing more ROS. Further experiments are needed to support this hypothesis, such as direct measurement of the extracellular ROS concentration. Still, this hypothesis is indirectly supported in this study by the fact that the proximity plays an important role in cell killing, since ROS is very unstable and reacts almost immediately, making it more difficult for ROS to kill cells that are too far away from the generation source.

Alternatively, it is possible that Mg ions are playing the primary role in cell toxicity and that galvanic coupling is more quickly generating high levels of Mg ions for an enhanced killing effect compared to Mg only particles. Mg ions alone can have cytotoxic effects at high enough concentrations and these may be a significant mechanism of killing. The work by Gu et al. [18], Gao et al. [26], and Wang et al. [37] studied Mg-ion effects on different cell lines including MC3T3 cells and showed some adverse effects on cells. However, the Mg ion concentrations to cause adverse effects were variable between them, with the study by Wang et al. reporting higher Mg ion concentrations than the maximum concentration used in this study for Mg ions to have cytotoxic effect on MC3T3 cells.

Despite the lower concentration of Mg ions produced in this study, compared to Wang et al., Mg particles that were actively corroding killed cells completely, which may indicate that Mg ions are not the primary cytotoxic factor.

These observations indicate that the particles are generators of species that ultimately affect the variability of cells proximal to the particle. It also implies that there may be an element of cellular consumption (or reaction) of these presumed ROS species that may be at play, so that the cellular density proximal to the particles may reduce the killing effect [29].

Future studies will explore the effect of pH alone on cell viability, the role of cellular density on efficacy of particles, the effect of proximity of particles to cells, and the time-course of the killing effects. In addition, efforts for direct measurement of ROS generation will be explored to assess whether, in fact, reduction reactions do generate intermediate radical species.

The weaknesses of the current study involve high variability of killing based on certain factors. First, not all Mg particles are sputtered with enough or any Ti, and/or the sputtered Ti layer are not electrically connected to the Mg substrate. Mg particles are widely and randomly

distributed and spread out on the dish to insure maximum sputtering of these Mg particles with Ti; however, since it is impossible to get a perfect monolayer of Mg particles, there must be some particles that are underneath other particles that do not get any exposure to Ti during sputtering. The fraction of these particles are unknown and this factor will vary for each sputtering process. Second, the random distribution of particles yielded higher local particle density in some regions and much lower particle density in other regions. This randomness yielded a wider variability of cell viability in the measurements. Third, although careful measures are taken to prevent significant loss of the particles during the processes of measuring, sputtering, and transferring the particles from the dish (in which they were sputtered) to the tube to make aliquots of the appropriate concentration, there still was a loss of particles, which will also vary. Loss of particles will lead to lower concentration than the calculated concentrations, ultimately affecting cell viability. Fourth, the size and shape of particles, and the potential variability in the sputtering will affect the rates of corrosion and the duration of the effect. In this work, the particles were highly variable in sizes and shapes giving varying corrosion rates and durations of actions, although most particles remained present for most of the initial time period of 24 h. In addition, the distribution of shapes and sizes and the nature of the sputtering process (line-of-sight) adds a level of variability that may have influenced the results presented. Despite these weaknesses, the results of this study still show that Mg and Mg-Ti particles kill cells in a dosage-dependent manner and that Mg-Ti kills cells more efficiently than Mg alone.

Galvanic coupling of Mg-Ti particles, or even Mg and Ti implants may be beneficial in a number of different applications including cancer therapy and local bacterial infections. In orthopedic applications, for example, Ti is one of the most widely used materials. Galvanically coupling a Ti implant with Mg (either in particle form or embedded in the device) may be able to

kill bacteria growing as biofilms on the implant surface or prevent biofilms from forming at the implant surface. Implant-centered infections are known to be very persistent and hard to treat even with antibiotics, usually resulting in the removal of the implant [45-46]. As stated previously, Mg has already been reported to prevent infections at the surgical site [5]. Even though the killing of Mg-Ti does not discriminate bacteria and mammalian cells, proximity will be an advantage since the galvanic couple can prevent biofilm formation at the implant surface without harming more remote tissue or bone surrounding the implant.

In addition, this effect will be transient whereby Mg will corrode for a few weeks after the surgery to prevent any post-surgery infections and then once completely corroded, the reduction reactions will stop and the Mg will degrade away, leaving only the Ti implant intact. The only challenge is to design an implant that incorporates Mg without disintegrating the implant in terms of its strength and performance. Here, it is important to note that very small quantities of Mg are sufficient to lower the potential of the implant to -1 V (vs. Ag/AgCl) or more [47].

Mg and/or Mg-Ti particles may be used to kill bacterial infections that are more resistant to antibiotics, in the form of cream or in aqueous solution. Also, since Mg has been reported to be able to reduce tumors, particles of Mg or Mg-Ti can be designed to target and kill tumors. Again, because of the relatively short duration of the effect, these particles can be delivered to kill in proximity to the particles themselves and then after a period of time from 12 to 40 hours, the particles will corrode away and the local biological system can recover. Particle delivery may be possible by direct injection to the tumor site, or by perhaps using receptor-ligand like approaches to have the particles target specific tumor cells. These concepts are in the early conceptual stages of development. The duration will depend on particle size (larger results in

longer), shape, and roughness. For Mg-Ti particles, the oxidation products will be magnesium hydroxide (MgOH) and the remaining thin (about 5 nm thick) Ti half-shell. Mg oxidation products are non-toxic and the infinitesimal amount of Ti remaining is not likely to have any significant effects on the local tissue as Ti particles are not known to elicit significant adverse biological reactions in vivo [48-50].

There are previous studies reporting other galvanically-coupled particles to control biological processes. Cao et al. embedded silver (Ag) nanoparticles on Ti surface via Ag plasma immersion ion implantation process so that these Ag nanoparticles can inhibit the growth of bacteria, with a potential application of utilizing this method on Ti-based implantable devices [51]. Although the exact mechanism is still being debated, one hypothesis is that the Ag ions released is contributing to cell death, by disrupting the cell membrane [51]. However, in this case, the standard electrode potential of Ti is more cathodic than the standard electrode potential of Ag, unlike Mg and Ti coupling, where Mg is more cathodic. So while the Mg-Ti galvanic coupling enhances the rates of oxidation reaction of Mg and reduction reaction of water and oxygen, Ti-Ag galvanic coupling will actually slow the oxidation reaction of Ag. In fact, this will cause the Ti surrounding the Ag to potentially oxidize. The antimicrobial effect of Ag is dependent upon size and shape, where Ag is most effective as nanoparticles, small enough to interact with the bacterial membrane and enter inside the cell, reacting with sulfur-containing proteins and phosphorus-containing DNA, and ultimately disrupting the normal functions of the bacteria [52]. Ag also produces ROS that influence the bacterial cells [53]. However, large release of Ag ions can travel and accumulate at distant locations and adversely affect human body [53].

Galvanic coupling of other metals is possible and may have similar effects in terms of cell killing. For example, iron (Fe), zinc (Zn), and copper (Cu) are all essential metals that are found in the body that can easily replace Mg in the galvanic couple. However, the electrode potential difference between Zn, for example, and Ti is smaller than the electrode potential difference between Mg and Ti, and so the corrosion rate of Zn will not be as accelerated as that of Mg.

While the use of Mg and galvanic coupling of Mg and Ti in particle or other form opens up possibilities for therapeutic effect, these results also raise questions concerning the use of bulk Mg alloy implants since the reduction reactions associated with the rapid corrosion of these devices may generate significant reactive oxygen intermediates that may lead to significant cellular killing in the vicinity of the device, regardless of the non-toxic nature of the oxidation products. This work is only preliminary in the advancement of an alternative therapeutic approach to cancer or infection and much additional investigation is needed. However, the basic killing effect of such galvanically coupled particles has been demonstrated in this study.

3.5 Conclusion

This study has demonstrated that both Mg and Mg-Ti galvanically-coupled particles are cytotoxic with Mg-Ti particles more potent than Mg particles alone. Also, the pH shift seen in the two groups was similar while the killing efficiency was greater with the galvanically coupled Mg-Ti particles, demonstrating that there are more factors affecting cell viability than just the pH of the solution.

These galvanically coupled particles (and alloys) represent a novel concept in the potential treatment of infection or cancer and future work on this approach should explore the

specific mechanism of action which we hypothesize is related to the reactive oxygen intermediates generated during the associated reductions.

3.6 Acknowledgements

This work was supported, in part, by DePuy Synthes and the Cheney International Faculty Fellowship at the University of Leeds.

3.7 Supplementary Images

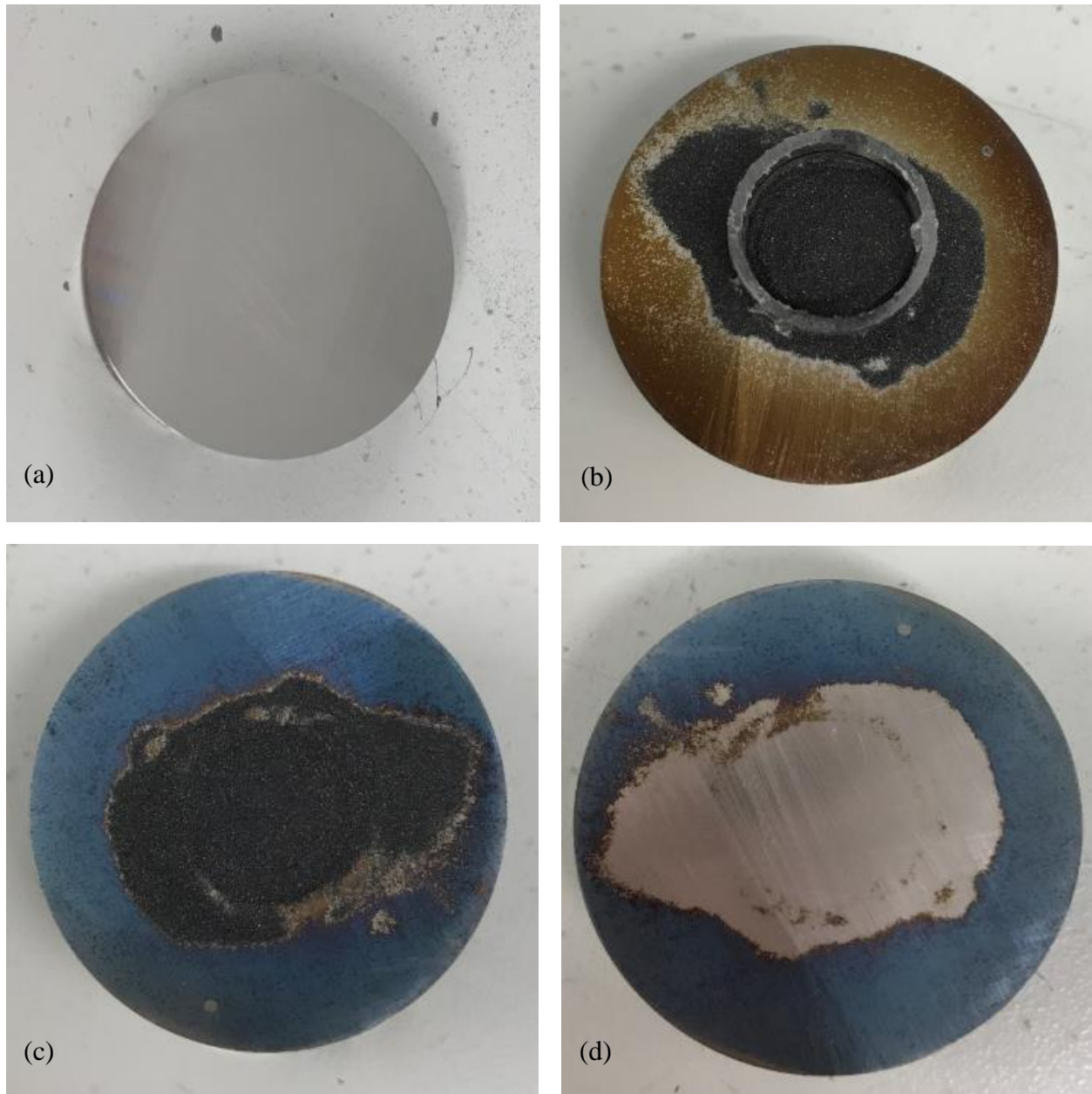


Fig. 3.10 (a) Stainless steel (SS) disc after polished with 320, 400, and 600 grit sandpapers, (b) stainless steel disc with Mg powder placed inside the plastic ring (although there is leakage) and sputtered for ten minutes, showing yellowish discoloration of the SS disc, (c) SS disc with Mg powder sputtered for more than 20 minutes, showing blue discoloration of the SS disc, and (d) SS disc after Mg powder has been removed to show that there is no discoloration where the Mg powder has been since SS underneath Mg powder was not exposed.

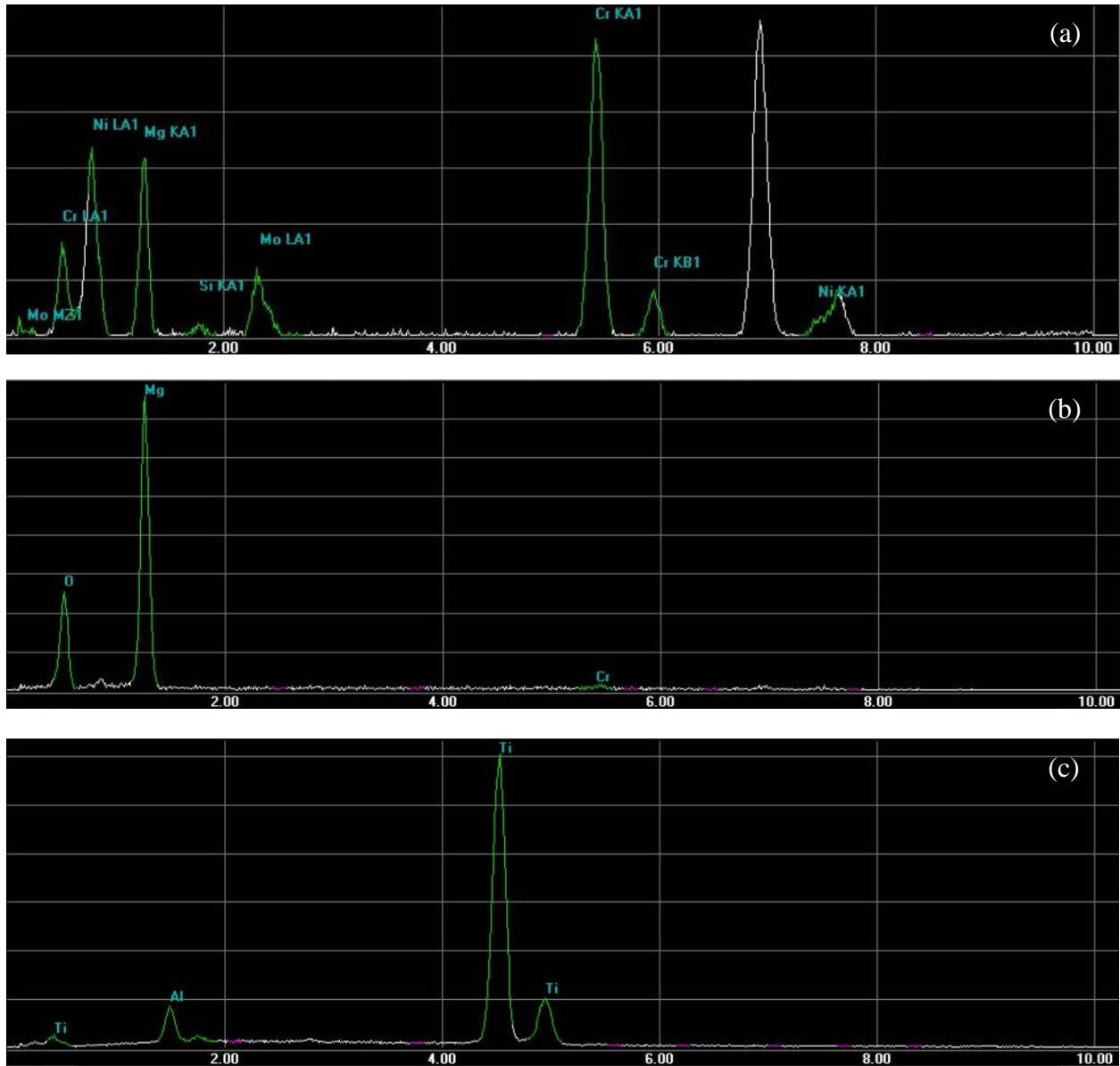


Fig. 3.11 EDS on (a) mostly stainless steel (SS) disc (Mg is detected as well because there also must be some Mg particles), (b) mostly Mg powder (where Mg powder is densely packed), and (c) Ti6Al4V disc. Although Ti has been sputtered for very long time, and there was discoloration of the disc, Ti could not be detected on both SS disc and Mg powder. EDS was measured on Ti6Al4V disc to show that EDS can detect Ti, just in larger amount.

Mg Trial 1				Concentration		
Z	Element	Line	K-Ratio	wt%	at%	Cmpd wt%
8	O KA1	0.523	0.1441	25.442	34.153	25.442
12	Mg KA1	1.254	0.6337	74.558	65.847	74.558
			Total	100	100	100
Mg Trial 2				Concentration		
Z	Element	Line	K-Ratio	wt%	at%	Cmpd wt%
8	O KA1	0.523	0.0862	16.012	22.468	16.012
12	Mg KA1	1.254	0.7603	83.988	77.532	83.988
			Total	100	100	100
Mg Trial 3				Concentration		
Z	Element	Line	K-Ratio	wt%	at%	Cmpd wt%
8	O KA1	0.523	0.018	3.543	5.288	3.543
12	Mg KA1	1.254	0.9432	96.457	94.712	96.457
			Total	100	100	100

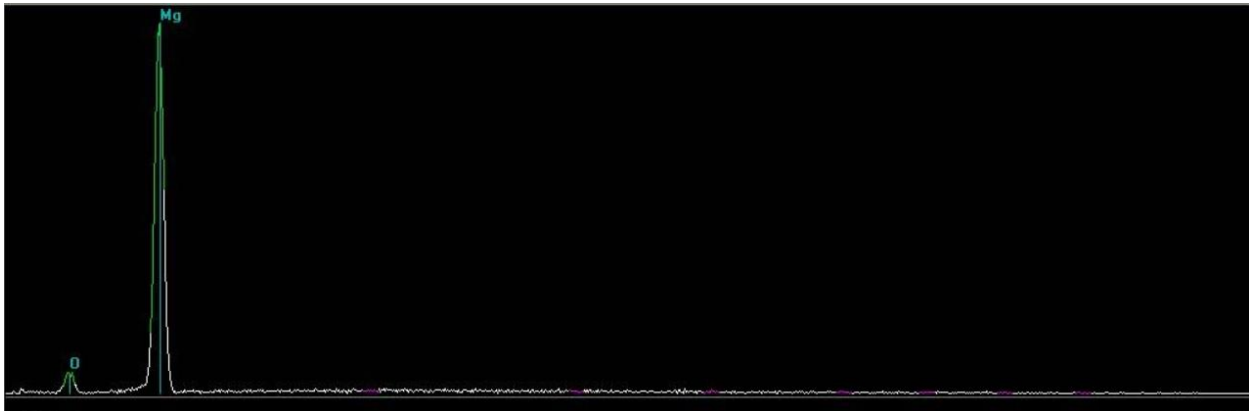


Fig. 3.12 EDS on Mg powder shows magnesium (Mg) and oxygen (O).

Mg-Ti Trial 1				Concentration		
Z	Element	Line	K-Ratio	wt%	at%	Cmpd wt%
8	O KA1	0.523	0.0872	16.173	22.676	16.173
12	Mg KA1	1.254	0.7581	83.827	77.324	83.827
22	Ti KA1	4.51	0	0	0	0
			Total	100	100	100
Mg-Ti Trial 2				Concentration		
Z	Element	Line	K-Ratio	wt%	at%	Cmpd wt%
8	O KA1	0.523	0.0225	4.421	6.568	4.421
12	Mg KA1	1.254	0.9295	95.579	93.432	95.579
22	Ti KA1	4.51	0	0	0	0
			Total	100	100	100
Mg-Ti Trial 3				Concentration		
Z	Element	Line	K-Ratio	wt%	at%	Cmpd wt%
8	O KA1	0.523	0.0462	8.883	12.906	8.883
12	Mg KA1	1.254	0.8617	91.117	87.094	91.117
22	Ti KA1	4.51	0	0	0	0
			Total	100	100	100

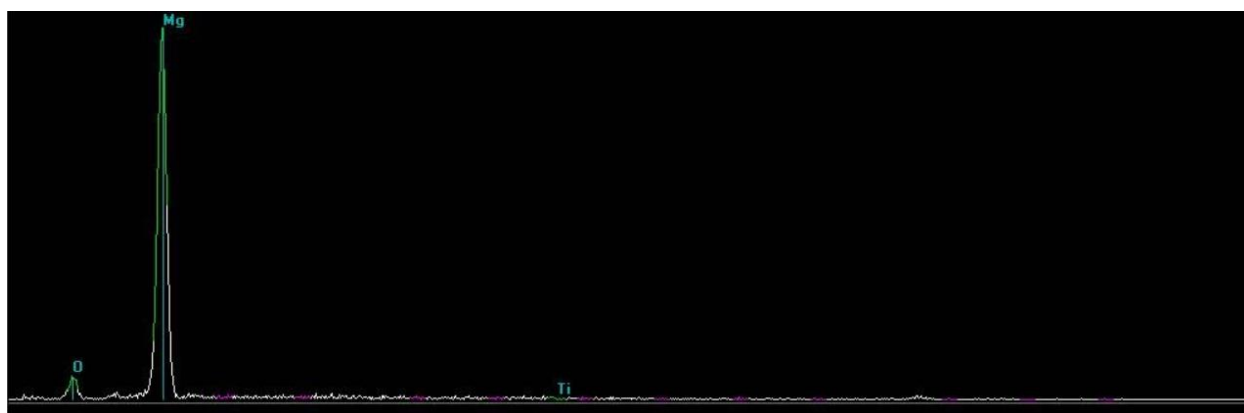


Fig. 3.13 EDS on Mg-Ti powder still shows only magnesium (Mg) and oxygen (O).

References

1. Waizy H, Seitz JM, Reifenrath J, Weizbauer A, Bach FW, Meyer-Lindenberg A, Denkena B, Windhagen H. Biodegradable Magnesium Implants for Orthopedic Applications, *J. Mater. Sci.* 2013; 48: 39-50.
2. Wong HM, Yeung KWK, Lam KO, Tam V, Chu PK, Luk KDK, Cheung KMC. A Biodegradable Polymer-Based Coating to Control the Performance of Magnesium Alloy Orthopaedic Implants, *Biomaterials* 2010; 31: 2084-96.
3. Waksman R, Erbel R, Di Mario C, Bartunek J, de Bruyne B, Eberli FR, Erne P, Haude M, Horrigan M, Ilesley C, Böse D, Bonnier H, Koolen J, Lüscher, Weissman NJ. Early- and Long-Term Intravascular Ultrasound and Angiographic Findings after Bioabsorbable Magnesium Stent Implantation in Human Coronary Arteries, *JACC: Cardiovasc. Interv.* 2009; 2: 312-20.
4. Barlis P, Tanigawa J, Di Mario C. Coronary Bioabsorbable Magnesium Stent: 15-Month Intravascular Ultrasound and Optical Coherence Tomography Findings, *Eur. Heart J.* 2007; 28: 2319.
5. Witte F. The History of Biodegradable Magnesium Implants: A Review, *Acta Biomater.* 2010; 6: 1680-92.
6. Wilflingseder P, Martin R, Papp Ch. Magnesium Seeds in the Treatment of Lymph- and Haemangiomas, *Chir. Plastica* 1981; 6: 105-16.
7. Staindl O. Treatment of Haemangiomas of the Face with Magnesium Seeds, *Arch. Otorhinolaryngol.* 1989; 246: 213-17.

8. Witte F, Kaese V, Haferkamp H, Switzer E, Meyer-Lindenberg A, Wirth CJ, Windhagen H. In Vivo Corrosion of Four Magnesium Alloys and the Associated Bone Response, *Biomaterials* 2005; 26: 3557-63.
9. Kraus T, Fischerauer SF, Hänzi AC, Uggowitz PJ, Löffler JF, Weinberg AM. Magnesium Alloys for Temporary Implants in Osteosynthesis: In Vivo Studies of Their Degradation and Interaction with Bone, *Acta Biomater.* 2012; 8: 1230-38.
10. Zhang E, Xu L, Yu G, Pan F, Yang K. In Vivo Evaluation of Biodegradable Magnesium Alloy Bone Implant in the First 6 Months Implantation, *J. Biomed. Mater. Res. A* 2009; 90A: 882-93.
11. Janning C, Willbold E, Vogt C, Nellesen J, Meyer-Lindenberg A, Windhagen H, Thorey F, Witte F. Magnesium Hydroxide Temporarily Enhancing Osteoblast Activity and Decreasing the Osteoclast Number in Peri-Implant Bone Remodelling, *Acta Biomater.* 2010; 6: 1861-68.
12. Katayanagi K, Miyagawa M, Matsushima M, Ishikawa M, Kanaya S, Ikehara M, Matsuzaki T, Morikawa K. Three-Dimensional Structure of Ribonuclease H from *E. Coli*, *Nature* 1990; 347: 306-9.
13. Needham JV, Chen TY, Flake JJ. Novel Ion Specificity of a Carboxylate Cluster Mg(II) Binding Site: Strong Charge Selectivity and Weak Size Selectivity, *Biochemistry* 1993; 32: 3363-7.
14. Yang W, Hendrickson WA, Crouch RJ, Satow Y. Structure of Ribonuclease H Phased at 2 Å Resolution by MAD Analysis of the Selenomethionyl Protein, *Science* 1990; 249: 1398-405.

15. Cowan JA. Structural and Catalytic Chemistry of Magnesium-Dependent Enzymes, *Biometals* 2002; 15: 225-235.
16. Witte F, Hort N, Vogt C, Cohen S, Kainer KU, Willumeit R, Feyerabend F. Degradable Biomaterials Based on Magnesium Corrosion, *Curr. Opin. Solid State Mater. Sci.* 2008; 12: 63-72.
17. Song G. Control of Biodegradable Magnesium Implant Material, *Corros. Sci.* 2007; 49: 1696-701.
18. Gu X, Zheng Y, Cheng Y, Zhong S, Xi T. In Vitro Corrosion and Biocompatibility of Binary Magnesium Alloys, *Biomaterials* 2009; 30: 484-98.
19. Tan ALK, Soutar Am, Annergren IF, Liu YN. Multilayer Sol-Gel Coatings for Corrosion Protection of Magnesium, *Surf. Coat. Tech.* 2005; 198: 478-82.
20. Li L, Gao J, Wang Y. Evaluation of Cyto-Toxicity and Corrosion Behavior of Alkali-Heat-Treated Magnesium in Simulated Body Fluid. *Surf. Coat. Tech.* 2004; 185: 92-8.
21. Saris NEL, Mervaala E, Karppanen H, Khawaja JA, Lewenstam A. Magnesium: An Update on Physiological, Clinical and Analytical Aspects, *Clin. Chim. Acta* 2000; 294: 1-26.
22. Song G, Song S. A Possible Biodegradable Magnesium Implant Material, *Corros. Sci.* 2007; 9: 298-302.
23. Zeng R, Dietzel W, Witte F, Hort N, Blawert C. Progress and Challenge for Magnesium Alloys as Biomaterials, *Adv. Eng. Mater.* 2008; 10: B3-B14.
24. Williams D. New Interests in Magnesium, *Med. Device Technol.* 2006; 17: 9-10.
25. Liu C, Xin Y, Tian X, Chu PK. Degradation Susceptibility of Surgical Magnesium Alloy in Artificial Biological Fluid Containing Albumin, *J. Mater. Res.* 2007; 22: 1806-14.

26. Gao JC, Qiao LY, Xin RL. Effect of Mg²⁺ Concentration on Biocompatibility of Pure Magnesium, *Front Mater. Sci.* 2010; 4: 126-31.
27. Robinson DA, Griffith RW, Shechtman D, Evans RB, Conzemi MG. In Vitro Antibacterial Properties of Magnesium Metal Against *Escherichia Coli*, *Pseudomonas Aeruginosa* and *Staphylococcus Aureus*, *Acta Biomater.* 2010; 6: 1869-77.
28. Dhar HP, Howell DW, Bockris JOM. The Use of In Situ Electrochemical Reduction of Oxygen in the Diminution of Adsorbed Bacteria on Metals in Seawater, *J. Electrochem. Soc.* 1982; 129: 2178-82.
29. Sivan S, Kaul S, Gilbert JL. The Effect of Cathodic Electrochemical Potential of Ti-6Al-4V on Cell Viability: Voltage Threshold and Time Dependence, *J. Biomed. Mater. Res. B* 2013; 101: 1489-497.
30. Ehrensberger MT, Sivan S, Gilbert JL. Titanium Is Not the Most Biocompatible Metal Under Cathodic Potential: The Relationship Between Voltage and MC3T3 Preosteoblast Behavior on Electrically Polarized CpTi Surfaces, *J. Biomed. Mater. Res. A* 2010; 93: 1500-509.
31. Haeri M, Wollert T, Langford GM, Gilbert JL. Electrochemical Control of Cell Death by Reduction-Induced Intrinsic Apoptosis and Oxidation-Induced Necrosis on CoCrMo Alloy *In Vitro*, *Biomaterials* 2012; 33: 6295-304.
32. Shetty, Dipika. *The Influence of Microparticles of Mg, Ti, and Mechanically Alloyed (50/50) MgTi on Mammalian Cell (MC3T3-E1) Viability*. Syracuse University, 2011.
33. Stohs S. Oxidative Mechanisms in the Toxicity of Metal Ions. *Free Radical Biol. Med.* 1995; 18: 321-36.

34. Sun Z, Wataha JC, Hanks CT. Effects of Metal Ions on Osteoblast-Like Cell Metabolism and Differentiation, *J. Biomed. Mater. Res.* 1997; 34: 29-37.
35. Wataha JC, Hanks CT, Sun Z. Effect of Cell Line on *In Vitro* Metal Ion Cytotoxicity, *Dent. Mater.* 1994; 10: 156-61.
36. Li Y, Wong C, Xiong J, Hodgson P, Wen C. Cytotoxicity of Titanium and Titanium Alloying Elements, *J. Dent. Res.* 2010; 89: 493-97.
37. Wang J, Witte F, Xi T, Zheng Y, Yang K, Yang Y, Zhao D, Meng J, Li Y, Li W, Chan K, Qin L. Recommendation for Modifying Current Cytotoxicity Testing Standards for Biodegradable Magnesium-Based Materials, *Acta Biomater.* 2015; 21: 237-49.
38. Circu ML, Aw TY. Reactive Oxygen Species, Cellular Redox Systems, and Apoptosis, *Free Radical Bio. Med.* 2010; 48: 749-62.
39. Fink SL, Cookson BT. Apoptosis, Pyroptosis, and Necrosis: Mechanistic Description of Dead and Dying Eukaryotic Cells, *Infect. Immun.* 2005; 73: 1907-16.
40. Visai L, De Nardo L, Punta C, Melone L, Cigada A, Imbriani M, Arciola CR. Titanium Oxide Antibacterial Surfaces in Biomedical Devices, *Int. J. Artif. Organs* 2011; 34: 929-46.
41. Blake DM, Maness PC, Huang Z, Wolfrum EJ, Huang J. Application of the Photocatalytic Chemistry of Titanium Dioxide to Disinfection and the Killing of Cancer Cells, *Separ. Purif. Method* 1999; 28: 1-50.
42. Tsuang YH, Sun JS, Huang YC, Lu CH, Chang WHS, Wang CC. Studies of Photokilling of Bacteria Using Titanium Dioxide Nanoparticles, *Artif. Organs* 2008; 32: 167-74.

43. Maness PC, Smolinski S, Blake DM, Huang Z, Wolfrum EJ, Jacoby WA. Bactericidal Activity of Photocatalytic TiO₂ Reaction: Toward an Understanding of Its Killing Mechanism, *Appl. Environ. Microb.* 1999; 65: 4094-8.
44. Fujishima A, Rao TN, Tryk DA. Titanium Dioxide Photocatalysis, *J. Photochem. Photobiol. C: Photochem. Rev.* 2000; 1: 1-21.
45. Ha KY, Chung YG, Ryoo SJ. Adherence and Biofilm Formation of Staphylococcus Epidermidis and Mycobacterium Tuberculosis on Various Spinal Implants, *Spine* 2005; 30: 38-43.
46. Campoccia D, Montanaro L, Arciola CR. The Significance of Infection Related to Orthopedic Devices and Issues of Antibiotic Resistance, *Biomaterials* 2006; 27: 2331-9.
47. Gilbert JL. Electrochemical Coupling of Metallic Biomaterial Implants for Biological Effect. Syracuse University (Syracuse, NY, US), assignee. Patent US9039764 B2. 26 May 2015.
48. Woodman JL, Jacobs JJ, Galante JO, Urban RM. Metal Ion Release from Titanium-Based Prosthetic Segmental Replacements of Long Bones in Baboons: A Long-Term Study, *J. Orthop. Res.* 1983; 1: 421-30.
49. Jacobs JJ, Skipor AK, Black J, Urban RM, Galante JO. Release and Excretion of Metal in Patients Who Have a Total Hip-Replacement Component Made of Titanium-Base Alloy, *J. Bone Joint Surg.* 1991; 73: 1475-86.
50. Bianco PD, Ducheyne P, Cuckler JM. Titanium Serum and Urine Levels in Rabbits with a Titanium Implant in the Absence of Wear, *Biomaterials* 1996; 17: 1937-42.
51. Cao H, Liu X, Meng F, Chu PK. Biological Actions of Silver Nanoparticles Embedded in Titanium Controlled by Micro-Galvanic Effects, *Biomaterials* 2011; 32: 693-705.

52. Morones JR, Elechiguerra JL, Camacho A, Holt K, Kouri JB, Ramírez JT, Yacaman MJ.
The Bactericidal Effect of Silver Nanoparticles, *Nanotechnology* 2005; 16: 2346-53.
53. Gallo J, Holinka M, Moucha CS. Antibacterial Surface Treatment for Orthopaedic
Implants, *Int. J. Mol. Sci.* 2014; 15: 13849-80.

4 The Effect of Cell Density, Proximity, and Time on the Cytotoxicity of Mg and Galvanically Coupled Mg-Ti Particles In Vitro

4.1 Introduction

Magnesium metal (Mg) and its alloys have been gaining attention as a biodegradable implant material due to many desirable properties. First, Mg has a similar density as that of natural bone, compared to other metals, such as titanium (Ti), cobalt-chromium alloy (CoCr), and stainless steel (SS) [1]. Physical and mechanical properties like elastic modulus and compressive yield strength of Mg is also closer to that of natural bone, reducing stress shielding, which is a common problem for other metallic implants [1]. Second, Mg ions are commonly found in the body, which are stored in muscle, soft tissue, and bone [2]. Third, Mg ions released from Mg-containing implants during degradation are known to stimulate bone regeneration, due to Mg ions increasing osteoblast activity [3-5].

Although the biological response to the implant may vary depending on the metal alloy type, tissue type, degree of vascularization, and other factors, generally Mg-based implants are considered very biocompatible, where Mg ion toxicity, alkaline toxicity, and hydrogen gas-induced necrosis have not been reported as major issues in *in vivo* studies. Significant increase in bone mineralization around the Mg-based implants were reported weeks after the surgery [3]. There were no adverse effects of hydrogen gas, which disappeared over time [3]. A study showed that there were different degradation rates based on the location of Mg alloy in the cortical bone or in the bone marrow, with an increased degradation rate in bone marrow compared to that of cortical bone [4]. There was bone tissue formation around the implant, with two distinct membranes between the implant and the bone, with a membrane closest to the Mg implant being fibrovascular and the other membrane close to the bone being synovial [4]. This

study also reported no gas bubbles [4]. Another study also reported new bone formation around the Mg implant without any inflammatory response, although significant amount of hydrogen gas was produced and initially impeded cortical bone healing process [5]. But without any intervention, hydrogen gas no longer became an issue as hydrogen gas evolution decreased over time [5].

Despite the common conception that Mg and Mg-based alloys are biocompatible, Mg and Mg-based alloys can actually be cytotoxic. The cytotoxicity of Mg is similar to that of applying cathodic potentials at the metal surface, which drives reduction reactions of water and oxygen due to excess electrons. Studies have shown that cathodic polarization of metal surface below -300 mV show significant reduction in cell area and cell viability [6-8]. Cathodic voltages over time increase reduction reactions, and Bokris et al. showed that reduction reactions can produce reactive oxygen species (ROS) [9]. ROS are widely known to play a role in inducing cell apoptosis, damaging DNA, or modifying proteins by cleaving disulfide bonds, as an example [10-13]. Harris et al. discovered that some types of tungsten-nickel-cobalt alloy particles produce enough ROS to cause oxidative damage to DNA and proteins [14]. Therefore, ROS generated from reduction reactions associated with oxidation of metal alloys are important to consider in terms of cytotoxicity of metallic biomaterials.

This study focuses on galvanically coupling Mg with Ti to accelerate the corrosion rate, a.k.a. the oxidation and reduction reaction rates, so that theoretically, more ROS can be generated in a shorter period of time, increasing the cytotoxicity of Mg. There has been very little work on the galvanic coupling of Mg metals with other metallic biomaterials to assess the effects of such couples. Kim and Gilbert recently showed that when Mg particles were galvanically coupled to Ti thin films formed by sputtering Ti onto the Mg particles, enhanced

killing effects were seen with Mg-Ti particles compared to Mg alone on MC3T3 cells *in vitro*, and that the killing effects were particle concentration dependent [15]. Di Virgilio et al. did similar work and evaluated *in vitro* cytotoxicity and genotoxicity of Mg particles by evaluating cell viability (in terms of particle concentrations), micronucleus induction in binucleated cells for chromosome breakage and/or whole chromosome loss, and DNA damage [16]. This study used the same Mg particles purchased from Alfa Aesar, with the same average size of the particles, as the particles used for this work. Similar to Kim and Gilbert's study [15] (Chapter 3), Di Virgilio et al. also found that rat osteosarcoma cell viability was concentration-dependent, where cell viability dropped as the concentration increased. Although most of Mg particles remained on the surface of the cells after 2 hours of treatment, some particles of smaller sizes, within 60 to 200 nm diameter, were found inside the cytoplasm within the vesicles (but not in the nucleus) [16]. Comet assay and micronucleus assay have been used to detect genotoxic effects of Mg particles, where Comet assay detects single and double DNA strand breaks, and micronucleus assay detects chemicals which induce the formation of small membrane bound DNA fragments (a.k.a. micronucleus), which are detected in cells with some DNA damage. Comet assay gave negative results, while micronucleus assay was positive on cells treated with low concentrations of Mg (ex. 25 µg/ml), which this study explained as the result of the physical presence of Mg particles in the cells affecting the cell division process, leading to chromosome loss [16]. Virgilio et al. concluded that the increase of pH, hydrogen evolution, and cell internalization of submicron particles resulted in cytotoxic and genotoxic effects. However, as this study reported, the particles they purchased from Alfa Aesar had the average size of $58.9 \mu\text{m} \pm 20.7 \mu\text{m}$ (SD), which are mostly bigger than an average mammalian cell. Although there are variations in size of these particles, most of the particles are large, in µm, not in nm. And so, while a few particles

may be small enough to be ingested, many particles cannot be ingested by phagocytosis, pinocytosis, or receptor-mediated endocytosis as the study suggested [16].

In this chapter, the cytotoxicity of Mg and Mg-Ti microparticles was evaluated in terms of particle concentration, cell density, time, and cell-particle cluster proximity. Cell viability and cell morphology were measured to evaluate cytotoxicity resulting from these particles in vitro, and pH of the solution at different particle concentrations for Mg and Mg-Ti was measured to assess the relative roles of reduction reactions and pH on cell killing.

4.2 *Materials and Methods*

4.2.1 *Preparation of Mg-Ti Microparticles*

Titanium (Alfa Aesar, Stock #:13975 and Lot #: C19N26), with 99.99% Ti purity, was sputtered onto Mg particles (Goodfellow, Product #: MG006021), with 99.8% Mg purity, for 5 minutes at 1.2 kV, 50 mA, and 100-200 mTorr. The presence of the Ti layer was evaluated as discussed previously [15]. Being a line-of-sight process, the sputtered Mg particles were only partially coated with a thin film of Ti, which allowed the Mg to directly corrode and the Ti surface to serve as the site of reduction reactions.

4.2.2 *Cell Density Effect*

Mouse pre-osteoblast cells, MC3T3 (ATCC #: CRL-2593), were seeded in a 6-well plate ($A= 9.6 \text{ cm}^2$) with cell densities of 5,000, 10,000, 20,000, and 30,000 cells/cm², and were left for $t= 12$ hours at 37 Celsius and 5% CO₂ for cell attachment onto the surface. Mg and Mg-Ti microparticle concentrations ranging from 50 to 1750 µg/ml were given to the cells of different cell density groups for $t= 24$ hours, with 2 ml of the solution given per well. The particles were randomly scattered throughout the dish.

Live/dead assay (Invitrogen #: L3224) was performed at t= 24 hours to measure cell viability using an optical microscope (Leica Instruments). Ten images were taken randomly per sample for three separate samples, and number of live and dead cells was counted manually using Image J for each image (n=30 images). Viability was determined as the number of live cells divided by the total number of cells (live and dead cells) in each image.

$$\%CV = \frac{\# \text{ of live cells}}{\# \text{ of live cells} + \# \text{ of dead cells}}$$

The results from the 10,000 cells/cm² group were reported in another paper to evaluate the effect of particle concentration on cell viability for a single cell density, but the data is shown in this paper again for comparison purposes with the other cell densities [15] (5,000, 20,000, and 30,000 cells/cm², not reported previously).

In selected cases, low voltage scanning electron microscopy (SEM) imaging (JEOL 5600, Dearborn MA) was used to assess the interactions between cells and particles. The low kV imaging mode, using secondary electrons, allows for highlighting of cellular features relative to the background tissue culture plastic and adsorbed proteins.

Not only percent viability over different particle concentrations were reported for different cell densities, the change of cell viability (CV) drop over the change of particle concentrations (PC) ranging from 0 to 100 µg/ml, essentially the slope ($\Delta CV/\Delta PC$), was measured for each cell density.

4.2.3 Time Effect

All cell culture conditions were the same as described in Section 4.2.2. This includes cell seeding and particle concentrations. For the present experiment, the 10,000 cells/cm² group was treated with either Mg or Mg-Ti for different times: t= 1, 3, 6, 12, 18, 24, 48, and 72 hours to assess how the particle corrosion processes affected cell viability over this timeframe. Live/dead

assay was used to determine cell viability (n=3 samples, and 10 micrographs per sample). The 24-hour group is the same data from Section 4.2.2, where the data were used to assess viability of the 10,000 cells/cm² density group, and again, these data have been reported in an earlier paper from our group (Chapter 3 of this thesis) [15]. Percent cell viability, as well as absolute numbers of live cells and dead cells were assessed over the timeframe of the experiments as there was some recovery and growth in viable cell numbers over this timeframe for some conditions. The number of live cells and dead cells reported is the sum of live or dead cells that were counted manually from the ten images per trial and total three trials per concentration (note: sum and not average, and therefore, no standard deviations).

4.2.4 Proximity Effect

Cells were seeded with a cell density of 10,000 cells/cm² in a 70 mm petri dish (A= 38.5 cm²) in complete media (AMEM + 10% FBS + 1% PSG) for t= 12 hours for attachment. 20% (w/v) pluronic F-127 solution was made by dissolving 2.0 g of F-127 (Sigma-Aldrich P2443) in 10 ml of complete media at 4 Celsius. Once the cells attached, the media was aspirated and 8 ml of the 20% pluronic F-127 solution was added over the top of the attached cells, which resulted in a gel approximately 2 mm in height. The cells were not in the gel matrix, but the gel was layered on top of the cells. Cells remained viable under this gel for the duration of the experiment.

The dish was then left in the incubator at 37 Celsius and 5% CO₂ for 6 hours so that the pluronic solution was allowed to gel. 0.05 g of Mg or Mg-Ti microparticles were then added at the center of the dish. A round plastic ring, with a diameter of 0.5 cm, was lightly placed on top of the gel and particle solution (0.05 g of Mg or Mg-Ti in 1 ml of complete media) was pipetted into the ring to create a particle bulk at the center of the dish with roughly an average diameter of

0.5 cm. This plastic ring was dipped in 70% ethanol overnight to sterilize since this material could not be autoclaved.

After 24 hours, live/dead assay was performed to measure cell viability as a function of distance away from the center of particle bulk, $n=3$. pH was measured after Mg or Mg-Ti microparticles were added in order to see the changes of pH, using a micro needle-tip pH electrode (Fischer Scientific, Catalog #: 13299510), as a function of distance away from the particles.

4.2.5 *Statistical Analysis*

Two-way analysis of variance (ANOVA) statistical methods were used to analyze the results, along with post hoc Tukey tests, using SPSS Statistics Software, version 17.0.

Statistically significant differences were determined with an alpha level (significance level) of 0.05.

4.3 *Results*

4.3.1 *Cell Density Effect*

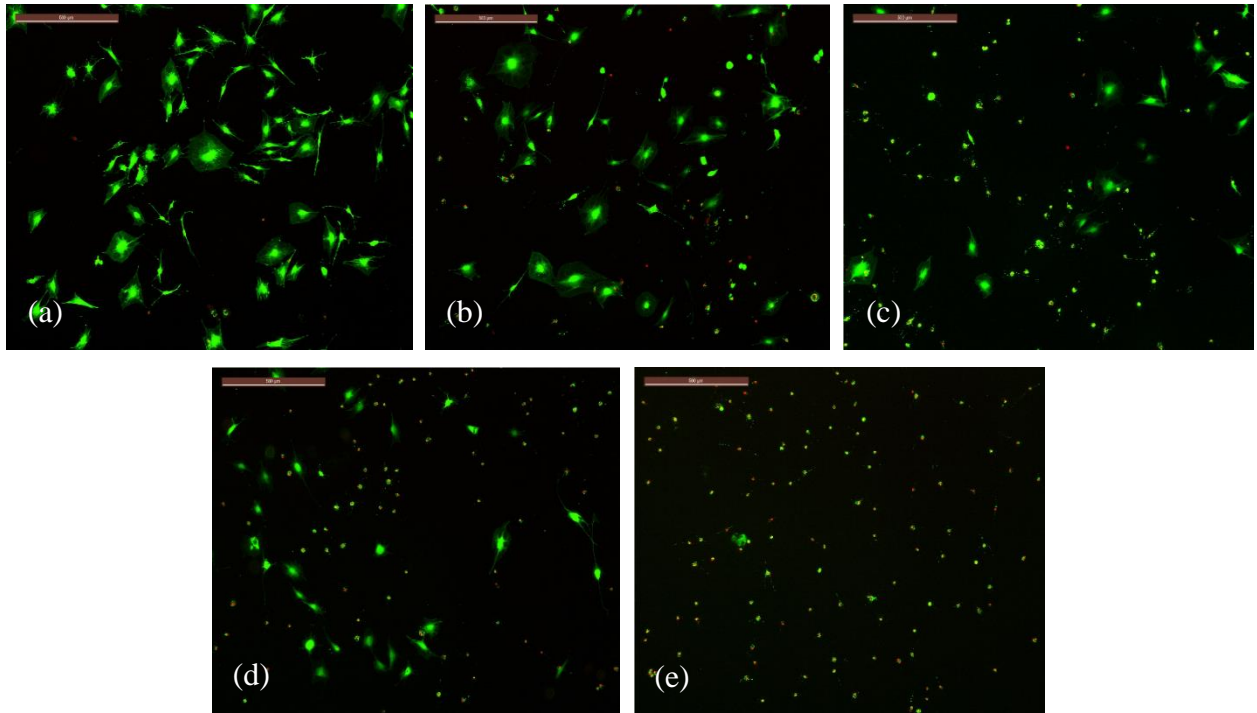
Fig. 4.1 shows live/dead images of different cell densities treated with either 50 or 500 $\mu\text{g/ml}$ of Mg or Mg-Ti particles (live/dead images of other concentrations are shown in [Section 4.7 Supplementary Images](#)). These panels of live/dead images for the different cell densities with varying particle concentrations demonstrate several features worthy of note. First, the 5,000 cells/ cm^2 panel appear to show significantly more cell killing at lower particle concentrations, below 250 $\mu\text{g/ml}$, while at higher cell densities, greater fractions of viable cells are seen. In addition, for the 20,000 and 30,000 cells/ cm^2 cases, the cells appear to surround the Mg or Mg-Ti particles and are viable (e.g., see [Fig. 4.2a](#) arrows for Mg particles surrounded by viable MC3T3 cells).

Fig. 4.2 provides both fluorescent live/dead imaging and SEM imaging of cells interacting with Mg-Ti particles after 24 hours of interaction. The cells are viable, even though they are very close to the particles. SEM images show cells on top of the particles which have filopodia of their membrane still attached to the surface, trapping the particles underneath them (Fig. 4.2b-d).

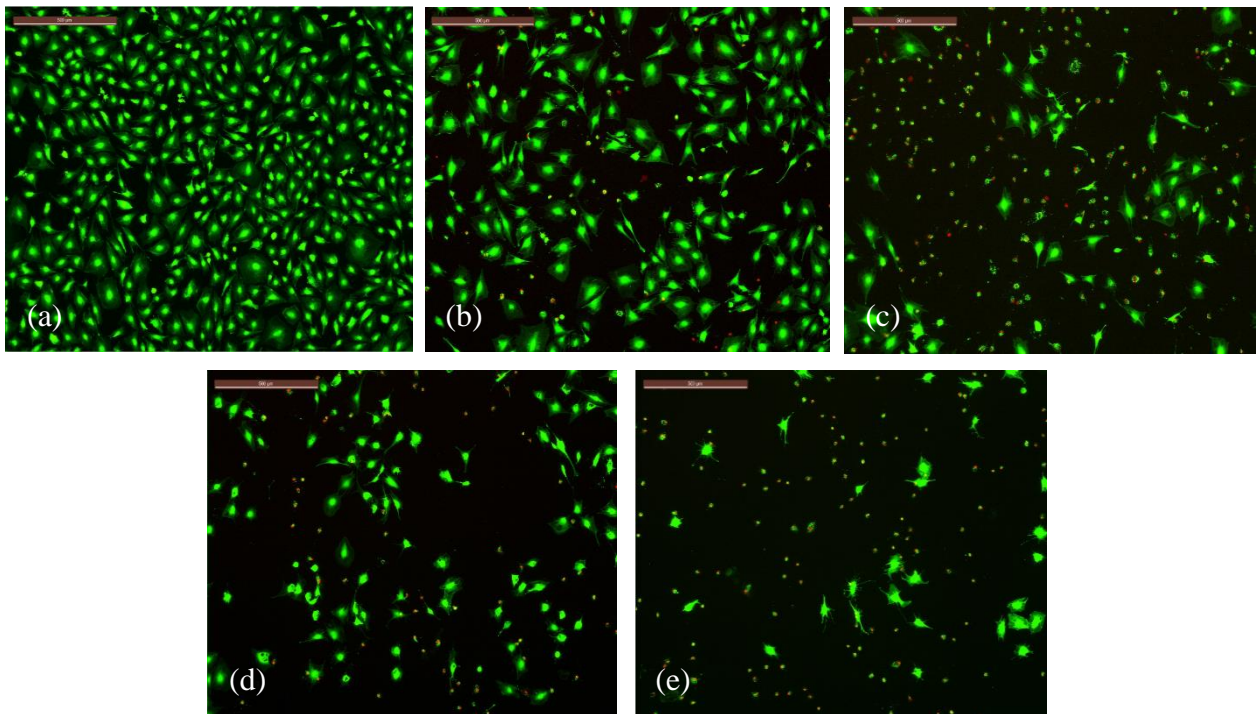
Fig. 4.3 shows cell viability-particle concentrations of Mg and Mg-Ti at different cell densities. Overall, cell viability is always significantly lower for Mg-Ti at all particle concentrations than Mg group for all cell density groups ($p < 0.05$). The 5,000 cells/cm² group treated with Mg shows a different behavior than the rest of the groups (Fig. 4.3a). Cell viability of Mg-treated group at 5,000 cells/cm² decreases initially at low concentrations (from 50 to 100 $\mu\text{g/ml}$) but then maintains a steady viability of approximately 20-30% despite the increase in particle concentrations (from 250 to 1500 $\mu\text{g/ml}$). Cell viability of control group at this cell density is not very high, with an average cell viability of 74% (which is significantly different from the cell viabilities of control groups at higher cell densities around 99%, see Fig. 4.3b-d). Fig. 4.3b is the same figure from Fig. 3.7 from Chapter 3, which is shown here again for comparison purposes. The concentration required to kill all cells completely at 5,000 cells/cm² and 10,000 cells/cm² for Mg-Ti are the same, around 750 $\mu\text{g/ml}$. At 10,000 cells/cm², twice the concentration of Mg (1500 $\mu\text{g/ml}$) is required to kill cells completely, compared to Mg-Ti. Fig. 4.3c and 4.3d shows higher cell density groups of 20,000 and 30,000 cells/cm², which also show that 1000-1500 $\mu\text{g/ml}$ of Mg and Mg-Ti concentrations are required to kill cells completely. While graphs from Fig. 4.3 compares cell viability between Mg and Mg-Ti treated groups of the same cell density, graphs from Fig. 4.3 are re-graphed to compare cell viability of different cell densities in Fig. 4.4. There was more rapid drop of cell viability for lower cell density than

higher cell density in both cases, although this is more clearly shown for Mg than Mg-Ti. Post hoc Tukey test shows that there is no statistical difference in cell viability among cell density groups for Mg or Mg-Ti ($p > 0.05$), except for Mg 5,000 cells/cm² group compared to other Mg cell density groups ($p < 0.05$). Although the statistical analysis shows that cell density did not have a significant effect on cell viability, average cell viability was different for low particle concentrations, depending on cell densities. For example, at 50 µg/ml, the average cell viability for Mg groups (Fig. 4.4a) of 5,000, 10,000, 20,000, and 30,000 cells/cm² are 46.01%, 85.73%, 99.56%, and 99.57%, respectively, while the average cell viability for MgTi groups (Fig. 4.4b) for 5,000, 10,000, 20,000, and 30,000 cells/cm² are 37.66%, 66.29%, 99.18%, and 99.34%, respectively. This shows that when cells are treated with low concentrations of Mg or Mg-Ti, the cells will be very viable if cell density is high, while the cells will die if cell density is low. Fig. 4.3c and Fig. 4.3d are exactly the same graphs as Fig. 4.3a and Fig. 4.3b, respectively, but the particle concentrations were divided by the relative cell density ratio, where particle concentrations for 5,000 cell/cm² group was divided by 1, 10,000 cells/cm² by 2 (since 10,000 is 2 x 5,000), 20,000 cells/cm² by 4 (since 20,000 is 4 x 5,000), and 30,000 cells/cm² by 6 (since 30,000 is 6 x 5,000). By doing so, the cell viability of different cell densities overlap more closely, which indicates that there is a particle density threshold that needs to be reached to start killing cells.

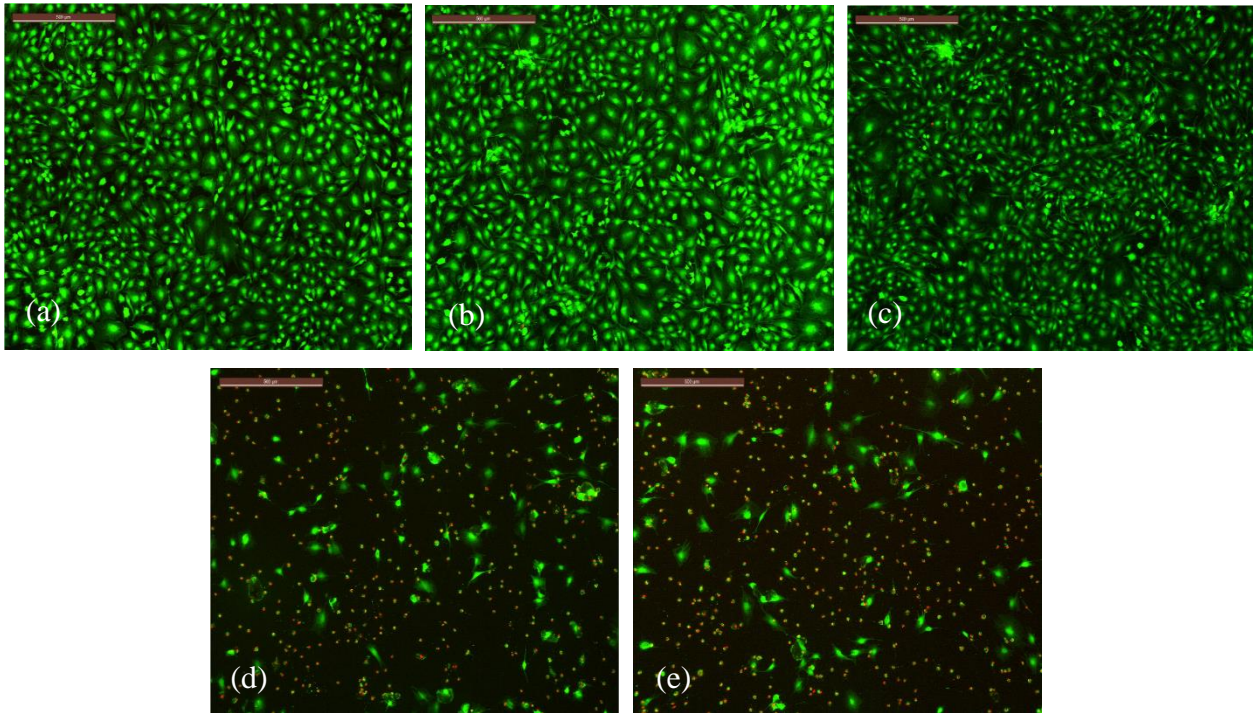
(i) 5,000 cells/cm²



(ii) 10,000 cells/cm²



(iii) 20,000 cells/cm²



(iv) 30,000 cells/cm²

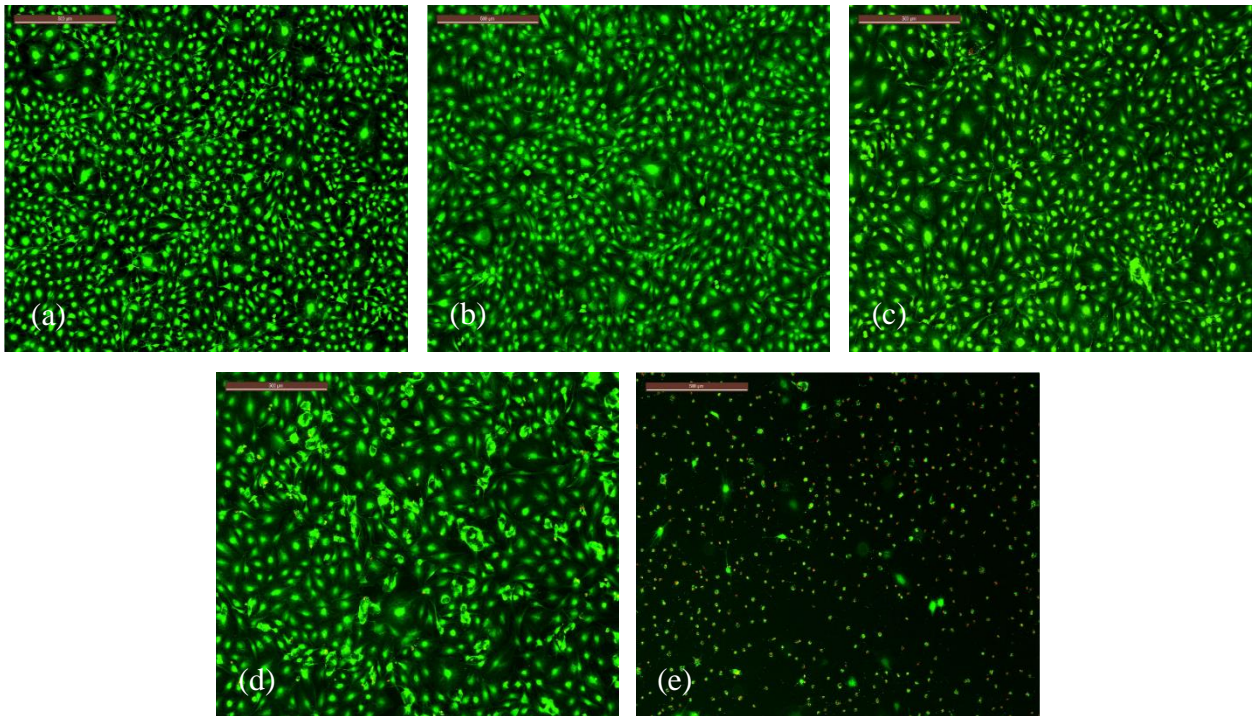


Figure 4.1 Live/dead images of MC3T3 cells with cell densities of (i) 5,000, (ii) 10,000, (iii) 20,000, and (iv) 30,000 cells/cm². (a) Control, (b) 50 µg/ml Mg, (c) 50 µg/ml Mg-Ti, (d) 500 µg/ml Mg, and (e) 500 µg/ml Mg-Ti, n=3. The scale bar = 500 µm.

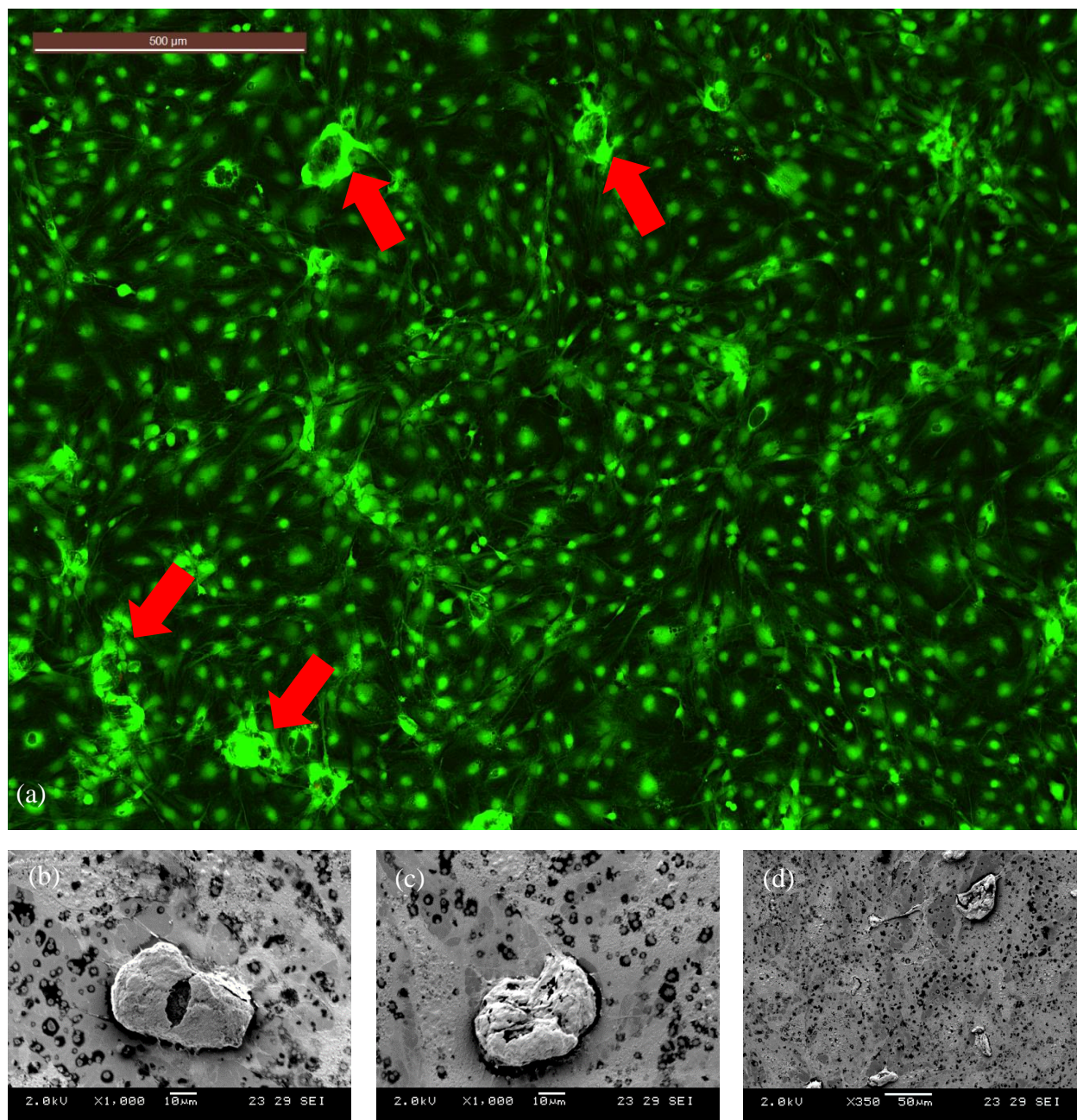
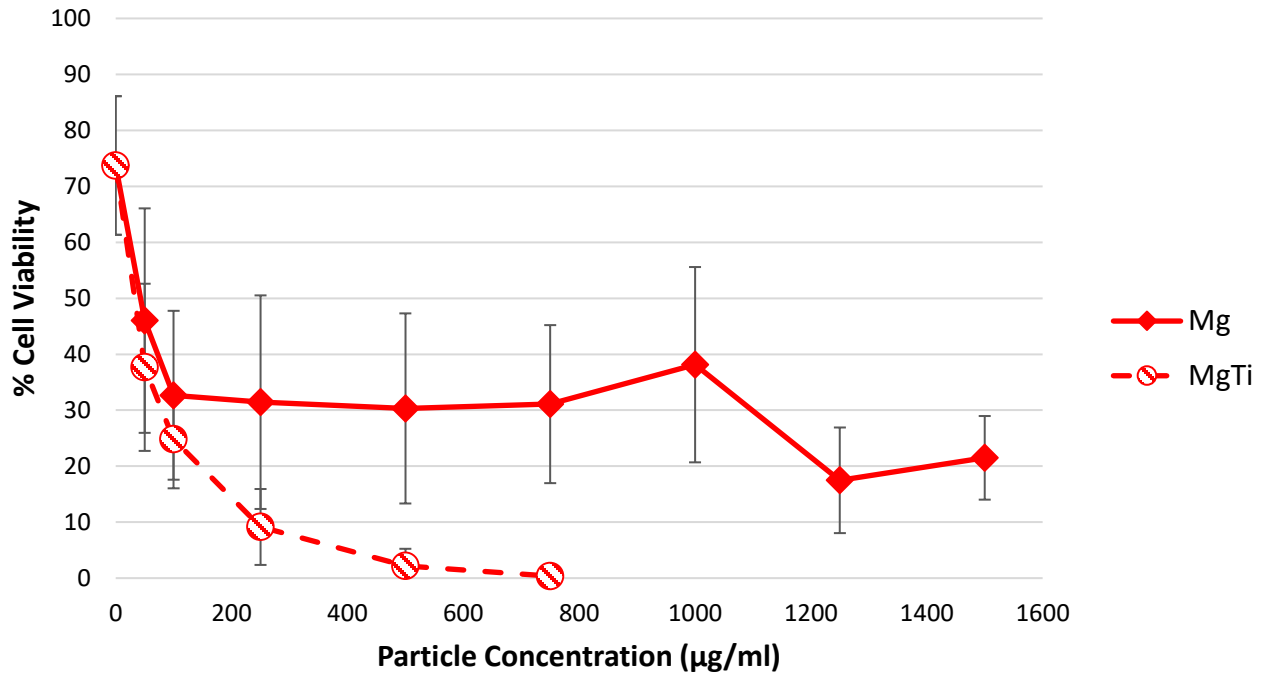


Figure 4.2 (a) Live/dead image of cells enveloping the particles. The cells are working together to engulf a large particle, which is impossible for an individual cell. This image was taken from a sample with cell density of 30,000 cells/cm² treated with 100 μg/ml of Mg-Ti. (b-d) SEM images of cells on top of the particles. Cells have somehow migrated on top of the cells, and while the cell body is on the particle, the cell filapodia are still attached to the surface. SEM images were taken from a sample with cell density of 30,000 cells/cm² treated with 500 μg/ml of Mg.

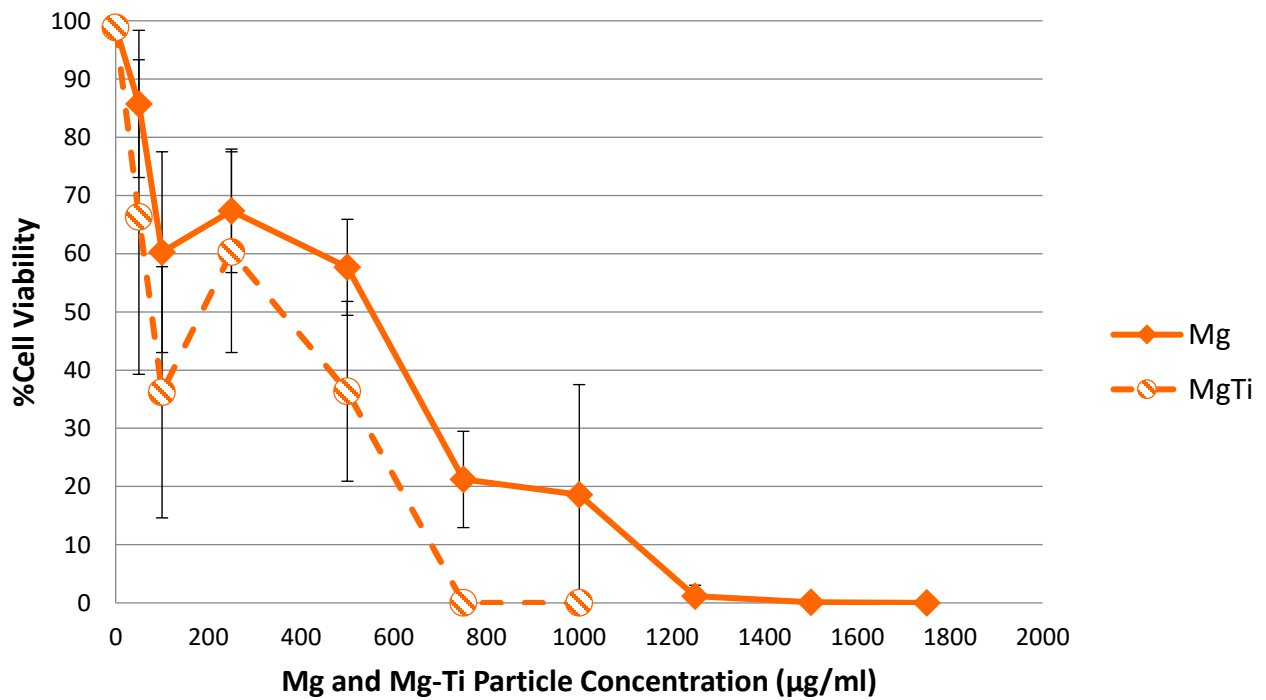
(a)

Cell Density: 5,000 cells/cm²



(b)

Cell Density: 10,000 cells/cm²



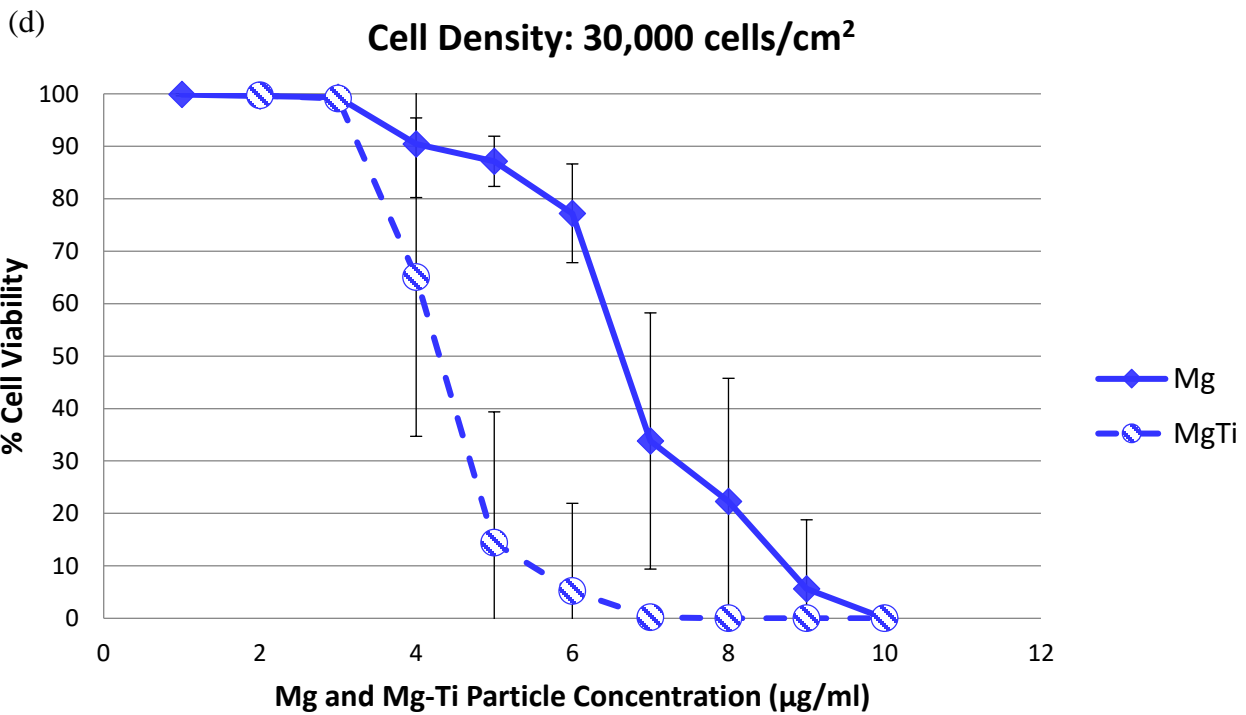
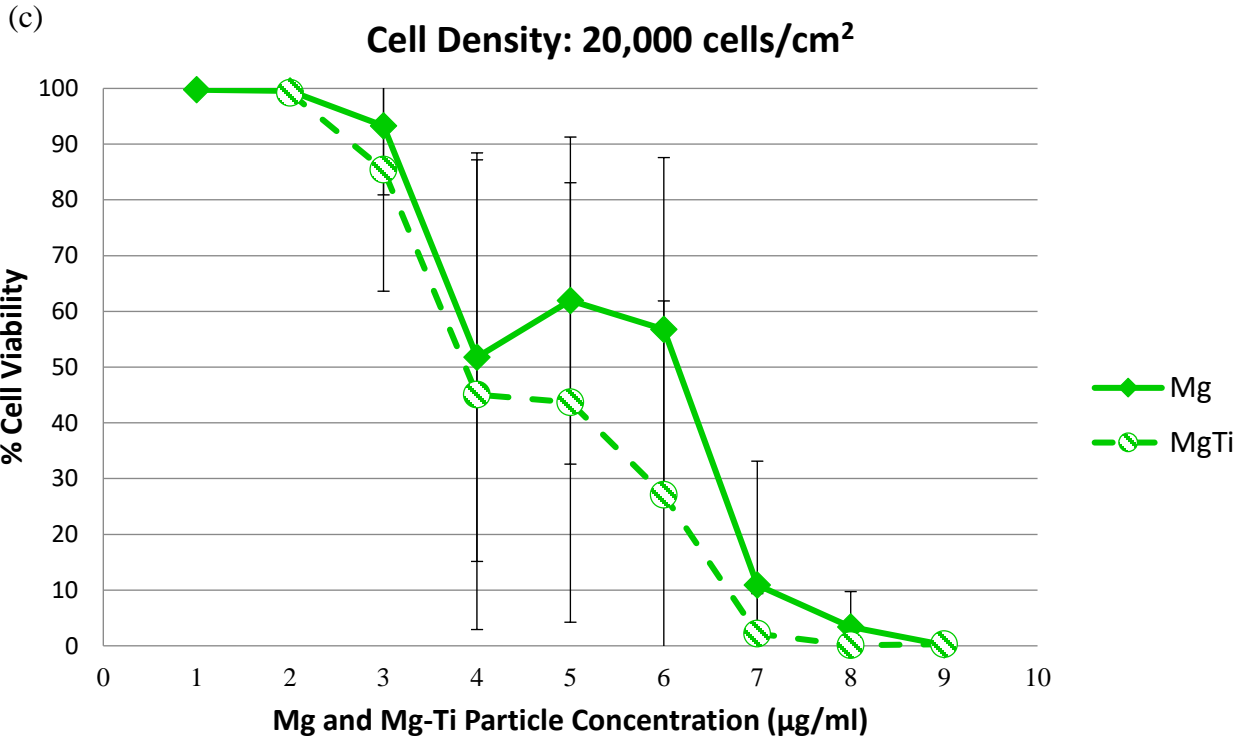
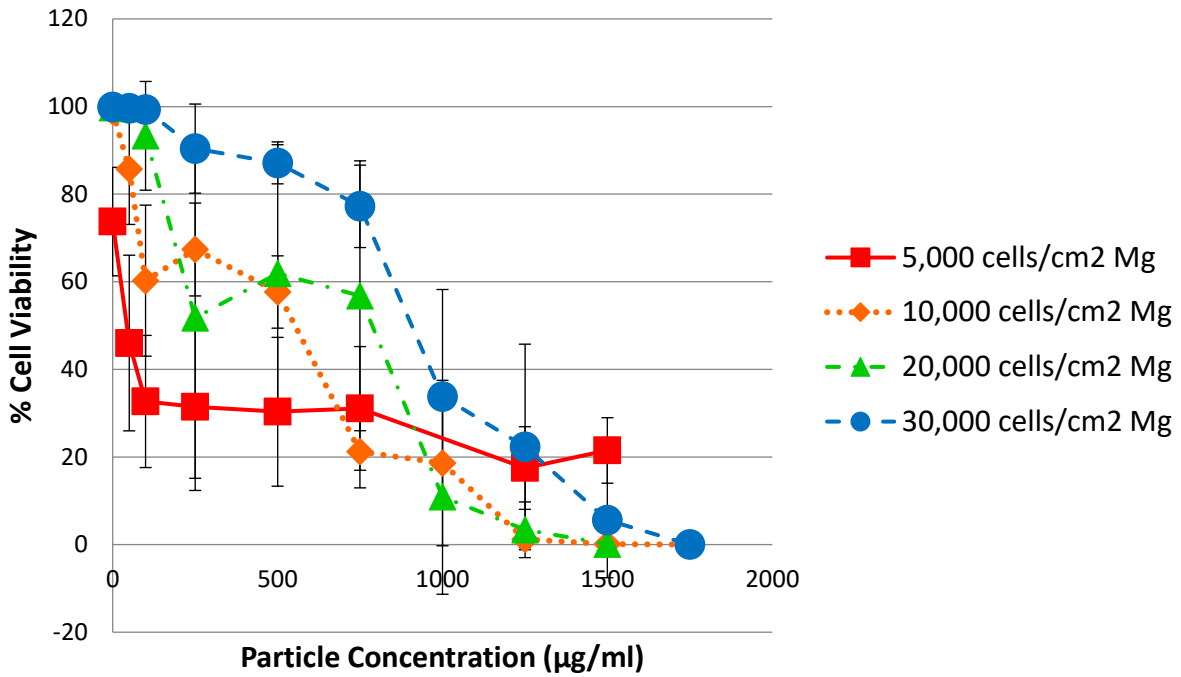
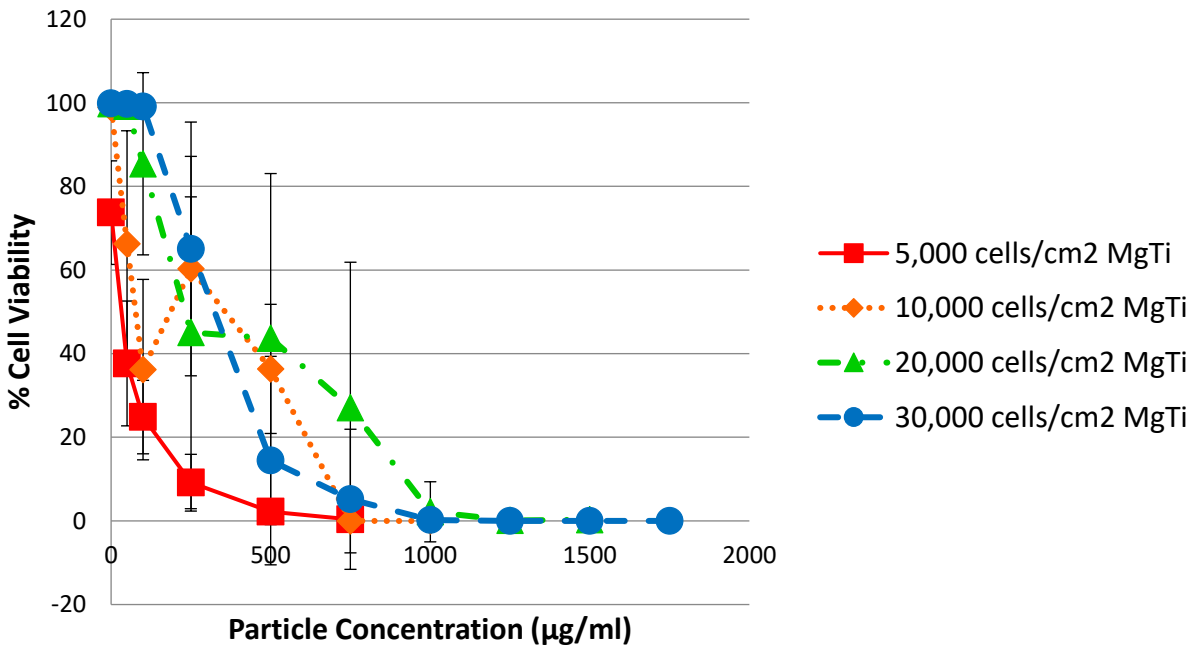


Figure 4.3 Cell viability graphs of Mg and Mg-Ti at different cell densities of (a) 5,000 cells/cm², (b) 10,000 cells/cm², (c) 20,000 cells/cm², and (d) 30,000 cells/cm², n=3. Cell viability is always significantly lower for those treated with Mg-Ti compared to Mg, $p < 0.05$.

(a) **% Cell Viability vs. Mg Particle Concentration at Different Densities**



(b) **% Cell Viability vs. Mg-Ti Particle Concentration at Different Densities**



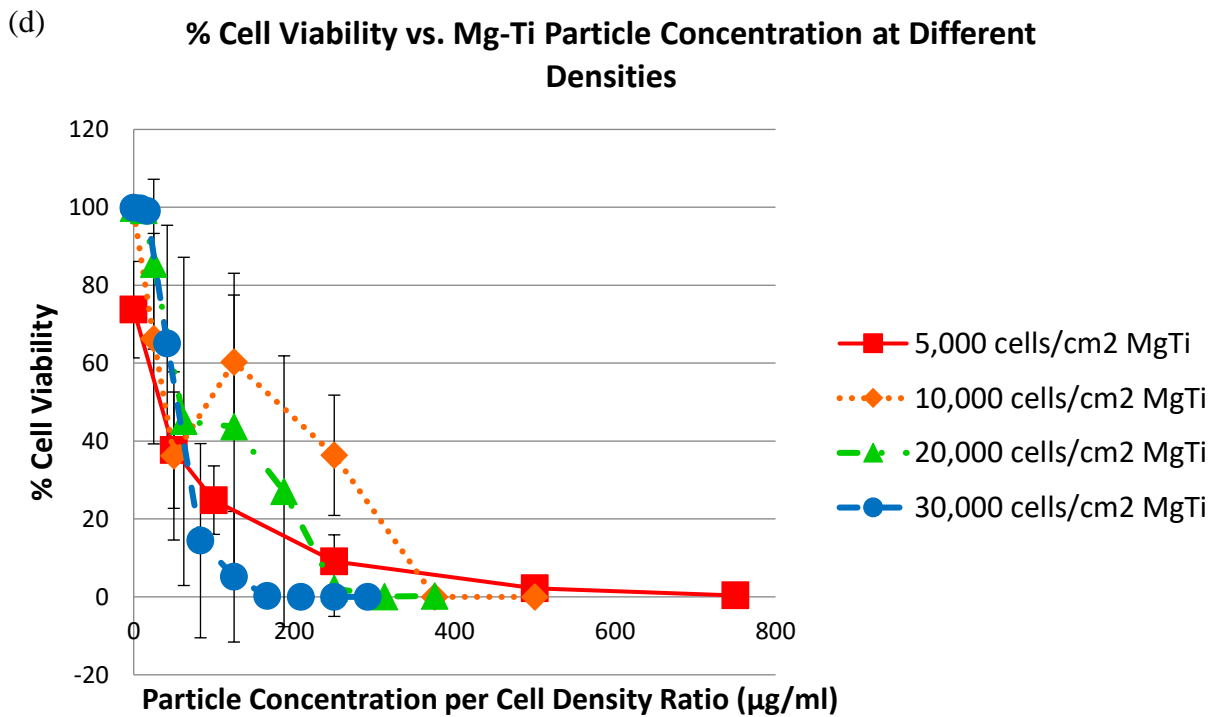
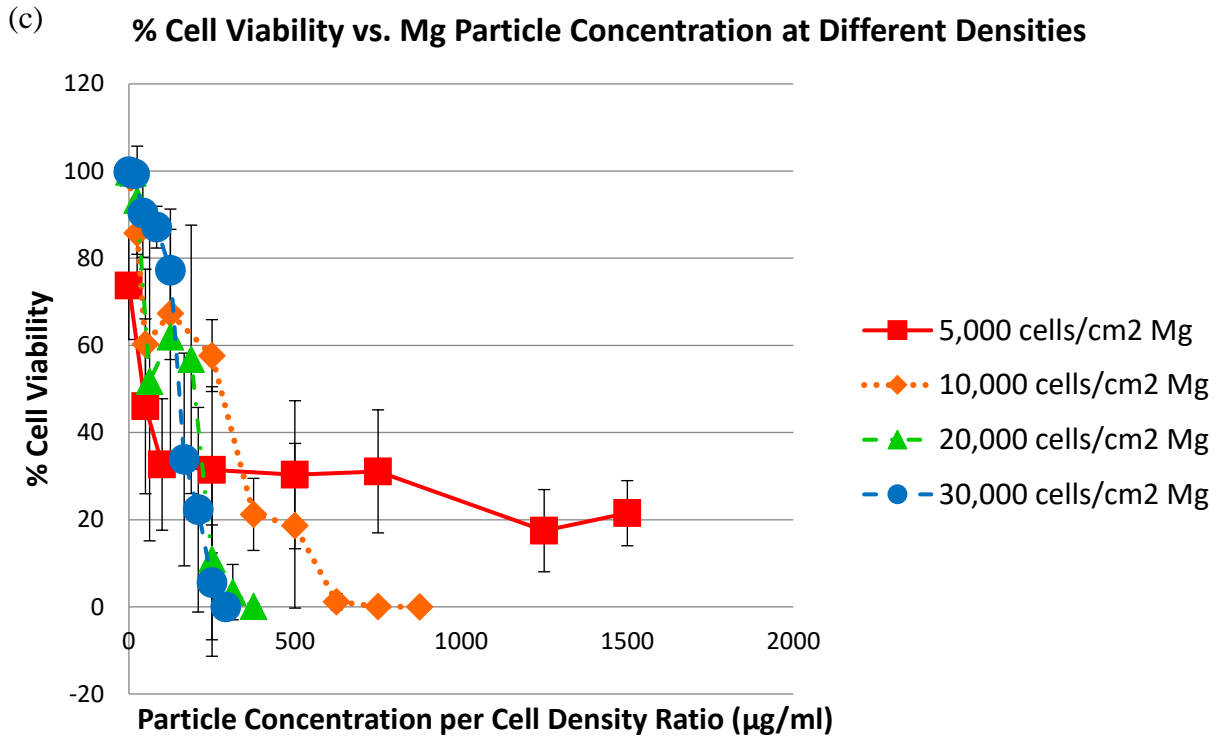


Figure 4.4 Graphs showing how cell viability as a function of particle concentration drops at a different rate when cell density is varied for (a) Mg and (b) Mg-Ti, $n=3$. The graphs (a) and (b) were re-graphed as (c) Mg and (d) Mg-Ti by dividing the particle concentration by relative cell density ratio, where 5,000 cells/cm² was divided by 1, 10,000 cells/cm² by 2, 20,000 cells/cm² by 4, and 30,000 cells/cm² by 6, $n=3$.

Fig. 4.5 shows the slopes of cell viability plotted from 0 to 250 $\mu\text{g/ml}$ (the slopes of the first three points from Fig. 4.4a and Fig. 4.4b) for different cell densities and particle groups, plotted against cell densities. The more negative the slope indicates the faster the rate of drop of cell viability as particle concentration was increased from 0 to 250 $\mu\text{g/ml}$. Lower cell density groups, 5,000 cells/ cm^2 and 10,000 cells/ cm^2 , had more negative slopes, and higher cell density groups, 20,000 cells/ cm^2 and 30,000 cells/ cm^2 , had less negative slopes, where 30,000 cells/ cm^2 group had a slope of almost zero, which shows that cell viability did not drop over this concentration range. Post hoc Tukey test shows that the drop of cell viability for these concentrations is significantly different between 5,000 cells/ cm^2 and 20,000 cells/ cm^2 , 5,000 cells/ cm^2 and 30,000 cells/ cm^2 , 10,000 cells/ cm^2 and 20,000 cells/ cm^2 , and 10,000 cells/ cm^2 and 30,000 cells/ cm^2 , $p < 0.05$, but not different between 5,000 cells/ cm^2 and 10,000 cells/ cm^2 , and not different between 20,000 cells/ cm^2 and 30,000 cells/ cm^2 .

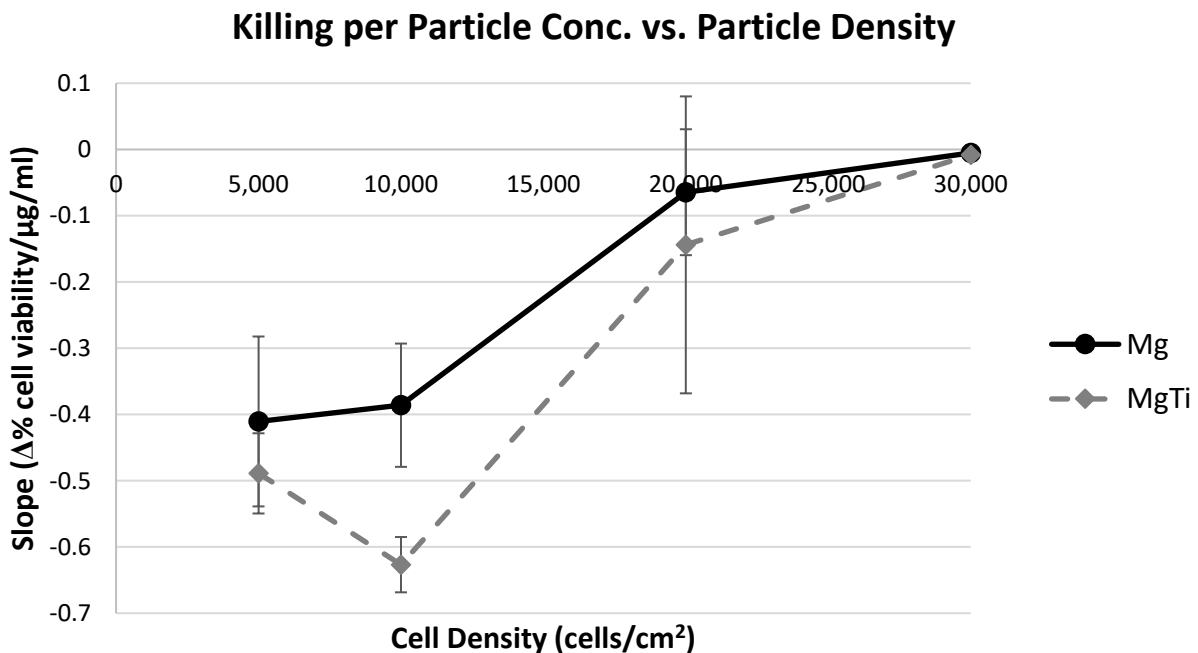


Figure 4.5 The slopes of % average cell viability versus particle concentration, taken for different cell densities between 0 and 100 $\mu\text{g/ml}$ for Mg group and Mg-Ti group, $n=3$. The more negative the slope, the faster the rate of cell killing. The lower the cell density, the slope also became more negative.

4.3.2 Time Effect

Fig. 4.6 shows cell viability over time for different particle concentrations of Mg and Mg-Ti groups. While control groups maintain almost no change in cell viability, with most of the cells viable over time, groups treated with different particle concentrations show high variability. For Mg (Fig. 4.6a), cell viability of low concentrations of 50, 100, and 250 $\mu\text{g/ml}$ drop from $t=0$ to 18 hours, but then slowly recover from 24 hours to 3 days, where cell viability for 50 and 100 $\mu\text{g/ml}$ recover fully, and for 250 $\mu\text{g/ml}$, cell viability recovers back to above 90%. Cell viability of medium concentrations of 500, 750, and 1000 $\mu\text{g/ml}$ also drop from $t=0$ hour to 18 hours, and then seem to recover just a little after 24 hours, but never recover fully (above 90%) like the low concentrations. For high concentrations of 1250, 1500, and 1750 $\mu\text{g/ml}$, cell viability dropped quickly to zero from $t=0$ to 24 hours, and since there are no live cells, there is no recovery afterwards.

Mg-Ti group (Fig. 4.6b) also shows similar trends, where cell viability of 50 $\mu\text{g/ml}$ recover fully, while cell viability of 100, 250, and 500 $\mu\text{g/ml}$ fall quickly and then recover somewhat, and cell viability of 750 $\mu\text{g/ml}$ and above drop to zero within 24 hours and never recover. While Mg group shows complete cell death within 24 hours and no recovery at 1250 $\mu\text{g/ml}$, Mg-Ti group shows complete cell death and no recovery at 750 $\mu\text{g/ml}$.

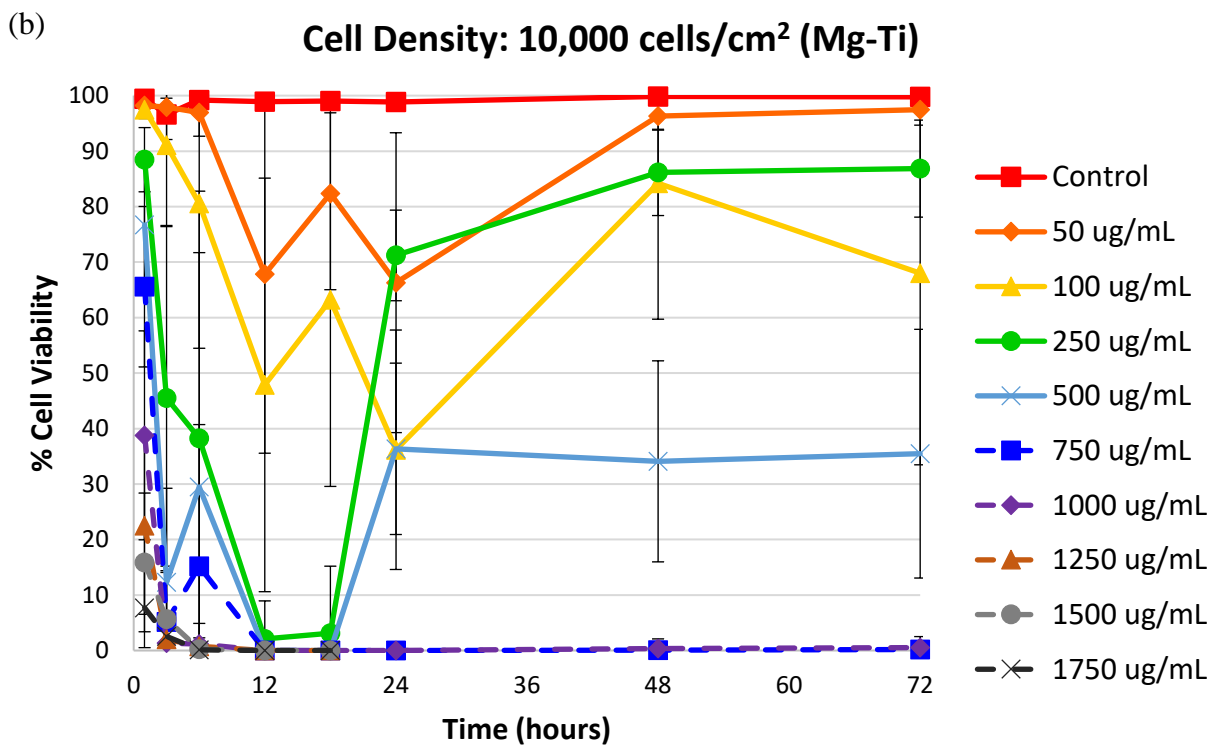
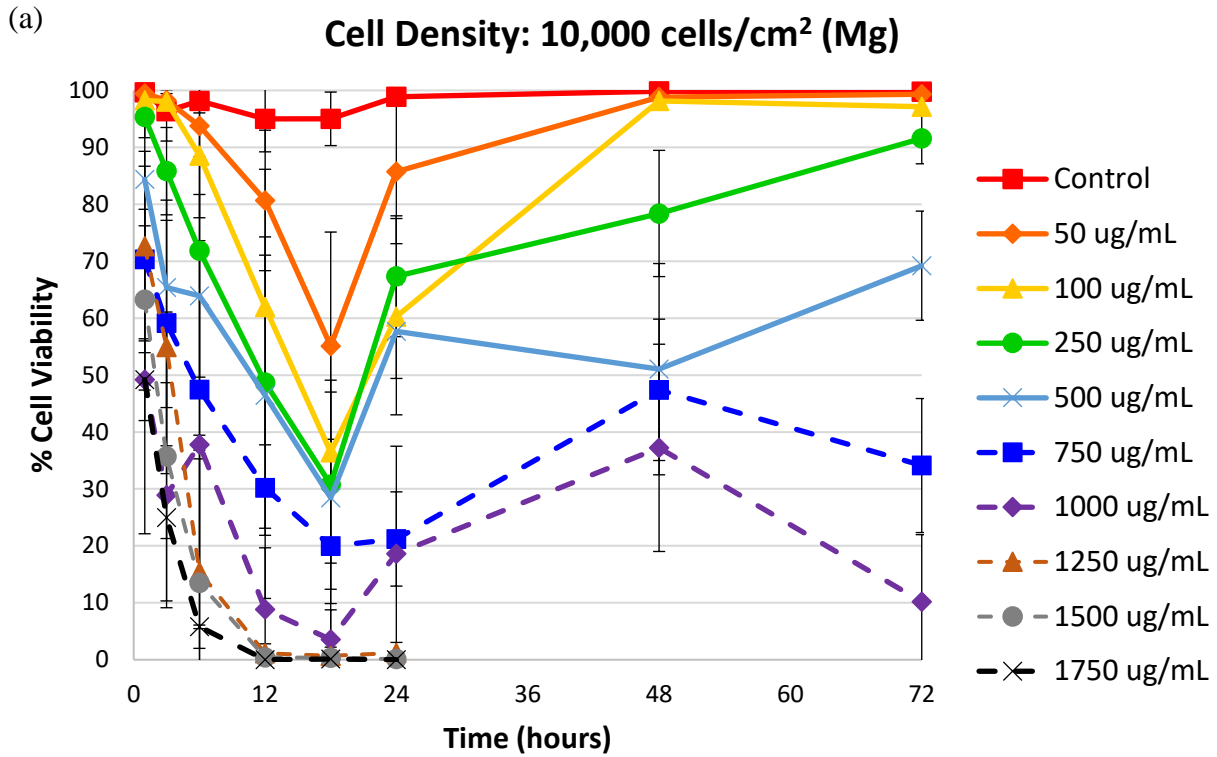


Figure 4.6 Graphs showing how cell viability changes over time at different particle concentrations for 10,000 cells/cm² cell density group (a) Mg and (b) Mg-Ti, n=3. At low particle concentrations, the cells can recover by t=48 hours, but as the particle concentration is increased, cells cannot recover.

Mg and Mg-Ti groups are re-graphed together for the same particle concentrations in Fig. 4.7. For control group (no particles), cell viability remains very high from $t=0$ to 72 hours (Fig. 4.7a). For 250 $\mu\text{g/ml}$ group, the average cell viability for Mg and Mg-Ti drops to 30% and 3% by 18 hours, but they eventually recover back to 92% and 87%, respectively, by the end of 72 hours (Fig. 4.7b). For 750 $\mu\text{g/ml}$ group, cell viability of Mg and Mg-Ti quickly drops to 70% and 66% by $t=1$ hour, from where Mg exponentially decay to 20% by $t=18$ hours, and although there is a slight increase of cell viability after 24 hours, there is no significant cell recovery. For Mg-Ti, there is 0% cell viability by $t=12$ hours and since all cells completely died, there is no cell recovery. For 1500 $\mu\text{g/ml}$, cell viability of Mg and Mg-Ti is 63% and 16% at $t=1$ hour, and by $t=12$ hours, both Mg and Mg-Ti show 0% cell viability, and therefore no cell recovery after $t=24$ hours.

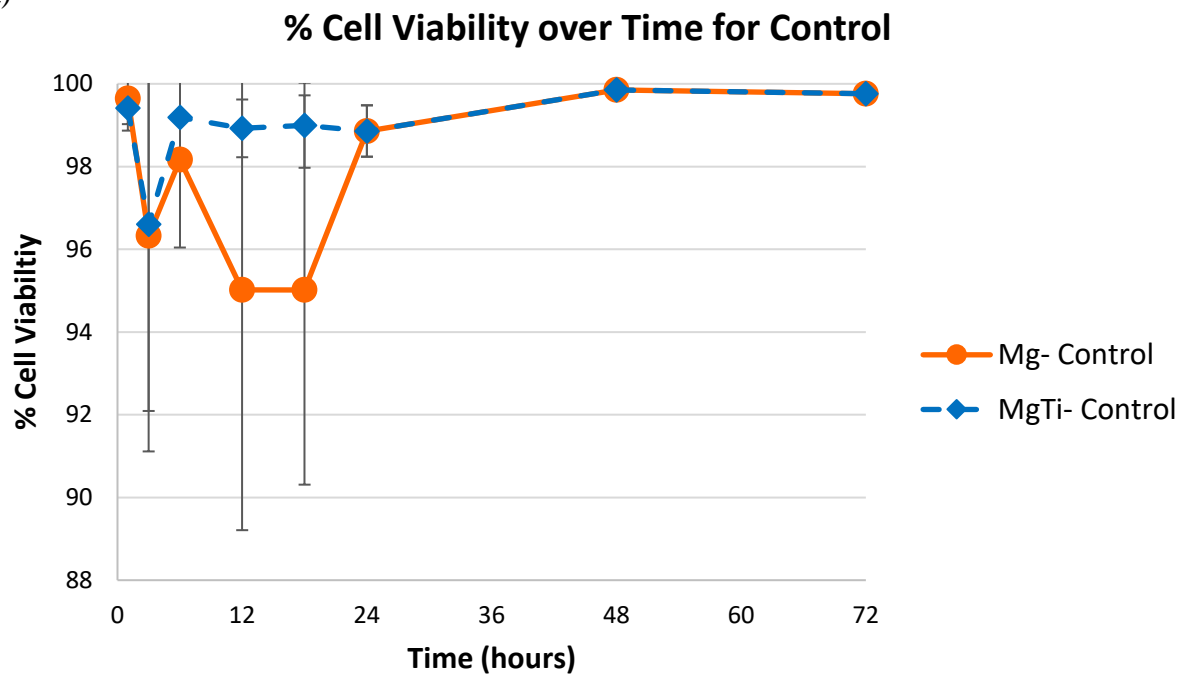
Instead of % cell viability, Fig. 4.8 shows the total number of live and dead cells for selected concentration of 50 $\mu\text{g/ml}$ and 500 $\mu\text{g/ml}$ for Mg and Mg-Ti groups over time. For low concentration of 50 $\mu\text{g/ml}$ of both Mg and Mg-Ti, the number of live cells decreased slightly within 24 hours and then increased, indicating that once the particles finished corroding, the remaining live cells proliferated to yield more cells. The number of dead cells, on the other hand, is very low throughout the entire time. Cells are able to proliferate after 24 hours, and this explains the increase in cell viability. For higher concentrations of 500 $\mu\text{g/ml}$, the Mg group shows a slight decrease in the number of live cells initially and then both the number of live and dead cells remain relatively steady, which means remaining live cells do not get killed after 24 hours but these cells do not proliferate either. The increase of dead cells within the first 24 hours for Mg-Ti at 500 $\mu\text{g/ml}$ explains the decrease of cell viability within this time frame, and the remaining live cells stay alive after 24 hours without any cell proliferation. Any slight decrease

in the number of dead cells is likely the result of a loss of dead cells from the surface. And note that 250 $\mu\text{g/ml}$ of Mg-Ti killed more cells by $t= 18$ hours (3.11% live), compared to 750 $\mu\text{g/ml}$ of Mg, which killed to 19.95%, by $t= 18$ hours as well. And yet, 250 $\mu\text{g/ml}$ of Mg-Ti group was able to recover significantly, while 750 $\mu\text{g/ml}$ of Mg group could not. This suggests that remaining number of live cells is not significant to recovery, but remaining ROS or toxic species that are affecting cell proliferation.

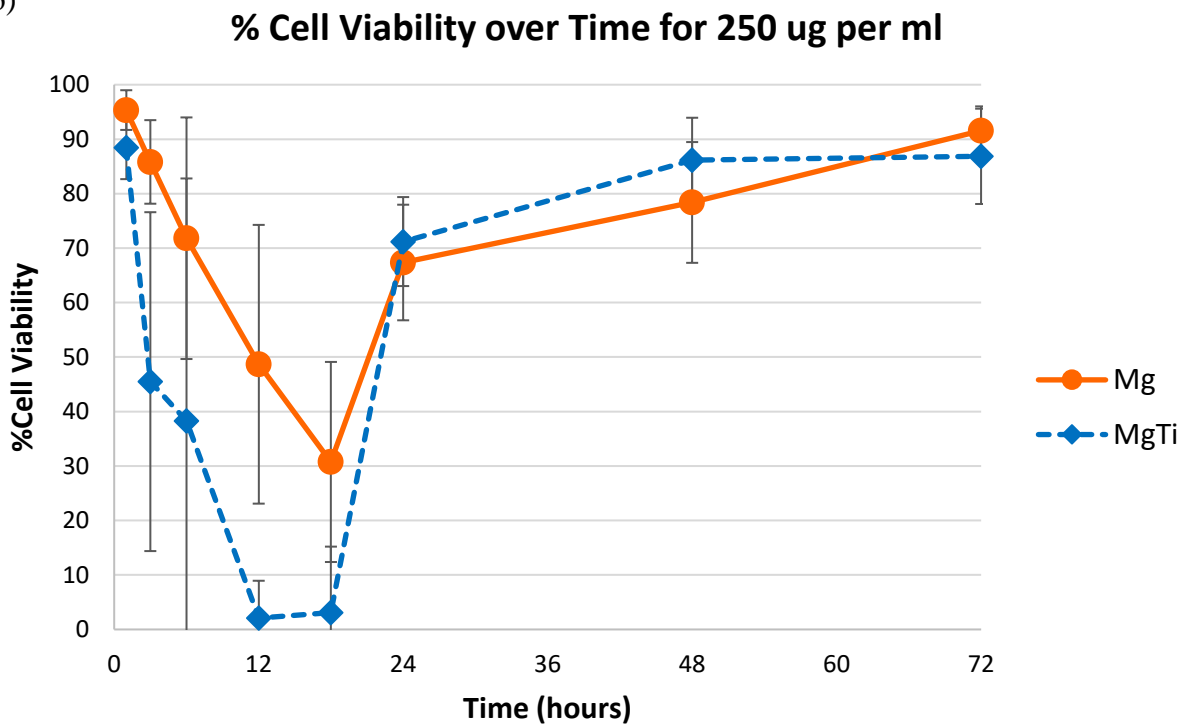
The slopes were measured from $t= 0$ to 18 hours and from $t= 24$ to 72 hours per particle concentration of Mg and Mg-Ti groups to find the killing and recovery rates (Fig. 4.9). As shown in Fig. 4.9a, the slope is more negative for higher particle concentrations, which means that the cells are being killed more quickly. The slope plateaus for Mg at 1250 $\mu\text{g/ml}$ and for Mg-Ti at 250 $\mu\text{g/ml}$, which means that Mg-Ti is killing faster at much lower particle concentration. Fig. 4.9b shows the recovery rates after $t= 24$ hours, where higher the particle concentrations, the lower the recovery rate. And of course, there is a low recovery rate for lower particle concentrations because not many cells were killed to begin with. The highest recovery rate for both Mg and Mg-Ti is when the cells are treated with 250 $\mu\text{g/ml}$, which means that at this concentration, surviving cells proliferated and re-populated.

The pH was measured for different particle concentrations, from 0 to 2500 $\mu\text{g/ml}$, over time from $t= 0$ to 72 hours (Fig. 4.10). As shown, for both Mg and Mg-Ti treated samples, the pH starts around 7.4 (no particles) and is increased to 9 as the particle concentration is increased to 2500 $\mu\text{g/ml}$. There is not much pH change over time, although the pH may drop slightly, which is more evident for higher particle concentrations. And there is no significant difference in pH between Mg and Mg-Ti groups, $P > 0.05$.

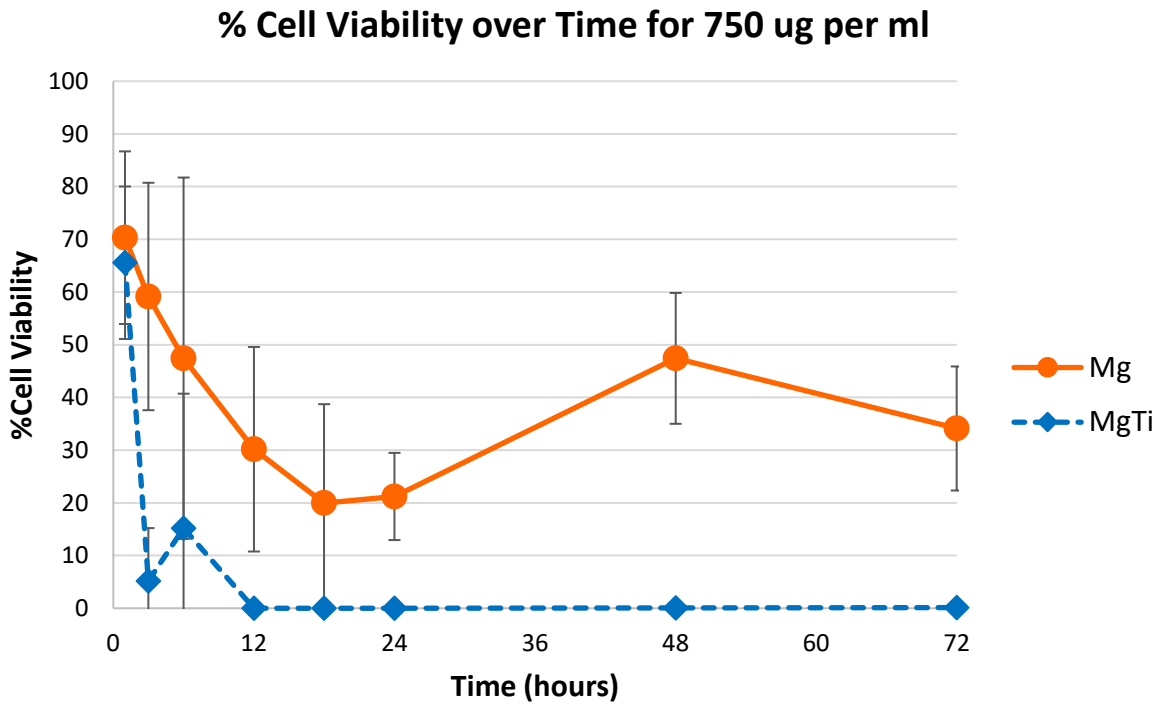
(a)



(b)



(c)



(d)

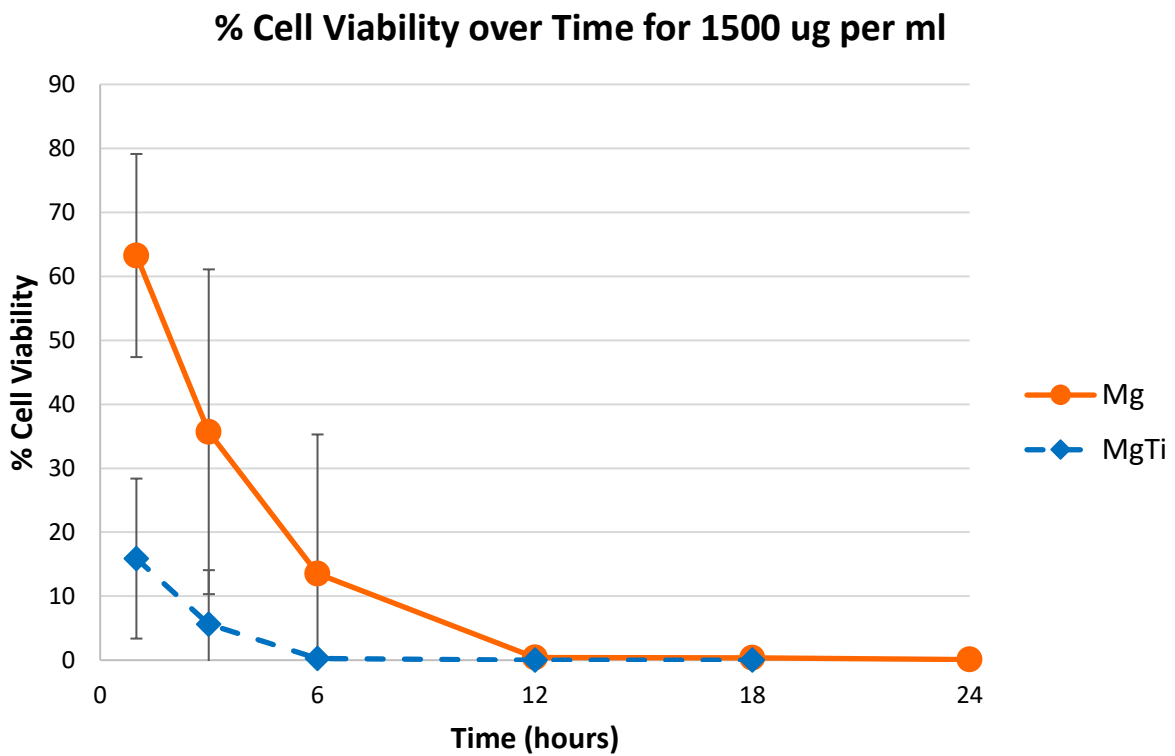


Figure 4.7 Mg and Mg-Ti groups graphed over time at concentrations of: (a) 0 $\mu\text{g/ml}$ (control), (b) 250 $\mu\text{g/ml}$, (c) 500 $\mu\text{g/ml}$, (d) 750 $\mu\text{g/ml}$, and (e) 1500 $\mu\text{g/ml}$, $n=3$. Mg-Ti groups kill more cells over time than Mg groups.

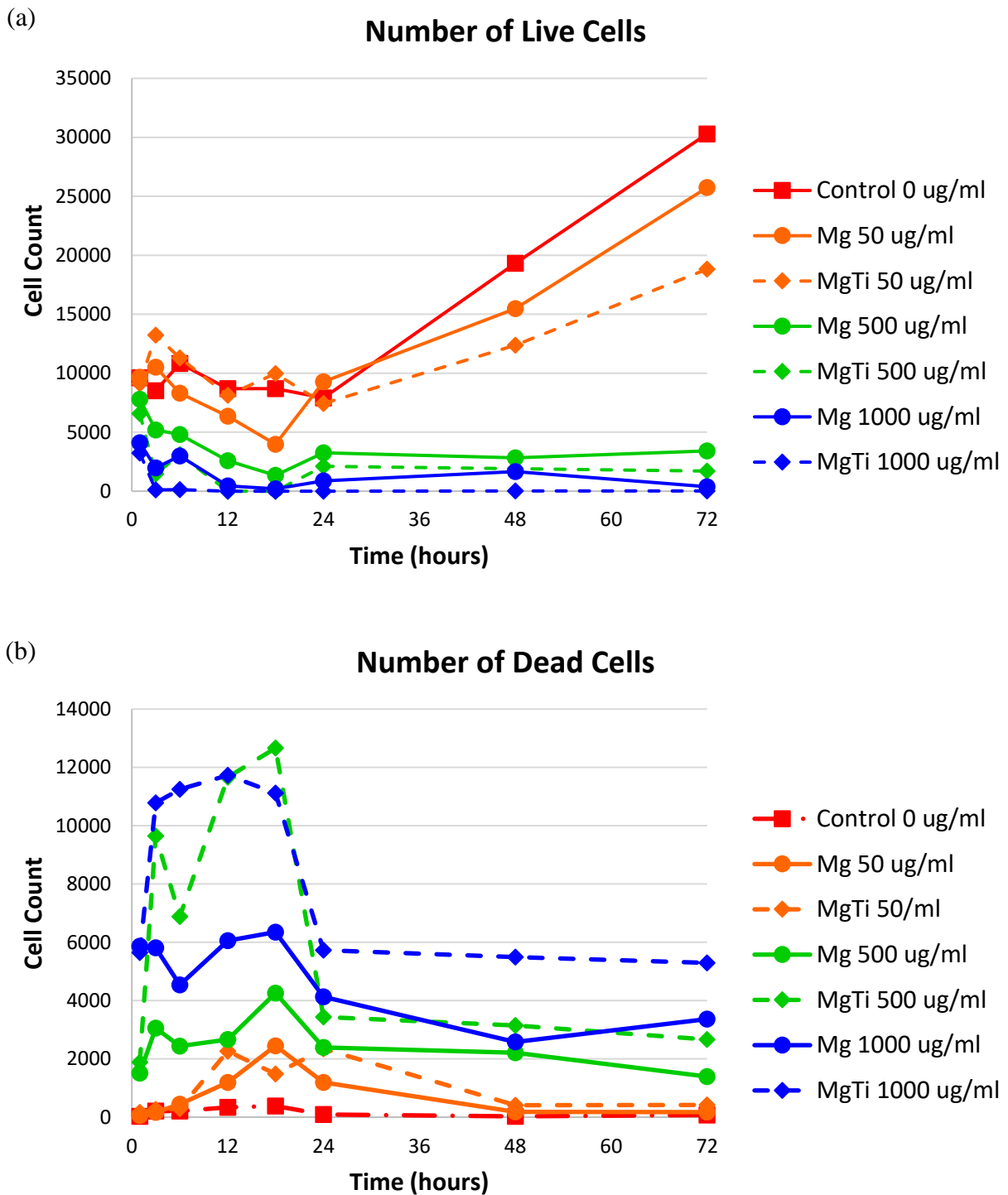
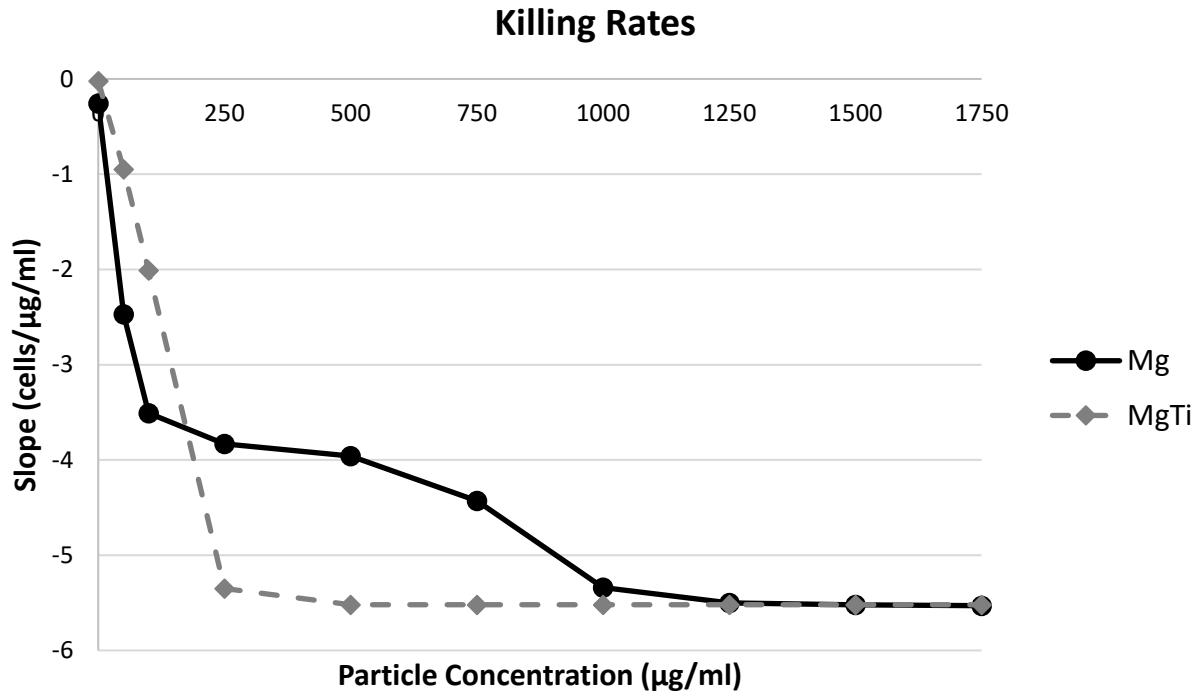


Figure 4.8 The total number of live and dead cells over time for Mg and Mg-Ti groups at control, 50, 500, and 1000 $\mu\text{g/ml}$ collected from 3 different samples.

(a)



(b)

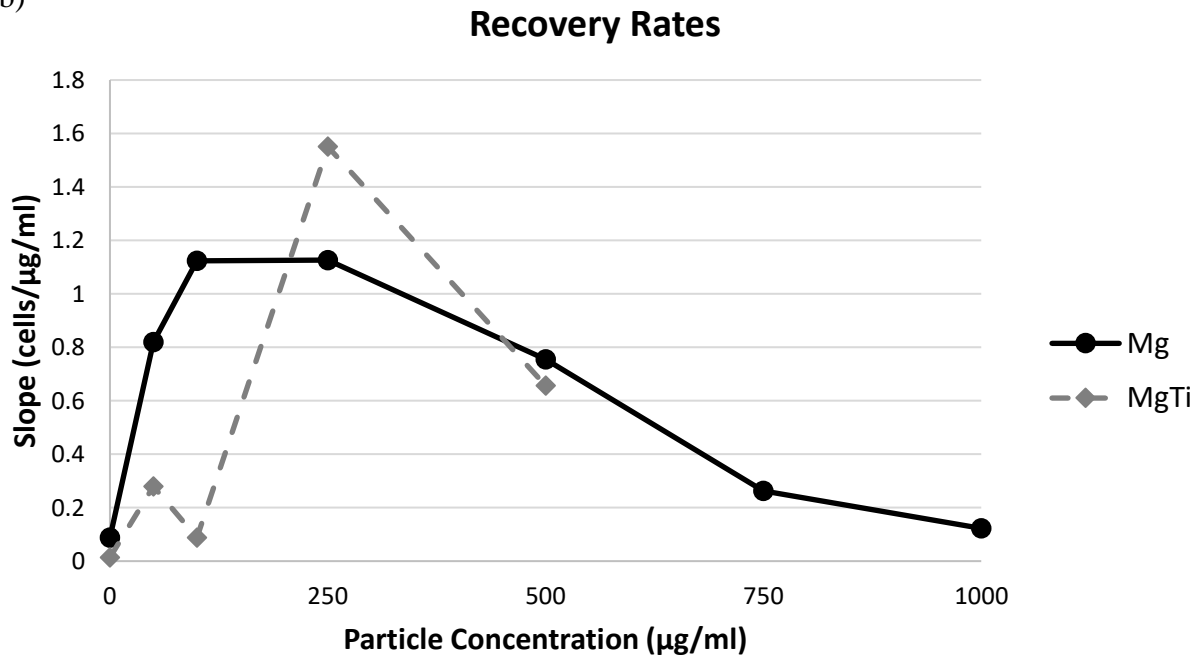
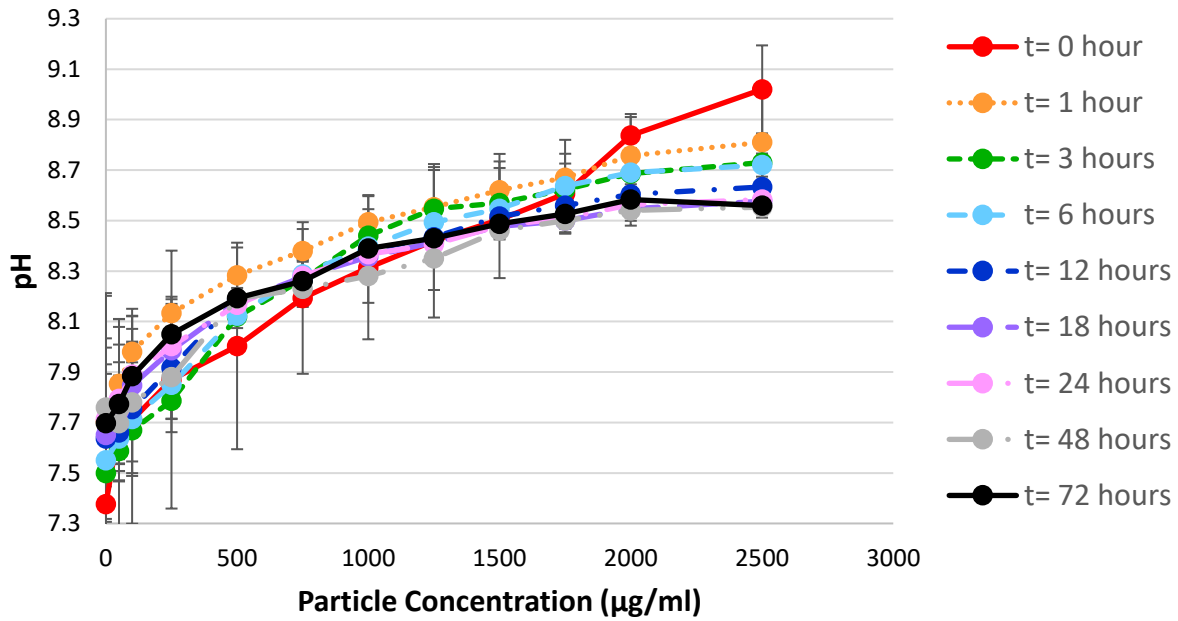


Figure 4.9 The slopes of % average cell viability over particle concentrations for cell density of 10,000 cells/cm² were measured from t= 0 to 18 hours to measure (a) killing rates, and from t= 24 to 72 hours to measure (b) recovery rates. Because these slopes were measured from the average % cell viability, there are no standard deviations.

(a)

Mg Particle Concentrations vs. pH



(b)

Mg-Ti Particle Concentrations vs. pH

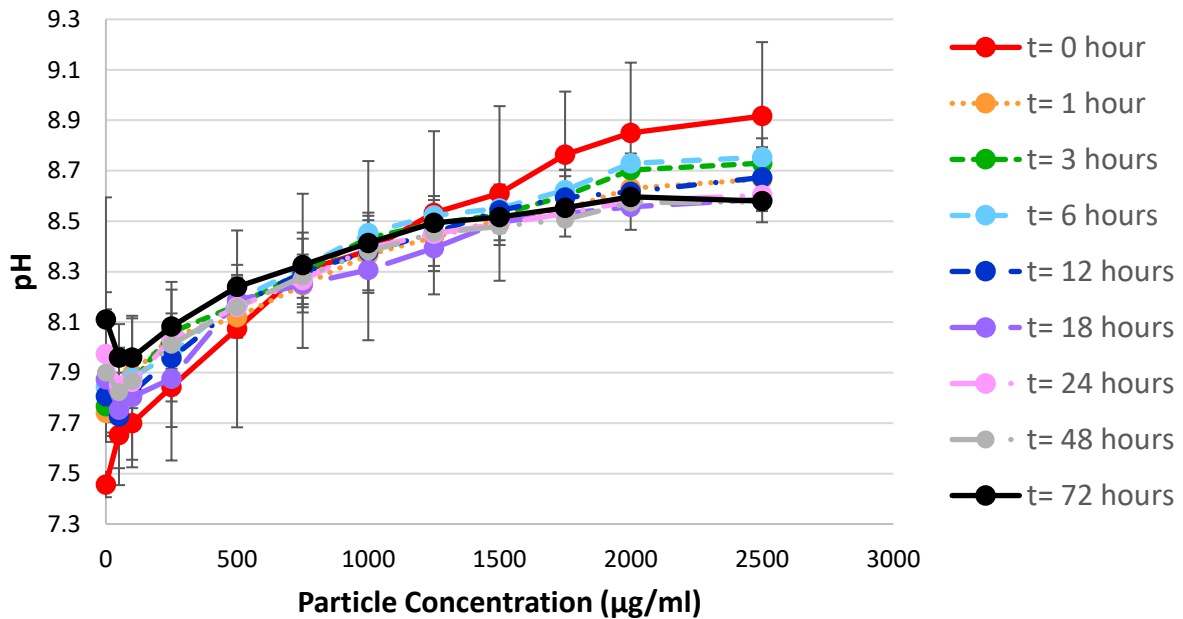


Figure 4.10 Graphs showing pH values of complete media (AMEM + 10% FBS + 1% PSG) with different particle concentrations (from 0 to 1750 µg/ml) corroding from t=0 to 72 hours, where (a) shows Mg and (b) shows Mg-Ti, n=3.

4.3.3 Proximity Effect

Fig. 4.11 shows live/dead images of cells as a function of distance away from the bulk particles and also an image of the dish to give an idea of how the particles are trapped within the pluronic matrix. Cells exactly underneath the particles completely died, while the cells at the edge of the particle zone were more alive. The transition is very stark and is demonstrated in the montage of images in Fig. 4.12. Cell viability was measured over distance away from the bulk particles to see how close the particles have to be to the cells to have a killing effect (Fig. 4.13). When the particles were added to the gel, most of the particles seemed to sink a little into the gel due to their weight. The distance between the particles and the cells exactly underneath the particles is not known, but since the height of the gel is 2 mm, the distance is within 2 mm. Only the horizontal distance was measured away from the particles. Cell viability is zero at the site of the particles, but cell viability increases with distance, where approximately 80% of cells are viable 1 cm away from the center of the bulk particles. This sharp transition was the case for both Mg and Mg-Ti group, and so there were no significant difference in cell viability between Mg and Mg-Ti group, $p > 0.05$. The pH was measured as a function of distance over different periods of time as well (Fig. 4.14). There was no significant difference of pH across distance, even at $t = 0$ hour, which was almost immediately after the particles were added to the pluronic gel ($p > 0.05$), indicating that the pluronic gel was very permeable and the hydroxide ions were able to travel and spread very quickly.

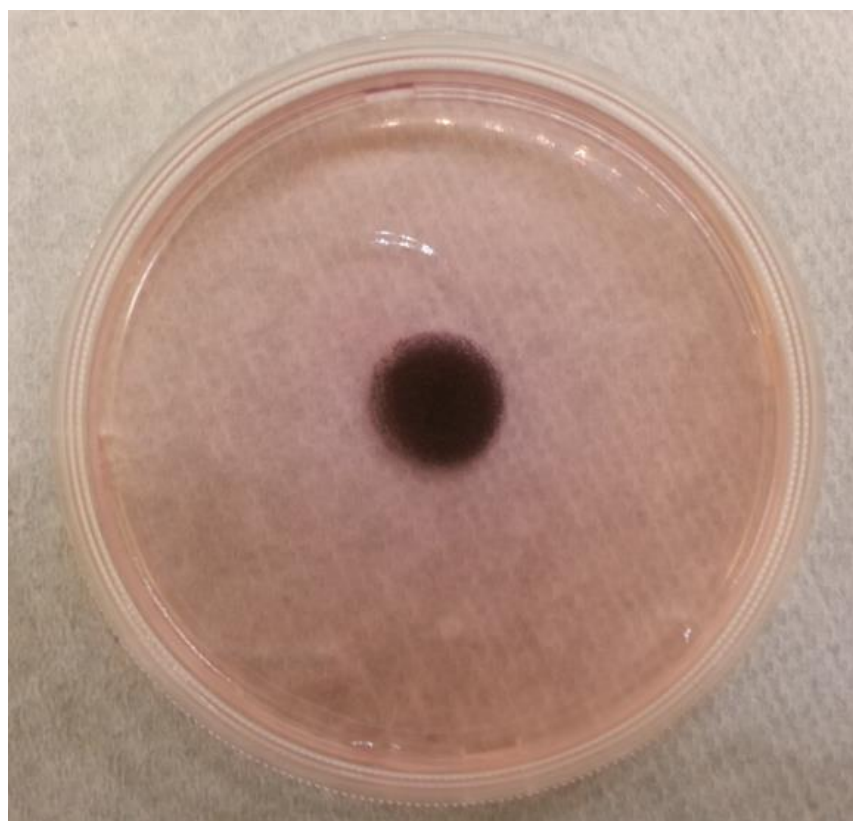
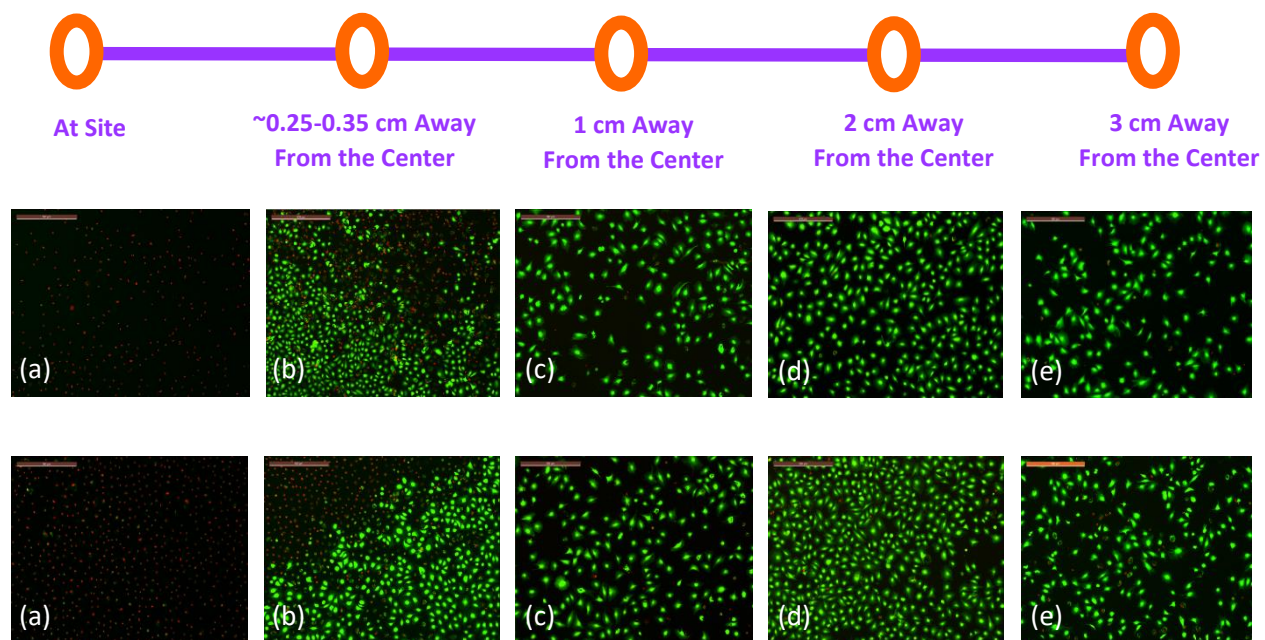


Figure 4.11 0.05 g of Mg (top row) and Mg-Ti (bottom row) are located at the center of the dish and live/dead images taken at (a) at site, (b) ~0.25-0.35 cm away, (c) 1 cm away, (d) 2 cm away, and (e) 3 cm away from the center of the bulk particles, where the diameter of the bulk particles is approximately 0.5 cm, n=3.

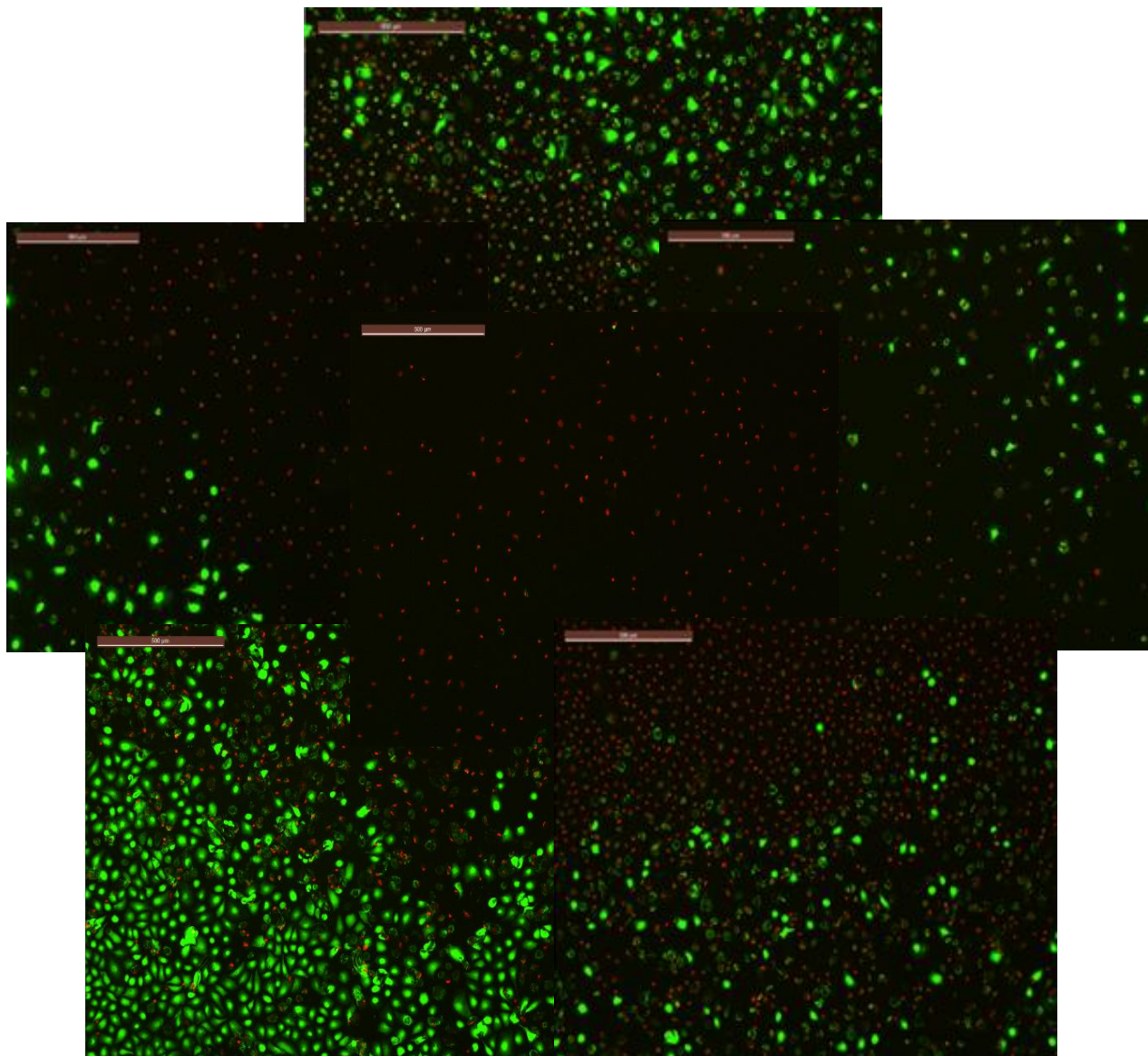


Figure 4.12 Images grouped to roughly show that the cells underneath the particles died completely, and the difference between the center and the edge of the particle bulk is very stark.

Proximity vs. % Cell Viability

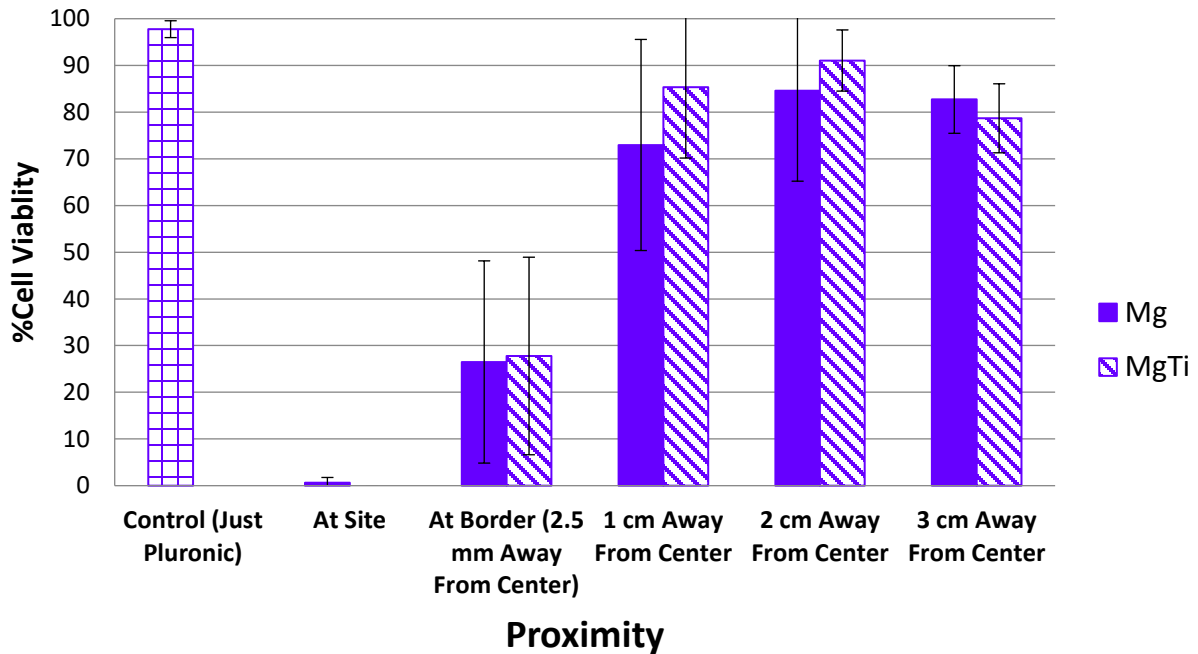


Figure 4.13 Graph showing cell viability as a function of proximity, distance away from the center of the bulk particles, n=3. Cells are almost completely dead at the center, but significant number of cells survived even 1 cm away.

pH vs. Proximity (cm) over Time

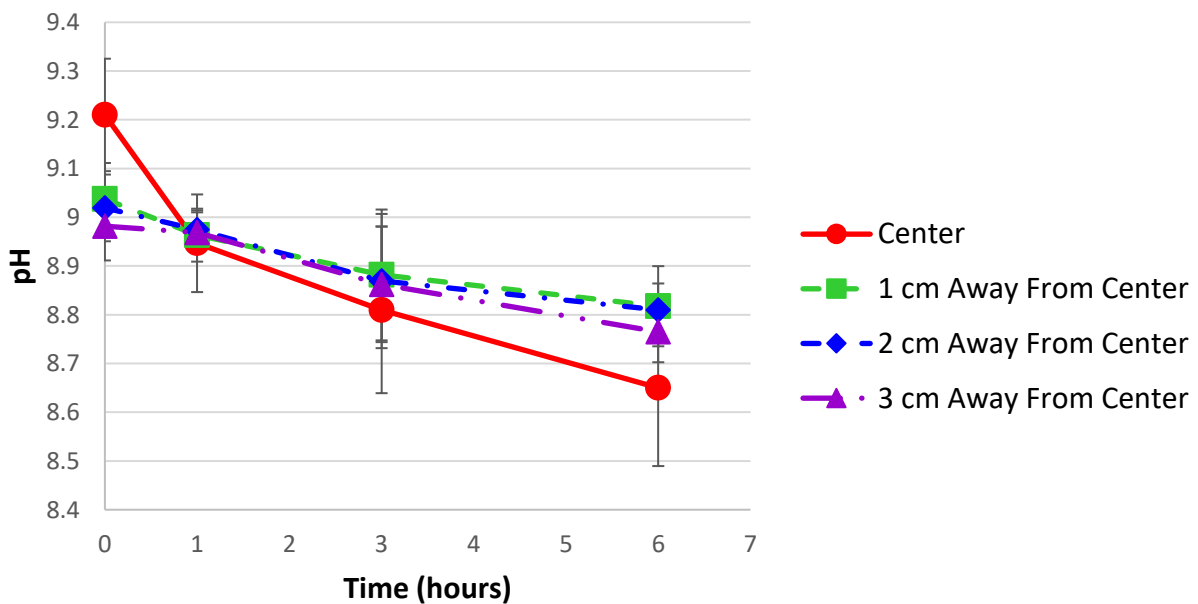


Figure 4.14 Graph showing pH as a function of proximity, distance away from the center of the bulk particles, n=3. There is no significant difference in pH at different locations.

4.4 Discussion

This study demonstrated that cytotoxicity of Mg and Mg-Ti galvanically coupled particles was determined by particle concentration, cell density, time, and proximity. Mg and Mg-Ti kill cells in a dosage dependent manner, with Mg-Ti killing cells more effectively than Mg alone. In a previous study, cell viability was shown to be a function of particle concentration and had variable in viability within the sample due to factors like local cell density and local particle concentration [15]. This study varied cell density to determine if it would have an effect on the efficacy of particle cytotoxicity. Post hoc Tukey test comparing the cell viability between different cell densities at different particle concentrations showed no statistical significant effects of cell density. However, when the rate of cell viability drop (the slope from the cell viability and particle concentration graph) was measured for lower particle concentrations from 0 to 250 $\mu\text{g/ml}$, the change in cell viability over the change of particle concentrations were significantly different from each other between lower cell densities (5,000 and 10,000 cells/cm^2) and higher cell densities (20,000 cells/cm^2 and 30,000 cells/cm^2). This shows that when cells are confluent, the particles cannot kill as readily at lower dosage.

5,000 cells/cm^2 cell density group showed different characteristic behavior when treated with particles, compared to the other cell densities. Even the 5,000 cells/cm^2 cell density control group had low cell viability of around 73%. It is hypothesized that MC3T3 cells are adherent cells that may not survive as well when they are not in a confluent layer. At this low cell density, the cells were seeded very sparsely, so that there were many single cells that were too far away from other cells for any cellular communication. When Mg particles were introduced, cell viability of this low cell density group exponentially dropped, but then was able to maintain a certain level of cell viability of approximately 20-30% at higher concentrations. But this was not

the case for Mg-Ti group. For Mg-Ti group, cell viability exponentially decayed to zero. The reason for this observation is not readily explained experimentally, but happened for all samples of the Mg group (n=3). This phenomenon may be explained, based on the work done by Wilson et al. Wilson et al. showed that there is a relationship between apoptosis and gap junctional intercellular communication (GJIC), where cells undergoing apoptosis had increased GJIC [17]. Also, Wilson et al. noticed that early apoptotic cell bodies were still coupled to healthy cells via gap junctions, allowing cell-cell communication. When cells are induced to undergo apoptosis, a majority of cells undergo apoptosis, but a subpopulation of cells initiate mitosis, suggesting that these cells are functioning to rescue the population. Besides the apoptosis inducer (ex. ROS), cells may be more prone to undergo cell apoptosis if surrounding cells undergo cell apoptosis, releasing chemical signals via gap junctions to signal other cells. When cells are seeded sparsely, an apoptotic body will not cause other cells to undergo apoptosis since there is no cell-cell communication. However, for Mg-Ti group, cells may still be killed because there are enough toxic species to kill the cells even without cell-cell communication. This is just a speculation based on previous studies and theories; further analysis is needed to explain this phenomenon.

When cell density increased, the cells were better able to tolerate the cytotoxicity of the particles at lower concentrations. When cell density was high, cells near particles worked together to engulf the particle, which could not be seen when cell density was low. Those cells on top of, or near the particles were very viable, despite their close proximity to the particle. This finding implies that there needs to be sufficient cytotoxic species generated to induce cellular apoptosis for cells around that specific particle. When there are only few cells, a particle can generate enough cytotoxic species to kill them, but if there are too many cells around a

particle, there will not be enough of cytotoxic species to go around for the cells to die, indicating a threshold.

Cell viability was measured at different time periods to determine the duration of cytotoxicity of these particles. 10,000 cells/cm² cell density was chosen arbitrarily. The particles actively killed and then once they were finished corroding, the remaining cells either remained viable or even proliferated, depending on the particle concentrations. Based on the cell viability-time plots (Fig. 4.6), which showed either recovery or maintenance of cell viability after 24 hours, it is assumed that most Mg and Mg-Ti particles finish corroding between 18 and 24 hours. For low particle concentrations (up to 500 µg/ml), some cells are killed by t= 18 hours, but they can recover, usually due to proliferation of remaining live cells. For higher particle concentrations (from 750 µg/ml and above), remaining live cells stay alive, but do not proliferate (unless the concentration is too high that all cells are killed). This indicates that at intermediate particle concentrations, some cells remain alive because the particles do not produce high enough toxic species to kill all the cells, but they seem to prevent the remaining cells from proliferating. And it is interesting to note that at some concentrations (ex. 250 µg/ml of Mg-Ti), many cells were killed within 18 hours, even below 5%, and yet, they recovered significantly, while at some higher concentrations (ex. 750 µg/ml of Mg), more cells were alive at 18 hours, but they did not proliferate. This shows that for cells to recover, the number of live cells is not as significant as the concentration of ROS or toxic species produced that must be affecting cell proliferation. Bergamini et al. supports this result, as Bergamini et al. stated that low dose of ROS stimulates mitogenic cell proliferation, while intermediate dose of ROS induces cell growth arrest, and high dose of ROS induces cell death via apoptosis and necrosis [18].

If all the cells were killed during active particle corrosion in the first 24 hours, then the cell viability remained zero after 24 hours. Just to make sure that cell recovery at lower particle concentration is not due to the decrease of dead cells (from dead cells falling off the surface), the number of live and dead cells were counted and indeed, live cell count increased for some concentrations. This study shows that the particle corrosion is very short and temporary, but very effective in killing cells at higher particle concentrations.

The pH was measured over time as well to determine if the increase in pH is the main killing effect of Mg-Ti galvanic couple. Although the pH did increase as the particle concentration increased, the pH did not vary over a wide range but stayed between 7.4 and 9.1. All cells died at 1750 $\mu\text{g/ml}$ or lower at all cell densities, and the pH at this particle concentration was around 8.7. Although the Mg-Ti killed more cells than Mg, there was no difference in pH measurements. Also, pH did not explain the killing and recovery phases. For example, at 250 $\mu\text{g/ml}$, for both Mg and Mg-Ti, the cell viability decreased, more significantly for Mg-Ti than Mg, before 24 hours, and then recovered almost completely after 24 hours. However, the pH measured at this particle concentration over time did not vary significantly for both Mg and Mg-Ti, where pH read around 7.8-8.1. If pH was consistent over time, it is unclear why cells would die in significant number in the first 24 hours but then recover afterward. In addition, our earlier work demonstrated that within the range of pH measured in this work, MC3T3 cells remained substantially viable in pH solutions in this range [15].

When cell viability was measured as a function of distance away from the bulk cluster of particles, again pH did not seem to be the primary killing effect. Cell viability increased with the increasing distance away from the particles, where the cells immediately underneath the particles were completely dead, while the cells immediately next to the particle cluster, even at the

borderline, were more viable. These results show that even though pH is relatively homogeneous, proximity has a significant effect on cell viability, indicating that some factor other than pH is significantly killing the cells. Clearly, this experiment shows that particles have to be very proximal, within 2 mm, in order to be able to completely kill cells.

Pluronic gel did not have any significant effect on the cell viability, which indicates that pluronic gel, at 20% concentration, did not hinder oxygen and nutrient diffusion to the cells underneath. However, the clustered particles at the center could have limited oxygen transfer to the cells directly underneath the particles, potentially contributing to cell death. Baumann et al. investigated cell viability of different cell types under oxygen deficient system, where glucose oxidase depletes oxygen from the cell culture medium by oxidizing glucose and reducing molecular oxygen to hydrogen peroxide [19]. Under this oxygen deficient model, oxygen is completely depleted to zero within 2 minutes, and when cell viability was measured after 2 hours, approximately 10% cells survived for CHO/AA8 Chinese hamster cells and EMT6 murine mammary carcinoma cells, and approximately 85% cells survived for U251 human glioma cells [19]. In the proximity experiment, molecular oxygen level was not measured, but oxygen must not be completely depleted, even if reduced, under the pluronic gel with the particles present. But the cells directly underneath the particles completely died within 1 hour, which is less than the cells in the oxygen deficient system from the study performed by Baumann et al. Therefore, the cells from the proximity experiment could not have died solely due to reduced oxygen diffusion. In order to eliminate these factors, the proximity design can be modified. Instead of seeding the cells at the bottom, pouring the pluronic gel on top of the cells, and adding the particles on top of the gel, the particles can be at the bottom and the cells mixed in the pluronic gel matrix poured on top of the particles. In this way, the cells can be on top of the particles, and

oxygen and nutrient can diffuse more easily to the cells, and yet if the cells close to the particles die, the study can safely conclude that the cells died due to the redox reactions of the Mg and Mg-Ti particles.

Overall, this study shows that cells are killed by Mg and Mg-Ti particles in particle dosage, time, and proximity-dependent manner. Cell density did not have a significant effect on the cytotoxicity of Mg and Mg-Ti particles except at low particle concentrations, where the cell viability remained high (same as control group) only for the high cell density groups. And at low concentrations, the cells were able to tolerate the particles even at very close proximity, indicating that the generation of cytotoxic species has not reached a threshold, while at higher concentrations, cells in close proximity to the particles did not survive. Also, the killing was time-dependent, where there were clearly two distinct phases, killing and recovery phases, where the corrosion of Mg or Mg-Ti particles killed cells within 18 to 24 hours, and if enough cells remained alive, they stayed alive after the corrosion ceased and then proliferated, which depended on the dosage and the cell density.

As mentioned in the previous study, the pH does not explain the increased cytotoxicity of the galvanic couple of Mg and Ti compared to that of Mg alone, since the pH measurements are comparatively the same for both groups. The pH also does not explain the killing and recovery phases, since pH readings do not change over time. The pH also does not explain why more cells closer to the particles were killed compared to the cells further away from the particles, since pH measurements were uniform across distance. Although this study did not directly prove that ROS generation due to reduction reaction is killing the cells, there are good indicators that ROS may be the cause of cytotoxicity of Mg and Mg-Ti particles. ROS are unstable species that rapidly react, which means that ROS cannot travel very far, and this may explain why the cells

only close to the particles are killed. Also, higher cell density can tolerate a particle better even in close proximity because there are not enough ROS produced to trigger cellular apoptosis at lower particle concentrations. Further analysis and investigations are needed to prove that ROS generation is the cause of Mg toxicity.

The cytotoxic effects of Mg and Mg-Ti are very short lived and temporary, and the target area is apparently small. These two factors can be advantageous in designing this material for therapeutic purposes, such as killing bacterial infections or tumors. For example, designing an orthopedic implant where Ti is commonly used, galvanically coupling Mg in the metal implant can help prevent biofilm formation on the implant surface, which is known to be very resistant to antibiotics, often resulting in the removal of the implant [20-23]. But since Mg and Mg-Ti couples only kill cells in close proximity, this galvanic couple can kill or prevent biofilm formation at the surface, without harming bone or tissue surrounding the implant. In fact, as mentioned earlier, release of Mg ions can travel to bone forming site and enhance bone formation. Since Mg corrodes very quickly, the cytotoxic effect will be temporary, lasting from few days to few weeks, only to prevent or kill post-surgery infections, and then Mg will be fully degraded and gone, so that the normal biological functions can take over. Also, after surgical removal of malignant tumors, the insertion of Mg or Mg-Ti at the tumor site may be able to kill remaining tumor cells to prevent tumor re-growth. Further analysis is needed for designing Mg or Mg-Ti couples for their potential therapeutic effect, such as investigating the cytotoxicity of this galvanic couple on bacterial and tumor cells. However, this study shows that Mg and Mg-Ti shows a great promise in killing cells in a mechanism other than increase of pH, and this finding can be very useful.

4.5 Conclusion

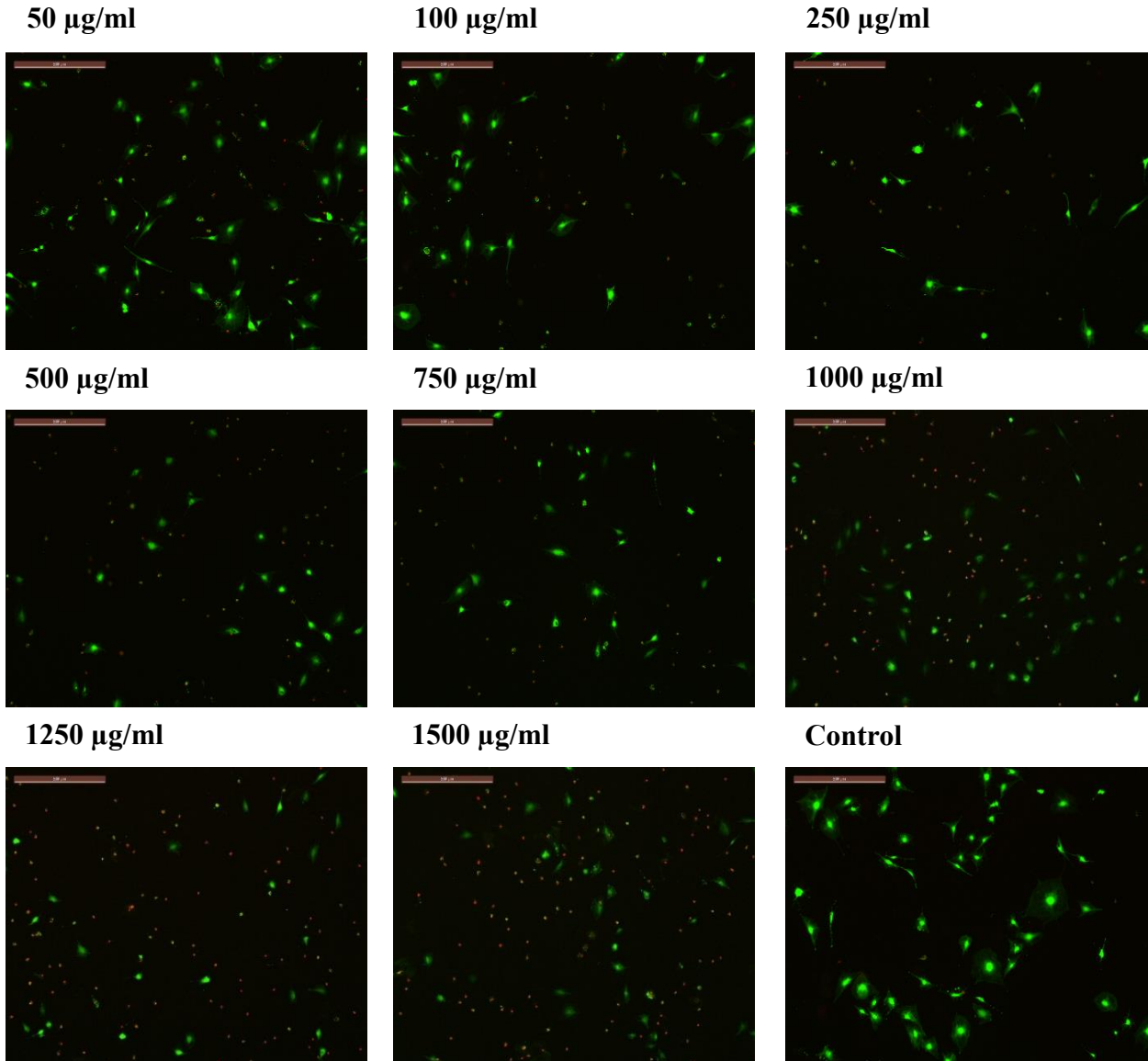
In conclusion, this study has shown that Mg and Mg-Ti particles exhibit killing effects on MC3T3 cells in a dose dependent manner where the cell density did not affect the killing. However, the rates of cell viability drop with increasing particle concentrations, especially at low particle concentration range, were significantly different between low cell densities and higher cell densities. There are two phases in the process: killing and recovery. The killing phase occurs within the first 24 hours during the particle corrosion, and then the recovery phase occurs after at the end of the particle corrosion. At lower particle concentrations, the remaining live cells can proliferate, but at higher concentrations, they do not. Proximity plays an important role in killing cells. Cells close to the particles (whether as an individual or bulk) are killed more effectively than cells further off. Increase of pH may negatively affect cell viability, but does not seem to play a primary role in killing. pH does not explain why Mg-Ti is more effective in killing than Mg alone, nor does it explain why killing occurs only during the first 24 hours, or why only those cells in close proximity to the particles are killed.

4.6 Acknowledgements

This work was supported, in part, by DePuy Synthes.

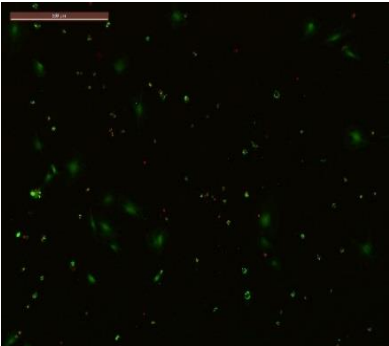
4.7 *Supplementary Images*

5,000 cells/cm², Mg-Treated for t= 24 hours

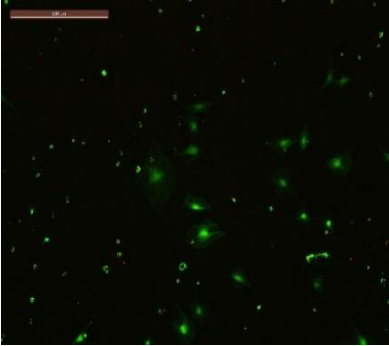


5,000 cells/cm², Mg-Ti-Treated for t= 24 hours

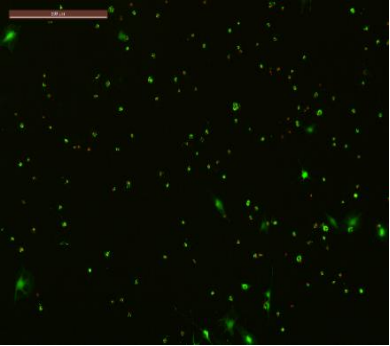
50 µg/ml



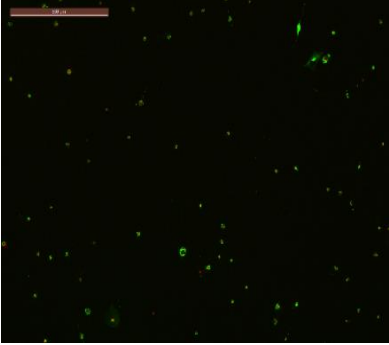
100 µg/ml



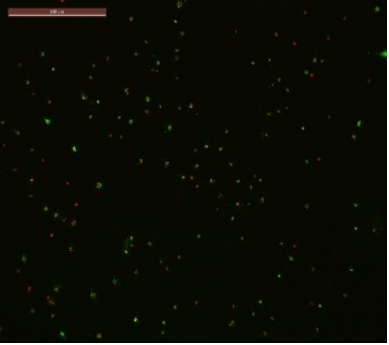
250 µg/ml



500 µg/ml

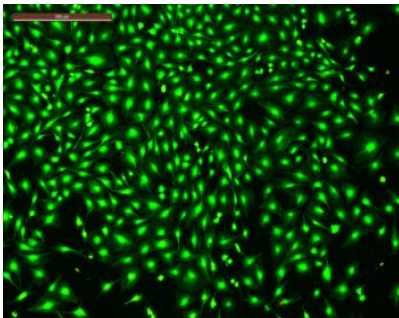


750 µg/ml

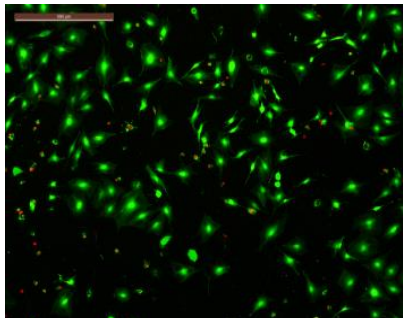


10,000 cells/cm², Mg-Treated for t= 24 hours

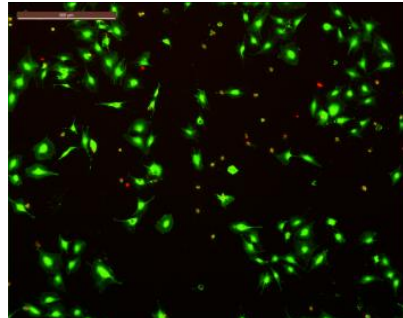
50 µg/ml



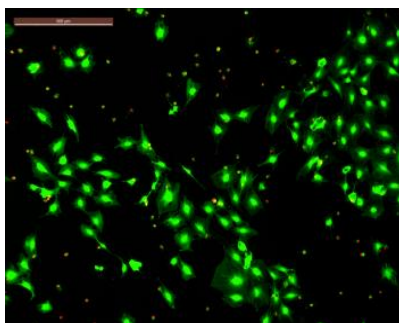
100 µg/ml



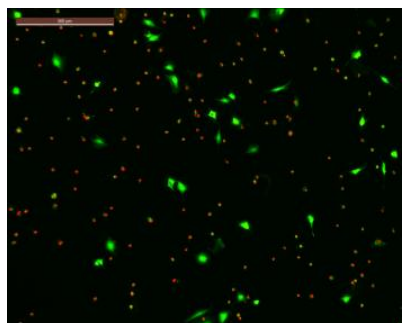
250 µg/ml



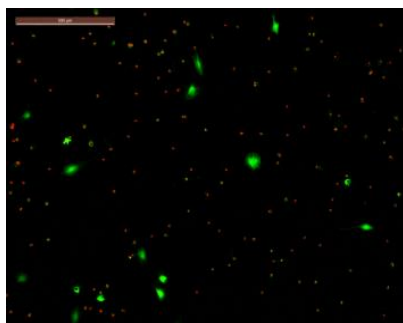
500 µg/ml



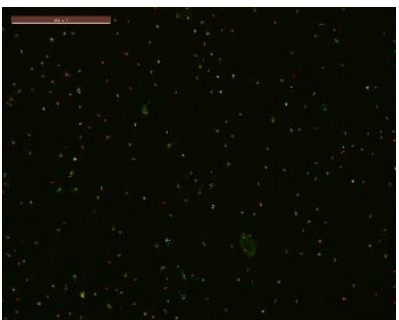
750 µg/ml



1000 µg/ml



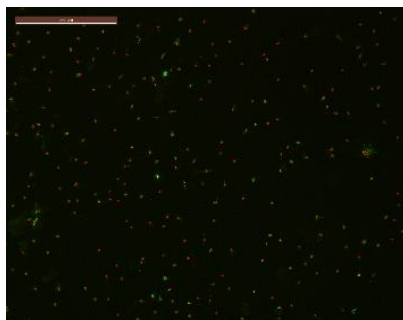
1250 µg/ml



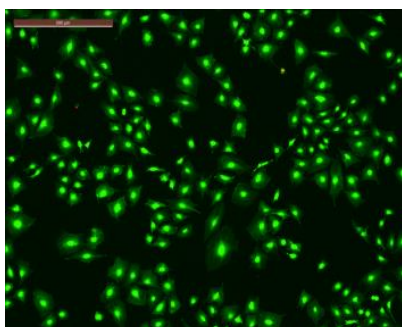
1500 µg/ml



1750 µg/ml

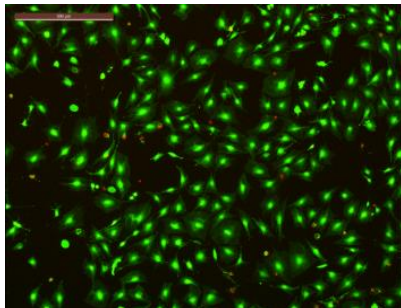


Control

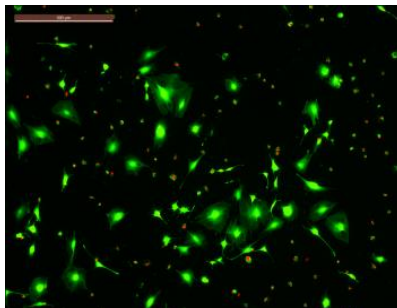


10,000 cells/cm², Mg-Ti-Treated for t= 24 hours

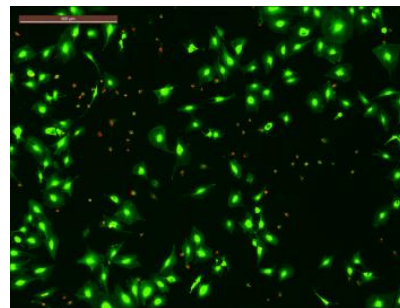
50 µg/ml



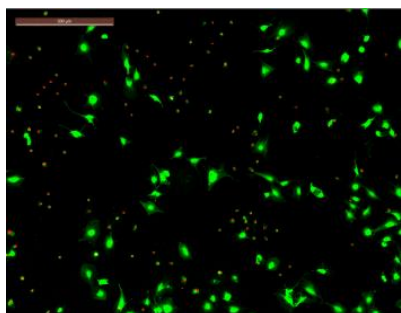
100 µg/ml



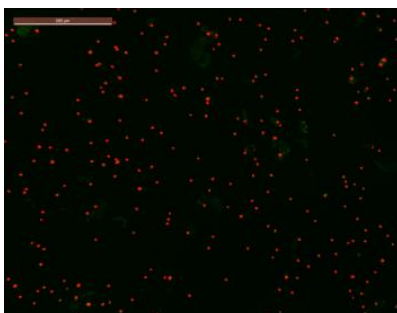
250 µg/ml



500 µg/ml



750 µg/ml

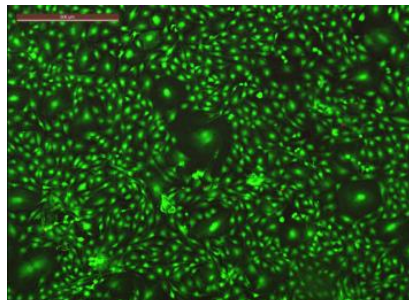


1000 µg/ml

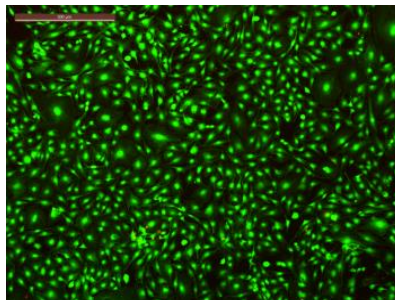


20,000 cells/cm², Mg-Treated for t= 24 hours

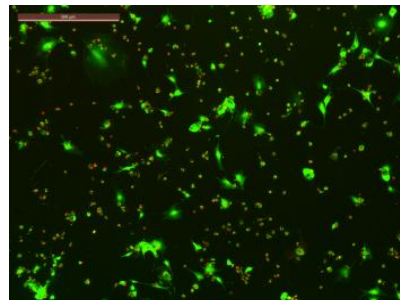
50 µg/ml



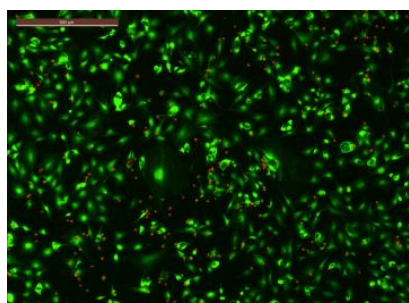
100 µg/ml



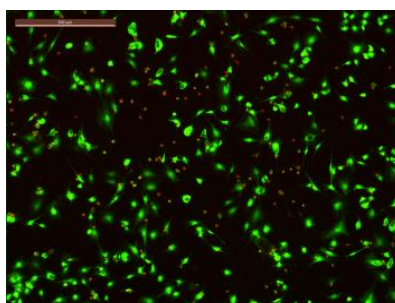
250 µg/ml



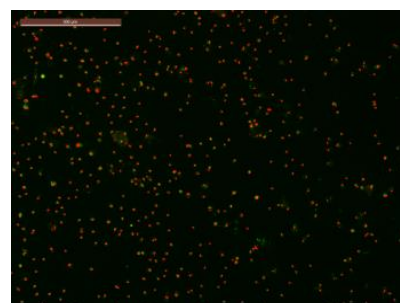
500 µg/ml



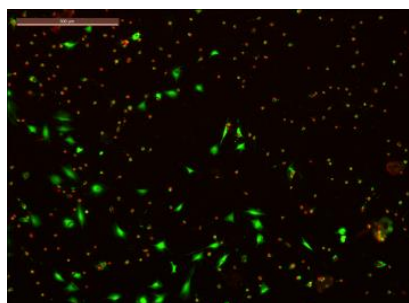
750 µg/ml



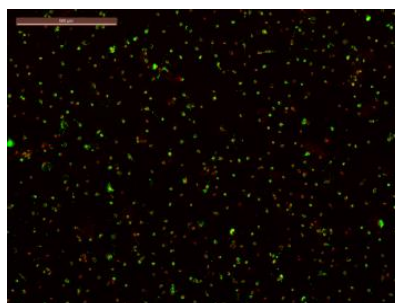
1000 µg/ml



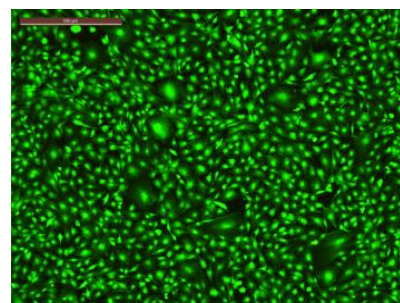
1250 µg/ml



1500 µg/ml

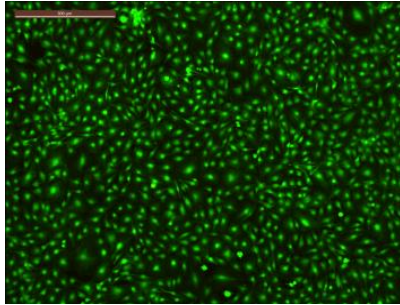


1750 µg/ml

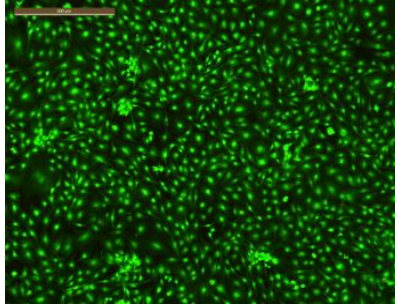


20,000 cells/cm², Mg-Ti-Treated for t= 24 hours

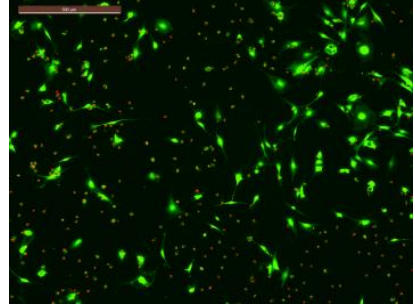
50 µg/ml



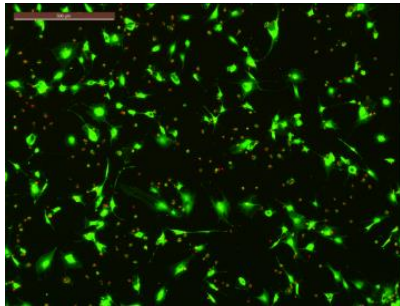
100 µg/ml



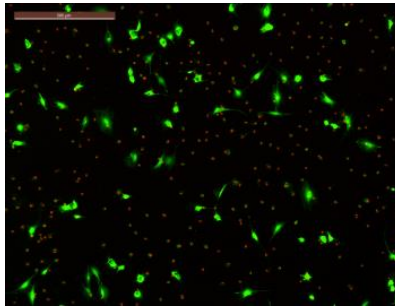
250 µg/ml



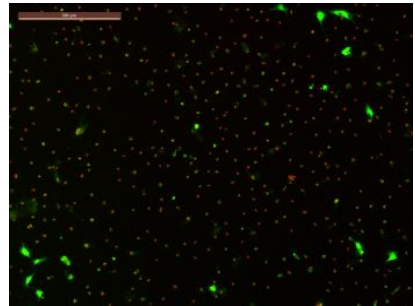
500 µg/ml



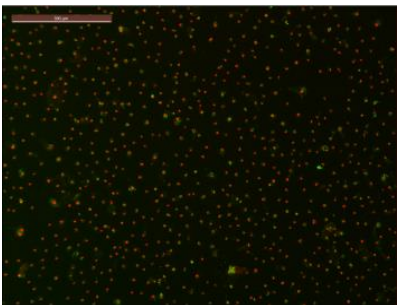
750 µg/ml



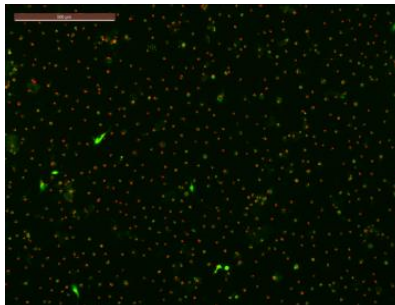
1000 µg/ml



1250 µg/ml

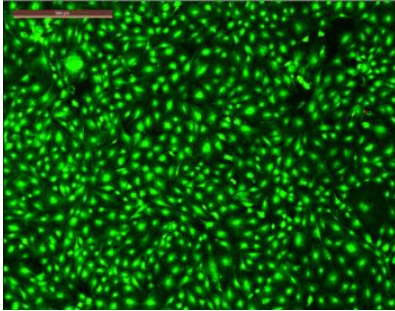


1500 µg/ml

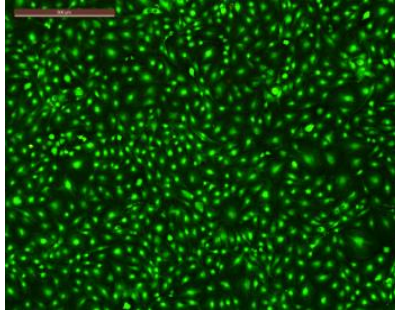


30,000 cells/cm², Mg-Treated for t= 24 hours

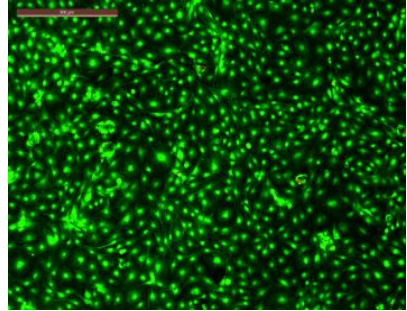
50 µg/ml



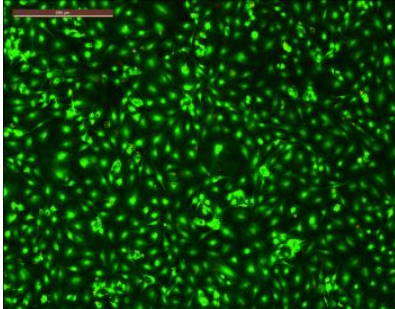
100 µg/ml



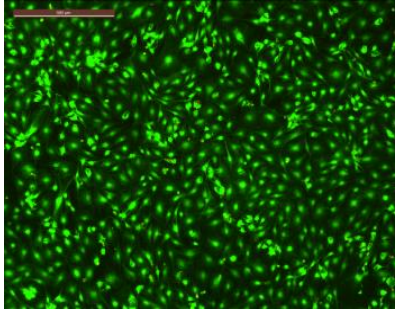
250 µg/ml



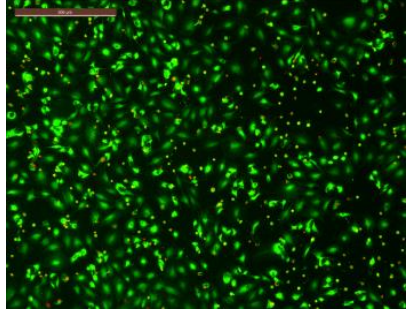
500 µg/ml



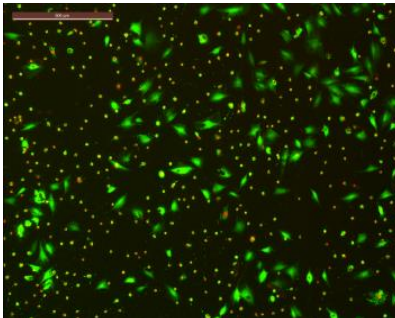
750 µg/ml



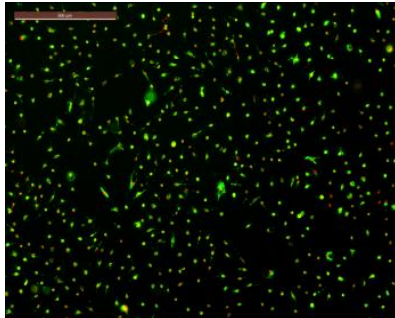
1000 µg/ml



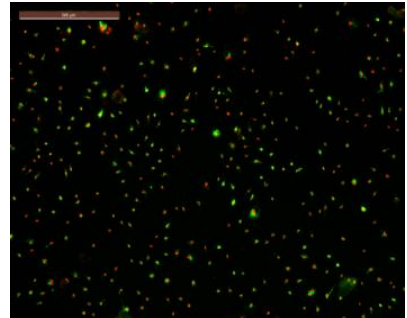
1250 µg/ml



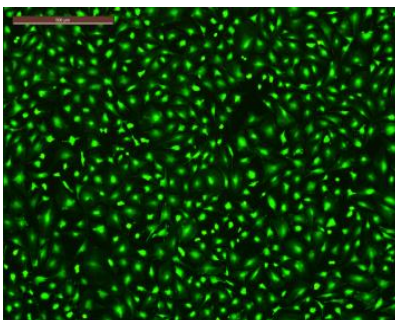
1500 µg/ml



1750 µg/ml

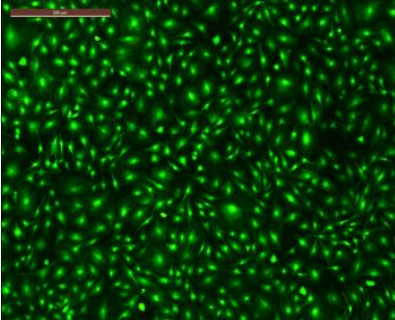


Control

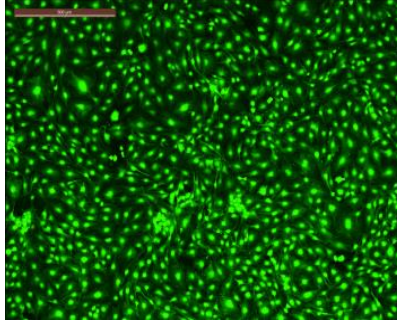


30,000 cells/cm², Mg-Ti-Treated for t= 24 hours

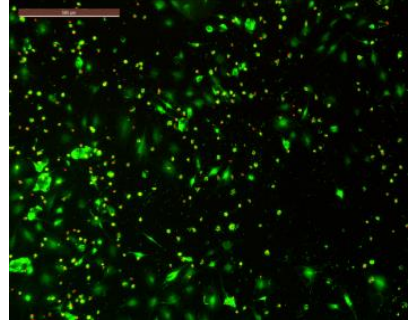
50 µg/ml



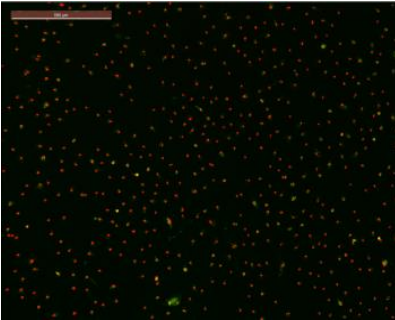
100 µg/ml



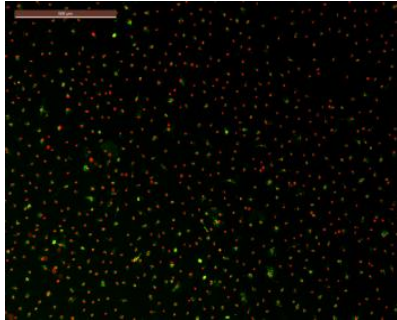
250 µg/ml



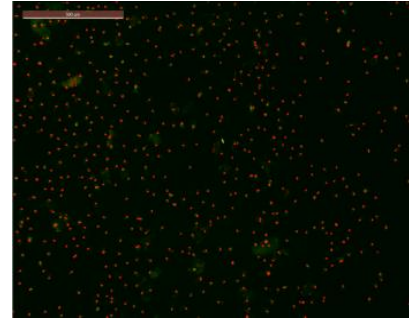
500 µg/ml



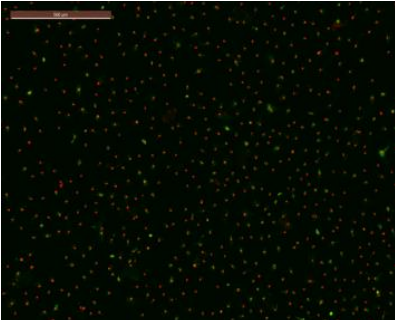
750 µg/ml



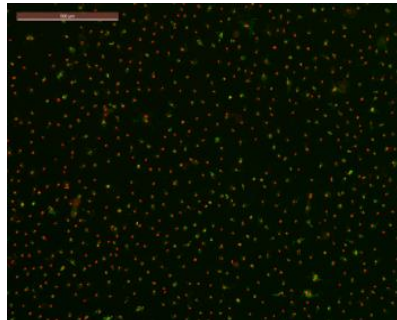
1000 µg/ml



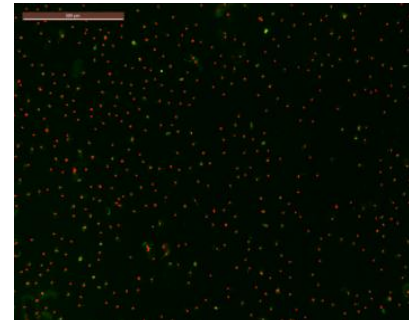
1250 µg/ml



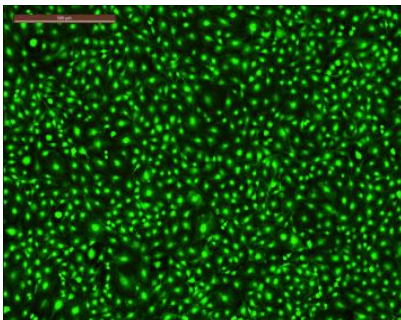
1500 µg/ml



1750 µg/ml

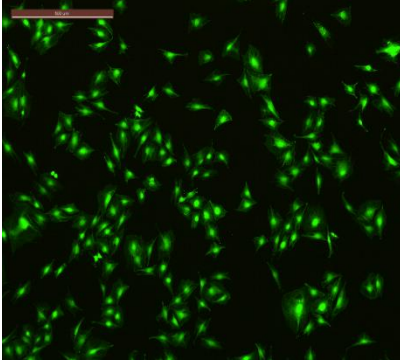


Control

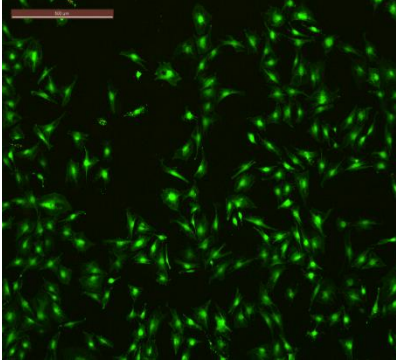


Control, 10,000 cells/cm², at different

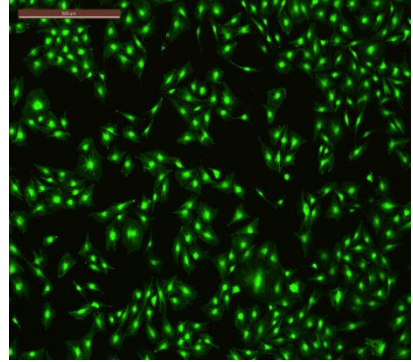
T= 1 hour



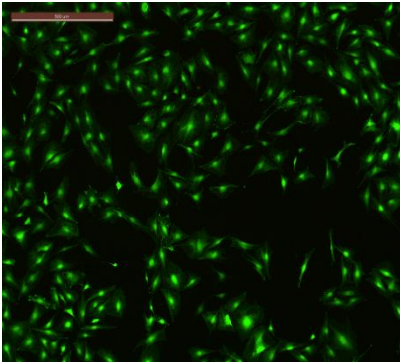
T= 3 hours



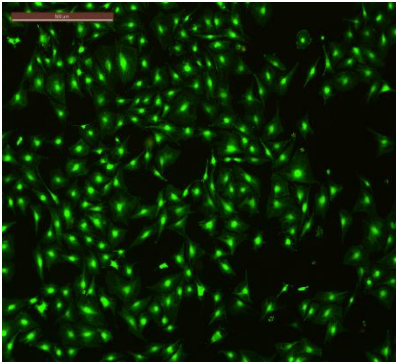
T= 6 hours



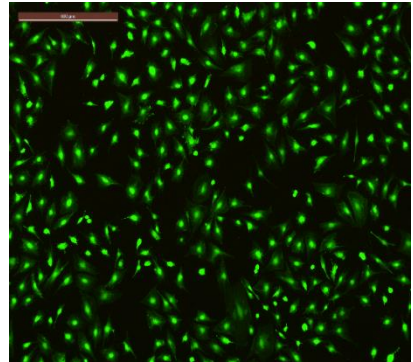
T= 12 hours



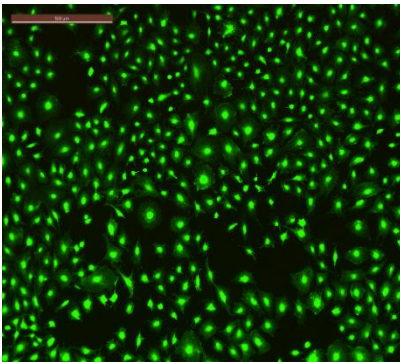
T= 18 hours



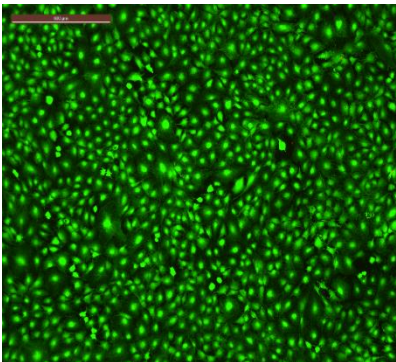
T= 24 hours



T= 48 hours

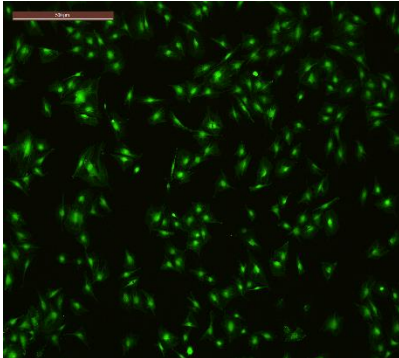


T= 72 hours

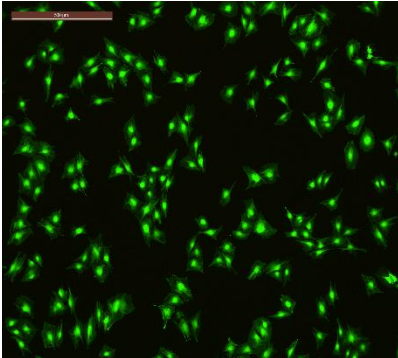


Mg 50 $\mu\text{g/ml}$, 10,000 cells/ cm^2 , at different times

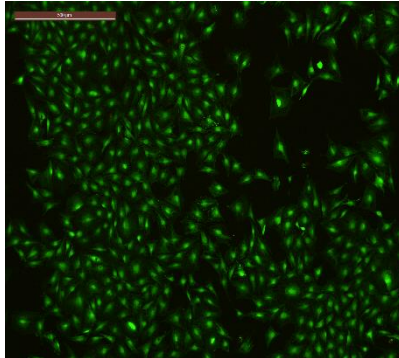
T= 1 hour



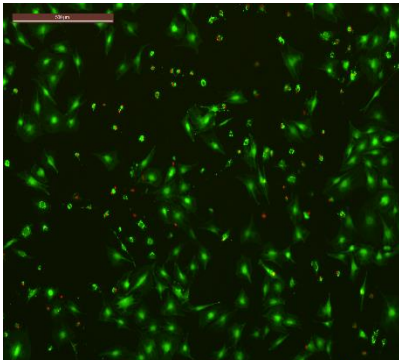
T= 3 hours



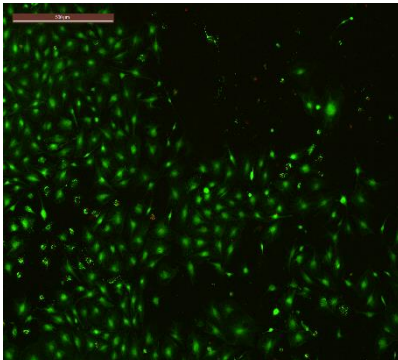
T= 6 hours



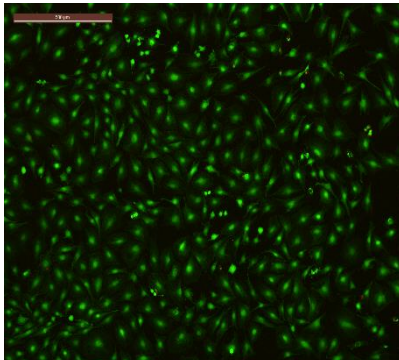
T= 12 hours



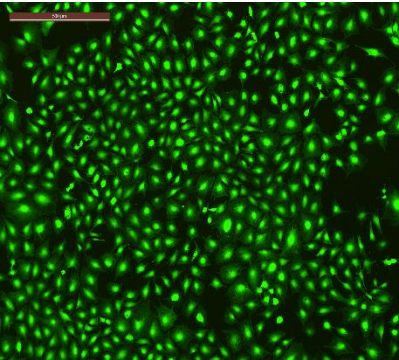
T= 18 hours



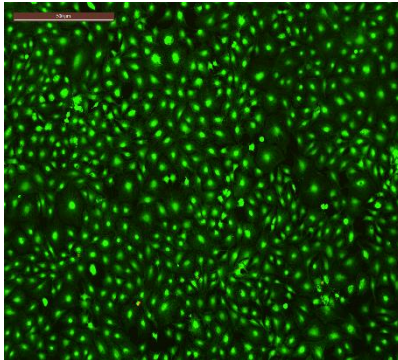
T= 24 hours



T= 48 hours

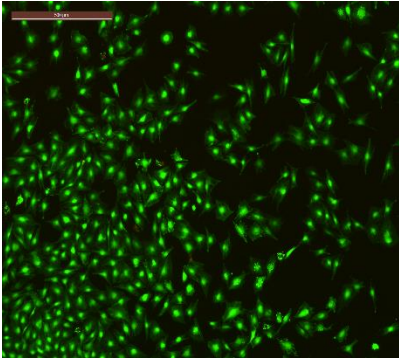


T= 72 hours

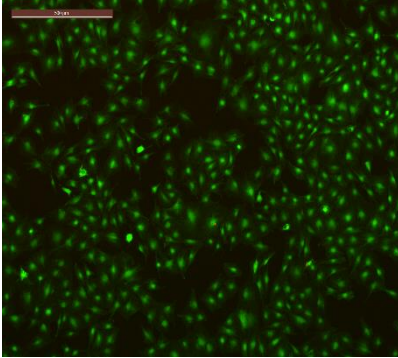


Mg-Ti 50 $\mu\text{g/ml}$, 10,000 cells/ cm^2 , at different times

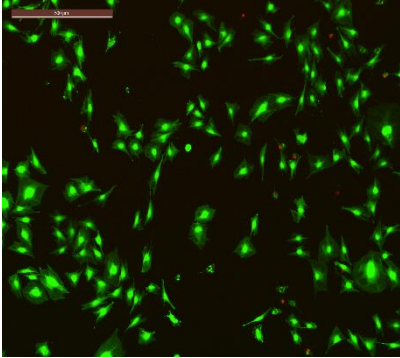
T= 1 hour



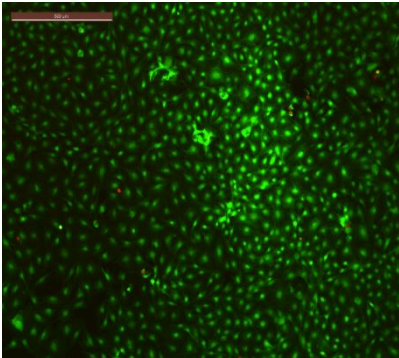
T= 3 hours



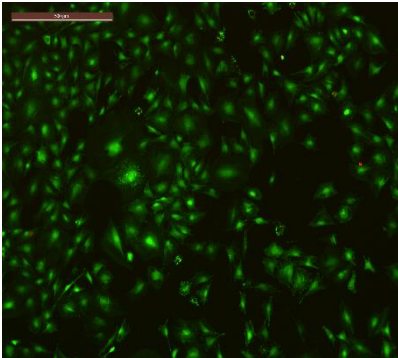
T= 6 hours



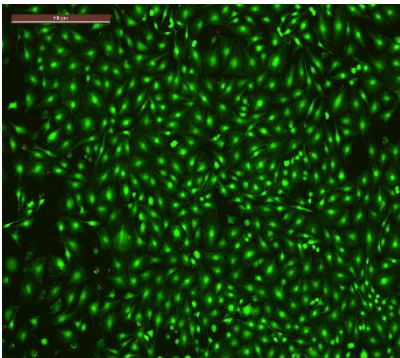
T= 12 hours



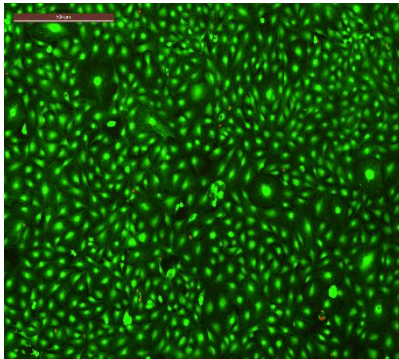
T= 18 hours



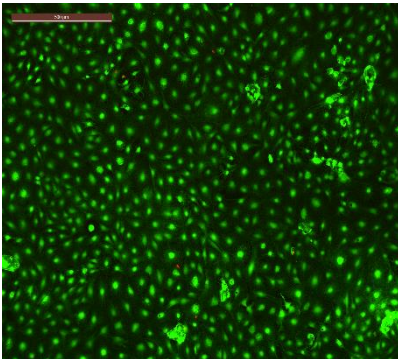
T= 24 hours



T= 48 hours

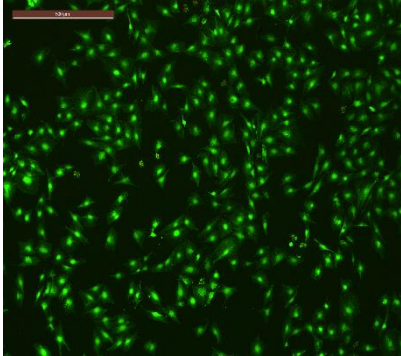


T= 72 hours

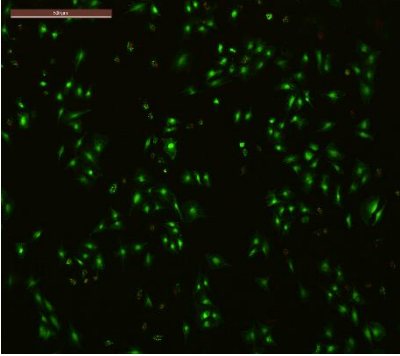


Mg 500 $\mu\text{g/ml}$, 10,000 cells/ cm^2 , at different times

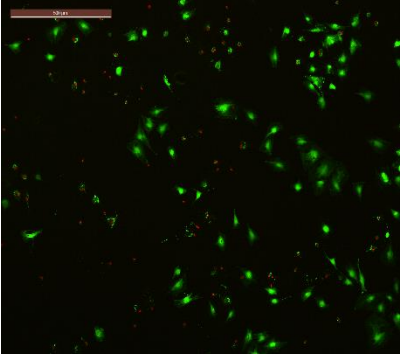
T= 1 hour



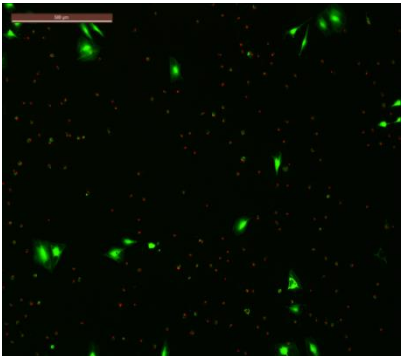
T= 3 hours



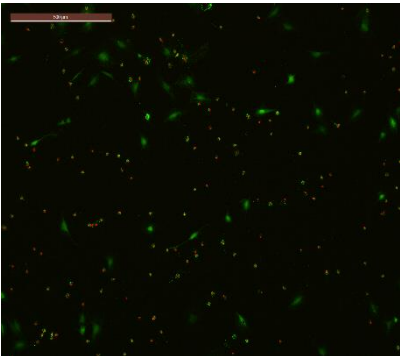
T= 6 hours



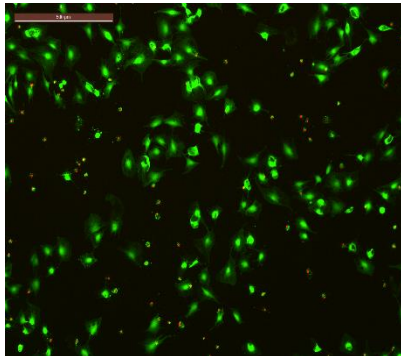
T= 12 hours



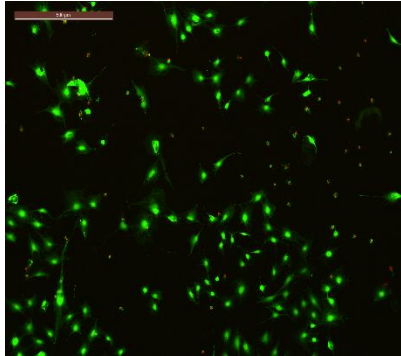
T= 18 hours



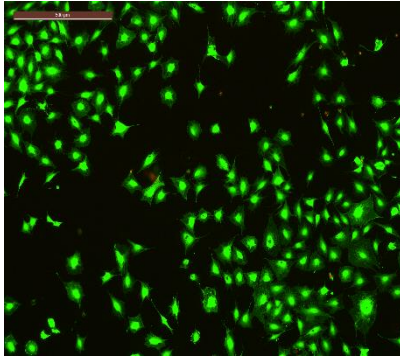
T= 24 hours



T= 48 hours

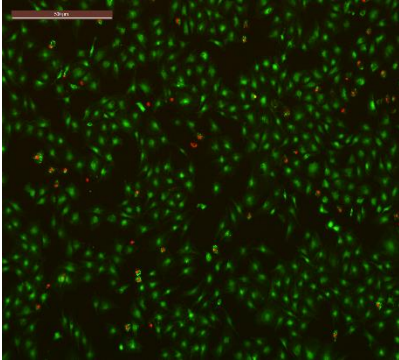


T= 72 hours

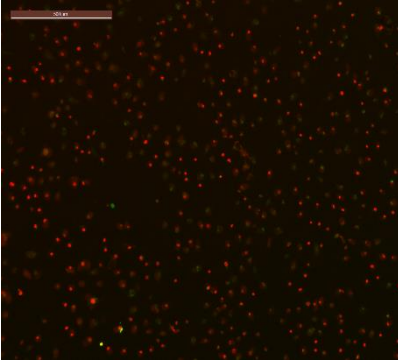


Mg-Ti 500 $\mu\text{g/ml}$, 10,000 cells/ cm^2 , at different times

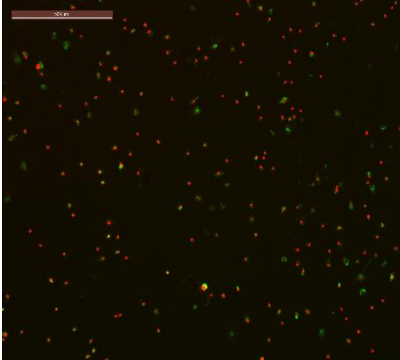
T= 1 hour



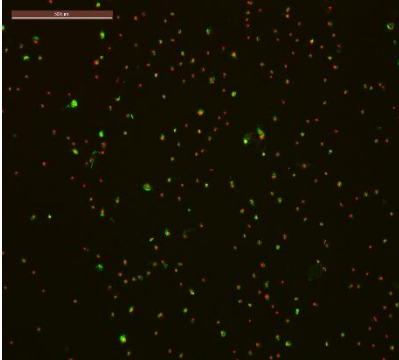
T= 3 hours



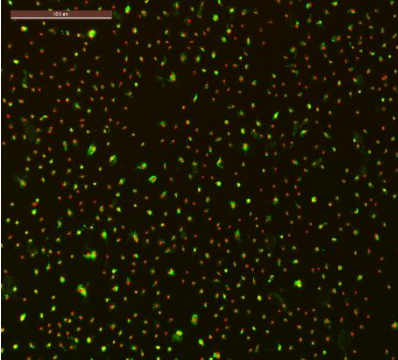
T= 6 hours



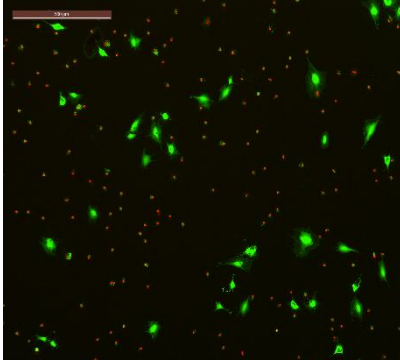
T= 12 hours



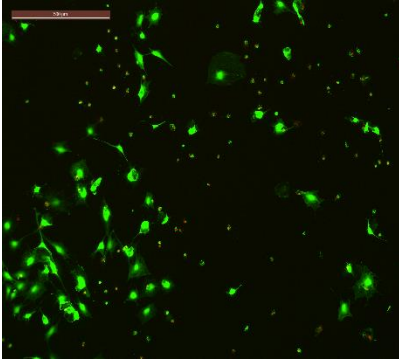
T= 18 hours



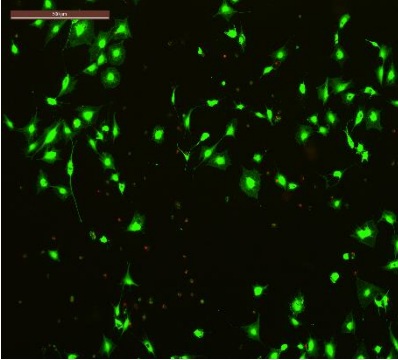
T= 24 hours



T= 48 hours

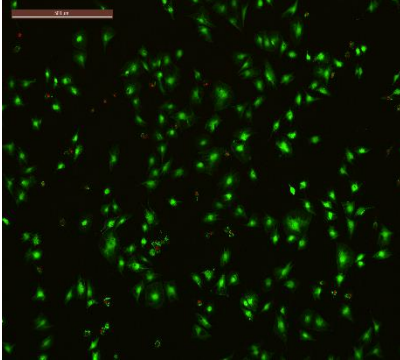


T= 72 hours

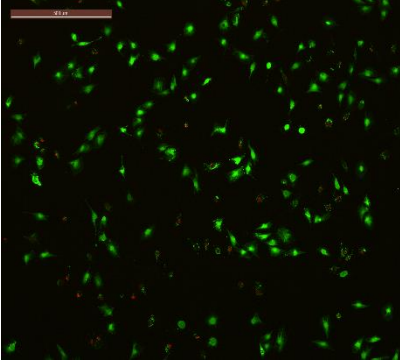


Mg 1500 $\mu\text{g/ml}$, 10,000 cells/ cm^2 , at different times

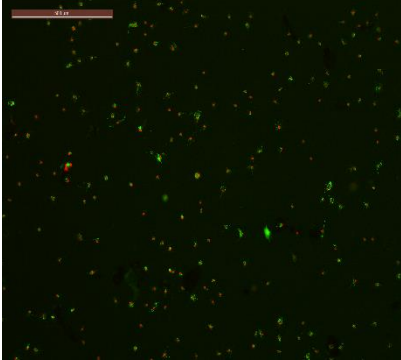
T= 1 hour



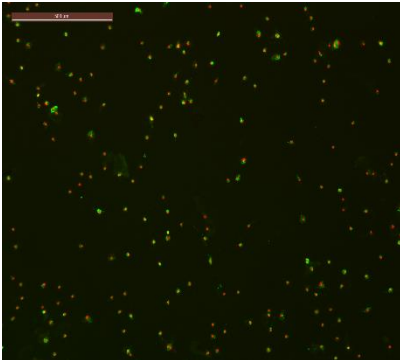
T= 3 hours



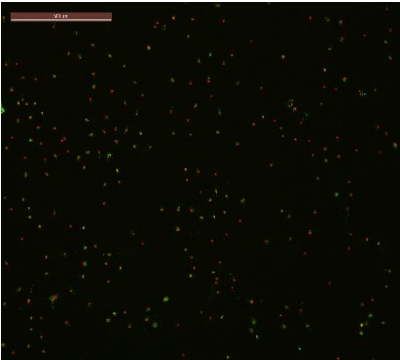
T= 6 hours



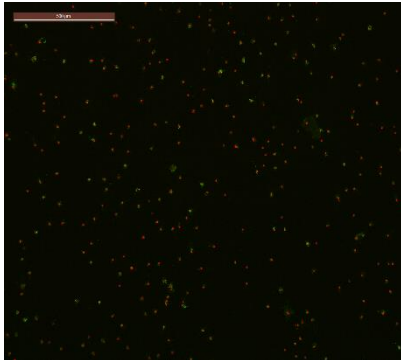
T= 12 hours



T= 18 hours

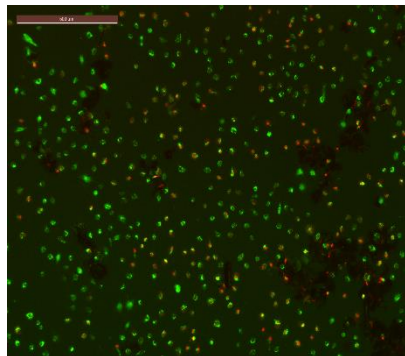


T= 24 hours

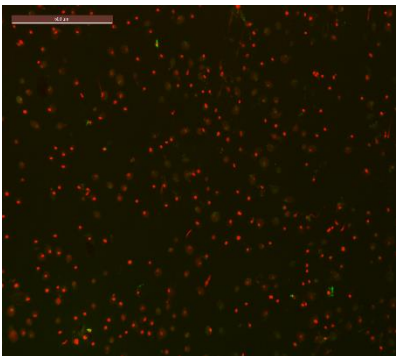


Mg-Ti 1500 $\mu\text{g}/\text{ml}$, 10,000 cells/ cm^2 , at different times

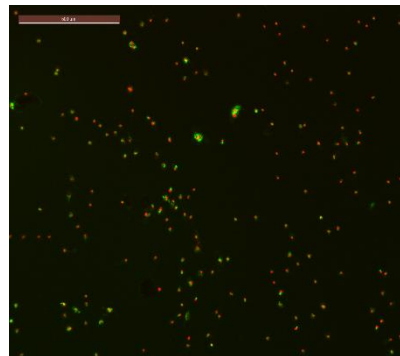
T= 1 hour



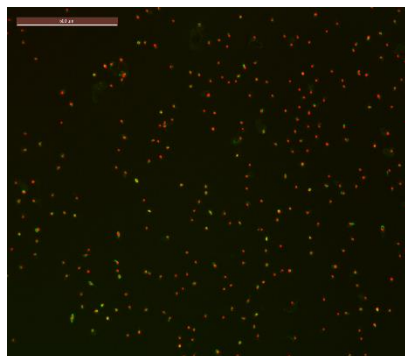
T= 3 hours



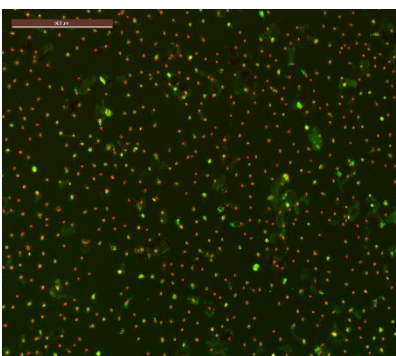
T= 6 hours



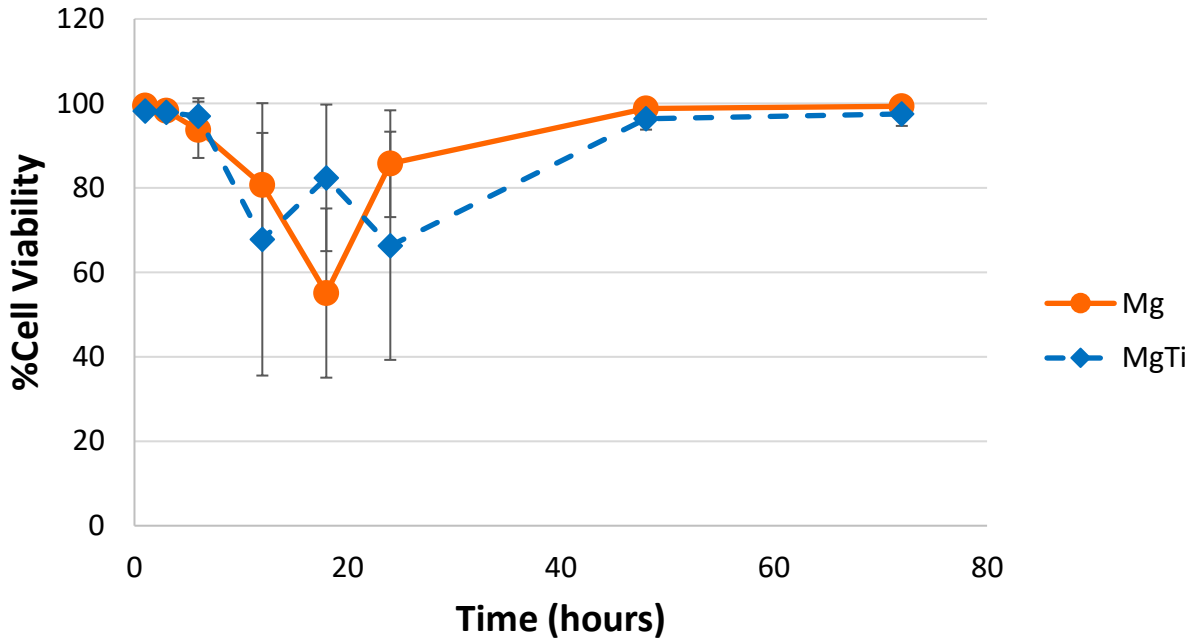
T= 12 hours



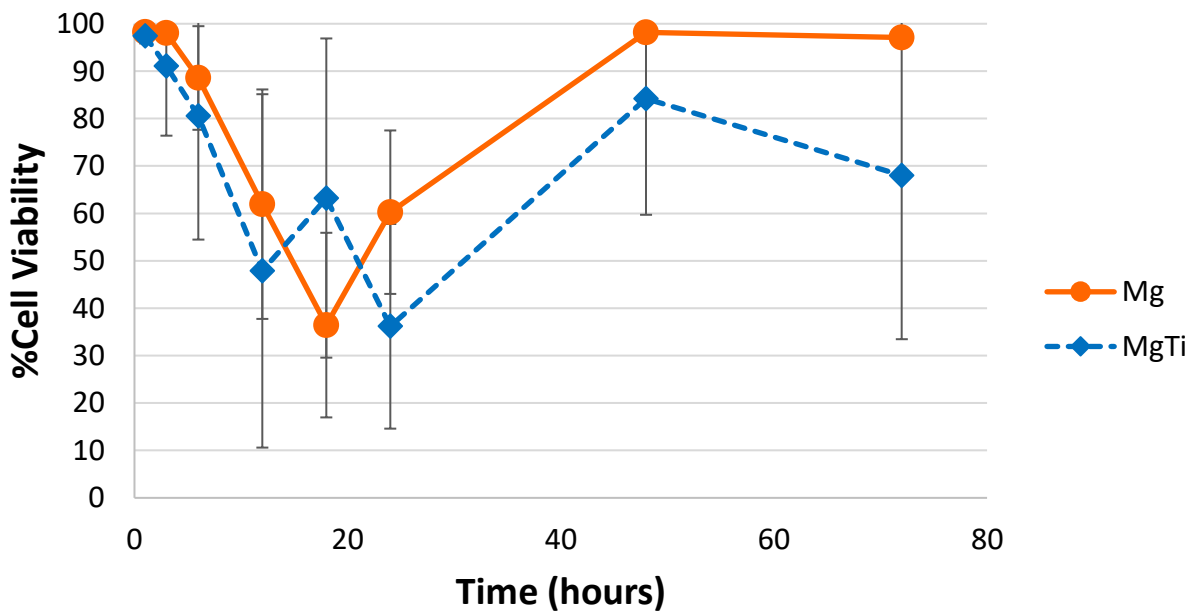
T= 18 hours



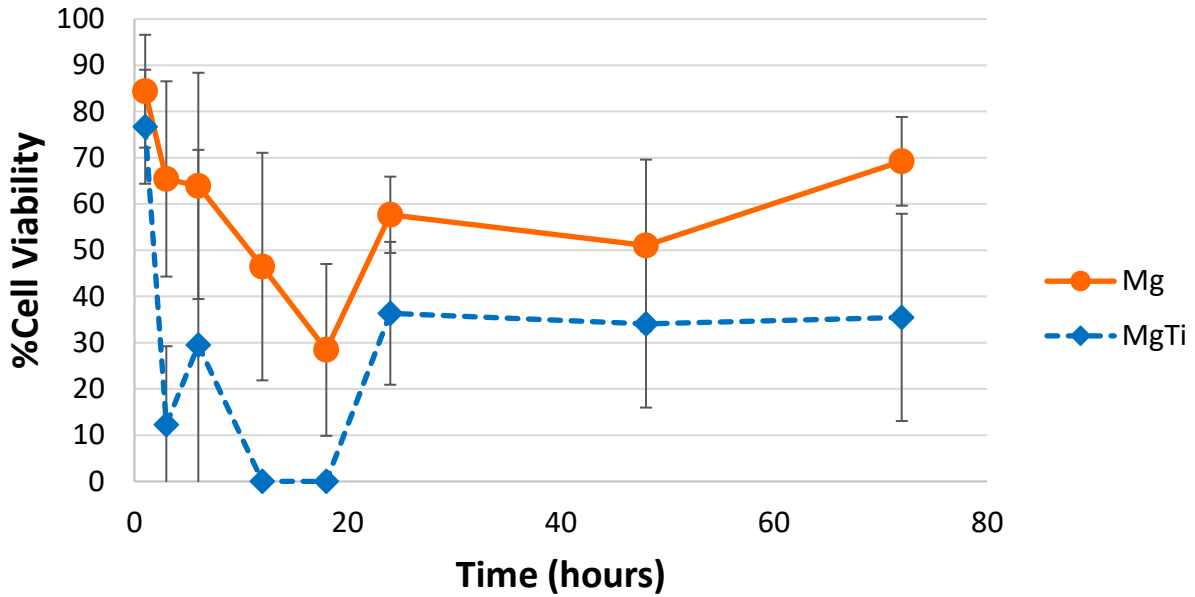
% Cell Viability over Time for 50 ug per ml



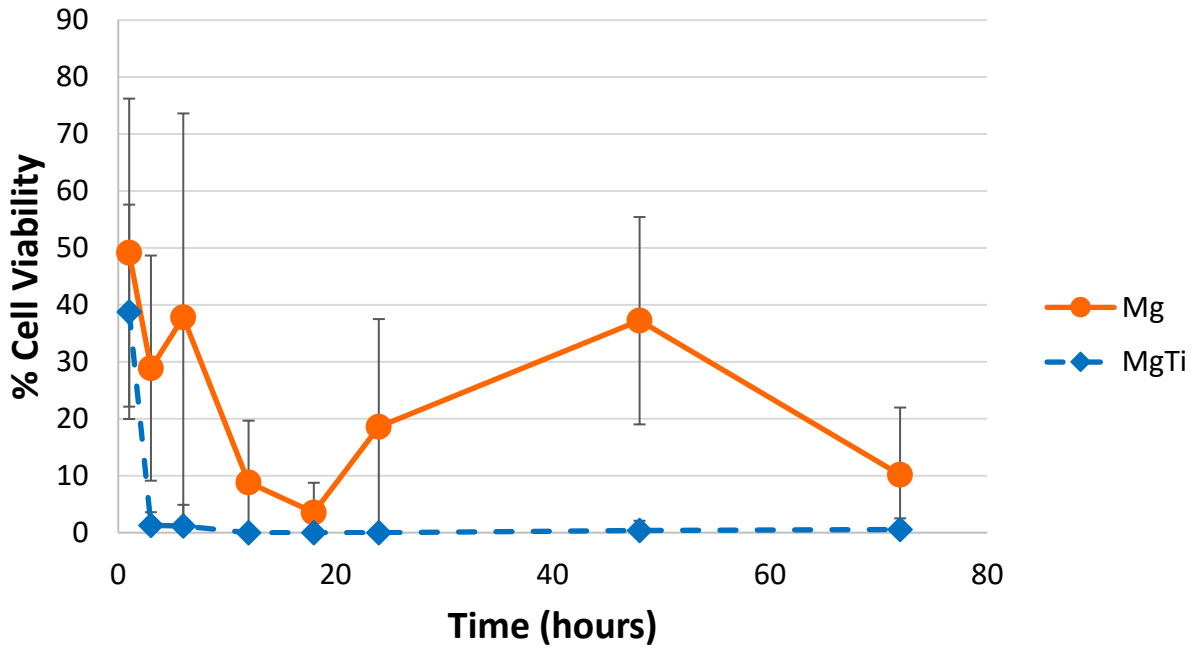
% Cell Viability over Time for 100 ug per ml



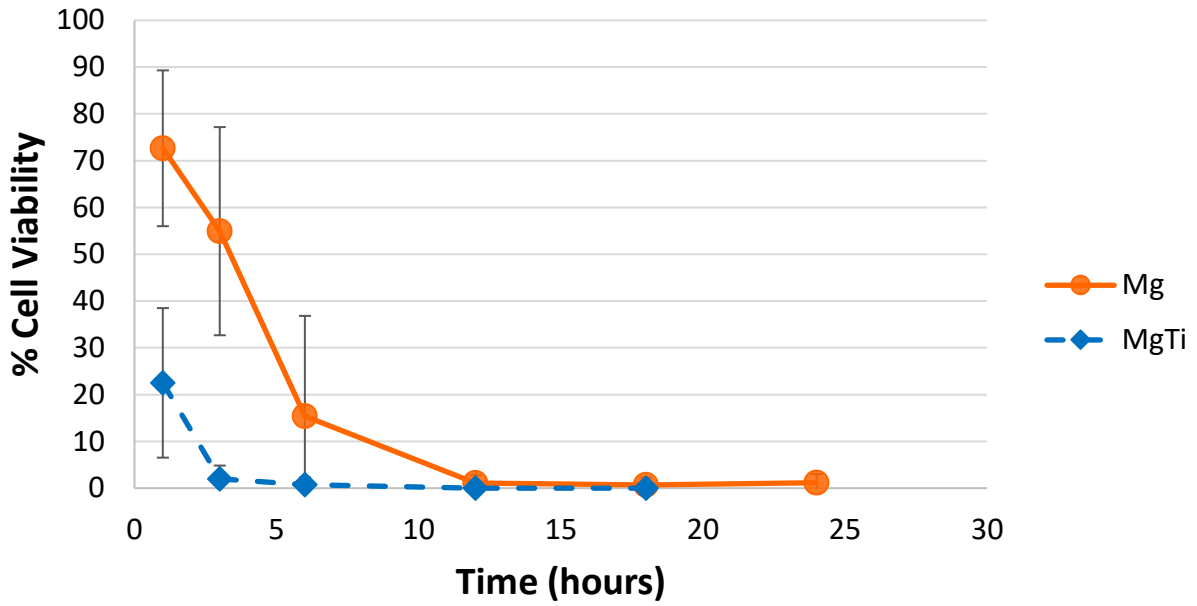
% Cell Viability over Time for 500 ug per ml



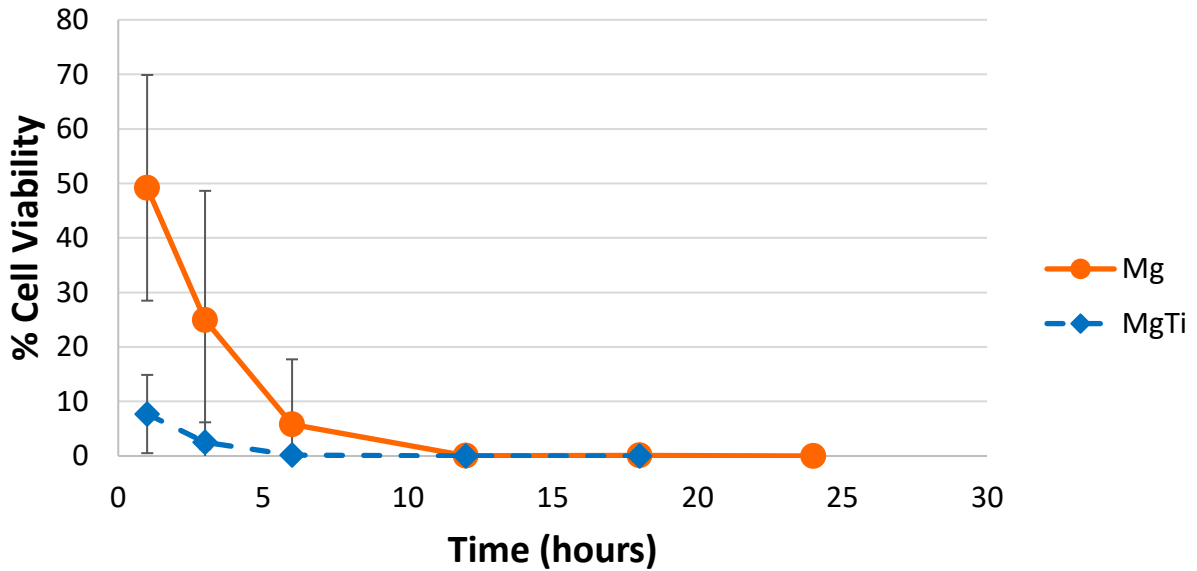
% Cell Viability over Time for 1000 ug per ml



% Cell Viability over Time for 1250 ug per ml



% Cell Viability over Time for 1750 ug per ml



References

1. Staiger MP, Pietak AM, Huadmai J, Dias G. Magnesium and Its Alloys as Orthopedic Biomaterials: A Review, *Biomaterials* 2006; 27(9): 1728-734.
2. Saris NEL, Mervaala E, Karppanen H, Khawaja JA, Lewenstam A. Magnesium: An Update on Physiological, Clinical and Analytical Aspects, *Clin. Chim. Acta* 2000; 294(1-2): 1-26.
3. Witte F, Kaese V, Haferkamp H, Switzer E, Meyer-Lindenberg A, Wirth CJ, Windhagen H. In Vivo Corrosion of Four Magnesium Alloys and the Associated Bone Response, *Biomaterials* 2005; 26(17): 3557-63.
4. Zhang E, Xu L, Yu G, Pan F, Yang K. In Vivo Evaluation of Biodegradable Magnesium Alloy Bone Implant in the First 6 Months Implantation, *J. Biomed. Mater. Res. A*, 2009; 90A(3): 882-93.
5. Kraus T, Fischerauer SF, Hänzi AC, Uggowitzer PJ, Löffler JF, Weinberg AM. Magnesium Alloys for Temporary Implants in Osteosynthesis: In Vivo Studies of Their Degradation and Interaction with Bone, *Acta Biomater.* 2012; 8(3): 1230-8.
6. Ehrensberger MT, Sivan S, Gilbert JL. Titanium Is Not “the Most Biocompatible Metal” under Cathodic Potential: The Relationship between Voltage and MC3T3 Preosteoblast Behavior on Electrically Polarized CpTi Surfaces, *J. Biomed. Mater. Res. A* 2010; 93A(4): 1500-9.
7. Haeri M, Wollert T, Langford GM, Gilbert JL. Electrochemical Control of Cell Death by Reduction-Induced Intrinsic Apoptosis and Oxidation-Induced Necrosis on CoCrMo Alloy *In Vitro*, *Biomaterials* 2012; 33(27): 6295-304.

8. Sivan S, Kaul S, Gilbert JL. The Effect of Cathodic Electrochemical Potential of Ti-6Al-4V on Cell Viability: Voltage Threshold and Time Dependence, *J. Biomed. Mater. Res. B: Appl. Biomater.* 2013; 101(8): 1489-97.
9. Dhar HP, Howell DW, Bockris JO'M. The Use of *In Situ* Electrochemical Reduction of Oxygen in the Diminution of Adsorbed Bacteria on Metals in Seawater, *J. Electrochem. Soc.: Electrochem. Sci. Technol.* 1982; 129(10): 2178-82.
10. Cabisco E, Tamarit J, Ros J. Oxidative Stress in Bacteria and Protein Damage by Reactive Oxygen Species, *Int. Microbiol.* 2000; 3: 3-8.
11. Circu ML, Aw TY. Reactive Oxygen Species, Cellular Redox Systems, and Apoptosis, *Free Radic. Biol. Med.* 2010; 48(6): 749-62.
12. Fink SL, Cookson BT. Apoptosis, Pyroptosis, and Necrosis: Mechanistic Description of Dead and Dying Eukaryotic Cells, *Infect. Immun.* 2005; 73(4): 1907-16.
13. Martindale JL, Holbrook N. Cellular Response to Oxidative Stress: Signaling for Suicide and Survival, *J. Cell. Physiol.* 2002; 192(1): 1-15.
14. Harris RM, Williams TD, Hodges NJ, Waring RH. Reactive Oxygen Species and Oxidative DNA Damage Mediate the Cytotoxicity of Tungsten-Nickel-Cobalt Alloys in Vitro, *Toxicol. Appl. Pharm.* 2011; 250(1): 19-28.
15. Kim J, Gilbert JL. Cytotoxic Effect of Galvanically Coupled Magnesium-Titanium Particles, *Acta Biomater.* 2016; 30: 368-77.
16. Di Virgilio AL, Reigosa M, Lorenzo de Mele MF. Biocompatibility of Magnesium Particles Evaluated by *In Vitro* Cytotoxicity and Genotoxicity Assays, *J. Biomed. Mater. Res. B: Appl. Biomater.* 2011; 99B(1): 111-9.

17. Wilson MR, Close TW, Trosko JE. Cell Population Dynamics (Apoptosis, Mitosis, and Cell-Cell Communication) During Disruption of Homeostasis, *Exp. Cell Res.* 2000; 254(2): 257-68.
18. Bergamini CM, Gambetti S, Dondi A, Cervellati C. Oxygen, Reactive Oxygen Species and Tissue Damage, *Curr. Pharm. Des.* 2004; 10: 1611-26.
19. Baumann RP, Penketh PG, Seow HA, Shyam K, Sartorelli AC. Generation of Oxygen Deficiency in Cell Culture Using a Two-Enzyme System to Evaluate Agents Targeting Hypoxic Tumor Cells, *Radiat. Res.* 2008; 170(5): 651-60.
20. Secinti KD, Özalp H, Attar A, Sargon MF. Nanoparticle Silver Ion Coatings Inhibit Biofilm Formation on Titanium Implants, *J. Clin. Neurosci.* 2011; 18(3): 391-5.
21. Sheehan E, McKenna J, Mulhall KJ, Marks P, McCormack D. Adhesion of Staphylococcus to Orthopaedic Metals, an *In Vivo* Study, *J. Orthop. Res.* 2004; 22: 39-43.
22. Gallo J, Holinka M, Moucha CS. Antibacterial Surface Treatment for Orthopaedic Implants, *Int. J. Mol. Sci.* 2014; 15: 13849-80.
23. Campoccia D, Montanaro L, Arciola CR. The Significance of Infection Related to Orthopedic Devices and Issues of Antibiotic Resistance, *Biomaterials* 2006; 27: 2331-9.

5 In-Vitro Cytotoxicity of Galvanically Coupled Magnesium-Titanium Particles on Human Osteosarcoma SAOS2 Cells: A Potential Cancer Therapy

5.1 Introduction

Osteosarcoma is a malignant bone cancer that occurs mostly in children and young adults (age 0 to 24 years), where ages from 15 to 19 years have the highest incidence of osteosarcoma [1-2]. Osteosarcoma accounts for 5% of childhood cancer, or less than 1% of all cancers diagnosed in the United States, where out of 800 people diagnosed with osteosarcoma, half of them are children and teenagers [1-2]. Although osteosarcoma is prominent in children and young adults, osteosarcoma also affects the elderly, especially between the ages of 65 and 80 [1]. In young patients, osteosarcoma usually occurs in the metaphysis of the long bone that includes the growth plate, such as the distal femur, proximal tibia, and proximal humerus [1]. In older patients, osteosarcoma mostly occurs due to Paget disease or other types of bone lesions [1]. Before the 1980s, the five-year survival rate for osteosarcoma patients in the United States was approximately 20%, and then the survival rate increased drastically to approximately 70%, mainly due to chemotherapy [1]. If osteosarcoma is localized, the tumor can be removed by surgery; however, most osteosarcoma grows quickly, and therefore, even with surgical removal of the tumor, chemotherapy is usually essential to eliminate any remaining tumor. Despite these advances, the five-year survival rate for metastatic and recurrent tumors remains at less than 20% [2]. Besides the type of osteosarcoma (localized vs. metastatic vs. recurrent), the survival rate is affected by the location of the cancer, with the highest survival rate in patients with osteosarcoma in upper and lower short bones and the poorest survival rates in patients with

osteosarcoma in the pelvis [1]. Other factors also affect the survival rate of osteosarcoma, such as the age of the patient, gender, and tumor's ability to respond to chemotherapy [1-2]. Although osteosarcoma is sporadic and does not provide specific genetic abnormalities that can serve as a diagnostic marker of this disease, osteosarcoma has shown mutations in RB gene and p53 gene, which are both tumor suppressor genes, where 70% of osteosarcoma tumors have mutated RB gene [2]. Also, over-expression of oncogenes, such as *c-myc*, *c-fos*, *Her-2*, *MET*, *SAS*, and *GLI*, are known to cause osteosarcoma [2]. Despite the advances made in understanding the genetic cause of osteosarcoma, there are no definitive causal indicators of the disease, and therefore, there have been few advances in osteosarcoma treatment, and there have been no improvements in the osteosarcoma survival rates in the past decade [1].

Kim and Gilbert et al. recently found that magnesium (Mg) and galvanically coupled magnesium-titanium (Mg-Ti) particles have a cytotoxic effect on cells in-vitro [3]. This finding contradicts previous findings that Mg and Mg-based alloys are very biocompatible, especially in in vivo experiments [4-7]. There are in vitro experiments assessing cytotoxicity of Mg and Mg-based alloys, but these studies attribute the cause of cytotoxicity to the increase of pH, high concentrations of Mg ions, and/or release of alloyed elements [8-11]. Kim and Gilbert et al. previously hypothesized that one of the contributing factors to Mg and Mg-Ti cytotoxicity is the electrochemical production of reactive oxygen species (ROS) during corrosion, which will ultimately induce cell apoptosis or necrosis, depending on the concentration of ROS produced [3,12]. The reasons behind this hypothesis are as follows. First, Mg and Mg-Ti particles killed cells in dosage-dependent manner. Mg-Ti, due to galvanic coupling, enhanced the rate of Mg corrosion (rates of oxidation and reduction reactions). As a result, Mg-Ti killed more effectively than Mg alone. This showed that the rate of corrosion affected the cell viability, where faster

corroding Mg-Ti particles killed more cells, even though the particle concentrations of Mg-Ti are the same as that of Mg, meaning the final concentrations of by-products once the particles finish corroding, such as Mg ion concentrations and hydroxide ions, are the same for both particle types. And therefore, as expected, the pH measurements from Mg and Mg-Ti corrosion were not different. Hydrogen gas, $H_2(g)$, although not measured in this study, will have no effect in vitro since hydrogen gas produced will dissipate. Mg ion levels, based on other previous studies, was in the range where it will not cause cytotoxicity in vitro. Therefore, the hypothesis of this study is that the ROS generated during reduction of water and/or oxygen are affecting cell viability and proliferation depending on the concentration of ROS produced (which is proportional to the particle concentration), and this hypothesis is supported by the nature of the active corrosion (redox) reactions proposed. Furthermore, Kim and Gilbert et al. found that cells only proximal to the particles are affected and killed, while cells away from the particles remain viable [12]. This proximity range was very narrow, where the cells had to be very close to the particles, less than 1-2 mm away. Therefore, there was high variability of cell viability due to the random scattering of particles, where within a sample, regions where cells were near the particles were dead and cells away from the particles were alive. However, when the cell density was increased, cells behaved differently. Instead of undergoing cell apoptosis when near the particle, at high cell numbers, the cells enveloped the particles, and even the cells attached to the particles were viable. This indicated that the concentration of ROS needs to reach a local threshold concentration sufficient to kill the surrounding cells. If there are few cells near the particles, this threshold will be low, but if there are more cells near the particles, the threshold will be higher. The aim of this study was to see if Mg and Mg-Ti particles can kill cancer cells in vitro in a dose and time dependent manner. If cancer cells can be killed, Mg-Ti couples in geometries other

than particle-form may be considered as biomaterials for the manufacture of orthopedic implants to replace the tumor site (when cancer-affected bone is surgically removed), so that Mg-Ti can help to kill any potentially remaining tumors or prevent tumor regrowth, in addition to chemotherapy and radiation, to have a synergistic effect.

5.2 *Materials and Methods*

5.2.1 *Preparation of Mg-Ti Microparticles*

Titanium (Alfa Aesar, Stock #: 13975 and Lot #: C19N26), with 99.99% Ti purity, was sputtered onto Mg particles (Goodfellow, Product #: MG006021), with 99.8% Mg purity, for 5 minutes at 1.2 kV, 50 mA, and 100-200 mTorr. The presence of the Ti layer was evaluated as discussed previously [3]. Being a line-of-sight process, the sputtered Mg particles were only partially coated with a thin film of Ti which allowed the Mg to directly corrode and the Ti surface to serve as the site of reduction reactions.

5.2.2 *SAOS2 Cell Viability vs. Mg and Mg-Ti Particle Concentrations*

SAOS2 (ATCC #: HTB-85), human bone osteosarcoma cells, were cultured in Dulbecco's Modified Eagle Medium (DMEM, Catalog #: 10313-021), 15% fetal bovine serum (FBS, Invitrogen #: 16000044), and 1% penicillin-streptomycin-glutamine (PSG, Invitrogen #: 10378-016). Mg and Mg-Ti microparticle concentrations ranging from 50 to 2500 $\mu\text{g/ml}$ were given to the cells at a cell density of 30,000 cells/ cm^2 for different time periods, $t = 24, 48, \text{ and } 72$ hours, with 2 ml of the solution given per well ($A = 9.6 \text{ cm}^2$). The particles were randomly scattered throughout the dish.

Live/dead assay (Invitrogen #: L3224) was performed at the end of $t = 24, 48, \text{ and } 72$ hours to measure cell viability using optical microscope (Leica Instruments). Ten images were taken randomly per sample for three separate samples, and the number of live and dead cells was

counted manually using the cell counter feature of Image J for each image (n= 30 images).

Viability was determined as the number of live cells divided by the total number of cells (number of live and dead cells) in each image.

$$\%CV = \frac{\# \text{ of live cells}}{\# \text{ of live cells} + \# \text{ of dead cells}}$$

This method is identical to the method used to measure in-vitro cytotoxicity of Mg and Mg-Ti particles on MC3T3 cells reported in other papers [3, 12]. Relevant data from those previous studies is shown in this paper for comparison purposes with SAOS2 cells.

5.2.3 Analysis of SAOS2's Acquired Resistance to Cytotoxicity of Mg and Mg-Ti Particles

Once SAOS2 cells were mostly killed by Mg particles leaving few live cells, they were allowed to recover. The SAOS2 cells were killed by 1750 $\mu\text{g/ml}$ of Mg particles over $t = 24$ hours, which left the average of 42 surviving cells from the entire sample (starting from 30,000 cells/ cm^2 in 9.6 cm^2 dish, which yields total of 288,000 cells) by the end of $t = 24$ hours. At $t = 24$ hours, the sample was then gently washed using PBS to get rid of the Mg particles, and then replenished with fresh media for cell growth. After one week, these cells were then trypsinized and transferred from a dish to a T-75 flask (Corning #: 430725U) to further grow them into a confluent layer. These cells were grown for 48 days to get the number of cells needed to do a recovery experiment. In order to avoid multiple passaging of cells, which may affect the cells, when the cells were transferred from a dish to a T-75 flask, the cells were divided and transferred into multiple T-75 flasks, which then resulted an average of 1-10 cells per T-75 flask. Cells took 48 days to become confluent because very few or an isolated single cell didn't proliferate immediately and the initial proliferation took a long time before there were enough cells to increase the rate of proliferation. Once the "recovered" cells became confluent, these cells were

then again cultured in a 9.6 cm² dish with a cell density of 30,000 cells/cm². And again, the cells were treated with particle concentrations of 50-2500 µg/ml for t= 24 hours.

Like the experiment in Section 5.2.1, live/dead assay was performed at the end of t= 24 hours to measure cell viability using optical microscope (Leica Instruments). Ten images were taken randomly per sample for three separate samples, and number of live and dead cells was counted manually using Image J for each image (n= 30 images).

5.2.4 SEM Analysis of SAOS2 Morphology After Mg and Mg-Ti Particle Treatment

In selected cases, low voltage scanning electron microscopy imaging (SEM, JEOL 5600, Dearborn, MA) was used to assess the interactions between cells and particles. The particle concentrations used for SEM analysis are control (0 µg/ml), 100 µg/ml, 500 µg/ml, 1000 µg/ml, and 1500 µg/ml for both Mg and Mg-Ti. The cells were prepared for SEM analysis by fixing the cells in 4% formaldehyde for 15 minutes and then different gradients of ethanol mixed in PBS (50%, 75%, 90%, and 100% ethanol for 15 minutes each). The low kV imaging mode (4 kV) allows for highlighting of cellular features and adsorbed proteins relative to the background tissue culture plastic.

5.2.5 Time-Lapse of SAOS2 Cells and Mg Particle Interactions

Time-lapse was done for t= 24 hours (at 37 Celsius and 5% CO₂) for the selected concentrations of Mg groups, 250 µg/ml (low concentration) and 2000 µg/ml (high concentration), and observed the cell-particle interactions over time using differential interference contrast DIC mode in optical microscope (Leica Instruments).

5.2.6 Statistical Analysis

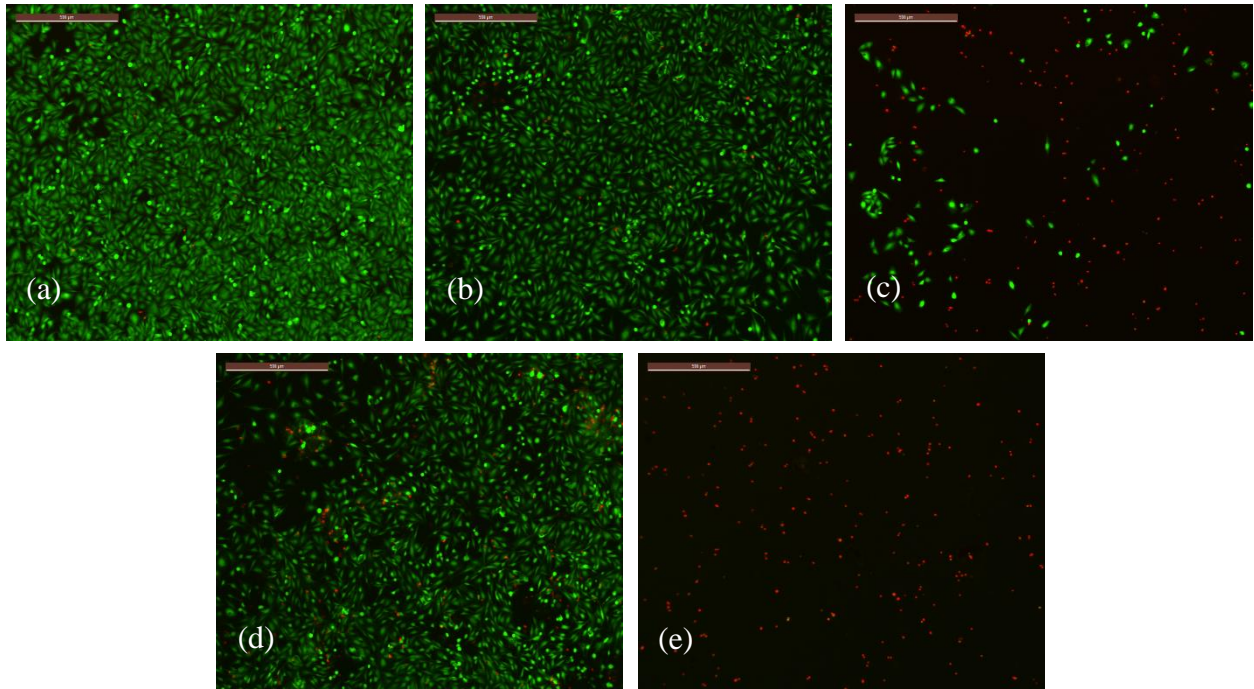
Two-way analysis of variance (ANOVA) statistical methods were used to analyze the results with the two factors being particle type and concentration, along with post-hoc Tukey

tests, using SPSS Statistics Software, version 17.0. Statistically significant differences were determined with $p < 0.05$.

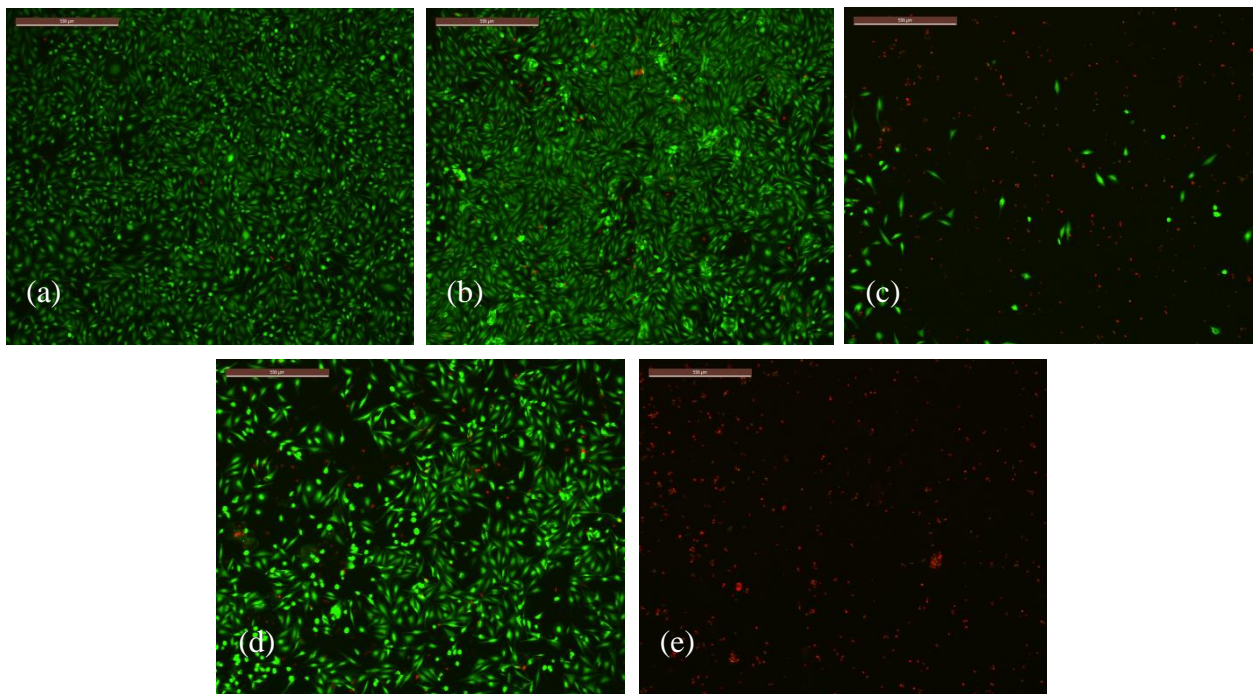
5.3 Results

Fig. 5.1 shows live/dead images of SAOS2 cells treated with either 500 and 1000 $\mu\text{g/ml}$ Mg or Mg-Ti particles for different time periods, $t = 24, 48,$ and 72 hours. Mg-Ti treated groups have significantly greater numbers of dead cells over live cells, compared to Mg groups, at all particle concentrations and at all times. Control samples show a significant increase of cells over time, indicating cell proliferation. Like MC3T3 cells at high cell density, SAOS2 cells envelop particles and even migrate onto the particles (Fig. 5.2(a)). At lower particle concentrations, SAOS2 cells are viable, even the cells in close proximity to the particles. At higher particle concentrations, SAOS2 cells around the particles are killed (Fig. 5.2(b)). There is an interesting feature worthy of note: while many cells appear to undergo cellular apoptosis (characteristic of apoptosis is cells retracting their membranes and balling-up), other cells have ruptured membranes, exposing red-stained nucleus while maintaining the cell-shape, which is a characteristic of necrosis (Fig. 5.2(c)). Exact ratios of cells that undergo apparent apoptosis and necrosis have not been measured.

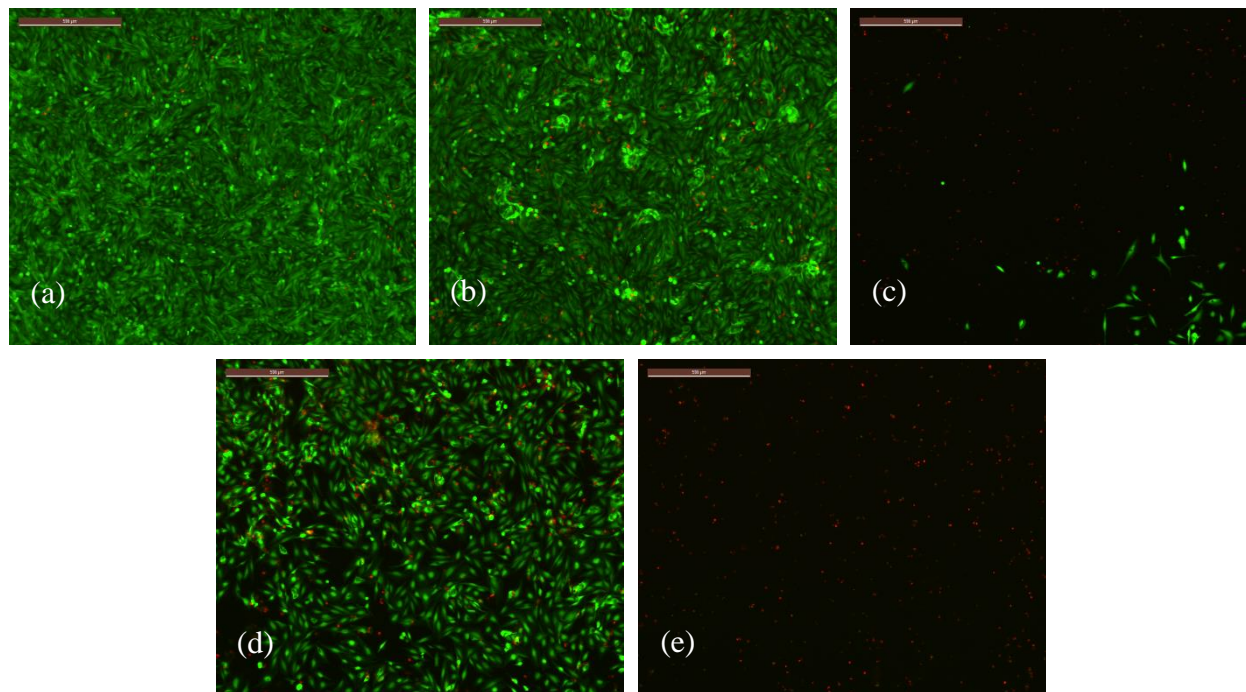
(i)



(ii)



(iii)



(iv)

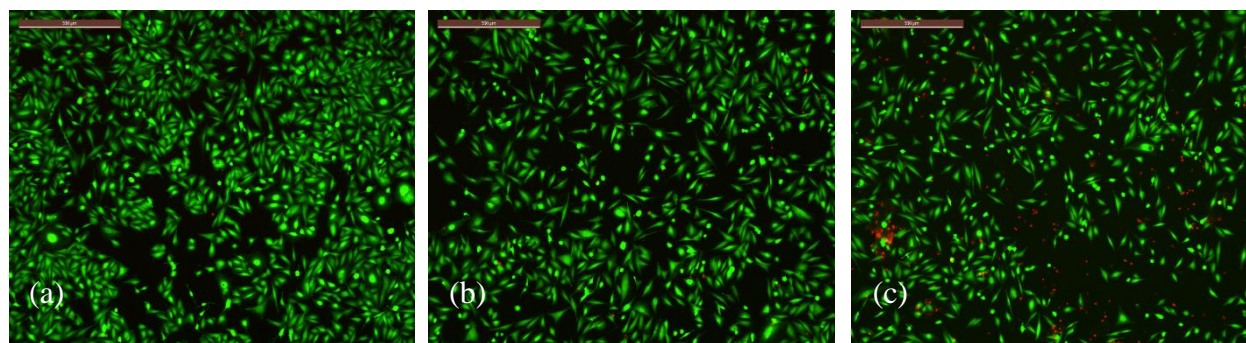


Figure 5.1 Live/dead images of SAOS2 cells, where (a) Control (no particles), (b) Mg 500 µg/ml, (c) Mg-Ti 500 µg/ml, (d) Mg 1000 µg/ml, and (e) Mg-Ti 1000 µg/ml for (i-iii) groups, where the cells have been treated with particles for (i) $t = 24$ hours, (ii) $t = 48$ hours, and (iii) $t = 72$ hours, $n = 3$. (iv) SAOS2 cells have been killed with Mg 1750 µg/ml for 24 hours, and the surviving cells were re-grown for almost seven weeks before treating them again with (a) Control (no particles), (b) Mg 500 µg/ml, and (c) Mg 1000 µg/ml for $t = 24$ hours, $n = 3$.

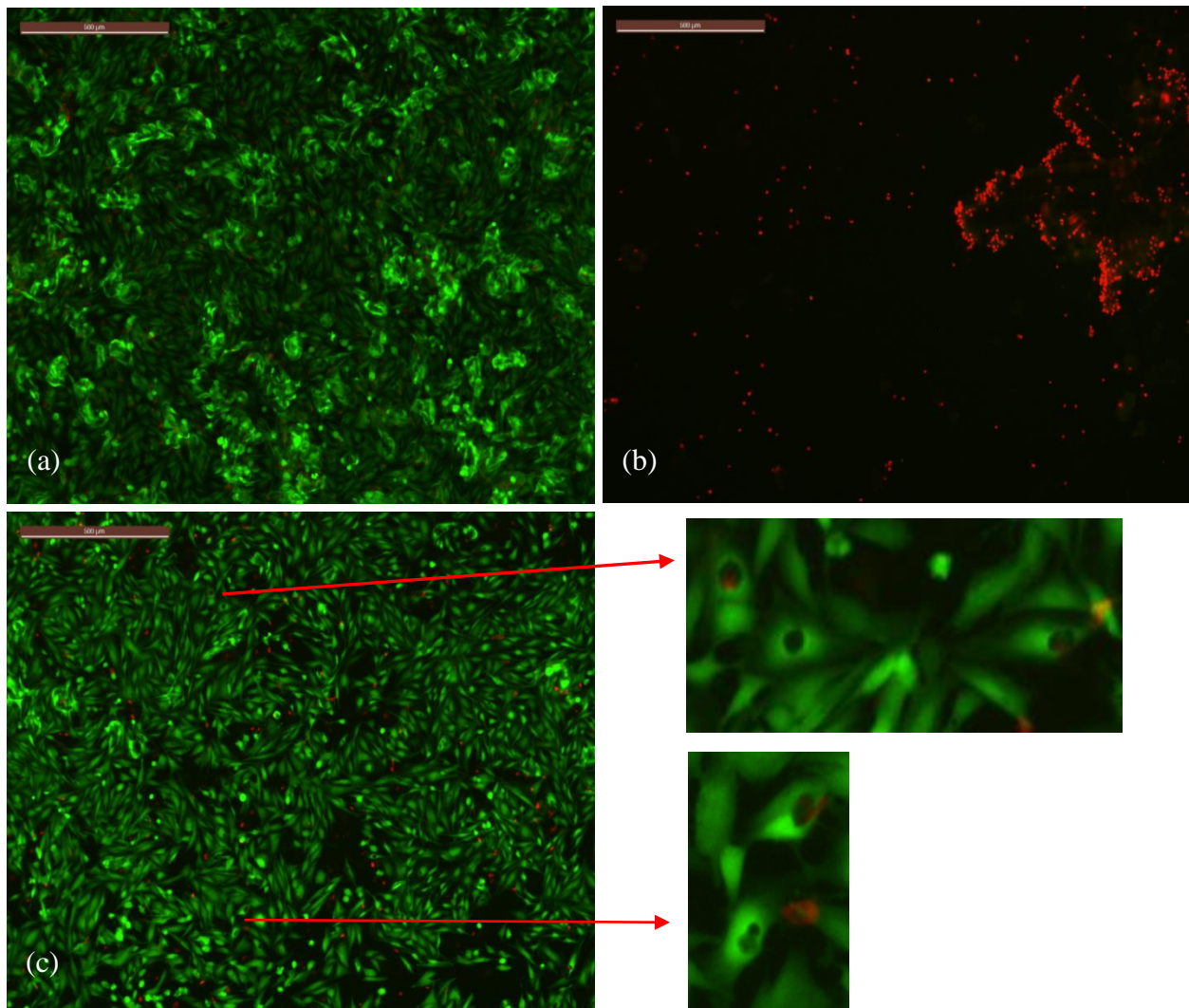
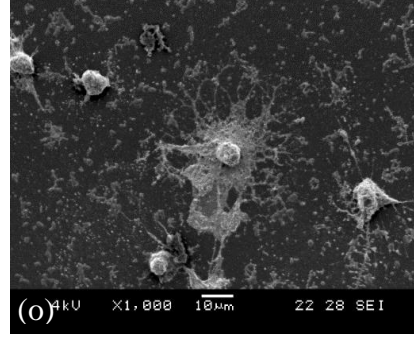
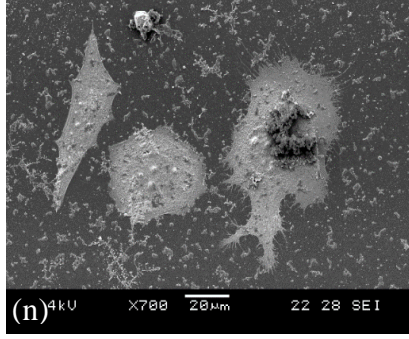
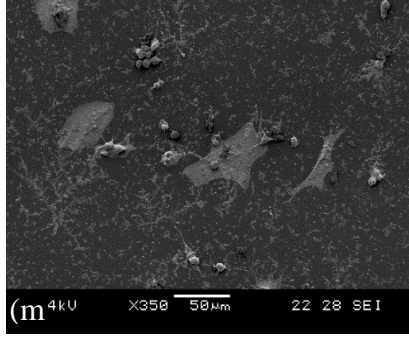
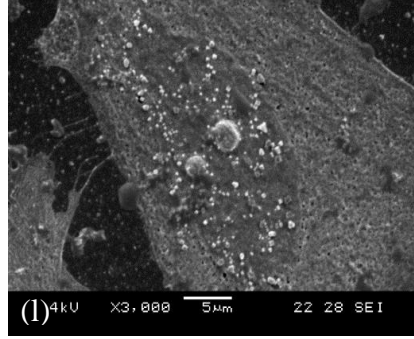
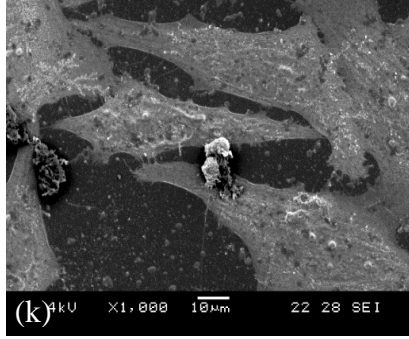
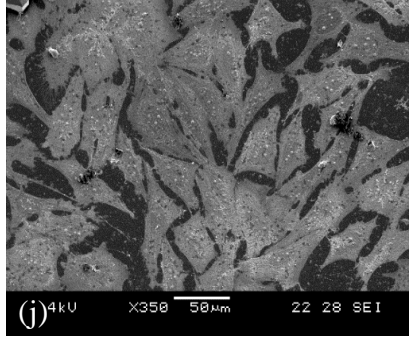
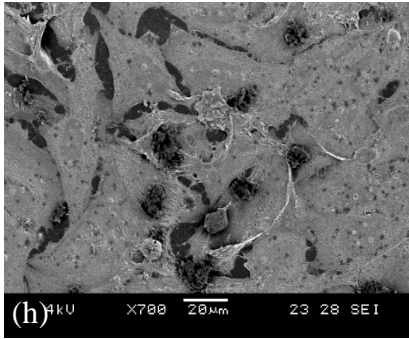
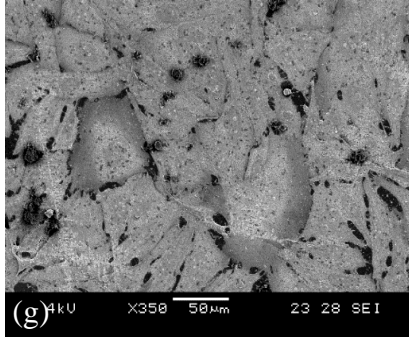
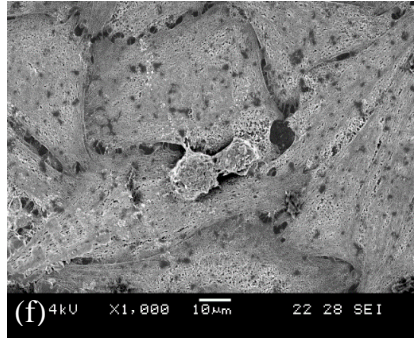
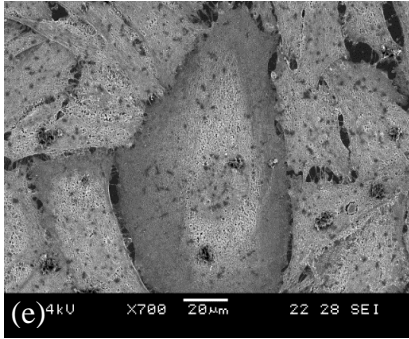
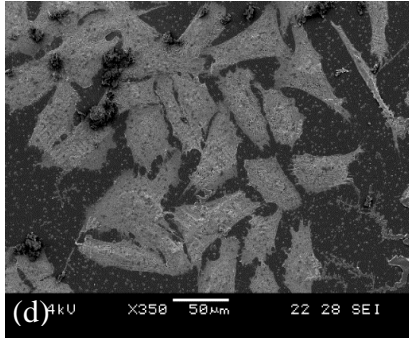
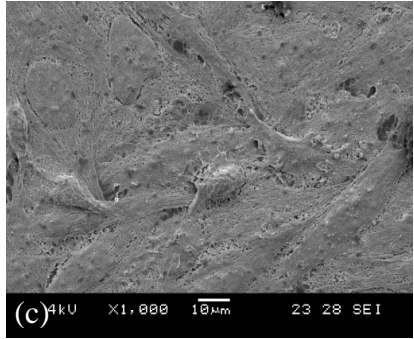
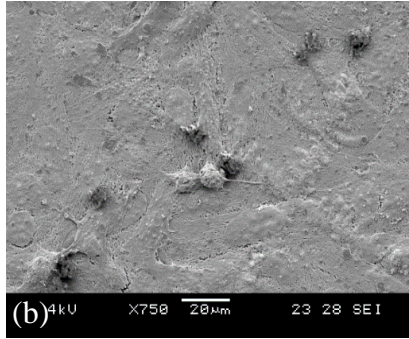
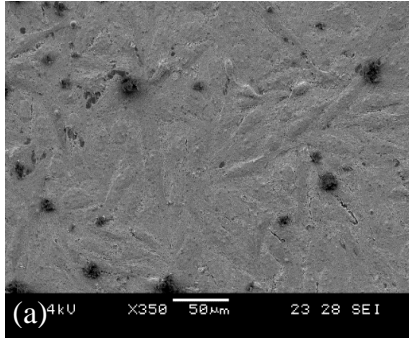


Figure 5.2 Cells interact with Mg and Mg-Ti particles. At high cell density, like MC3T3 cells, SAOS2 cells envelop the particles and even at proximity, many cells are viable, such as (a) treated with Mg 750 $\mu\text{g}/\text{ml}$. At higher particle concentrations, the cells that have attached to the particles are eventually killed, such as (b) treated with Mg 1750 $\mu\text{g}/\text{ml}$. (c) shows cells with their membranes punctured, with red-stained nucleus either remaining inside the cell or bleeding out. This image has taken from a sample treated with Mg 500 $\mu\text{g}/\text{ml}$ for $t = 24$ hours.

SEM analysis shows cell morphology more clearly (Fig. 5.3). Control groups show that most of SAOS2 cells are very well spread and adhered to the surface (Fig. 5.3(a-c)). SAOS2 cells at 30,000 cells/cm² show high confluency, where the surface is entirely covered by the cells. Although the cells are generally in a monolayer, some cells are on top of the other cells, which is a classic characteristic of cancerous cells. Compared to the control group, cells treated with Mg or Mg-Ti particles were generally less confluent, despite the fact that the seeding cell

density was the same. Besides the less confluency than the control group, cells treated with Mg 100-1000 $\mu\text{g/ml}$ were very well and adhered to the surface, indicating their viability (Fig. 5.3(e-f)). Some SAOS2 cells were of a much larger size, such as shown in Fig. 5.3(e), but as to the percentage of these super-sized cells in the population is not yet known. These cells are approximately 2-3 times the size of the normal cells, but are still morphologically similar in shape with other normal-sized cells. Abnormality in size indicate that SAOS2 cells are indeed cancerous, because cancerous cells can often be in different sizes, where some may be larger than normal, while others are smaller than normal. Cells treated with Mg 1500 $\mu\text{g/ml}$ show that the cell population has distinctly decreased, and the remaining cells are either retracting their filopodia in the process of balling up, or have already balled up, consistent with an apoptosis process. Cells treated with Mg-Ti particles show a similar pattern where cells treated with 100 $\mu\text{g/ml}$ are still viable (Fig. 5.3(p-r)), while cells treated with 500 and 1000 $\mu\text{g/ml}$ show mixtures of spread cells and balled-up cells (Fig. 5.3(s-u) and (v-x)). Cells treated with 1500 $\mu\text{g/ml}$ show most are completely balled-up, indicating non-viability (Fig. 5.3(y-aa)). SEM images also show two distinct modes of cell death: apoptosis and necrosis. Fig. 5.3(i, x) show cells that have punctured membranes, as shown in Fig. 5.2(c) in fluorescent images. There are also some debris on the cells, such as shown in Fig. 5.3(a, d, h, n, t, u, w, x), which seem to be remnants of other cells that have been killed by necrosis, releasing cell's content. Although these debris were also seen in control groups, there were much more debris on the particle-treated samples. The dark and white spots are protein agglomerates that have been highlighted compared to the petri dish, due to the low kV SEM emission characteristics of these materials in secondary emission mode.



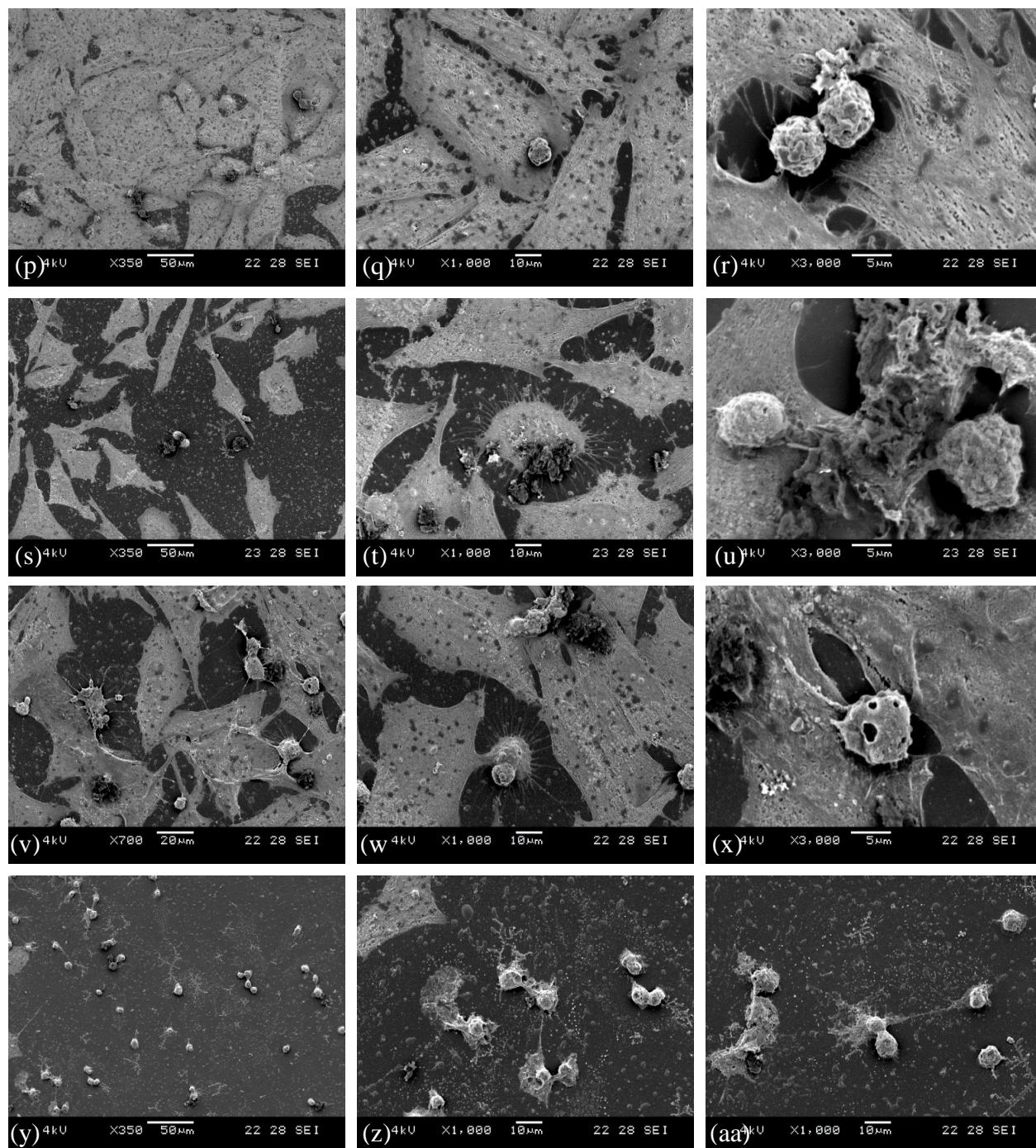


Figure 5.3 SEM images of (a-c) control, (d-f) Mg 100 µg/ml, (g-i) Mg 500 µg/ml, (j-l) Mg 1000 µg/ml, (m-o) Mg 1500 µg/ml, (p-r) Mg-Ti 100 µg/ml, (s-u) Mg-Ti 500 µg/ml, (v-x) Mg-Ti 1000 µg/ml, and (y-aa) Mg-Ti 1500 µg/ml. These SEM images were taken at low accelerating voltage of 4 kV, in order to highlight cellular features, such as filopodia and adsorbed proteins.

The cell viability over particle concentrations of Mg and Mg-Ti treated for different periods of time, summarized in Fig. 5.4(a-c), are particle dose-dependent, where the curves are sigmoidal in shape. The viability for Mg-Ti treated cells drops more quickly than those treated with Mg as the particle concentration is increased. Post hoc Tukey test shows that cell viability of different particle concentrations is statistically different from each other ($p < 0.05$), except the low particle concentration groups (50 and 100 $\mu\text{g/ml}$) are not different from the control group, and the high concentrations of 2000 and 2500 $\mu\text{g/ml}$ are not different from each other ($p > 0.05$). Post hoc Tukey test also shows that Mg-Ti groups are statistically different than Mg groups ($p < 0.05$) at all times ($t = 24, 48, \text{ and } 72$ hours). For $t = 24$ hours (Fig. 5.4(a)), cells are less than 1% viable at particle concentrations of 1250 $\mu\text{g/ml}$ or higher for Mg-Ti, while 6-8% of cells are still viable at 2000 and 2500 $\mu\text{g/ml}$ for Mg. 4-5% of cells are viable for Mg-Ti at 750 and 1000 $\mu\text{g/ml}$, which shows that more than twice the amount of Mg is needed to have the same killing effect as Mg-Ti. By $t = 48$ hours (Fig. 5.4(b)), cells treated with 1250 $\mu\text{g/ml}$ of Mg-Ti and higher have completely died. However, cells treated with Mg still have not reached complete cell death even at the highest particle concentration at this time, maintaining approximately 4% cell viability at 2500 $\mu\text{g/ml}$. Only by $t = 72$ hours (Fig. 5.4(c)), cells treated with Mg 2500 $\mu\text{g/ml}$ decrease to less than 1%; however, there are still few cells alive.

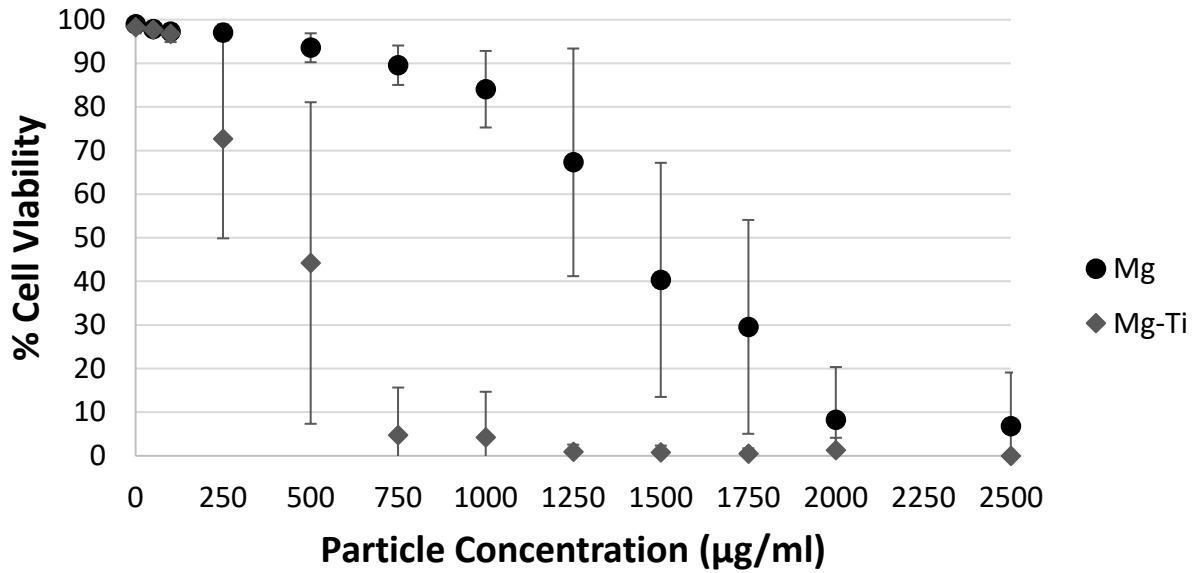
Fig. 5.5 shows the percent cell viability of “recovered” cells treated with different particle concentrations, where the recovered cells have been initially treated with Mg 1750 $\mu\text{g/ml}$ for $t = 24$ hours and then allowed to recover for several weeks. When SAOS2 cells were treated with Mg 1750 $\mu\text{g/ml}$, there were total of 44 cells alive for the particular sample used to recover them (the sample dish area is 9.6 cm^2 , which means average of 4-5 cells per cm^2). In this experiment, 44 cells took 48 days to grow approximately 1.1×10^8 cells, with a doubling time of 54.2 hours.

These cells were then again treated with the same range of Mg particle concentrations (0-2500 $\mu\text{g/ml}$) for $t=24$ hours. The percent cell viability curve of “recovered” cells is very similar to the percent cell viability of cells treated with Mg only once for $t=24$ hours shown in [Fig. 5.4\(a\)](#). Post hoc Tukey test shows that there is no significant difference in the cell viability of these two groups ($P > 0.05$).

In order to show how percent cell viability changes over time per particle concentration, the data in [Fig. 5.4\(a-c\)](#) has been re-plotted as a function of time, instead of as a function of particle concentration (see [Fig. 5.6](#)). [Fig. 5.6\(a-b\)](#) shows cell viability of SAOS2 cells over time for different particle concentrations of Mg and Mg-Ti, respectively. For Mg ([Fig. 5.6\(a\)](#)) of 0 $\mu\text{g/ml}$ (control) up to 250 $\mu\text{g/ml}$, there is no significant change in cell viability over time, maintaining over 94% of cell viability at all times. From 500 $\mu\text{g/ml}$ to 2500 $\mu\text{g/ml}$, cell viability may slightly decrease between $t=24$ and 72 hours, but most of the cell deaths have occurred by the first 24 hours. There are still many viable cells by $t=24$ hours (more than 50% of cells alive up to 1250 $\mu\text{g/ml}$), and yet these cells never recover over time (at least within $t=72$ hours). For Mg-Ti ([Fig. 5.6\(b\)](#)), the same trend is shown. For 0 to 100 $\mu\text{g/ml}$ groups, no significant change in cell viability over time is seen, maintaining over 95% of cell viability at all times. Cell viability of 250 $\mu\text{g/ml}$ and 500 $\mu\text{g/ml}$ groups have dropped significantly, compared to that of Mg groups, by $t=24$ hours, and like the Mg group, the remaining cells showed no recovery after $t=24$ hours. Cell viability of 750 $\mu\text{g/ml}$ and higher groups are not expected to recover in $t=72$ hours, because more than 90% of cells were killed by $t=24$ hours. In short, all the killings have occurred by $t=24$ hours for both Mg and Mg-Ti, since there is a jump in decrease of cell viability for intermediate and high particle concentrations.

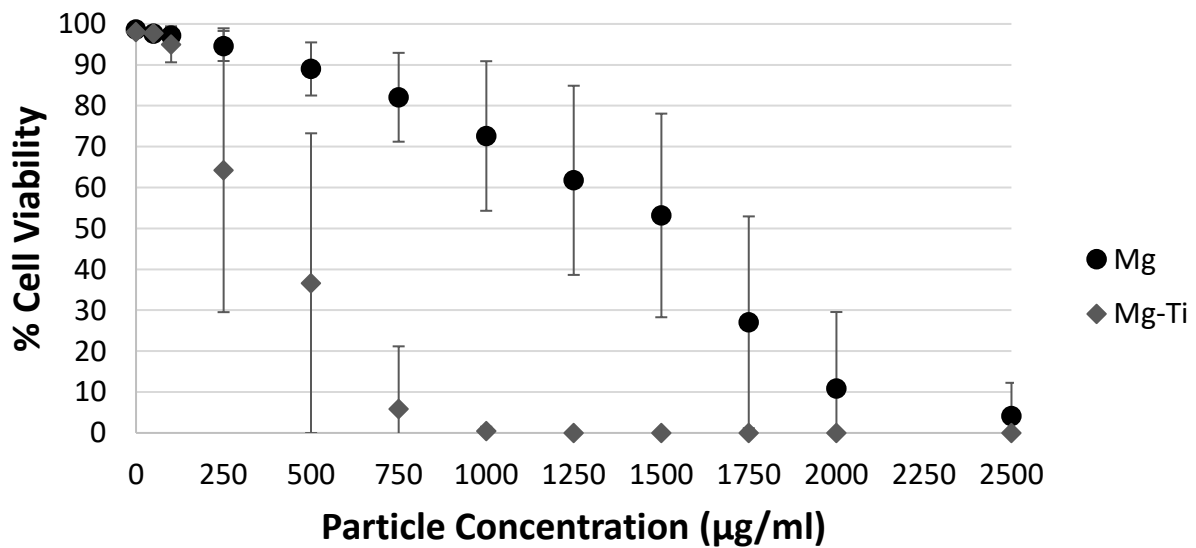
(a)

SAOS2 Cell Viability vs. Particle Concentration at t= 24 Hours



(b)

SAOS2 Cell Viability vs. Particle Concentration at t= 48 Hours



(c)

SAOS2 Cell Viability vs. Particle Concentration at t= 72 Hours

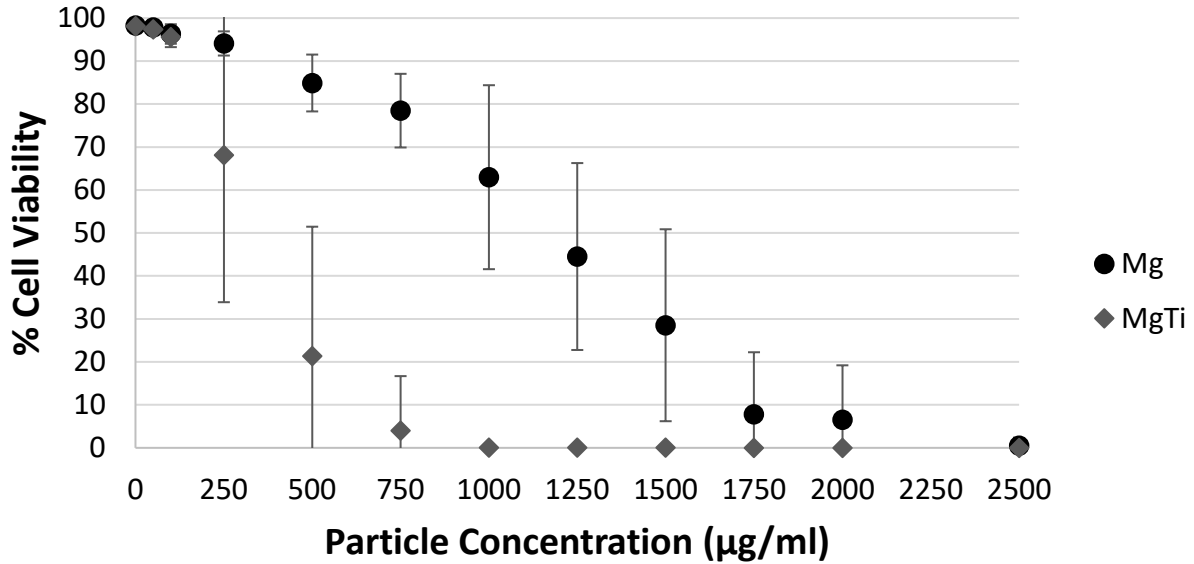


Figure 5.4 Graphs plotting % cell viability of SAOS2 cells as a function of Mg and Mg-Ti particle concentrations (0-2500 µg/ml) at (a) t= 24 hours, (b) t= 48 hours, and (c) t= 72 hours, n=3. Like MC3T3 cells, SAOS2 cells are killed in a particle dosage-dependent manner, where Mg-Ti killed cells more significantly than Mg.

Recovered SAOS2 Cell Viability

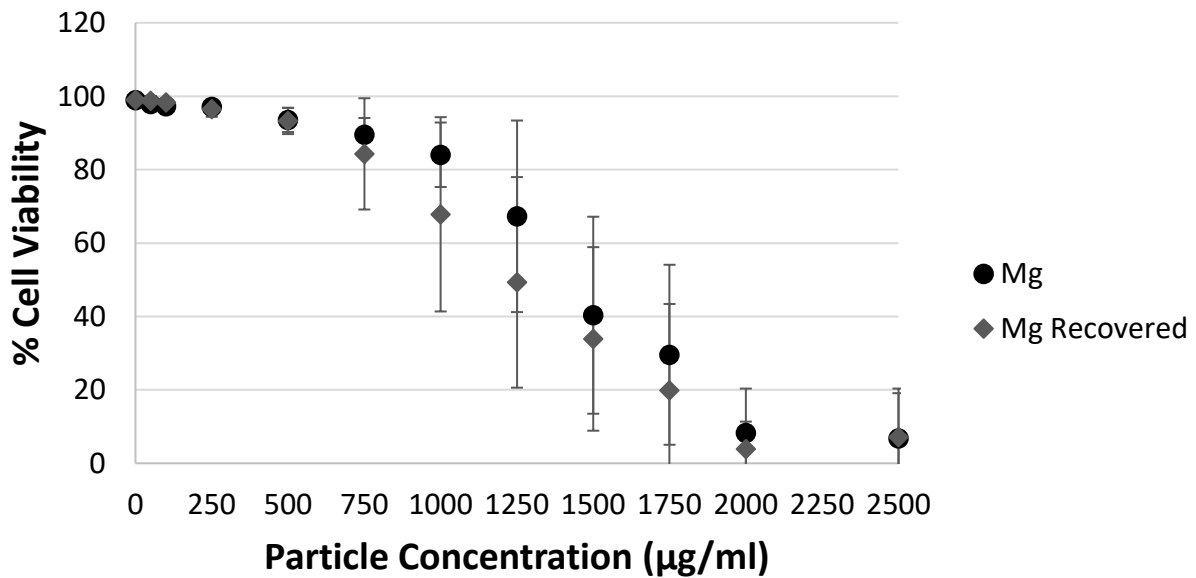


Figure 5.5 A graph of % cell viability of "recovered" SAOS2 cells killed again for t= 24 hours using the same Mg particle concentrations of 0-2500 µg/ml, which is compared to the cells killed only once with Mg shown in Fig. 5.4(a), n=3.

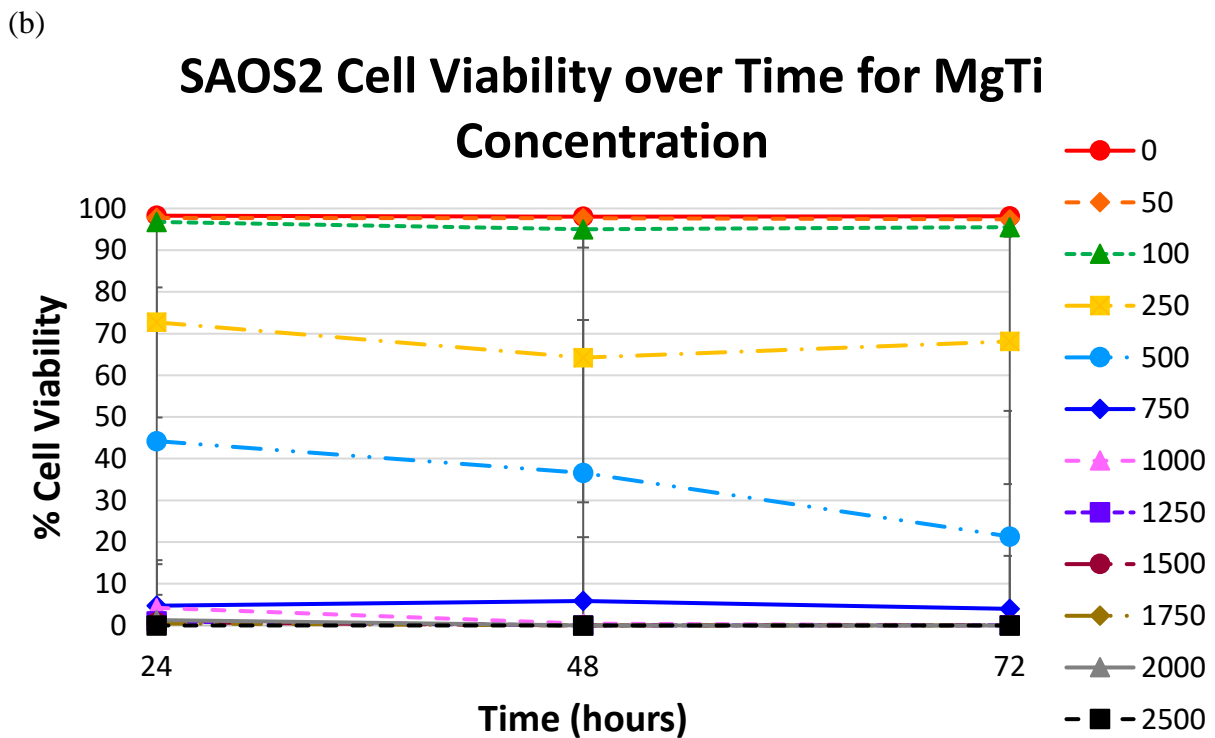
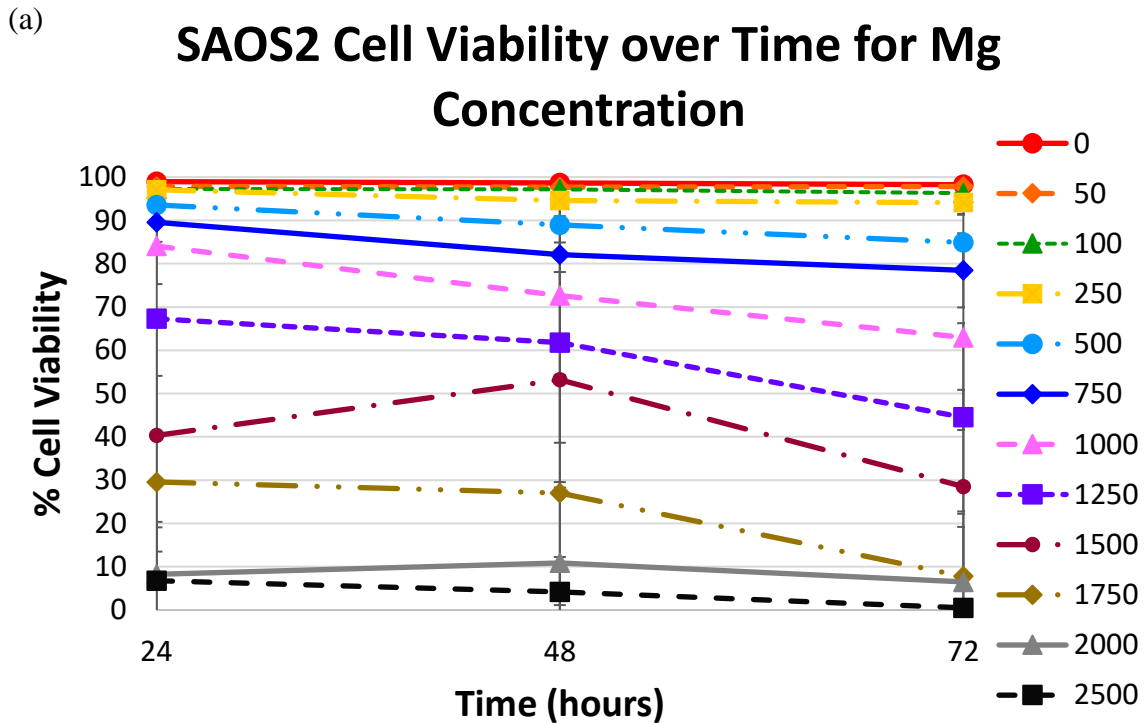


Figure 5.6 Graphs showing % cell viability of SAOS2 cells over time, from $t=24$ to 72 hours, for (a) Mg and (b) Mg-Ti, $n=3$. All the killings have occurred by 24 hours. There was no recovery of cells after 24 hours, even though for some particle concentrations, many cells remained viable.

MC3T3 vs. SAOS2 Cell Viability at t= 24 hours

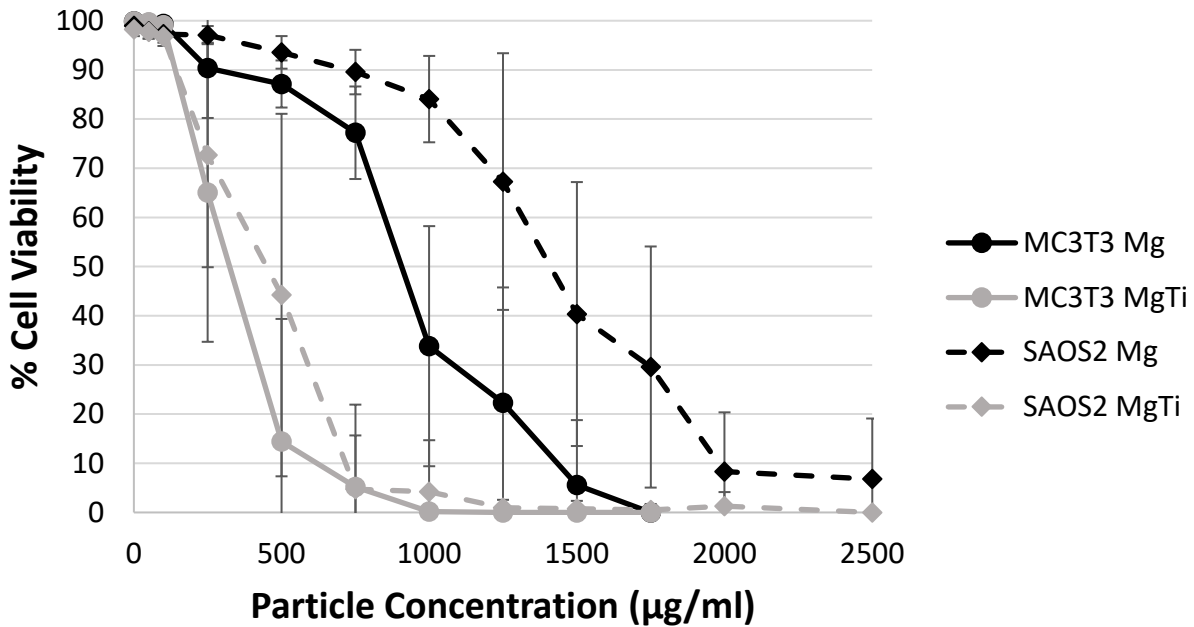
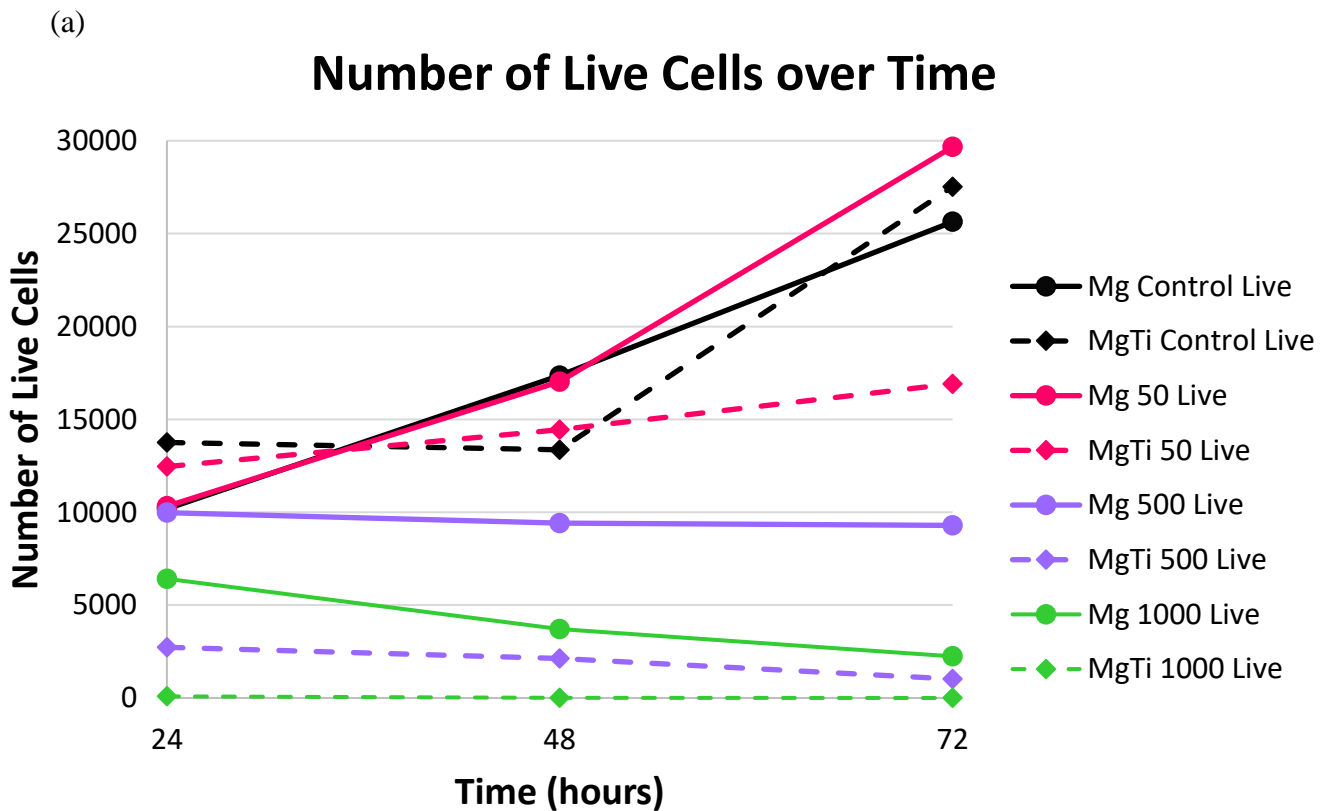


Figure 5.7 A graph comparing SAOS2 and MC3T3 cell viability treated with Mg and Mg-Ti particle concentrations for t= 24 hours. Post hoc Tukey test shows that MC3T3 cell viability is significantly different from SAOS2 cell viability for high Mg particle concentrations of 1000 to 1750 µg/ml ($p < 0.05$), where SAOS2 cells have higher cell viability than that of MC3T3 cells at the same particle concentration. However, there is no significant difference in cell viability between MC3T3 and SAOS2 cells for all particle concentrations, except 500 µg/ml, for Mg-Ti groups ($p > 0.05$).

Fig. 5.7 compares cell viability of SAOS2 cells treated with Mg and Mg-Ti to cell viability of MC3T3 cells treated with Mg and Mg-Ti from a previous study [12]. In order to accurately compare the differences in cell viability due to cell types, many factors, such as cell seeding density, particle concentrations, sample area (so that fraction of area covered by particles will remain the same), particle-treated time, etc. all remained the same. As shown, for Mg, SAOS2 cells had higher cell viability than MC3T3 cells at all particle concentrations. While MC3T3 cells completely died at Mg 1750 µg/ml, approximately 30% of SAOS2 cells were alive at this particle concentration. On the other hand, cell viability of both MC3T3 cells and SAOS2 cells treated with Mg-Ti were similar in the drop of cell viability as particle concentration was increased. Less than 1% of cells were viable at Mg-Ti 1000 µg/ml for MC3T3 cells and Mg-Ti

1250 $\mu\text{g/ml}$ for SAOS2 cells. Although most cells were killed at these concentrations, complete cell death only occurred at Mg-Ti 1250 $\mu\text{g/ml}$ for MC3T3 cells and Mg-Ti 2500 $\mu\text{g/ml}$ for SAOS2 cells, which was twice the concentration required to kill SAOS2 cells completely compared to MC3T3 cells. Post hoc Tukey tests shows that cell viability of MC3T3 cells was statistically different from that of SAOS2 cells for Mg 1000 $\mu\text{g/ml}$ and higher particle concentrations ($p < 0.05$), except for lower particle concentrations between 50-750 $\mu\text{g/ml}$. For Mg-Ti, cell viability of MC3T3 cells and SAOS2 cells were not significantly different for all particle concentrations ($p > 0.05$), except for 500 $\mu\text{g/ml}$.



(b)

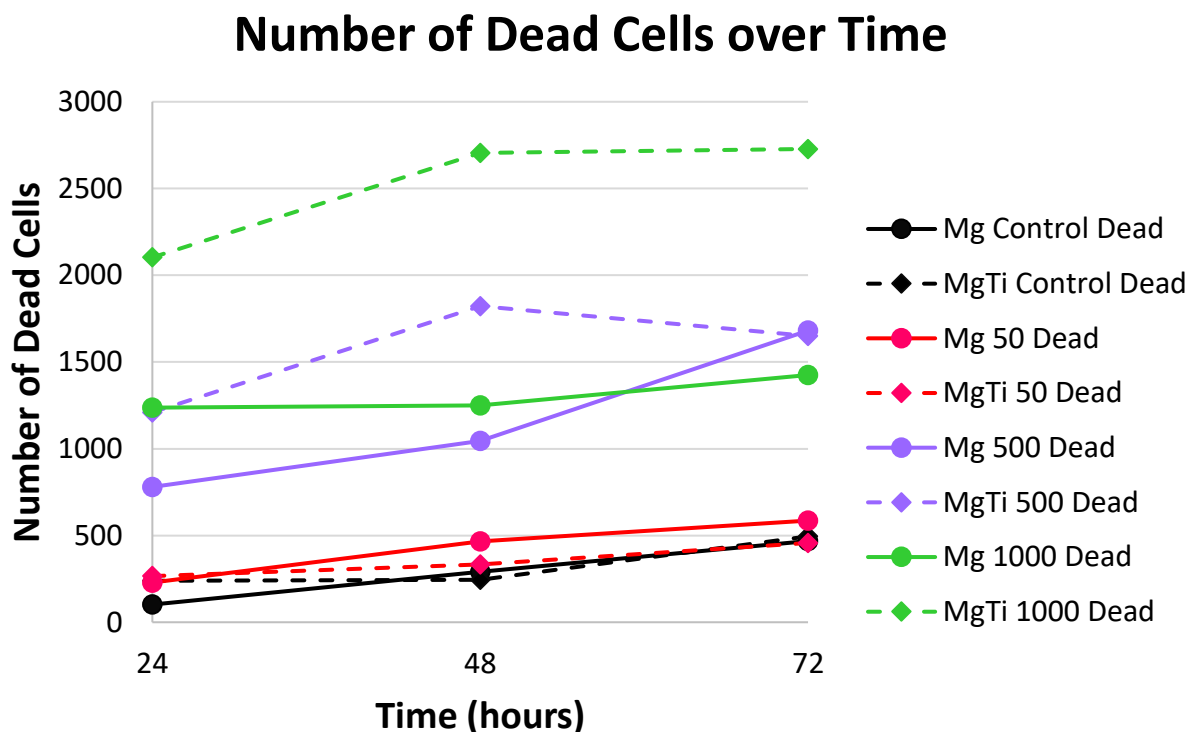


Figure 5.8 Total number of (a) live cells and (b) dead cells counted from ten images per sample, $n=3$, have been plotted for control, 50 $\mu\text{g/ml}$, 500 $\mu\text{g/ml}$, and 1000 $\mu\text{g/ml}$. For control groups and Mg 50 $\mu\text{g/ml}$, the number of live cells drastically increase, almost doubling and tripling from 1st day to 3rd day. Number of live cells treated with Mg-Ti 50 $\mu\text{g/ml}$ increased very slightly, which is less than that of the control group and Mg 50 $\mu\text{g/ml}$. For 500 and 1000 $\mu\text{g/ml}$, the number of live cells remain relatively the same for both Mg and Mg-Ti groups, indicating that there is no proliferation of remaining live cells. The number of dead cells are highest for higher particle concentrations, where Mg-Ti groups showed higher number of dead cells, compared to that of Mg group of the same concentration. Control groups and 50 $\mu\text{g/ml}$ showed relatively low number of dead cells, with a slight increase in number over time.

Fig. 5.8 shows the total number of live and dead cells, which were summed from all ten live/dead images per sample and three samples total. These graphs reveal different information that percent cell viability fails to show. For instance, live cells from control and Mg 50 $\mu\text{g/ml}$ groups increased over time, from $t=24$ hours to $t=72$ hours (Fig. 5.8a). Live cells of Mg control, Mg-Ti control and Mg 50 $\mu\text{g/ml}$ increased to 2.5, 2, and 2.8 times the original population (original population at $t=24$ hours compared to the final population at $t=72$ hours), respectively. However, live cells of Mg-Ti 50 $\mu\text{g/ml}$ only increased by 1.22, which is less compared to the control groups and Mg counterpart. Live cells of Mg and Mg-Ti particle groups

with higher concentrations (500 and 1000 $\mu\text{g/ml}$) do not increase in number (either maintain or slightly decrease), which indicates that unlike the control and Mg 50 $\mu\text{g/ml}$ groups, there was no cell proliferation. In fact, the number of live cells of Mg control and Mg 50 $\mu\text{g/ml}$ groups are very similar to that of Mg 500 $\mu\text{g/ml}$ at $t= 24$ hours, all around approximately 10,000 cells. And yet, cells from Mg control and Mg 50 $\mu\text{g/ml}$ groups proliferate, increasing in number by $t= 72$ hours, while cells from Mg 500 $\mu\text{g/ml}$ group don't proliferate, maintaining the same number of cells at the end of $t= 72$ hours. Number of dead cells (Fig. 5.8b) from control groups and Mg and Mg-Ti 50 $\mu\text{g/ml}$ groups are lowest, all under or approximately around 500 at all times. Mg 500 $\mu\text{g/ml}$, Mg-Ti 500 $\mu\text{g/ml}$, and Mg 1000 $\mu\text{g/ml}$ have dead cells in the range approximately between 800 and 1800, where the number of dead cells usually fall within this range at all times. Mg-Ti 1000 $\mu\text{g/ml}$ have high number of dead cells, always over 2000 cells, with approximately 2100 dead cells at $t= 24$ hours, and 2700 dead cells at $t= 48$ and 72 hours.

5.4 Discussion

The primary purpose of this study was to see if cancerous cells can be killed by the electrochemical effects of Mg particles or galvanically coupled Mg-Ti particles, and if so, to determine if the cytotoxicity of these particles is greater or less on cancerous cells than that compared to healthy mammalian cells. Kim and Gilbert et al. have previously studied cytotoxicity of Mg and galvanically coupled Mg-Ti particles on mouse pre-osteoblast MC3T3 cells, using the same particles and same experimental method as used in this study [3, 12]. Both MC3T3 and SAOS2 cells are widely used for in-vitro research of osteoblast cell models, and so despite the differences between them, these cells both have osteoblastic properties, and therefore, it is relevant to compare them in investigating the cytotoxicity of Mg and Mg-Ti particles, especially in terms of using these particles as an application to treating osteosarcoma [13-16].

There are different types of treatments for osteosarcoma, depending on the types of osteosarcoma. Briefly, osteosarcoma is usually high-grade, meaning they will quickly grow and spread (more common for adolescents and young adults), but some osteosarcoma can also be low-grade, which can usually be treated with surgery alone (more common for elderly) [17-18]. Most osteosarcoma requires a combination of chemotherapy, surgery, and radiation therapy, especially when osteosarcoma is high-grade, metastatic, and recurrent, where only 5-20% of patients survive by surgery alone before the combination therapy [17]. Depending on where the osteosarcoma occurred, removing tumor could be complicated or even impossible. For example, if osteosarcoma is in the limbs, removal of bone could result in requiring bone graft or implant to replace the missing bone. If osteosarcoma is in the spine or skull, surgery may not be able to remove the entire effected area, requiring other forms of treatment such as radiation and chemotherapy.

The treatment of osteosarcoma does not involve just efficiently removing the tumor itself but preventing metastasis into lungs and other bones. There are dormant metastatic cancer cells, hypothesized to be in the bone marrow, which can break their dormancy and colonize at distant secondary sites, where one of the most common metastasis site is lungs [18]. Therefore, in the era before chemotherapy, over 85% patients had metases of osteosarcoma [18]. If Mg or Mg-Ti can be incorporated into the bone graft or in the metal implant to replace the missing bone, then Mg or Mg-Ti alone, or in combination with chemotherapy or radiation, can kill the remaining tumor that was impossible to remove physically via surgery, and/or prevent the tumor from recurring by killing the dormant metastatic cells. Especially since radiation therapy is used to create free radicals that can damage DNA and kill cancer cells, Mg or Mg-Ti can be used synergistically with radiation therapy to create more free radicals to kill cancer cells more

effectively. Further investigation of potential use of Mg or Mg-Ti particles as osteosarcoma cancer treatment is needed, and this study is just the first step to investigate the cytotoxic properties of Mg or Mg-Ti against human osteosarcoma cells in-vitro.

Unfortunately, Mg and Mg-Ti particles cannot discriminate between healthy and cancerous cells, and will kill any cells that are in close proximity to the particles, less than 1-2 mm away [12]. However, Mg or Mg-Ti particles can be made more selective to bind to cancer cells by adding ligands or designing a delivery method that can accurately deliver the particles to the exact tumor site, in order to use the proximity as an advantage to effectively kill cancer cells without damaging too much of the healthy tissue surrounding the tumor. Although more Mg particles are required to kill SAOS2 cells than MC3T3 cells, there were no significant differences in killing SAOS2 cells and MC3T3 cells for Mg-Ti particles. This means that Mg-Ti can kill SAOS2 cells more effectively than Mg without too much damage to the healthy cells, since the concentration used can be lower than that of Mg.

Mg was not able to kill cancer cells completely as Mg-Ti even at the highest particle concentration (2500 $\mu\text{g/ml}$) used in this study at all times. At Mg 2500 $\mu\text{g/ml}$, cell viability at $t=$ 24, 48, and 72 hours were 6.78%, 4.17%, and 0.52%, respectively. Although this is significantly less than the control group, there were still few viable cancer cells left. This is significant because one SAOS2 cell is enough to start proliferating to make an entire confluent population of cells (although the time for proliferation may take several weeks).

Based on the recovered experiment, few SAOS2 cells can re-populate in a matter of a number of days, which was seen in this study. The doubling time of 54.2 hours reported in this study is slightly longer than the doubling time of 37 hours reported by Rodan et al. [14]. However, this makes sense since Rodan had a higher starting cell density of 5,000 cells/cm²,

compared to just total of 44 cells, and grew them for 7 days to reach the final cell density of 300,000 cells/cm². Therefore, it is crucial to kill all cancer cells, since even less than 1% of viable cells can eventually grow back. While Mg particles could not kill all cells even at high concentration at all times, Mg-Ti, on the other hand, killed all cells completely at 2500 µg/ml (t= 24 hours), 1250 µg/ml (t= 48 hours), and 1750 µg/ml (t= 72 hours). Technically, since all cells died from 1250 µg/ml by t= 48 hours, all cells should have died from 1250 µg/ml by t= 72 hours as well. However, the samples used to measure cell viability for t= 24, 48, and 72 hours are all different samples (in other words, the experiment did not use the same sample to measure changes in cell viability at different times), and so there is inevitable variability of cell viability due to the randomness of particle scattering, local variability in cell density, etc. However, despite these variabilities, Mg-Ti showed effective killing of all cells completely at higher particle concentrations that Mg could not.

The goal of the “recovered” cell experiment was to see if the cells not killed by higher particle concentrations would acquire resistance to the toxicity of Mg particles, and as a result, if the daughters of these cells would be harder to kill. Essentially, the “recovered” cells were killed twice. Cell viability of “recovered” cells showed no difference compared to the cell viability of cells treated with Mg particles only once for t= 24 hours. This means that although the cells survived the toxicity of Mg and proliferated to produce the daughter cells, the daughter cells did not acquire any resistance to the particle toxicity, and therefore, are prone to getting killed again, without having to increase the particle dosage or time of particle treatment.

Further analysis needs to be done to show that cells will not acquire resistance to the particle toxicity. For instance, the cells in this study were exposed to the particle toxicity only once before killing them again. However, this may not be enough for cells to acquire any

resistance. Cells may need to be exposed to the particles several times before the daughters of the surviving cells start to show increased resistance, either requiring much higher particle concentration or longer exposure to the particles to get killed. However, this short-term experiment shows promise that cancer cells can be effectively killed by Mg or Mg-Ti without easily acquiring resistance to the particle toxicity.

Live/dead fluorescence assay and SEM analysis indicate that SAOS2 cells seem to die by both apoptosis and necrosis. This is different from MC3T3 cells, which primarily died by apoptosis in the presence of Mg or Mg-Ti particles [3, 12]. Cell death via apoptosis for MC3T3 cells in the presence of Mg or Mg-Ti is similar to the findings of Sivan and Gilbert et al., which showed that cathodic potential applied on Ti6Al4V caused MC3T3 cells on the metal surface to ball up and die [19]. Haeri and Gilbert et al. also showed that cathodic potential applied on CoCrMo caused MC3T3 cells on the metal surface to undergo apoptosis [20]. Haeri and Gilbert et al. further analyzed the effect of cathodic and anodic potentials on cells at the metal surface (CoCrMo) and found that cells at cathodic potentials were significantly less viable and had lower projected area (indicating that cells have balled up), while cells at anodic potentials were also less viable, but had higher projected area than cells treated with cathodic potential (but lower than that of control (OCP)). Caspase staining showed that cells treated with cathodic potential of -500 mV had high fluorescence of caspase 3 and 9, while cells treated with anodic potential of +500 mV did not, indicating that only cells at cathodic potentials died via apoptosis (caspase 3 is expressed for both intrinsic and extrinsic apoptosis, and caspase 9 is expressed only for intrinsic apoptotic pathway). Haeri and Gilbert et al. stated that generation of reactive oxygen species (ROS), such as super oxide anion, hydroxyl, peroxy, alkoxyl, radicals, and hydrogen peroxide, as a result of the reduction reactions associated with metal corrosion, can damage DNA and

ultimately cause cell death. Moreover, the effect of ROS on cells is dose dependent, where ROS can kill cells either by apoptosis or necrosis. Likewise, Mg and Mg-Ti particles can produce ROS as well. When Mg or Mg-Ti particles corrode, Mg will oxidize to Mg ion, releasing two electrons. Electrons will reduce water and/or oxygen, while producing intermediate ROS, which can trigger apoptosis or necrosis in cells nearby. Therefore, it is possible that ROS are produced in dose-dependent manner and will kill MC3T3 cells or SAOS2 cells by necrosis or apoptosis. Cho et al. showed that ROS-induced cell death can occur both via necrosis and apoptosis [21]. Cho et al. used two types of irradiation to produce different types of ROS, one type primarily singlet oxygen and the other primarily hydrogen peroxide, and showed that both cause apoptosis and necrosis. Cho et al. showed that apoptosis occurred earlier than necrosis, and that this killing was ROS dose-dependent. In previous study, Kim and Gilbert et al. hypothesized that Mg and Mg-Ti must be killing MC3T3 cells due to the production of ROS by reduction for the following reasons. First, Mg-Ti is significantly more effective in killing cells than Mg alone, and yet, pH, which becomes more basic as Mg or Mg-Ti corrodes, is the same for both Mg and Mg-Ti, indicating that pH is not the cause of increased cytotoxicity of Mg-Ti. Second, Mg and Mg-Ti only killed cells in very close proximity to the cells, which means that the killing species does not travel very far, eliminating Mg ions (which is stable) and pH as the major killing species.

There may be the possibility of Mg ion toxicity in-vitro. However, Mg ions are known to be very biocompatible and also in-vitro cytotoxicity of Mg ions are well documented. Gu et al. pre-corroded pure Mg in DMEM serum free medium for 72 hours and then the supernatant fluid was withdrawn and centrifuged to prepare the extraction medium [22]. This study measured the Mg ion concentrations of the extraction medium to be around 175 µg/ml. MC3T3 cell viability was around 60% after 2 days of culture in the extraction medium, and then the cell viability

recovered to 90-100% after 4 and 7 days of culture in the extraction medium, showing that Mg ion concentration in this range does not affect cell viability. Gao et al. used cast 4N-Mg alloy to study the effect of Mg ion concentrations on L929 fibroblast and MC3T3 pre-osteoblast cells [8]. When Gao et al. treated L929 cells with 181 $\mu\text{g/ml}$ of Mg ion concentrations, the study observed that cell viability decreased just a little, while morphology remained the same. But higher Mg ion concentrations, from 343 to 415 $\mu\text{g/ml}$, have adverse effects on cells. % RGR (relative growth rates) measured using MTT assay showed that for MC3T3 cells, 198 $\mu\text{g/ml}$ of Mg ion concentration gives 101 RGR% (compared to 100 RGR% for negative control), while 504.7 $\mu\text{g/ml}$ gives 76 RGR%, at the end of 2 days, which shows that although Mg ion may have some cytotoxicity effect at higher Mg ion concentrations, cells are still viable. This study cannot fully attribute the cytotoxicity of the cells to Mg ions due to the fact that the sample used was not pure Mg (alloyed element can influence cytotoxicity). Wang et al. treated MC3T3 pre-osteoblast cells with different Mg ion concentrations (2-100 mM) and measured cell viability at $t = 2, 4,$ and 6 days [23]. Cells remained very viable for lower Mg ion concentrations (2-10 mM), and cell viability only began to decrease for higher Mg ion concentrations (20-100 mM) for all time periods. At 100 mM Mg ion concentration, cell viability of MC3T3 cells was around 30% by $t = 2$ days. 100 mM of Mg ions converts to 2430.5 $\mu\text{g/ml}$, which is very high. In this study, the particle concentrations used to kill all cells are 2500 $\mu\text{g/ml}$, respectively, and since one mole of Mg yields one mole of Mg ions, 2500 $\mu\text{g/ml}$ of Mg ions would have been produced if the particles have corroded completely at the end of 24 hours. However, based on the observation, Mg and Mg-Ti particles have not completely corroded away, meaning the Mg ion concentrations, although not directly measured, will not exceed 2500 $\mu\text{g/ml}$. Despite the lower concentration of Mg ions produced in this study, compared to Wang et al., Mg particles actively

corroding in the presence of cells have killed cells completely, which may indicate that Mg ions are not playing the primary role of cytotoxicity in this study. While cytotoxic effect of Mg ions still cannot be ruled out, previous studies indicate that Mg ions do not affect cell viability significantly, at least in the range of particle concentrations used in this study to kill cells completely.

Besides the killing effect, Mg and Mg-Ti particles have the ability to prevent cell proliferation. This was also seen for MC3T3 cells in the previous study [12], and SAOS2 cells show a similar pattern. Although the number of cells that survived could affect the proliferation rate (less cells will lead to less proliferation), this does not explain, for instance, how cells treated with Mg 500 $\mu\text{g/ml}$ does not proliferate at all, when cells in control groups, which have the same number of cells at $t= 24$ hours, proliferate. Interesting to note that while these cells do survive the particle treatment and remain viable, they just do not proliferate. Boonstra et al. discussed that there are four phases of cell cycle: DNA synthesis phase (S phase), the cell division phase (M phase), the gap phases, G1 phase between M and S phase, and G2 phase between S and M phases [24]. Boonstra et al. mentioned that cell cycle has checkpoints along the progression of cell cycle to check and repair DNA damage, where ultimately cells will decide either to continue to progress through the cell cycle, arrest in the quiescent phase (G0), or undergo apoptosis. These checkpoints are regulated by many factors, and one of these factors are ROS. ROS are known to cause temporary or permanent growth arrest, apoptosis, or necrosis, depending on the concentration level of ROS. Also, low concentration of ROS is known to enhance the cell cycle, and so the concentration of ROS is critical in determining the fate of the cell. Therefore, there is a critical threshold, where if the concentration of ROS exceeds that threshold, the cells nearby

the particles will be killed. But if the concentration of ROS is below that critical threshold, either the cells will or will not proliferate, but not be killed.

Further experiments are needed to investigate the exact mechanism of cytotoxicity caused by Mg and Mg-Ti. Direct measurement of extracellular ROS being produced during Mg and Mg-Ti particle corrosion may be one possibility. However, this study shows that Mg and Mg-Ti particles are effective in killing SAOS2 human osteosarcoma cells in a dose-dependent manner, where Mg-Ti particles are more effective than Mg alone. Galvanically coupled Mg-Ti, either in particle form shown in this study or in a different form, may be considered to treat human osteosarcoma, and this study shows a promise in using Mg or Mg-Ti in this application.

5.5 Conclusion

This study shows that SAOS2 osteosarcoma cells can be killed by Mg and Mg-Ti particles in a concentration dependent manner over time, where the active corrosion associated with killing occurs by $t = 24$ hours. Galvanically coupled Mg-Ti particles are more effective in killing SAOS2 cells than Mg particles only. Depending on the particle concentrations, cells remained viable and proliferated (low particle concentrations), remained viable but not proliferated (medium particle concentrations), or underwent apoptosis or necrosis (high particle concentrations). Overall, Mg and Mg-Ti particles, and especially Mg-Ti particles, are able to kill osteosarcoma cells effectively.

5.6 Acknowledgements

This work was supported, in part, by DePuy Synthes.

References

1. Mirabello L, Troisi RJ, Savage SA. Osteosarcoma Incidence and Survival Rates from 1973 to 2004, *Cancer* 2009; 115(7): 1531-43.
2. Wang LL. Biology of Osteogenic Sarcoma, *Cancer J.* 2005; 11(4): 294-305.
3. Kim J, Gilbert JL. Cytotoxic Effect of Galvanically Coupled Magnesium-Titanium Particles, *Acta Biomater.* 2016; 30: 368-77.
4. Witte F, Ulrich H, Ruder M, Willbold E. Biodegradable Magnesium Scaffolds: Part I: Appropriate Inflammatory Response, *J. Biomed. Mater. Res. A* 2007; 81A(3): 748-56.
5. Witte F, Ulrich H, Palm C, Willbold E. Biodegradable Magnesium Scaffolds: Part II: Peri-Implant Bone Remodeling, *J. Biomed. Mater. Res. A* 2007; 81A(3): 757-65.
6. Witte F, Kaese V, Haferkamp H, Switzer E, Meyer-Lindenberg A, Wirth CJ, Windhagen H. In Vivo Corrosion of Four Magnesium Alloys and the Associated Bone Response, *Biomaterials* 2005; 26: 3557-63.
7. Zhang E, Xu L, Yu G, Pan F, Yang K. In Vivo Evaluation of Biodegradable Magnesium Alloy Bone Implant in the First 6 Months Implantation, *J. Biomed. Mater. Res. A* 2009; 90A(3): 882-93.
8. Gao JC, Qiao LY, Xin Long. Effect of Mg²⁺ Concentration on Biocompatibility of Pure Magnesium, *Front. Mater. Sci. China* 2010; 4(2): 126-31.
9. Fischer J, Pröfrock D, Hort N, Willumeit R, Feyerabend F. Improved Cytotoxicity Testing of Magnesium Materials, *Mater. Sci. Eng. B* 2011; 176: 830-4.
10. Robinson DA, Griffith RW, Shechtman D, Evans RB, Conzemius MG. In Vitro Antibacterial Properties of Magnesium Metal Against Escherichia Coli, Pseudomonas Aeruginosa and Staphylococcus Aureus, *Acta Biomater.* 2010; 6: 1869-77.

11. Li L, Gao J, Wang Y. Evaluation of Cyto-Toxicity and Corrosion Behavior of Alkali-Heat-Treated Magnesium in Simulated Body Fluid. *Surf. Coat. Tech.* 2004; 185: 92-8.
12. Kim J, Gilbert JL. The Effect of Cell Density, Proximity, and Time on the Cytotoxicity of Mg and Galvanically Coupled Mg-Ti Particles In Vitro, In Progress.
13. Czekanska EM, Stoddart MJ, Richards RG, and Hayes JS. In Search of an Osteoblast Cell Model for In Vitro Research, *Eur. Cell. Mater.* 2012; 24: 1-17.
14. Rodan SB, Imai Y, Thiede MA, Wesolowski G, Thompson D, Bar-Shavit Z, Shull S, Mann K, Rodan GA. Characterization of a Human Osteosarcoma Cell Line (SAOS-2) with Osteoblastic Properties, *Cancer Res.* 1987; 47: 4961-6.
15. Ahmad M, McCarthy MB, Gronowicz G. An In Vitro Model for Mineralization of Human Osteoblast-Like Cells on Implant Materials, *Biomaterials* 1999; 20(3): 211-20.
16. Quarles LD, Yohay DA, Lever LW, Canton R, Wenstrup RJ. Distinct Proliferative and Differentiated Stages of Murine MC3T3-E1 Cells in Culture: An In Vitro Model of Osteoblast Development, *J. Bone Miner. Res.* 1992; 7(6): 683-92.
17. Durnali A, Alkis N, Cangur S, Yukruk FA, Inal A, Tokluoglu S, Seker MM, Bal O, Akman T, Inanc M, Isikdogan A, Demirci A, Helvaci K, Oksuzoglu B. Prognostic Factors for Teenage and Adult Patients with High-Grade Osteosarcoma: An Analysis of 240 Patients, *Med. Oncol.* 2013; 30: 624.
18. Gorlick R, Khanna C. Osteosarcoma, *J. Bone Miner. Res.* 2010; 25(4): 683-91.
19. Sivan S, Kaul S, Gilbert JL. The Effect of Cathodic Electrochemical Potential of Ti-6Al-4V on Cell Viability: Voltage Threshold and Time Dependence, *J. Biomed. Materials Res. Part B Appl. Biomater.* 2013; 101(8): 1489-497.

20. Haeri M, Wollert T, Langford GM, Gilbert JL. Electrochemical Control of Cell Death by Reduction-Induced Intrinsic Apoptosis and Oxidation-Induced Necrosis on CoCrMo Alloy *In Vitro*, *Biomaterials* 2012; 33(27): 6295-304.
21. Cho KS, Lee EH, Choi JS, Joo CK. Reactive Oxygen Species-Induced Apoptosis and Necrosis in Bovine Corneal Endothelial Cells, *Invest. Ophthalmol. Vis. Sci.* 1999; 40(5): 911-9.
22. Gu X, Zheng Y, Cheng Y, Zhong S, Xi T. In Vitro Corrosion and Biocompatibility of Binary Magnesium Alloys, *Biomaterials* 2009; 30: 484-98.
23. Wang J, Witte F, Xi T, Zheng Y, Yang K, Yang Y, Zhao D, Meng J, Li Y, Li W, Chan K, Qin L. Recommendation for Modifying Current Cytotoxicity Testing Standards for Biodegradable Magnesium-Based Materials, *Acta Biomater.* 2015; 21: 237-49.
24. Boonstra J, Post JA. Molecular Events Associated with Reactive Oxygen Species and Cell Cycle Progression in Mammalian Cells, *Gene* 2004; 337: 1-13.

6 In-Vitro Cytotoxicity of Galvanically Coupled Magnesium-Titanium

Particles on *Escherichia Coli* Cells: Potential Bacterial Infection

Therapy

6.1 Introduction

Orthopedic device-related infection (ODRI) occurs in less than 0.5-5% on implants (with less than 1-2% in institutions with highly trained surgeons). However, as the number of patients requiring orthopedic implants grows, so does the number of patients with ODRI [1-2]. More than 500,000 people receive total hip and knee replacements annually, more than 4.4 million people have at least 1 internal fixation device, and more than 1.3 million people have an artificial joint in the United States [1-2]. Based on the Nationwide Inpatient Sample (NIS) database, the average rate of infected knee arthroplasties was 0.92% and that of infected hip arthroplasties was 0.88% between 1990 and 2004 [3]. However, between 1990 and 2004, the incidence of infection for both hip and knee arthroplasties increased by nearly 2-fold in the United States, where for hip arthroplasties, the incidence was 0.80% in 1990 and 1.40% in 2004, and for knee arthroplasties, the incidence was 0.74% in 1990 and 1.36% in 2004 [3]. Although the reason is not clear, a gradual increase in the prevalence of antibiotic-resistant bacteria is consistent with the observed increase in the incidence of infections with hip and knee arthroplasties [3].

ODRI can be detected with cultures of local body fluids near the implant [4]. Once the ODRI is diagnosed, it can be treated with antibiotic therapy and surgical intervention [4]. About two thirds of infections are caused by either *Staphylococcus Aureus* or coagulase-negative staphylococci, where most of the implant infected with either *Staphylococcus Aureus* or candida require implant removal [4].

While the removal of the infected implant is the most effective way to eradicate ODRI, antibiotic therapy may be sufficient to treat less virulent types of bacterial infections and may be the only option for patients who will face high risk of intraoperative and/or postoperative complications [4]. ODRI is harder to treat than other types of bacterial infections because formation of biofilm on the implant surface increases the resistance of bacteria against antibiotics. Initially, the host-derived adhesins (such as fibrinogen, fibronectin, and collagen) layer forms on the surface of the implant, on top of which the free-floating (planktonic) bacteria attach. Bacterial division, recruitment of additional planktonic organisms, and secretion of bacterial products (major components like glycocalyx) will form a complex, three-dimensional biofilm, with tightly attached (sessile) bacteria and fluid channels for flow of nutrients and waste, which is very resistant to antibiotics for many possible reasons [5]:

1. Antibacterial agents cannot penetrate the full depth of the biofilm layer. Antibiotics may be deactivated before being able to diffuse into the inner most layer of the biofilm.
2. Some of the bacterial cells in the biofilm, such as persister cells, have slow or non-growing status, which makes them not very susceptible to antibacterial agents, compared to the planktonic counterparts.
3. Certain enzymes and substances in the biofilm may trap and damage the antibacterial agents, inhibiting antimicrobial activity.

Therefore, bacterial infections on the implant surface are not easily treatable using conventional antibiotics, even if the antibiotics are effective in killing the planktonic counterparts. In some cases, antibiotics treatment for ODRI not only increases the resistance of the bacterial infection, but also helps stimulate the growth of the biofilms [5]. For this reason, many studies have begun

to focus on killing biofilms using anti-antibiotic agents and/or other methods. One method involves modifying the implant surface, creating a hydrophilic and/or anionic surface so that bacteria cannot attach easily [5]. Another method is to develop surface coatings incorporating compounds with antibacterial properties like silver, or bacteriophages, which are viruses that can infect or destroy bacteria, or bioactive enzymes, which can lyse and destroy certain elements of the biofilm [5]. Finally, applying electrical simulation on the orthopedic implant surfaces also can detach the biofilm [5].

Application of electric fields and current density to enhance the biocides and antibacterial agents against bacterial biofilms is described as the *Bioelectric Effect* [6-8]. Costerton et al. reported that mature biofilms (grown longer than 7 days) are resistant to antibiotics and biocides at levels even 500 to 5,000 times higher than the concentration used to kill the planktonic cells [6-7]. However, Costerton et al. found that low-intensity electric fields (field strength of 1.5 to 20 V/cm and current densities of 15 $\mu\text{A}/\text{cm}^2$ to 2.1 mA/cm^2) can decrease the resistance of the biofilm, so that only 1.5 to 4 times the concentration used to kill the planktonic counterparts can be used to kill the biofilm bacteria [6-7]. The bioelectric effect enhanced the killing of biofilm cells of several species of gram-negative and gram-positive bacteria and fungi using different chemical classes of biocides and antibiotics [6-7]. Only the application of DC electric fields (not AC) produced the bioelectric effect and the electric field alone did not kill bacteria. The main hypothesis of this study was that the electric field allowed the antimicrobial agents to overcome the diffusion barriers, so that more antibiotics penetrated into the biofilm and killed the biofilm bacteria, by a form of electrophoresis [6-7]. However, Costerton et al. also suggested that application of electric field can also disrupt cell membrane potentials, affect the membrane proteins, such as electro-inserting proteins into the cell membrane, or alter the membrane protein

orientation and motilities [6]. Van der Borden et al. also showed that staphylococcal strains, *Staphylococcus Epidermidis* and *Staphylococcus Aureus*, can be detached from stainless steel by applying an electric current [8]. Van der Borden et al. applied a DC current ranging from 25-125 μA and detached an adherent staphylococcus biofilm from the surface of stainless steel and also prevented them from colonizing on the surface again [8]. This study found that increasing the electric current did not significantly affect the percentage of biofilm detachment, but the initial detachment rates increased proportionally with the increasing current, where the biofilm detached from 1000 cm/s at 15 μA to 7000 cm/s at 125 μA [8]. Van der Borden et al. explained that the initial detachment depended on the ionic-strength dependence, where the detachment mechanism was based on the reversal of charge transfer during bacterial adhesion to conducting surfaces [8].

While many studies focused on applying constant current, which controlled the *rate* of reactions, other studies focused on applying constant voltage, which controlled the *type* of reactions. Ehrensberger et al. showed that cathodic potential below -300 mV on commercially pure titanium (cpTi) reduced the cell viability of the mammalian cells on the metal surface within 24 hours, while anodic polarization (from -300 to +1000 mV) showed no difference in cell viability [9]. Haeri et al. also noticed a similar trend with CoCrMo alloy, where cell viability decreased at the cathodic potential below -400 mV [10]. Unlike cpTi, cells on CoCrMo alloy with anodic potential at +500 mV and greater showed decrease in cell viability, but the mechanism of cell death was different from those cells died of cathodic potential. Cells killed with cathodic voltages essentially “ball-up”, decreasing the cell area, which is a morphological characteristic of cell apoptosis, while cells killed with anodic voltages had increase in cell area, with punctured membranes, which is a morphological characteristic of cell necrosis. Staining the

cathodic and anodic voltage-treated samples for presence of caspase proteins, which are released during cell apoptosis process, indeed showed that while cells that were exposed to cathodic voltages expressed high concentrations of caspase proteins in the cells, the cells exposed to anodic voltages did not. In other words, cathodic voltage-treated cells undergo apoptosis, and anodic voltage-treated cells undergo necrosis, because of the type of reaction that dominates. In addition, not only was cell viability directly proportional to the magnitude of the cathodic potential, where more cells died at higher magnitude (dose-dependent), Sivan et al. showed that the killing was also time-dependent, where cells applied with higher cathodic voltages died more quickly [11].

There are two types of reactions that happen at the metal interface: reduction and oxidation. Metal atoms will spontaneously undergo oxidation reaction: $M \rightarrow M^{n+} + ne^{-}$, where the metal ions are released into the solution and electrons accumulate at the metal surface. Some metals will even form an oxide film, which is another type of oxidation reaction: $nM + mH_2O \rightarrow M_nO_m + 2mH^{+} + me^{-}$, and this oxide film protects the metal surface and reduces the corrosion rate. Reduction reactions of oxygen and water also occur at the metal surface to balance the oxidation reactions and possible reduction reactions are shown below:

- (1) $O_2 + 2H_2O + 4e^{-} \rightarrow 4OH^{-}$
- (2) $O_2 + 2H_2O + 2e^{-} \rightarrow 2OH^{-} + H_2O_2$
- (3) $H_2O + e^{-} \rightarrow OH^{-} + 1/2H_2$
- (4) $O_2 + H_2O + e^{-} \rightarrow HO_2^{\bullet} + OH^{-}$
- (5) $HO_2^{\bullet} + H_2O \rightarrow H_2O_2 + OH^{\bullet}$
- (6) $H_2O_2 + 2e^{-} \rightarrow 2OH^{-}$

Under the cathodic voltage, the reduction reactions of water and oxygen are dominant due to excess electrons at the metal surface, while under anodic voltage, the oxidation reaction of metal is dominant due to depletion of electrons at the metal surface. The oxidation reaction of metal releases metal ions (depending on the metal alloy type), such as Co^{2+} , Cr^{3+} , and Cr^{6+} for CoCrMo alloy, for example. These ions can be cytotoxic to the cells in time and dose-dependent manner [12]. The reduction reactions of oxygen and water also produce reactive oxygen species (ROS), where the effect of ROS on cellular behavior is known to be dose-dependent. At low concentrations, ROS is known to induce cell signaling and proliferation, at intermediate concentrations, ROS is known to cause growth arrest, and at high concentrations, ROS is known to disrupt normal cell function, damage DNA, RNA, cellular proteins, and lipids, and promote cell death [13-18].

Ehrensberger et al. studied the effect of the cathodic voltage on the viability of biofilms by applying static cathodic voltage on cpTi samples with pre-formed biofilm-like structures of methicillin-resistant *Staphylococcus aureus* (MRSA) [19]. The in vitro and in vivo studies both show that applying static cathodic potential of -1.8 V for 1 hour significantly reduced the colony-forming units of MRSA, not only on the metal surface but from the surrounding solution (in vitro) or from the surrounding bone tissue (in vivo) [19]. In addition, Ehrensberger et al. showed that cathodic electrical stimulation combined with vancomycin were more effective in treating MRSA than just vancomycin alone, when colony-forming units of MRSA were measured from the implant surface and bone [20]. Although the bacterial concentrations significantly reduced by 98% and 87% for implants and bone tissue, respectively, when they were harvested immediately after the cathodic electrical stimulation of -1.8 V for 1 hour, there were no difference between electrical simulated group and control group when harvested 1 week after

stimulation. This indicates that the antimicrobial effects of cathodic voltage electrical stimulation cannot be sustained once the stimulation is removed, and even a small percentage of bacteria can re-grow and re-populate in a short period of time. As previously mentioned, this study is different from studies that delivered constant current, because this study controlled the type of reaction undergoing on the metal surface rather than the rate of reaction. This study shows that controlling the type of reaction (mainly reduction reaction dominating by applying cathodic potential) killed biofilm bacteria very quickly, in just one hour, compared to days when static current was applied. This study also shows that there are no adverse effects on the surrounding tissue based on histology, compared to the discoloration of surrounding bone due to constant current. The voltage-dependent interfacial electrochemical processes at the oxide film surface is thought to be involved in the antimicrobial effects of cathodic voltage-controlled electrical stimulation. Although the application of static cathodic potential proved to be very effective, the three-electrode system used by Ehrensberger et al. is not easily applicable to the clinical setting. The three-electrode system for in vivo simulation (using a rat model) consisted of the working electrode (Ti implant), accessed via internal cortex incision, the reference electrode (Ag/AgCl), and the counter electrode (platinum), which were both placed subcutaneously adjacent to the Ti implant [19]. This method requires multiple incisions, and during the electrical stimulation, the incision has to remain open for electrical connections. Although this approach may be feasible for animal models and just short one-time simulation, this approach may bring more complications for humans when the simulation needs to be done for longer period of time or multiple times to eradicate the bacterial infections. The open wounds are susceptible to more bacterial infections, and besides, having electrical connections through an open wound may cause discomfort and pain to the patient.

Some studies have investigated the mechanism of which the application of cathodic voltage stimulation kills and prevents biofilm formation. Miyanaga et al. studied the viability of *Pseudomonas Aeruginosa* biofilm on carbon steel when cathodic voltage of -0.85 V was applied, compared to saturated silver-silver chloride electrode (SSE), for 5 hours [21]. Miyanaga et al. found that the viability of biofilm of 5 mm thickness decreased to 1% after cathodic voltage stimulation, and found that the pH distribution of the carbon steel surface was increased to approximately 11, concluding that the cells in the biofilm were killed by increase of pH, which is due to the production of hydroxides from reduction of water associated with oxidation of metal. This is a very similar conclusion to a study done by Robinson et al., which studied the cytotoxicity of pure Mg on bacterial cells [22]. Robinson et al. noted that CFUs of different bacterial cells, *Escherichia Coli*, *Staphylococcus Aureus*, and *Pseudomonas Aeruginosa* reduced when Mg samples corroded, and concluded that the decrease of bacterial viability was due to the increase of pH, since the increase of Mg ion concentration alone did not affect the bacterial cell viability. In both cases, steel (Fe) and magnesium (Mg) metal both corrode to release metal ions and two electrons, which then reduce the water, which will release hydroxide ions as a byproduct, increasing the pH of the solution. However, both studies did not consider the possibilities of intermediate oxygen species produced during reduction reactions of water, which at high concentrations can induce cell death.

Cytotoxicity of galvanically coupled Mg and Ti microparticles have been investigated for therapeutic purposes. Previous study found that galvanically coupled Mg-Ti particles have higher cytotoxic properties than Mg alone [23]. Cytotoxicity of both Mg and Mg-Ti particles was dependent on time, dose, and proximity, where higher concentrations of particles killed more cells more quickly in very close proximity to the particles, within 2 mm [24]. Oxidation

and reduction reactions associated with corrosion of pure Mg are: $\text{Mg} \rightarrow \text{Mg}^{2+} + 2\text{e}^-$ and $2\text{H}_2\text{O} + 2\text{e}^- \rightarrow 2\text{OH}^- + \text{H}_2$. Pure Mg is highly corrosive, with a standard electrode potential of -2.34 V in 25 Celsius, but the actual measured potential is -1.7 V in chloride containing solutions [25]. Therefore, Mg will spontaneously corrode in the body, producing Mg ions and electrons, which will then reduce water and oxygen. Mg ions are known to be very biocompatible because Mg ions are one of the most commonly found ions in the body, so the body can readily take up Mg ions and excrete any excess via urine [26-27]. Hydroxide ions can increase the pH up to approximately 11, and then magnesium hydroxide (MgOH) can passivate the Mg surface, reducing the corrosion rate. Although the corrosion of Mg and Mg-Ti particles increased the pH up to 9-10 within the range of particle concentrations used to kill cells, the cell viability of Mg and Mg-Ti particle-treated cells was significantly lower than the cell viability of cells treated with NaOH at the same level of pH [23]. The pH did not explain the higher cytotoxicity of Mg-Ti particles compared to Mg because the pH levels were the same for both groups at the same particle concentrations [23-24]. Also, the cell proliferation was seen at low particle concentrations, cell growth arrest at intermediate particle concentrations, and cell death at high particle concentrations, which is consistent with the finding that ROS induces cell proliferation, growth arrest, and cell death depending on the ROS dosage [13, 24, 28].

This study investigated the cytotoxicity of Mg and Mg-Ti particles on biofilms with a goal of potentially incorporating Mg into orthopedic implants to prevent biofilm formation on the metal surface. The hypothesis of this study is that Mg and Mg-Ti particles kill cells in similar principles as applying cathodic voltage, where the reduction reactions produce ROS in dosage dependent manner, which will ultimately disrupt and kill biofilms. In vitro experiment of

cathodic potentials on biofilms were also conducted to investigate the biofilm cell viability and morphology.

6.2 *Materials and Methods*

6.2.1 *Cathodic Potentials*

6.2.1.1 *Metal Sample Preparation*

Disks of grade 4 cpTi (ASTM-F67) were cut from the rod stock to fit the electrochemical chamber with an exposed area of 3.7135 cm². Surfaces were wet polished with 240, 320, 400, and 600 grit. Samples were then rinsed with deionized water, sonicated in 70% ethyl alcohol for 30 minutes, and UV sterilized for 10 minutes before experimental use. A custom-made electrochemical chamber was used for all electrochemical treatments of biofilms, which has been described previously [29]. All components of the electrochemical chamber were rinsed with 70% ethyl alcohol, autoclaved, and UV sterilized for 10 minutes. The discs were placed into a custom-made electrochemical cell culture chamber with electrical contacts to a cpTi disk as a working electrode, a graphite as a counter electrode, and a chlorided silver (Ag/AgCl) wire as a reference electrode. A rubber stopper with holes for counter and reference electrodes was used to seal the glass chamber. A sterilized O-ring was mounted between the glass chamber and the metal sample to prevent cell culture media from leaking. Air could exchange through the holes on the rubber stopper.

6.2.1.2 *Bacterial Culture and Application of Cathodic Voltage*

E. coli HM22 was first cultured overnight in 25 ml Lysogeny Broth (LB) supplemented with 25 µl diphenyl phosphorazidate (DPA) at 37°C and 200 rpm. LB media consists of 10 g tryptone, 5 g yeast extract, and 10 g NaCl per 1 liter of Millipore water. LB media was autoclaved for 25 minutes at 120 °C (before adding DPA) and stored at 4 °C. 1 ml of overnight

cell culture was plated on cpTi surface and kept at open circuit potential (OCP) at 37°C for 30 minutes. After 30 minutes, the surfaces were gently rinsed with saline solution (0.9% w/v NaCl) three times. Fresh medium (LB media or saline solution) were then added to immerse the counter and reference electrodes, which were connected to a potentiostat. The cpTi samples were held at -1 V or -1.2 V for 24 hours at 37°C, while the control samples were held at OCP (around -0.2 V in saline solution or from -0.3 to -0.39 V in LB media), n=3. Current density of each test was measured in 28-second intervals for 24 hours using an NI9004 A/D board (National Instruments) and Labview software. Average current densities were determined over 24 hours (data not shown in this study).

To assess cell viability, a LIVE/DEAD® *BacLight* bacterial viability kit (ThermoFisher Scientific, Catalog #: L7012) was used. Bacterial cells on Ti surfaces were first rinsed with a saline solution three times and then transferred to a six-well plate. Live and dead dyes (3µl per 1ml of PBS) were added. The plate was then covered with aluminum foil to prevent photo-bleaching and kept in an incubator at 37°C for 15 minutes. Samples were then taken out, gently inverted, and mounted for fluorescent imaging.

Cells were imaged with an inverted microscope (Zeiss Axiovert 40 CFL, Zeiss, Denmark) connected to a CCD mono 12-bit camera (Q-imaging, Canada). Live cells were imaged through FITC filter set and dead cells were imaged through Texas red dye filter set. Five images were taken randomly per sample, and the areas of live and dead cells were determined using Image J software (NIH). Cell viability was calculated as:

$$\% \text{ Cell Viability} = \frac{\% \text{ Area of Live Cells}}{\% \text{ Area of Live Cells} + \% \text{ Area of Dead Cells}}$$

The bacterial cells could not be individually counted, so the area of live cells was measured using the live cell only image, and the area of dead cells was measured using the dead cell only image to calculate the ratio.

6.2.1.3 *Morphological Assessment using SEM and AFM*

The sample surfaces were gently rinsed with a phosphate buffered saline (PBS) after voltage treatments and then fixed with 4% formaldehyde. The samples were then dehydrated in gradients of ethanol (50%, 70%, 90%, and 100% of ethanol in DI water) for 15 minutes each and then sputtered with gold for 30 seconds (100-200 mTorr, 50 mA). The cells were imaged with SEM (JEOL 5600, Japan) in secondary mode, low kV.

AFM (Veeco Instruments) was used to image the cells in deflection and height modes, to measure the longitudinal length, width, and height of the bacterial cells either intact or ruptured from the voltage treatments.

6.2.1.4 *Statistical Analysis*

T-test was performed to compare cell viability of the controls (OCP) and voltage-treated groups at -1 V and -1.2 V in LB media or NaCl solution with a P-value of 0.05, n=3. Two-way ANOVA was performed to show significance in cell viability between voltage-treated groups in NaCl solution compared to voltage-treated groups in LB media with a significance level of 0.01, n=3.

6.2.2 *Mg and Mg-Ti Particles*

6.2.2.1 *E. Coli Biofilm Preparation for Mg and Mg-Ti Particle Treatment*

E. Coli strain K12 was cultured overnight in 25 ml Lysogeny Broth (LB) at 37 °C and 200 rpm. LB media consists of 10 g tryptone, 10 g NaCl, and 5 g yeast extract per 1 liter of Millipore water. LB media was autoclaved for 25 minutes at 120 °C. 1 µl of the overnight

culture was plated in 5 ml of fresh media per well in 6-well plates ($A= 9.6 \text{ cm}^2$) at $37 \text{ }^\circ\text{C}$ for $t= 24 \text{ h}$ to grow a biofilm.

6.2.2.2 *Sputtering of Mg with Ti*

Mg particles (Goodfellow, Product #: MG006021), generated by mechanical abrasion, with 99.8% Mg purity, were galvanically coupled with Ti (Alfa Aesar, Stock #: 13975 and Lot #: C19N26), with 99.99% Ti purity. Mg particles have a maximum diameter of approximately $50 \text{ }\mu\text{m}$, but are very irregular in shape with rough surface. Mg and Ti were galvanically coupled via direct current sputtering (Denton Systems) for 5 minutes, at 1.2 kV, 50 mA, and 100-200 mTorr. The particle concentration range used for this experiment was from 0 to $50000 \text{ }\mu\text{g}$ for Mg and 0 to $30000 \text{ }\mu\text{g}$ for Mg-Ti. Since Mg particles get sputtered based on line-of-sight, Mg particles were scattered as much as possible. Therefore, no more than 0.005 g of Mg particles were sputtered in a dish with an area of 9.6 cm^2 ($d= 3.5 \text{ cm}$), and no more than 0.02 g of Mg particles were sputtered in a dish with an area of 38.5 cm^2 ($d= 7 \text{ cm}$) in order to maximize the exposure of Mg particles to Ti during sputtering.

6.2.2.3 *Distribution of Mg and Mg-Ti Particles*

Once the biofilm is ready, 5 ml of the LB media was aspirated (which removes many planktonic cells) and 1 ml of PBS is added. Mg or Mg-Ti particles of certain concentrations were mixed in with 2 ml of PBS and then added slowly and gently into the well in order to not disturb the biofilm. This resulted in a total of 3 ml of PBS sample. Mg and Mg-Ti particles were randomly scattered throughout the dish. The biofilm was treated with Mg or Mg-Ti particles for $t= 6 \text{ hours}$ in PBS. Negative control group is cells without any particle treatment, and positive control group is cells with ofloxacin-antibiotic treatment.

6.2.2.4 *Flow Cytometry*

At the end of $t = 6$ hours, the biofilm with the particles were sonicated for $t = 30$ seconds in order to remove the biofilm off the surface. The biofilm was more broken down by aspirating the solution with a 1000 μl micropipette multiple times. Then the cell solution with the particles were transferred into 15 ml centrifuge tube for 30-60 seconds, so that the particles could sink (the particles sink very quickly without having to centrifuge). Once the particles sank, 1 ml of cell solution, clear of Mg or Mg-Ti particles by not disturbing the particles at the bottom of the tube, was transferred to a new tube. Fluorescent live/dead assay kit (ThermoFisher Scientific, Catalog #: L7012) was used to measure the number of live and dead cells using flow cytometry (BD Accuri C6). This dye kit contains dye A, which has a mixture of SYTO-9, 1.67 mM, and propidium iodide, 1.67 mM and dye B, which has a mixture of SYTO-9, 1.67 mM, and propidium iodide, 18.3 mM. SYTO-9 usually stains all bacteria in population, those with intact membranes and those with damaged membranes, while propidium iodide (PI) penetrates only bacteria with damaged membranes, which reduces the SYTO-9 stain fluorescence when both dyes are present in the cell. Therefore, with an appropriate mixture of the SYTO-9 and PI, bacteria with intact cell membranes stain fluorescent green (excitation/emission maxima of 480/500 nm), while bacteria with damaged membranes stain fluorescent red (excitation/emission maxima of 490/635 nm).

6.2.2.5 *Treatment of Planktonic Cells with Mg and Mg-Ti Particles*

After the overnight culture from Section 6.2.2.1, 1 ml of the solution was transferred to a new flask with 19 ml of fresh LB media. 0.5 g of Mg particles were added into the flask for the experimental groups and none for the negative control groups. The flask was shaken at 200 rpm and 37 °C for $t = 24$ hours. Afterwards, the solution was transferred to a 50 ml centrifuge tube for the particles to sink, and then 1 ml of the cell solution, clear of Mg particles, was transferred to

another tube. Fluorescent dyes were added for flow cytometry analysis. This experiment did not have Mg-Ti samples because 0.5 g (per sample, n=3) of Mg-Ti particles were difficult to sputter because only 0.02 g of particles can be sputtered at a time.

So instead of killing large volume of planktonic cells (20 ml) using 0.5 g of particles, smaller volume of solutions was prepared. 0.1 g of particles were added in 4 ml of the cell solution. This 4 ml was taken out of the 20 ml solution, after thoroughly mixing 1 ml of cell overnight culture to 19 ml of fresh LB media. Instead of a flask, 50 ml tubes with conical shape at the bottom were used, and these tubes were shaken at 200 rpm and 37 °C for t= 24 hours. The tubes were left on the counter to let the particles sink, and then 1 ml of the cell solution was transferred to another tube. Fluorescent dyes were added for flow cytometry analysis.

6.2.2.6 *Preparation of Cells for SEM Images*

After the particle treatments, both biofilm and planktonic cells were prepared for SEM analysis using the same protocol as Section 6.2.1.3.

6.2.2.7 *Inhibition Zone Test*

100 mm diameter petri dishes were used to make agar plates. 100 µl of overnight culture was spread carefully on the agar plate. At the center of the dish, a clear plastic ring with a diameter of 16 mm was placed gently, not pressed against the agar plate to make depression marks, but enough to not cause any leakage. Particle concentrations of 0.005 g or 0.02 g of Mg and Mg-Ti particles were mixed with 100 µl of LB media and then carefully added into the ring, so that Mg or Mg-Ti particles were centered with a diameter of roughly 16 mm. Afterwards, the agar plate was left overnight for the cells to grow. Inhibition zone, a clear ring around the Mg or Mg-Ti particles, was measured using a ruler around 4 different locations of the ring (per sample, n=3) and then averaged.

6.2.2.8 *Statistical Analysis*

Two-way analysis of variance (ANOVA) statistical methods were used to analyze the results, along with post hoc Tukey tests, using SPSS Statistics Software, version 17.0.

Statistically significant differences were determined with $p < 0.05$.

6.3 *Results*

6.3.1 *Cell Viability of E. Coli Biofilm After Cathodic Voltage Treatment*

Fig. 6.1 shows the fluorescent images of *E. Coli* HM22 after live and dead stains of either OCP or cathodic voltage (-1 V or -1.2 V) treated samples in NaCl solution or LB media. Cells in biofilms were alive when they were in LB media, despite the cathodic voltage treatments, while many cells were dead when the metal sample was held at -1 V in NaCl solution. Fig. 6.2 shows the cell viability fraction of bacterial biofilm measured from live/dead images after -1 V or -1.2 V voltage treatments in either NaCl solution or LB media, compared to controls at OCP in NaCl solution or LB media. For LB media-treated groups, the average cell viability fraction of biofilms at -1 V was not significantly different from that of OCP ($p > 0.05$), while that of -1.2 V was significantly different from that of OCP and -1 V groups ($p < 0.05$). For NaCl solution-treated groups, the average cell viability fraction of biofilms at -1 V was significantly different from that of OCP ($p < 0.05$), and even compared to that of -1 V in LB media ($p < 0.05$), indicating that solutions can have an influence in cathodic voltage treatment.

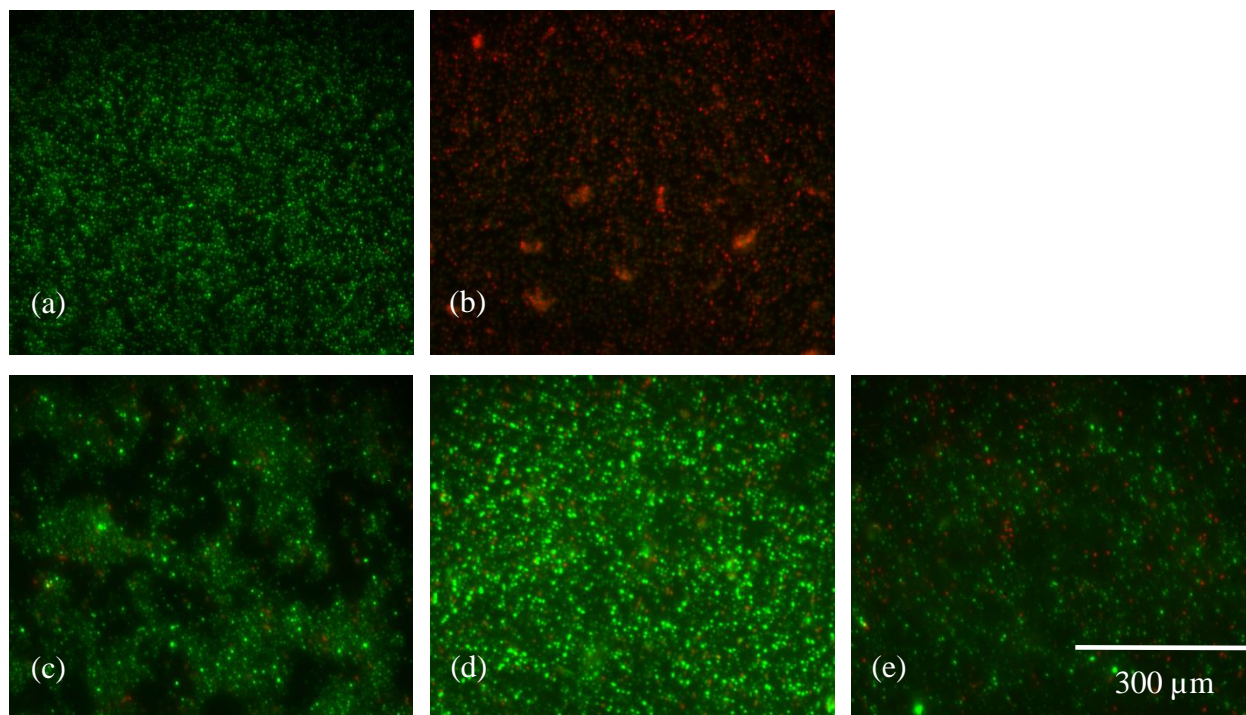


Figure 6.1 Fluorescent images of *E. Coli* HM 22 cells after live/dead stain. (a) Cells at OCP in NaCl solution, (b) cells at -1 V in NaCl solution, (c) cells at OCP in LB media, (d) cells at -1 V in LB media, and (e) cells at -1.2 V in LB media for $t= 24$ hours. All images were at 63x magnification. All the cells were dead after -1 V treatment in NaCl, while most of the cells in LB media remained alive, despite the voltage treatment.³⁰

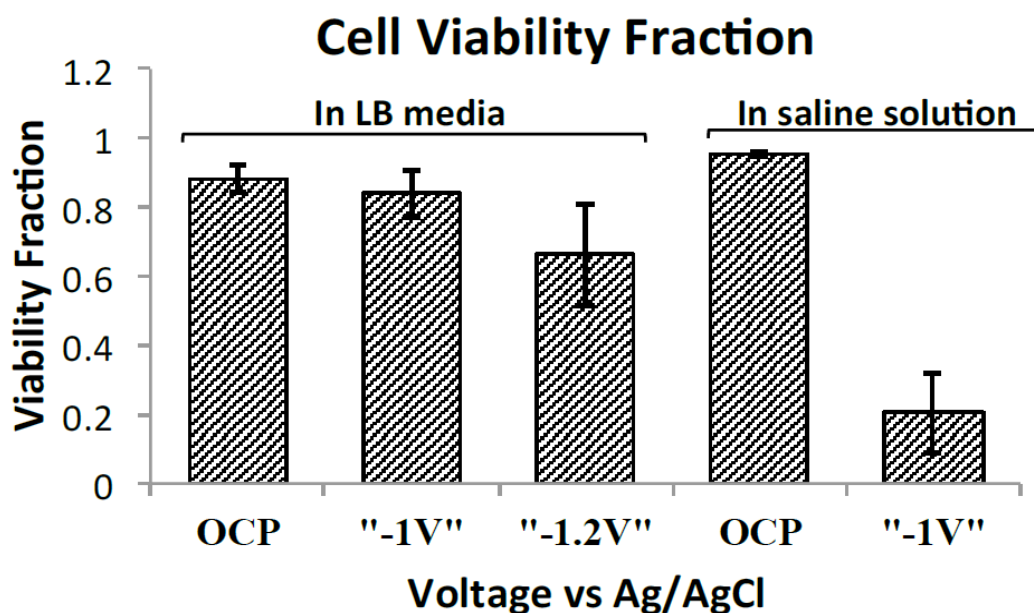


Figure 6.2 Cell viability fraction of bacterial biofilm measured from live/dead assay after OCP, -1 V, and -1.2 V voltage treatments in LB media or NaCl solution, $n=3$. Compared to voltage treatments of cells in LB media, the cells treated with -1 V in PBS show a significant decrease in cell viability.³⁰

6.3.2 Morphology Assessment of Cells using SEM

Cells at OCP in NaCl solution are very sparsely distributed, without any aggregation and three-dimensional structure/matrix (Fig. 6.3a). The cells at OCP in NaCl solution are attached as individuals in a monolayer, while cells at OCP in LB media are aggregated, forming a three-dimensional matrix-like structures that resembles more of a biofilm (Fig. 6.3c). The cells treated with -1 V in NaCl solution have cavitations (dark areas within the bacterial cell), and they look more balled up, or shortened longitudinally, compared to the control cells, which are rod-shaped (Fig. 6.3b). The cells treated with -1 and -1.2 V in LB media show mixtures of cells that are rod-shaped and balled-up, and few cells show cavitations (Fig. 6.3d and 6.3e).

6.3.3 Length, Width, and Height Measurements using AFM

Control cells at OCP have intact and smooth membranes, while cells treated with cathodic potentials are lysed, with dis-intact membranes (Fig. 6.4). Fig. 6.5 shows width and length of the cells, while Fig. 6.6 shows the height of the cells. Voltage treatment of -1 V in NaCl solution significantly reduced the length and the width of both intact and ruptured cells, compared to those of control cells at OCP ($p < 0.05$). The height of the ruptured cells at -1 V was significantly lower than that of control cells (intact) at OCP ($p < 0.05$), while the height of the intact cells at -1 V was not impacted by voltage ($p > 0.05$). In LB media, voltage treatment of -1 V significantly reduced the length and height of both intact and ruptured cells compared to that of the control cells at OCP ($p < 0.05$), whereas, the width of all cells was unaffected by the application of cathodic potentials ($p > 0.05$).

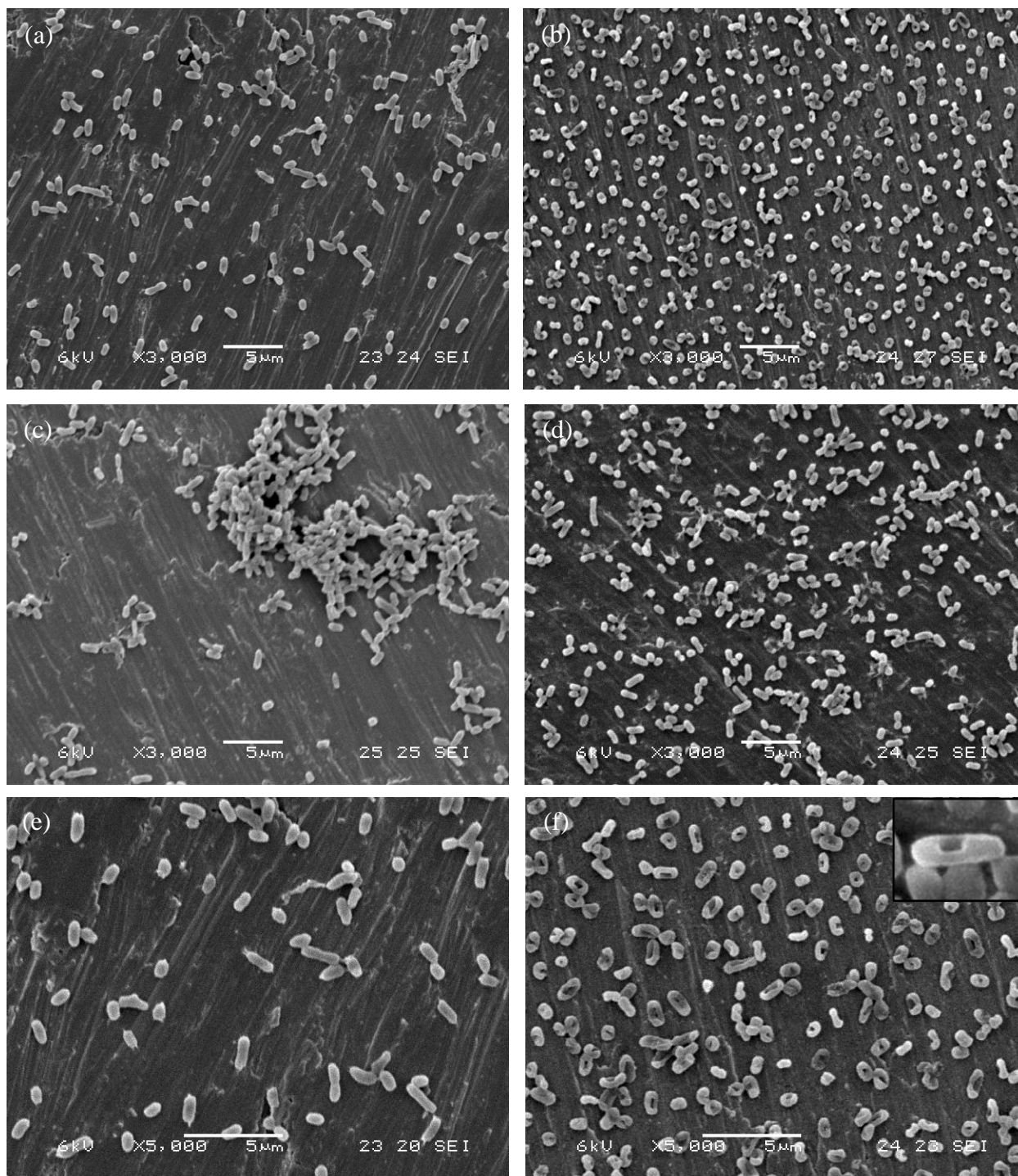
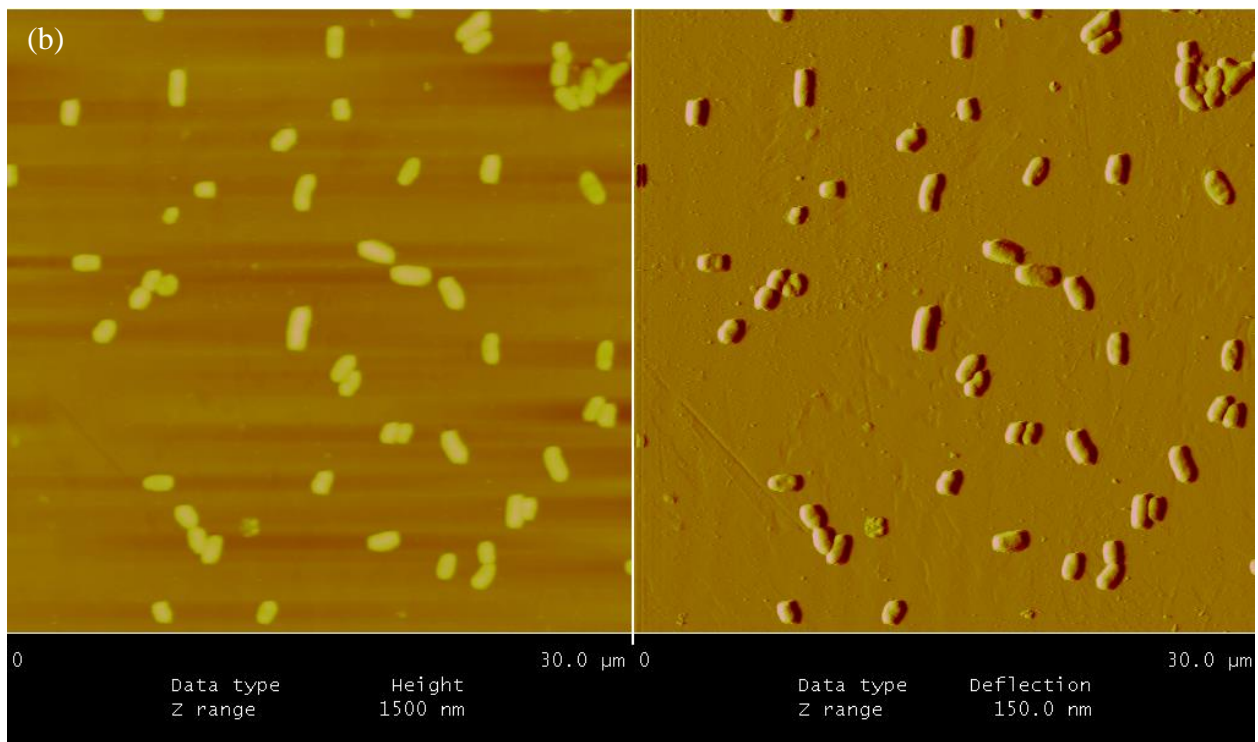
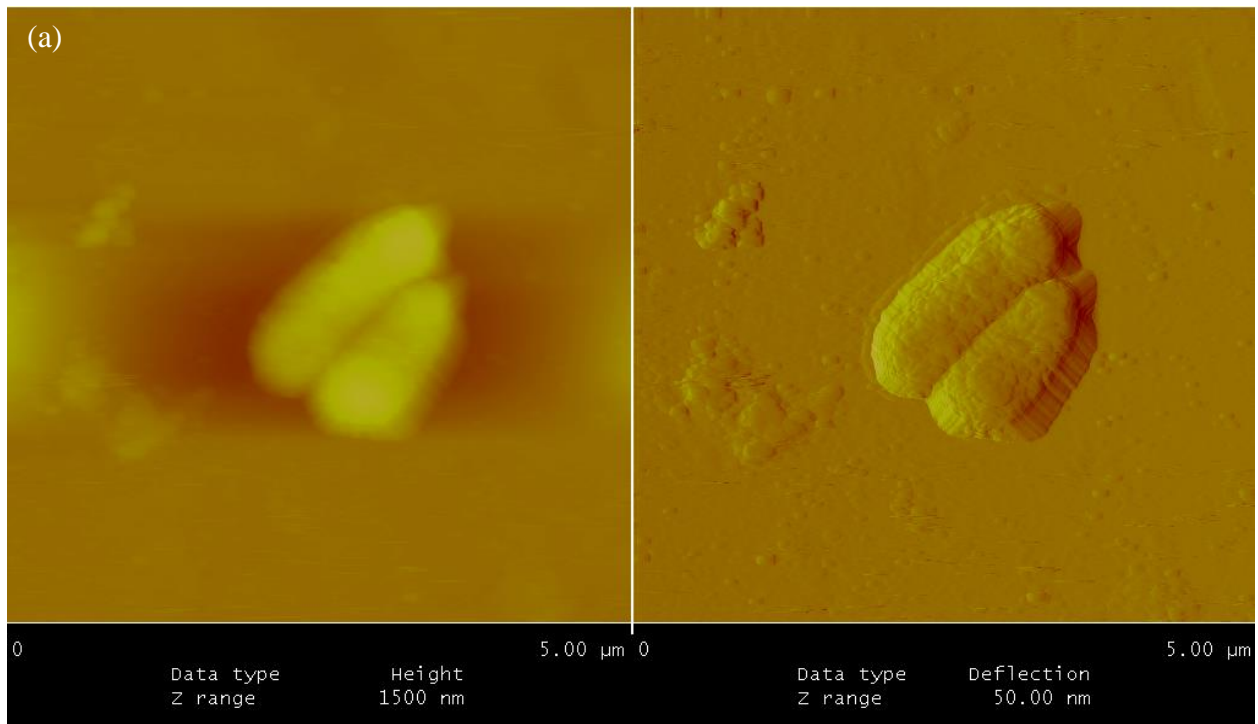
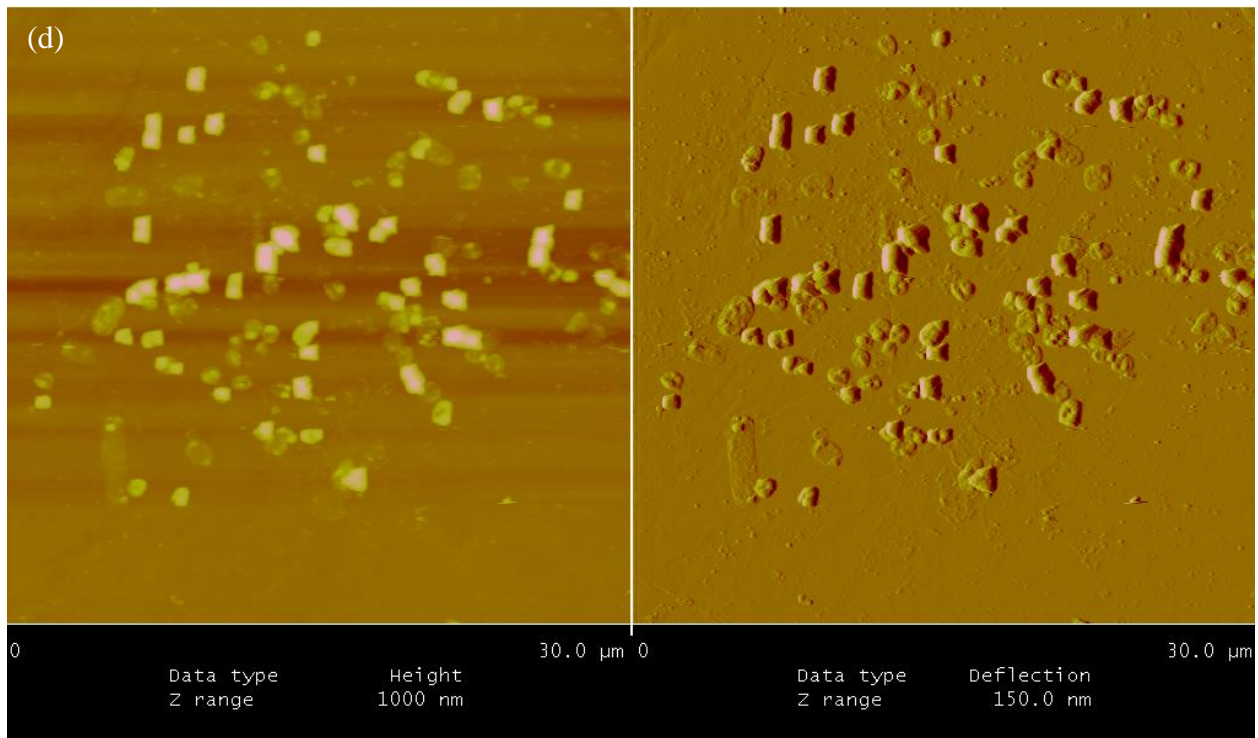
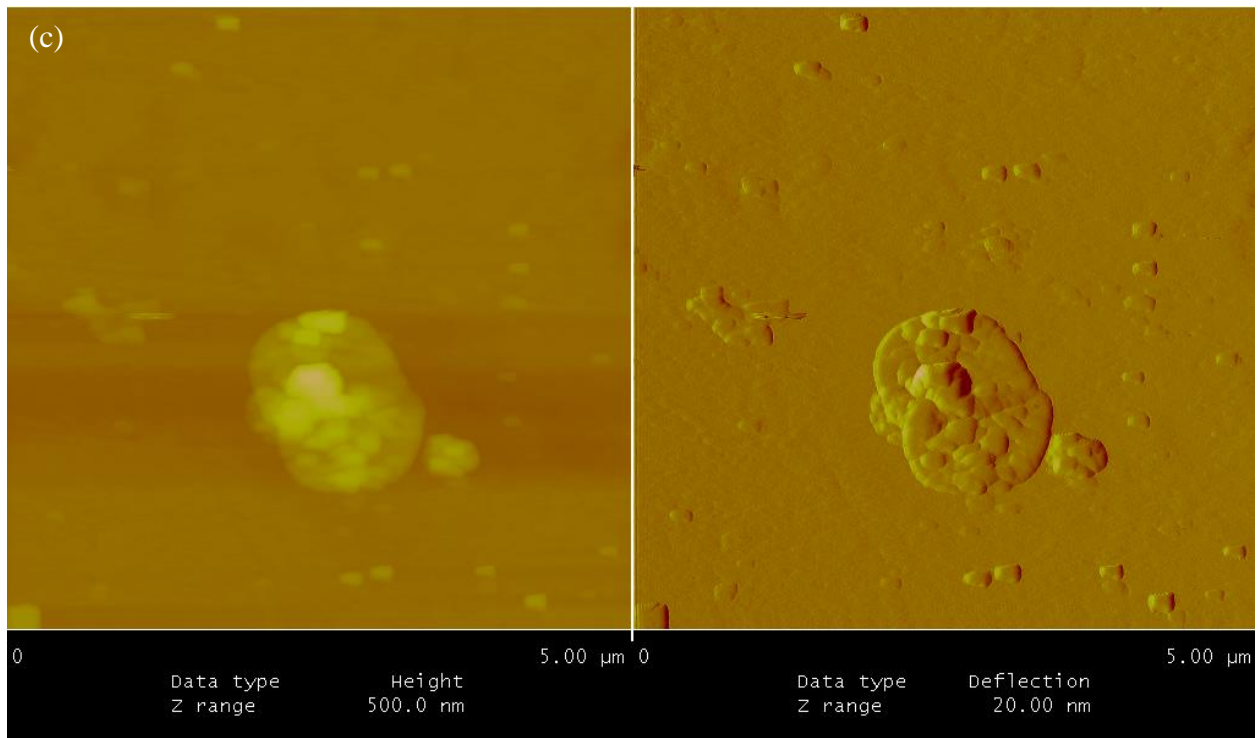


Figure 6.3 SEM images of *E. Coli* HM 22 cells after electrochemical treatment in secondary mode. (a) Cells at OCP in PBS, (b) cells at -1 V in PBS, (c) cells at OCP in LB media, and (d) cells at -1 V in LB media. Additional images are shown for (e) cells at OCP in PBS at higher magnification, and (f) cells at -1 V in PBS at higher magnification. Cells at OCP in PBS and LB media are rod-shaped, and the cells in LB media are starting to form clusters, which cannot be seen with cells in PBS. Most of the cells treated with -1 V voltage in PBS have cavitations in their surfaces and become shorter in the longitudinal direction, where there are more spherical than rod-shaped cells. For cells treated with -1 V in LB media, there are mixtures of cells with cavitation and shortened length and rod-shaped cells. Cells treated with -1 V voltage in LB media did not form clusters like the cells in OCP.³⁰





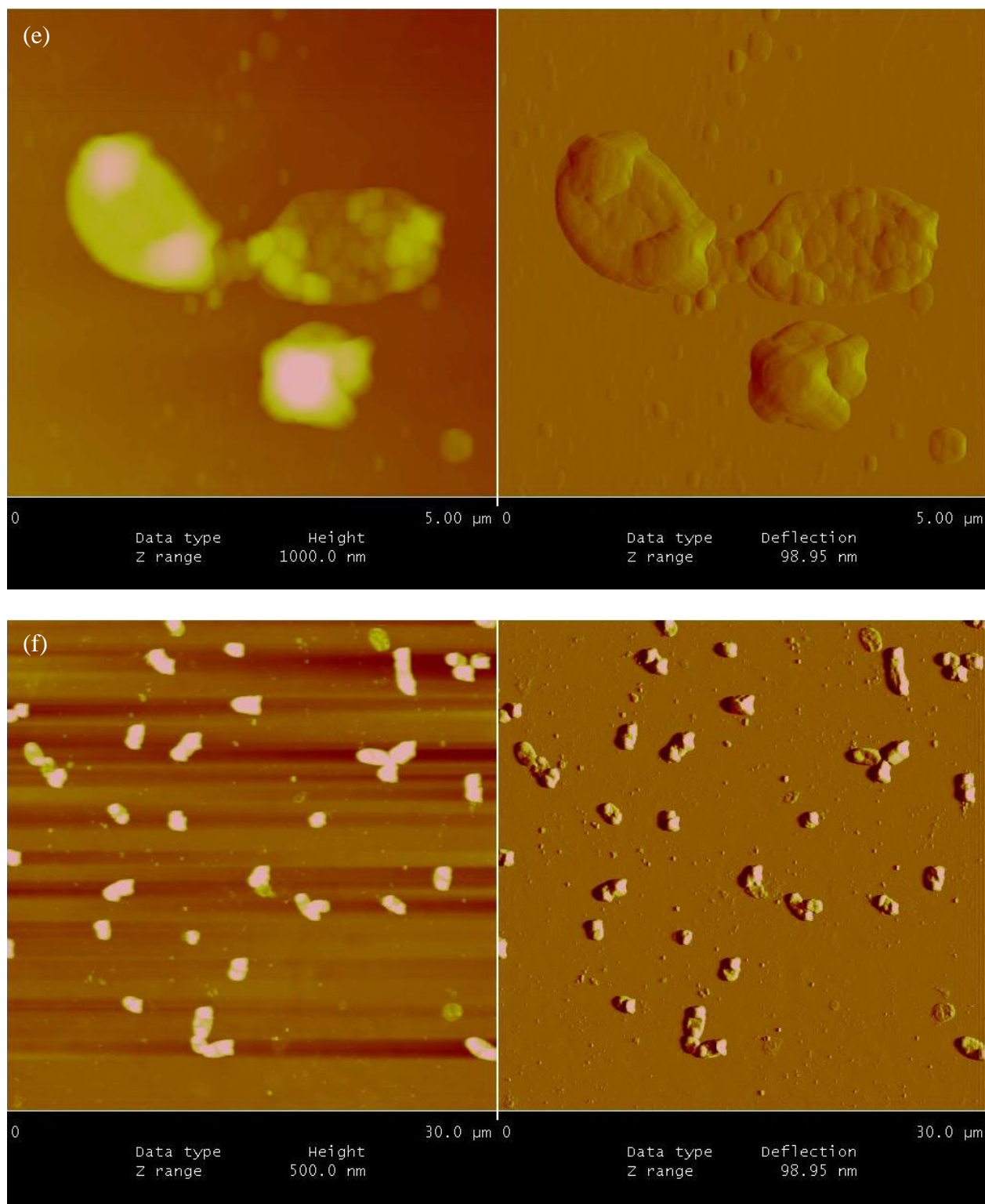


Figure 6.4 AFM images of *E. coli* HM 22 after 2 hours at (a) OCP (5 μm scale bar) in LB media, (b) OCP (30 μm scale bar) in LB media, (c) -1V (5 μm scale bar) in NaCl solution, (d) -1V (30 μm scale bar) in NaCl solution, (e) -1V (5 μm scale bar) in LB media, and (f) -1V (30 μm scale bar) in LB media. Cells at OCP have intact and smooth membranes and are rod-shaped. Many cells at -1V in NaCl solution and LB media are lysed, with blebbed membranes. All voltages were versus Ag/AgCl.³⁰

***E. coli* HM22 Length & Width**

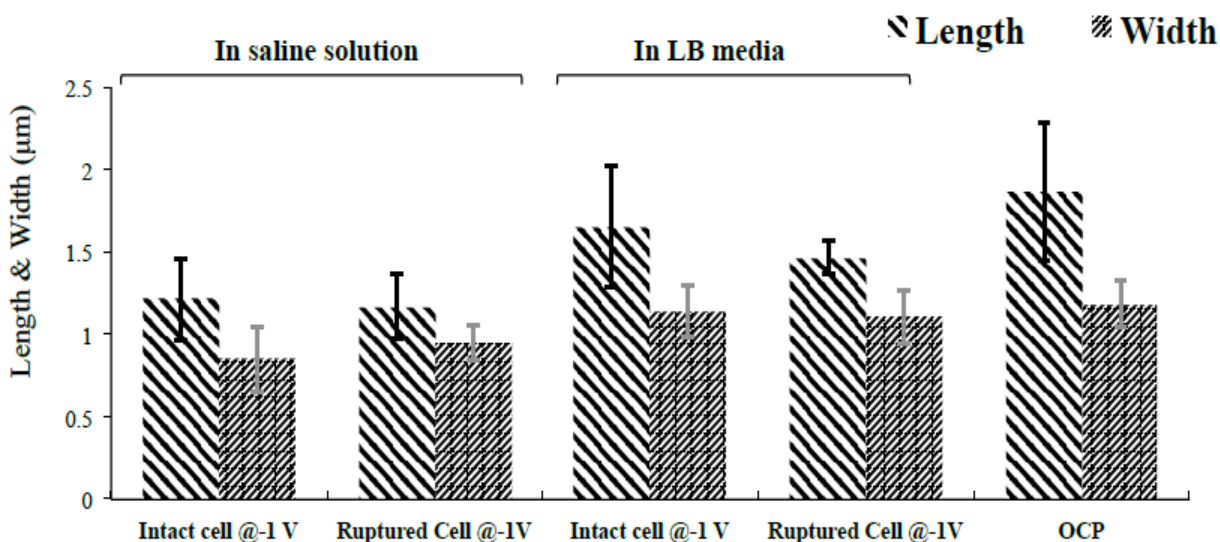


Figure 6.5 Cell length and width of bacteria on cpTi samples after two-hour voltage treatment in saline solution or LB media at -1 V, n=3. The OCP was measured in LB media for 2 hours, n=3. Post hoc Tukey test shows that voltage treatment of -1 V in saline solution reduced the length and the width of both intact and ruptured cells, compared to those of control cells at OCP ($p < 0.05$).³⁰

***E. coli* HM22 Height**

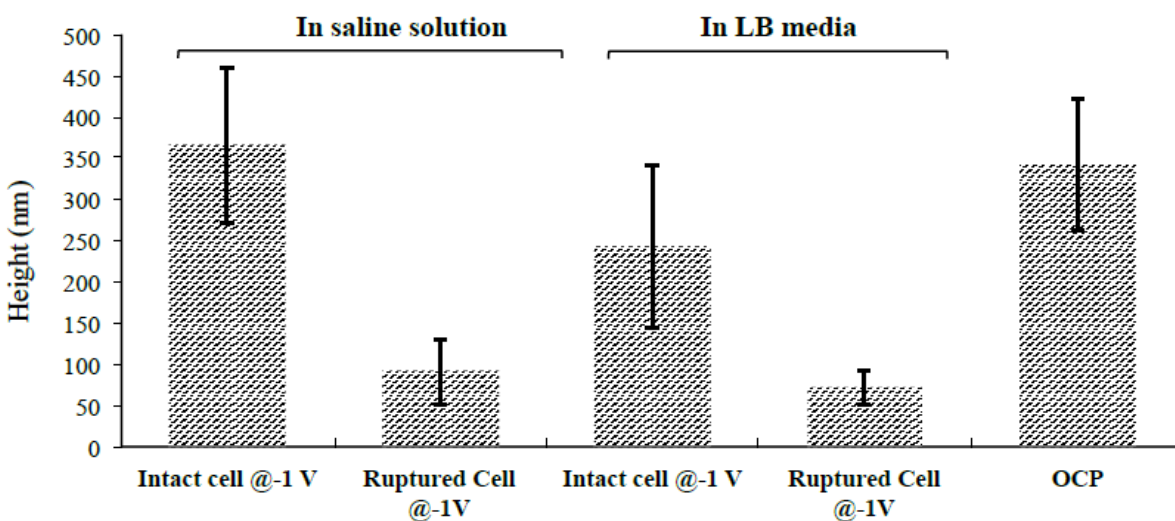


Figure 6.6 Cell height of bacteria on cpTi samples after two-hour voltage treatment in saline solution or LB media for 24 hours -1 V, n=3. The OCP was measured in LB media for 2 hours, n=3. Post hoc Tukey test shows that the height of the ruptured cells due to voltage treatment decreased significantly to that of intact cells found in control and at -1 V ($p < 0.05$).³⁰

6.3.4 Cell Viability of *E. Coli* Biofilm After Mg and Mg-Ti Particle Treatment

Fig. 6.7 shows fluorescent images of biofilms treated with Mg for low concentrations between 0 and 3500 μg . There is less green fluorescence as the particle concentration is increased, although this cannot be measured quantitatively just based on live/dead images. Fig. 6.8 shows raw data retrieved from flow cytometer. Graph (a) shows correlated measurements of FSC (forward-scattered light, which measures diffracted light, proportional to cell-surface area or size) and SSC (side-scattered light, which measures refracted and reflected light, proportional to cell granularity or internal complexity), which allow for differentiation of cell types in a heterogeneous cell population. Graphs (b) and (c) show FSC measurements of live cells fluorescing with SYTO-9 (only live cells will fluoresce SYTO-9 since PI in dead cells reduce the fluorescence of SYTO-9) and dead cells fluorescing with PI. Graph (d) shows correlated FSC measurements of SYTO-9 and PI. Graphs (e) and (f) show cell counts of cells fluorescing in SYTO-9 and PI, respectively. Fig. 6.8(i) is measured from negative control without dyes, so any signals detected in this reading is considered “noise.” Based on this reading, Graph (d) has red lines drawn to show that any signals detected in the left-bottom corner (LL) are considered “noise.” If cells are detected in the bottom-right corner (LR), high signal of SYTO-9 and low signal of PI, cells are considered viable. If cells are found in the top-left corner (UL), high signal of PI but low signal of SYTO-9, cells are not viable. If cells are in the top-right corner (UR), high signal of both SYTO-9 and PI, then cells are not viable due to the high signal of PI. Fig. 6.8(ii) shows negative control with dyes, which shows that 92.1% of cells are in LR (viable) and 7.2% of cells are in UR (not viable) from graph (d). These are relative ratios, and the actual cell numbers of viable and non-viable cells are shown in graphs (e) and (f), where the exact numbers can be found in table (g). Fig. 6.8(iii) shows cells treated with Mg 7500 μg , where now, most of

cells are in the UR region (80.3%, non-viable), and fewer cells in LR region (17.5%, viable), due to the particle treatment. The correlated FSC measurements of SYTO-9 and PI from graph (d) shows that there are two distinct cell populations of different sizes, although there is only one type of cell in this experiment. This is not observed in negative control groups, very low particle concentration-treated groups (1000 and 2500 μg), or high particle concentration-treated groups (45000 and 50000 μg), but only in ofloxacin antibiotic-treated groups and medium particle concentration-treated groups (5000-40000 μg) (Fig. 6.8(i)-(v)). This phenomenon is also not seen in planktonic negative control groups and planktonic Mg and Mg-Ti treated groups (Fig. 6.8(vi)-(vii)).

Fig. 6.9 shows % average live and dead cells in biofilms after 6-hour treatment using Mg or Mg-Ti particles. As particle concentration increases from 0 to 50,000 μg or 0 to 30,000 μg for Mg or Mg-Ti, respectively, % live cells decreases, while % dead cells increases. At 0 μg (negative control group), 78.6% are alive and 18% are dead, and 91.8% are live and 7.5% are dead, for Mg and Mg-Ti experiments, respectively. At the highest particle concentration of 50,000 μg for Mg, % live cells drop to 2.7% and % dead cells increase to 94.5%. At the highest particle concentration of 30,000 μg for Mg-Ti, % live cells drop to 11.6% and % dead cells increase to 86.3%. Fig. 6.9b compares the % live cells of Mg and Mg-Ti from 0 to 30,000 μg to show whether Mg-Ti can kill biofilm more effectively than Mg alone. Post hoc Tukey test shows that the % cell viability (or % live cells) of higher particle concentrations from 7,500 μg to 50,000 μg show no significant difference ($p > 0.05$). There is also a significant difference between Mg and Mg-Ti groups ($p < 0.05$), but unlike the hypothesis, the results show that % cell viability of Mg-Ti is higher than that of Mg. Fig. 6.10 shows % live and dead cells of biofilms treated with 50 and 100 $\mu\text{g/ml}$ of ofloxacin, where 62.6% are live and 33.2% are dead for 50

$\mu\text{g/ml}$, and 52% are live and 45.6% are dead for 100 $\mu\text{g/ml}$. The average % live cells are significantly higher for antibiotic-treated cells than Mg and Mg-Ti-treated cells ($p < 0.05$), where the average % live cells fall below 20% for both Mg and Mg-Ti groups by 10,000 μg .

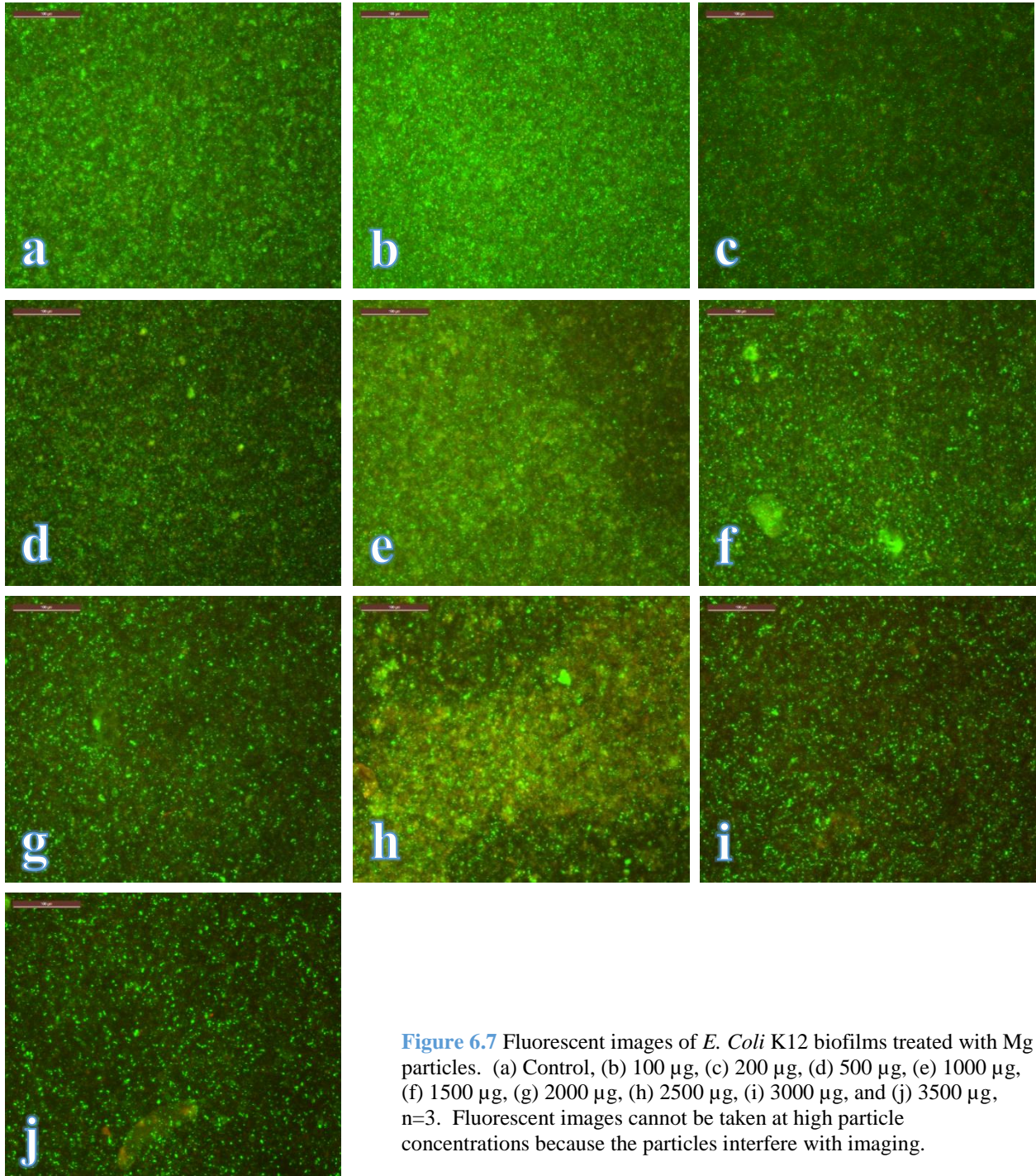
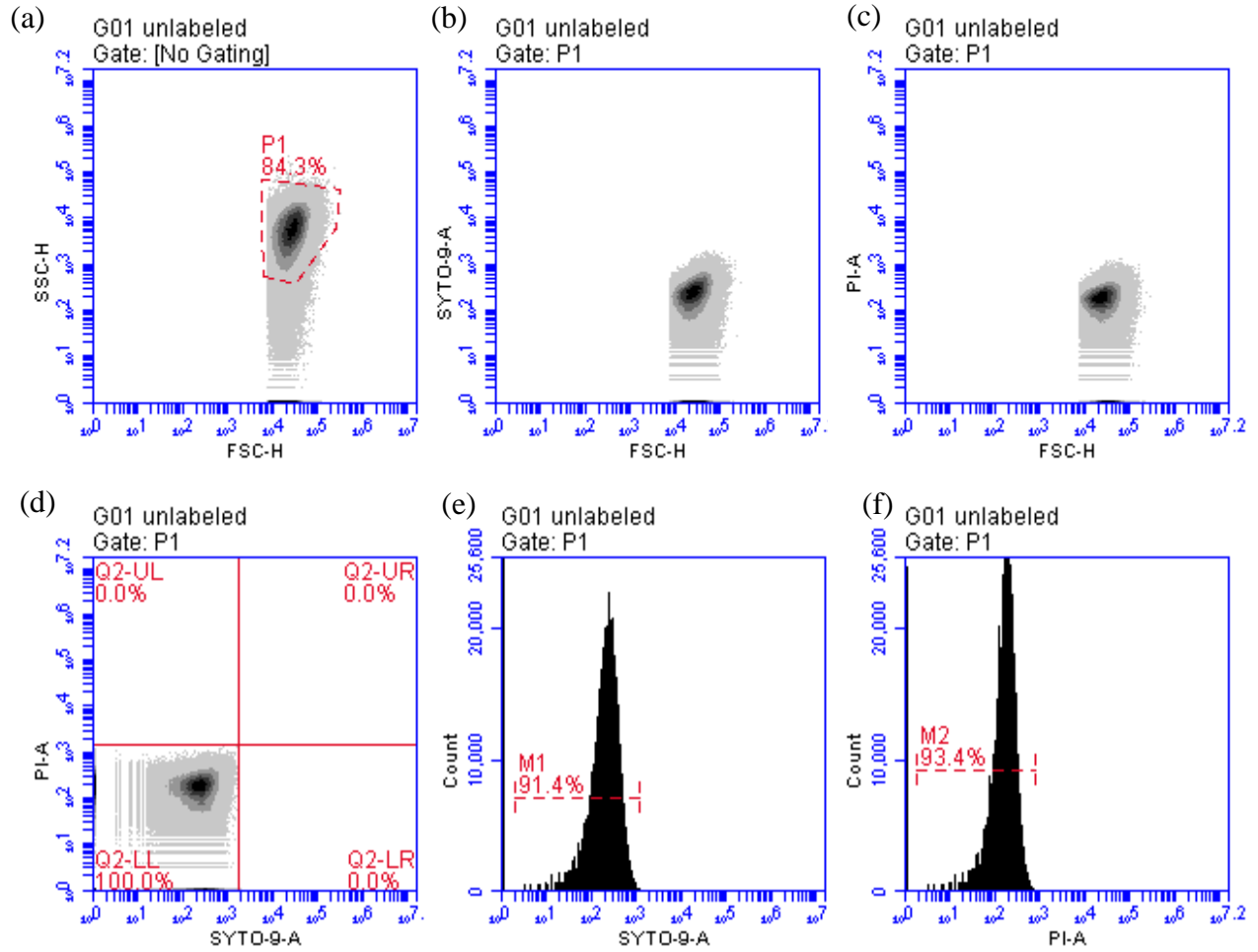


Figure 6.7 Fluorescent images of *E. Coli* K12 biofilms treated with Mg particles. (a) Control, (b) 100 μg , (c) 200 μg , (d) 500 μg , (e) 1000 μg , (f) 1500 μg , (g) 2000 μg , (h) 2500 μg , (i) 3000 μg , and (j) 3500 μg , $n=3$. Fluorescent images cannot be taken at high particle concentrations because the particles interfere with imaging.

i) **Negative Control without Dyes:**



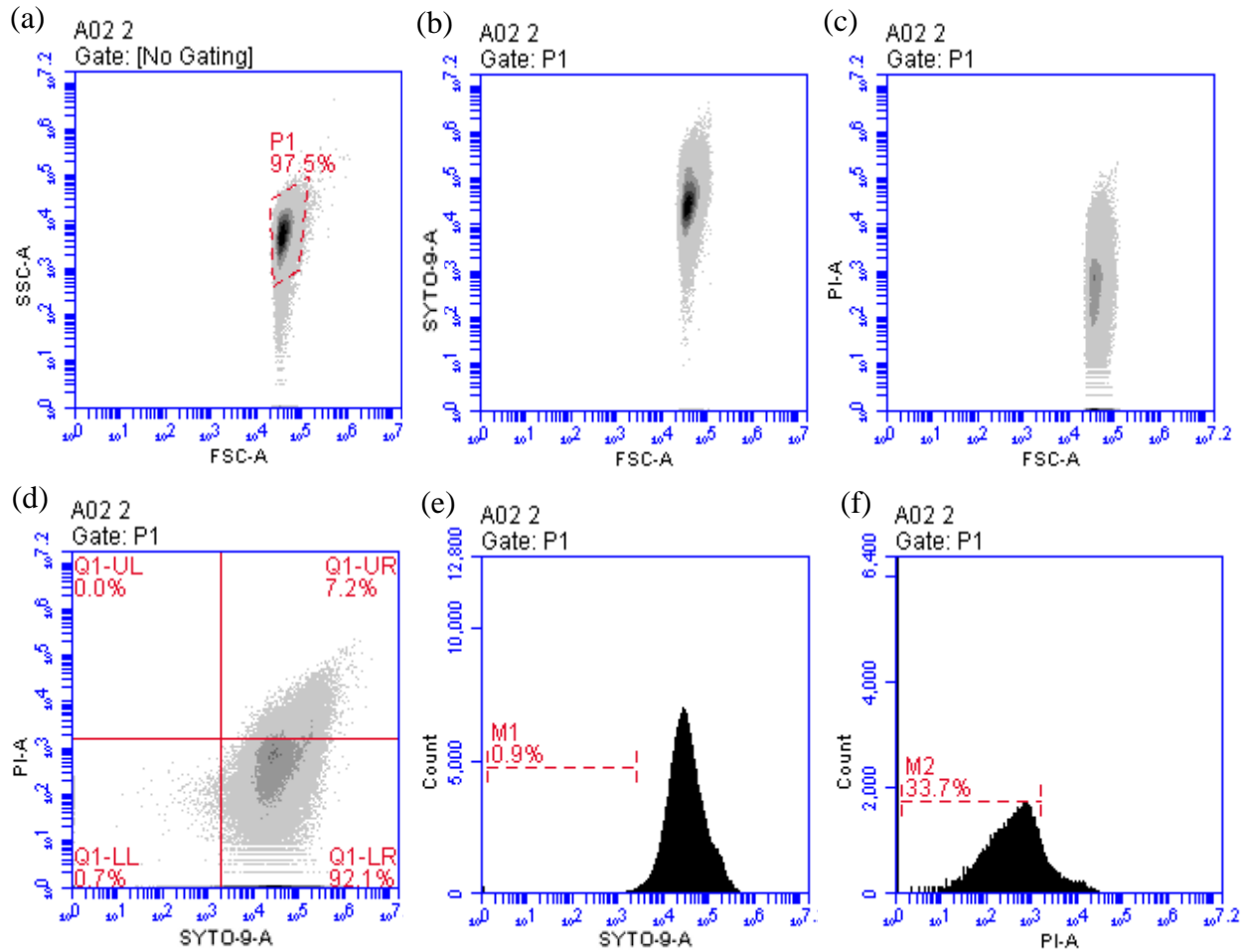
(g)

<input type="checkbox"/> Plot 5: G01 unlabeled Gated on P1	Count	Volume (µL)	% of This Plot	% of All	Mean SYTO-9-A	Mean PI-A	CV SYTO-9-A	CV PI-A	Me
This Plot	382,275	26	100.00%	84.34%	220.31	167.00	76.08%	63.94%	
Q2-UL	0	26	0.00%	0.00%	0.00	0.00	0.00%	0.00%	
Q2-UR	0	26	0.00%	0.00%	0.00	0.00	0.00%	0.00%	
Q2-LL	382,266	26	100.00%	84.33%	220.27	167.00	76.02%	63.93%	
Q2-LR	9	26	0.00%	0.00%	1,755.78	294.11	4.32%	98.91%	

<input type="checkbox"/> Plot 6: G01 unlabeled Gated on P1	Count	Volume (µL)	% of This Plot	% of All	Mean SYTO-9-A	CV SYTO-9-A	Median SYTO-9-A
This Plot	382,275	26	100.00%	84.34%	220.31	76.08%	
M1 (2.0 / 1,248.0)	349,531	26	91.43%	77.11%	240.33	66.03%	

<input type="checkbox"/> Plot 7: G01 unlabeled Gated on P1	Count	Volume (µL)	% of This Plot	% of All	Mean PI-A	CV PI-A	Median PI-A
This Plot	382,275	26	100.00%	84.34%	167.00	63.94%	
M2 (2.0 / 840.0)	357,107	26	93.42%	78.78%	178.53	55.89%	

ii) Negative Control with Dyes:



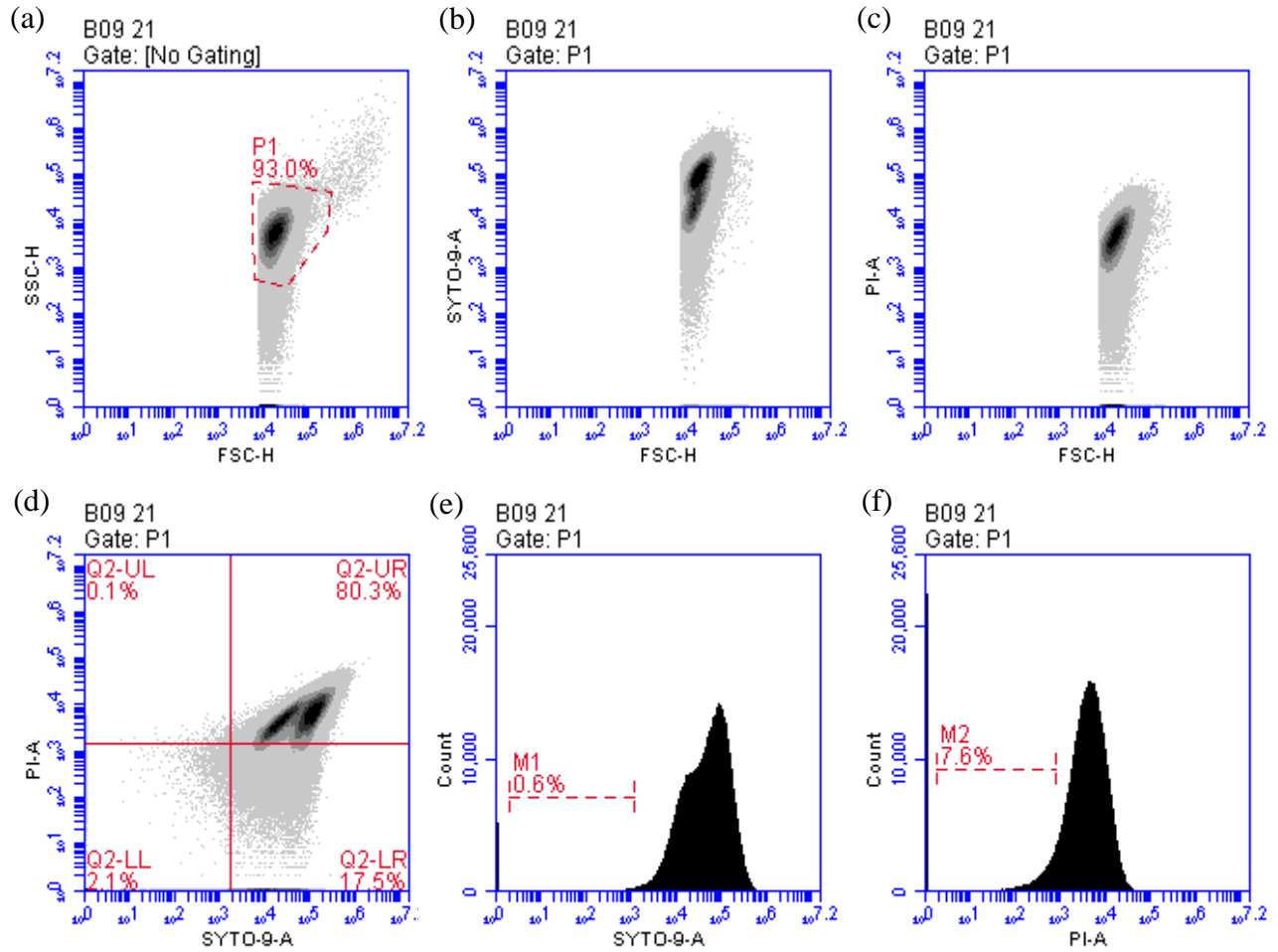
(g)

Gated on P1		Count	Volume (µL)	% of This Plot	% of All	Mean FL1-A	CV FL1-A	Median FL1-A
This Plot		149,032	25	100.00%	96.07%	51,569.07	569.45	126.70%
Q1-UL		0	25	0.00%	0.00%	0.00	0.00	0.00%
Q1-UR		10,452	25	7.01%	6.74%	157,151.38	6,055.64	90.27%
Q1-LL		1,013	25	0.68%	0.65%	770.10	36.30	85.90%
Q1-LR		137,567	25	92.31%	88.68%	43,921.26	156.55	106.09%

Plot 8: A02 2 Gated on P1		Count	Volume (µL)	% of This Plot	% of All	Mean FL1-A	CV FL1-A	Median FL1-A
This Plot		149,032	25	100.00%	96.07%	51,569.07	126.70%	
M1 (1.0 / 2,7...		1,348	25	0.90%	0.87%	1,655.13	45.61%	

Plot 9: A02 2 Gated on P1		Count	Volume (µL)	% of This Plot	% of All	Mean FL2-A	CV FL2-A	Median FL2-A
This Plot		149,032	25	100.00%	96.07%	569.45	448.26%	
M2 (1.0 / 1,6...		50,374	25	33.80%	32.47%	461.20	91.01%	

iii) Mg 7500 µg:



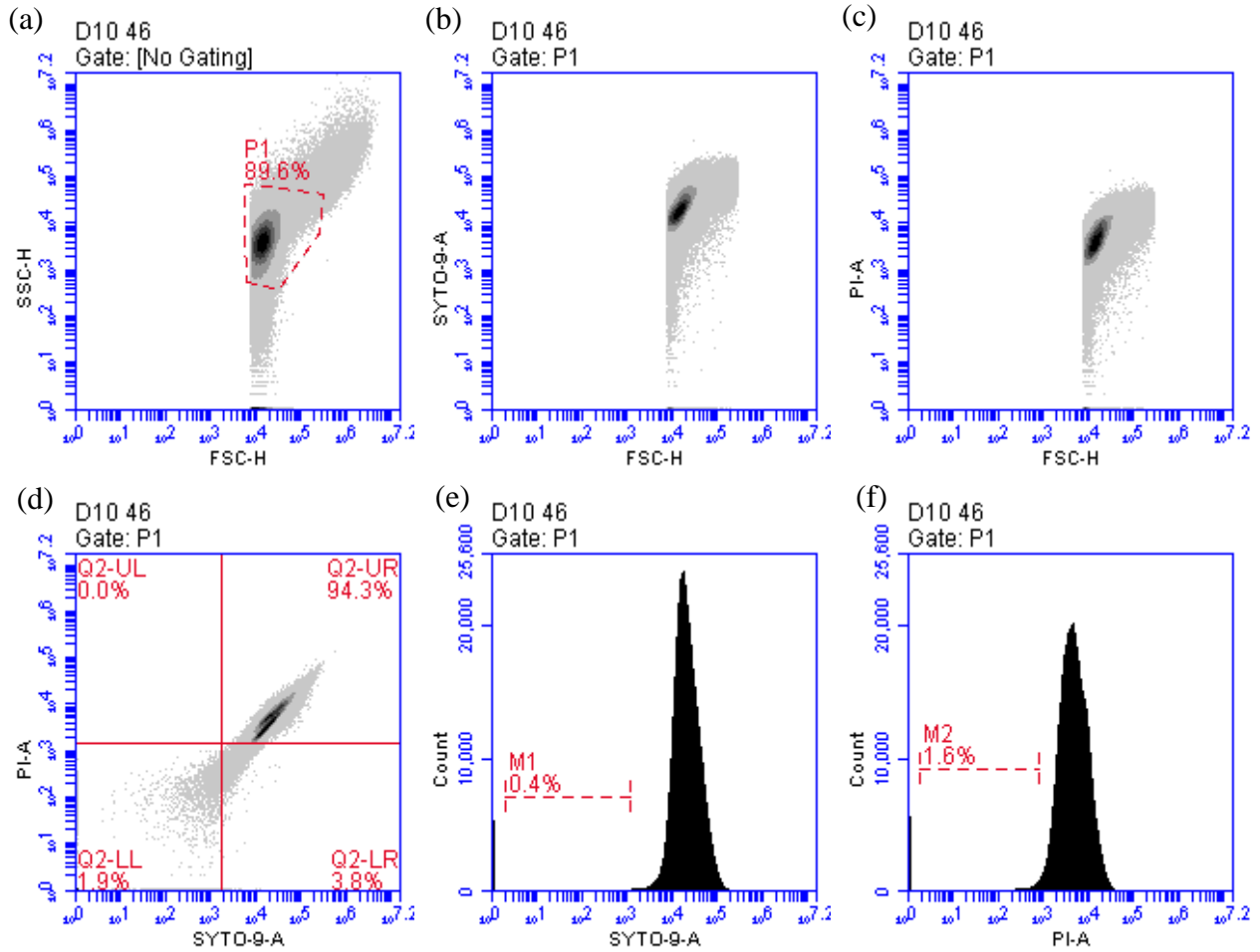
(g)

<input type="checkbox"/> Plot 5: B09 21 Gated on P1	Count	Volume (µL)	% of This Plot	% of All	Mean SYTO-9-A	Mean PI-A	CV SYTO-9-A	CV PI-A
This Plot	407,590	25	100.00%	92.99%	79,689.19	5,441.11	104.49%	99.02%
Q2-UL	389	25	0.10%	0.09%	774.93	2,088.60	78.86%	40.46%
Q2-UR	327,460	25	80.34%	74.71%	92,249.32	6,638.18	94.47%	80.82%
Q2-LL	8,478	25	2.08%	1.93%	349.26	136.41	152.40%	218.32%
Q2-LR	71,263	25	17.48%	16.26%	31,843.94	589.85	97.32%	79.62%

<input type="checkbox"/> Plot 6: B09 21 Gated on P1	Count	Volume (µL)	% of This Plot	% of All	Mean SYTO-9-A	CV SYTO-9-A	Median SYTO-9-A
This Plot	407,590	25	100.00%	92.99%	79,689.19	104.49%	
M1 (2.0 / 1,24...)	2,436	25	0.60%	0.56%	662.24	53.83%	

<input type="checkbox"/> Plot 7: B09 21 Gated on P1	Count	Volume (µL)	% of This Plot	% of All	Mean PI-A	CV PI-A	Median PI-A
This Plot	407,590	25	100.00%	92.99%	5,441.11	99.02%	
M2 (2.0 / 840.0)	30,796	25	7.56%	7.03%	453.59	52.76%	

iv) Mg 50000 µg:



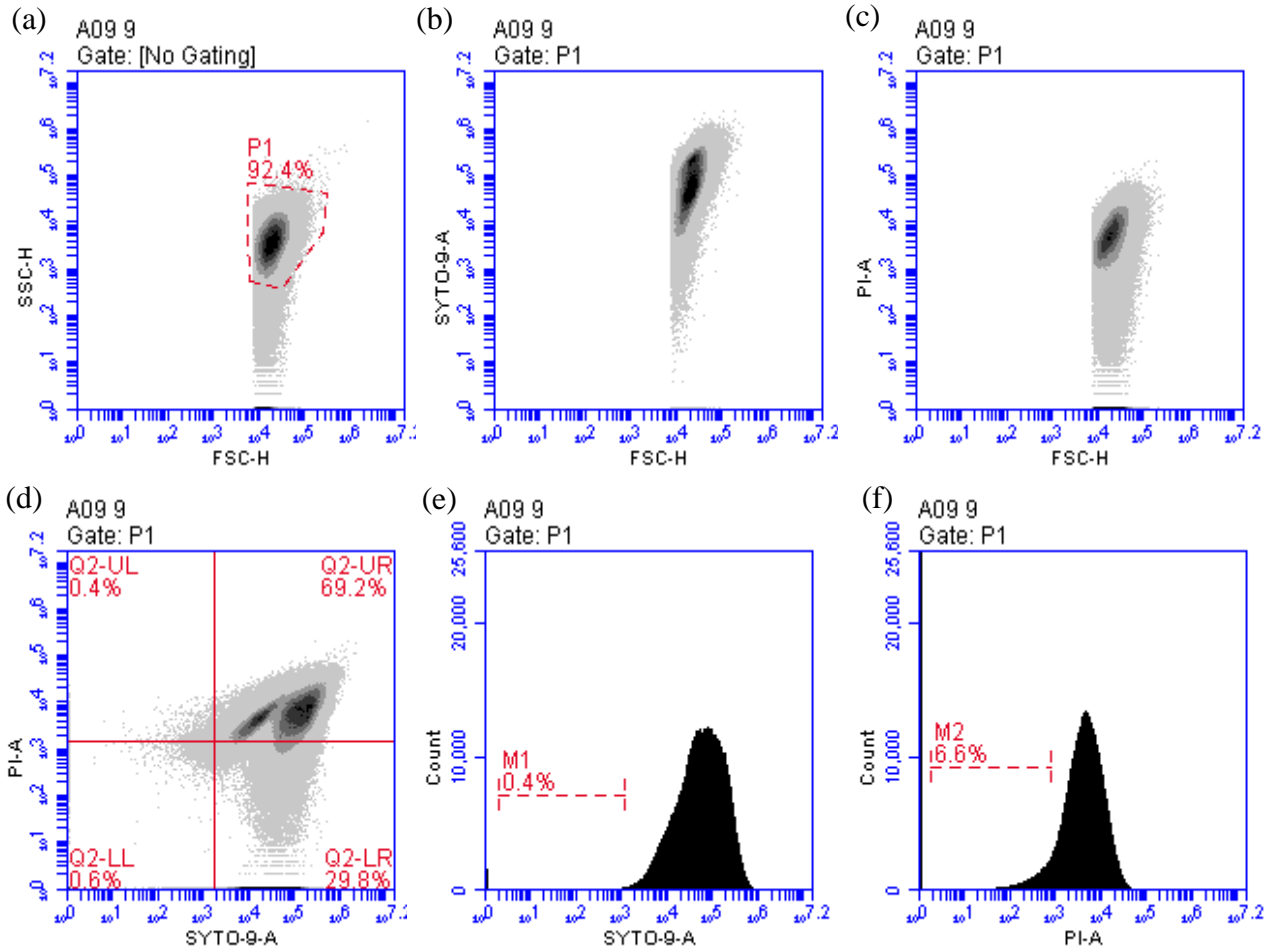
(g)

<input type="checkbox"/> Plot 5: D10 46	Count	Volume (µL)	% of This Plot	% of All	Mean SYTO-9-A	Mean PI-A	CV SYTO-9-A	CV PI-A
Gated on P1								
This Plot	391,267	25	100.00%	89.62%	26,969.24	6,032.77	79.65%	82.41%
Q2-UL	1	25	0.00%	0.00%	1,520.00	1,466.00	0.00%	0.00%
Q2-UR	368,852	25	94.27%	84.48%	28,364.73	6,359.03	75.19%	77.59%
Q2-LL	7,586	25	1.94%	1.74%	215.87	46.27	201.25%	241.50%
Q2-LR	14,828	25	3.79%	3.40%	5,944.82	980.01	36.09%	31.71%

<input type="checkbox"/> Plot 6: D10 46	Count	Volume (µL)	% of This Plot	% of All	Mean SYTO-9-A	CV SYTO-9-A	Median SYTO-9-A
Gated on P1							
This Plot	391,267	25	100.00%	89.62%	26,969.24	79.65%	
M1 (2.0 / 1,24...	1,657	25	0.42%	0.38%	571.31	65.48%	

<input type="checkbox"/> Plot 7: D10 46	Count	Volume (µL)	% of This Plot	% of All	Mean PI-A	CV PI-A	Median PI-A
Gated on P1							
This Plot	391,267	25	100.00%	89.62%	6,032.77	82.41%	
M2 (2.0 / 840.0)	6,181	25	1.58%	1.42%	463.91	54.21%	

v) Ofloxacin 100 µg/ml:



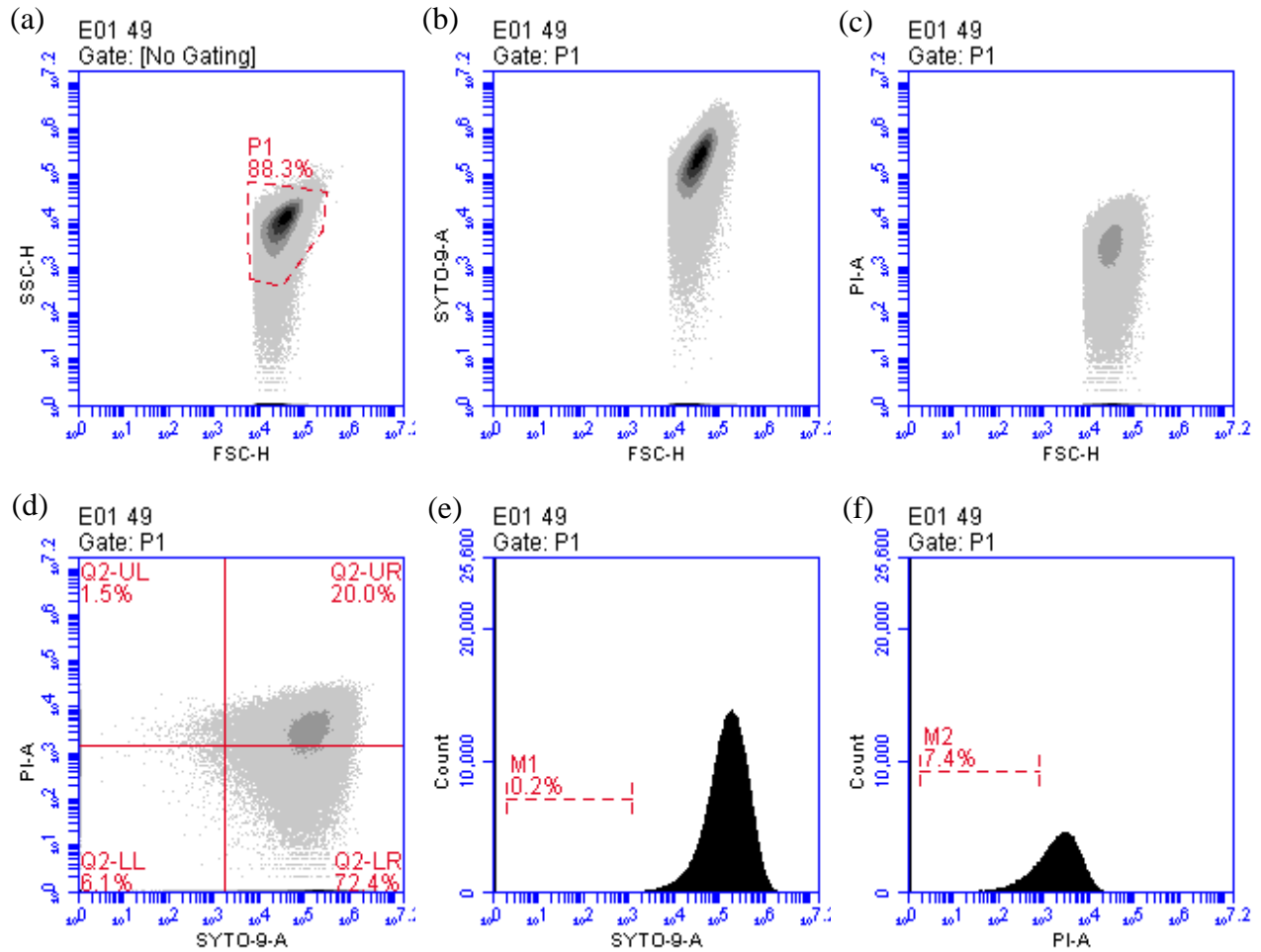
(g)

<input type="checkbox"/> Plot 5: A09 9 Gated on P1	Count	Volume (µL)	% of This Plot	% of All	Mean SYTO-9-A	Mean PI-A	CV SYTO-9-A	CV PI-A
This Plot	403,417	25	100.00%	92.42%	102,213.78	5,123.05	110.49%	121.19%
Q2-UL	1,492	25	0.37%	0.34%	635.98	2,885.02	96.07%	67.82%
Q2-UR	279,239	25	69.22%	63.97%	126,589.46	7,268.68	99.04%	87.65%
Q2-LL	2,587	25	0.64%	0.59%	534.10	530.83	109.75%	88.48%
Q2-LR	120,099	25	29.77%	27.51%	48,990.67	261.04	84.91%	161.70%

<input type="checkbox"/> Plot 6: A09 9 Gated on P1	Count	Volume (µL)	% of This Plot	% of All	Mean SYTO-9-A	CV SYTO-9-A	Median SYTO-9-A
This Plot	403,417	25	100.00%	92.42%	102,213.78	110.49%	
M1 (2.0 / 1,2...)	1,571	25	0.39%	0.36%	690.80	50.87%	

<input type="checkbox"/> Plot 7: A09 9 Gated on P1	Count	Volume (µL)	% of This Plot	% of All	Mean PI-A	CV PI-A	Median PI-A
This Plot	403,417	25	100.00%	92.42%	5,123.05	121.19%	
M2 (2.0 / 840.0)	26,561	25	6.58%	6.08%	415.25	59.11%	

vi) Planktonic Cells Negative Control:



(g)

<input type="checkbox"/> Plot 5: E01 49 Gated on P1	Count	Volume (μ L)	% of This Plot	% of All	Mean SYTO-9-A	Mean PI-A	CV SYTO-9-A	CV PI-A
This Plot	386,462	25	100.00%	88.34%	230,780.56	1,065.76	108.40%	229.02%
Q2-UL	5,935	25	1.54%	1.36%	67.54	3,824.07	391.82%	67.45%
Q2-UR	77,171	25	19.97%	17.64%	197,878.40	4,671.40	103.52%	73.32%
Q2-LL	23,718	25	6.14%	5.42%	25.79	115.68	653.87%	260.04%
Q2-LR	279,638	25	72.36%	63.92%	264,328.98	92.76	98.53%	293.30%

<input type="checkbox"/> Plot 6: E01 49 Gated on P1	Count	Volume (μ L)	% of This Plot	% of All	Mean SYTO-9-A	CV SYTO-9-A	Median SYTO-9-A
This Plot	386,462	25	100.00%	88.34%	230,780.56	108.40%	
M1 (2.0 / 1,24...)	884	25	0.23%	0.20%	619.97	57.44%	

<input type="checkbox"/> Plot 7: E01 49 Gated on P1	Count	Volume (μ L)	% of This Plot	% of All	Mean PI-A	CV PI-A	Median PI-A
This Plot	386,462	25	100.00%	88.34%	1,065.76	229.02%	
M2 (2.0 / 840.0)	28,505	25	7.38%	6.52%	409.14	58.74%	

vii) Planktonic Cells Treated with Mg 0.05 g/20 ml:

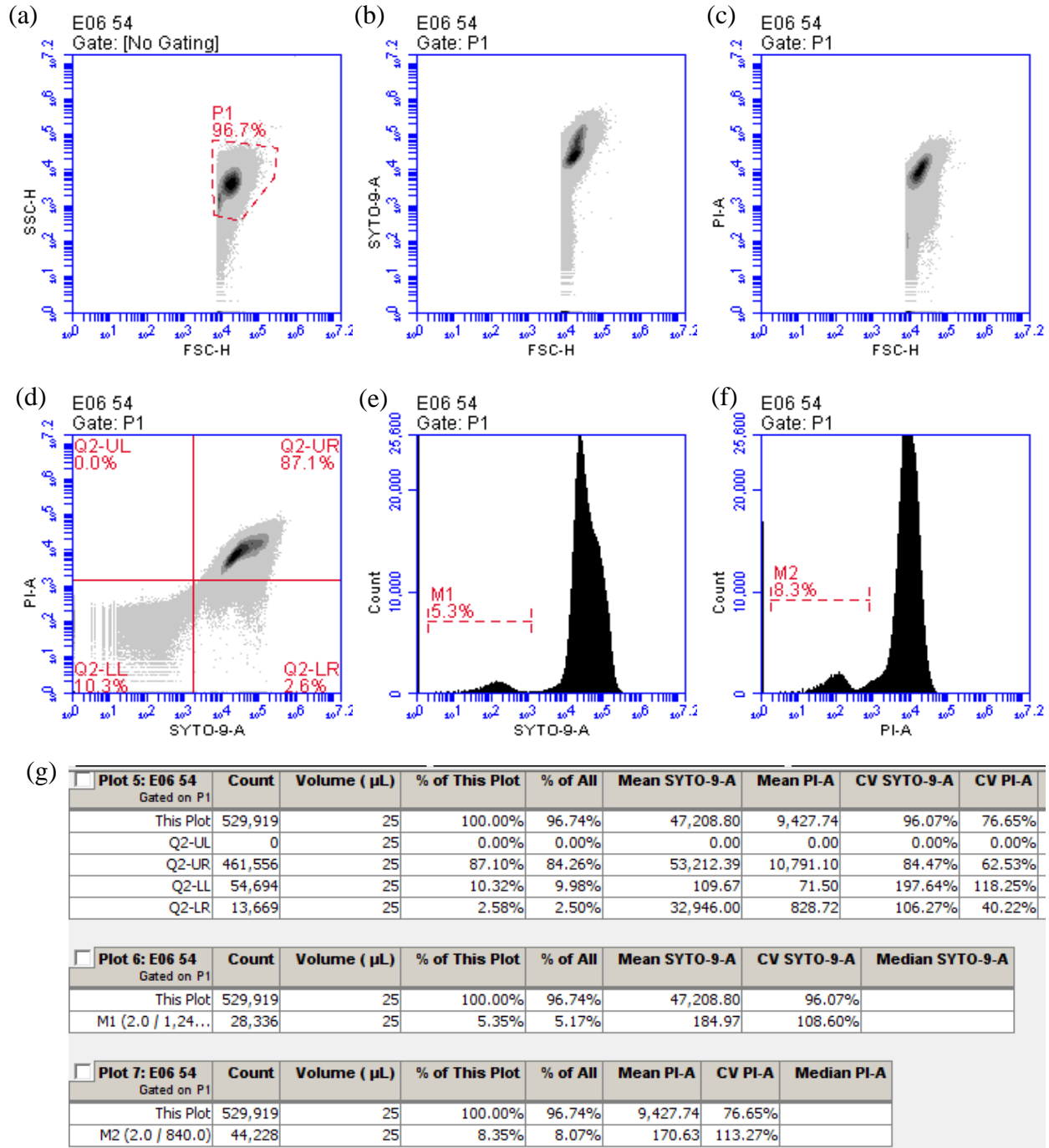


Figure 6.8 Flow cytometry data counting live and dead cells. Cells are stained with SYTO-9 and propidium (PI), where live cells fluoresce green and dead cells fluoresce red. Graph (a) shows correlated measurements of FSC and SSC, graph (b) shows FSC measurements of SYTO-9, graph (c) shows FSC measurements of PI, graph (d) shows correlated measurements of FSC of SYTO-9 and PI, graph (d) shows cell count of cells with SYTO-9, graph (e) shows cell count of cells with PI, and table (f) shows the actual cell numbers measured from the reading. Data is shown for (i) negative control without dyes, (ii) negative control with dyes, (iii) biofilm cells treated with Mg 7500 µg, (iv) biofilm cells treated with Mg 50000 µg, (v) positive control with 100 µg/ml of ofloxacin, (vi) negative control planktonic cells, and (vii) planktonic cells treated with Mg 0.05g per 20 ml, n=3.

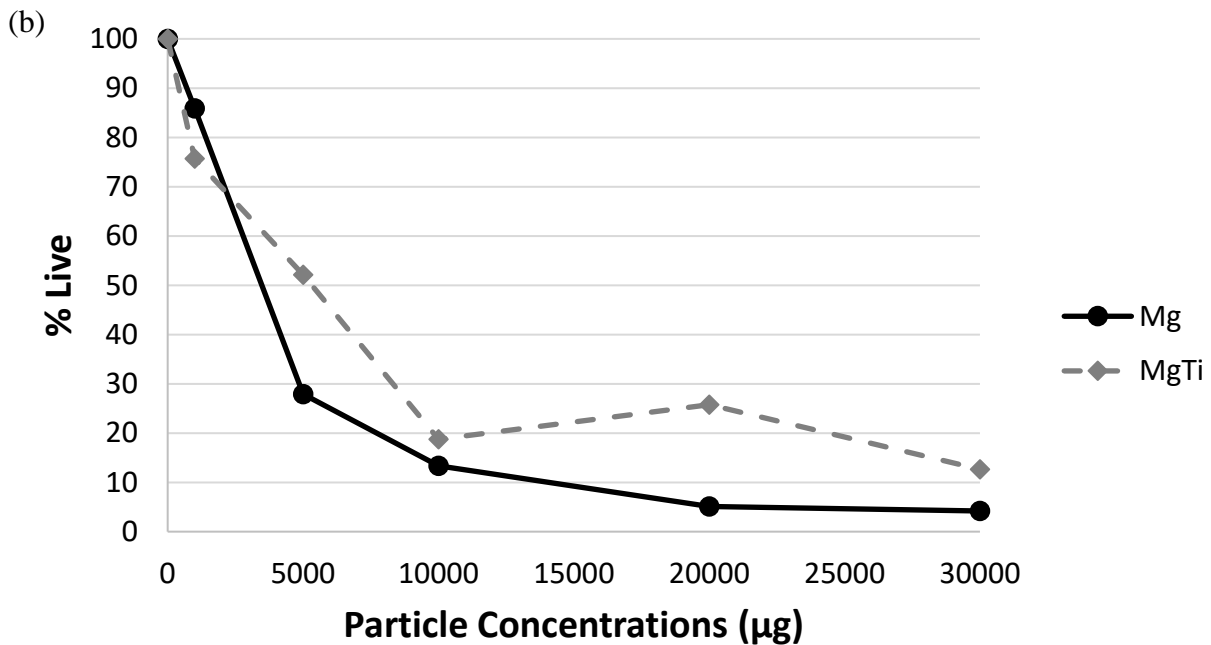
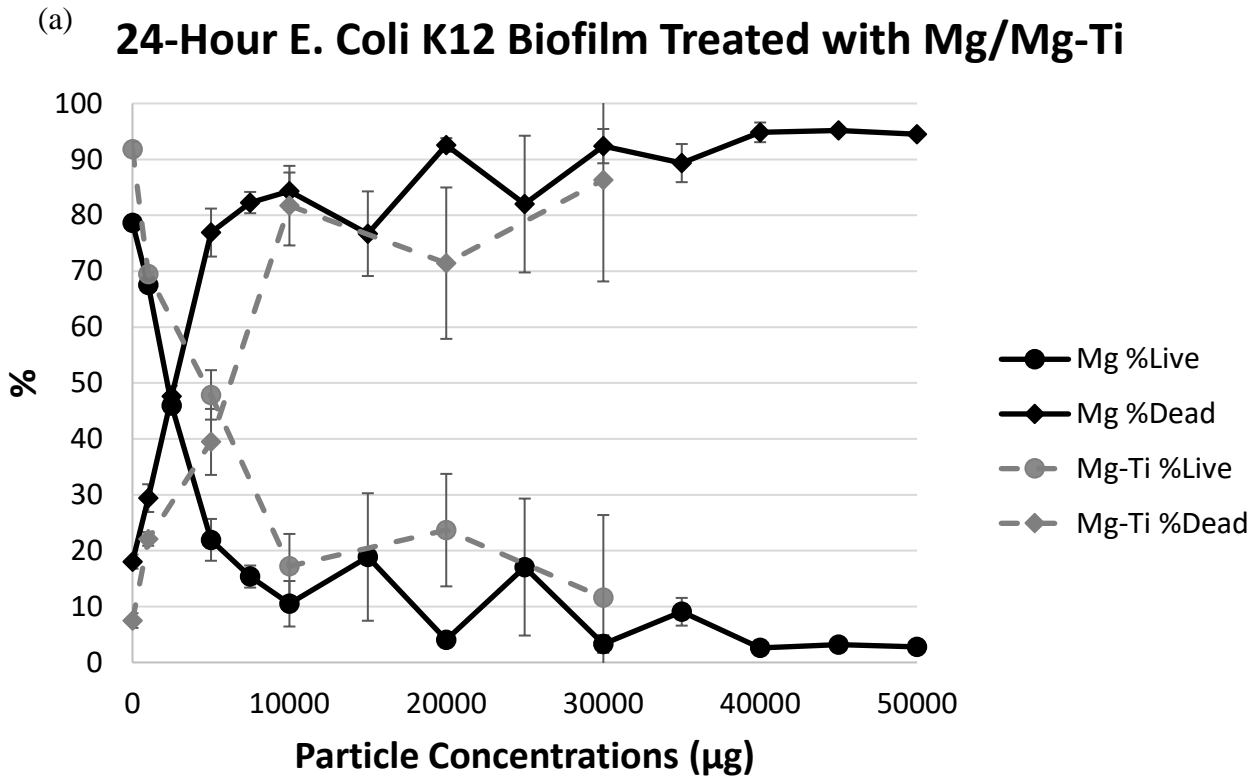


Figure 6.9 Cell viability of *E. Coli* K12 biofilms after Mg and Mg-Ti particle treatment for $t=6$ hours in PBS, $n=3$. The biofilm was grown in a cell-treated cell culture dish ($A=9.6\text{ cm}^2$) for $t=24$ hours in LB media before the particle treatment. The cells were treated with Mg from 0 to 50000 μg and Mg-Ti from 0 to 30000 μg in a total volume of 3 ml of PBS. The particles were randomly scattered in the dish. The % live cells decreased and the % dead cells increased as the particle concentration increased. (a) shows complete data of % live and % dead from both Mg and Mg-Ti groups for all concentrations, and (b) shows % live between Mg and Mg-Ti groups for comparison.

Ofloxacin

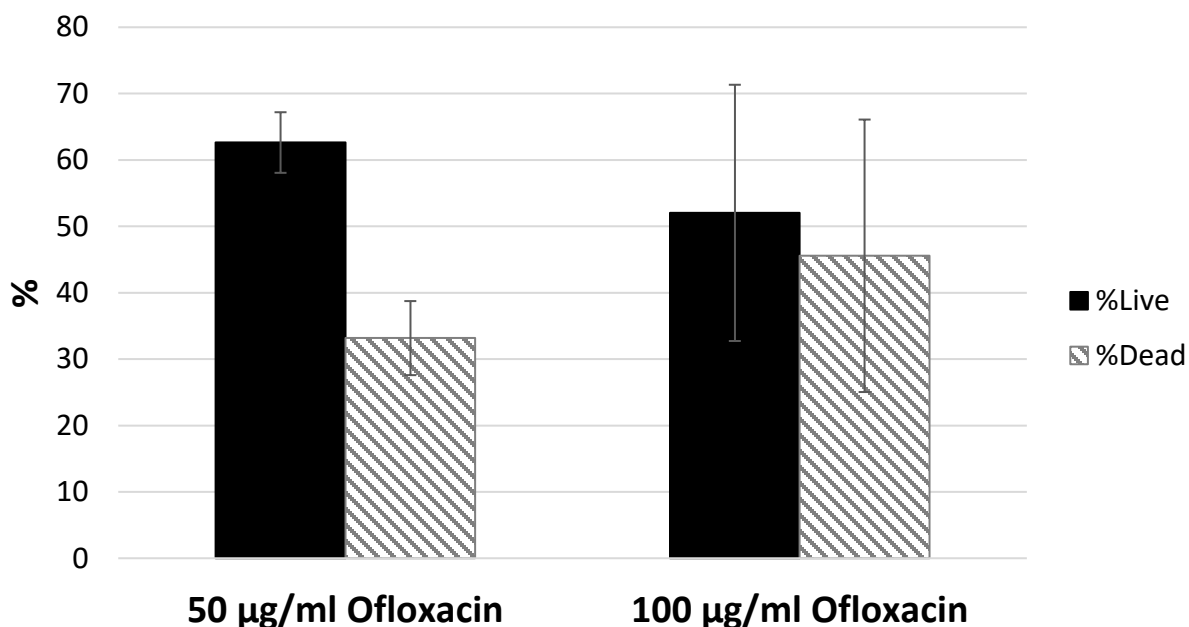
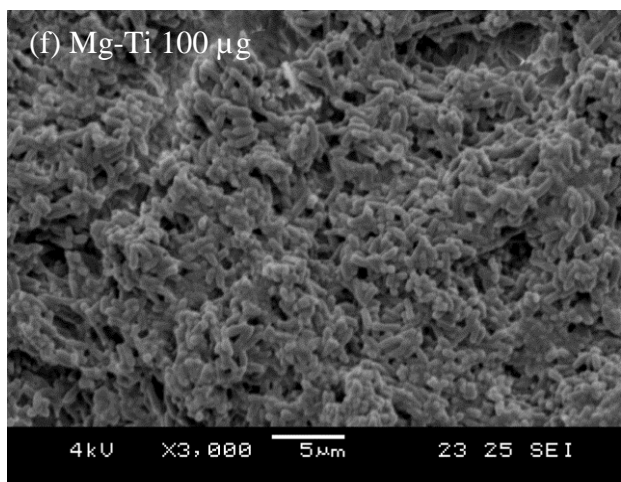
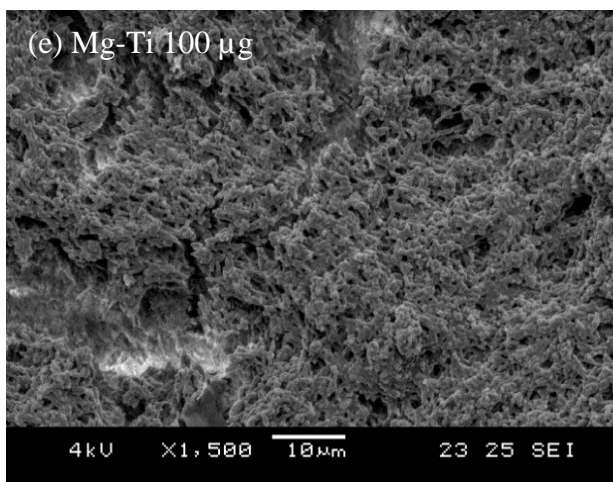
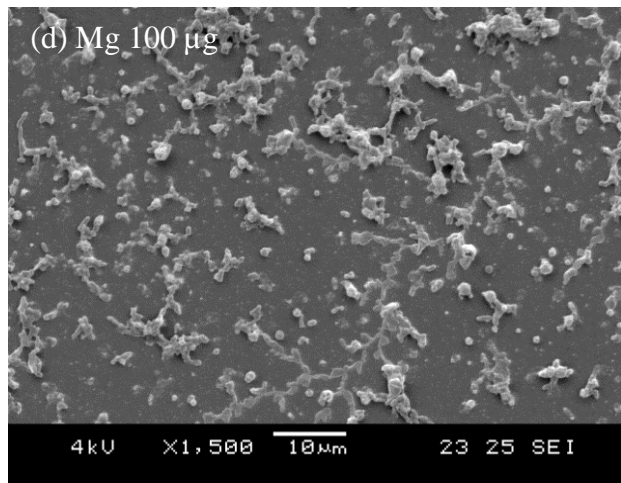
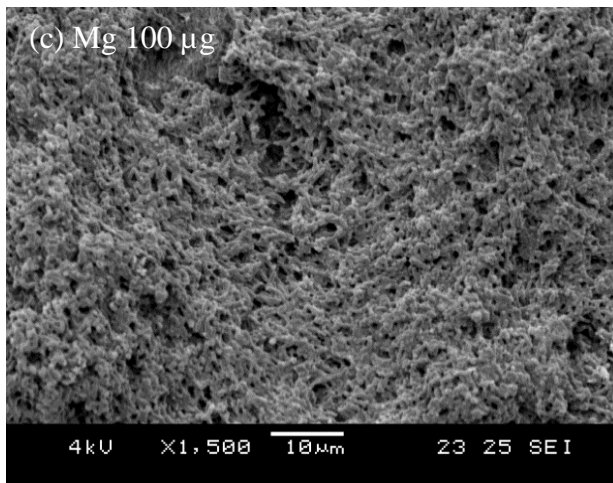
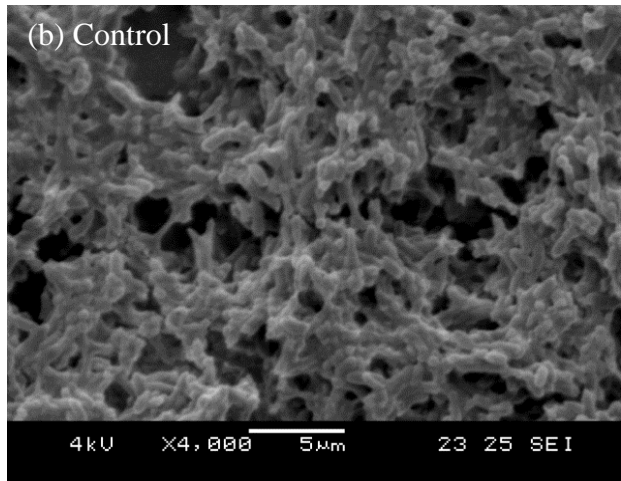
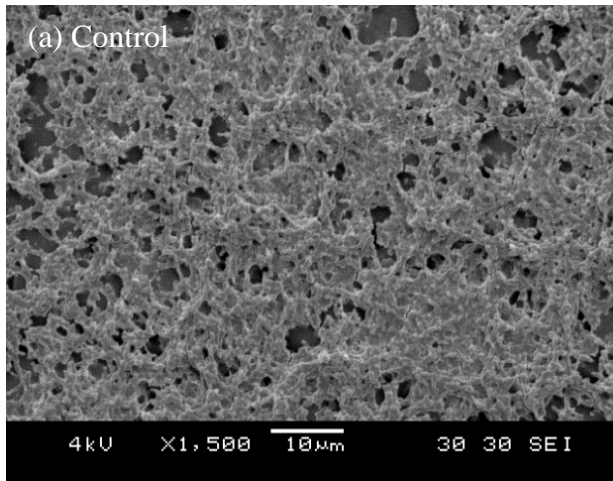


Figure 6.10 Cell viability of *E. Coli* K12 biofilms after ofloxacin antibiotic treatment for $t=6$ hours in PBS, $n=3$. Like the cells treated with Mg and Mg-Ti particles, biofilms were grown in a cell-treated cell culture dish ($A=9.6$ cm^2) for $t=24$ hours in LB media before the antibiotic treatment. Even with high concentrations of antibiotics, more than 50% of cells in biofilm survived. There were no significant differences in % live and % dead between 50 $\mu\text{g/ml}$ and 100 $\mu\text{g/ml}$, $p > 0.05$.

6.3.5 Morphology Assessment of Biofilm Cells using SEM

[Fig. 6.11](#) shows SEM images of fully grown biofilms (grown for 24 hours in LB media) treated with Mg and Mg-Ti particles for $t=6$ hours in PBS. [Fig. 6.11a-b](#) show three-dimensional biofilms fully grown and covering the surface. [Fig. 6.11c-d](#) show biofilms treated with 100 μg of Mg, where most regions have highly confluent cells (more densely covering the surface than the control group), but there are also very few regions with no biofilm, but only just few balled up cells and fragments of dead cells, indicating that the Mg particles may have been locally aggregated in this location, killing the biofilm, instead of homogenously spread out and scattered throughout the dish. Biofilms treated with 100 μg of Mg-Ti also show dense layer of cells, even more confluent than the control group, like the Mg ([Fig. 6.11e-f](#)). [Fig. 6.11g-j](#) show biofilms

treated with 2500 μg of Mg and Mg-Ti, where the particles are covered with cells. The particles cannot be washed off because the particles have been integrated into the biofilm. Unfortunately, biofilms of higher concentrations were not able to be imaged, because they were saturated with the particles.



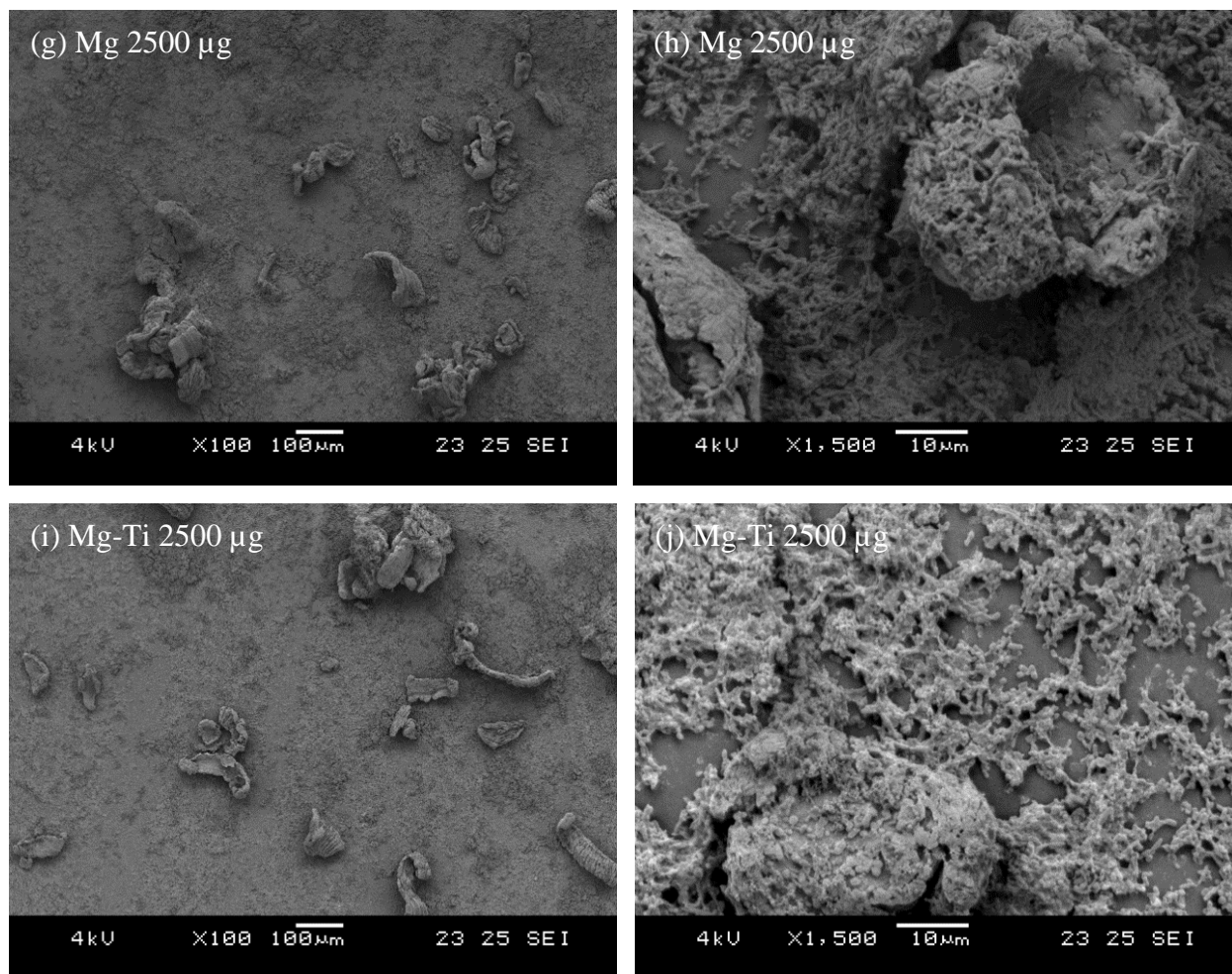


Figure 6.11 SEM images of biofilm cells after Mg and Mg-Ti treatment. Only negative control (a-b), Mg and Mg-Ti 100 µg (c-f), and Mg and Mg-Ti 2500 µg (g-j) are shown. SEM images of only low particle concentrations are shown because the higher particle concentration groups have too many particles in the sample, preventing proper SEM imaging. SEM images show the structure of the *E. Coli* K12 biofilm and its interaction with the particles. (a) shows biofilm grown for 24 hours on cell-treated polystyrene (PS) and (b) shows a close-up view. As expected, biofilm is consisted of many layers of cells. (c) shows biofilm treated with 100 µg of Mg, where in this particular site, the biofilm is very intact. (d) shows another area of the same sample treated with 100 µg of Mg as in (c), but in this location, there are hardly any cells to make up the biofilm. This discrepancy of local cell viability depends on the scattering of Mg particles. Some areas can have higher aggregation of the Mg particles, which will increase the local density of the particles, killing more cells than other areas. The variability of local cell viability also indicates that Mg particles only kill biofilm in close proximity around the particles, and so the cells do not get killed homogeneously across the sample. (e) and (f) show biofilm treated with 100 µg of Mg-Ti, where again like the 100 µg of Mg, the biofilm thickness is higher than that of control, although the thickness is not directly measured (just based on the observation). Therefore, at this particle concentration, Mg or Mg-Ti may be inducing cell proliferation and biofilm growth. At 2500 µg of both Mg (g-h) and Mg-Ti (i-j), many particles are visible, when compared to the bacterial cells (in nm range), the particles are much bigger (in µm range). Many cells have grown over the particles, integrating the particles into the biofilm, even though the particles have been added after 24-hour pre-formation of the biofilm.

6.3.6 Cell Viability of *E. Coli* Planktonic Cells After Mg and Mg-Ti Particle Treatment

The planktonic cells were treated with Mg or Mg-Ti particles either in larger volume (in flask; 0.5 g per 20 ml) or in smaller volume (in 50 ml conical tube; 0.1 g per 4 ml). The purpose of re-doing the experiment in smaller volume was due to the large amount of Mg particles that needed to be sputtered. So instead of using 0.5 g of particles per 20 ml, the samples were reduced to 0.1 g of particles per 4 ml, so that the weight to volume (w/v) ratio of the particles and the solution remain the same. Since the w/v ratio remain the same, the cell viability was expected to be the same, but [Fig. 6.12a](#) shows that more planktonic cells have been killed in the flask than the planktonic cells in the conical tube, and the post hoc Tukey test shows that this difference in viability is significant ($p < 0.05$). However, the cell viability of the control groups between the flasks and the tubes are also significantly different from each other ($p < 0.05$), where the cell viability of the control groups in the tubes are significantly higher than that of the control groups in the flasks. Therefore, [Fig. 6.12a](#) was re-graphed and % cell viability was normalized by dividing the % cell viability of all the groups by % cell viability of the control, where % cell viability of control equals 1 ([Fig. 6.12b](#)). Even after the normalization, post hoc Tukey test shows that Mg-Ti killed more planktonic cells than Mg ($p < 0.05$). Also, Mg killed more planktonic cells in the flask than in the tube ($p < 0.05$).

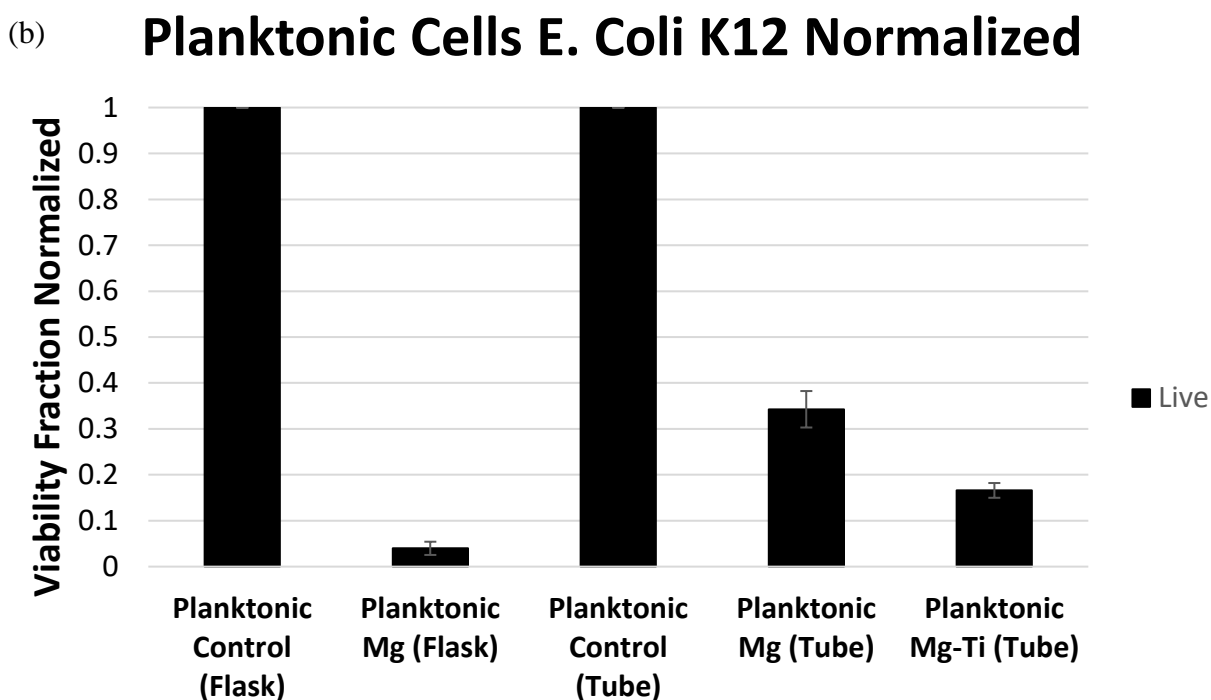
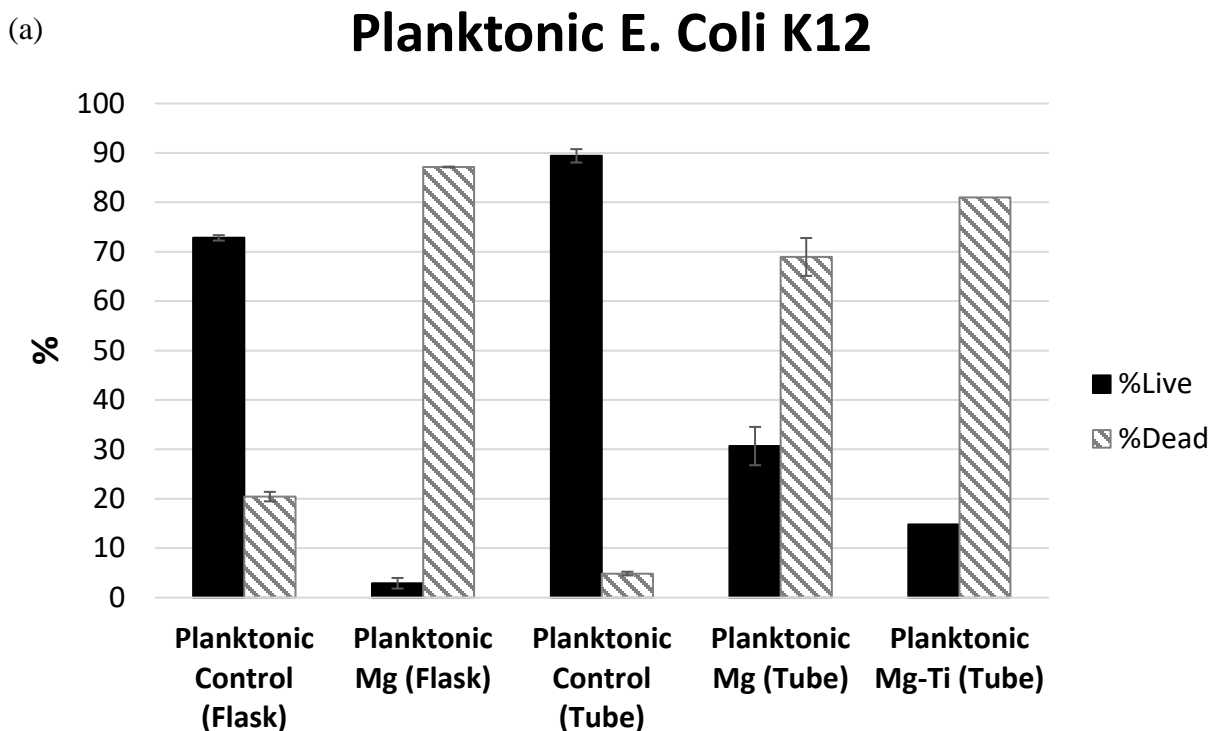


Figure 6.12 Cell viability of *E. Coli* K12 planktonic cells after Mg and Mg-Ti treatment, n=3. For larger volume experiment, planktonic *E. Coli* K12 cells were grown in 25 ml of LB media for t= 18 hours, and then 1 ml of the planktonic cells were re-suspended in 19 ml of fresh LB media with 0.5 g of Mg particles in a flask for t= 24 hours. For smaller volume experiment, 0.1 g of Mg particles were corroded in 4 ml of cell solution for t= 24 hours. (a) % live and % dead cells and (b) viability fraction normalized by control, n=3.

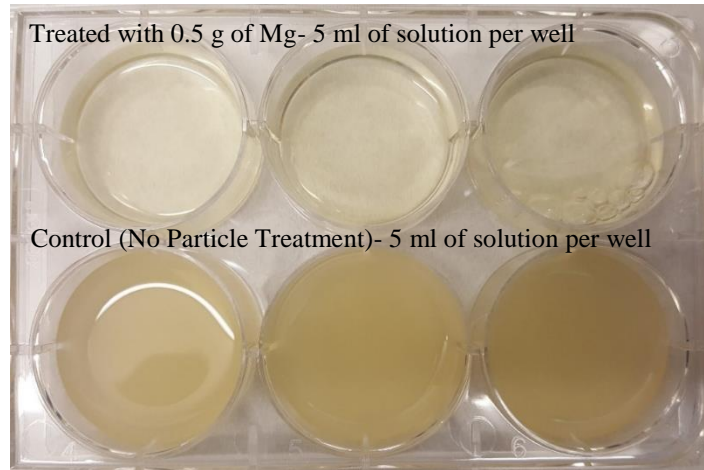


Figure 6.13 Image of the solutions after treating 20 ml volume to 0.5 g of Mg for $t=24$ hours. The solutions were transferred from a flask to the 6-well plate for visual purposes, 5 ml of solutions per well. As shown, the samples treated with 0.5 g of Mg are clear in optical density, while the control samples are very cloudy, indicating a significant difference in cell population.

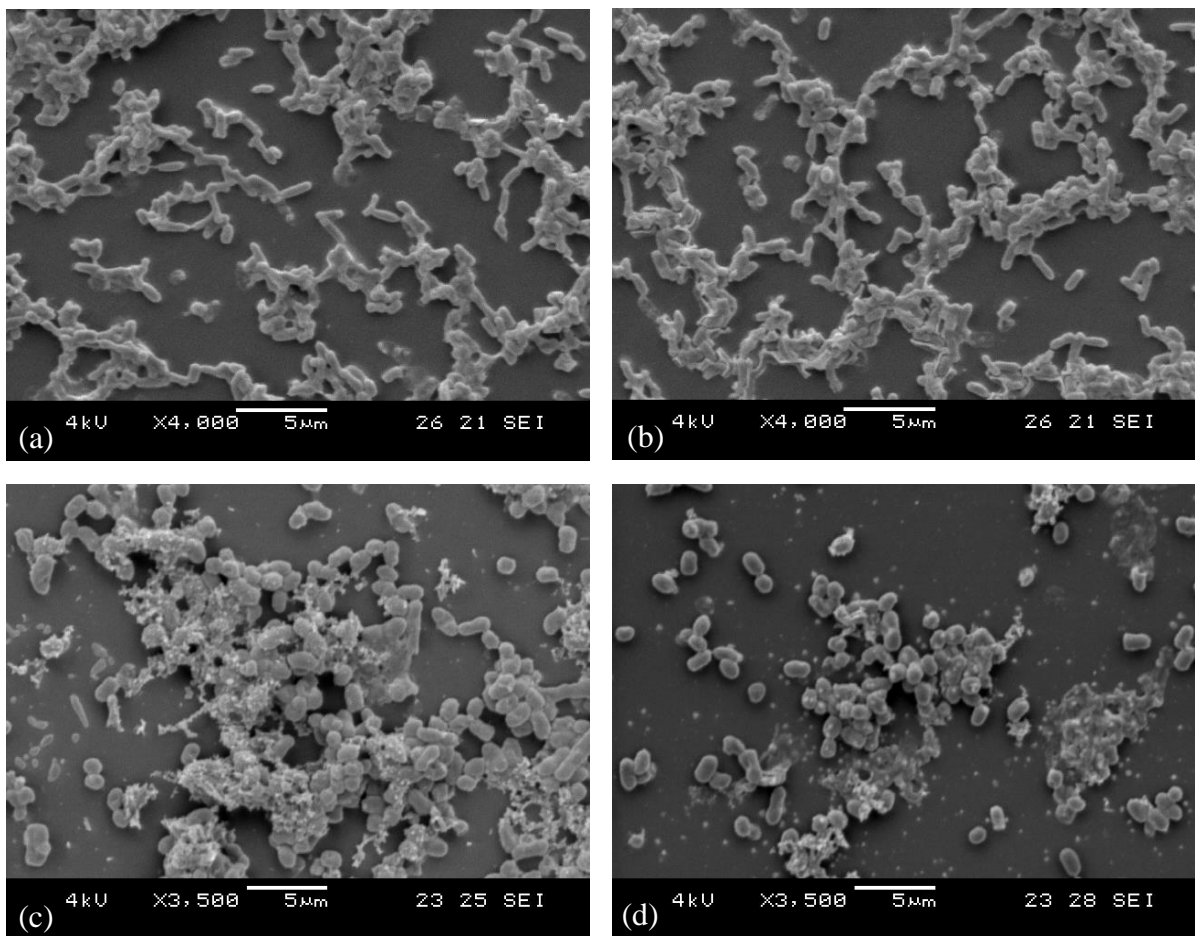
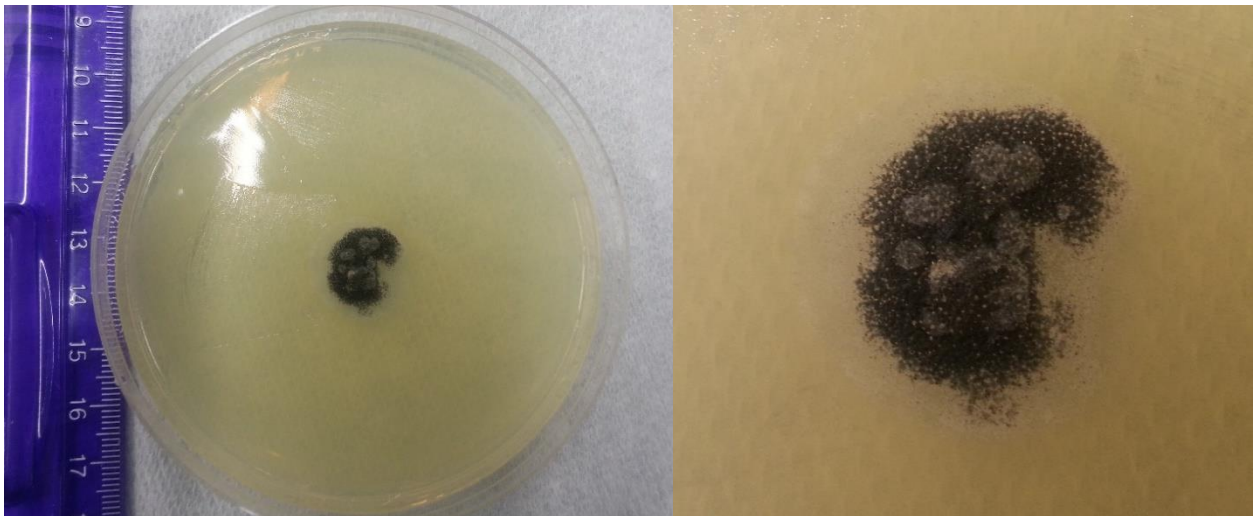


Figure 6.14 SEM images of (a-b) control planktonic cells and (c-d) 0.5 g of Mg-treated planktonic cells. Compared to the control cells, the longitudinal lengths of Mg-treated cells have decreased, giving a round appearance than a rod-shaped.

6.3.7 Inhibition Zone Test

Fig. 6.15 shows the images taken after 0.02 g of Mg and Mg-Ti particle treatment overnight. The inhibition zone could not be measured for particle concentrations of 0.005 g for both Mg and Mg-Ti because the particles fully corroded and the cells grew in the particle zone, and there was no inhibition zone to measure (no pictures shown). Fig. 6.16 shows that the average thickness of the inhibition zones for 0.02 g of Mg and Mg-Ti particles are 1.5 mm and 2 mm, respectively. Post hoc Tukey test shows that there is no statistical difference between the two groups ($p > 0.05$).

(a) Mg 0.02 g



(b) MgTi 0.02 g

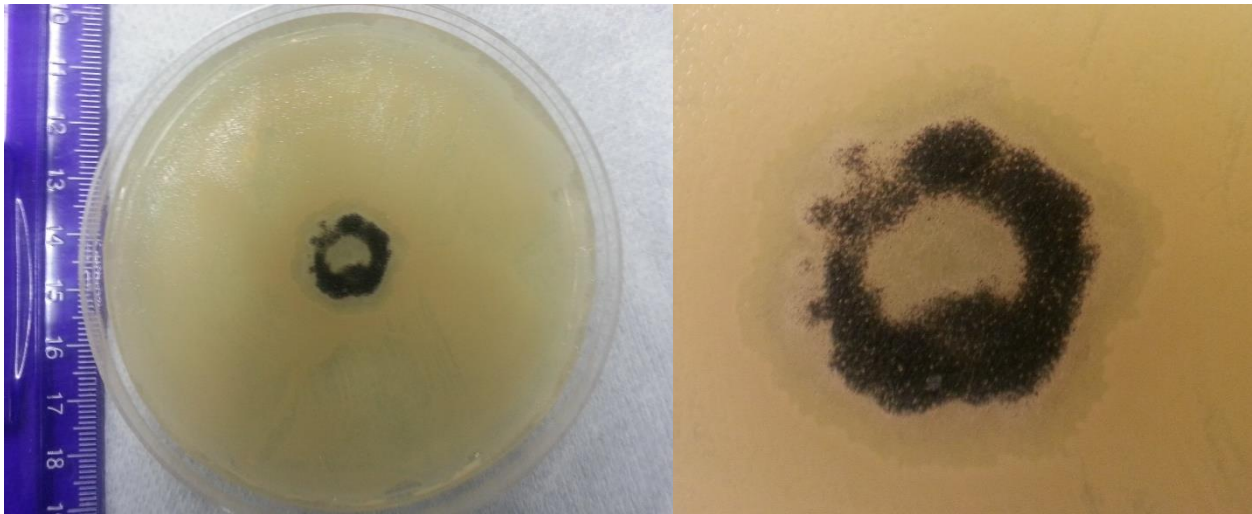


Figure 6.15 Similar to the antibiotic resistance test, this is a particle proximity test to see how close the bacterial cells can grow near the particles. A ring with a diameter of 1.6 cm was placed in the center and then added 0.005 g or 0.02 g of Mg or Mg-Ti (in 100 μ l of LB media) in the ring to make a circular shape. There was no leakage of the particles. The inhibition ring zone is much smaller than a typical inhibition ring caused by an antibiotic. First, the particles were not able to corrode on the agar plate as they would in solution, which probably decreased the toxicity. Also, the particles are known to have small toxicity range of less than 2 mm from a previous study.

Distance between E.Coli Cells and Particles

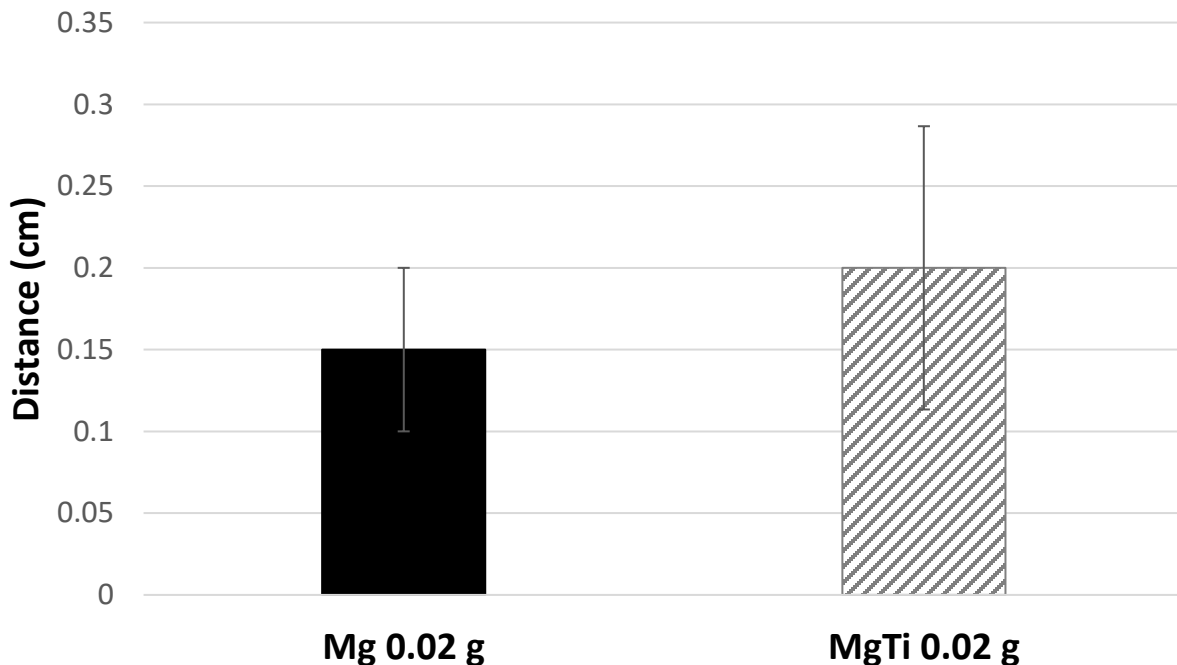


Figure 6.16 The thickness of the inhibition zone for Mg and Mg-Ti. The average distance the cells colonized away from the particles for Mg is 0.15 cm (1.5 mm) and for Mg-Ti is 0.2 cm (2 mm). Post hoc Tukey test shows that there is no difference between Mg and Mg-Ti inhibition zones.

6.4 Discussion

The first part of this study used cathodic potentials to kill biofilms *in vitro* to show that cathodic potentials do have an adverse effect on the viability of the biofilms. This finding is supported by the *in vivo* studies done by Ehrensberger et al., which showed that the bacterial infection on the Ti implant can be reduced by the electrical stimulation alone, although the reduction of biofilm is more significant when the electrical stimulation is combined with antibiotics, especially if the electrical stimulation was done immediately after the operation (insertion of the implant into the body) [19-20, 31]. *In vitro*, bacteria were allowed to form biofilms on the commercially pure titanium (cpTi) coupon for 18 hours at 100 rpm and 37 Celsius, before applying either OCP or -1.8 V for 1 hour. CFUs of cells were measured from the saline solution and also from the cpTi coupon, and Ehrensberger et al. found there were 1-2 orders of magnitude reduction in CFUs for -1.8 V treated samples compared to that of OCP [19]. One study by Ehrensberger et al. showed that -1.8 V electrical stimulation for 1 hour alone *in vivo* can significantly decrease the CFUs by 1 order of magnitude in bone and by 2 orders of magnitude on the implant [19]. Another study by Ehrensberger et al. showed that the electrical stimulation of -1.8 V for 1 hour *in vivo* alone did not decrease the CFUs significantly at the implant, bone, and synovial fluid, but rather a combination of electrical stimulation and vancomycin treatment reduced the CFUs by 99.8% (3-4 orders of magnitude) [31]. Regardless, this study and the studies done by Ehrensberger et al. showed that cathodic voltage treatment can reduce biofilms at the metal surface both *in vitro* and *in vivo*, either without or with the combination of antibiotics.

The purpose of this study was to show how the cells in biofilms are affected by the application of cathodic potentials, based on the viability and morphological assessments.

Application of cathodic potentials of -1 V and -1.2 V in PBS induced bacterial cell death, where the bacteria balled up and showed cavitations (disruption of the membrane) and/or membrane rupture. Application of cathodic potentials in LB media does not affect the cell viability and morphology as NaCl solution (when all the other factors remain the same), which indicates that the solution plays an important role. LB media contains tryptone, NaCl, and yeast extract, which provides free amino acids, proteins, B-complex vitamins, and other elements needed for bacterial growth, whereas PBS only contains NaCl. Therefore, free amino acids, proteins, B-complex vitamins, and other elements in the LB media must reduce the adverse effects of cathodic potentials. Based on the previous studies by Ehrensberger, Haeri, and Sivan et al., the application of cathodic potentials causes reduction reactions to dominate at the metal surface due to accumulation of excess electrons, presumably producing ROS that induce cell death [9-11]. For *E. Coli*, ROS, such as hydrogen peroxide H_2O_2 or superoxide $O_2^{\cdot-}$, target and damage proteins such as alcohol dehydrogenase, elongation factor G, the heat-shock protein DNA K, and the β -subunit of F_0F_1 -ATPase [32-33]. This will in turn cause growth arrest of cells, and even cell death, depending on the degree of oxidative stress. ROS are usually known to target DNA, RNA, proteins, and lipids [16]. Free radicals can attack polyunsaturated fatty acids in membranes and cause lipid peroxidation, which decreases membrane fluidity and disrupt membrane-bound proteins [16]. ROS can also attack the base and sugar moieties of the DNA strands, breaking the DNA backbone, adducts of base and sugar groups, cross-link other molecules, and form lesions to block DNA replication [16]. Proteins can also be oxidized, which can cause reduction of disulfide bonds, cross-linking between proteins, fragmentation of peptides, and much more [16]. ROS are very reactive, where a freely diffusing ROS molecule (non-charged) has an average diffusion coefficient D of $1 \times 10^{-5} \text{ cm}^2$ (in water) [34]. Pryor and

Winterbourn calculated to estimate the mean square displacement of ROS, where hydroxyl radical can only diffuse few angstroms, while superoxide and hydrogen peroxide can diffuse a few tens of micrometers [34-36]. Although superoxide may not readily cross bilayers due to the charge, hydrogen peroxide can [34-36]. So some ROS are more stable than other types of ROS, and can be internalized by the cell and attack the intracellular proteins, DNA, and RNA, while other ROS can only affect the extracellular proteins and free amino acids in the solution. Therefore, some ROS can be “quenched” by the elements found in the LB media (and these elements may or may not be so essential for cell survival or at least not cause immediate cell death), before ROS can directly attack and induce cell death. This may be the reason why the cell viability of biofilms in LB media is significantly higher than the cell viability of biofilms in NaCl solution, despite the same electrical stimulation and experimental method. Another reason why the cell viability of biofilms in LB media is higher is that cells can proliferate quickly since LB contains nutrients, while NaCl does not. Further analysis needs to be done to determine the cause of the solution effect.

Mg and Mg-Ti particles were able to kill biofilm more effectively than high concentrations of antibiotic ofloxacin. 5 µg/ml of ofloxacin can kill planktonic bacteria *E. coli* HM21 (a derivative of *E. coli* K12) from 100% to below 0.01% in 3 hours [37]. On the other hand, ofloxacin did not kill *Pseudomonas aeruginosa* biofilms as effectively, where 0.1 µg/ml did not kill at all (compared to control, 8 log CFU/peg) and 100 µg/ml reduced the biofilm to 5 log CFU/peg, which is 37.5% reduction from control [38]. This is similar to the ofloxacin treatment on a 24-hour biofilm of *E. coli* K12, which resulted in 48% reduction of biofilm at 100 µg/ml. Despite the high ofloxacin dosage, biofilms cannot be completely eradicated with the antibiotic alone, unlike the planktonic cells. 37.5% or 48% reductions of biofilms are not

significant, since the biofilms can easily grow back and recover after the antibiotic treatment. Also, high concentrations of antibiotics can make the cells resistant to antibiotics, and so the biofilms may be harder to kill after the high dose treatment. Compared to antibiotics, Mg and Mg-Ti were able to reduce the 24-hour biofilm more significantly, where the highest concentration of 50 mg (0.05 g) Mg killed 97.2% of the biofilm, and 30 mg (0.03 g) Mg-Ti killed 88.4% of the biofilm. Average particle density on the biofilm for these concentrations are 5208 $\mu\text{g}/\text{cm}^2$ and 3125 $\mu\text{g}/\text{cm}^2$, respectively, although the random scattering of the particles will vary the local particle density within the sample. Cell viability plateaued around 2-3% from 30000 μg Mg, despite the increase of particle concentrations up to 50000 μg Mg. Higher particle concentrations of Mg-Ti are expected to kill cells down to 2-3% as Mg, if the cell viability was measured beyond 30000 μg . When cell viability of Mg and Mg-Ti were compared, the statistical analysis showed that there was significant difference in cell viability between the particle types, where cell viability of Mg-Ti is higher than Mg. This finding is different from previous studies, where Mg-Ti was more effective in killing murine pre-osteoblast cells and human osteosarcoma cells [23-24]. However, this result may not be due to the fact that Mg-Ti could not kill as effectively or more efficiently than Mg alone for biofilms, but rather a difference in the experimental methods. To measure murine osteoblast and human osteosarcoma viabilities, the cells were treated with the particles, where the particles were randomly scattered throughout the sample, and the images were taken at random places within the sample (ten images per sample, n=10). To calculate cell viability, the cells were manually counted for live and dead cells from the images. Therefore, the variability of cell viability was high even within one sample, since the random scattering of particles affected the local densities of cell viability. However, to measure cell viability of biofilms, the particles were randomly scattered, and then instead of

taking images at random places to count live and dead cells, the biofilms were detached from the surface, and the cells were counted per volume of solution using flow cytometer. There is no variability within the sample since the biofilm is detached and the solution containing the biofilm is mixed before the cell count. For the mammalian cell experiments, the variability of cell viability due to random scattering of particles can be measured by calculating the standard deviations within the sample (from the ten images per sample). However, this variability cannot be measured in the biofilm experiment. If the particles were all aggregated in one region, killing the biofilms in that area, leaving the rest of the regions with more viable biofilms, the cell viability of that biofilm will be higher than a sample with the particles homogeneously scattered, killing more area of the biofilm. Higher cell viability can be due to the aggregation of the particles to a local region, but also due to other reasons, such as stronger biofilms for that particular sample compared to other samples. Although this study could not show that Mg-Ti can kill biofilms more effectively than Mg, it showed that Mg and Mg-Ti can kill biofilms more significantly than conventional antibiotics.

There were two distinct different cell-sized populations for medium particle concentration-treated biofilms and ofloxacin antibiotic-treated biofilms, which were not found in other groups. This is explained by SEM images and AFM measurements. Cells killed by cathodic voltages or Mg/Mg-Ti particles seem to decrease in size, because they “ball-up.” For control and low particle-treated groups, most cells were viable, so there were no different sized cell populations. For high particle-treated groups, most cells were dead, so again, there were no different sized cell populations. But for medium particle-treated and antibiotic groups, there were mixtures of live and dead cells, where live cells have longer width and length, compared to

the dead cells, yielding in two distinct cell populations. Again, flow cytometry reading by FSC and SCC confirms the morphological differences in cells seen in SEM and AFM.

24-hour biofilms were used to show that Mg and Mg-Ti can kill more developed biofilms, and not just pre-mature biofilms grown for few minutes or hours. -1 V of cathodic treatment for 30-minute biofilms in NaCl solution showed the average cell viability of 20%, which is significantly higher than the average cell viability of 2.77% for 24-hour biofilms treated with 0.05 g of Mg in NaCl solution, despite the fact that the biofilms were grown longer for Mg/Mg-Ti experiment. Mg has standard electrode potential of -2.34 V (or -1.7 V in chloride containing solution), which is much more cathodic than -1 V, which means more reduction reactions, ultimately producing more ROS, over the same period of time. Also, the Mg microparticles have larger surface area than a bulk sample, and larger surface area means more oxidation and reductions can occur at the surface exposed in solution.

Even though Mg and Mg-Ti particles killed the cells to 2-3%, bacterial cells can easily grow back and form biofilms, and therefore, treatment is only considered successful if the biofilms can be killed below 0.01%. Ehrensberger et al. showed that cathodic potential of -1.8 V applied on the Ti implant in vivo in combination with antibiotic vancomycin (0.5 µg/ml) for 1 hour reduced the CFUs of the biofilms by 99.8% on the implant, surrounding bone, and synovial fluid, compared to control [31]. Mg and Mg-Ti particles can also be used with the treatment of antibiotics to have a synergistic effect of killing biofilms more effectively than just Mg and Mg-Ti particles alone. Mg and Mg-Ti can resolve the issue of having to make additional incisions to insert counter and reference electrodes to apply cathodic potentials, as well as having to leave the incisions open during cathodic voltage treatments, since Mg and Mg-Ti can spontaneously corrode, producing the same effect as applying cathodic potential. Depending on the severity

and type of infection, Mg and Mg-Ti particle size and dosage can be controlled. While Ehrensberger et al. focused on treating already-formed biofilm using cathodic treatment, Mg can be incorporated into the Ti implant surface to prevent biofilm attachment for several weeks after the surgery (highest risk for postoperative infections), which may be easier than trying to eradicate already-formed biofilm. In other words, Mg and Mg-Ti can be used as preventive measures as well as the actual treatment.

6.5 Conclusion

This study showed that cathodic stimulation of biofilms can decrease the cell viability of biofilms by rupturing and forming cavitations on the cell membranes. Mg and Mg-Ti particles were able to kill biofilms more effectively than conventional antibiotics alone, where Mg and Mg-Ti particles killed in a dosage-dependent manner. Even the highest particle concentrations of Mg and Mg-Ti alone could not kill the biofilms below 0.01%, giving the possibility for the biofilms to grow back once the Mg and Mg-Ti treatment is done. However, this study still shows promise in ODRI treatment, where Mg and Mg-Ti can be used synergistically with conventional antibiotics.

6.6 Acknowledgements

This work was supported, in part, by DePuy Synthes.

References

1. Widmer AF. New Developments in Diagnosis and Treatment of Infection in Orthopedic Implants, *Clin. Infect. Dis.* 2001; 33(1): 94-106.
2. Campoccia D, Montanaro L, Arciola CR. The Significance of Infection Related to Orthopedic Devices and Issues of Antibiotic Resistance, *Biomaterials* 2006; 27: 2331-9.
3. Kurtz SM, Lau E, Schmier J, Ong KL, Zhao Ke, Parvizi J. Infection Burden for Hip and Knee Arthroplasty in the United States, *J. Arthroplasty* 2008; 23(7): 984-91.
4. Darouiche RO, M.D. Treatment of Infections Associated with Surgical Implants, *N. Engl. J. Med.* 2004; 350: 1422-9.
5. Connaughton A, Childs A, Dylewski S, Sabesan VJ. Biofilm Disrupting Technology for Orthopedic Implants: What's on the Horizon? *Front. Med.* 2014; 1: 22.
6. Costerton JW, Ellis B, Lam K, Johnson F, Khoury AE. Mechanism of Electrical Enhancement of Efficacy of Antibiotics in Killing Biofilm Bacteria, *Antimicrob. Agents Chemother.* 1994; 38(12): 2803-9.
7. Khoury AE, Lam K, Ellis B, Costerton JW. Prevention and Control of Bacterial Infections Associated with Medical Devices, *ASAIO Journal* 1992; 38: M174-8.
8. Van der Borden A, Van der Mei H, Busscher HJ. Electric-Current-Induced Detachment of *Staphylococcus Epidermidis* Strains from Surgical Stainless Steel, *J. Biomed. Mater. Res. Part B Appl. Biomater.* 2004; 68: 160-4.
9. Ehrensberger MT, Sivan S, Gilbert JL. Titanium Is Not “the Most Biocompatible Metal” under Cathodic Potential: The Relationship between Voltage and MC3T3 Preosteoblast Behavior on Electrically Polarized CpTi Surfaces, *J. Biomed. Mater. Res. A* 2010; 93A(4): 1500-9.

10. Haeri M, Wollert T, Langford GM, Gilbert JL. Electrochemical Control of Cell Death by Reduction-Induced Intrinsic Apoptosis and Oxidation-Induced Necrosis on CoCrMo Alloy *In Vitro*, *Biomaterials* 2012; 33(27): 6295-304.
11. Sivan S, Kaul S, Gilbert JL. The Effect of Cathodic Electrochemical Potential of Ti-6Al-4V on Cell Viability: Voltage Threshold and Time Dependence, *J. Biomed. Mater. Res. B: Appl. Biomater.* 2013; 101(8): 1489-97.
12. Fleury C, Petit A, Mwale F, Antoniou J, Zukor DJ, Tabrizian M, Huk OL. Effect of Cobalt and Chromium Ions on Human MG-63 Osteoblasts In Vitro: Morphology, Cytotoxicity, and Oxidative Stress, *Biomaterials* 2006; 27(18): 3351-60.
13. Bergamini CM, Gambetti S, Dondi A, Cervellati C. Oxygen, Reactive Oxygen Species and Tissue Damage, *Curr. Pharm. Des.* 2004; 10: 1611-26.
14. Harris RM, Williams TD, Hodges NJ, Waring RH. Reactive Oxygen Species and Oxidative DNA Damage Mediate the Cytotoxicity of Tungsten-Nickel-Cobalt Alloys *In Vitro*, *Toxicol. Appl. Pharmacol.* 2011; 250: 19-28.
15. Ziech D, Franco R, Georgakilas AG, Georgakila S, Malamou-Mitsi V, Schoneveld O, Pappa A, Panayiotidis MI. The Role of Reactive Oxygen Species and Oxidative Stress in Environmental Carcinogenesis and Biomarker Development, *Chem. Biol. Interact.* 2010; 188: 334-9.
16. Cabiscol E, Tamarit J, Ros J. Oxidative Stress in Bacteria and Protein Damage by Reactive Oxygen Species, *Internatl. Microbiol.* 2000; 3: 3-8.
17. Circu ML, Aw TY. Reactive Oxygen Species, Cellular Redox Systems, and Apoptosis, *Free Radic. Biol. Med.* 2010; 48: 749-62.

18. Martin KR, Barrett JC. Reactive Oxygen Species as Double-Edged Swords in Cellular Processes: Low-Dose Cell Signaling Versus High-Dose Toxicity, *Hum. Exp. Toxicol.* 2002; 21: 71-5.
19. Ehrensberger MT, Tobias ME, Nodzo SR, Hansen LA, Luke-Marshall NR, Cole RF, Wild LM, Campagnari AA. Cathodic Voltage-Controlled Electrical Stimulation of Titanium Implants as Treatment for Methicillin-Resistant Staphylococcus Aureus Periprosthetic Infections, *Biomaterials* 2015; 41: 97-105.
20. Nodzo SR, Tobias M, Ahn R, Hansen L, Luke-Marshall NR, Howard C, Wild L, Campagnari AA, Ehrensberger MT. Cathodic Voltage-Controlled Electrical Stimulation Plus Prolonged Vancomycin Reduce Bacterial Burden of a Titanium Implant-Associated Infection in a Rodent Model, *Clin. Orthop. Relat. Res.* 2016; 474: 1668-75.
21. Miyanaga K, Terashi R, Kawai H, Unno H, Tanji Y. Biocidal Effect of Cathodic Protection on Bacterial Viability in Biofilm Attached to Carbon Steel, *Biotechnol. Bioeng.* 2007; 97(4): 850-7.
22. Robinson DA, Griffith RW, Shechtman D, Evans RB, Conzemi MG. In Vitro Antibacterial Properties of Magnesium Metal against *Escherichia Coli*, *Pseudomonas Aeruginosa*, and *Staphylococcus Aureus*, *Acta Biomater.* 2010; 6: 1869-77.
23. Kim J, Gilbert JL. Cytotoxic Effect of Galvanically Coupled Magnesium-Titanium Particles, *Acta Biomater.* 2016; 30: 368-77.
24. Kim J, Gilbert JL. The Effect of Cell Density, Proximity, and Time on the Cytotoxicity of Mg and Galvanically Coupled Mg-Ti Particles In Vitro, In Progress.

25. Revie, R. Winston, and Herbert H. Uhlig. "Thermodynamics: Corrosion Tendency and Electrode Potentials." *Corrosion and Corrosion Control*. 4th ed. Hoboken: John Wiley & Sons, 2008. 21-41.
26. Saris NEL, Mervaala E, Karppanen H, Khawaja JA, Lewenstam A. Magnesium: An update on physiological, clinical and analytical aspects. *Clin Chim Acta* 2000; 294: 1-26.
27. Song G, Song S. A possible biodegradable magnesium implant material. *Corros Sci* 2007; 9: 298-302.
28. Kim J, Gilbert JL. In-Vitro Cytotoxicity of Galvanically Coupled Magnesium-Titanium Particles on Human Osteosarcoma SAOS2 Cells: A Potential Cancer Therapy, In *Progress*.
29. Haerihosseini, Seyed Morteza. "Voltage Effects on Cells Cultured on Metallic Biomedical Implants" (2012). *Biomedical and Chemical Engineering- Dissertations*. Paper 66. http://surface.syr.edu/bce_etd/66.
30. Guo, J. (2013). *Bacterial Biofilms on Electrochemically Active Cathodic Titanium Surfaces* (Order No. 1546328). Available from Dissertations & Theses @ Syracuse University; ProQuest Dissertations & Theses Global. (1450054358). Retrieved from <http://search.proquest.com.libezproxy2.syr.edu/docview/1450054358?accountid=14214>.
31. Nodzo S, Tobias M, Hansen L, Luke-Marshall NR, Cole R, Wild L, Campagnari AA, Ehrensberger MT. Cathodic Electrical Stimulation Combined with Vancomycin Enhances Treatment of Methicillin-Resistant *Staphylococcus Aureus* Implant-Associated Infections, *Clin. Orthop. Relat. Res.* 2015; 473: 2856-64.
32. Cabiscol E, Piulats E, Echave P, Herrero E, Ros J. Oxidative Stress Promotes Specific Protein Damage in *Saccharomyces Cerevisiae*, *J. Biol. Chem.* 2000; 275(35): 27393-98.

33. Tamarit J, Cabiscol E, Ros J. Identification of the Major Oxidatively Damaged Proteins in *Escherichia Coli* Cells Exposed to Oxidative Stress, *J. Biol. Chem.* 1998; 273(5): 3027-32.
34. Krumova K, Cosa G. Chapter 1: Overview of Reactive Oxygen Species, in *Singlet Oxygen: Applications in Biosciences and Nanosciences, Volume 1*, 2016, 1, pp. 1-21.
35. Pryor WA. Oxy-Radicals and Related Species: Their Formation, Lifetimes, and Reactions, *Annu. Rev. Physiol.* 1986; 48: 657-67.
36. Winterbourn CC. Reconciling the Chemistry and Biology of Reactive Oxygen Species, *Nat. Chem. Biol.* 2008; 4: 278-86.
37. Kaldalu N, Mei R, Lewis K. Killing by Ampicillin and Ofloxacin Induces Overlapping Changes in *Escherichia coli* Transcription Profile, *Antimicrob. Agents Chemother.* 2004; 48(3): 890-6.
38. Brooun A, Liu S, Lewis K. A Dose-Response Study of Antibiotic Resistance in *Pseudomonas Aeruginosa* Biofilms, *Antimicrob. Agents Chemother.* 2000; 44(3): 640-6.

7 Effect of Mg and Mg-Ti Corrosion Preconditioning on Biological Medium and Cell Viability

7.1 Introduction

Although magnesium (Mg) is considered to be a biocompatible metal [1-5], there are certain adverse effects to be considered when Mg corrodes in solution. It releases Mg ions, hydroxide ions (OH⁻) ions, and hydrogen gas (H₂). Mg is considered biocompatible for many reasons. Mg is one of the most abundant ions found in the body, which can be stored in bone, muscle, and soft tissue [6-7]. Witte et al. summarized the physiological roles of Mg ions: (1) co-regulator of energy metabolism, cell proliferation, protein synthesis, and DNA synthesis, (2) regulator of more than 350 proteins, (3) co-regulator and activator of integrins during cell migration, (4) stabilizer of DNA and RNA, etc. [5]. Therefore, Mg ions released from the metal can be taken up and utilized by the body, if Mg ions are released at a tolerable level.

Song et al. stated that the intake of Mg of an average human body for metabolic activities is usually about 300-400 mg/day [7]. So according to the measured average corrosion rate (i.e. average weight loss) of Mg in the normal stimulated body fluid as 19-44 mg/cm²/day, the dissolved Mg²⁺ ions will be easily consumed by the body if the total surface area of a Mg implant is less than 9 cm² [7]. If Mg ion level exceeds the level the body can consume, then Mg toxicity can occur. Mild Mg cytotoxicity includes vomiting, nausea, feeling of warmth, flushing, hypotension, bradycardia, cardiac arrhythmias, somnolence, double vision, slurred speech, and weakness when the plasma concentration of Mg is around 3.5-5 mmol/l [6]. Extreme Mg toxicity includes hyporeflexia, muscular paralysis, respiratory arrest, and cardiac arrest when the plasma concentration of Mg exceeds to 5-15 mmol/l [6]. However, toxicity due to Mg ion

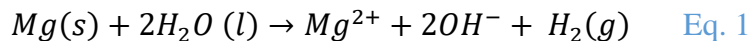
overdose is very rare in the body because the body can efficiently excrete excess Mg ions via urine, and Mg toxicity usually only occurs in bodies with kidney failures [6-8].

In vitro cytotoxicity due to Mg ions have been measured on fibroblast L929 and pre-osteoblast MC3T3-E1 cells, where different levels of Mg ion concentrations induced different cell behavior [9]. Lower Mg ion concentrations below 152 mg/l (6.25 mmol/l or 152 µg/ml) promoted cell proliferation, while intermediate Mg ion concentrations around 181 mg/l (7.45 mmol/l or 181 µg/ml) had no effect, and higher Mg ion concentrations between 343-415 mg/l (14.11-17.07 mmol/l or 343-415 µg/ml) showed adverse effects on cell viability [9]. Another study also treated MC3T3 pre-osteoblast cells with Mg ion concentrations ranging from 2-100 mM and measured cell viability at $t = 2, 4, \text{ and } 6$ days, with a starting density of 3,000 cells/well (in 96 well plates, $A = 0.3 \text{ cm}^2$, 10,000 cells/cm²) [10]. At the highest Mg ion concentration of 100 mM (2430.5 µg/ml), cell viability was around 30% by $t = 2$ days [10], also showing that MC3T3 cells show high tolerance for Mg ions. Comparing in vivo and in vitro studies, in vitro Mg toxicity level seems to be much higher than in vivo Mg toxicity, where up to approximately 8 mmol/l Mg ions have positive or no effect on cells, although this high level of Mg ions in plasma is known to cause severe Mg toxicity in the body.

Chapter 2 of this dissertation shows that pre-osteoblast MC3T3-E1 cells treated with even very low Mg particle concentrations ranging from 50 to 100 µg/ml show a decrease in cell viability (less than 75% of cells are alive), not cell proliferation. And as stated above, while highest Mg ion concentration of 100 mM (2430.5 µg/ml) did not kill all cells (30% alive), the same type of cells, MC3T3, treated with 1500 µg/ml of Mg or 750 µg/ml of Mg-Ti were killed completely by $t = 24$ hours (in Chapter 2). The difference is that Mg or Mg-Ti directly corroding in the presence of cells produces more than just Mg ions (such as hydrogen gas, hydroxide ions,

and ROS) and therefore, Mg or Mg-Ti particles are able to kill much more effectively. Also, Mg ion-induced toxicity does not explain why twice the concentration of Mg (1500 µg/ml) was needed to kill the same number of cells, compared to Mg-Ti (750 µg/ml), when Mg or Mg-Ti of the same particle concentrations must release the same amount of Mg ions.

Corrosion of Mg not only releases Mg ions, but also by-products of hydrogen gas H₂ and hydroxide ions OH⁻. Pure Mg, without any coating or alloying with other elements, will corrode very quickly, especially in acidic pH solution (which occurs during inflammation at surgery/implantation site) or even in physiological pH of 7.4 [11]. Mg corrosion is also influenced by chloride concentrations found in physiological fluid, where the corrosion rate increases proportional to the increase of the chloride concentration of the solution [12]. Based on the overall equation (Eq. 1), 1 mole of Mg theoretically produces 1 mole of H₂, which is equivalent to 1 gram of Mg producing 0.923 liter of H₂ gas.



When 5 g of Mg screw, with a total surface area of 5.9 cm², is implanted, the hydrogen gas evolution rate is 236 ml/day (40 ml/cm²/day), which is a very large hydrogen gas volume [7]. Song et al. also stated that for pure Mg nail with a smaller surface area of 0.977 cm² (2 cm in length and 0.15 cm in diameter) yields approximately 25 ml/day, which is still a large hydrogen gas volume for a body to consume [13]. In in vivo animal study, the adsorption of hydrogen gas was dependent on the diffusion coefficient of hydrogen in the tissue, and so the overall rate of hydrogen adsorption was calculated to be about 0.954 ml per hour (22.9 ml/day) [5,14]. And so if the corrosion of Mg produces hydrogen gas faster than the adsorption rate by the body, hydrogen gas will accumulate and form pockets in the tissue, which can cause necrosis and separate the tissue layers [7]. For Mg stents, the generated gas bubbles can block flowing blood,

which may even cause death [7]. So theoretically, hydrogen gas volume can pose a serious threat if produced in large volume very quickly. However, Witte et al. showed that during in vivo study, all Mg-based implants exhibited visible gas bubbles, which appeared within one week of surgery and then disappeared after 2-3 weeks without causing any adverse side effects [15]. Even though the commercially pure Mg exhibits very high hydrogen evolution rate, the hydrogen gas can easily be punctured and be syringed out as well if the gas begins to accumulate, which can be easily detected [15]. Besides commercially pure Mg, Mg alloys exhibit hydrogen gas evolution rates between 0.008 and 1.502 ml/cm²/day, which is closer to the postulated acceptable level of 0.01 ml/cm²/day by the body [11,13]. Therefore, hydrogen gas produced by Mg does not pose a serious threat to the use of Mg as an implant material. Song et al. stated that corrosion of Mg also results in alkalization of simulated body fluid (SBF), where the pH value of the SBF increases to over 9 in about 10 hours and then finally stabilize around 10.5 [7]. This concerns the local pH increase of the body fluid near the Mg implant, where the alkalization of the body fluid can adversely affect physiological reaction balances in the human body [7]. However, interestingly, in vivo studies of Mg or Mg-based alloy implants did not observe any significant effects in nearby tissues due to alkalization, or notice any unusual symptoms from animals possibly due to alkalization [15-16]. Alkalization, however, may have an adverse effect in vitro, such as shown by Robinson et al., which showed that viability of bacterial cells at alkaline pH significantly decreased [17].

While other studies focus on slowing the corrosion rate of Mg to use Mg as a potential biodegradable implant material, this study focuses on galvanically coupling Mg with Ti to increase its corrosion rate, so that Mg-Ti can ultimately be used to kill and/or prevent bacterial infections (such as biofilm formation on the implant surface) and cancerous tumors for

therapeutic effect. If the corrosion rate is decreased by coating the surface or alloying other elements, hydrogen gas and hydroxide ions will also be produced at much slower rates, which can easily be absorbed by the body, and so many studies conclude that Mg and Mg-based alloys are very biocompatible and have great potentials as biodegradable implant materials. However, this study is focused on increasing the corrosion rate of Mg by galvanically coupling with more noble metal, Ti, and therefore, the hydrogen gas and hydroxide ion evolution rates will be much higher, which may cause cytotoxicity. Previous study by Kim and Gilbert showed that Mg microparticles kill murine pre-osteoblast MC3T3 cells in a dosage dependent manner, while galvanically coupled Mg-Ti kill cells more effectively, requiring lower particle concentrations to kill same number of cells than Mg alone [18]. The pH increased proportionally as Mg/Mg-Ti particle concentrations increased, but there was no statistical difference in pH measurements between Mg and Mg-Ti groups, which showed that pH did not cause the significant increase of killing in Mg-Ti groups [18]. The overall pH of the solution, not the local pH at the particle surface, was measured. Therefore, the local pH at the Mg surface may be higher for Mg-Ti than Mg, but the solution pH was the same for Mg and Mg-Ti, which indicates that faster corrosion rate due to galvanic coupling of Mg and Ti did not produce significantly higher hydroxide ions to increase the pH of the entire solution of the sample. Additionally, the highest solution pH measured was 8.3-8.6 (for highest particle concentrations that resulted in complete cell killing), which was significantly lower than theoretically calculated values (1750 $\mu\text{g/ml}$ of Mg should theoretically yield pH of 13.16; 750 $\mu\text{g/ml}$ of Mg-Ti should theoretically yield pH of 12.79; calculation not shown), probably due to the buffers in the cell culture media. If pH was the major cause of Mg cytotoxicity, the solution pH should be higher, and the pH of Mg-Ti should be higher than the pH of Mg. Although Chapter 2 shows parts of NaOH-controlled pH viability

data to compare with Mg and Mg-Ti particles, this chapter will discuss in further details the effects of pH due to Mg and Mg-Ti particle corrosion and pre-conditioning effect (pre-corrosion of particles in cell culture medium). The goal of this chapter is to analyze the pH of the solution due to Mg or Mg-Ti particle corrosion to determine whether the cytotoxicity of Mg or galvanically coupled Mg-Ti is due to alkaline pH.

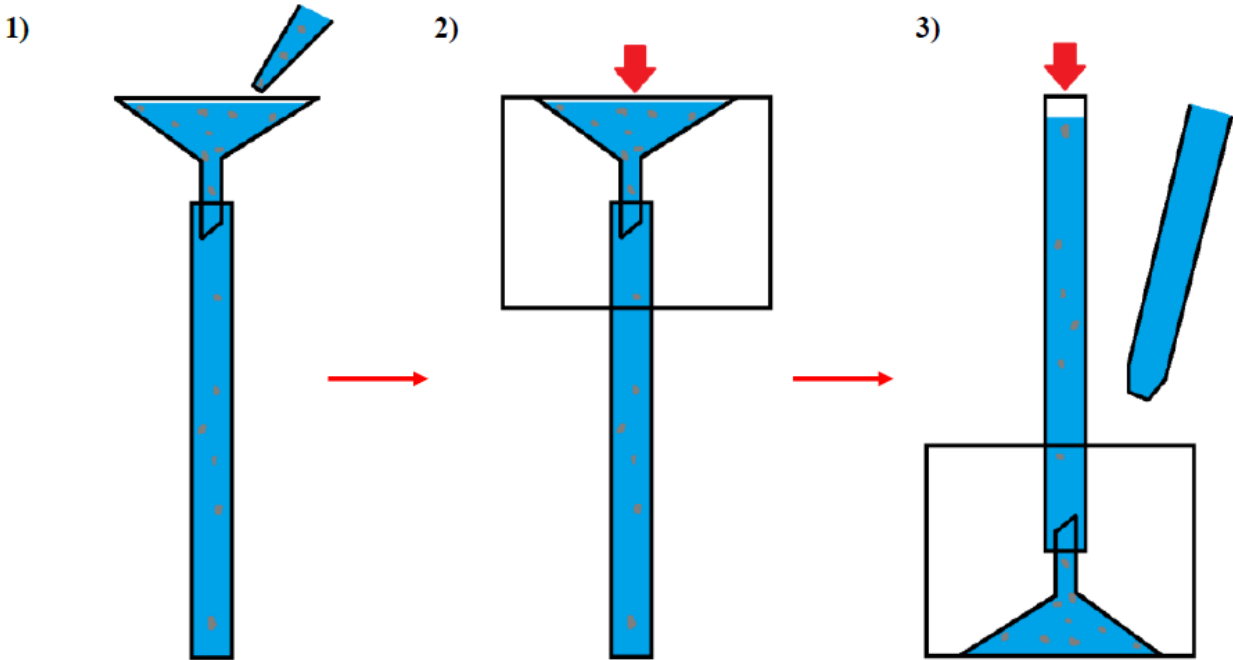
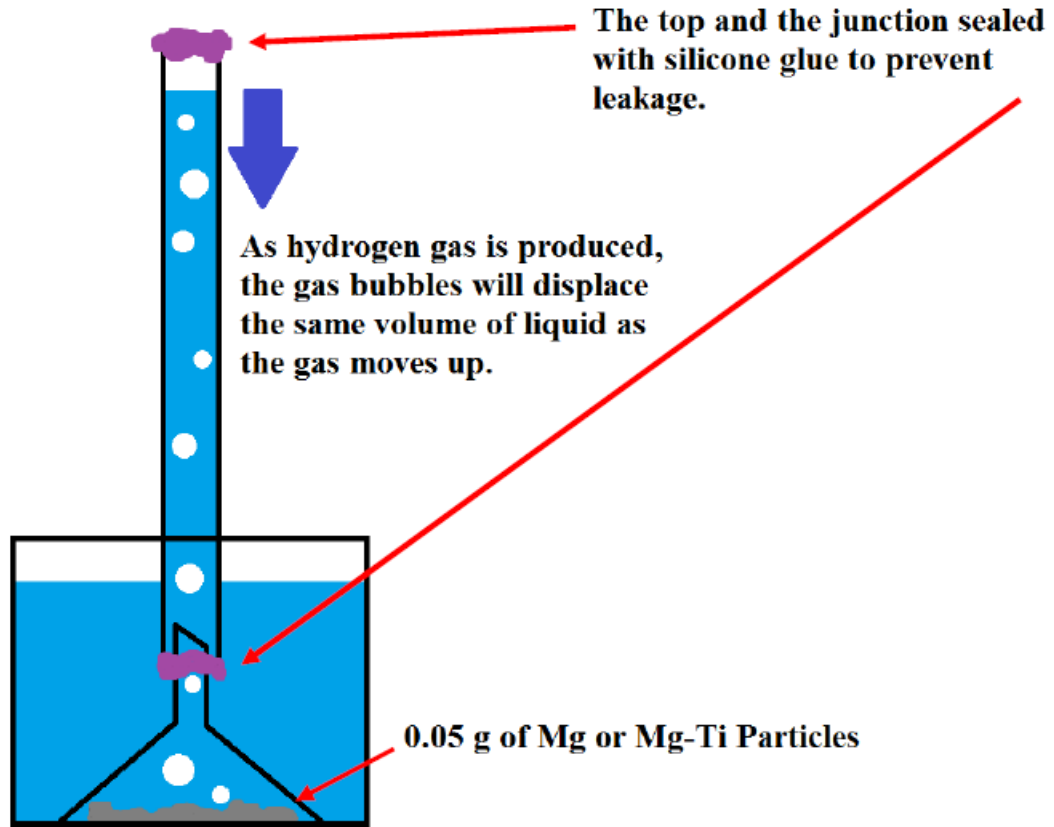
7.2 *Materials and Methods*

7.2.1 *Hydrogen Gas Volume*

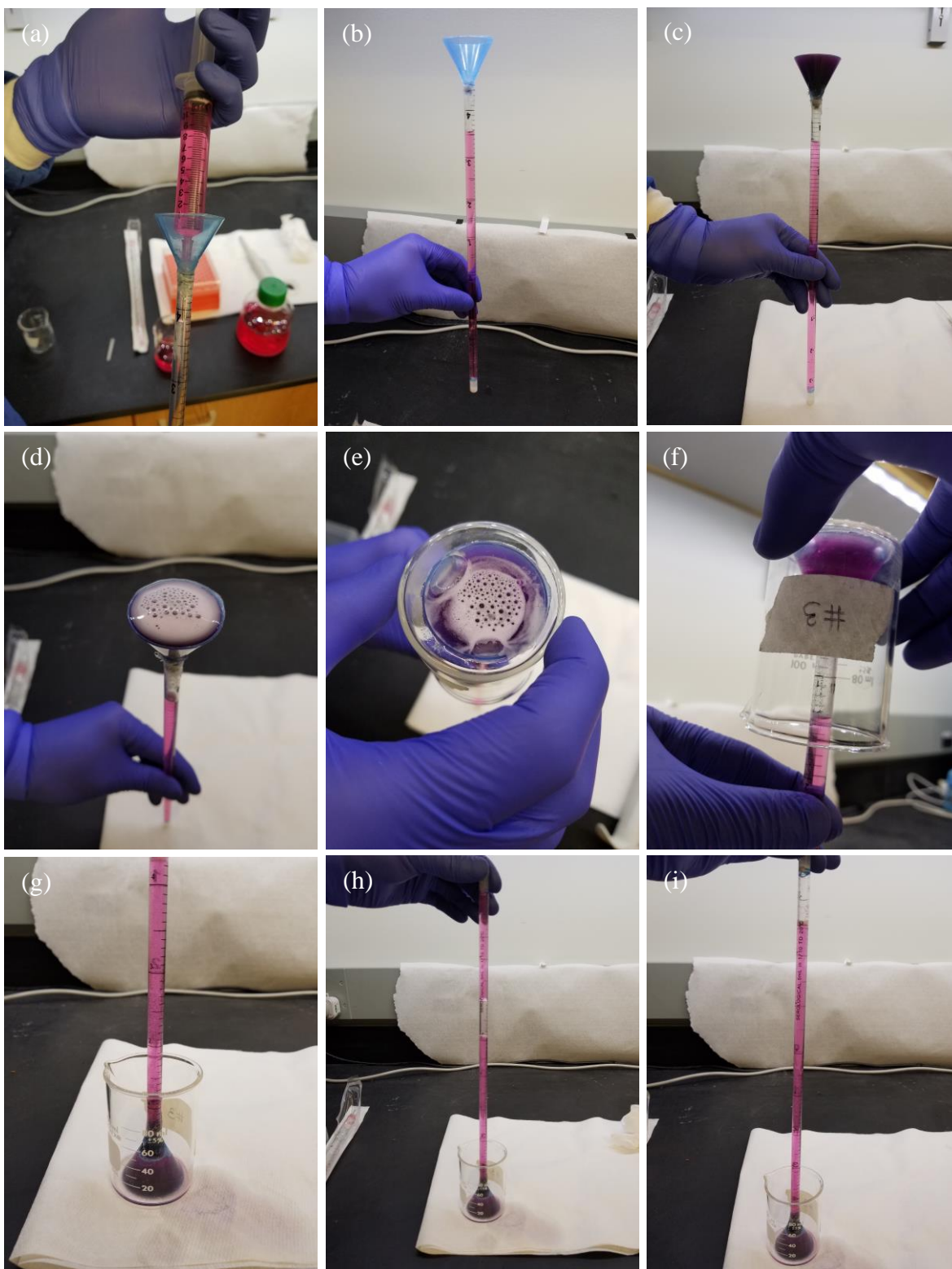
Hydrogen gas volume was measured using the same method as Song et al. used [10]. Fig. 7.1 shows the schematic set-up and step-by-step process of the experiment. Please note the careful steps taken to limit the loss of the particles. 5 ml pipette was used as the column and the top end was glued with silicone so that hydrogen gas cannot escape. The junction between the column and the cone is also glued. At the bottom of the cone, 0.05 g of Mg and Mg-Ti particles corroded in cell culture media (AMEM + 10% FBS + 1% PSG) to measure hydrogen gas volume from $t = 0$ to 72 hours. 0.05 g of Mg or Mg-Ti particles were added inside the funnel and as the particles corroded, hydrogen gas was produced, which floated up to the top of the pipette and displaced the same volume of liquid. Part I of Fig. 7.1 shows the schematic set-up of the experiment. Part II of Fig. 7.1 shows the step-by-step procedures. First, the media was injected into the pipette using a syringe as shown in Fig. 7.1 Part IIa. The media was not filled all the way to the top so that when the pipette was inverted, the liquid was within the markers (to read the volume displacement, in ml). 0.05 g of Mg or Mg-Ti was added into the cone. To do so, 0.05 g of particles was pre-mixed with small amounts of media (~1 ml) and then pipetted into the cone. Because there was an air gap between the liquid in the cone and the liquid in the pipette, the particles did not immediately fall into the pipette. Additional media was added so that the

cone was filled completely, but not overflowing. The beaker was gently placed over the cone and then the pressure was applied. The entire system was then quickly inverted, without causing any spillage. The pressure was still applied on the pipette as the liquid was displaced. Once the liquid displacement was finished, 30 ml of media was added to the beaker. The hand still applied pressure on the pipette so that the pipette did not move while the media was being added. Once done, the hand gently let go of the pipette.

I. Schematic Set-Up



II. Step-by-Step Procedures



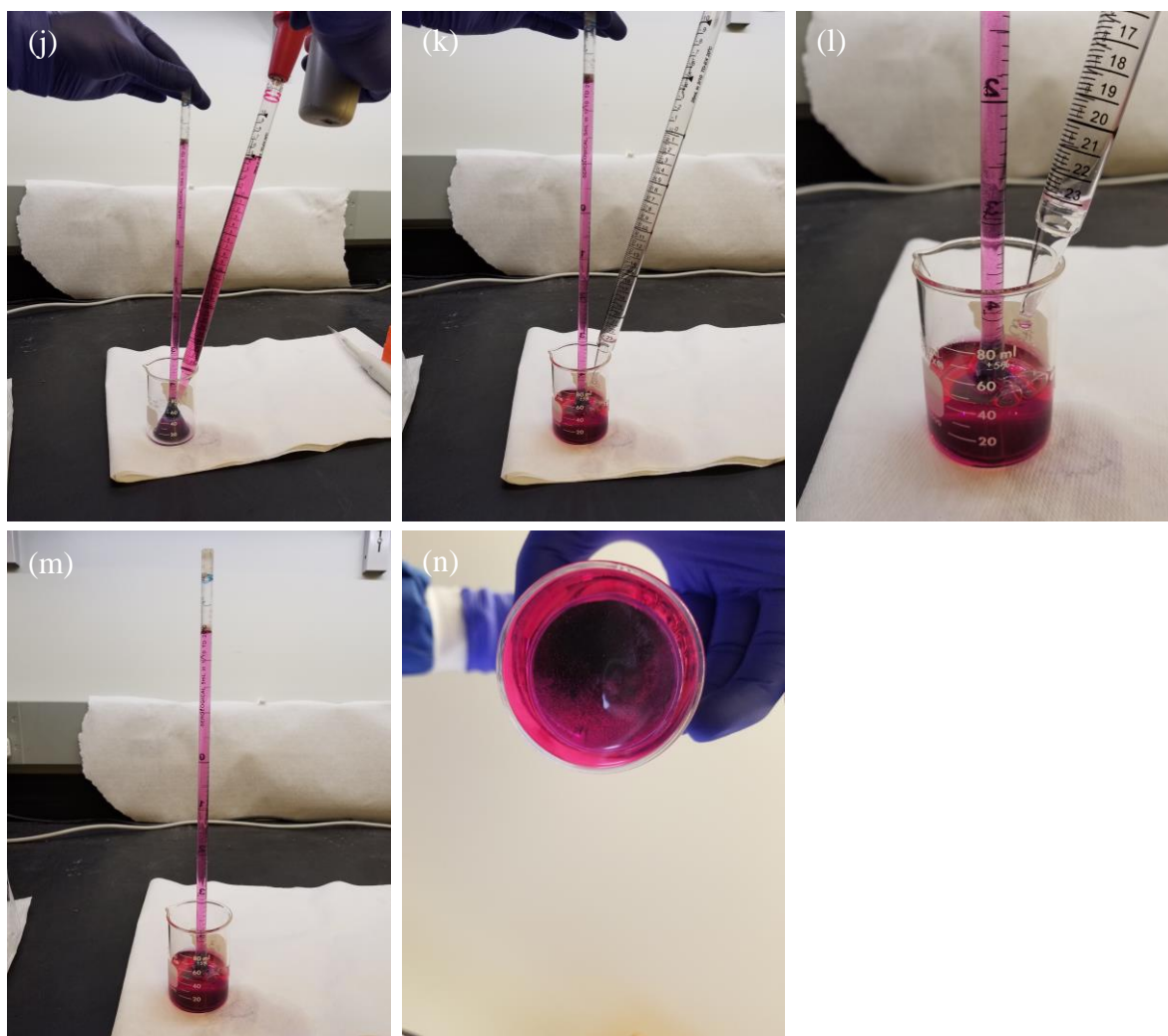


Figure 7.1 Part I shows the schematic set-up of the experiment. 5 ml of pipette was used to measure the hydrogen gas volume. The tip (where it narrows) was cut and then a funnel was glued using silicone glue. The other end of the pipette tip was also glued to prevent hydrogen gas evaporation to the atmosphere. 0.05 g of Mg or Mg-Ti particles were added inside the funnel and as the particles corroded, hydrogen gas was produced, which floated up to the top of the pipette and displaced the same volume of liquid. Part II shows the step-by-step procedures. (a) First, the media was injected into the pipette using a syringe as shown. (b) The media was not filled all the way to the top so that when the pipette was inverted, the liquid was within the markers (to read the volume displacement, in ml). (c) 0.05 g of Mg or Mg-Ti was added into the cone. To do so, 0.05 g of particles was pre-mixed with small amounts of media (~1 ml) and then pipetted into the cone. Because there was an air gap between the liquid in the cone and the liquid in the pipette, the particles did not immediately fall into the pipette. (d) Additional media was added so that the cone was filled completely, but not overflowing. (e) The beaker was gently placed over the cone and then (f) the pressure was applied. (g) The entire system was then quickly inverted, without causing any spillage. (h) The pressure was still applied on the pipette as the liquid was displaced. (i-l) Once the liquid displacement was finished, 30 ml of media was added to the beaker. The hand still applied pressure on the pipette so that the pipette did not move while the media was being added. (m) Once done, the hand gently let go of the pipette. (n) This image shows the close-up of the bottom of the beaker, to ensure that the particles are all within the cone.

7.2.2 *Pre-Conditioning Media Part I*

0.05 g of Mg or Mg-Ti particles were added in 15 ml of complete media (AMEM + 10% FBS + 1% PSG) in 37 Celsius for either $t = 1$ hour or 5 days, occasionally stirring the particle solution so that many particles were exposed to the solution. This solution was then centrifuged at 200 rpm for 2 mins so that the corrosion products and left-over particles can sink so that only now the “pre-conditioned” media can be pipetted. 2 ml of this “pre-conditioned” media was then given to the MC3T3 cells with cell density of 10,000 cells/cm² in 9.6 cm² per sample for $t = 24$ hours. The negative control group for this experiment is just cells given regular media, without any pre-conditioning using particles. At the end of $t = 24$ hours, live/dead assay (Invitrogen #: L3224) was performed to measure cell viability using an optical microscope (Leica Instruments). Ten images were taken per sample at random for three separate samples ($n=3$, total 30 images per sample) and the number of live and dead cells was counted manually in each image using the manual cell counter feature of Image J software (Image J, NIH Bethesda MD).

7.2.3 *Pre-Conditioning Media Part II*

Section 7.2.1 “pre-conditions” the media after the media has been made by mixing 10% FBS and 1% PSG in AMEM. In this experiment, 0.5 g of Mg particles was added in 50 ml of AMEM and 50 ml of FBS for $t = 5$ days at 4 Celsius in order to make “pre-conditioned” AMEM and FBS to determine the “pre-conditioning” effects on AMEM and FBS separately. From now on, the “regular” AMEM and FBS will be labeled as RA and RF, respectively, and the “pre-conditioned” or modified AMEM and FBS will be labeled as MA and MF, respectively. Afterwards, complete media was made as the following: RA + 10% RF (negative control), RA + 10% MF, MA + 10% RF, and MA + 10% MF. In this experiment, PSG was eliminated to simplify the solution to determine which components of the media is affected by the corrosion of

the particles. PSG does not significantly alter the cell viability, since penicillin-streptomycin is antibiotics to prevent bacterial contamination and L-glutamine is known to help cell proliferation. And therefore, as long as the cell culture method/technique maintains sterility, cells can be cultured without PSG; cells just may take little longer time to proliferate. MA + 10% MF group is essentially the same as the “pre-conditioned” media from Section 7.2.2, except for the difference in the order in which the “pre-conditioned” media was made. In this section, AMEM and FBS were pre-conditioned separately and then the complete media was made afterwards, while in Section 7.2.2, the complete media was made and then the complete media was pre-conditioned using the particles. 2 ml of each media was then given to MC3T3 cells with cell density of 10,000 cells/cm² in 9.6 cm² per sample for t= 24 hours and then live/dead assay was performed to measure cell viability.

7.2.4 *pH Effect*

In order to determine if pH is the major cause of cytotoxicity of Mg and Mg-Ti particles, pH of complete media (AMEM + 10% FBS + 1% PSG) was changed using sodium hydroxide (NaOH) base. Different concentrations of sodium hydroxide (NaOH, Fischer Scientific, Lot #: 033125-24) were added in 10 ml of complete media to vary the pH levels from 7 to 11, and the pH of the media was measured using the pH meter (Omega PHB-45). After adding different concentrations of NaOH, osmolality was calculated to make sure the solution is not too hypertonic or hypotonic. The concentrations of NaOH added did not affect the osmolality of the solution (the calculation not shown). 2 ml of the complete media with different pH ranging from 7 to 11 was given to MC3T3 cells with cell density of 10,000 cells/cm² in 9.6 cm² per sample for either t= 1 hour or 24 hours and then live/dead assay was performed to measure cell viability.

The pH values were also measured at the end of each time period (1 hour or 24 hours) since pH can shift due to the 5% CO₂ buffer in the incubator.

The pH values of these solutions (RA + 10% RF, RA + 10% MF, MA + 10% RF, MA + 10% MF) were adjusted back close to the physiological pH of 7.4 using hydrochloric acid (HCl, Fluka Analytical Lot #: SZBB3080V). These solutions were then given to the MC3T3 cells with cell density of 10,000 cells/cm² in 9.6 cm² for 24 hours and then live/dead assay was performed to measure cell viability.

pH was measured every 24 hours for RA, RF, MA, MF solutions while the particles were corroding from t= 0 to 120 hours. Once the media solutions were made (RA + 10% RF, RA + 10% MF, MA + 10% RF, MA + 10% MF), the pH was again measured. After the pH was adjusted back to physiological pH using HCl, the pH was also measured. The pH was all measured using the pH meter (Omega PHB-45).

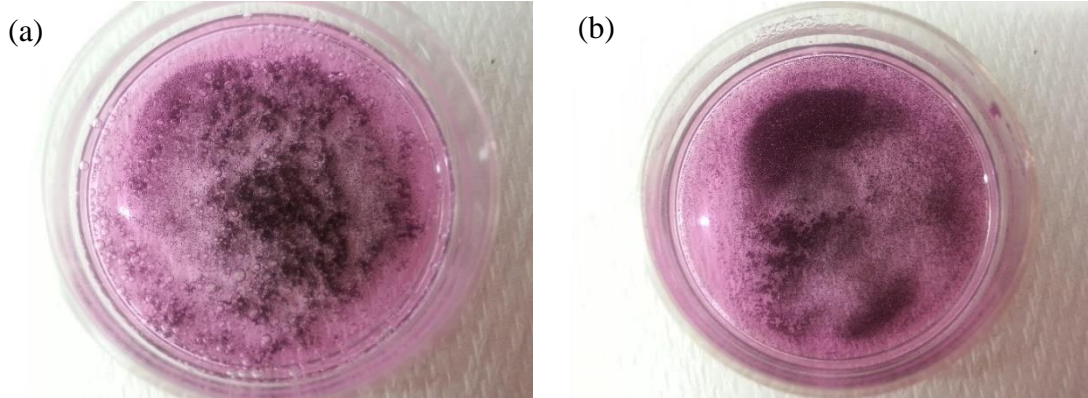
7.3 Results

7.3.1 Hydrogen Gas Volume

Fig. 7.2 shows 0.01 g of Mg and Mg-Ti particles corroding in complete media (AMEM + 10 % FBS + 1% PSG) for 12 hours. Optical images show hydrogen gas evolving from Mg particles very clearly, and the hydrogen bubbles growing bigger over time. However, for Mg-Ti particles, there were very small few hydrogen gas bubbles initially, but then once they popped, no new hydrogen gas bubbles formed. This could possibly mean that hydrogen gas is not produced when Mg-Ti particles corrode; however, hydrogen gas volume needs to be quantitatively measured in order to confirm that hydrogen gas is not produced during Mg-Ti particle corrosion. So hydrogen gas was measured for 0.05 g of Mg and Mg-Ti particles, which shows that Mg-Ti particles produced more hydrogen gas volume than Mg (Fig. 7.3). 0.05 g of

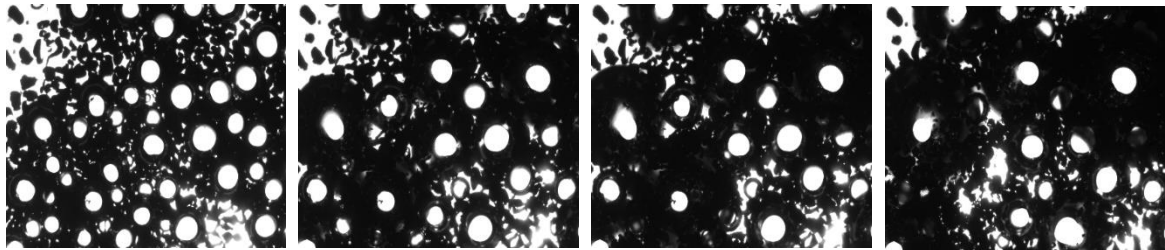
Mg-Ti produced a total volume of 2.9 ml of H_2 by $t= 18$ hours and did not produce any more H_2 after that. 0.05 g of Mg steadily produced H_2 , producing a total volume of 1.32 ml at the end of $t= 72$ hours. At $t= 18$ hours, when Mg-Ti finished producing H_2 , Mg only produced 0.8 ml of H_2 .

i)



ii)

Mg: (a) $t = 1$ sec (b) $t = 3$ hours (c) $t = 6$ hours (d) $t = 12$ hours



Mg-Ti: (a) $t = 1$ sec (b) $t = 3$ hours (c) $t = 6$ hours (d) $t = 12$ hours

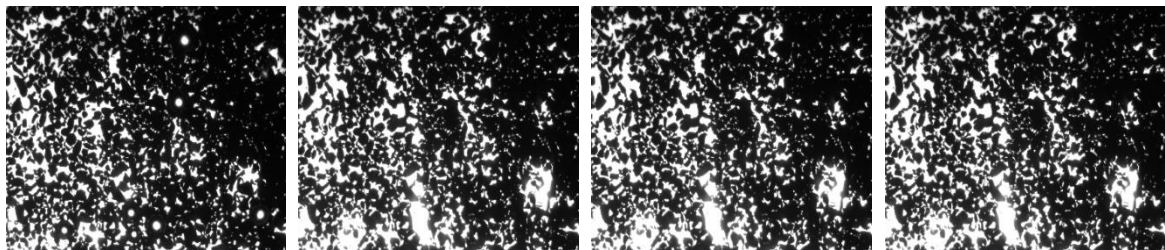


Figure 7.2 i) Pictures of (a) 0.01 g of Mg and (b) 0.01 g of Mg-Ti in complete media for $t= 3$ days. For Mg, there are still hydrogen gas bubbles seen even at 3 days, while no hydrogen gas bubbles are visible for Mg-Ti. ii) Images are taken with optical microscope using time-lapse. Mg and Mg-Ti particles are corroded in complete media (AMEM + 10% FBS + 1% PSG) for (a) $t= 1$ sec, (b) $t= 3$ hours, (c) $t= 6$ hours, and (d) $t= 12$ hours, up to $t= 3$ days, which is not shown. However, the time-lapse images also show that only Mg particles visibly produce hydrogen gas bubbles.

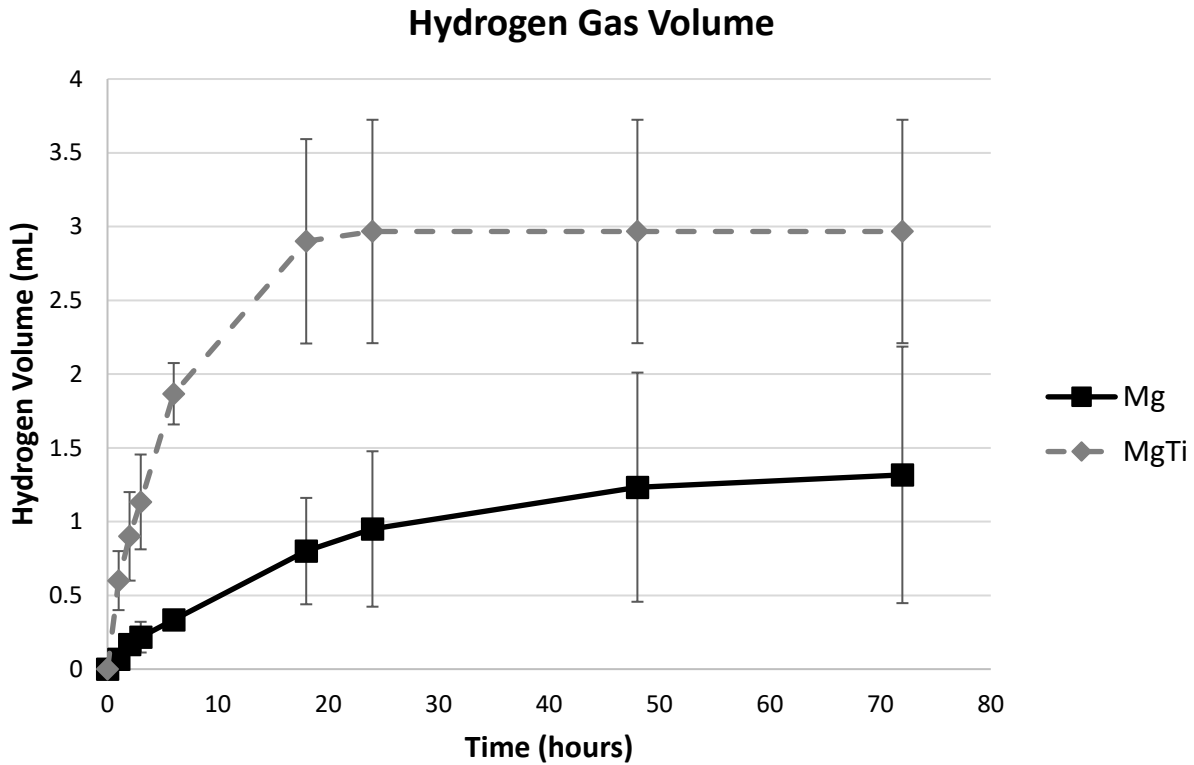


Figure 7.3 Hydrogen gas volume measured over time for 0.05 g of Mg and Mg-Ti corroding in complete media, $n=3$. There is significantly higher volume of hydrogen gas produced over time for the same amount of Mg-Ti than Mg, where Mg-Ti produces approximately twice the hydrogen gas volume than Mg, $p < 0.05$. Also, based on the hydrogen gas volume measured over time, Mg-Ti finished corroding more quickly, by $t= 18$ hours, compared to Mg, which kept producing hydrogen gas steadily over $t= 72$ hours.

7.3.2 Pre-Conditioning Media Part I

Fig. 7.4 shows live/dead images of cells treated with either regular media (control group) or “pre-conditioned” media using 0.05 g of Mg or Mg-Ti particles (experimental groups) for $t= 24$ hours. While control groups were very viable, many cells have been killed using “pre-conditioned” media, whether the media was “pre-conditioned” for $t= 1$ hour or 5 days. As shown in Fig. 7.5, the cell viability of the control groups is very high, approximately 95%. However, cells treated with “pre-conditioned” media using Mg particles show 1.7% and 0% cell viability for the conditioning times of 1 hour and 5 days, respectively. Likewise, cells treated with “pre-conditioned” media with Mg-Ti particles show 0.622% and 0% cell viability for the conditioning times of 1 hour and 5 days, respectively. Post hoc Tukey test shows that while cell viability

between control groups and “pre-conditioned” media groups using Mg and Mg-Ti particles are significantly different ($p < 0.05$), cell viability between “pre-conditioned” Mg and “pre-conditioned” Mg-Ti groups are not different from each other ($P > 0.05$).

pH was measured over time during the particle corrosion in the media from $t = 0$ hour to 5 days (Fig. 7.6). For control (regular media), the pH was between 7.6 and 8.1 during this time period. For “pre-conditioned” media using Mg and Mg-Ti particles, the pH immediately jumped to 9.3, even when the pH was measured immediately after adding the particles (within 30 seconds). The highest pH was measured as 9.91 and 9.73 for “pre-conditioned” media using Mg and Mg-Ti particles, respectively, at $t = 72$ hours, and the final pH was measured as 9.72 and 9.75, respectively, at $t = 120$ hours. Post hoc Tukey test shows that the pH values are all significantly different from each other ($p < 0.05$), although the pH values of Mg and Mg-Ti groups are very close to each other.

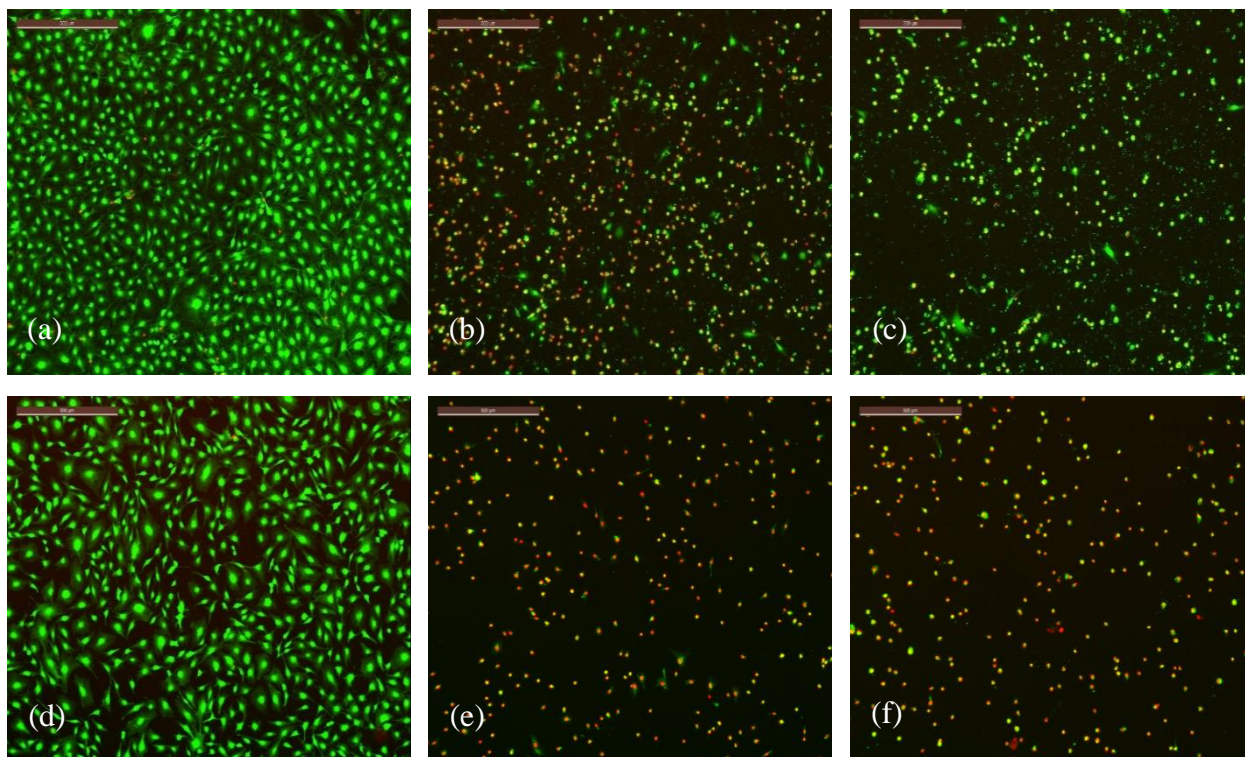


Figure 7.4 Live/dead images of MC3T3 cells treated with the following media for $t=24$ hours: (a) control (regular media) for $t=1$ hour, (b) 0.05 g of Mg pre-corroded in complete media for $t=1$ hour, (c) 0.05 g of Mg-Ti pre-corroded in complete media for $t=1$ hour, (d) control (regular media) for $t=5$ days, (e) 0.05 g of Mg pre-corroded in complete media for $t=5$ days, and (f) 0.05 g of Mg-Ti pre-corroded in complete media for $t=5$ days, $n=3$. Unlike the control groups, cells treated with “pre-conditioned” media, regardless of the conditioned time and particle type (Mg vs. Mg-Ti) that conditioned the media, were killed almost completely.

Cell Viability for Pre-Conditioned Media (0.05g Mg or Mg-Ti / 15 ml)

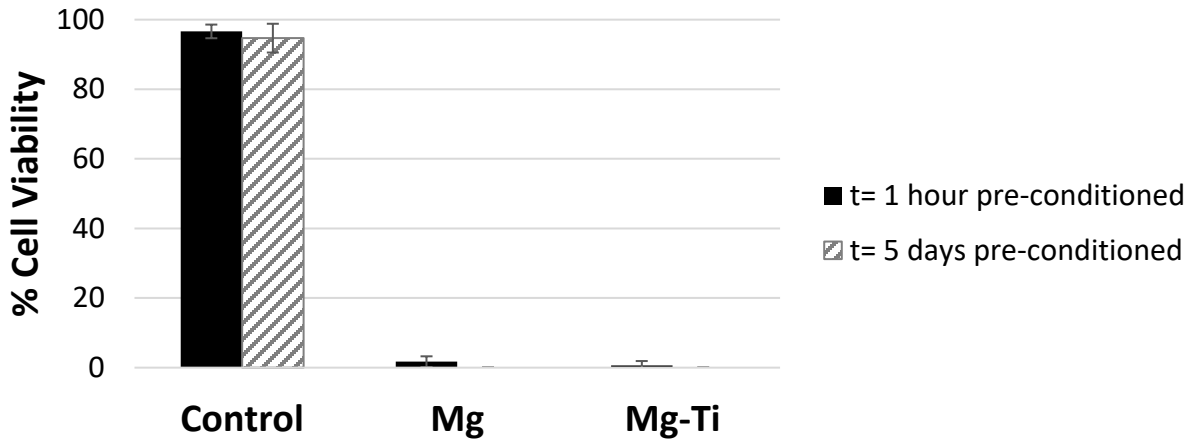


Figure 7.5 Cell viability measured for MC3T3 cells treated with pre-conditioned media for 24 hours. The pre-conditioned media has been made by corroding 0.05 g of Mg or Mg-Ti particles for $t= 1$ hour or 5 days in 15 ml of complete media, $n=3$. Post hoc Tukey test shows that there is a significant difference in cell viability between control and Mg/Mg-Ti groups, $p < 0.05$, but not between Mg and Mg-Ti groups, $p > 0.05$.

Conditioning Media: pH over time

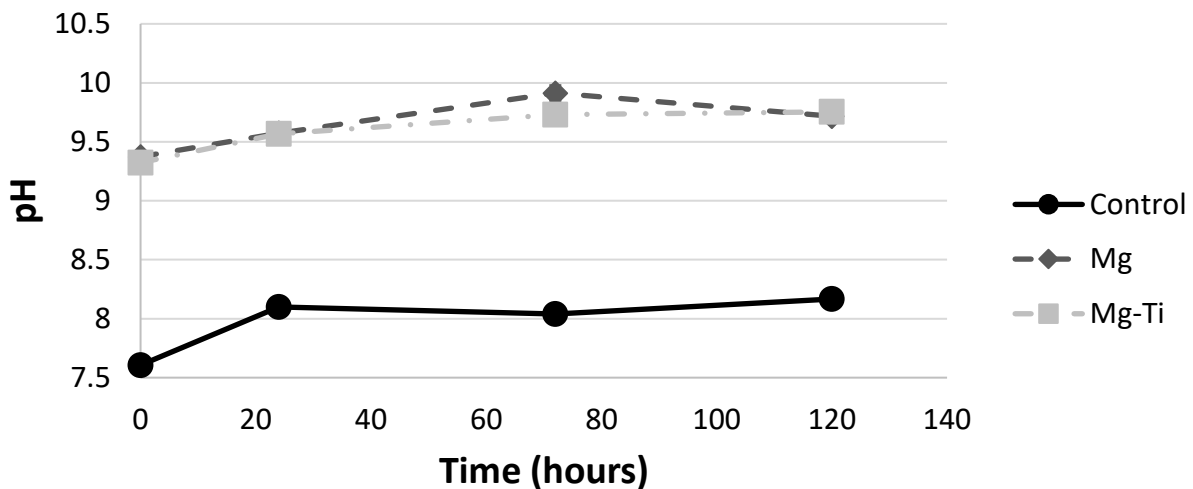


Figure 7.6 pH measured over time from $t= 0$ hour to 120 hours (5 days) for 0.05 g of Mg or Mg-Ti particles pre-corroded in 15 ml of complete media (AMEM + 10% FBS + 1% PSG), compared to control group, which is complete media without any particles, $n=3$. The pH shifted immediately after the particles have been added (within 1 minute) to pH of 9.3 and stayed between 9.5 and 9.9 over time. The pH of the control group at $t= 0$ hour was 7.6 and slightly increased to 8.1 by the end of $t= 5$ days. The pH measurements are significantly different among control, Mg and Mg-Ti groups, $p < 0.05$. Although post hoc Tukey test showed that the pH measured for Mg and Mg-Ti is significantly different, the pH values between Mg and Mg-Ti are only slightly different, with the differences all within 0.2.

7.3.3 Pre-Conditioning Media Part II

Fig. 7.7 shows AMEM and FBS pre-conditioned with 0.5 g of Mg particles (in 50 ml of AMEM or FBS solutions). From now on, AMEM and FBS pre-conditioned with Mg particles will be referred to as modified AMEM and modified FBS, respectively. AMEM and FBS were not pre-conditioned with Mg-Ti in this experiment because the results in Section 7.3.2 indicated that the galvanic coupling did not affect the pre-conditioning of the media, and did not cause any difference in cell viability. Compared to just regular AMEM and FBS, the modified AMEM and modified FBS are very cloudy, indicating that the chemical composition of the solution has been altered. Regular AMEM is red, indicating that the pH of the AMEM solution is basic, due to phenol red, pH indicator. This is a natural occurrence when the media is stored in the fridge over time, without any buffer, such as 5% CO₂. In order to identify the difference in solution composition of regular and modified solutions, these solutions were dried in the desiccator in order to image using SEM (Fig. 7.8). Modified AMEM shows clustered and aggregated particles, which is not seen in regular AMEM, but there is no morphological difference between regular FBS and modified FBS, which both become flakes as the solution has been dried.

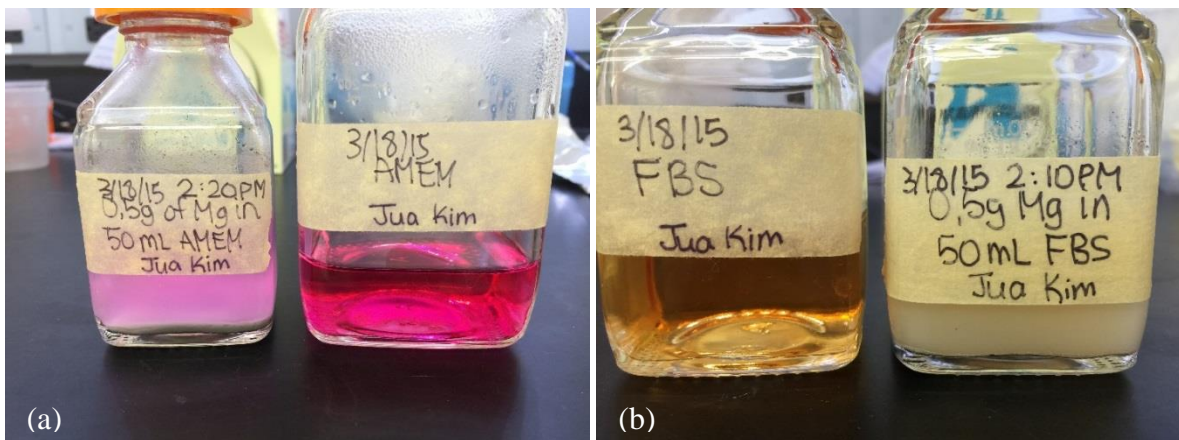


Figure 7.7 (a) 0.5 g of Mg pre-corroded in 50 ml AMEM solution for $t = 5$ days at 4 Celsius, compared to regular AMEM. (b) 0.5 g of Mg-Ti pre-corroded in 50 ml FBS solution for $t = 5$ days at 4 Celsius, compared to regular FBS. The solution opacity looks clearly different. Both FBS and AMEM solutions with particles have more cloudy-appearance than its control counterparts, indicating that solution composition/chemistry due to particle corrosion have changed.

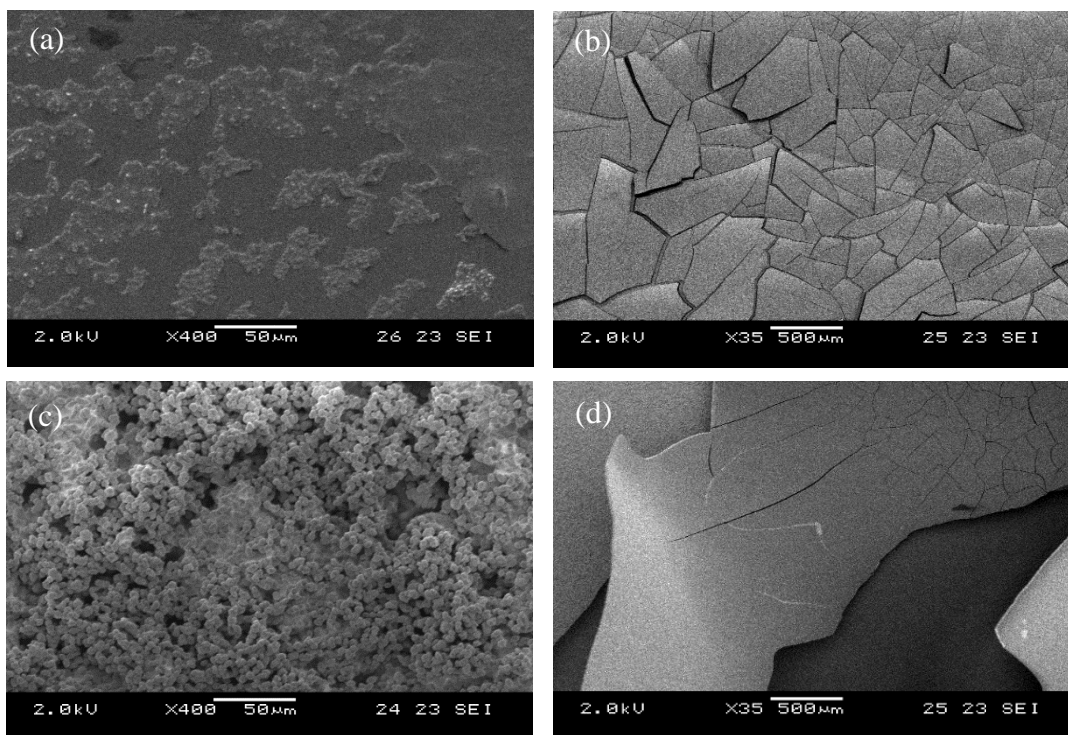


Figure 7.8 SEM images of (a) regular AMEM, (b) regular FBS, (c) modified AMEM treated with Mg, and (d) modified FBS treated with Mg. The solutions in the plastic dish were left in the desiccator and then sputtered with gold for SEM imaging. There were lots of particulates that were morphologically different for modified AMEM, compared to regular AMEM. The regular FBs and modified FBS did not show any morphological difference; there were just dried flakes of FBS.

The pH was measured for regular AMEM, modified AMEM, regular FBS, and modified FBS over time, while the particles were corroded from $t = 0$ hour to $t = 120$ hours (Fig. 7.9). To make sure all the solutions were under the same conditions, 50 ml of the solutions were stored in glass bottles in the fridge at 4 Celsius, including the control groups (regular AMEM and regular FBS), while the particles were corroding for modified AMEM and modified FBS. Regular AMEM and regular FBS solutions did not show significant increase in pH because there were no particles corroding in solution. Again, the slight shift of pH over time in regular AMEM and FBS is a natural occurrence when the solution is stored without any buffer. Regular AMEM and regular FBS had lower pH than its pre-conditioned counterparts, where the pH of regular AMEM and FBS ranged between 7.4 and 8.9 over time, while the pH of the modified AMEM and FBS ranged between 8.63 and 11.95 over time. For modified AMEM and FBS, the pH increased the

first 72 hours (3rd day), from approximately 9 to 12, then started to plateau by 96 hours (4th day), and then dropped slightly at 120 hours (5th day). Post hoc Tukey test shows that pH of regular AMEM is different from that of modified AMEM, $p < 0.05$, and pH of regular FBS is different from that that of modified FBS, $p < 0.05$.

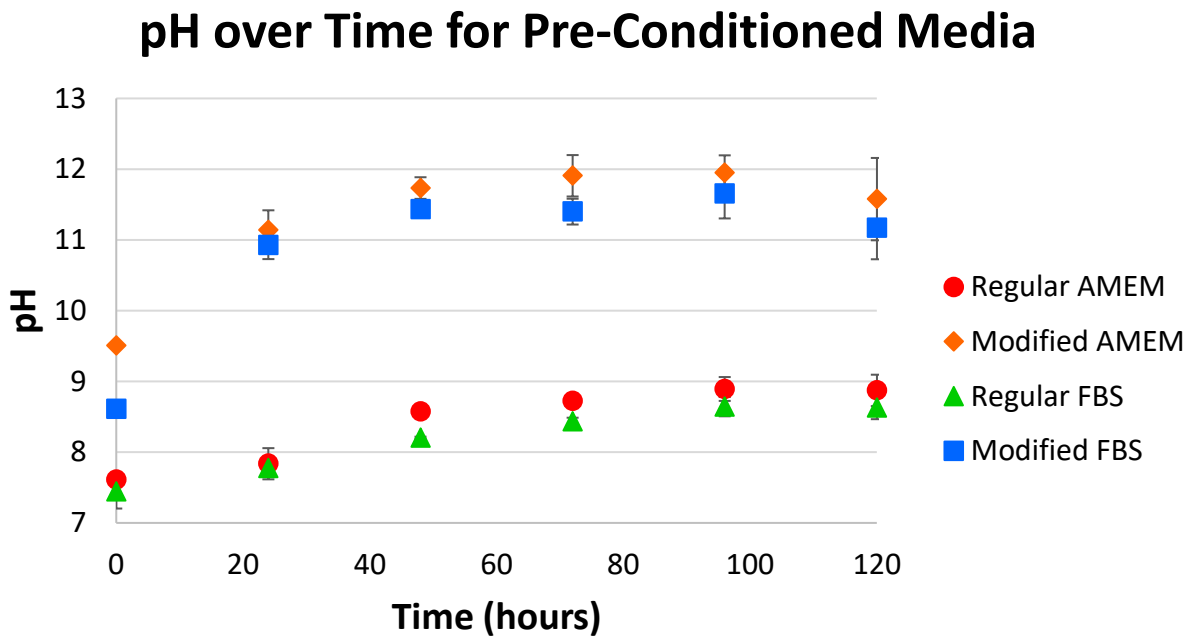


Figure 7.9 pH measurements over time for the following solutions: Regular AMEM, Modified AMEM, Regular FBS, Modified in FBS from $t=0$ to 120 hours, $n=3$. The pH of regular AMEM and modified AMEM are significantly different from each other, $p < 0.05$, and likewise, the pH of regular FBS and modified FBS are significantly different from each other, $p < 0.05$.

Fig. 7.10 shows pH measurements after mixing regular AMEM, modified AMEM, regular FBS, and modified FBS in following combinations: (A) regular AMEM + 10% regular FBS (i.e. control), (B) regular AMEM + 10% modified FBS, (C) modified AMEM + 10% regular FBS, and (D) modified AMEM + 10% modified FBS. The pH increased from (A) to (D), as the ratio volume of the modified solution increased. Group A is a negative control group since no pre-conditioning has been performed in either components of the solution, but another control group has been prepared. Unlike group A, which has been made from smaller amount (50 ml) of AMEM and FBS solutions stored separately in glass bottles for 5 days, this control

group has been made directly from new, unopened bottles (500 ml per bottle) that came from the manufacturing company. There should be no difference in group A and control group (using new products) other than the fact that they have been stored in different bottles and the new products were sealed properly (but at same temperature of 4 Celsius). However, group A showed higher pH than the control group. The average pH of control, A, B, C, and D before pH adjustment is as follows: 8.6, 9.43, 10.53, 11.52, and 12.08, where group D had the highest pH value. The pH was then re-adjusted using hydrochloric (HCl) acid to 7.95~8.5. Instead of using hydrochloric acid to adjust the pH, A and D were mixed in 1:1 ratio to dilute solution D, which resulted in group E, with an average pH of 10.77.

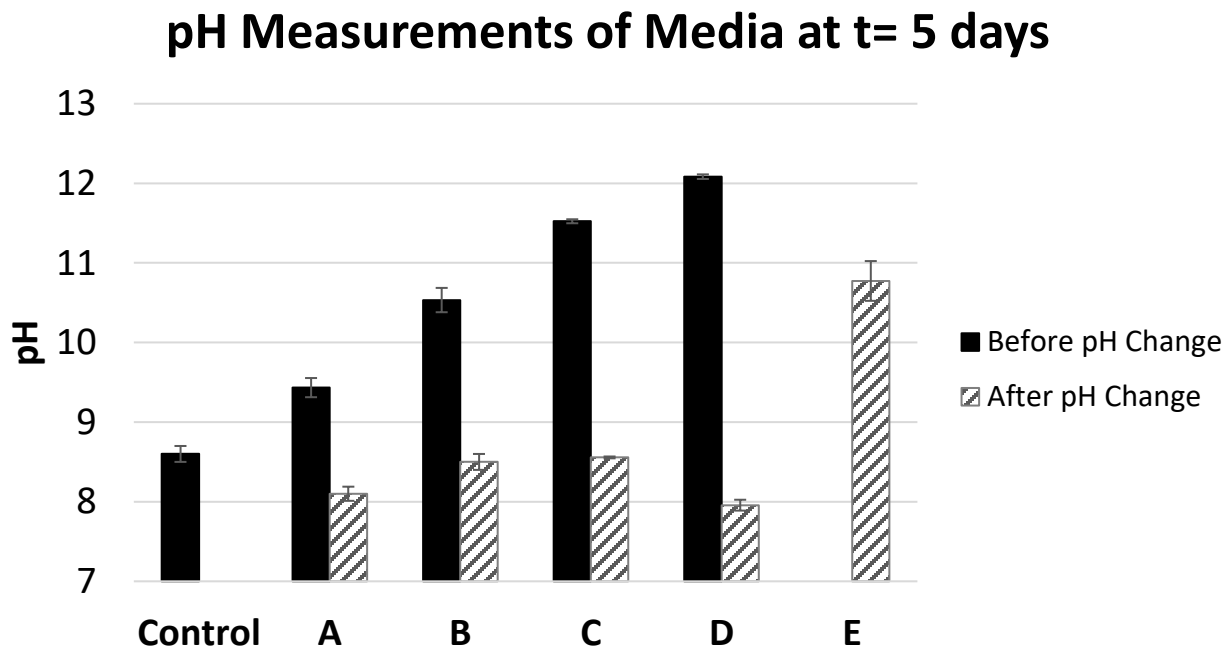
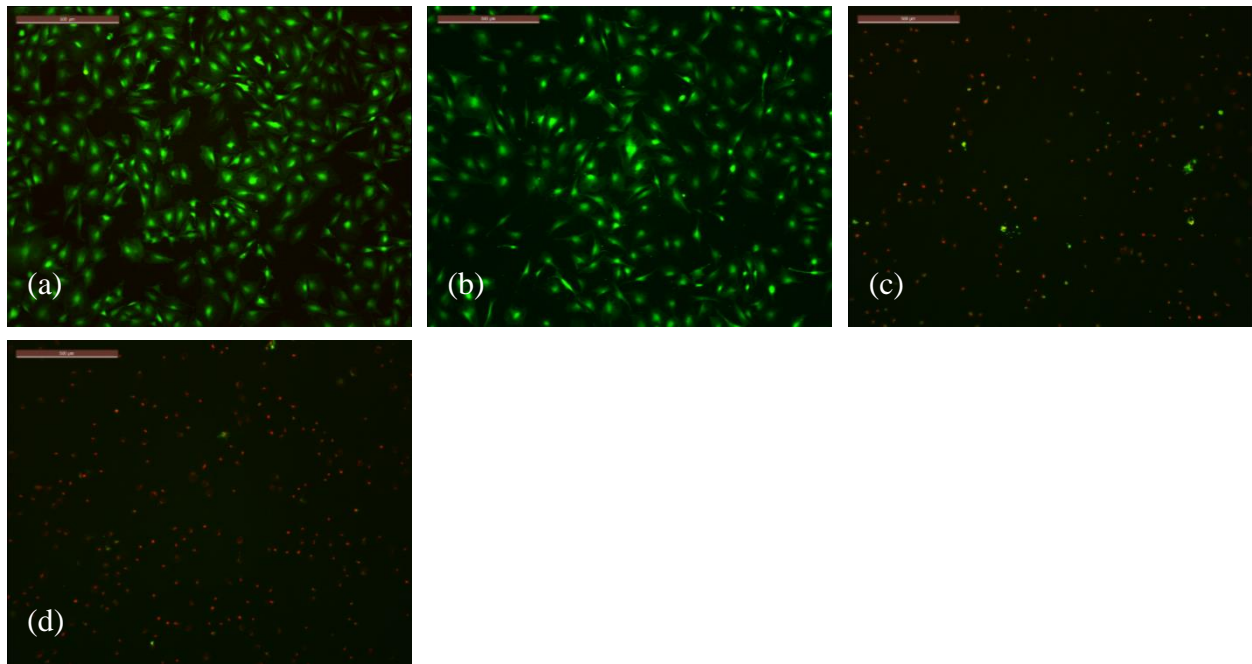


Figure 7.10 pH measurements before and after pH changes of regular media using new products (control), (A) Regular AMEM + 10% Regular FBS (RR), (B) Regular AMEM + 10% Modified FBS (RM), (C) Modified AMEM + 10% Regular FBS (MR), and (D) Modified AMEM + 10% Modified FBS (MM), and (E) 50% (A) + 50% (D), n=3. The pH for groups A-D ranged from 8.5-12.1, and then the pH was re-adjusted closer to physiological pH using HCl. The pH after HCl for groups A-D ranged from 7.95-8.5. Although the pH could have been brought closer to the physiological pH of 7.4, adding more HCl would have started to affect the osmolality of the solution. Group E has a pH of 10.77, which is approximately the average pH of A and D, and this makes sense since E is a result of 50:50 ratio of A and D.

The solutions A-E, both before and after pH adjustments, have been given to the cells for $t=24$ hours to show the “pre-conditioning” effect of the solution on cell viability. Fig. 7.11 shows live/dead images of MC3T3 cells treated with solutions A-E, before and after pH adjustments. As shown, before pH adjustments, cells treated with A and B are viable, while most cells treated with C and D are dead. After pH adjustments, cells treated with A and B are still viable. While there are slightly more cells alive treated with C after pH adjustment compared to cells treated with C before pH adjustment, cells treated with D are completely dead despite the pH adjustment. Cells treated with E shows mixtures of live and dead cells. Fig. 7.12 shows cell viability data of these groups. Group A has no significant difference in cell viability before and after pH adjustment, with the average cell viability of 99.71% and 99.47%, respectively, $p > 0.05$. Group B has significant difference in cell viability before and after pH adjustment, with the average cell viability of 96.78% and 76.69%, respectively, $p < 0.05$. Group C has significant difference in cell viability before and after pH adjustment, with the average cell viability of 0% and 7.05%, respectively, $p < 0.05$. Lastly, group D has significant difference in cell viability before and after pH adjustment, with the average cell viability of 0% and 0.14%, respectively, $p < 0.05$. Groups A-D, before and after pH adjustment, are all significantly different from group E, which has an average cell viability of 40.98%, $p < 0.05$.

Before pH Adjustment:



After pH Adjustment:

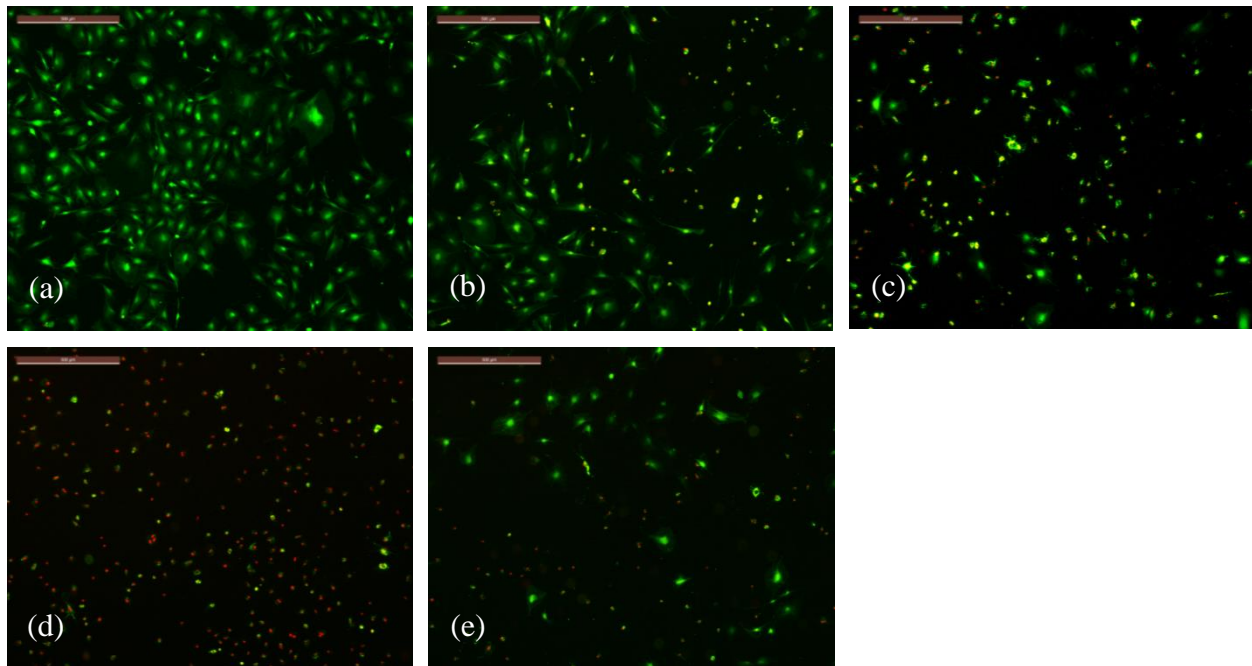


Figure 7.11 Live/dead images of MC3T3 cells treated with (A) Regular AMEM + 10% Regular FBS (RR), (B) Regular AMEM + 10% Modified FBS (RM), (C) Modified AMEM + 10% Regular FBS (MR), and (D) Modified AMEM + 10% Modified FBS (MM) for $t=24$ hours, and (E) 50% (Regular AMEM + 10% Regular FBS) + 50% (Modified AMEM + 10% Modified FBS) (50%), $n=3$. Cells were treated with the following solutions either with or without pH adjustment using HCl solution. Group E is a result of mixing (A) and (D) by 1:1 ratio to change the pH without adding the HCl solution (and therefore, there is no cell viability reading “before pH change”).

Cell Viability for Pre-Conditioned AMEM/FBS

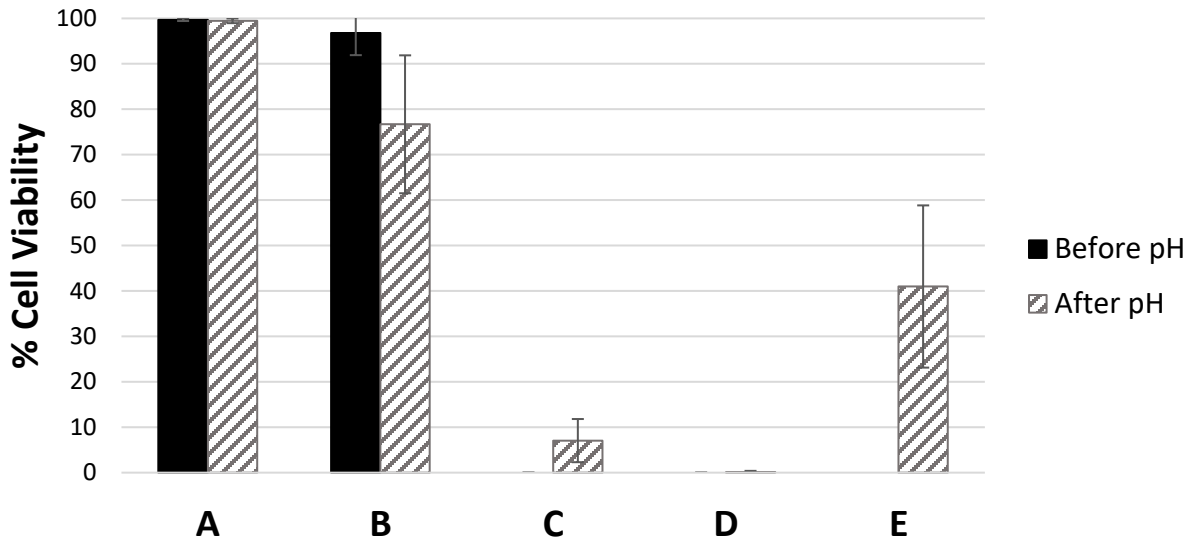


Figure 7.12 Cell viability of MC3T3 cells treated with media with the following treatment conditions A-E that are explained in Fig. 7.10-7.11, n=3. Group A, which is control, shows high cell viability. Group B also shows high cell viability, although after the pH adjustment, cell viability is slightly lower than that of before pH adjustment. Groups C and D have very low cell viability, regardless of pH adjustments. Since group C also shows very low cell viability as group D, this indicates that modified AMEM has an effect on cell viability more significantly than modified FBS. Group E shows cell viability approximately between that of A and D.

7.3.4 pH Effect (Comparing Cell Viability of Mg and Mg-Ti Treated vs. NaOH Treated)

In order to assess whether the direct killing of cells from exposure to particles and indirect killing of cells from “pre-conditioned” media are due to pre-corrosion of particles, cell viability was measured as a function of pH. Fig. 7.13 shows the actual pH that was measured over time. Because the media was exposed to 5% CO₂ buffer in the incubator, the pH neutralized over time, so that for example, for pH of 11, pH decreased to 9.69 by t= 1 hour and 8.2 by t= 24 hours. However, despite the fact that the pH did neutralize, the cell viability was still decreased over time as a function of pH. Fig. 7.14 shows cell viability of cells treated with different pH for either t= 1 hour or t= 24 hours. Cell viability did not change as pH increased when cells have only been treated for t= 1 hour, but cell viability decreased as low as 21% for pH of 11 for t= 24 hours. The cell viability of cells treated with NaOH have been compared to cell

viability of cells treated with Mg and Mg-Ti particles. Instead of plotting cell viability as a function of particle concentrations, which have been published before, cell viability has been plotted as a function of pH in order to compare to the cell viability of cells treated with Mg or Mg-Ti particles to that of cells treated with NaOH (Fig. 7.15). Cells treated with Mg and Mg-Ti particles had a decrease in cell viability as pH increased; however, cells treated with Mg and Mg-Ti particles killed cells by $t = 1$ hour while NaOH did not have any effect on cell viability at this time. Post hoc Tukey test shows that there is a statistical difference in cell viability among cells treated with NaOH, Mg particles, and Mg-Ti particles for $t = 1$ hour, $p < 0.05$. But when cells are treated for $t = 24$ hours, there is no statistical difference between Mg and Mg-Ti-treated groups, $p > 0.05$, but there is statistical difference between NaOH and Mg/Mg-Ti-treated groups, $p < 0.05$. Please note that before, post hoc Tukey test compared cell viability of Mg or Mg-Ti treated cells at the same particle concentrations, which shows significant difference between Mg and Mg-Ti. However, in this case, post hoc Tukey test compared cell viability of Mg or Mg-Ti treated cells at the same pH, which does not show significant difference between Mg and Mg-Ti, at least for the time point of $t = 24$ hours.

pH changes over time

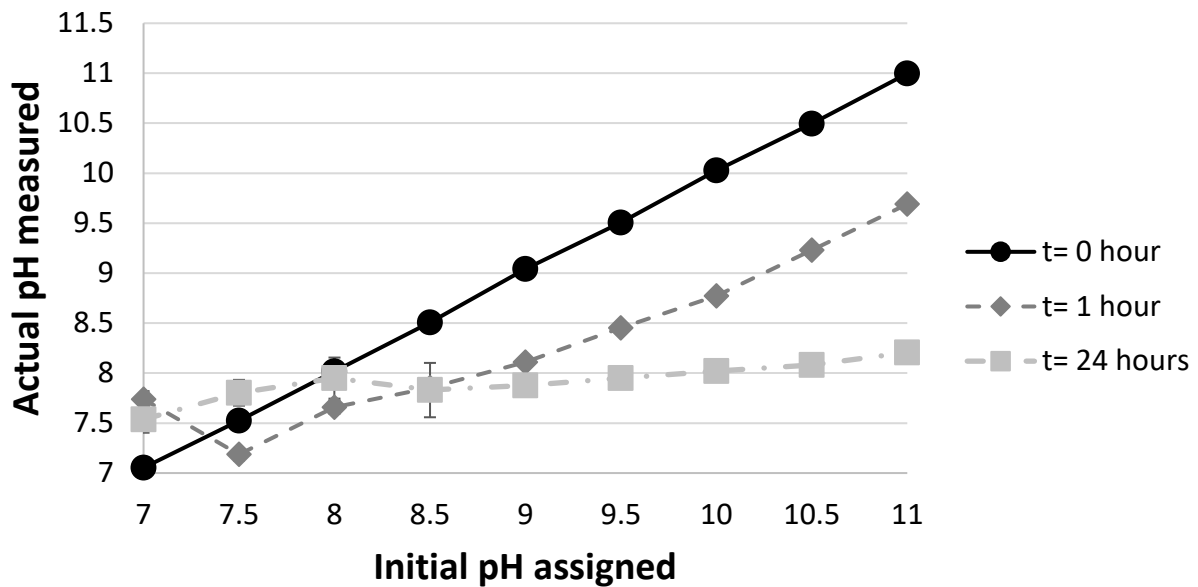


Figure 7.13 pH of complete media (AMEM + 10% FBS + 1% PSG) adjusted with HCl or NaOH from 7 to 11. The pH was measured at t= 0 hour (immediately after adding HCl or NaOH), t= 1 hour, and t= 24 hours, n=3. The pH shifted over time and the range of pH from 7 to 11 measured initially flattened to the range from 7.5 to 8.2, due to the buffering of 5% CO₂ and buffers present in the media.

pH vs. % Cell Viability

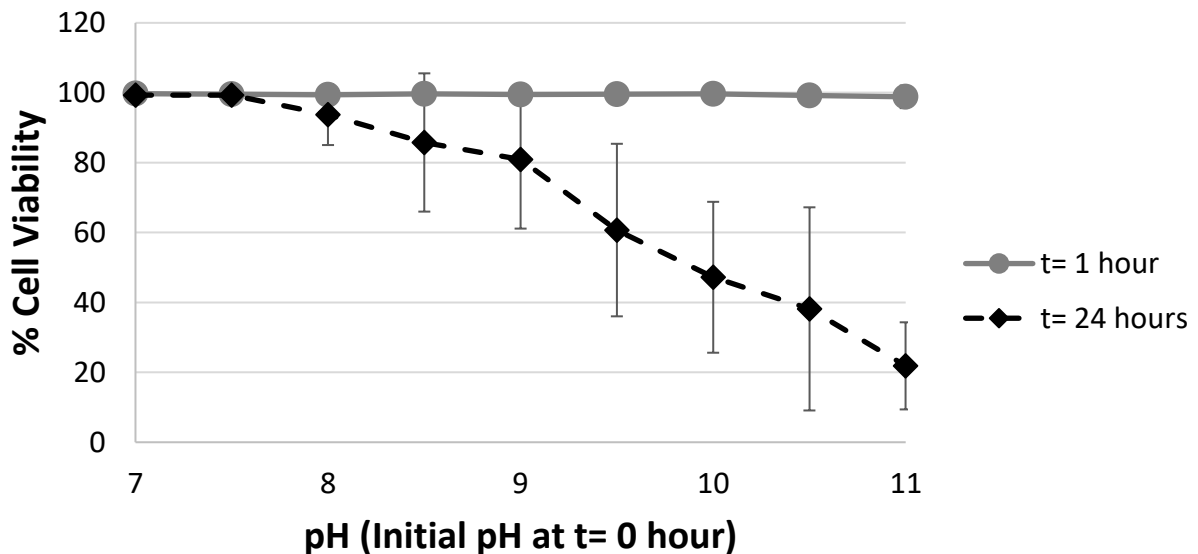
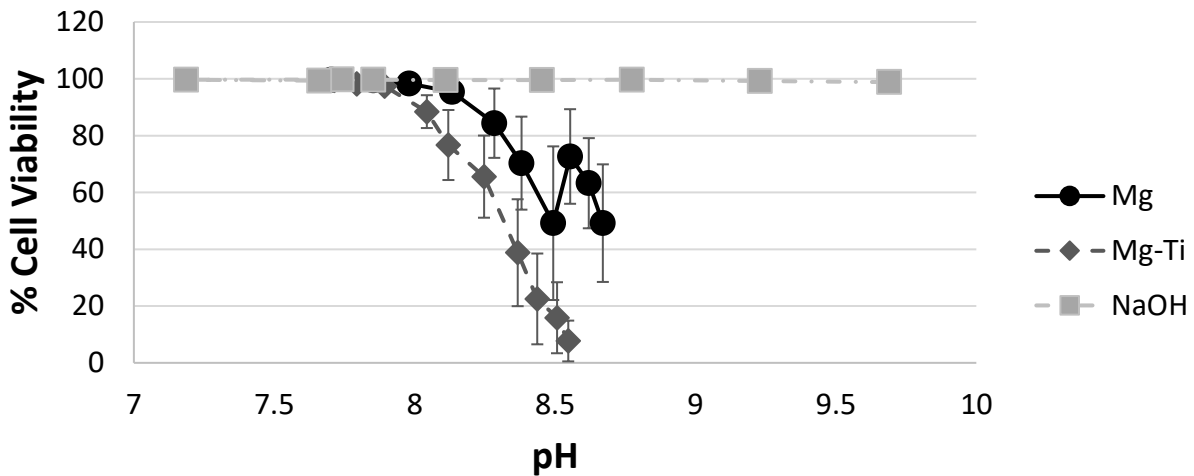


Figure 7.14 Cell viability of MC3T3 cells treated with different pH of complete media, n=3. After t= 1 hour, the cells were still viable, even at the pH of 11. However, at t= 24 hours, the cell viability decreased as a function of pH, where the cell viability was lowest at the highest pH of 11.

(a) Comparing % CV Mg and Mg-Ti Induced pH vs. NaOH Induced pH at t= 1 hour



(b) Comparing % CV Mg and Mg-Ti Induced pH vs. NaOH Induced pH at t= 24 hours

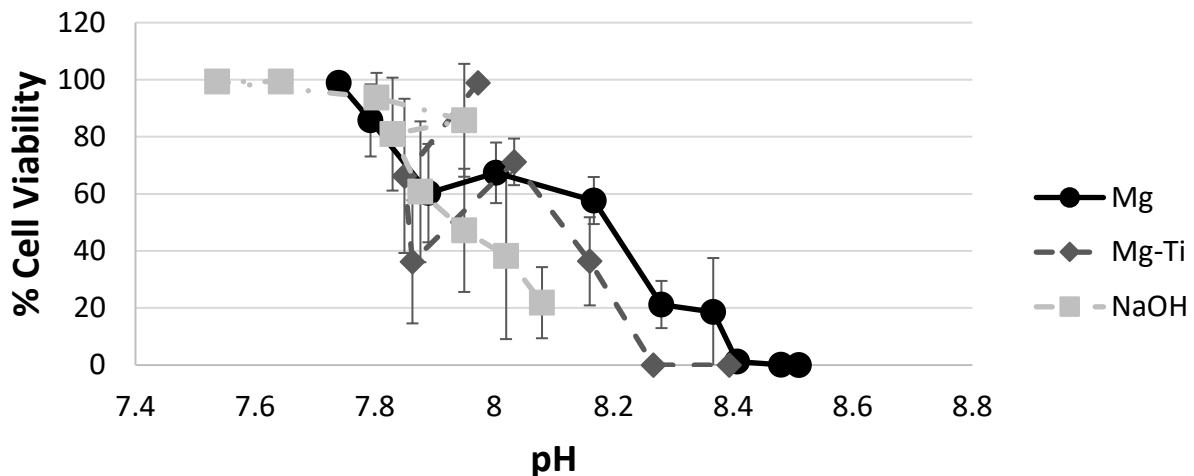


Figure 7.15 Comparison of cell viability of MC3T3 cells treated with Mg and Mg-Ti particles to cell viability of MC3T3 cells treated with NaOH to compare the pH effect, n=3. As shown in (a), at t= 1 hour, the NaOH induced killing did not have any effect yet at this time point, even at the highest pH of 11. However, Mg and Mg-Ti particles had significant decrease in cell viability at t= 1 hour, where the highest particle concentration had pH of 8.5, for both Mg and Mg-Ti. Post hoc Tukey tests showed that at t= 1 hour, Mg and Mg-Ti groups were significantly different from NaOH group and from each other ($p < 0.05$), except NaOH group compared to control groups (0 $\mu\text{g/ml}$ and no NaOH), n=3. (b) At t= 24 hours, cell viability of NaOH group decreased proportionally to the increase of pH. Post hoc Tukey test showed that at t= 24 hours, Mg and Mg-Ti groups were significantly different from NaOH group ($p < 0.05$), but not from each other, n=3.

Cell viability between cells treated with Mg/Mg-Ti modified media and cells treated with NaOH was also compared (Fig. 7.16). As shown, compared to NaOH group, which had cell viability of 93.7% and 60.71% at pH values of 8 and 9.5, respectively, group A had cell viability of 99.5%, for both before and after pH adjustment of 9.42 and 8.03. The pH adjusted using NaOH had lower cell viability at this pH level. For group B, cell viability was 96.7% and 76.69% before and after pH adjustment of 10.4 and 8.4, respectively, which can be compared relatively to NaOH group of pH 10.5, which resulted in cell viability of 38.16%, and pH of 8.5, which resulted in cell viability of 85.77%. For group B, cell viability was actually higher before adjusting the pH adjustment using HCl, again, resulting in lower cell viability despite the decrease of pH. And NaOH group at pH of 10.5 had much lower cell viability than compared to group B before pH adjustment. For group C, the cell viability was 0% and 7.05% before and after pH adjustment of 11.5 and 8.5, which can be compared to the NaOH group with cell viability of 85.77% and 21.86% at pH of 8.5 and 11. Unfortunately, cell viability for NaOH group was only measured up to pH of 11 because addition of too much NaOH to increase the pH may result in significant change of cell osmolality. However, group C shows that despite the re-adjustment of pH from 11.5 to 8.5, cell viability did not increase significantly, not even close to 85%, which is the cell viability at pH of 8.5. For group D, the cell viability was 0% and 0.13% before and after pH adjustment of 12.05 and 7.88, respectively, which can be compared to the NaOH group with cell viability of 93.71% and 21.86% at pH of 8 and 11. Again, despite the fact that pH was similar, NaOH group and group D after pH adjustment did not result in similar cell viability. Group D, despite the pH change, resulted in significant cell killing. Lastly, group E

had cell viability of 40.98% with pH of 10.83, which can be compared to pH of 11, which can be compared to either 38.16% of pH 10.5 and 21.96% of pH 11.

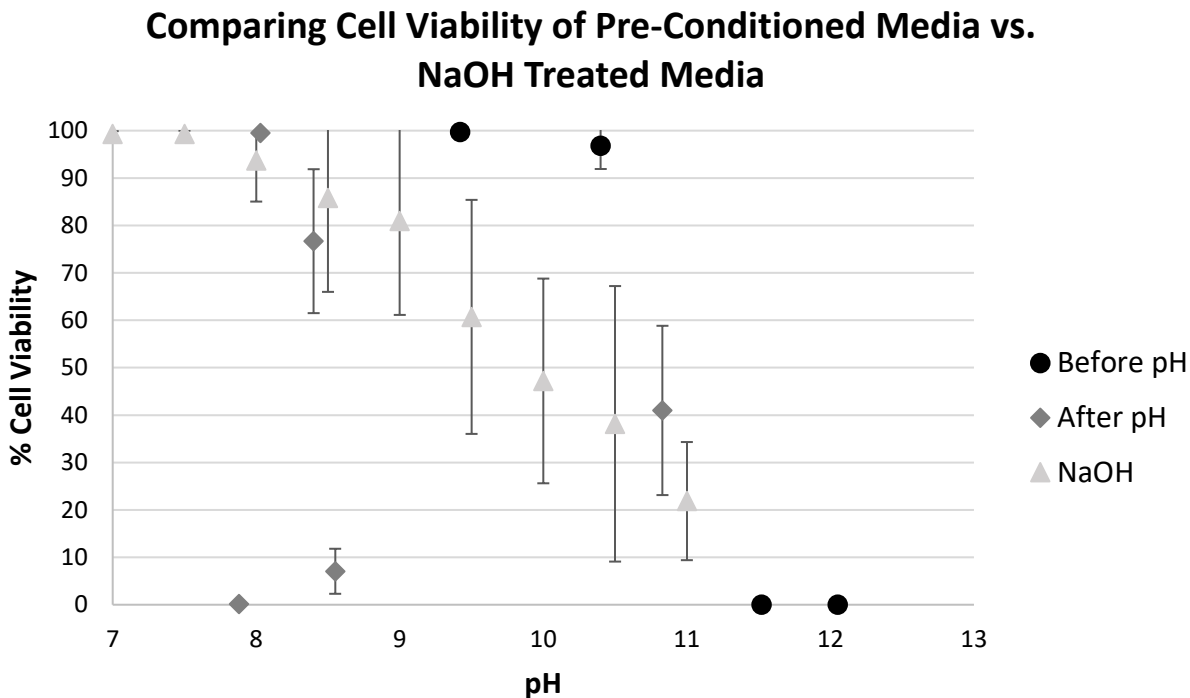


Figure 7.16 Comparison of cell viability between pre-conditioned media before and after adjusting pH groups (from Fig. 7.12) and NaOH-treated groups, n=3. Cell viability of pre-conditioned media before pH adjustment (groups A-D) dropped proportionally to the increase of pH. Cell viability of NaOH group also dropped proportionally to the increase of pH. However, cell viability of pre-conditioned media after pH adjustment (groups A-E) showed no correlation to pH levels. This shows that while pH is a contributing factor, pH is not the major factor killing cells after the media is pre-conditioned.

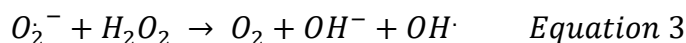
7.4 Discussion

There are important observations that should be made from this study. When same concentrations of Mg and Mg-Ti particles were corroded and hydrogen gas was measured over time, Mg-Ti particles produced more hydrogen gas than Mg. Chapter 4, however, showed that the pH values between Mg and Mg-Ti are the same. This is not possible based on the reduction reaction of water, where two moles of water (H_2O) reduce to produce one of mole hydrogen gas (H_2) and two moles of hydroxide ions (OH^-). One possibility is that Mg-Ti undergo different redox reactions than the one proposed for Mg. Many studies reported that pure Mg corrode to

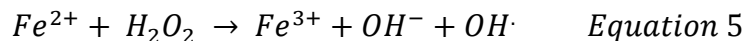
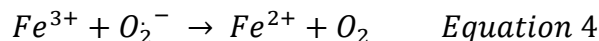
release two electrons, which then breaks the water into hydroxide and hydrogen gas. However, this may be just one type of reaction, and there may be other types of reactions that can occur. ROS are thought to occur in the presence of free metal ions via two types of reactions: Fenton reaction and Haber-Weiss reaction [19-20]. Fenton reaction involves oxidizing a free metal ion, for example Iron(II), by hydrogen peroxide, to Iron(III) to form a hydroxyl radical and a hydroxide ion (Equation 1). Another hydrogen peroxide molecule then can reduce Iron(III) back to Iron(II) to form a hydroperoxyl radical and a proton (Equation 2).



Equation 1 becomes part of Haber-Weiss reaction, where the net reaction of Haber-Weiss is:

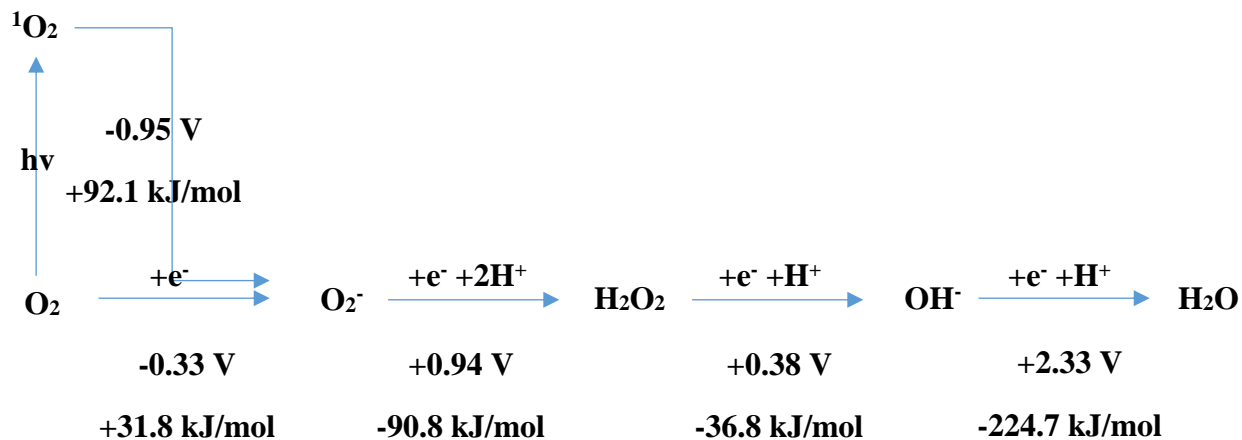


Where a typical iron-catalyzed Haber-Weiss reaction can be broken down to,

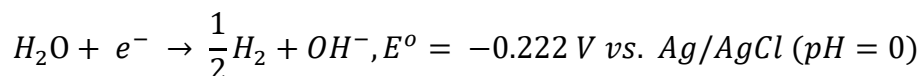
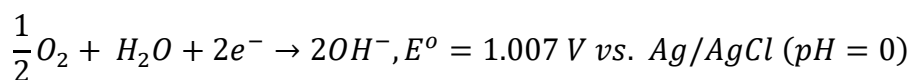


where a metal ion is used as a catalyst, to generate more toxic radicals from less reactive hydrogen peroxide and superoxide [21]. Although Fenton and Haber-Weiss reaction involves Fe^{2+}/Fe^{3+} metal ions as catalysts, but other metal cations can be involved, such as Mg^+/Mg^{2+} . Dioxygen (O_2) can also be converted into ROS by either energy transfer or monovalent reduction [22]. Singlet oxygen (1O_2), in which two electrons have opposite spins, can be formed when O_2 absorbs energy. Singlet oxygen then can go through a stepwise monovalent reduction resulting in the sequential formation of superoxide anion ($\cdot O_2^-$), hydrogen peroxide (H_2O_2), hydroxyl radical ($\cdot OH$), and finally, water (H_2O) (Fig. 7.17). The first reduction step is endergonic,

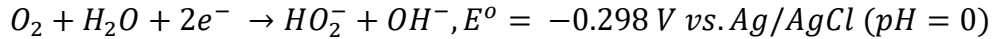
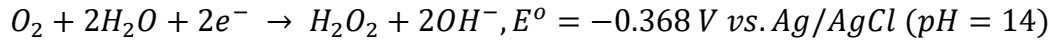
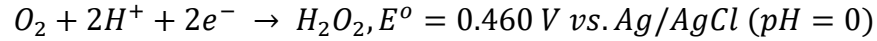
requiring energy and electron donation from transition metal ions, but the following one-electron reduction steps are exergonic and can occur spontaneously [22-23].



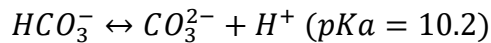
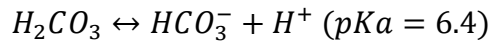
The superoxide produced from the dioxide or singlet oxygen is very short-lived (approximately 2 to 4 μs) and not readily diffusible, but may cause lipid peroxidation, thereby weakening cell membranes [22,24]. Hydrogen peroxide is a relatively long-lived (1 ms) and stable, so it can diffuse through membranes and reach cellular components such as nucleus distant from its site of synthesis [22,25]. Hydroxyl radical is highly reactive, which is considered one of the most harmful form of ROS, and has a half-life of 1 pico-second and has a very high affinity for biological molecules [22,26]. Since Mg^+ is not very stable ($\Delta G = +848.9 \text{ kJ/mol}$) than Mg^{2+} ($\Delta G = -454.8 \text{ kJ/mol}$), Mg^+ readily gives up the electron that is required for this monovalent reductions of dioxide oxygen to produce different types of ROS [27]. Ti from Mg-Ti also plays an important role, providing the surface for the reductions of water and oxygen to take place. The reductions of H_2O and O_2 at the Ti surface depends on the voltage, where reduction of H_2O arises at more negative potentials than the reduction of O_2 [19].



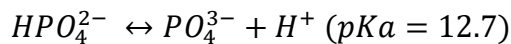
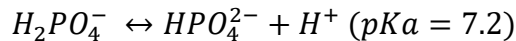
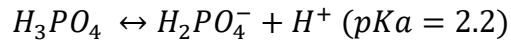
Clech et al. showed that under cathodic voltages (below -400 mV vs. Ag/AgCl), titanium oxide (TiO₂) surfaces can produce hydrogen peroxide (H₂O₂) [19,28]. And these are possible intermediate reactions that produce hydrogen peroxide.



Different types of reductions can occur; however, there are no reduction reactions that can produce hydrogen gas, but not hydroxide ions. So another possibility is that Mg-Ti does produce higher amounts of hydroxide ions compared to Mg due to faster corrosion rate, but the excess hydroxide ions produced by Mg-Ti must be taken up by the buffers found in cell culture media. The cell culture media (Minimum Essential Medium (MEM) Alpha Medium, Corning, Catalog #: 10-022-CV) used in the experiments has two buffers: sodium dihydrogen phosphate (NaH₂PO₄·H₂O, 140 mg/l) and sodium bicarbonate (NaHCO₃, 2200 mg/l). Sodium bicarbonate is one of the most common buffers found in the body.



Carbonic acid (H₂CO₃) can dissociate into bicarbonate (HCO₃⁻) and a proton (H⁺), and HCO₃⁻ can dissociate into carbonate (CO₃²⁻) and a proton (H⁺), depending on the pH. Sodium dihydrogen phosphate (NaH₂PO₄) is also commonly used as a buffer.



Phosphate Buffering

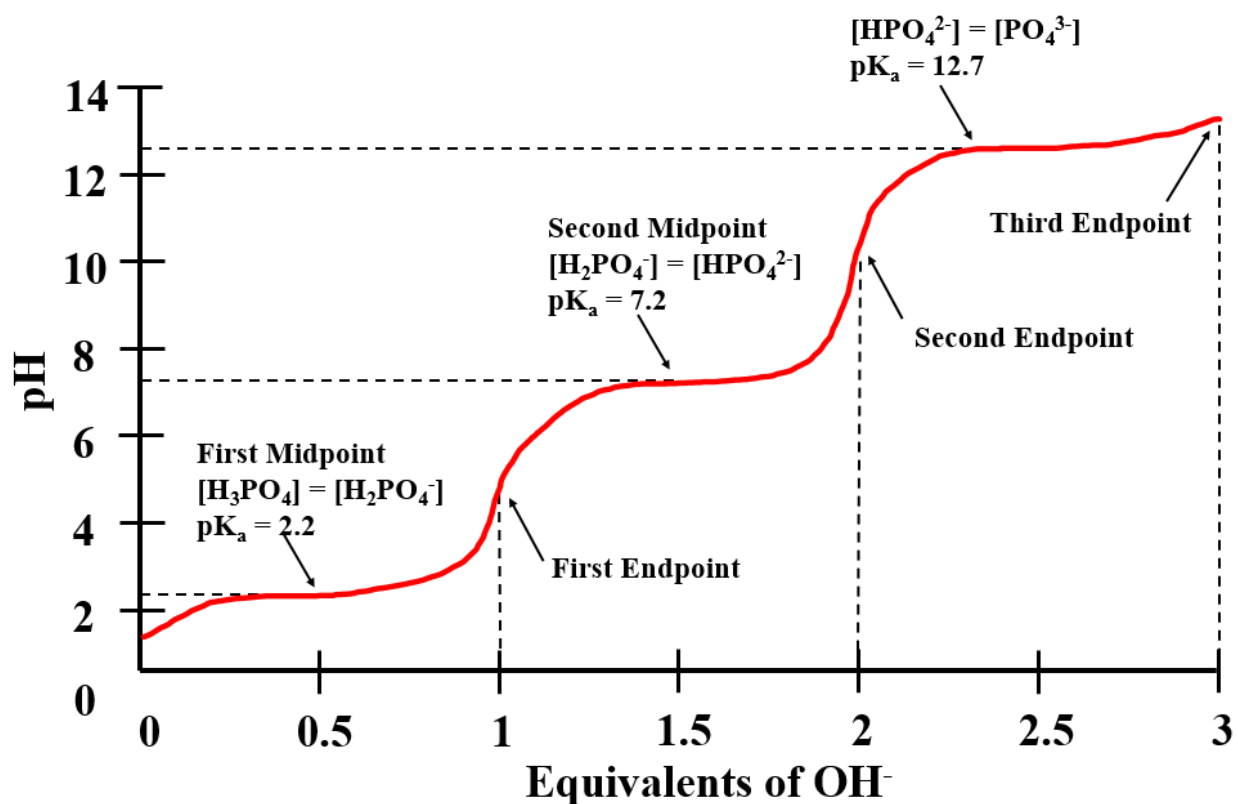
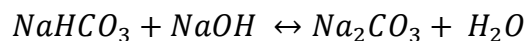
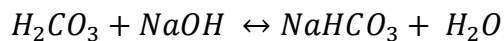


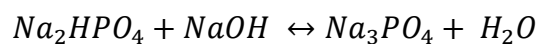
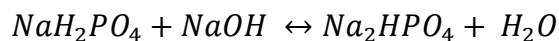
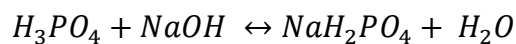
Figure 7.17 pH titration curve with phosphate buffering.²⁹

These buffers can also react with sodium hydroxide (NaOH), and produce water as a by-product.

For carbonate-based buffers,



For phosphate-based buffers,



One of the highest Mg concentrations used to kill all cells was 1750 µg/ml (mg/l). Since one mole of Mg produces two moles of OH⁻, 2448 mg/l of OH⁻ will be produced if 1750 mg/l of Mg is fully corroded. The calculation is shown.

$$\frac{1750 \text{ mg}}{l} \text{ Mg} * \frac{1 \text{ mol}}{24305 \text{ mg}} \text{ Mg} * \frac{2 \text{ mol OH}^-}{1 \text{ mol Mg}} * \frac{17000 \text{ mg}}{1 \text{ mol OH}^-} = 2448 \text{ mg/l OH}^- \text{ produced}$$

$$\frac{2448 \text{ mg}}{l} \text{ OH}^- * \frac{1 \text{ g}}{1000 \text{ mg}} * \frac{1 \text{ mol}}{17 \text{ g}} = 41.616 \frac{\text{mol}}{l} (\text{M})\text{OH}^-$$

$$[41.616] = 10^{-pOH}$$

$$pOH = 1.62$$

$$pH = 14 - 1.62 = 12.38$$

When 2448 mg/l of OH⁻ is produced, theoretically pH should be 12.38, but the actual pH values measured for this concentration is around 8.7, and therefore, the decrease of OH⁻ must be due to buffers, making the pH values of Mg and Mg-Ti to be the same between 7-9.

When cell culture media was “pre-conditioned” by pre-corroding the Mg or Mg-Ti particles and the pre-conditioned media was given to the cells, the cells died. When AMEM and FBS were “pre-conditioned” separately, the solution morphology changed, where the “pre-conditioned” solution had cloudy appearance, compared to its control counterparts, which was clear, indicating that some structural changes of different elements in solution have taken place. Translucent solution transforming into opaque solution must mean that constituents suspended in solution have visibly gotten bigger to scatter light. SEM images of “pre-conditioned” AMEM showed aggregates of some particulates that were not found in control AMEM. The pH of the “pre-conditioned” AMEM and FBS were higher, up to 12, than the pH values of Mg and Mg-Ti particles ranging from 0-2500 µg/ml for t= 3 days, up to 9 (Chapter 4). This makes sense because 0.5 g in 50 ml solution yields 10,000 µg/ml and the solution corroded for longer period

of time, $t= 5$ days. However, pH was not a significant factor in cytotoxicity of “pre-conditioned” solutions. The pH values were different for each group, where RR (made of regular AMEM and regular FBS) had the lowest pH of 9.43 and MM (made of modified AMEM and modified FBS) had the highest pH of 12.08. This is due to the volume ratios of AMEM and FBS, where complete media consists of AMEM+ 10% FBS, so that the pH of complete media is closer to the pH of AMEM than FBS. So the pH of RM, made of regular AMEM and modified FBS, will be lower than that of MR, made of modified AMEM and regular FBS. The pH from RR, RM, MR, to MM increase linearly. However, cell viability does not decrease linearly. There is a significant drop of cell viability for MR and MM. In fact, for RM, the pH is 10.5, and for MR, the pH is 11.5, where the difference of pH is 1. However, RM has cell viability of 96% while MR has cell viability of 0%. pH was eliminated as a factor, by decreasing the pH values of these groups, to close to physiological pH. After the pH change, RM has cell viability of 77%, which is actually lower than before pH change, probably addition of NaOH increased the osmolality of the solution, disrupting cell function and causing some cell death. MR has cell viability of 7%, which is higher than before pH change, but still significantly lower in cell viability compared to RM. For MM, all cells died regardless of pH change. If pH is the sole or major factor in cytotoxicity, cell viability after pH change should be significantly higher. Regardless of pH, cell viability of MR and MM was significantly lower than that of RR and RM. This showed that AMEM significantly influences cell viability, since RM (modification of FBS alone) did not affect cell viability that significantly. This does not mean, however, that FBS is not modified, but that cells did not necessarily need the elements in FBS to survive for short-term.

Cell viability of cells treated with different pH levels (NaOH alone) was compared to Mg and Mg-Ti particles (part of this data has been shown in Chapter 3). Different concentrations of

NaOH was added in cell culture media to make pH ranging from 7 to 11. However, over time, this range narrowed, as the 5% CO₂ buffer and the buffers in media brought the pH level down. While cell viability of NaOH group was viable at t=1 hour, cell viability decreased proportional to the pH level by t= 24 hours, with cell viability of 21% for pH 11 group (initial pH was 11 at t= 0 hour, but decreased to 8.2 by t= 24 hours). When cells of NaOH group were compared to Mg and Mg-Ti particle-treated groups for these time periods (t= 1 hour and t= 24 hours), there was something very interesting to note. Although the pH alone did kill cells, pH did not kill cells as quickly as Mg or Mg-Ti. At t= 1 hour, even pH of 11 had high cell viability of 100%, but Mg and Mg-Ti group had cell viability exponentially decaying to 50% and 7%, respectively, at pH of 8.5-8.7. So even before pH has any effect on cells, something else killed the cells for those treated with Mg or Mg-Ti particles very quickly, within t= 1 hour. Cell viability of NaOH treated groups was also compared to that of “pre-conditioned” groups to show that pH gave no correlation to the cell viability for those treated with “pre-conditioned” solutions.

So based on this study, alkaline pH is not a major reason for cytotoxicity of Mg or Mg-Ti directly killing the cells or cytotoxicity of “pre-conditioned” media. Mg or Mg-Ti kill cells more effectively and more quickly than alkaline pH. Alkaline pH is also not the cause of enhanced cytotoxicity of Mg-Ti. The only toxic species known to kill cells this quickly in dosage dependent manner is ROS. High concentrations of ROS are known to directly induce cell death [30-31]. Protein or amino acid oxidation, which is covalent modification of a protein or amino acid, can occur due to ROS, altering protein functions [21]. Certain types of amino acids, such as sulfur-containing amino acids, are very susceptible to oxidation [31]. Oxidation of sulfhydryl groups, reduction of disulfide bonds, protein-protein cross-linking, and peptide fragmentation due to ROS have also been reported [32]. For example, oxidation of cysteine causes disulfide

cross-linking while oxidation of tyrosine cause Tyr-Tyr cross-links [33]. And these free amino acids are found in AMEM (formulation of AMEM shown in Fig. 7.18) [34]. Although not all proteins are known in FBS and the concentrations of FBS vary in different batches, proteins that are found in FBS are albumin, globulin, fetuin, fibronectin, transferrin, protease inhibitors, and etc. [35].

All these elements are susceptible to ROS attack, and therefore proteins and amino acids can be modified. Further analysis is needed to prove that significant concentration of ROS is being generated due to Mg or Mg-Ti corrosion and further investigation is needed to prove that proteins and amino acids in the cell culture medium are indeed been modified due to Mg or Mg-Ti corrosion.

Cat. No.	10-022	15-012	50-012	Components (continued)	(10- 022)	(15- 012)	(50- 012)
Description	Liquid , 1x	Liquid , 1x	Powder	<i>Amino Acids</i>			
Units	mg/L	mg/L	mg/L				
				Ascorbic acid	50	50	50
				Biotin	0.1	0.1	0.1
				D-Calcium pantothenate	1	1	1
				Choline chloride	1	1	1
				Folic acid	1	1	1
				<i>l</i> -inositol	2	2	2
				Nicotinamide	1	1	1
				Pyridoxine * HCl	1	1	1
				Riboflavin	0.1	0.1	0.1
				Thiamine * HCl	1	1	1
				Vitamin B12	1.36	1.36	1.36
				<i>Inorganic Salts</i>			
CaCl ₂ (anhydrous)	200	200	200				
KCl	400	400	400				
MgSO ₄ (anhydrous)	97.7	97.7	97.7				
NaCl	6800	6800	6800				
NaH ₂ PO ₄ * H ₂ O	140	140	140				
NaHCO ₃	2200	2200	--				
				<i>Amino Acids</i>			
L-Alanine	25	25	25	<i>Other</i>			
L-Arginine * HCl	126.4	126.4	126.4	D-Glucose	1000	1000	1000
L-Asparagine * H ₂ O	50	50	50	Lipotic acid	0.2	0.2	0.2
L-Aspartic Acid	30	30	30	Phenol red * Na	10	10	10
L-Cysteine * HCl * H ₂ O	100	100	100	Sodium pyruvate	110	110	110
L-Cysteine * 2HCl	31.2	31.2	31.2	<i>Nucleosides</i>			
L-Glutamic Acid	75	75	75	Thymidine	10	--	--
L-Glutamine	292	--	292	Adenosine	10	--	--
Glycine	50	50	50	Cytidine	10	--	--
L-Histidine * HCl * H ₂ O	41.9	41.9	41.9	Guanosine	10	--	--
L-Isoleucine	52.5	52.5	52.5	Uridine (anhydrous)	10	--	--
L-Leucine	52.5	52.5	52.5	2'-Deoxyadenosine * H ₂ O	10	--	--
L-Lysine * HCl	72.5	72.5	72.5	2'-Deoxycytidine * HCl	11	--	--
L-Methionine	15	15	15	2'-Deoxyguanosine * H ₂ O	10	--	--
L-Phenylalanine	32.5	32.5	32.5	Add			
L-Proline	40	40	40	NaHCO ₃			
L-Serine	25	25	25	Powder (g/L)	--	--	2.2
L-Threonine	47.6	47.6	47.6	7.5% solution (mL/L)	--	--	29.33
L-Tryptophan	10	10	10	L-Glutamine			
L-Tyrosine * 2Na * 2H ₂ O	51.9	51.9	51.9	Powder (mg/L)	--	292	292
L-Valine	46.8	46.8	46.8	200 mM Solution (mL/L)	--	10	10

Figure 7.18 Formulations of AMEM by Corning, MediaTech Inc. ³⁴

7.5 Conclusion

In conclusion, Mg-Ti corrodes more quickly than Mg due to galvanic coupling, producing larger hydrogen gas volume. ROS are produced as Mg or Mg-Ti corrodes, which kill cells directly but also indirectly by modifying proteins and free amino acids. Although not directly proven which ROS are produced by Mg or Mg-Ti corrosion yet, ROS produced by Mg or Mg-Ti kill cells very effectively and more quickly compared to alkaline pH.

7.6 Acknowledgements

This work was supported, in part, by DePuy Synthes.

References

1. Gu XN, Zheng YF. A Review on Magnesium Alloys as Biodegradable Materials, *Front. Mater. Sci. China* 2010; 4(2): 111-5.
2. Zhang E, Zu L, Yu G, Pan F, Yang K. In Vivo Evaluation of Biodegradable Magnesium Alloy Bone Implant in the First 6 Months Implantation, *J. Biomed. Mater. Res. A* 2009; 90A(3): 882-93.
3. Di Mario C, Griffiths H, Goktekin O, Peeters N, Verbist J, Bosiers M, Deloose k, Bernhard H, Rohde R, Kasese V, Ilsley C, Erbel R. Drug-Eluting Bioabsorbable Magnesium Stent, *J. Interv. Cardiol.* 2004; 17(6): 391-5.
4. Chen Y, Xu Z, Smith C, Sankar J. Recent advances on the development of magnesium alloys for biodegradable implants, *Acta Biomater.* 2014; 10: 4561-73.
5. Witte F, Hort N, Vogt C, Cohen S, Kainer KU, Willumeit R, Feyerabend F. Degradable Biomaterials Based on Magnesium Corrosion, *Curr. Opin. Solid State Mater. Sci.* 2008; 12(5-6): 63-72.
6. Saris NEL, Mervaala E, Karppanen H, Khawaja JA, Lewenstam A. Magnesium: An Update on Physiological, Clinical, and Analytical Aspects, *Clin. Chim. Acta* 2000; 294: 1-26.
7. Song G, Song S. A Possible Biodegradable Magnesium Implant Material, *Corros. Sci.* 2007; 9: 298-302.
8. Seal CK, Vince K, Hodgson MA. Biodegradable Surgical Implants Based on Magnesium Alloys- A Review of Current Research, *IOP Conf. Series: Mater. Sci. Eng.* 2009; 4: 012011.

9. Gao JC, Qiao LY, Xin Long. Effect of Mg²⁺ Concentration on Biocompatibility of Pure Magnesium, *Front. Mater. Sci. China* 2010; 4(2): 126-31.
10. Wang J, Witte F, Xi T, Zheng Y, Yang K, Yang Y, Zhao D, Meng J, Li Y, Li W, Chan K, Qin L. Recommendation for Modifying Current Cytotoxicity Testing Standards for Biodegradable Magnesium-Based Materials, *Acta Biomater.* 2015; 21: 237-49.
11. Zeng R, Dietzel W, Witte F, Hort N, Blawert C. Progress and Challenge for Magnesium Alloys as Biomaterials, *Adv. Eng. Mater.* 2008; 10(8): B3-B14.
12. Song G, Atrens A, St John D, Wu X, Nairn J. The Anodic Dissolution of Magnesium in Chloride and Sulphate Solutions, *Corr. Sci.* 1997; 39(10-11): 1981-2004.
13. Song G. Control of Biodegradation of Biocompatible Magnesium Alloys, *Corr. Sci.* 2007; 49: 1696-1701.
14. Hiromoto S, Tomozawa M. Hydroxyapatite Coating of AZ31 Magnesium Alloy by a Solution Treatment and its Corrosion Behavior in NaCl Solution, *Surf. Coat. Technol.* 2011; 205(19): 4711-9.
15. Witte F, Kaese V, Haferkamp H, Switzer E, Meyer-Lindenberg A, Wirth CJ, Windhagen H. In Vivo Corrosion of Four Magnesium Alloys and the Associated Bone Response, *Biomaterials* 2005; 26: 3557-63.
16. Zhang E, Xu L, Yu G, Pan F, Yang K. In Vivo Evaluation of Biodegradable Magnesium Alloy Bone Implant in the First 6 Months Implantation, *J. Biomed. Mater. Res. Part A.* 2009; 90A(3): 882-93.
17. Robinson DA, Griffith RW, Shechtman D, Evans RB, Conzemi MG. In Vitro Antibacterial Properties of Magnesium Metal against Escherichia Coli, Pseudomonas Aeruginosa and Staphylococcus Aureus. *Acta Biomater.* 2010; 6(5): 1869-877.

18. Kim J, Gilbert JL. Cytotoxic Effect of Galvanically Coupled Magnesium-Titanium Particles, *Acta Biomater.* 2016; 30: 368-77.
19. Sivan, Shiril, "Electrochemical Aspects of Metallic Biocompatibility" (2015). *Dissertations - ALL*. Paper 238. <http://surface.syr.edu/etd/238>.
20. Barbusiński K. Fenton Reaction- Controversy Concerning the Chemistry, *Ecol. Chem. Eng. S* 2009; 16(3): 347-58.
21. Kehrer JP. The Haber-Weiss Reaction and Mechanisms of Toxicity, *Toxicol.* 2000; 149: 43-50.
22. Akinci S. "Chapter 2. Drought and Its Consequences to Its Plants- From Individual to Ecosystem." *Responses of Organisms to Water Stress*. By Ciríaco da Silva E, Bandeira de Albuquerque M, Dias de Azevedo Neto A, Dias da Silva Junior C. Rijeka, Croatia: InTech, 2013. 17-47.
23. Azevedo Neto AD, Gomes-Filho E, Prisco JT. Salinity and Oxidative stress. In: Khan NA, Singh S (ed.) *Abiotic stress and plant responses*. New Delhi: I.K. International; 2008. 57-82.
24. Smirnoff N. The Role of Active Oxygen in the Response of Plants to Water Deficit and Desiccation, *New Phytologist.* 1993; 125: 27-58.
25. Willekens H, Chamnongpol S, Davey M, Schraudner M, Langebartels C, Van Montagu M, Inzé D, Van Camp W. Catalase is a Sink for H₂O₂ and is Indispensable for Stress in C₃ Plants, *EMBO Journal* 1997; 16: 4806-16.
26. Dat J, Vandenabeele S, Vranová E, Van Montagu M, Inzé D, Van Breusegen F. Dual Action of the Active Oxygen Species During Plant Stress Responses, *Cell Mol. Life Sci.* 2000; 57: 779-95.

27. Dean JA. *Lange's Handbook of Chemistry*, 12th ed.; McGraw-Hill: New York, New York, 1979; p. 9-4–9-94.
28. Clechet P, Martelet C, Martin J, Olier R. Photoelectrochemical Behaviour of TiO₂ and Formation of Hydrogen Peroxide, *Electrochim. Acta*. 1979; 24(4): 457-461.
29. Ramanathan N. "Acid-Base Equilibria, PH and Buffers." *LinkedIn SlideShare*. LinkedIn, 8 Aug. 2013. Web. 18 Sept. 2016.
30. Martin KR, Barrett JC. Reactive Oxygen Species as Double-Edged Swords in Cellular Processes: Low-Dose Cell Signaling Versus High-Dose Toxicity, *Hum. Exp. Toxicol*. 2002; 21: 71-5.
31. Bergamini CM, Gambetti S, Dondi A, Cervellati C. Oxygen, Reactive Oxygen Species and Tissue Damage, *Curr. Pharm. Des*. 2004; 10: 1611-26.
32. Cabiscol E, Tamarit J, Ros J. Oxidative Stress in Bacteria and Protein Damage by Reactive Oxygen Species, *Internatl. Microbiol*. 2000; 3: 3-8.
33. Stadtman ER. Oxidation of Free Amino Acids and Amino Acid Residues in Proteins by Radiolysis and by Metal-Catalyzed Reactions, *Annu. Rev. Biochem*. 1993; 62: 797-821.
34. *Minimum Essential Medium (MEM) Alpha Medium*. Corning, MediaTech, Inc. <<http://cellgro.com/products/classical-media/minimum-essential-medium-mem-alpha-medium/minimum-essential-medium-mem-alpha-medium.html>>.
35. Jha N. "Culture Media for Animal Cells: An Overview." *Biology Discussion*. Biology Discussion, 16 Oct. 2015. Web. 18 Sept. 2016. <<http://www.biologydiscussion.com/biotechnology/animal-biotechnology/culture-media-for-animal-cells-an-overview/10499>>.

8 Characterization of Mg-Ti Particle Corrosion in Different Solutions

8.1 *Introduction*

There are many studies showing the effects of proteins on metal corrosion [1-12], where usually proteins either accelerate or decelerate the metal corrosion, depending on the metal alloy type, protein type, and pH. One of the principal proteins studied is albumin because albumin is the most common protein found in the extracellular fluid [1]. One study shows that when albumin was added to the PBS, albumin increased the corrosion resistance of Ti alloy, especially at higher pH [2]. This study explains that this is due to albumin's isoelectric point of 4.5, allowing albumin to be negatively charged at pH higher than 4.5, so that negatively charged albumin can form metal/protein/hydroxide complex, which then adsorbs to the metal surface and restricts metal dissolution [2]. Another study shows that the presence of collagen or albumin mainly affects the cathodic polarization behavior, while they have no effect on the anodic behavior of the Ti alloy [3]. XPS analysis showed that the composition of the surface oxide films had no difference in the presence or absence of collagen, not being incorporated into the oxide film but acting as a cathodic corrosion inhibitor by reducing the concentration of oxygen [3]. For albumin, the inhibition mechanism of metal corrosion is proposed as preferential adsorption on the metal surface, thus blocking sites where oxygen should react with the metal surface [3]. This hypothesis is further supported by the fact that albumin has no effect on metal corrosion in the HEPES buffered solutions, since albumin adsorption to the metal surface competes with the adsorption of HEPES molecules, which contain polar SO_3^- end and nitrogen group that promote adsorption on polar surfaces [3]. For pure Mg, protein-containing solutions generally retard the corrosion rate of Mg, where the corrosion rate of pure Mg in NaCl solution is about 100 times larger than the corrosion rate of pure Mg in E-MEM + FBS, which is very

similar to human blood plasma [4-5]. The total Mg^{2+} release is lower for E-MEM + FBS than any other solutions (NaCl, E-MEM, Earle's solution), suggesting that the protein adsorption onto the Mg surface significantly reduces the Mg ion dissolution [4].

As much as proteins affect metal corrosion, metal corrosion affects proteins as well. Cathodic reduction of metal surfaces produces ROS, which can alter proteins. Some protein modifications are documented as oxidation of sulfhydryl groups, reduction of disulfides, oxidative adduction of amino acid residues close to metal-binding sites via metal-catalyzed oxidation, reaction with aldehydes, protein-protein cross-linking, and peptide fragmentation [13-15]. When proteins are exposed to ROS, protein modifications lead to protein's functional changes that disturb cellular metabolism [13]. Cytosolic proteins maintain their cysteines reduced in the native form, while secreted proteins maintain their cysteines in disulfide bonds, and therefore, unwanted disulfide bonds may be produced among cytosolic proteins due to ROS exposure, a situation called "disulfide stress" [13,16]. However, disulfide bonds are reversible and so the damage is not permanent. Oxidation of amino acids in a protein, however, is irreversible and is achieved via two mechanisms: ionizing radiation and metal ion-catalyzed oxidation reactions. Radiolysis of water produces hydroxyl radicals ($HO\cdot$), which then react with an α -hydrogen atom of an amino acid to form a carbon centered radical. In the presence of oxygen, an alkoxy radical ($RO\cdot$) is produced, which then cleaves the peptide bond by diamide or α -amidation pathway [13,17]. In the absence of oxygen, the carbon-centered radical reacts with another protein to form protein-protein crosslinked derivatives [13, 18]. For metal-catalyzed oxidation of proteins, amino acid residues are oxidized by hydroxyl radical (produced by Fenton reaction) close to the cation-binding site [13]. The main protein modifications due to metal-catalyzed oxidation are loss of catalytic activity of proteins, amino acid modifications, carbonyl

group formation, fragmentation, formation of protein-protein crosslinks, formation of S-S disulfide bonds, and increased susceptibility to proteolysis (breakdown of proteins to amino acids) [13]. Amino acid modifications are as follows in Fig. 8.1.

Amino Acid	Oxidation Products
Arginine	Glutamic Semialdehyde
Cysteine	Disulfides, Cysteic Acid
Glutamyl	Oxalic Acid, Pyruvic Acid
Histidine	2-Oxohistidine, Asparagine, Aspartic Acid
Lysine	2-Aminoadipic Semialdehyde
Methionine	Methionine Sulfoxide, Methionine Sulfone
Phenylalanine	2,3-Dihydroxyphenylalanine, 2-,3-, and 4-Hydroxyphenylalanine
Proline	2-Pyrrolidone, 4-and5-Hydroxyproline Pyroglutamic Acid, Glutamic Semialdehyde
Threonine	2-Amino-3-Ketobutyric Acid
Tryptophan	2-,4-,5-,6-, and 7-Hydroxytryptophan, Nitrotryptophan, Kynurenine, 3-Hydroxykynurenine, Formylkynurenine
Tyrosine	3,4-Dihydroxyphenylalanine, Tyr-Tyr Cross-Link, Try-O-Tyr, Cross-Linked Nitrotyrosine

Figure 8.1 A table showing amino acids in proteins that can be oxidized and the oxidized products that are formed.^{13,19}

Some enzymes with active iron-sulfur carriers are highly sensitive to inactivation by O_2^- , such as *E. coli* aconitase [13,20]. Oxidized proteins can be removed by proteasomes, which are found in cells to degrade unneeded or damaged proteins. Ubiquitin, a regulatory protein, binds to a substrate protein (called ubiquitination) to signal for the degradation of the substrate protein by proteasome [13]. There are also various heat-shock proteins, which act as chaperones to help refold damaged proteins into proper tertiary forms [13]. However, despite the mechanisms to reduce damaged proteins, heavily oxidized proteins, which are extensively cross-linked and aggregated, cannot be degraded easily, and can also inhibit proteases from degrading other oxidized proteins, causing their accumulation [13].

Previous study by Kim and Gilbert et al. showed that corrosion of Mg or Mg-Ti particles in cell culture medium containing free amino acids and proteins have altered the solution

properties, such as its opacity, indicating that the constituents in the solution have been modified. When pre-conditioned media was given to the cells, they died, even though there were no particles directly corroding in the presence of cells. The by-products, such as hydroxide ions, Mg ions, and hydrogen gas, have been eliminated as major causes of the cytotoxicity of pure Mg and also the enhanced cytotoxicity of galvanically coupled Mg-Ti. Hydrogen gas escapes to the atmosphere, so it has been eliminated as a factor. Although the actual Mg ion concentrations and osmolality were not experimentally measured, the theoretical calculation of expected Mg ion concentrations and osmolality (when Mg particles fully corroded) were still well within the reasonable range for the cells. pH was measured, which showed that increased pH due to hydroxide ions could not explain the enhanced cytotoxicity of Mg-Ti compared to Mg and also the killing of cells by pre-conditioned media. Direct particle-killing killed cells more quickly than alkaline pH, which showed that something else was killing cells even before alkaline pH had any cytotoxic effect. Therefore, an alternative mechanism of killing was identified. The hypothesis of the previous study was that the ROS generated by corrosion of Mg or Mg-Ti (where Mg-Ti generated higher concentration of ROS due to faster corrosion) not only can directly kill cells nearby the particles, but also may affect the free amino acids and proteins in solution, modifying their structure, thus making them harmful to the cells. In order to prove this hypothesis, this study investigated the corrosion effect of Mg or Mg-Ti on a single-protein fibrinogen solution to see if there is any structural modification of fibrinogen.

Fibrinogen is a glycoprotein that helps to form blood clots. The fibrinogen molecule has a molecular weight of 340 kDa, that can be converted to fibrin by thrombin during blood clot formation [20]. Fibrinogen has a rod-like shape with dimensions of 9 x 45 x 6 nm and has a negative net charge at physiological pH because fibrinogen has an isoelectric point at pH of 5.2

[20]. At the molecular level, fibrinogen is a dimer with two outer D domains, each connected by a coiled-coil segment to its central E domain [21]. The fibrinogen molecule consists of two sets of three polypeptide chains termed $A\alpha$, $B\beta$, and γ , which are joined together in the N-terminal E domain by five symmetrical disulfide bridges (Fig. 8.2) [21]. $A\alpha$ chain consists of 610, $B\beta$ chain 461, and γ chain 411 amino acid residues, where the molecular weight of $A\alpha$, $B\beta$, and γ chains are 63.5 kDa, 56 kDa, and 47 kDa [21]. The concentrations of fibrinogen in the blood plasma ranges from 200-400 mg/dl in an average human body.

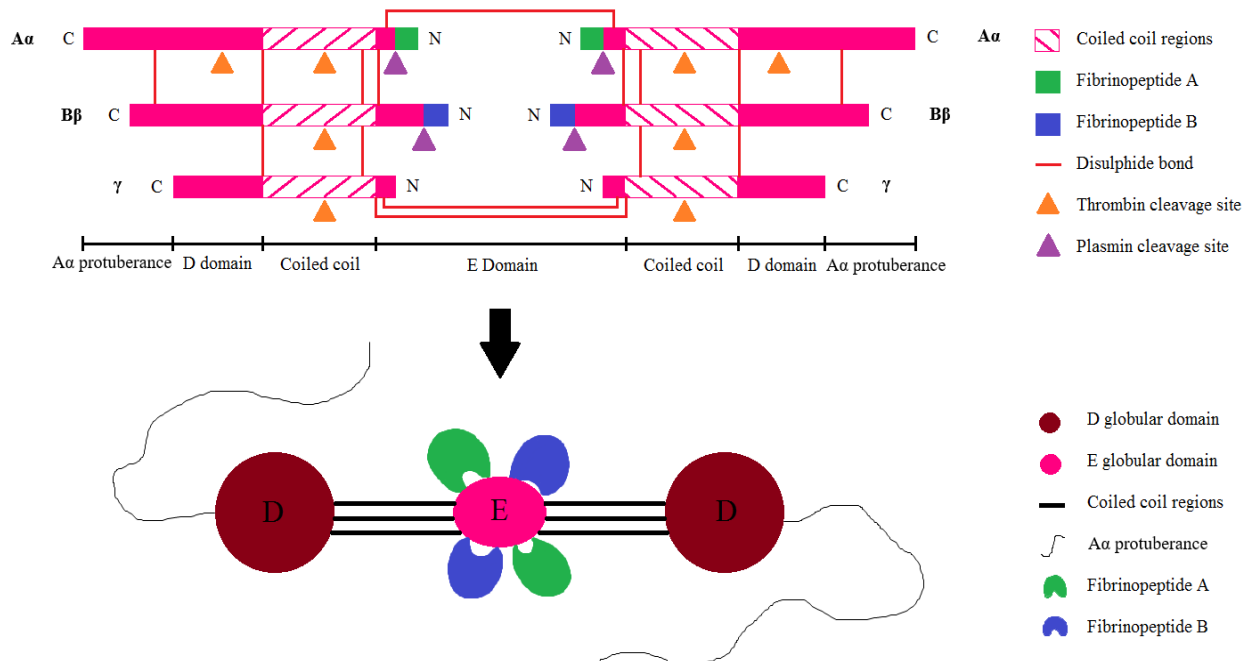


Figure 8.2 The polypeptide organization of fibrinogen (top) and the domain organization of fibrinogen (bottom), where fibrinogen consists of two sets of $A\alpha$, $B\beta$, and γ polypeptide chains, which are connected by disulfide bonds.²²

The hypothesis of this study is that the corrosion reactions associated with Mg and Mg-Ti particles result in electrochemical interactions between the Mg metal, its degradation products (ex. Mg oxides), and proteins which may alter the structure and/or function of proteins. To prove this hypothesis, Mg and Mg-Ti particles are corroded in a single protein solution (i.e. fibrinogen dissolved in PBS) to determine whether the ROS produced by Mg or Mg-Ti would

cleave the dimer into two monomers, since disulfide bonds are very susceptible to ROS attack, as one type of protein modification.

8.2 *Materials and Methods*

8.2.1 *Mg Oxide Crystal Formation in Different Solutions*

0.01 g of Mg or Mg-Ti particles were corroded in 5 ml of different solutions from $t= 1$ hour to 24 hours. Different solutions include phosphate buffered saline (PBS; Life Technologies, Catalog #: 10010023), Minimum Essential Medium (MEM) Alpha Medium (AMEM; Cellgro, Catalog #: 15-012-CV), Dulbecco's Modified Eagle Medium (DMEM; Life Technologies, Catalog #: 10313021), fetal bovine serum (FBS, Cert., USA Origin, Life Technologies, Catalog #: 16000044), horse serum (HS, Cert., New Zealand Origin, Life Technologies, Catalog #: 16050122), AMEM + 10% FBS, DMEM + 10% FBS, and lysogeny broth (LB) media (10 g tryptone, 5 g yeast extract, and 10 g NaCl in 1 L of Millipore water).

8.2.2 *Gel Electrophoresis*

8.2.2.1 *Sample Preparation*

Fibrinogen (type I-S: from bovine plasma) was purchased from Sigma-Aldrich (Material #: F8630-1G, Batch #: SLBJ3957V). Fibrinogen concentration of 2 mg/ml (the same concentration of fibrinogen found in blood plasma) was dissolved in PBS. Negative control is just fibrinogen in PBS. 0.05 g of Mg or Mg-Ti was corroded in 20 ml of fibrinogen solution for $t= 3$ days.

8.2.2.2 *SDS Page Preparation/Protocol*

An intact SDS PAGE electrophoresis system includes: a tank, lid with power cables, electrode assembly, cell buffer dam, casting stands, casting frames, combs (usually 10-wells or 15-wells), and glass plates (thickness 0.75 mm, 1.0 mm, or 1.5 mm) (purchased from Bio-Rad).

The SDS PAGE gel in a single electrophoresis run can be divided into stacking gel and separating gel. Stacking gel (acrylamide 5%) is poured on top of the separating gel (after solidification) and a gel comb is inserted in the stacking gel (to make the wells). The acrylamide percentage in SDS PAGE gel depends on the size of the target protein in the sample (see details below).

Acrylamide %	M.W. Range (kDa)
7%	50-500
10%	20-300
12%	10-200
15%	3-100

Volumes of stacking gel and separating gel differ according to the thickness of gel casting:

Thickness of the gel	Vol. of stacking gel	Vol. of separating gel
0.75mm	2ml	4ml
1.0mm	3ml	6ml
1.5mm	4ml	8ml

- **For a 5 ml stacking gel:**

H ₂ O	2.975 ml
0.5 M Tris-HCl, pH 6.8	1.25 ml
10% (w/v) SDS	0.05 ml
Acrylamide/Bis-Acrylamide (30%:0.8% w/v)	0.67 ml
10% (w/v) Ammonium Persulfate (AP)	0.05 ml
TEMED	0.005 ml

- **For a 10ml separating gel:**

Acrylamide Percentage	6%	8%	10%	12%	15%
H ₂ O	5.2ml	4.6ml	3.8ml	3.2ml	2.2ml
Acrylamide/Bis-acrylamide (30%/0.8% w/v)	2ml	2.6ml	3.4ml	4ml	5ml

1.5M Tris-HCl (pH=8.8)	2.6ml	2.6ml	2.6ml	2.6ml	2.6ml
10% (w/v) SDS	0.1ml	0.1ml	0.1ml	0.1ml	0.1ml
10% (w/v) ammonium persulfate (AP)	100µl	100µl	100µl	100µl	100µl
TEMED	10µl	10µl	10µl	10µl	10µl

Note: AP and TEMED must be added right before each use.

- **5X Sample buffer (loading buffer):**

SDS	10% (w/v)
Dithiothreitol, or Beta-Mercapto-Ethanol	10 mM
Glycerol	20% (v/v)
Tris-HCl, pH 6.8	0.2 M
Bromophenolblue	0.05% (w/v)

Note: Make sure the target protein is dissolved completely in the liquid phase, and no inappropriate ingredients are present (e.g. guanidine hydrochloride can interact with SDS and cause precipitation). Generally, treat the sample either with sonicator or lysis buffer, or both to sufficiently make the target protein dissolved.

- **1x Running Buffer:**

Tris-HCl	25 mM
Glycine	200 mM
SDS	0.1% (w/v)

Note: Approximate volume of less than 1 liter is needed depending on the type of the electrophoresis system.

First, the separating gel (10% acrylamide) was made as described above. 10% acrylamide was chosen because fibrinogen has a molecular weight of 340 kDa, with $\alpha\alpha$, $B\beta$, and γ chains 63.5 kDa, 56 kDa, and 47 kDa, respectively, and so the molecular weights of the chains are within 20-300 kDa. The casting frames were then set on the casting stands. The separating

gel solution was swirled gently but thoroughly to ensure mixing and then pipetted into the gap between the glass plates. To make the top of the separating gel evenly horizontal, water or isopropanol was filled into the top of the gap until the liquid overflowed. Then waited for 20-30 minutes for the separating gel to gel.

Once the separating gel was gelled, the water or isopropanol on top of the separating gel was discarded. Then the stacking gel solution was pipetted until overflow. The well-forming comb was carefully inserted without trapping air under the teeth of the comb. Waited another 20-30 minutes for the stacking gel to gel. Once the stacking gel was completely gelled, the comb was taken out carefully. The glass plates were taken out of the casting frame and set them in the cell buffer dam. The running buffer (electrophoresis buffer) was poured into the inner chamber until the buffer surface reached the required level in the outer chamber. To prepare the samples for gel electrophoresis, the sample was mixed with sample buffer (loading buffer) and both were heated in boiling water for 5-10 minutes. Prepared samples were loaded into the wells without any overflow. The first lane was loaded with protein markers, which show different molecular weights. Then the top was covered with the electrodes connected. As for the total running time, SDS-PAGE was stopped when the down-most sign of the protein marker almost reached the foot line of the glass plate. Generally, about 1 hour is needed for a 120 V voltage and a 12% separating gel (if the separating gel has a higher percentage, a longer time is required). Note that various factors can affect the properties of the resulting gel. Higher concentration of ammonium sulfate and TEMED will lead to faster gelation, but will lower the gel stability and elasticity. The optimal temperature for gel gelation is 23°C-25°C. Lower temperature will lead to turbid, porous, and inelastic gels. The pH should be neutral and the gelation time should be limited to 20-30 minutes.

8.2.3 X-Ray Diffractometer (XRD) Analysis

For XRD (Rigaku RINT2200 diffractometer) scans, the following samples were used.

1. Mg powder as purchased from Goodfellow (Product #: MG006021) → Mg Before
2. Mg-Ti powder where Mg (Goodfellow) was sputtered with Ti for 5 minutes at 1.2 kV, 50 mA, and 100-200 mTorr → Mg-Ti Before
3. 0.1 g of Mg powder corroded in 10 ml of PBS solution for $t = 4$ days and then dried in the desiccator → Mg After
4. 0.1 g of Mg-Ti powder corroded in 10 ml of PBS solution for $t = 4$ days and then dried in the desiccator → Mg-Ti After
5. Fibrinogen powder as purchased from Sigma-Aldrich → Fb
6. 0.1 g of Mg powder corroded in 10 ml of PBS with 2 mg/ml fibrinogen for $t = 4$ days and then dried in the desiccator → Mg + Fb
7. 0.1 g of Mg-Ti powder corroded in 10 ml of PBS with 2 mg/ml fibrinogen for $t = 4$ days and then dried in the desiccator → Mg-Ti + Fb

XRD diffraction patterns were obtained with Ni-filtered Cu K_{α} radiation ($\lambda = 1.54068 \text{ \AA}$) generated at 30 kV and 30 mA at a scanning speed of $0.5^{\circ}2\theta/\text{min}$ in the range of $1-50^{\circ}2\theta$ and then analyzed using MDI (Jade version 5) software. Using clean alligator clip and spatula (cleaned with ethanol), some of the powder samples mentioned above were loaded in clear scotch tape and then the tape was folded in half. This tape was then taped to the sample holder, ensuring that the powder was at the center.

8.2.4 Fourier Transform Infrared Radiation (FTIR) Analysis

The samples mentioned in Section 8.2.3 were also analysed with FTIR (PerkinElmer Instrument and Spectrum One software) in reflectance mode. The background sample used was CoCrMo alloy.

8.3 Results

Mg particles formed cuboidal Mg oxides within $t = 1$ hour in FBS or HS solution, which decreased in size over time and completely disappeared by $t = 24$ hours (Fig. 8.3). Mg particles in AMEM became transparent over time, showing that Mg metal corroded, replaced by Mg oxides (Fig. 8.4). Most particles were completely transparent, except the few that were big in size, which still had not finished corroding. Mg particles in complete media (AMEM + 10% FBS) also became transparent over time, but some Mg particles formed needle-shaped Mg oxides (Fig. 8.5). The conditions in which these Mg oxide needles formed were not clear, because these oxides did not always form. Sometimes, individual Mg particles became transparent, forming Mg oxide, while other times, Mg particles aggregated and formed these Mg oxide needles. One condition that needs to meet to form Mg oxide needles is that the particle concentrations have to be high so that the particles can easily aggregate. These Mg oxide needles were also seen in AMEM, DMEM, AMEM + 10% FBS, DMEM + 10% FBS, and NaCl solutions as well (not shown because they look the same as shown in Fig. 8.5(e)). Interestingly, Mg needle oxides were not seen in serum-only solutions (FBS or HS), even if there were high concentrations of Mg particles. Mg needle oxides were formed if AMEM or DMEM were present, and since AMEM + 10% FBS or DMEM + 10% FBS solutions have higher volume ratio of AMEM or DMEM compared to FBS, Mg oxide needles were formed over cuboidal Mg oxides, which were seen in serum-only solutions. Mg oxides in LB media showed completely different shape, which was rectangular, where some were branched (Fig. 8.6). Not all Mg

particles formed these rectangular-shaped oxides, however, and so again, as to why some Mg particles formed these rectangular-shaped oxides are not clear. SEM images show more close-up view of Mg oxide needles (Fig. 8.7). A single Mg needle is hexagonal in shape, although the actual size and length may vary. Usually, many Mg oxide needles spurted from one single origin, almost forming a sphere. Mg-Ti particles in different solutions developed same oxides as Mg, and therefore, the images are not shown to reduce repetitive images.

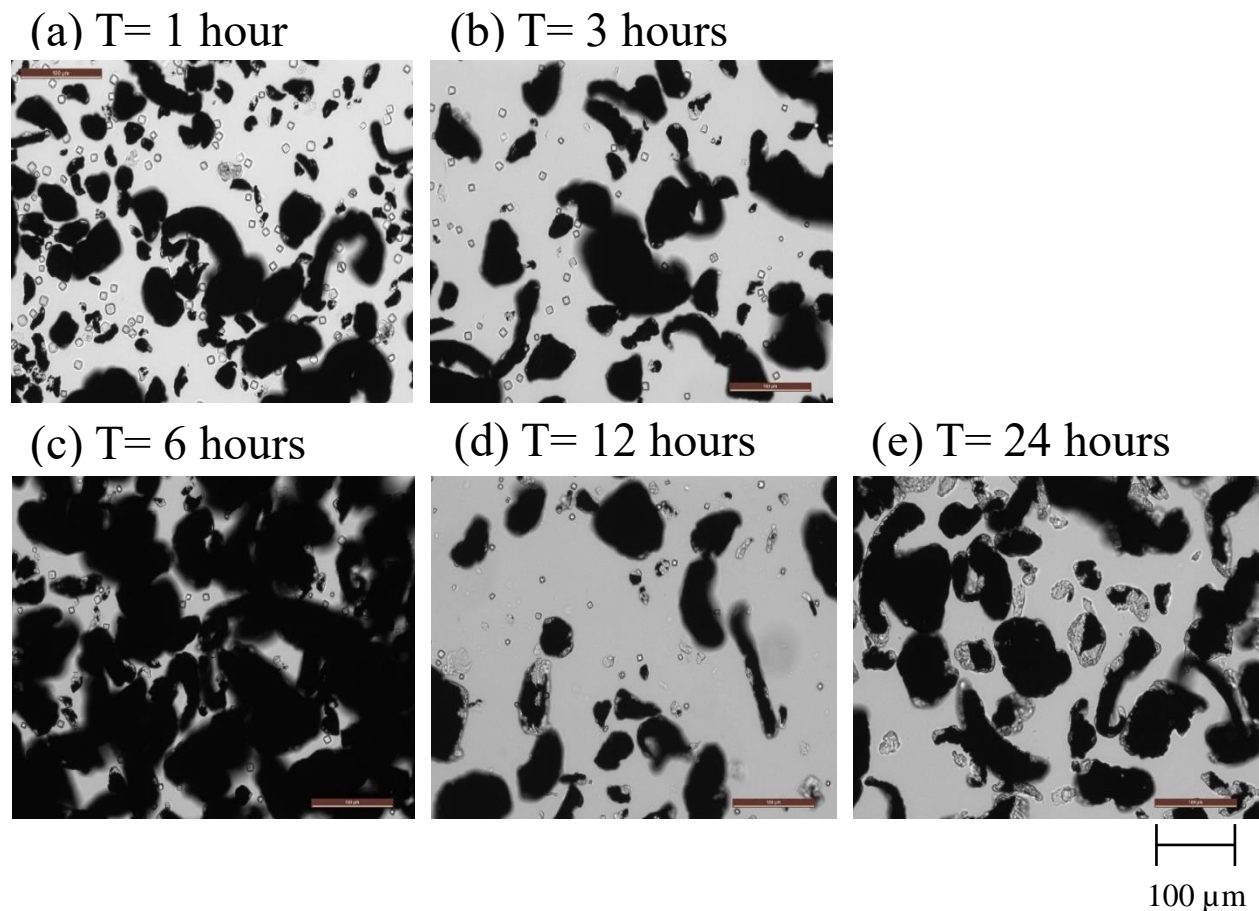


Figure 8.3 0.01 g of Mg particles in 5 ml of FBS solution from $t= 1$ hour to 24 hours, $n=3$. Cuboidal Mg oxides form within $t= 1$ hour and then disappear by $t= 24$ hours. All images were taken at 20x magnification.

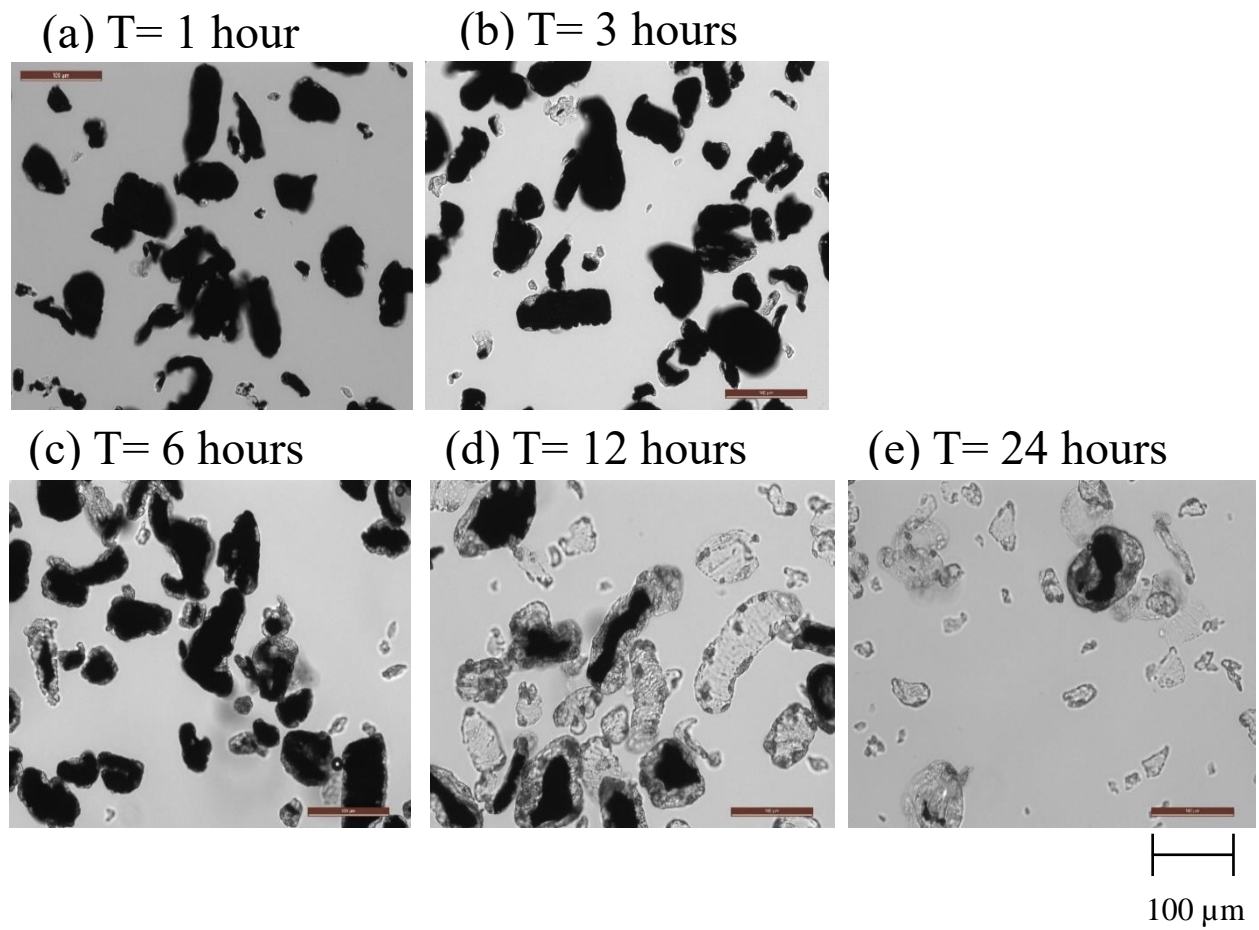


Figure 8.4 0.01 g of Mg particles in 5 ml of AMEM solution from t= 1 hour to 24 hours, n=3. Mg particles become transparent over time, where Mg metal is oxidized to form Mg oxide. All images were taken at 20x magnification.

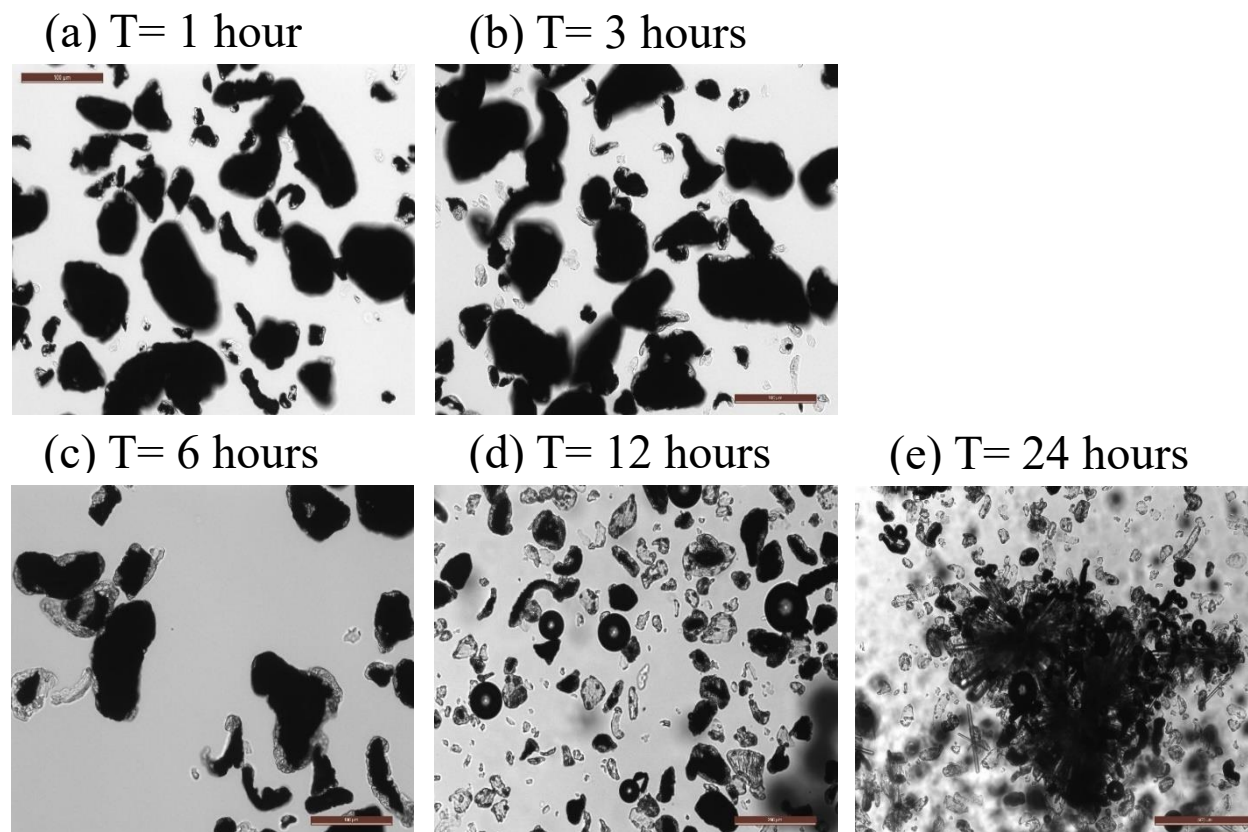


Figure 8.5 0.01 g of Mg particles in 5 ml of AMEM + 10% FBS solution from $t=1$ hour to 24 hours, $n=3$. Mg particles become transparent over time, where Mg metal is oxidized to form Mg oxide. Mg oxide needles are formed in areas where particles are aggregated. Images (a)-(c) were taken at 20x (the scale bar 100 μm), (d) taken at 10x (the scale bar 50 μm), and (e) at 5x (the scale bar 20 μm).

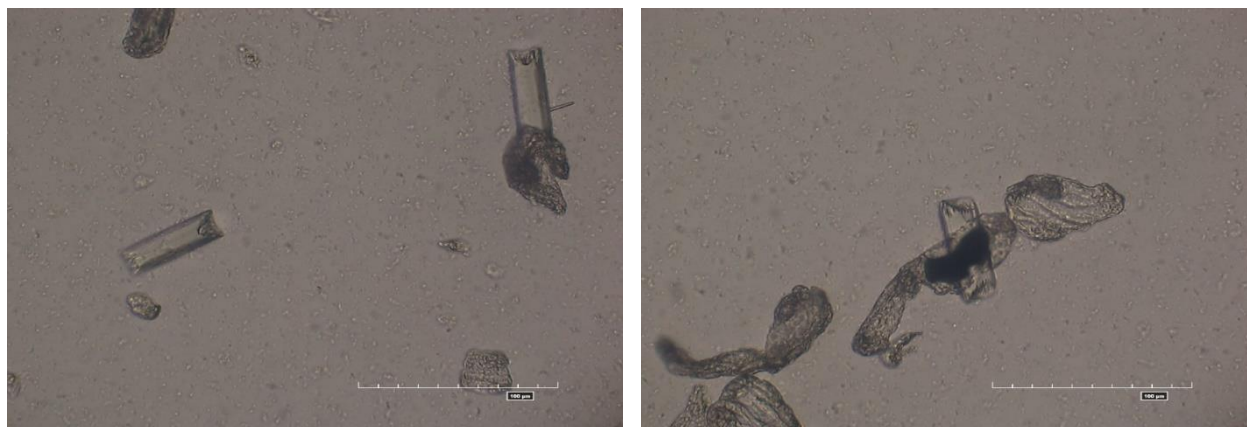


Figure 8.6 0.01 g of Mg particles in 5 ml of LB media for $t=24$ hours, $n=3$. Mg particles become transparent over time, and some may form rectangular oxides. All images were taken at 20x magnification.

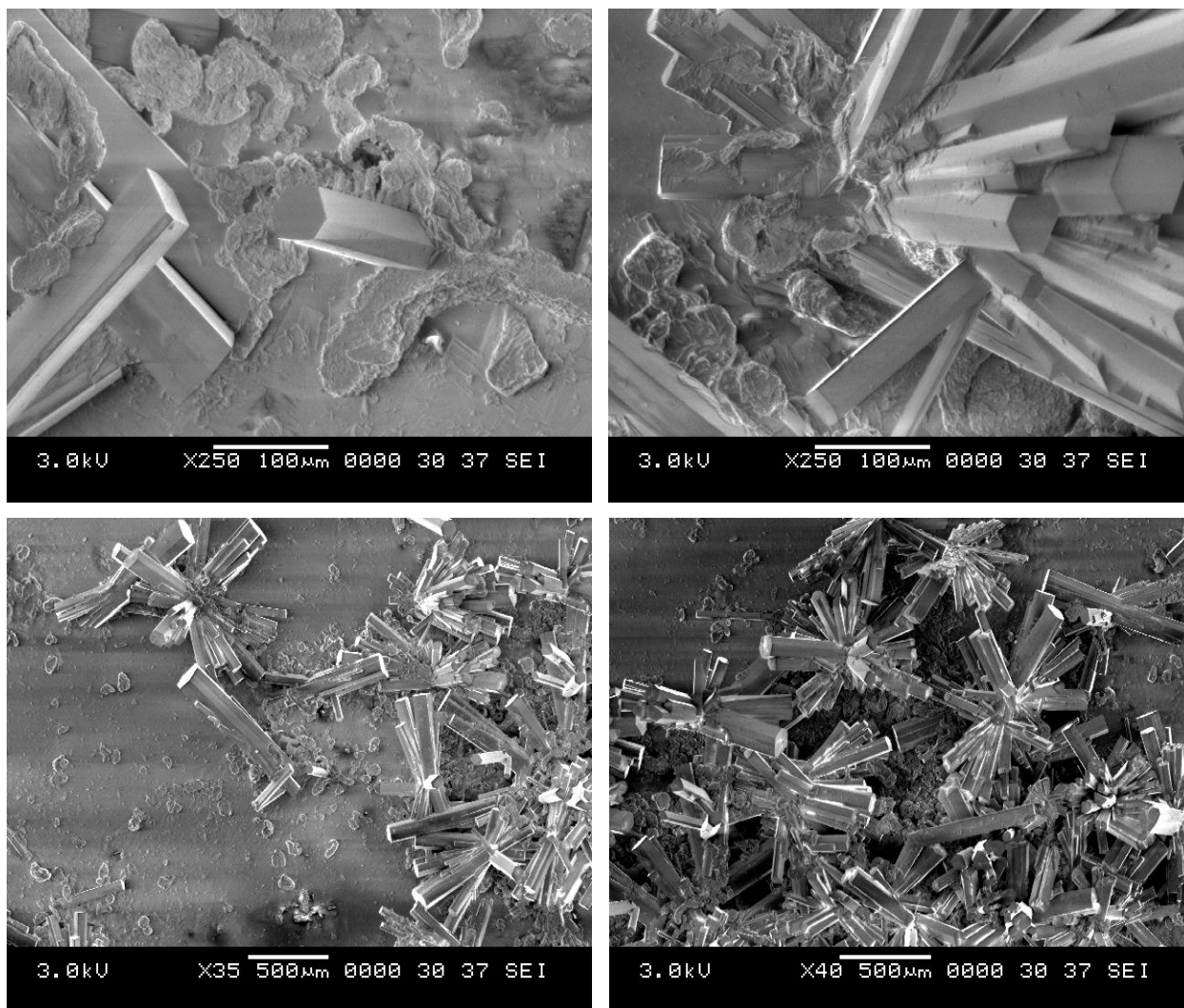


Figure 8.7 0.01 g of Mg particles in 5 ml of AMEM + 10% FBS for $t = 24$ hours. Mg particles form these needle-shaped oxides, where each needle is hexagon-shaped.

Not only the constituents in solutions affect the growth and shape of Mg oxides, but Mg corrosion affects the constituents in solutions (refer to [Fig. 7.7](#)). Because there are too many constituents in AMEM and FBS, it was not clear which elements were being modified due to Mg corrosion. Therefore, fibrinogen protein was chosen to further investigate whether proteins are modified due to Mg corrosion. Fibrinogen was chosen because it is a dimer, with two sets of monomers bridged by disulfide bonds.

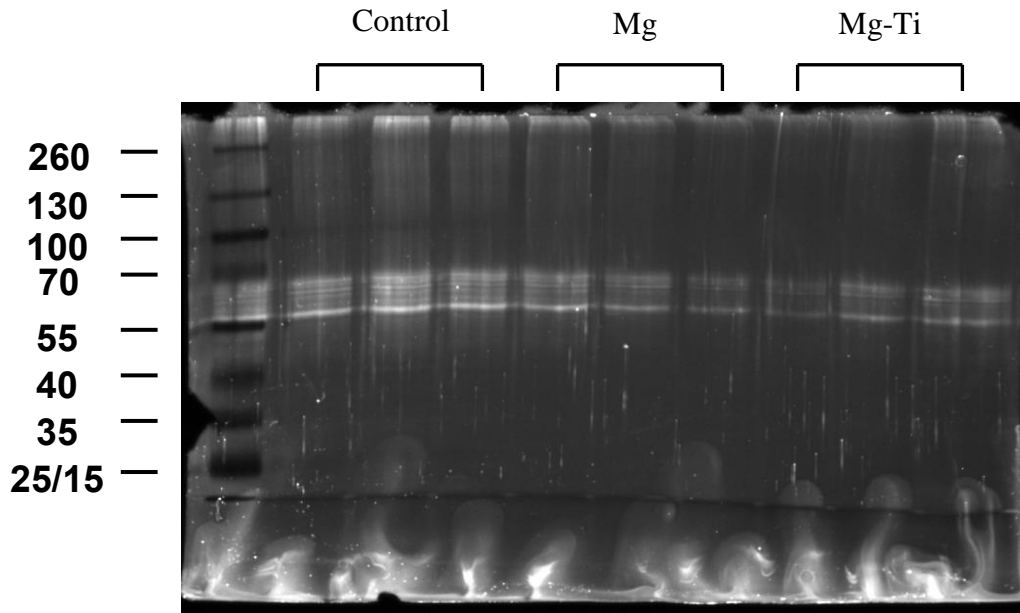


Figure 8.8 Gel electrophoresis of control (just fibrinogen dissolved in PBS), Mg-treated fibrinogen, MgTi-treated fibrinogen, n=3. The first row consists of protein markers (shown in black bands with the molecular weights labeled on the left accordingly in kDa), but part of control group leaked. The molecular weights are within 70 and 55 kDa, because the molecular weights of A α , B β , and γ chains are 63.5 kDa, 56 kDa, and 47 kDa, respectively. Fibrinogen molecule has a molecular weight of 340 kDa, which is too large to travel, and so may remain in the wells if fibrinogen is not reduced.

Gel electrophoresis of fibrinogen, Mg-treated fibrinogen, and MgTi-treated fibrinogen is shown in [Fig. 8.8](#). 10% acrylamide gel reduced the fibrinogen into its A α , B β , and γ chains because the bands shown are between the protein markers of 70 and 55 kDa, which makes sense since the molecular weights of A α , B β , and γ chains are 63.5 kDa, 56 kDa, and 47 kDa, respectively. Fibrinogen molecule, which weighs 340 kDa, is too large to travel for this gel electrophoresis, and so some molecules that have not been broken down to its polypeptide chains were still in the wells. When compared to other gel electrophoresis of fibrinogen performed by Gorkun et al., this gel electrophoresis data is very consistent [\[23\]](#). Gel electrophoresis of plasma fibrinogen show that there should be three predominant bands that correspond to the A α , B β , and γ chains [\[23\]](#). There is also a minor band, which shows smaller A α chain species [\[23\]](#). Although the gel electrophoresis done in this study seems to show multiple bands and distinct dominant

bands are not as clear, the range of molecular weights of the polypeptide chains is very consistent. There are ten wells, where the first lane (leftmost) should only consist of the protein markers, the next three lanes control (only fibrinogen), the three lanes after Mg-treated fibrinogen, and the last three lanes MgTi-treated fibrinogen. However, due to inexperience use of gel electrophoresis, control leaked to the protein-marker well as the samples were being pipetted into the wells, and so the protein marker lane also shows control. When Mg or Mg-Ti particles were corroded in fibrinogen solution, the particles aggregated the proteins into metal-protein complexes, which were very solid and hard to dissolve (Fig. 8.9). Mg oxide needles and particles seemed glued by fibrinogen, making large solid rock-like Mg oxides/Mg metal/protein complex. So gel electrophoresis was done using the remaining liquid samples, which shows no difference among control, Mg-treated, and MgTi-treated samples, except for the intensity of the bands, where the bands fluoresce less for Mg and MgTi-treated samples compared to control. However, this does not mean that Mg or Mg-Ti corrosion did not alter fibrinogen, since metal-protein complexes (the solid precipitates) were not analyzed using gel electrophoresis.

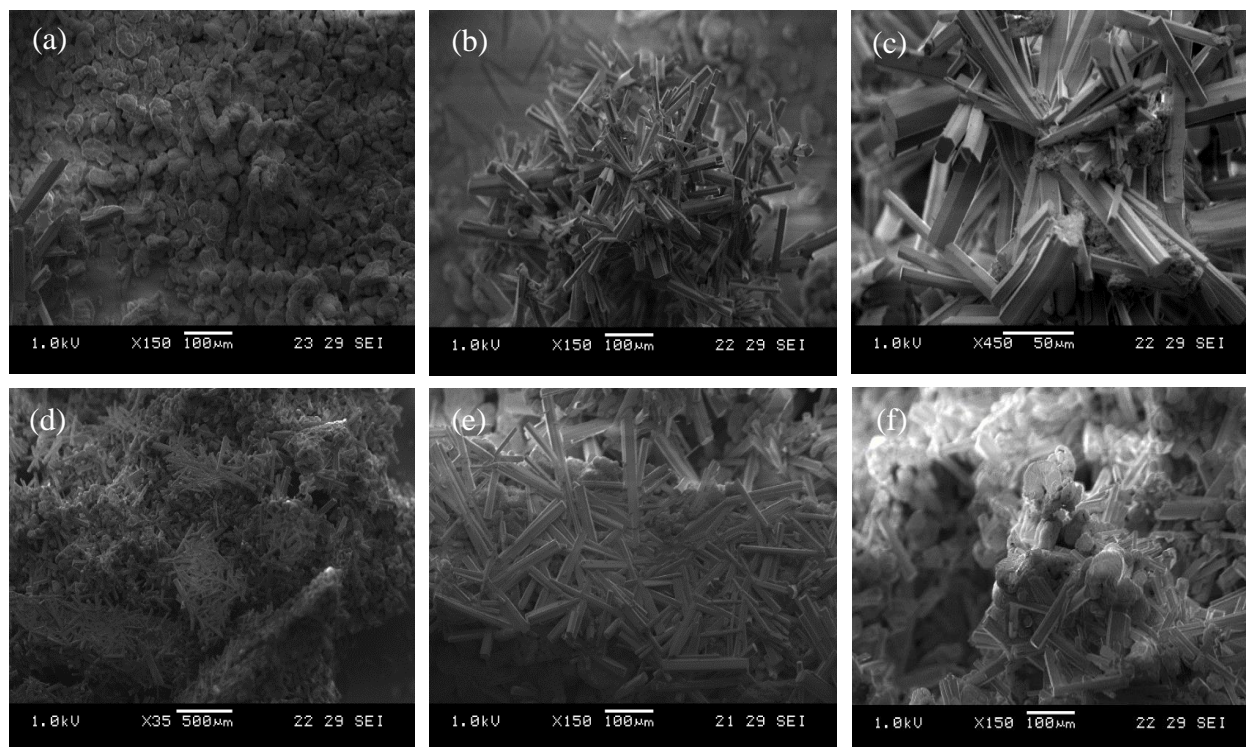


Figure 8.9 SEM images of (a)-(c) 0.1 g of Mg in 10 ml of PBS with fibrinogen (2 mg/ml) and (d)-(f) 0.1 g of Mg-Ti in 10 ml of PBS with fibrinogen (2 mg/ml). Although predominantly showing Mg oxide needles and Mg particles, these oxide needles seemed “glued” by fibrinogen.

These metal-protein complexes formed by pre-corroding Mg or Mg-Ti in fibrinogen solution were analyzed using XRD. XRD data for Mg or Mg-Ti particles before and after corrosion, termed Mg(before) and Mg(after), and likewise Mg-Ti(before) and Mg-Ti(after), were obtained in this study. Mg(before) showed three peaks at 32°, 34°, and 36° that showed up in all Mg-based material (Fig. 8.10(a)). There was a fourth peak at 38°, which was probably due to MgO(111) since part of Mg may be oxidized by oxygen O₂ when exposed to air. There was also a peak below 50°, which indicated Mg(102). There was a small, broad peak right below 20°, which may be due to Mg or MgO, although not certain. After corroding Mg, the three peaks at 32°, 34°, and 36° completely disappeared. There were two small peaks at 31° and 38°, which might indicate Mg(OH)₂. There was a new peak at 27° and a bi-peak around 45°, which did not align with any of the known peaks for MgO or Mg(OH)₂, but clearly, the atomic and molecular structure of Mg has changed after corrosion. When Mg was galvanically coupled to Ti, the XRD

peaks were exactly the same as that of Mg, which made sense since sputtering a very thin layer of Ti (~nm) could not have changed the structure of Mg. Interestingly, when Mg-Ti was corroded, however, galvanic coupling of Ti did make a difference since the diffraction peaks of Mg-Ti(after) were slightly different compared to that of Mg(after) (Fig. 8.10(a)). First, the peak at 27° that showed up for Mg(after) was significantly reduced for Mg-Ti(after) (only a slight bump), and the intensity of peak at 31° had significantly increased. The fourth peak at 38° had increased in intensity as well (as bi-peak). As mentioned earlier, these two peaks at 31° and 38° might indicate Mg(OH)₂ and if so, the higher intensity of these peaks for Mg-Ti(after) compared to Mg(after) makes sense, since faster corrosion of Mg due to galvanic coupling must have produced higher concentrations of Mg(OH)₂ at the Mg particle surface. Again, there was a peak at 45° as Mg, which only showed up after the particle corrosion. Another interesting observation to note was that for Mg, the peak below 20° decreased in intensity after Mg corrosion, but for Mg-Ti, the peak intensity increased after Mg-Ti corrosion, although this change was slight.

Fibrinogen (Fb) powder was analyzed, which showed a broad peak at 20° and a sharp peak at 31° (Fig. 8.11(a)). Fig. 8.11(b) shows XRD analysis of Mg or Mg-Ti corroded in the absence or presence of Fb, where XRD graphs of Mg or Mg-Ti in the absence of Fb is the same data from Fig. 8.10, referred to as Mg(after) and Mg-Ti(after). For Mg, the peaks below 20°, and at 31° and 38° increased, while the peaks at 27° and 45° decreased due to Fb. Entirely new peaks appeared at 35° and 37°, where the peaks 37° and 38° appeared as bi-peak. For Mg-Ti, the peak

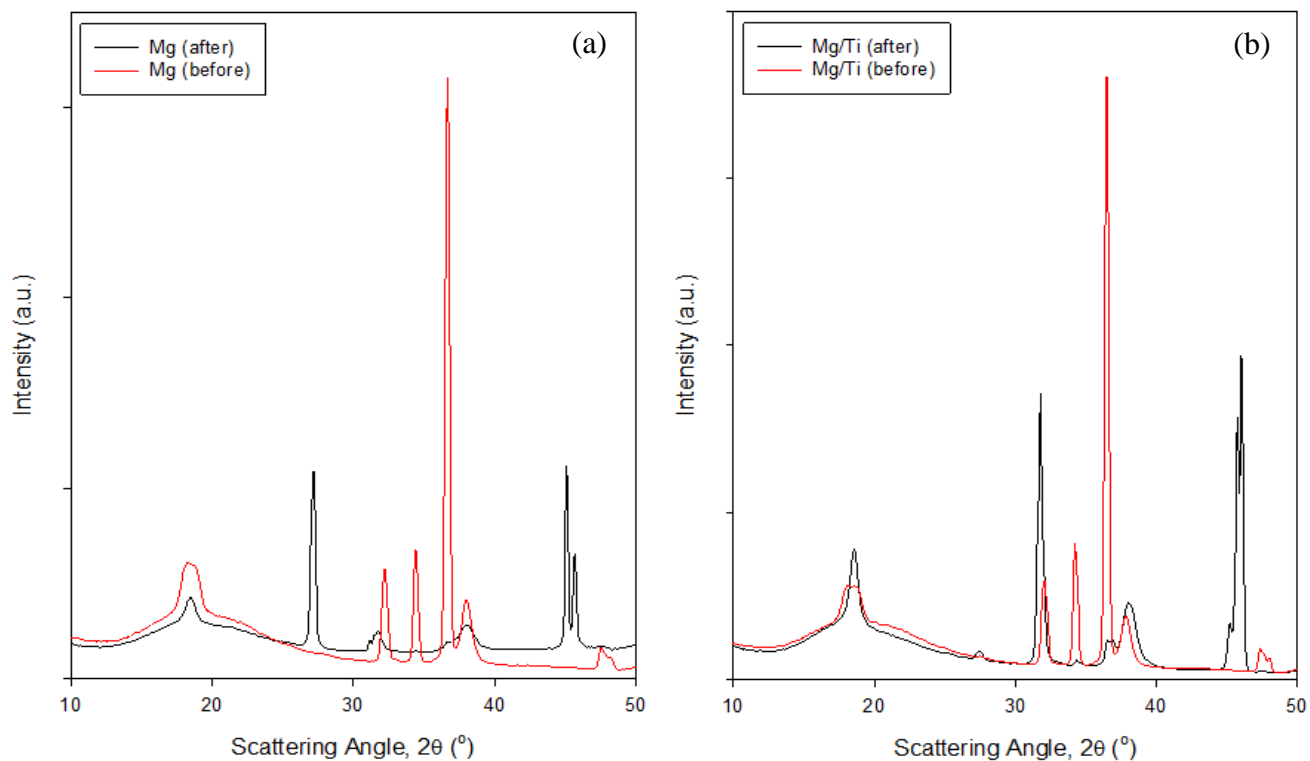


Figure 8.10 XRD analysis of (a) Mg (before)- red line and Mg (after)- black line, and (b) Mg-Ti (before)- red line and Mg-Ti (after)- black line.

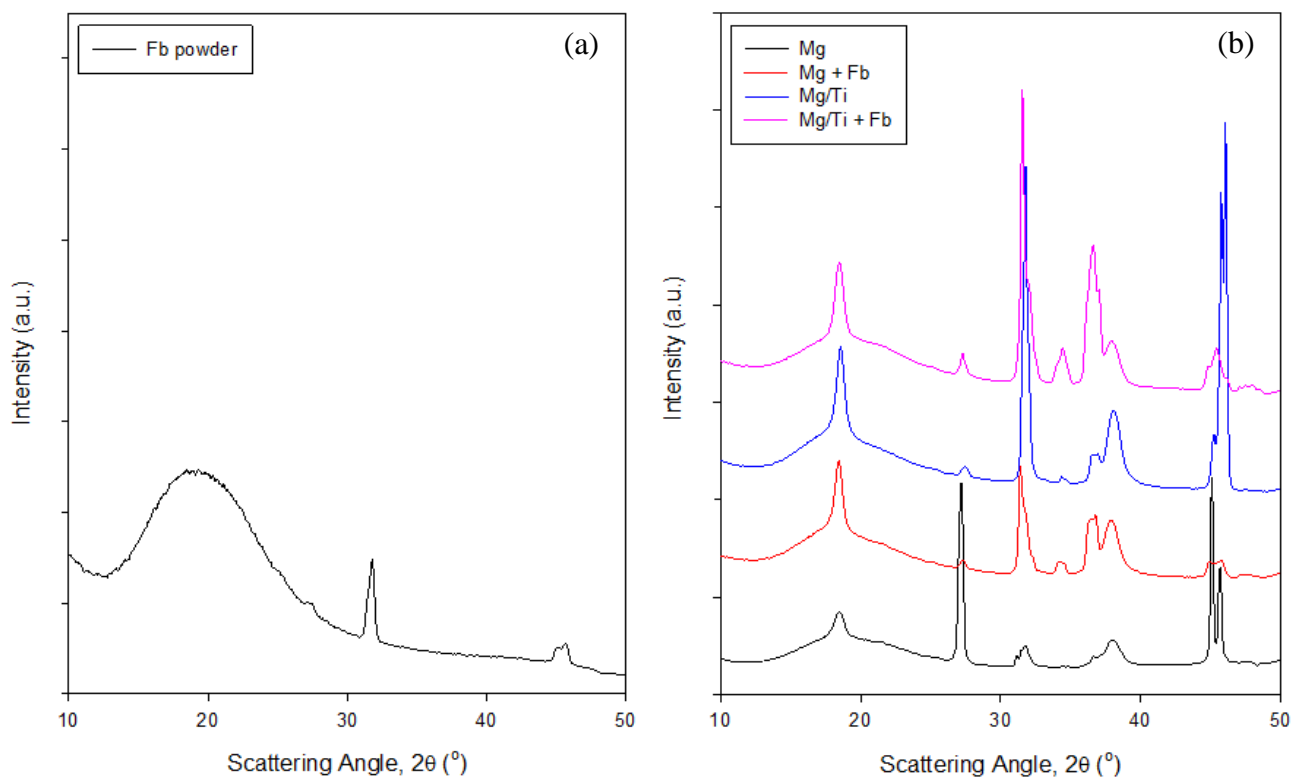


Figure 8.11 XRD analysis of (a) just fibrinogen (Fb) powder and (b) Mg with or without Fb and Mg-Ti with or without Fb. Mg and Mg-Ti without fibrinogen in graph (b) are Mg (after) and Mg-Ti (after) from Fig. 8.10.

below 20° was not affected by the presence of Fb for Mg-Ti. The peak at 27° does not appear significantly for Mg-Ti as Mg, but when Mg-Ti is corroded in the presence of Fb, the intensity of this peak increased slightly. Mg-Ti corrosion alone already shows a high peak at 31°, which does not change due to Fb. But the intensity of bi-peak at 37-38° is higher and also the peak at 35° shows up when Fb is present. The peak at 45° is reduced by Fb, although not completely. In order to compare more closely, Mg-Ti corroded with or without Fb is re-shown in [Fig. 8.12](#). Again, the peaks perfectly align between Mg-Ti w/o Fb and Mg-Ti w/ Fb, except the peaks between 35° and 38°, and at 45°. The peak at 35° is a new peak, which was absent when Mg-Ti corroded without Fb. The bi-peak at 37°-38° is present for Mg-Ti without Fb, but the intensity of the peak is smaller at 37° and higher at 38°, which is switched for Mg-Ti with Fb, where the peak is higher at 37° and smaller at 38° instead. These peaks may be due to MgO or Mg(OH)₂, since peaks characterizing MgO and Mg(OH)₂ do show up in this diffraction angle range. The peak at 45° only showed up after Mg or Mg-Ti corrosion and not for Mg or Mg-Ti metal, which significantly reduced when Fb protein was present. Also, the overall graph comparing all the groups are shown in [Fig. 8.13](#).

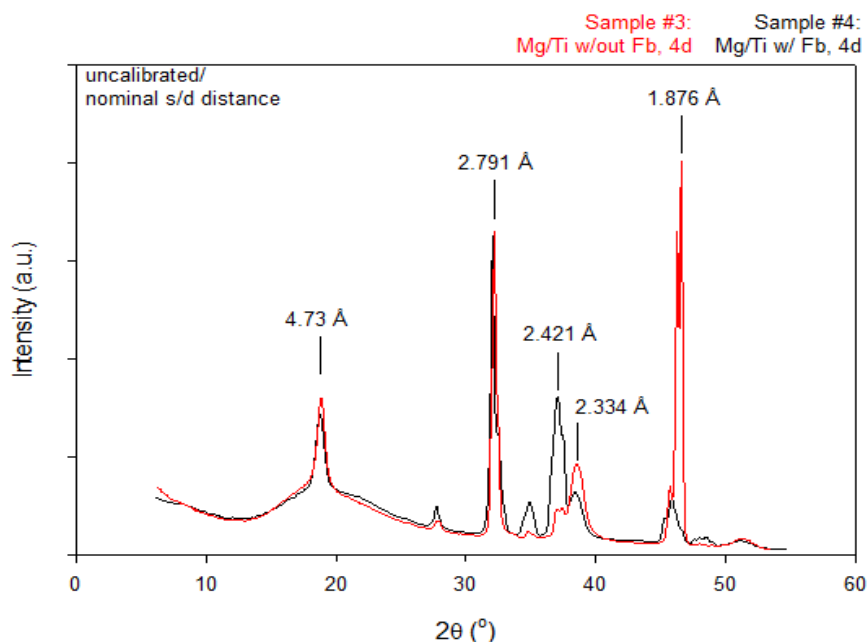


Figure 8.12 XRD analysis comparing Mg-Ti with and without Fb.

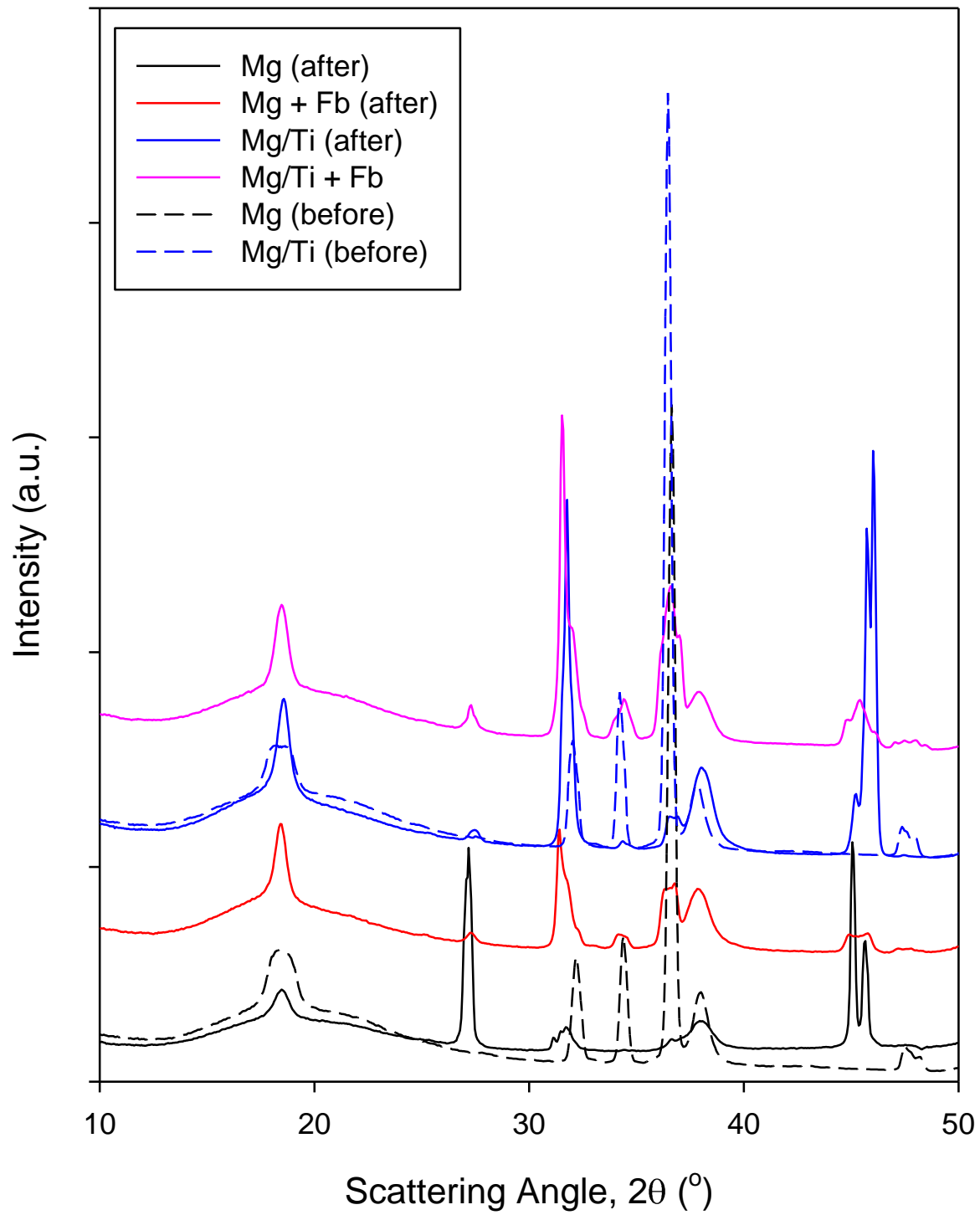
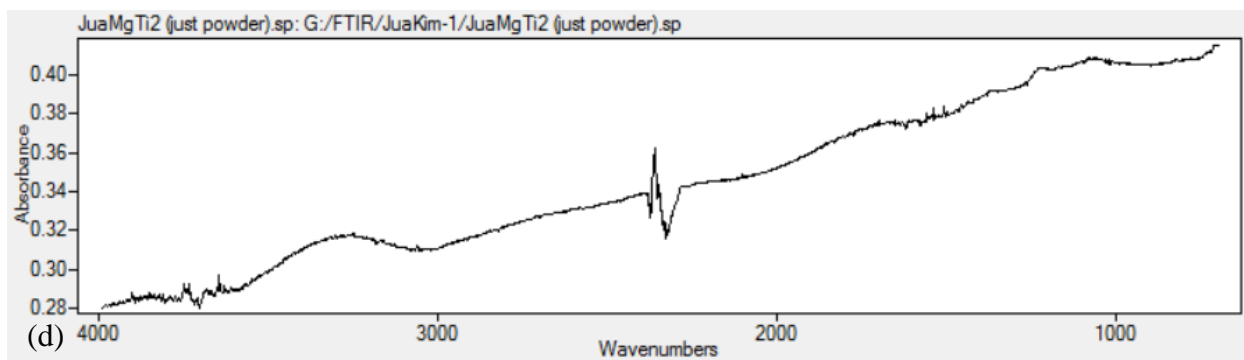
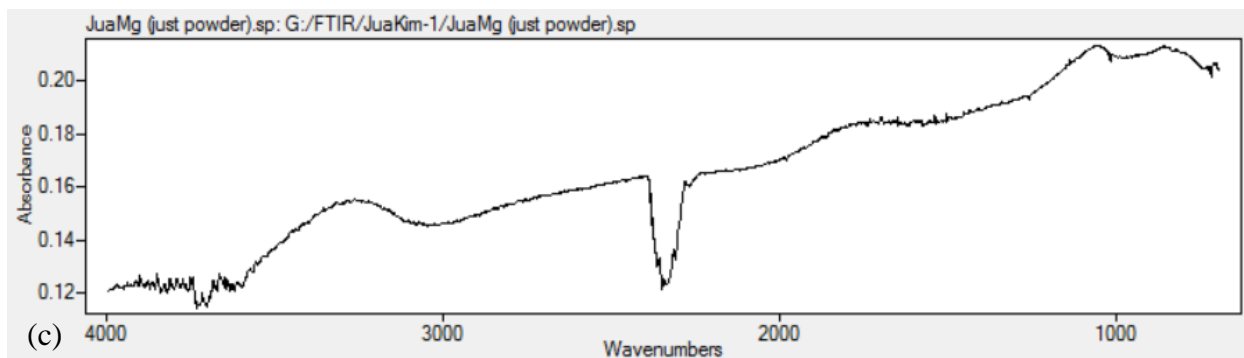
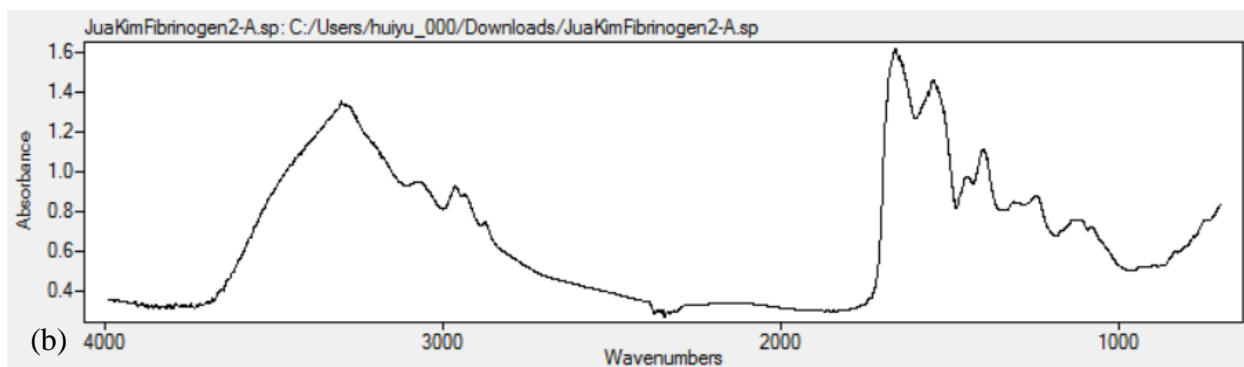
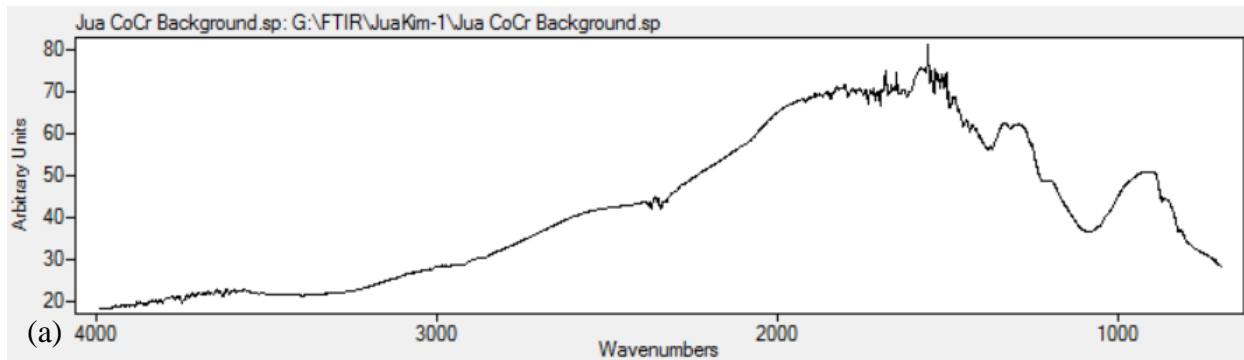


Figure 8.13 Overall XRD graphs comparing all the groups.



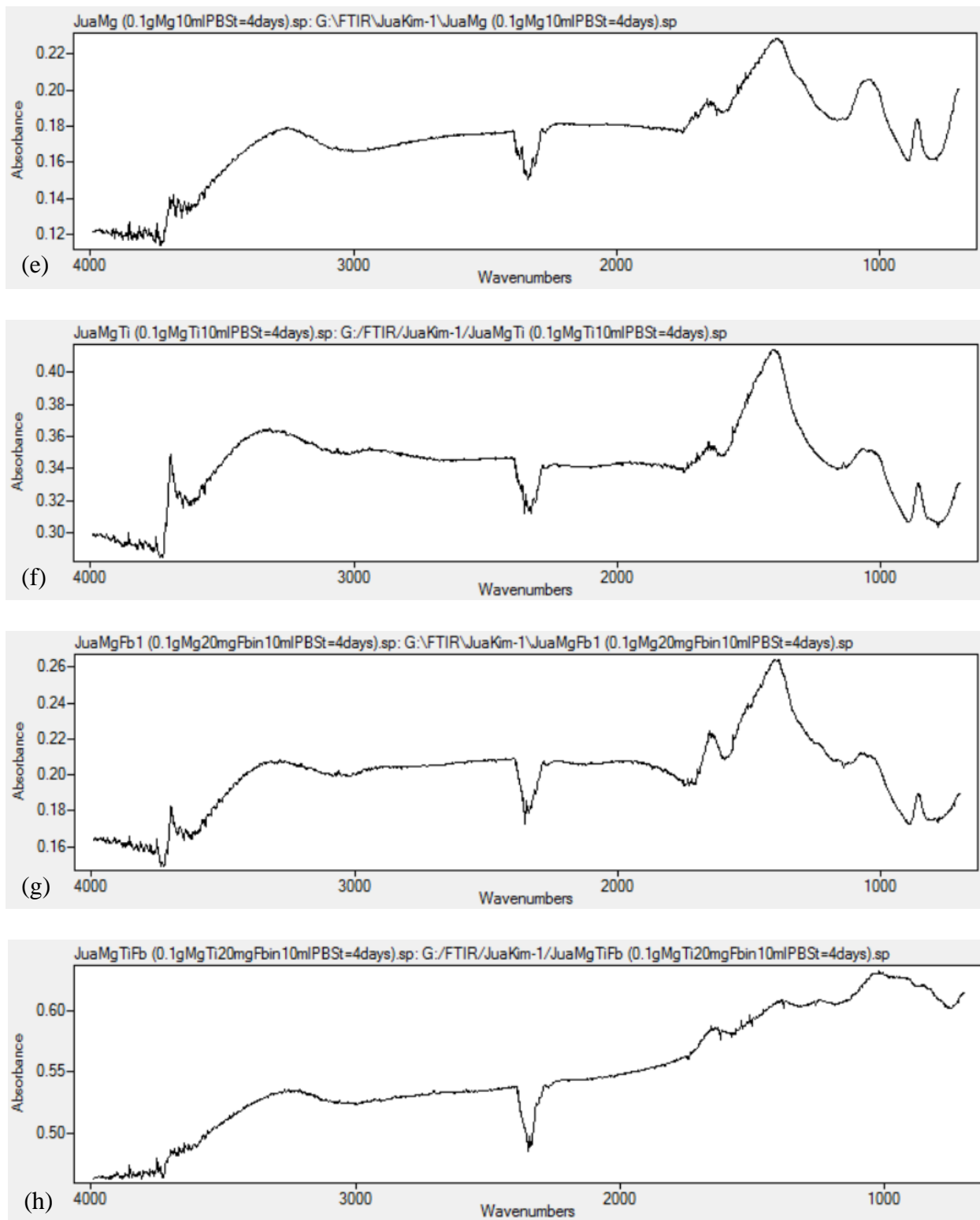


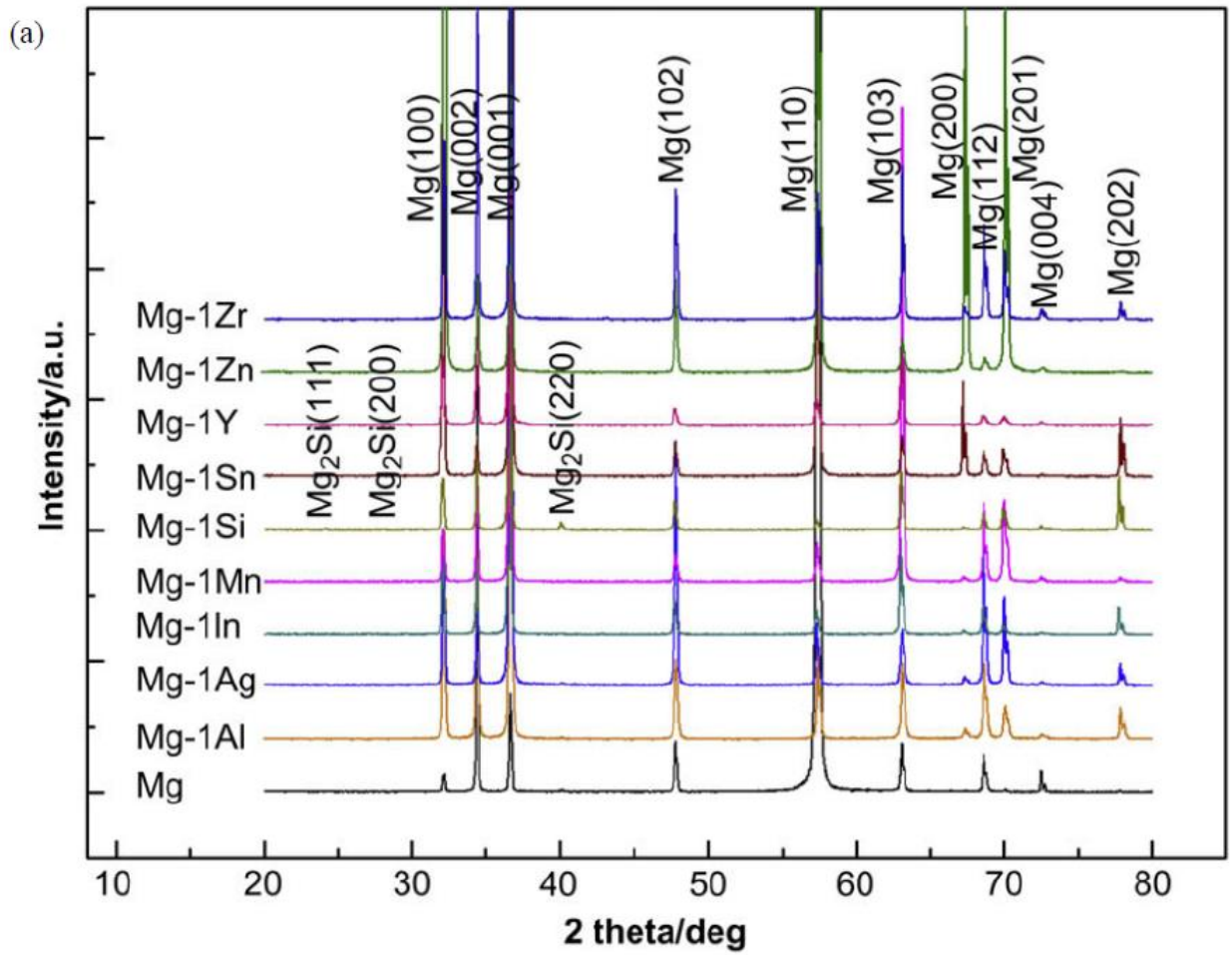
Figure 8.14 FTIR spectrums for (a) CoCr background, (b) fibrinogen, (c) Mg before corrosion, (d) Mg-Ti before corrosion, (e) Mg corroded in PBS for $t=4$ days, (f) Mg-Ti corroded in PBS for $t=4$ days, (g) Mg corroded in fibrinogen solution for $t=4$ days, and (h) Mg-Ti corroded in fibrinogen solution for $t=4$ days.

Fig 8.14 shows FTIR spectrums. Fibrinogen has a broad peak at 3300 cm^{-1} , which is due to the stretching vibration of N-H bond, and the peaks at 1666 and 1545 cm^{-1} are due to amide bonds [24-26]. Mg and Mg-Ti have a peak at approximately 2300 cm^{-1} , which show up in all Mg or Mg-Ti containing samples. When Mg or Mg-Ti were corroded in PBS, two peaks showed up approximately at 1300 - 1600 cm^{-1} . Since the peaks at 1300 - 1600 cm^{-1} show up in Mg or Mg-Ti particles corroded in PBS without the presence of fibrinogen, these peaks cannot be due to the bonds found in fibrinogen. When Mg or Mg-Ti were corroded in fibrinogen solution, the characteristic peaks of fibrinogen were not observed in the FTIR spectrum.

8.4 Discussion

Both XRD and FTIR data show that there are changes in crystallography and chemical bonds when Mg or Mg-Ti particles corrode in the presence and absence of fibrinogen. To interpret the XRD data obtained in this study, the data was compared to the XRD data from other studies, shown in Fig. 8.15 for comparison purposes. Gu et al. performed XRD on cast pure Mg or Mg-X alloys (where X= Al, Ag, In, Mn, Si, Sn, Y, Zn, and Zr) [27]. There were three distinct peaks at 32° , 34° , and 36° , which indicated Mg (100), Mg(002), and Mg (001), respectively, which can be seen in this study and other studies as well [27-30]. These peaks are seen consistently not just for pure Mg but also Mg-based alloys. There was a smaller peak at 48° , indicating Mg (102) [27-30], which was also seen for Mg(before) and Mg-Ti(before), but not for Mg(after) and Mg-Ti(after). XRD analysis of pure Mg by Gu et al. showed diffraction angles up to 80° , and for pure Mg, there were four peaks at diffraction angles between 55° and 75° , which indicated Mg (110), Mg (103), Mg (112), and Mg (004) [27], but these peaks were not relevant in this study because diffraction angles higher than 50° were not measured. Based on other studies, $\text{Mg}(\text{OH})_2$ has a distinct peak below 20° , and two other peaks between 30° and 40° , a

small peak right below 35° (100) and a large peak right below 40° (101) [28-29]. The XRD data from this study showed that both Mg and Mg-Ti before and after corrosion had a peak below 20°, indicating possibly that there was some hydroxide layer at the Mg or Mg-Ti surface even before the particle corrosion. Other peaks of Mg(OH)₂ were not found in this study. Other studies also showed that MgO (200) have a peak around 42° [28-29]. However, after Mg and Mg-Ti corrosion, MgO peak was not found at 42° in this study.



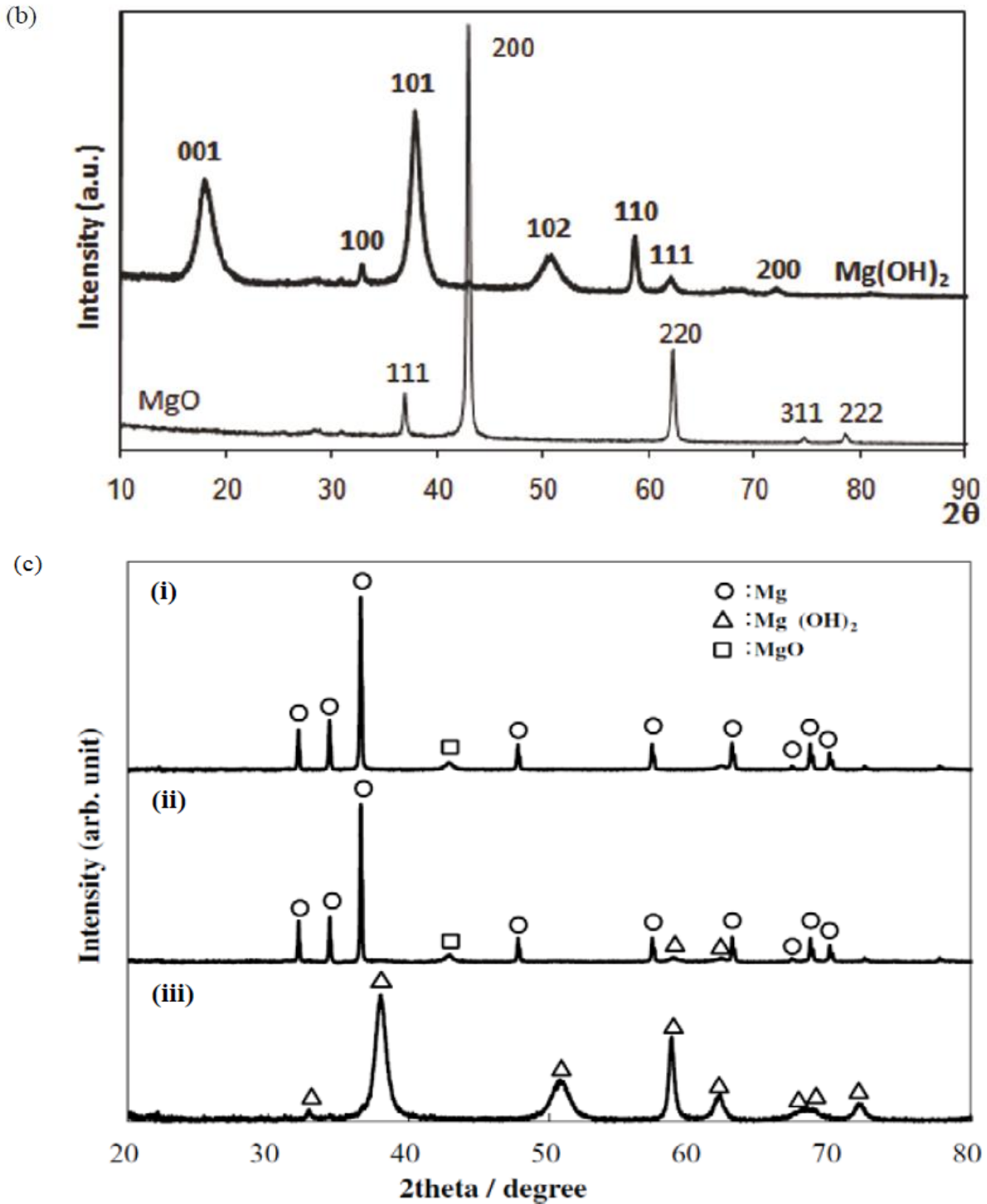


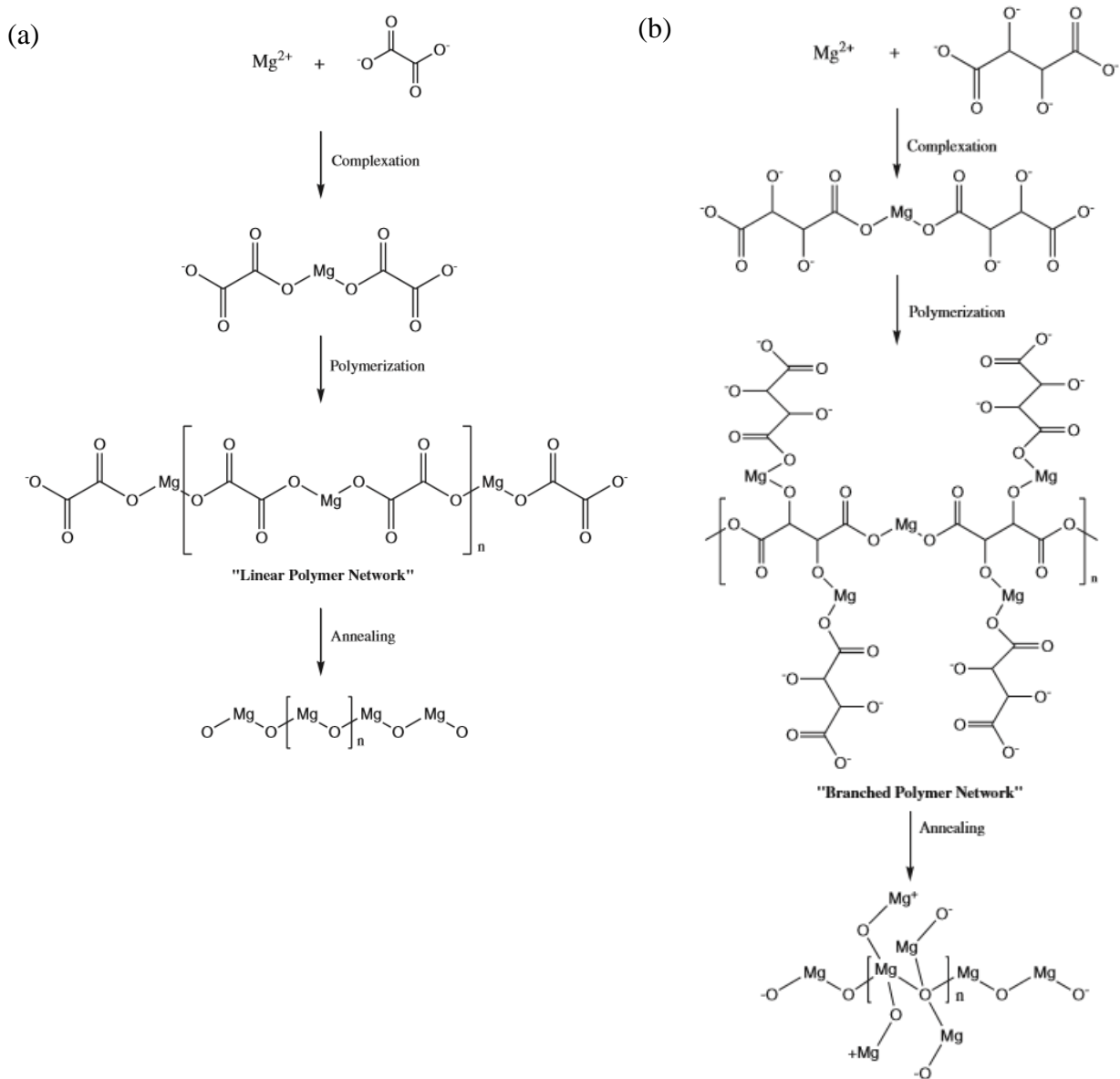
Figure 8.15 XRD analysis of (a) as-cast pure Mg and Mg-1X alloy (X= Al, Ag, In, Mn, Si, Sn, Y, Zn, Zr) samples at room temperature²⁷, (b) pure MgO (thin line) and MgO loaded with 1 wt% Au by DIM (thick line), which shows 99% Mg(OH)₂ phase²⁸, and (c-i) Mg nano-powder before corrosion, (c-ii) Mg nano-powder during corrosion, (c-iii) Mg nano-powder after corrosion is complete²⁹. These XRD graphs show characteristic peaks of 32°, 34°, 36°, and 48°, which all show up for all Mg and Mg-based alloys. These characteristic peaks only show up before corrosion and all disappear after corrosion. Mg(OH)₂ can be distinguished by a large peak right below 40°, while MgO can be distinguished by a large peak right above 40°.

When Mg metal is exposed in air, a thin film of MgO can form [31]. When Mg metal is in solution, a thin film consisting of either MgO or Mg(OH)₂ is known to form at the surface, depending on the electrode potential and solution pH [31]. However, an initial layer of MgO is quickly replaced by the more stable Mg(OH)₂ in an aqueous solution because MgO lacks the qualities of hardness and insolubility, and so MgO reacts with H₂O to form hydroxide [31-35]. Mg(OH)₂ is a hexagonal crystalline, which forms platelet-like crystals [36]. However, Mg(OH)₂ oxide crystals can have different shapes and sizes, which in turn play critical roles in determining their different chemical and physical properties [36-40]. These shapes can include lamellar-, needle-, rod-, flower-, and tube-shaped oxide particles that can be synthesized by precipitation reaction of magnesium salt (MgSO₄) and an alkaline solution (OH⁻) or by hydrothermal reactions [39, 41-47]. For example, Ding et al. formed different morphology of Mg(OH)₂ crystals by the hydrothermal method using different Mg sources, different solvents, and different alkaline levels [45]. Fig. 8.16 shows different crystals formed in different conditions [45]. Even though the mechanism is not very well understood, ethylenediamine plays an important role in synthesizing rod-like and lamellar-shaped oxides, while similar structures like pyridine or diethylamine cannot [37]. Mastuli et al. also synthesized nano-sized MgO crystallites by sol-gel method using different complexing agents, such as magnesium acetate tetrahydrate (Mg(CH₃COO)₂*4H₂O) with oxalic acid dehydrate (C₂H₂O₄*2H₂O) or tartaric acid (C₄H₆O₆) [48]. Fig. 8.17 shows the synthesis of MgO using different acids. These methods formed crystallites less than 100 nm, where oxalic acid produced smaller crystal compared to tartaric acid, because oxalic acid has two complexation sites to bind Mg²⁺ ions and polymerize, while tartaric acid provides four complexation sites, thus producing larger crystals [48].

Sample No.	Mg Source	Solvent	Temp (°C)	Time (Hrs)	Phase	Morphology	Size (nm, TEM)
1	Mg	Ethylenediamine-H ₂ O (8:1, v/v)	180	20	Mg(OH) ₂ Hexagonal	Rod-like	20x200
2	Mg	Ethylenediamine-H ₂ O (1:6, v/v)	180	20	Mg(OH) ₂ Hexagonal	Lamellar	50-100
3	Mg	NH ₃ *H ₂ O (pH 10)	180	20	Mg(OH) ₂ Hexagonal	Lamellar, Tube-like	25-200, 40x600
4	MgSO ₄	Ethylenediamine-H ₂ O (4:1, v/v)	180	20	Mg(OH) ₂ Hexagonal	Needle-like	10-20 x 50-100
5	MgSO ₄	Ethylenediamine-H ₂ O (1:1, v/v)	180	20	Mg(OH) ₂ Hexagonal	Lamellar	100- 150
6	MgSO ₄	NH ₃ *H ₂ O (pH 11)	110	20	Mg(OH) ₂ Hexagonal	Lamellar	150
7	Mg(NO ₃)*6H ₂ O	Ethylenediamine	180	20	Mg(OH) ₂ Hexagonal	Lamellar	80-100
8	Mg(NO ₃)*6H ₂ O	NH ₃ *H ₂ O (pH 10)	180	20	Mg(OH) ₂ Hexagonal	Lamellar	100- 200
9	Mg(NO ₃)*6H ₂ O	NaOH (0.1 M)	80	2	Mg(OH) ₂ Hexagonal	Lamellar	50

Figure 8.16 This table shows Mg(OH)₂ oxide crystals with different morphologies formed under different experimental conditions, such as different Mg source, different solvent, temperature, reaction time.⁴²

While these other studies used specific chemical reactions and different agents to control the size and shape of the MgO or Mg(OH)₂ crystals, this study allowed the Mg oxide or hydroxide crystals to spontaneously form at room temperature in different solutions. And yet, based on the solution type alone, MgO or Mg(OH)₂ crystals grew in different shapes, showing that the constituents in the solution can affect the crystal growth. Although it is not certain at this point the specific mechanisms of different oxide-shaped growth in different solutions, few mechanisms can be hypothesized based on previous studies. For instance, ethylenediamine is a bidentate ligand, which has two binding sites at the ends of the molecules for the metal ion, where the lone pair of electrons on the nitrogen from amine groups (-NH₂) react with the metal ions (Fig. 8.18). This may be why pyridine or diethylamine cannot replace ethylenediamine, because pyridine does not have electron lone pair on the nitrogen atom, while diethylamine has the nitrogen atom in the middle of the molecule, which may not be easily accessible for metal ion binding.



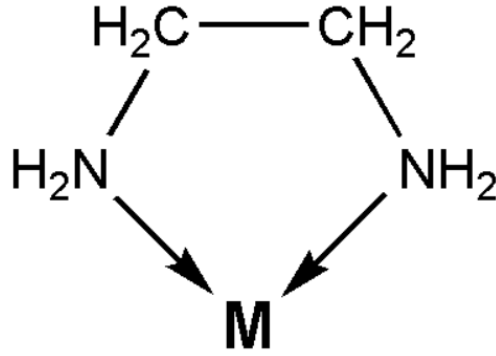


Figure 8.18 The NH_2 groups from ethyldiamine can attack the metal ion, forming a covalent bond with the metal ion with the two lone pairs on the outer energy level, where ethyldiamine acts as a lewis base (electron donors).

Oxalate and tartaric acids have hydroxyl ($-\text{OH}$) groups, which are the complexation sites for metal ions to bind. In AMEM, there are vitamins that have hydroxyl and amine groups that can behave similarly to ethyldiamine and oxalate or tartaric acids (Fig. 8.19). AMEM has ascorbic acid, biotin, D-calcium pantothenate, choline chloride, folic acid, *i*-inositol, nicotinamide, pyridoxine*HCl, riboflavin, thiamine*HCl, and vitamin B12 (see Fig. 7.18), where the concentration of ascorbic acid is the highest, 50 mg/l, while the concentrations of the rest of the vitamins are about 1 mg/l [46]. DMEM has similar components to that of AMEM: ascorbic acid phosphate, choline chloride, D-calcium pantothenate, folic acid, niacinamide, pyridoxine hydrochloride, riboflavin, thiamine hydrochloride, and *i*-inositol [47]. Also, AMEM, DMEM, and PBS all contain inorganic salts, such as sodium chloride, which can dissociate into a cation and an anion, where the anion can react with metal ions. Therefore, binding of these acids and inorganic salts to Mg ions while Mg ions react with water to form oxides or hydroxides may guide the crystals to form in different crystal morphologies. Individual oxide needle formed in AMEM, DMEM, or PBS is a hexagon (Fig. 8.7), and since $\text{Mg}(\text{OH})_2$ is known to be hexagonal, $\text{Mg}(\text{OH})_2$ oxides must be dominant in these solutions. MgO crystal is cuboidal, which is seen in FBS. And these cuboidal oxides disappear over time (Fig. 8.3), and this is consistent with the fact that MgO is known to be replaced by more stable $\text{Mg}(\text{OH})_2$ in aqueous solution. In other

words, MgO is dominant in FBS at early time point, and then MgO is slowly replaced by Mg(OH)₂ by MgO reacting with water ($2 \text{ Mg} + \text{O}_2 \rightarrow 2 \text{ MgO}$; $\text{MgO} + \text{H}_2\text{O} \rightarrow \text{Mg(OH)}_2$). This is a different reaction from Mg metal directly reacting with water to form Mg(OH)₂, which forms hydrogen gas in the process ($\text{Mg} + 2 \text{ H}_2\text{O} \rightarrow \text{Mg(OH)}_2 + \text{H}_2$). Different reactions occurring may mean that different intermediate species (a.k.a. ROS) are produced during the process, which may also affect the cytotoxicity of Mg or Mg-Ti particles in different solvents. Further analysis is needed.

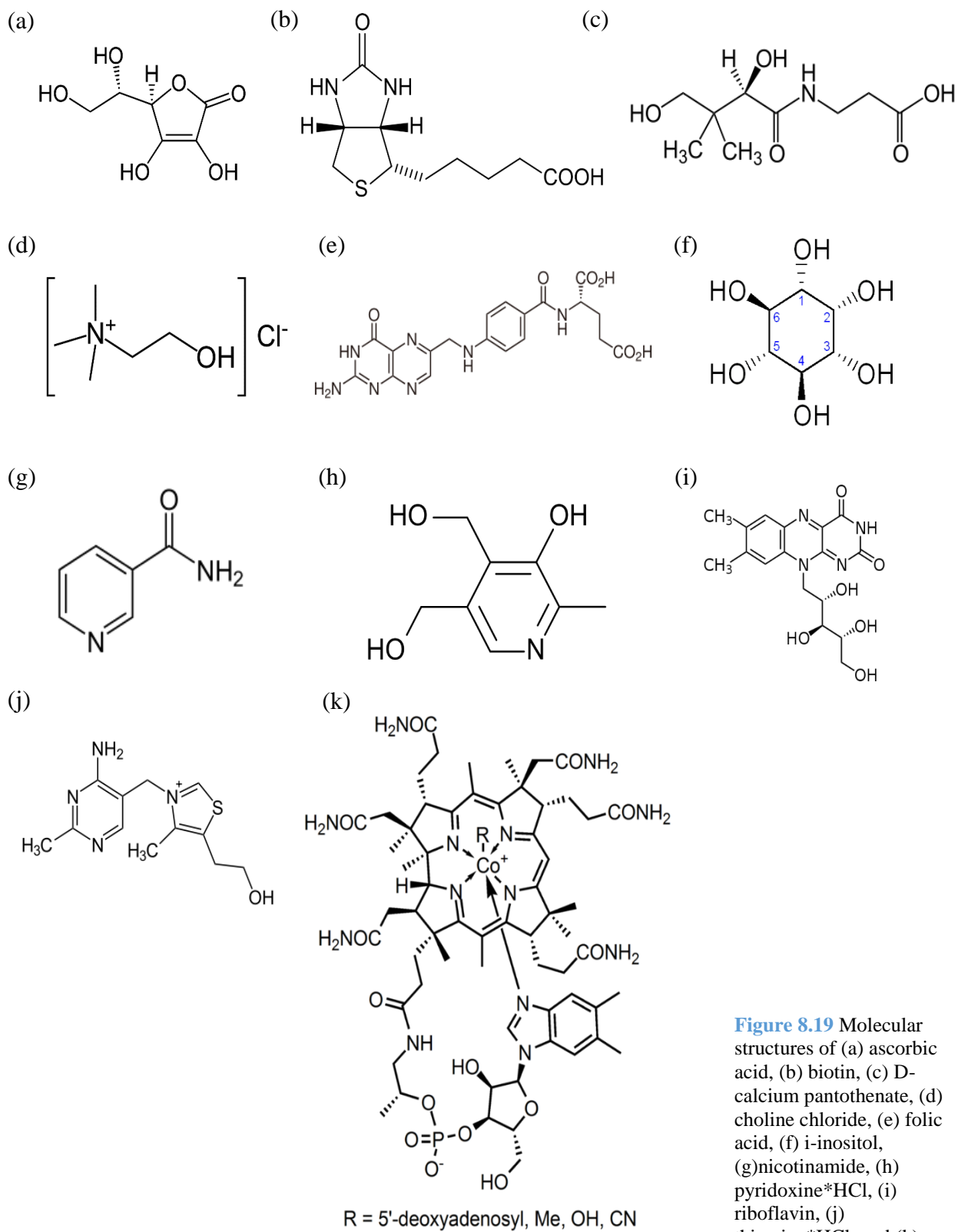


Figure 8.19 Molecular structures of (a) ascorbic acid, (b) biotin, (c) D-calcium pantothenate, (d) choline chloride, (e) folic acid, (f) *D*-inositol, (g) nicotinamide, (h) pyridoxine*HCl, (i) riboflavin, (j) thiamine*HCl, and (k) vitamin B12.

Not only different solvents affect the way Mg corrode, but the corrosion of Mg or Mg-Ti can affect the proteins and free amino acids in the solution. Although the initial hypothesis was that corroding Mg or Mg-Ti particles in a single-protein fibrinogen solution will cause the fibrinogen to break down into monomers due to the breakage of the disulfide bonds, this was not the case. Proteins aggregated with the metal particles to form a protein-metal complex, which could not be analyzed using gel electrophoresis. These metal-protein complexes were very solid and their solubility was very low, even at high temperatures (lower than melting point of fibrinogen 201-300 °C). The remaining fibrinogen solution that did not react with the metal to form metal-protein complex had no significant difference from negative control, where the acrylamide gel reduced the fibrinogen to its peptide chains, which all had molecular weights between 55 and 70 kDa. Although the same volume was used for gel electrophoresis analysis, there were less fibrinogen in Mg or Mg-Ti groups compared to control, just based on visual observation (the bands were fluorescing with less intensities). This is because as mentioned, the proteins were used up to form metal-protein complexes for the experimental groups, confirming that the solids rocks that precipitated out of the solution do contain fibrinogen proteins. XRD was then used to analyze these metal-protein complexes in powder-form, which showed that Mg or Mg-Ti were not different in crystal structures due to galvanic coupling, but due to corrosion and presence of fibrinogen. XRD clearly showed that the corrosion of Mg or Mg-Ti in the presence or absence of fibrinogen was significantly different, but the data could not show that the fibrinogen protein itself was changed. FTIR was performed on different metal-protein complexes, to see if any new bonds have been formed, but there was no significant difference in FTIR measurements among the samples (except fibrinogen-only sample), probably because there were significantly more of Mg or Mg-Ti than fibrinogen (v/v ratio), and so FTIR was primarily

reading just the Mg or Mg-Ti oxides. Despite the fact that this study was not able to directly show that fibrinogen has been altered, clearly, the metal-protein complexes have been formed, which means that the fibrinogen has been modified and aggregated, unusable for the cells, which then indirectly and adversely affects the cell viability. Protein-metal complexes and protein aggregation may also explain the fact that pre-conditioned media has cloudier look than its control counterparts (Fig. 7.7).

8.5 Conclusion

In conclusion, different solvents affect the growth and size of Mg or Mg-Ti oxide or hydroxide. Single-protein solution showed that proteins aggregate to form metal-protein complex, which was low in solubility. XRD graphs show that proteins affect the MgO or Mg(OH)₂ crystallization as well. Although further analysis is needed, protein aggregation is one mechanism of protein modification that cause the “modified” media from Chapter 7 to be cytotoxic, independent of alkaline pH.

8.6 Acknowledgements

This work was supported, in part, by DePuy Synthes.

References

1. Williams RL, Brown SA, Merritt K. Electrochemical Studies on the Influence of Proteins on the Corrosion of Implant Alloys, *Biomaterials* 1988; 9(2): 181-6.
2. Khan MA, Williams RL, Williams DF. The Corrosion Behaviour of Ti-6Al-4V, Ti-6Al-7Nb, and Ti-13Nb-13Zr in Protein Solutions, *Biomaterials* 1999; 20(7): 631-7.
3. Hiromoto S, Mischler S. The Influence of Proteins on the Fretting-Corrosion Behaviour of a Ti6Al4V Alloy, *Wear* 2006; 261(9): 1002-11.
4. Yamamoto A, Hiromoto S. Effect of Inorganic Salts, Amino Acids, and Proteins on the Degradation of Pure Magnesium In Vitro, *Mater. Sci. Eng. C* 2009; 29(5): 1559-68.
5. Yang L, Hort N, Willumeit R, Feyerabend F. Effects of Corrosion Environment and Proteins on Magnesium Corrosion, *Corr. Eng. Sci. Technol.* 2012; 47(5): 335-9.
6. Williams DF, Clark GCF. The Accelerated Corrosion of Pure Metals by Proteins, *Tra. Soc. for Biomater.* 1981; 4: 17.
7. Clark GCF, Williams DF. The Effects of Proteins on Metallic Corrosion, *J. Biomed. Mater. Res. A* 1982; 16(2): 125-34.
8. Merritt K, Brown SA. Effect of Proteins and pH on Fretting Corrosion and Metal Ion Release, *J. Biomed. Mater. Res. A* 1988; 22(2): 111-20.
9. Cheng X, Roscoe SG. Corrosion Behavior of Titanium in the Presence of Calcium Phosphate and Serum Proteins, *Biomaterials* 2005; 26(35): 7350-6.
10. Huang H-H. Effect of Fluoride and Albumin Concentration on the Corrosion Behavior of Ti-6Al-4V Alloy, *Biomaterials* 2003; 24(2): 275-82.

11. Kocijan A, Milošev I, Pihlar B. The Influence of Complexing Agent and Proteins on the Corrosion of Stainless Steels and Their Metal Components, *J. Mater. Sci. Mater. Med.* 2003; 14(1): 69-77.
12. Lewis AC, Kilburn MR, Papageorgiou I, Allen GC, Case CP. Effect of Synovial Fluid, Phosphate-Buffered Saline Solution, and Water on the Dissolution and Corrosion Properties of CoCrMo Alloys as Used in Orthopedic Implants, *J. Biomed. Mater. Res. A* 2005; 73A(4): 456-67.
13. Cabiscol E, Tamarit J, Ros J. Oxidative Stress in Bacteria and Protein Damage by Reactive Oxygen Species, *Internatl. Microbiol.* 2000; 3: 3-8.
14. Fucci L, Oliver CN, Coon M, Stadtman ER. Inactivation of Key Metabolic Enzymes by Mixed Function Oxidation Reactions: Possible Implication in Protein Turnover and Ageing, *Proc. Natl. Acad. Sci. USA* 1983; 80: 1521-5.
15. Stadtman ER. Metal Ion-Catalyzed Oxidation Proteins: Biochemical Mechanism and Biological Consequences, *Free Rad. Biol. Med.* 1990; 9: 315-25.
16. Åslund F, Zheng M, Beckwith J, Storz G. Regulation of the OxyR Transcription Factor by Hydrogen Peroxide and the Cellular Thiol-Disulfide Status, *Proc. Natl. Acad. Sci. USA* 1999; 96: 6161-5.
17. Berlett BS, Stadtman ER. Protein Oxidation in Aging, Disease, and Oxidative Stress, *J. Biol. Chem.* 1997; 272: 20313-6.
18. Stadtman ER. Oxidation of Free Amino Acids and Amino Acid Residues in Proteins by Radiolysis and by Metal-Catalyzed Reactions, *Annu. Rev. Biochem.* 1993; 62: 797-821.
19. Stadtman ER. Protein Oxidation and Aging, *Science* 1992; 257: 1220-4.

20. Fowler WE, Erickson HP. Trinodular Structure of Fibrinogen, *J. Mol. Biol.* 1979; 134: 241-9.
21. Mosesson MW. Fibrinogen and Fibrin Structure and Functions, *J. Thrombosis and Haemostasis* 2005; 3(8): 1894-1904.
22. McDowall, Jennifer. "Fibrinogen." *InterPro: Protein Sequence Analysis & Classification*. EMBL-EBI, Wellcome Genome Campus, Hinxton, Cambridgeshire, CB10 1SD, UK, 1 Nov. 2006. Web. 26 Sept. 2016.
<http://www.ebi.ac.uk/interpro/potm/2006_11/Page1.htm>.
23. Gorkun OV, Veklich YI, Weisel JW, Lord ST. The Conversion of Fibrinogen to Fibrin: Recombinant Fibrinogen Typifies Plasma Fibrinogen, *Blood* 1997; 89: 4407-14.
24. Lu DR, Park K. Effect of Surface Hydrophobicity on the Conformational Changes of Adsorbed Fibrinogen, *J. Colloid Interface Sci.* 1991; 144(1): 271-81.
25. Tunc S, Maitz M, Steiner G, Vázquez L, Pham MT, Salzer R. In Situ Conformational Analysis of Fibrinogen Adsorbed on Si Surfaces, *Colloids Surf. B Biointerfaces* 2005; 42: 219-25.
26. "Thin Film Sample Measurement Methods and Precautions : SHIMADZU (Shimadzu Corporation)." *SHIMADZU*. Shimadzu Corporation, 2016. Web. 24 Nov. 2016.
<<http://www.shimadzu.com/an/ftir/support/tips/letter7/tech.html>>.
27. Gu X, Zheng Y, Cheng Y, Zhong S, Xi T. In Vitro Corrosion and Biocompatibility of Binary Magnesium Alloys, *Biomaterials* 2009; 30: 484-98.
28. Carabineiro SA, Bogdanchikova N, Pestryakov A, Tavares PB, Fernandes LSG, Figueiredo JL. Gold Nanoparticles Supported on Magnesium Oxide for CO Oxidation, *Nanoscale Res. Lett.* 2011; 6: 435.

29. Uda M, Okuyama H, Suzuki TS, Sakka Y. Hydrogen Generation from Water Using Mg Nanopowder Produced by Arc Plasma Method, *Sci. Technol. Adv. Mater.* 2012; 13(2): 1-7.
30. Meenashisundaram KG, Nai MH, Alamjid A, Gupta M. Reinforcing Low-Volume Fraction Nano-TiN Particulates to Monolithical, Pure Mg for Enhanced Tensile and Compressive Response, *Materials* 2016; 9: 134.
31. Song G, Atrens A. Corrosion Mechanisms of Magnesium Alloys, *Adv. Eng. Mater.* 1999; 1(1): 11-33.
32. Hubert K. Anodic Formation of Coatings on Magnesium, Zinc, and Cadmium, *J. Electrochem. Soc.* 1953; 100(8): 376-82.
33. Frühwirth O, Herzog GW, Hollerer I, Rachetti A. Dissolution and Hydration Kinetics of MgO, *Surf. Technol.* 1985; 24(3): 301-17.
34. Hawke D. Corrosion and Wear Resistance of Magnesium Die Castings, *SYCE 8th International Die Casting Exposition and Congress*, Detroit 1975, Paper No. G-T75-114.
35. Makar GL, Kruger J. Corrosion of Magnesium, *Int. Mater. Rev.* 1993; 38(3): 138-53.
36. Gao Y, Wang H, Su Y, Shen Q, Wang D. Influence of Magnesium Source on the Crystallization Behaviors of Magnesium Hydroxide, *J. Crystal Growth* 2008; 310: 3771-8.
37. Peng ZA, Peng X. Mechanisms of the Shape Evolution of CdSe Nanocrystals, *J. Am. Chem. Soc.* 2001; 123: 1389-95.
38. Yan L, Zhuang J, Sun X, Deng Z, Li Y. Formation of Rod-Like Mg(OH)₂ Nanocrystallites under Hydrothermal Conditions and the Conversion to MgO Nanorods by Thermal Dehydration, *Mater. Chem. Phys.* 2002; 76: 119-22.

39. Lv J, Qiu L, Qu B. Controlled Growth of Three Morphological Structures of Magnesium Hydroxide Nanoparticles by Wet Precipitation Method, *J. Crystal Growth* 2004; 267: 676-84.
40. Wang X, Chen X, Gao L, Zheng H, Zhang Z, Qian Y. One-Dimensional Arrays of Co_3O_4 Nanoparticles: Synthesis, Characterization, and Optical and Electrochemical Properties, *J. Phys. Chem. B* 2004; 108: 16401-4.
41. Henrist C, Mathieu JP, Vogels C, Rulmont A, Cloots R. Morphological Study of Magnesium Hydroxide Nanoparticles Precipitated in Dilute Aqueous Solution, *J. Crystal Growth* 2003; 249: 321-30.
42. Lv X, Hari-Bala, Li M, Ma X, Ma S, Gao Y, Tang L, Zhao J, Guo Y, Zhao X, Wang Z. In Situ Synthesis of Nanolamellas of Hydrophobic Magnesium Hydroxide, *Colloid Surf. A: Physicochem. Eng. Aspects* 2007; 296: 97-103.
43. Giorgi R, Bozzi C, Dei L, Gabbiani C, Ninham BW, Baglioni P. Nanoparticles of $\text{Mg}(\text{OH})_2$: Synthesis and Application to Paper Conservation, *Langmuir* 2005; 21: 8495-501.
44. Yan C, Xue D, Zou L, Yan X, Wang W. Preparation of Magnesium Hydroxide Nanoflowers, *J. Crystal Growth* 2005; 282: 448-54.
45. Ding Y, Zhang G, Wu H, Hai B, Wang L, Qian Y. Nanoscale Magnesium Hydroxide and Magnesium Oxide Powders: Control over Size, Shape, and Structure via Hydrothermal Synthesis, *Chem. Mater.* 2001; 13: 435-40.
46. Li Y, Sui M, Ding Y, Zhang G, Zhuang J, Wang C. Preparation of $\text{Mg}(\text{OH})_2$ Nanorods, *Adv. Mater.* 2000; 12(11): 818-21.

47. Fan W, Sun S, Song X, Zhang W, Yu H, Tan X, Cao G. Controlled Synthesis of Single-Crystalline Mg(OH)₂ Nanotubes and Nanorods via a Solvothermal Process, *J. Solid State Chem.* 2004; 177: 2329-38.
48. Mastuli MS, Kamarulzaman N, Nawawi MA, Mahat AM, Rusdi R, Kamarudin N. Growth Mechanisms of MgO Nanocrystals via a Sol-Gel Synthesis Using Different Complexing Agents, *Nanoscale Res. Lett.* 2014; 9: 134.
49. *Minimum Essential Medium (MEM) Alpha Medium (Catalog #: 15-012-CV)*. Corning, MediaTech, Inc. <<http://cellgro.com/products/classical-media/minimum-essential-medium-mem-alpha-medium/minimum-essential-medium-mem-alpha-medium.html>>.
50. *Advanced DMEM (Catalog #: 12491)*. ThermoFisher Scientific. <<http://www.thermofisher.com/us/en/home/technical-resources/media-formulation.1.html>>.

9 SEM Method Technique: Imaging Cells on Non-Conducting

Substrate

9.1 Introduction

Scanning electron microscopy (SEM) is a very useful imaging equipment that produces images by scanning a sample with a focused beam of electrons in a raster scan pattern. A schematic illustration of SEM is shown in Fig. 9.1 [1-2].

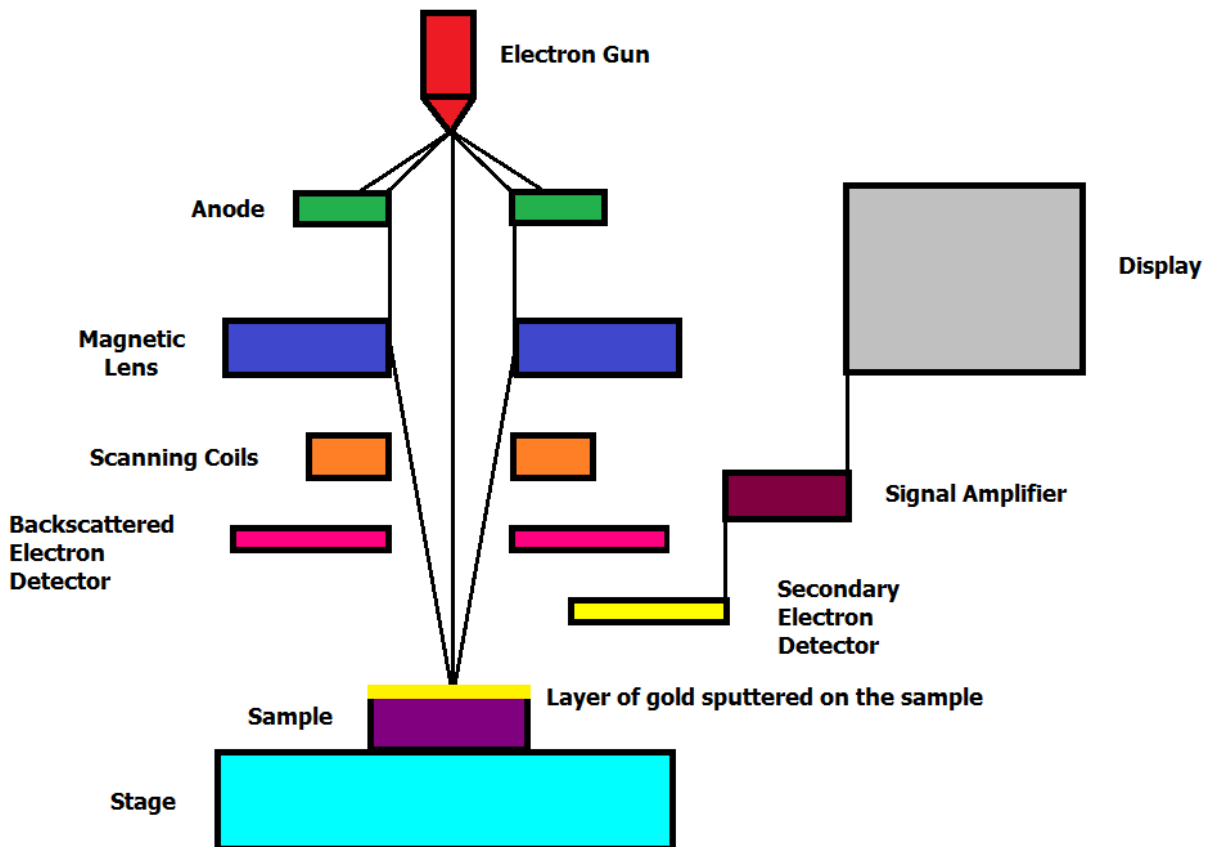


Figure 9.1 Schematic diagram of SEM.

SEM consists of an electron gun or a filament, of which the most common filament used in SEM is made of tungsten [1-2]. A voltage is applied to the tungsten filament, so that when the filament gets hot, electrons are emitted thermionically. A strong electric field exists between the filament and the anode plate, which causes the electrons to accelerate towards the anode from the

filament (cathode). In fact, the electrons accelerate so quickly that the electrons stream pass the anode plate and down the electron column to the sample, without remaining at the anode plate. Magnetic lens system consists of three parts: condenser lens, objective lens, and scanning coils. Condenser lens controls the intensity of the electron beam reaching the sample, while the objective lens brings the electron beam into focus (de-magnifies) on the sample. Objective lens aperture reduces and excludes scattered electrons so that high resolution secondary electron images can be obtained. A pair of scanning coils deflects the electron beam in x and y axes in a raster pattern to control the movement of the electron beam scanning across the surface of the sample. When the electron beam hits the sample, backscattered and secondary electrons are ejected from the surface, which are collected by the detectors and converted into an image.

When the incident electrons hit the sample, they will hit the sample atoms and become scattered, so that they follow complicated twisting paths. There are two types of scattering: elastic and inelastic [1-2]. In elastic scattering, the electron can hit the atomic nuclei and change the electron trajectory, without the electron losing its kinetic energy and velocity, mainly due to the large difference between the mass of the electron and atomic nuclei. In inelastic scattering, the incident electrons will hit the orbital electrons of the sample atoms, which does not change the trajectory of the incident electron significantly, but the energy is lost. Secondary electrons are the orbital electrons of the sample atoms knocked off from its orbital by the incident electron and come off the surface. Secondary electrons are emitted by atoms near the sample's surface, so imaging by secondary electron mode gives high resolution. On the other hand, backscattered electrons are the incident electrons that have changed their trajectories so that they re-emerge from the surface. The escape depth of backscattered electrons can be greater than that of secondary electrons, and so the topographical characteristics are not as clear as the secondary

electron mode; however, the backscattered electrons are sensitive to the atomic mass of the nuclei they scatter from, so in backscattered electron mode, the images may show chemical composition of the sample.

SEM has its advantages and disadvantages, compared to the optical microscope, which uses light rays [1-2]. SEM's first advantage is higher resolution, where SEM gives a specimen resolution of about 25 angstroms, compared to that of optical microscope of about 0.25 microns, due to the physical limit of the wavelength of light. Therefore, SEM gives higher magnification, where SEM can magnify up to 500,000 times while optical microscope can magnify up to 600 times. SEM's second advantage is higher depth of field than optical microscopy, which is the distance of the nearest and farthest object from the detector that appears still sharp and in focus, so that the SEM image gives 3D-like topographical images, instead of 2D plane images.

However, SEM has its disadvantages as well. First, the images generated by SEM are only in black and white, while images generated by optical microscope can be viewed in natural colors. Second, SEM has very limited field of view (~100 μm maximum diameter), while optical microscope has large field of view (~2 mm maximum diameter). Third, electron beam can be deflected even by air, and therefore, sample imaging can only be done in vacuum. Fourth, the sample must be completely dry, making it impossible to observe living specimens or wet samples. Therefore, the preparation of the sample for SEM imaging of cells and tissue can be time-consuming and/or complicated. Usually a basic protocol for preparing cells for SEM imaging involves:

- (1) completely rinse the growth media off the cells by washing with PBS

- (2) fix the cells using chemicals like formaldehyde or glutaraldehyde to preserve the structures of the tissue both physically and chemically by creating covalent chemical bonds between proteins in the tissue
- (3) post-fix with osmium tetroxide, which is a good fixative and stain for lipids in membranous structures and vesicles
- (4) dehydrate the cells by rinsing the cells with different gradients of ethanol, usually starting from 50% ethanol up to 100% ethanol

This sample preparation is to preserve the cell structure while dehydrating in order to image the cells in vacuum. A thin conducting layer of metal, usually gold, needs to be sputtered on the non-conducting sample, in order to prevent electron accumulation and damage to the sample [1-2]. SEM usually has an accelerating voltage adjustable from 200 V to 30 kV [1-2]. Generally, higher accelerating voltage increases the speed of the beam so that the incident electrons can penetrate more deeply into the sample surface. Higher accelerating voltages (15-30 kV) generally allows higher resolution and image sharpness at high magnifications, but usually high accelerating voltages do not work for non-conducting samples due to electron accumulation (charging effect) [1-2]. Therefore, usually non-conducting substrates are imaged at lower accelerating voltages of 10 kV, because lower accelerating voltage results in smaller penetration depth, which will decrease the number of electrons becoming trapped in the non-conducting sample causing the sample to charge [1-2]. Low accelerating voltage also yields finer details, while higher accelerating voltage may veil these details due to too much signal from backscattered electrons [1-2]. Also, different material surfaces have different ability to emit electrons under low accelerating voltage conditions. Therefore, chemical heterogeneity (i.e., an altered local chemical make up) may result in local variations in the brightness or darkness of the

signal coming from the SEM. In addition, this sensitivity of emission efficiency varies with the accelerating voltage of the incident electrons.

Together, the effects of accelerating voltage and chemical variation of emission behavior can be used to generate low-accelerating-voltage images of biological samples which contain a variety of biochemical species and constituents that result in variations in the contrast (brightness and darkness) developed in biological samples. This chapter investigates the secondary electron emission characteristics of biological systems in a cell culture, to identify optimal low kV imaging conditions that can capture the characteristics and morphologies of the cells.

9.2 *Materials and Methods*

9.2.1 *Experiment: Mg and Mg-Ti Particle Treatment*

Mouse pre-osteoblast cells, MC3T3 (ATCC #: CRL-2593), were seeded in a petri dish (surface area $A = 9.6 \text{ cm}^2$) with cell densities of 5,000, 10,000, 20,000, and 30,000 cells/cm² and were left for $t = 12$ hours at 37 Celsius and 5% CO₂ for cell attachment onto the surface. Mg and Mg-Ti microparticle concentration of 500 μg was given to the cells of different cell densities for $t = 24$ hours, with 2 ml of the solution per well. The particles were randomly scattered throughout the dish.

9.2.2 *Cell Preparation for SEM Imaging*

The growth media was aspirated and completely rinsed off the cells using PBS. Mg and Mg-Ti particles were aspirated and rinsed away with the growth media and PBS, although not completely. This process made the remaining particles move so the particles shown in SEM images does not give any information about where the particles had been during particle corrosion and cell killing. The cells were then fixed with 4% formaldehyde (mixed with PBS) for 20 minutes at room temperature. The cells were then rinsed again with PBS before the

dehydration process. The cells were dehydrated using different gradients of ethanol: 50%, 75%, 90%, and 100% ethanol (made by mixing 100% ethanol and PBS), for 15 minutes each. The samples were then left in the desiccator overnight to completely dry.

9.2.3 SEM Imaging

The samples were imaged either with or without sputtering of gold. The samples were sputtered with gold for 30 seconds at 1.2 kV, 50 mA, and 100-200 mTorr (Denton Systems). The accelerating voltage was also varied from 1 kV to 8 kV. Some sputtered samples were grounded using metal wires and conductive tape to connect the sample to the metal stage of the SEM to increase the conductivity of the sample while other samples were not grounded (i.e., gold coated but not grounded).

Systemic variations in accelerating voltage was performed and images were obtained over a range of voltages (1 to 8 kV) for the different surfaces (non-coated, coated and ground, coated and not ground). Differences in relative image contrast (i.e., brightness and darkness) for different features within these images were identified and related to the specific structures present (i.e., polystyrene substrate, cell membrane, protein clusters, etc.).

The changes in brightness were documented over accelerating voltage.

9.3 Results

When the sample is not sputtered, SEM images without significant charging artifact can only be taken at 1 kV and hardly any details can be observed (Fig. 9.2a). Only objects with some elevated height can be distinguished, such as partially or completely balled up cells and many particulates that are covering the surface (Fig. 9.2a). The red circles show cells that have retracted their membranes in the process of balling up, which can be detected in both at 1 kV and 4 kV (Fig. 9.2). Besides the cells circled in red, the other cells look very washed out, and there is

no clear distinction in boundaries between the cells and the background polystyrene at 1 kV. However, when the same sample is sputtered with gold so that the accelerating voltage can be increased to 4 kV, the image can now clearly show spread-out cells with its nucleus and microfilaments. In addition, the adsorbed particles surrounding the cells and on cell membranes can be distinguished as well.

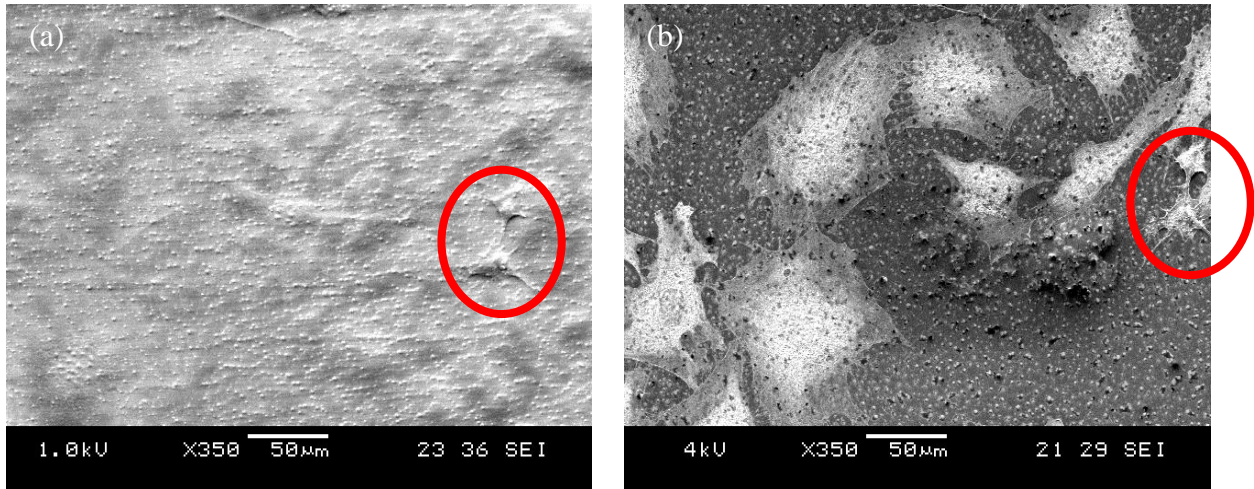
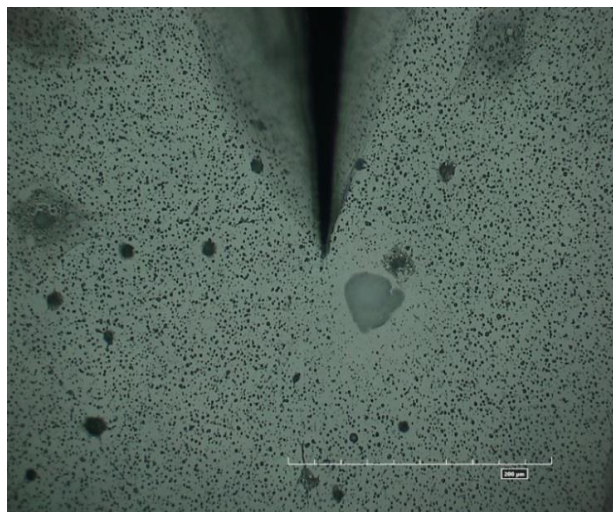


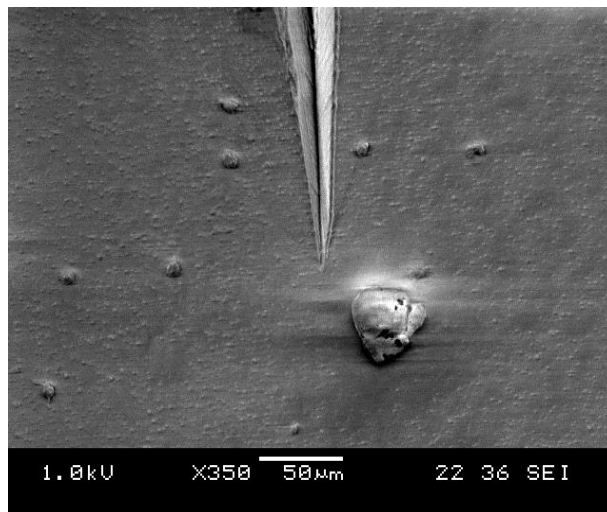
Figure 9.2 (a) Non-sputtered and imaged at 1 kV; (b) sputtered with gold for 30 seconds and imaged at 4 kV at the same location (two red circles show the same cells). The non-sputtered sample at 1 kV does not show spread out cells very clearly. Balled-up cells, which are greater in height, can be better distinguished. However, there are more details shown in the sputtered sample imaged at higher accelerating voltage. The spread-out cells are clearly visible, in contrast with the background.

The non-sputtered sample imaged using SEM at 1 kV is also compared to the image using digital microscope (Fig. 9.3). Again, the images taken using digital microscope shows more details, where the cell membranes of both spread out cells and balled-up cells are sharp and clear against the background. For example, the cells circled in red show balled-up cells that have microfilaments stretched out in many directions, which cannot be seen in SEM at 1 kV.

a) Digital Microscope



b) SEM



c) Digital Microscope



d) SEM

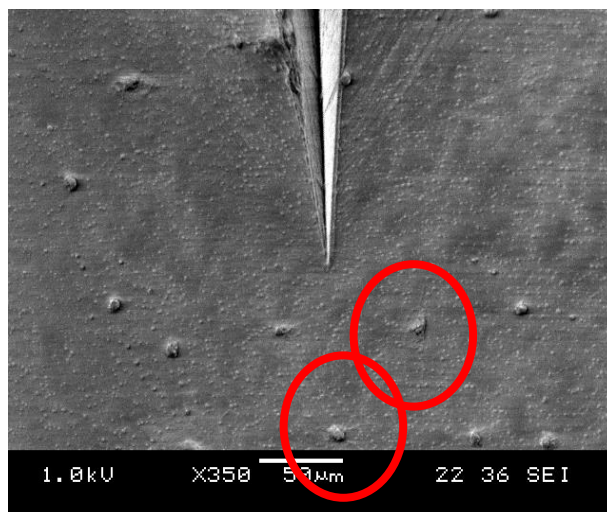
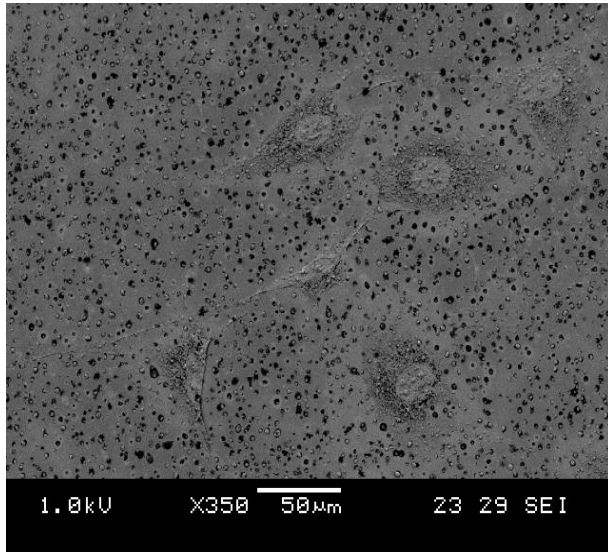
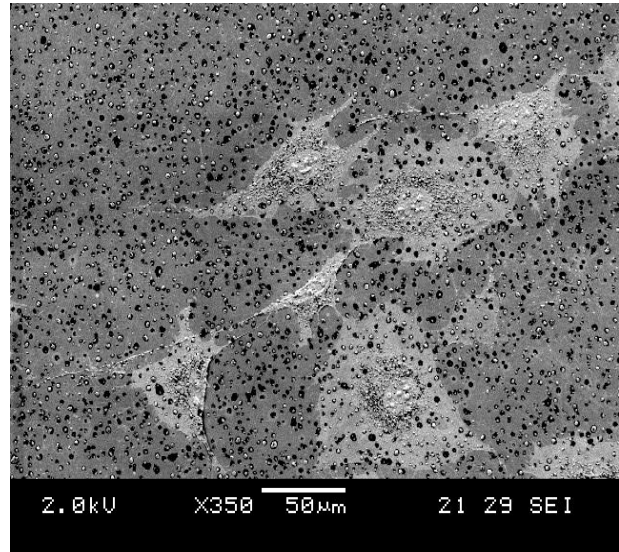


Figure 9.3 Images taken using digital microscope and SEM, where (a) and (b) are taken at the same location, and (c) and (d) are taken at the same location. For SEM, the samples are non-sputtered, and the images are taken at 1 kV. Only the balled-up cells, blade marks, and large Mg particles can be distinguished at 1 kV. The red circles show how even for the balled-up cells, the SEM only shows the cell bodies, while the digital microscope also shows the retracting filopodia. The blade mark on the sample was made to be able to find the same location.

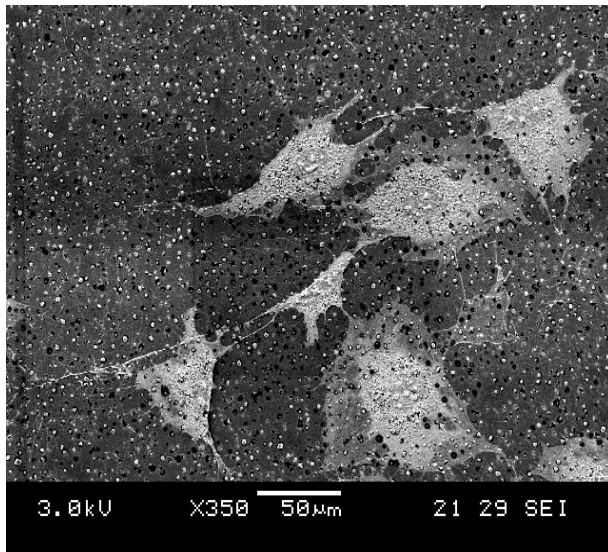
a) 1 kV



b) 2 kV



c) 3 kV



d) 4 kV

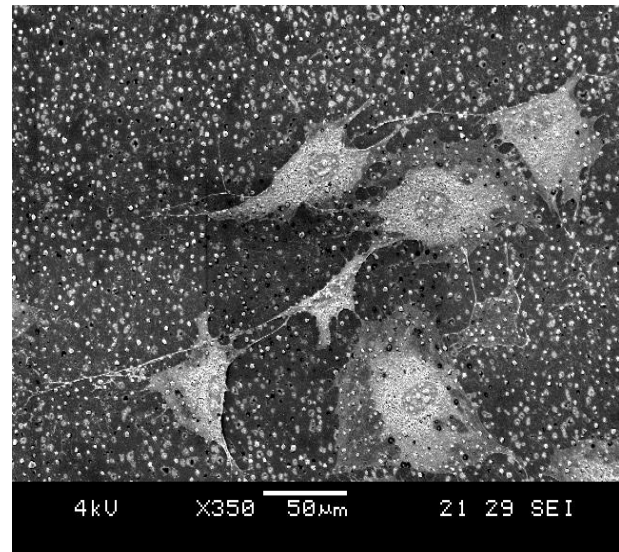
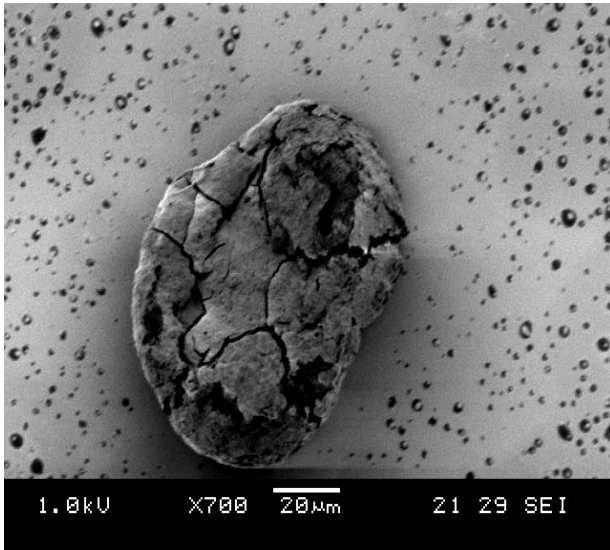
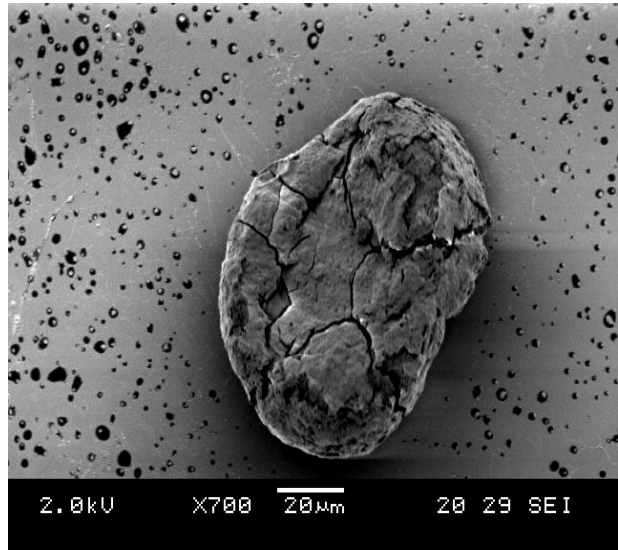


Figure 9.4 Cells with cell seeding density of 5,000 cells/cm² treated with 500 μg/ml for t= 24 hours and imaged from 1-4 kV accelerating voltages. The cells can be seen at 1 kV, but difficult to tell how far the cells are spread out on the surface. As the accelerating voltage is increased, the cells start to become brighter, showing more details of the cells, such as the nucleus and microfilaments. The particulates covering the surfaces and cells also become brighter along with the cells as the accelerating voltage is increased, indicating that the particulates are made up of same type of materials (i.e. organic substances).

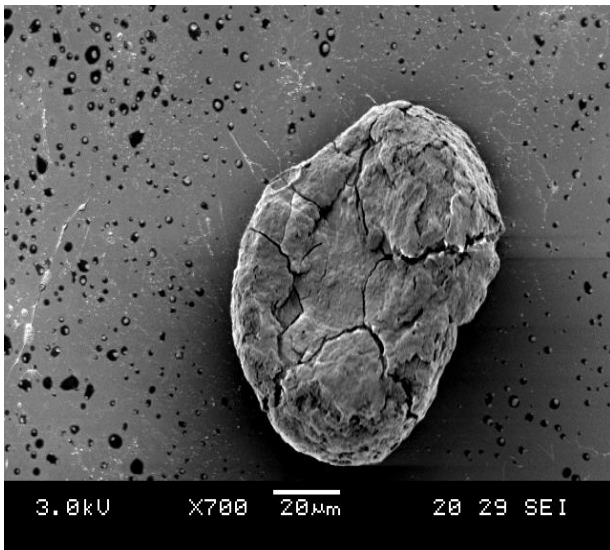
a) 1 kV



b) 2 kV



c) 3 kV



d) 4 kV

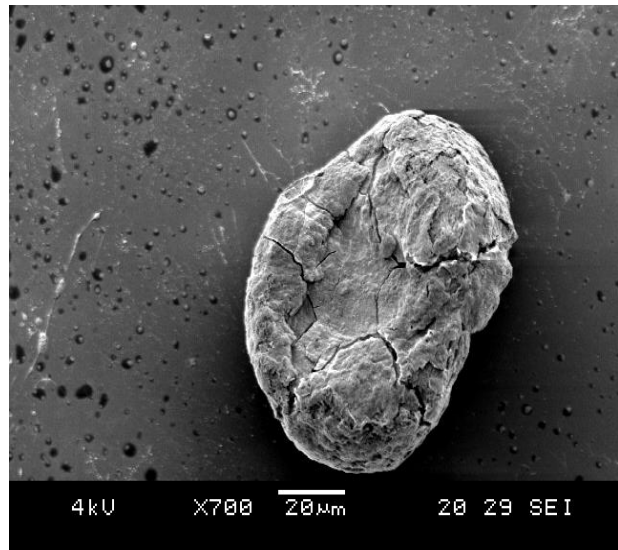
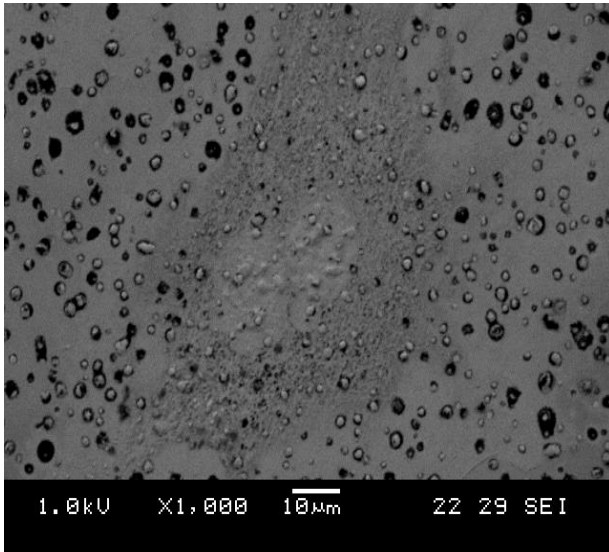
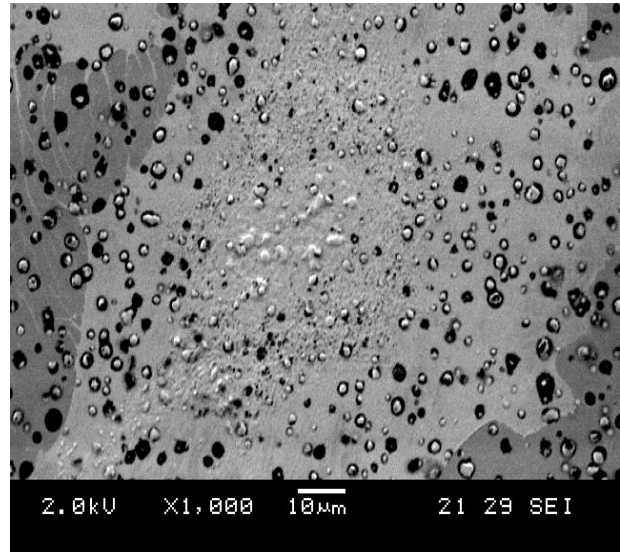


Figure 9.5 A Mg-Ti particle imaged at accelerating voltages of 1-4 kV. The particle becomes brighter as the accelerating voltage is increased. The particulates that became bright along with cells in Fig. 9.4 did not become bright with the Mg-Ti particle, which indicates that the particulates, organic in substance, is chemically different than a Mg-Ti particle, which is inorganic.

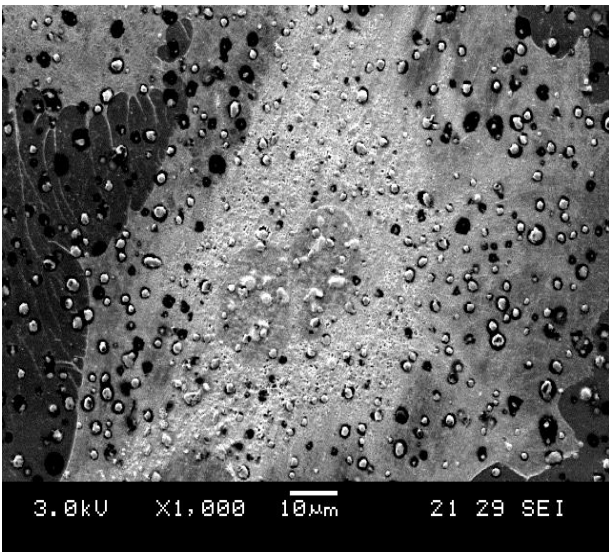
a) 1 kV



b) 2 kV



c) 3 kV



d) 4 kV

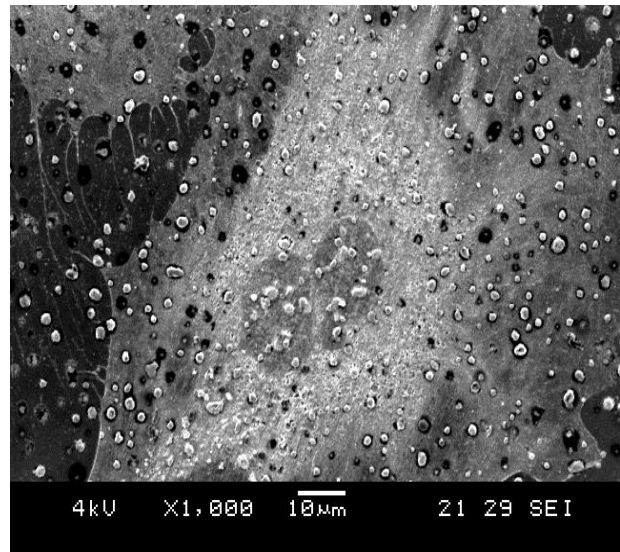


Figure 9.6 A cell imaged at accelerating voltages of 1-4 kV. The cell imaged at 1 kV cannot be easily distinguished, since the boundary of cell membrane cannot be seen. A part of a cell at the upper-left corner cannot be seen at this voltage at all. At 2 kV, the cell boundary is now more clearly visualized, with microfilaments as well. At 3 and 4 kV, the details of the cell nucleus can be seen, where the cell has a nucleus split into two, in the process of cell division, which was hard to tell in 1-2 kV accelerating voltages.

The same locations have been imaged with accelerating voltages from 1 to 4 kV after sputtering with gold for 30 seconds but not grounded (Fig. 9.4-9.6). Fig. 9.4 shows that at 1 kV, the cells and the background have similar contrast, as the same as the non-sputtered sample at 1 kV shown in Fig. 9.2, making it difficult to distinguish the cells and other constituents in the images and the background. However, as the accelerating voltage is increased to 3 and 4 kV, the cells become brighter, as the background becomes darker due to the differences in secondary electron emission characteristics of these different chemistries. The spherical particulates start out dark and become brighter like the cells, as dark halos at 1 kV and then bright white spots by 4 kV.

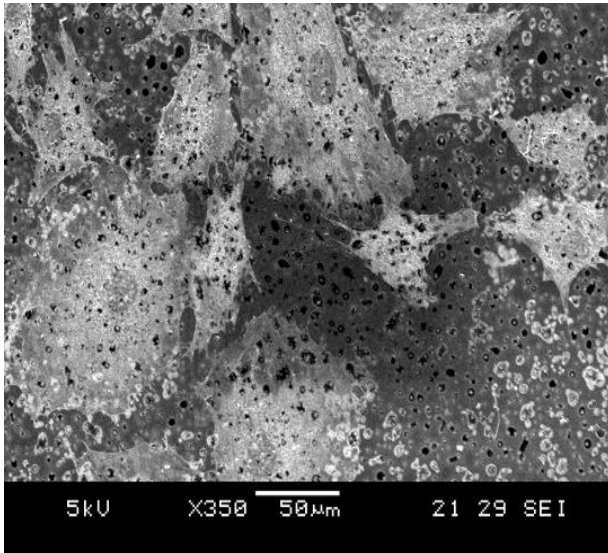
Fig. 9.5 shows an inorganic material, Mg particle, imaged from 1-4 kV. Interestingly, as the accelerating voltage is increased, Mg particles do become brighter, but not the spherical particulates, the same particulates that became brighter along with the cells from Fig. 9.4.

Fig. 9.6 shows a close-up cell imaged from 1-4 kV, where the cell nucleus can really be distinguished at the accelerating voltage of 3-4 kV. This cell is actually in the process of dividing, where the nucleus has already divided into two. However, this is not noticeable at the accelerating voltage of 1-2 kV. At 1 kV, the cell boundary is not distinguishable from the background, and at 2 kV, the cell boundary can be distinguished, but not the cell nucleus.

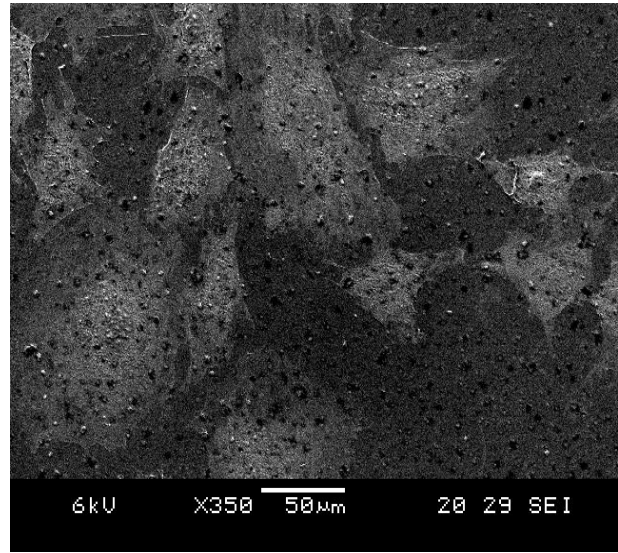
When the accelerating voltage is increased above 4 kV for the same samples as that of Fig. 9.4-9.6 (samples coated but not grounded), the image starts to deteriorate and details are again lost (Fig. 9.7). The images taken at high accelerating voltage above 4 kV look very grainy. After exposing the sample to a high accelerating voltage of 8 kV, the cells imaged at 1 kV afterwards look swollen and puffy (Fig. 9.8). However, when the samples are sputtered with

gold and then grounded to the metal stage of SEM using metallic wires or conducting tape, the sample can be imaged very clearly even at the accelerating voltage of 15 kV (Fig. 9.9).

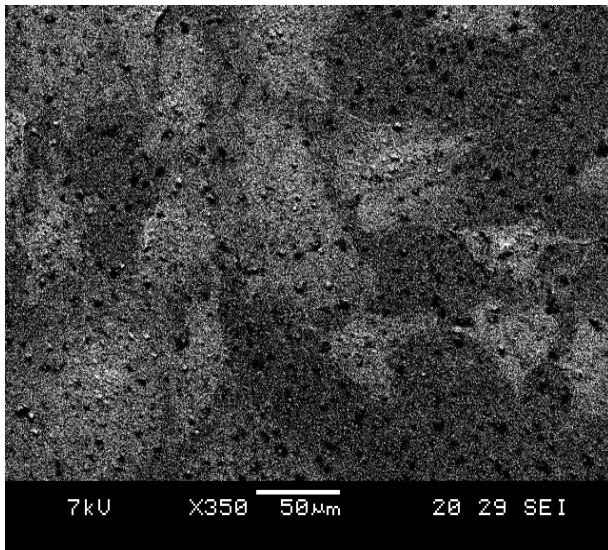
a) 5 kV



b) 6 kV



c) 7 kV



d) 8 kV

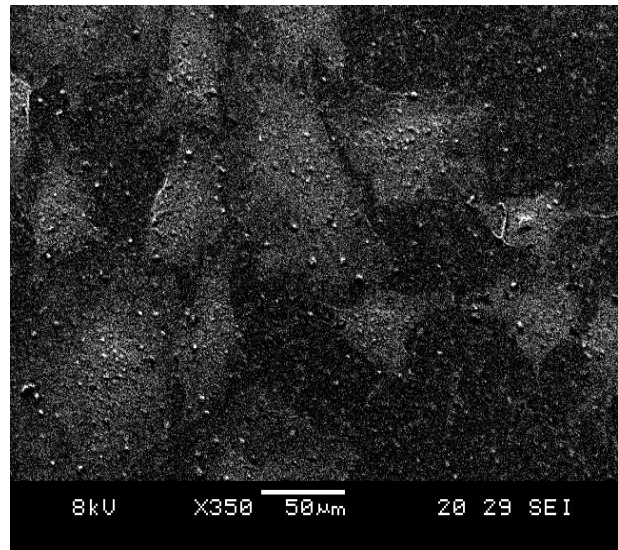
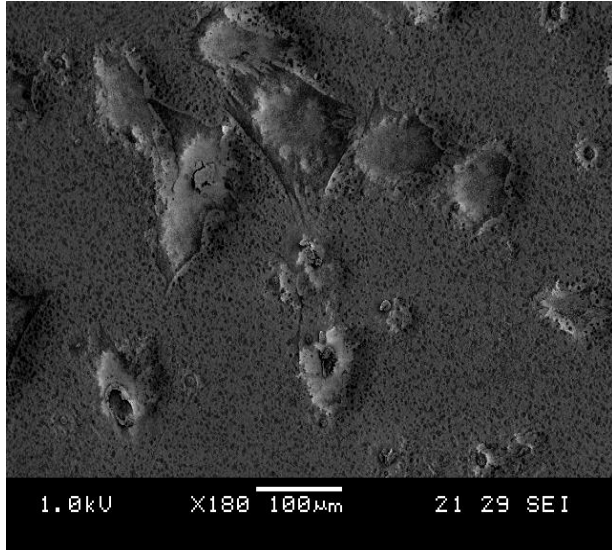
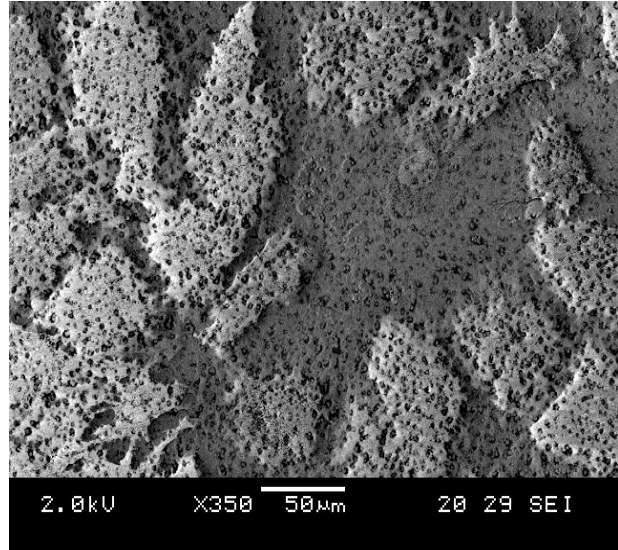


Figure 9.7 Gold-coated cells imaged at accelerating voltages from 5-8 kV. The details of the nucleus and microfilaments are lost, although the cells can still be seen. The images look very grainy, as if there is not a lot of signal being detected (i.e. not enough secondary electrons).

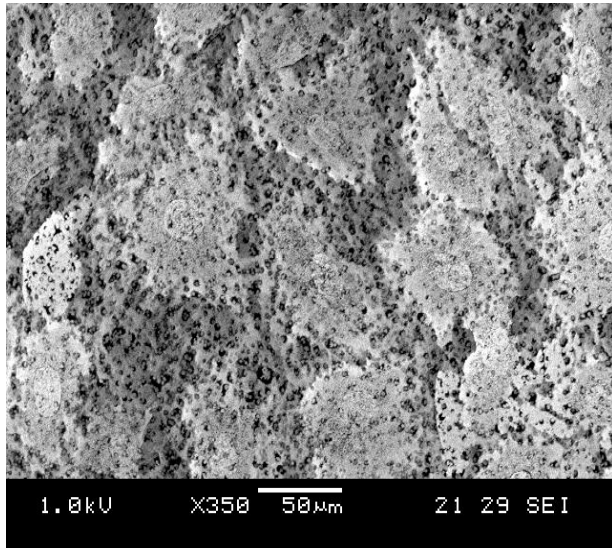
a) 1 kV



b) 2 kV



c) 1 kV



d) 2 kV



Figure 9.8 Gold-coated cells imaged at 1-2 kV after being exposed to the accelerating voltage of 8 kV for few minutes. At this high accelerating voltage of 8 kV, the electrons penetrate deeper into the sample than lower accelerating voltages. Because the sample is not conductive, the electrons accumulate and get trapped underneath the sample surface, and then the electrons will start to repel each other. The samples are now permanently “charged” with electrons, and so when the samples are imaged even at optimal accelerating voltage of 4 kV, the cells look very puffy and swollen.

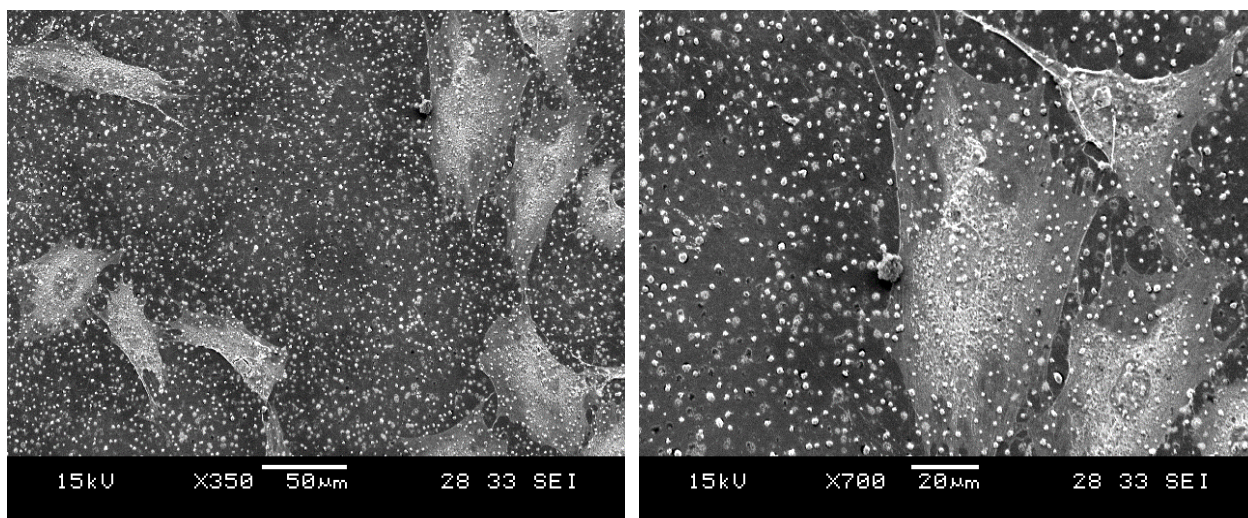


Figure 9.9 Cells imaged at 15 kV after sputtering the sample with gold for 30 seconds and then grounding the sample to the metal stage of SEM using metallic wires or conducting tape. The images look very detailed, even though the accelerating voltage was increased to 15 kV. This is because grounding the sample using metallic wires or conducting tape creates a pathway for electrons to flow out of the sample, instead becoming permanently trapped, as shown in Fig. 9.8.

9.4 Discussion

This study shows that the cells imaged on a non-conducting substrate can be imaged under low accelerating voltage of 4 kV, which captures the finest details of not only cell shape, but also local chemically-based variations in emission behavior (e.g., cell nucleus, microfilaments, and protein particles). Accelerating voltage under 3 kV loses many of the fine details of the image probably because the accelerating voltage is too low and many incident electrons do not penetrate the sample deep enough to give any surface structures. Imaging cells on a non-conducting substrate with accelerating voltages of 3-4 kV was only possible with sputtering of gold for at least 30 seconds to give a thin conducting layer. Sputtering gold longer will result in a thicker film, increasing the depth the electrons have to penetrate into the sample, and so the surface structure details will get lost. Increasing the accelerating voltage above 4 kV resulted in the deterioration of the sample image, where the image became grainy. Despite the thin conducting layer of gold, accelerating voltage higher than 4 kV resulted in incident electrons

penetrating more deeply, probably beyond the conducting layer, so that the electrons become permanently trapped in the sample. Therefore, after exposing the sample to a high accelerating voltage, the cells looked very puffy even when imaged at the optimal accelerating voltages of 3-4 kV, due to the repulsion of electrons. The cells looked puffier than the background because the cells were absorbing the electrons more than the polymer background. There were also some interesting observations to be made. The unknown particulates that were covering the sample (small white/black dots covering the cells and the background) changed in brightness when the accelerating voltage increased from 1 kV to 4 kV. When the cells were imaged, the particulates and the cells became brighter together as the accelerating voltage increased. However, when the metal particle was imaged, the metal particle increased in brightness as the accelerating voltage increased, but the particulates became dark, in contrast to the metal particle. SEM is known to show different chemical composition based on the signal, and it is hypothesized that although these particulates are unknown, they are organic material, similar to the cells, rather than inorganic like the metal. They are not salt crystals, which can form during the dehydration process of cells, but they have snow-flake like structures (data not shown). Grounding the sample to the SEM metal stage allowed imaging of the cells at higher accelerating voltage of 15 kV without losing any fine details because the wires allowed a path for electrons to leave the sample without getting trapped. The wire or conducting tape was connected to the gold layer to ensure connection. Being able to increase the accelerating voltage to at least 15 kV is important especially for any EDS analysis that needs to be done.

This accelerating voltage effect on cellular and biological imaging has important consequences for analysis of retrieved implants in that it is possible to identify specific biological constituents in an SEM image by the changing emission characteristics seen for different

accelerating voltages [3]. In a previous paper regarding inflammatory cell-induced corrosion, 4 kV secondary images were taken to distinguish cells and cell-like remnants from the metal alloy and other non-biological features on the metallic surface [3]. Higher accelerating voltages, on the other hand, showed more surface topography of the metal [3]. The samples were imaged without any gold coating, but the images were still clear at 4 kV because the biological samples were on the metal surface, which is conductive, unlike the samples in this study, where the biological samples were on a plastic surface.

9.5 Conclusion

In conclusion, the secondary emission characteristics of biological systems are variable due to chemical variations in the emission behavior in the SEM. These contrast variations depend on the accelerating voltage used to image the surface and whether sputtering of metal such as gold is present. The accelerating voltage is a very important factor in imaging of cells on a non-conducting substrate, where low accelerating voltage of 4 kV was determined to be the most optimal voltage that resulted in high resolution and large contrast variations between different constituents of the cell culture, which provided a sharp image with fine details.

9.6 Acknowledgements

This work was supported, in part, by DePuy Synthes.

References

1. Cheney B. "Introduction to Scanning Electron Microscopy." (n.d.): 1-13. Materials Engineering Department at San Jose State University. Web. 5 Oct. 2016.
<http://www.sjsu.edu/people/anastasia.micheals/courses/MatE143/s1/SEM_GUIDE.pdf>
.
2. JEOL. A Guide to Scanning Electron Microscope Observation. Web. 5 Oct 2016.
<http://www.jeol.co.jp/en/applications/pdf/sm/844_en.pdf>.
3. Gilbert JL, Sivan S, Liu Y, Kocagoz SB, Arnholt CM, Kurtz SM. Direct *In Vivo* Inflammatory Cell-Induced Corrosion of CoCrMo Alloy Orthopedic Implant Surfaces, *J. Biomed. Mater. Res. A* 2015; 103(1): 211-23.

10 Overall Conclusion

The overall objective of this dissertation was to investigate the in vitro cytotoxicity of Mg and Mg-Ti. The key research findings of this work are as follows:

- Galvanic coupling of Mg and Ti increased the cytotoxicity compared to Mg alone.
- Cytotoxicity of Mg or Mg-Ti was dependent on particle dosage, proximity between particles and cells, and time. Cells were killed at higher particle concentrations (dependent on cell types), near the particles (less than 2 mm away) in short period of time (within 18 hours).
- Mg or Mg-Ti not only killed murine pre-osteoblast MC3T3 cells, but also cancerous human osteosarcoma SAOS2 cells, and bacterial *Escherichia coli* cells (both planktonic and biofilms).
- The particle concentration required to kill cells completely (or almost completely) was the lowest for MC3T3 cells (3500 µg) and highest for bacterial biofilms (50000 µg). Despite the fact that the particle concentrations used to kill bacterial biofilms were about x14 times the concentration used to kill MC3T3 cells, biofilms were not killed completely (2% survival).
- Compared to an antibiotic ofloxacin, Mg or Mg-Ti killed biofilms significantly.
- pH level of the media was the same for Mg and Mg-Ti, indicating that the increased cytotoxic effect of Mg-Ti is not entirely or even principally due to pH.
- Cells treated with NaOH from pH of 7 to 11 had significantly higher cell viability compared to cells treated with Mg or Mg-Ti at the same measured pH level.
- Besides directly corroding the particles, pre-corroding Mg or Mg-Ti in cell culture media altered the media, which then killed the cells.

- Pre-conditioned media killed the cells even after the pH was re-adjusted to physiological pH.
- Pre-conditioned media showed different morphology compared to the control counterparts, where the pre-conditioned media looked cloudy and opaque, indicating that there are larger particulates obstructing light.
- Corrosion of Mg or Mg-Ti in different media solutions caused oxide or hydroxide growth in different shapes, indicating that different reactions might have taken place.
- Mg or Mg-Ti was corroded in a single protein fibrinogen solution, which showed aggregation of fibrinogen with metal/metal oxides, forming a protein-metal complex.
- The presence of fibrinogen resulted in systematic changes in the XRD spectra of the Mg corrosion products in terms of peaks present and relative peak heights in XRD spectra. This implies that fibrinogen affects the crystal forming behavior of $\text{Mg}(\text{OH})_2$ in culture.
- Secondary emission characteristics of biological species are dependent on the chemistry and the accelerating voltage used to obtain SEM images. Coating with a conductor and imaging at low kV can distinguish cells from substrates and also proteins from other biological structures. Voltage-dependent emission characteristics of biological species in low kV SEM imaging is a potentially powerful approach to documenting and characterizing the local chemical species present during SEM imaging.

11 Future Work/Potential Applications

Unlike the common conception that Mg is very biocompatible, this study showed that Mg is very cytotoxic to cells near the metal, where cytotoxicity depends on particle dosage, proximity, and time. And by galvanically coupling Mg with Ti, which increases the corrosion rate of Mg, Mg-Ti is more cytotoxic than Mg. This galvanic couple can potentially be used to target and kill cancerous tumor or bacterial infections.

This study concluded that the cytotoxicity of Mg and Mg-Ti is not due to alkaline pH, but rather hypothesized to be due to the production of ROS during the corrosion of Mg, since the cytotoxic effect was very fast and adjacent (and also based on previous studies of cells dying due to cathodic polarization). Future experiments can involve directly measuring ROS produced at the surface of Mg or Mg-Ti. One method involves adding fluorescent dyes that can stain different ROS to determine which types of ROS is being produced. Another method involves adding different concentrations of antioxidants, such as superoxide dismutase (SOD), that can quench ROS along with Mg or Mg-Ti and measuring cell viability to see if there is any significant difference in viability compared to cells treated with just Mg or Mg-Ti. If certain ROS is the cause of particle cytotoxicity, then quenching will prevent cell killing.

While pre-corroding Mg or Mg-Ti in cell culture media caused a change in the media, which then killed the cells, it is not yet clear what exactly changed in the media. Single protein fibrinogen solution study showed that fibrinogen aggregated with metal oxides formed a protein-metal complex, which was analyzed, but there are many other elements in the media that can also be studied. Future experiments can involve investigating other types of proteins or free amino acids. Also, other techniques besides gel electrophoresis and XRD can be used, such as differential scanning calorimetry (DSC) to measure the protein's glass transition temperature

(T_g) and melting temperature (T_m), to see if there is any transition in T_g or T_m after exposure to Mg or Mg-Ti corrosion, causing the protein structure to change.

Mg or Mg-Ti can kill all types of cells, not just cancerous or bacterial cells, but even healthy cells. Therefore, it is important to design this galvanic couple to target effectively to maximize the killing of targeted cells or tissue, while minimizing the adverse effect on healthy cells or tissue surrounding the targeted site. One method is designing this galvanic couple with ligands, for example, to bind to specific cells or tissue to kill. Another method is designing a Ti-based implant to incorporate some small fraction of Mg at the surface to prevent any biofilm formation at the metal surface.

As this research project moves forward, galvanic couple of Mg and Ti can replace the cathodic polarization treatment to kill bacterial infections on metallic implants, where the Mg-Ti is more clinically applicable than the three-electrode system used for cathodic polarization treatment. Mg-Ti can also be used to kill tumor synergistically with radiation and chemotherapy. While Mg or Mg-Ti showed effective killing of cells in vitro, the cytotoxicity of Mg or Mg-Ti have not been systematically investigated in vivo, which may be different. Therefore, it is essential to perform animal studies to evaluate the potential of Mg-Ti as a therapeutic material to target and kill bacterial infections and tumors.

12 Biographical Data

NAME OF AUTHOR: Jua Kim

PLACE OF BIRTH: Seoul, South Korea

DATE OF BIRTH: May 17, 1987

UNDERGRADUATE AND GRADUATE SCHOOLS ATTENDED:

Syracuse University, Syracuse, NY

Syracuse University, Syracuse, NY

DEGREES AWARDED:

Bachelors of Science in Bioengineering, 2009, Syracuse University

Masters of Science in Bioengineering, 2012, Syracuse University